Imperial College London

# Establishing Scanning Ion Conductance Microscopy for Enhanced Nano-scale Characterisation of Carbonate and Sandstone Rocks

Sarah Frances Lowe

2023

Department of Materials

Imperial College London

A thesis submitted in part fulfilment of the requirements for the degree of

Doctor of Philosophy at Imperial College London

# Acknowledgements

First of all I would like to thank my sponsors at Shell for their funding, without which this project would not have been possible. In particular I would like to thank Steffen Berg and Apostolos Georgiadis, who both gave up numerous hours to support me academically and personally throughout my PhD. Thanks as well Apostolos, for making the effort to keep in touch through lockdown, reading my thesis as I wrote it, and being a friend to me.

Thank you to my academic supervisors, Mary Ryan and Tim Albrecht, for your guidance throughout the years, providing your scientific expertise and being the voices of experience when I needed direction.

I would also like to thank the other researchers on the Digital Rocks Programme, in particular the members of the Luckham group, who took me in as one of their own. Maja, I'm sure that I'm not alone in feeling that the program would not have been the same without you - you brought us all together like a big sister. Ese and Sheri, thank you for your support and friendship, especially since you both became mums during your projects - you both had a lot on, but took the time to look out for others. Paul, thank you for your support on both a personal and academic level, in particular, thank you for looking over my thesis and your helpful feedback!

Thank you to the members of support staff at Imperial across the Chemistry, Materials and Chemical Engineering Departments that took the time to make stressful situations better: Bhavna, Alba, Doris and Annalisa. All of you have been so understanding and helpful, and always have time for the students you look after.

On a personal level, thank you to my endlessly supportive and loving husband, Jack. Without you motivating and believing in me, for being so selfless, and taking external stresses off me when I most needed it, I don't think I could have done it. I could not imagine a better partner in life.

Thank you to my parents and my brother, Sam, for supporting me both emotionally and financially, for motivating me the right amount, and for encouraging me throughout, even though you do think chemistry is witchcraft, Dad. Thank you as well to my father-in-law, Chris, for acting more like a big brother to me. I'm sorry that you passed before you could see me submit this.

Although not involved in my PhD, thank you to Amy; our interactions when I was at JM laid the groundwork for me to start believing that a PhD was something that I could actually do. Of course, an honorary mention must also go to Rani, for sharing the burdens and joys of running the belly dance society together.

Finally, thank you to my friends who carried out their PhDs at the same time as me - I can't list everything you've done, but: Tristan, crosswords will forever make me think of you; Jon, thank you for being a shoulder to cry on; Aigerim, for your constant motivation and pure excitement for science; Caoimhe, for our heart-to-hearts, and for your company in 1.14; Joe, for being my Pokemon GO buddy; and Francesca and Maeve, for our manicure and wine nights. You all helped me.

# Statement of Originality

I declare that the work presented herein, unless otherwise stated, was carried out by myself at Imperial College London for the purpose of fulfilling the requirements of my doctorate.

# Copyright Declaration

The copyright of this thesis rests with the author. Unless otherwise indicated, its contents are licensed under a Creative Commons Attribution-Non Commercial 4.0 International Licence (CC BY-NC).

Under this licence, you may copy and redistribute the material in any medium or format. You may also create and distribute modified versions of the work. This is on the condition that: you credit the author and do not use it, or any derivative works, for a commercial purpose.

When reusing or sharing this work, ensure you make the licence terms clear to others by naming the licence and linking to the licence text. Where a work has been adapted, you should indicate that the work has been changed and describe those changes.

Please seek permission from the copyright holder for uses of this work that are not included in this licence or permitted under UK Copyright Law.

# Abstract

Scanning ion conductance microscopy (SICM), an electrochemical scanning probe microscopy (SPM), has been used for the first time to generate topographical images of reservoir rock analogues for oil and gas recovery applications. Validation of these images was provided by low-vacuum scanning electron microscopy (SEM) and atomic force microscopy (AFM). Low-vacuum SEM micrographs provided the wider field of view required to understand the context of the smaller SICM images, in addition to showcasing the heterogeneity of these materials. Ketton, Estaillades and Indiana, three carbonate outcrop rocks, were found to have six, four and five distinct surface types respectively. These classifications provided an invaluable framework for the SICM validation in this work. AFM has previously provided maps of outcrop rocks in the literature, and as such was utilised here to provide a comparison of feature heights for validation of the SICM images. It was ultimately concluded that SICM was a better-suited SPM than AFM for these materials, due to the slower scan speeds, greater hop heights and longer probes.

SICM was also found to be a suitable tool for the mapping of materials which had been exposed to crude oil, despite the images being less well-resolved than for the unaltered surfaces. The blurring present in these images is proposed to be the

result of partial crude oil removal by the electrolyte, however the feature shapes and sizes were aligned with what was observed in the low-vacuum SEM micrographs, so were deemed to be a success.

There is potential for surface charge mapping on the SICM to provide added value to oil and gas recovery research; preliminary topographical mapping work towards surface charge mapping of outcrop rocks in both aqueous and organic solvents is presented, along with considerations for future work with additives to probe condition-dependant surface charge behaviours.

# Contents

**List of Figures** **15**

**List of Tables** **34**

**List of Acronyms** **36**

**1 Introduction** **39**

1.1 Motivation and context . . . . . 39

1.1.1 Oil and Gas Extraction Processes . . . . . 39

1.1.2 Special Core Analysis . . . . . 41

1.1.3 Wettability . . . . . 42

1.1.4 Digital Rock . . . . . 44

1.2 Scanning Ion Conductance Microscopy . . . . . 46

1.2.1 SICM setup . . . . . 46

1.2.2 Tip-sample distance approximation . . . . . 48

1.2.3 Topographical mapping . . . . . 49

1.2.4 Surface charge mapping . . . . . 54

1.3 Atomic Force Microscopy . . . . . 57

1.3.1 AFM setup . . . . . 57

1.3.2 Topographical scanning modes . . . . . 58

1.3.3 Surface charge mapping . . . . . 61
1.4 Comparison of AFM and SICM . . . . . 62
1.5 Limitations of Scanning Probe Microscopies . . . . . 64
1.6 Scanning Electron Microscopy . . . . . 66
1.6.1 Scanning Electron Microscope Setup . . . . . 68
1.6.2 Low-vacuum scanning . . . . . 70
1.7 Outcrop Rocks . . . . . 72
1.7.1 Carbonates: Ketton, Estaillades and Indiana . . . . . 72
1.7.2 Sandstone: Bandera Brown . . . . . 74
1.8 Thesis Outline . . . . . 76

**2 Methods** **77**

2.1 Samples . . . . . 77
2.1.1 Outcrop Rocks . . . . . 77
2.1.2 Ageing Protocol . . . . . 79
2.1.3 Polystyrene on Glass . . . . . 81
2.2 Scanning Ion Conductance Microscopy . . . . . 82
2.2.1 Topographical Mapping . . . . . 82
2.2.2 Surface Charge Mapping . . . . . 83
2.2.3 Nanopipettes . . . . . 84
2.2.4 Ag/AgCl Electrode Preparation . . . . . 87
2.3 Atomic Force Microscopy . . . . . 88
2.4 Low-Vacuum Scanning Electron Microscopy . . . . . 89

**3 Carbonates** **90**

3.1 Overview . . . 90
3.2 Low-Vacuum Scanning Electron Microscopy . . . 91
3.2.1 Calcite . . . 91
3.2.2 Ketton . . . 97
3.2.3 Estaillades . . . 106
3.2.4 Indiana . . . 112
3.3 Scanning Ion Conductance Microscopy . . . 122
3.3.1 Calcite . . . 122
3.3.2 Ketton . . . 132
3.3.3 Estaillades . . . 139
3.3.4 Indiana . . . 150
3.3.5 Summary of SICM imaging . . . 160
3.4 Atomic force microscopy . . . 162
3.4.1 Ketton . . . 162
3.4.2 Estaillades . . . 166
3.4.3 Indiana . . . 170
3.4.4 Summary of AFM imaging . . . 173
3.5 Summary and conclusions . . . 175

**4 Surface Charge Mapping** **178**

4.1 Overview . . . 178
4.2 Relevance for Digital Rock . . . 179
4.2.1 pH-dependent crude oil adhesion to clay surfaces . . . 180
4.2.2 Low-salinity flooding . . . 182

4.2.3 Redox activity in iron-bearing minerals . . . 185
4.2.4 Organic and aqueous environments . . . 186
4.3 Surface Charge Mapping Progress . . . 187
4.3.1 Organic Electrolytes in the SICM . . . 187
4.3.2 Polystyrene on Glass . . . 190
4.4 Summary and conclusions . . . 213

**5 Carbonate Ageing Studies 215**

5.1 Overview . . . 215
5.2 Estimated Cell Pressure During Ageing . . . 217
5.3 Low-Vacuum Scanning Electron Microscopy . . . 220
5.3.1 Calcite . . . 220
5.3.2 Estaillades . . . 245
5.4 Atomic Force Microscopy . . . 262
5.4.1 Aged Calcite . . . 262
5.4.2 Aged Estaillades . . . 267
5.5 Scanning Ion Conductance Microscopy . . . 271
5.5.1 Aged Calcite . . . 272
5.5.2 Aged Estaillades . . . 277
5.6 Summary and conclusions . . . 279

**6 Bandera Brown 281**

6.1 Overview . . . 281
6.2 Unaltered Bandera Brown Studies . . . 283
6.2.1 Low Vacuum Scanning Electron Microscopy . . . 283

6.2.2 Scanning Ion Conductance Microscopy . . . 318
6.2.3 Summary . . . 327
6.3 Aged Bandera Brown Studies . . . 329
6.3.1 Low Vacuum Scanning Electron Microscopy . . . 330
6.3.2 Scanning Ion Conductance Microscopy . . . 339
6.3.3 Post-Ageing, post-SICM Low Vacuum SEM Studies . . . 344
6.4 Summary . . . 354

**7 Discussion** **356**

7.1 Digital Rock and SICM . . . 356
7.2 Carbonates . . . 358
7.2.1 Ketton . . . 362
7.2.2 Estaillades . . . 368
7.2.3 Indiana . . . 372
7.2.4 Summary . . . 377
7.3 Bandera Brown . . . 379
7.3.1 Mineral identification with low-vacuum SEM . . . 379
7.3.2 The composition of Bandera Brown . . . 391
7.3.3 Mineral Relevance for PNM . . . 394
7.3.4 Topographical mapping with SICM . . . 400
7.4 Ageing Studies . . . 402
7.4.1 SICM and AFM imaging . . . 406
7.4.2 Aged sample variability . . . 407
7.4.3 The impact of SICM imaging . . . 411

7.5 Progress towards surface charge mapping . . . . . 420

**8 Future Work** **426**

8.1 Integration with modelling . . . . . 427

8.2 Additives . . . . . 428

8.2.1 Kaolinite . . . . . 428

8.2.2 Redox-active iron-bearing species . . . . . 431

8.3 Changing electrolytes . . . . . 434

8.3.1 Low salinity flooding . . . . . 436

8.3.2 Aqueous vs organic electrolytes . . . . . 436

8.4 Bandera Brown surface heterogeneity insights . . . . . 440

8.5 Integration of other techniques . . . . . 443

**9 Conclusions** **445**

**Bibliography** **449**

**A Methods** **462**

A.1 Calibration Standard . . . . . 462

A.2 Nanopipette Characterisation . . . . . 464

A.2.1 Re-arrangement of nanopipette conductance equation . . . . . 464

A.2.2 Worked example of nanopipette characterisation . . . . . 466

**B Carbonates** **468**

B.1 Calcite . . . . . 468

B.1.1 Low-Vacuum Scanning Electron Microscopy . . . . . 468

B.1.2 Energy-Dispersive X-Ray Spectroscopy . . . . . 486
B.2 Ketton . . . . . 492
B.3 Estaillades . . . . . 499
B.3.1 Low-Vacuum Scanning Electron Microscopy . . . . . 499
B.3.2 Energy-Dispersive X-ray Spectroscopy . . . . . 514
B.4 Indiana . . . . . 516

**C Bandera Brown** **520**

C.1 Low-Vacuum Scanning Electron Microscopy . . . . . 520

**D Polystyrene on Glass** **532**

# List of Figures


1.1 Diagram of the typical set up for enhanced oil recovery . . . . . 41

1.2 Wettability determination from a contact angle measurement . . . . 43

1.3 A representation of a typical SICM set up. . . . . 47

1.4 Diagram of a nanopipette tip . . . . . 49

1.5 Hopping mode . . . . . 52

1.6 Surface charge hopping mode . . . . . 56

1.7 Atomic force microscope setup . . . . . 58

1.8 Sketch of the force-distance curve of an AFM tip . . . . . 59

1.9 Scanning probe microscopy inaccuracies . . . . . 65

1.10 Electron and X-ray emissions from SEM beam interaction . . . . . 66

1.11 Auger Electron Generation . . . . . 67

1.12 Scanning electron microscope column and sample chamber . . . . . 69

2.1 Photograph of examples of Estaillades and Indiana samples . . . . . 78

2.2 Histogram of nanopipette diameters . . . . . 86

3.1 Crystal structure of calcite . . . . . 92

3.2 Calcite: SEM Overlay 1 . . . . . 93

3.3 Calcite: SEM Overlay 2 . . . . . 93

3.4 Calcite: high magnification SEM micrograph of surface type 1 . . . 95

3.5 Calcite: high magnification SEM micrograph of surface type 2 . . . 95
3.6 Calcite: high magnification SEM micrographs of surface type 4 . . . 96
3.7 Ketton: SEM Overlay 1 . . . . . 97
3.8 Ketton: SEM Overlay 2 . . . . . 98
3.9 Ketton: high magnification SEM micrograph of surface types 1 and 2 99
3.10 Ketton: high magnification SEM micrograph of surface type 2 . . . 100
3.11 Ketton: high magnification SEM micrographs of surface types 3 and 4101
3.12 Ketton: high magnification SEM micrograph of surface type 3 . . . 102
3.13 Ketton: high magnification SEM micrograph of surface type 4 . . . 102
3.14 Ketton: high magnification SEM micrograph of surface type 5 . . . 103
3.15 Ketton: high magnification SEM micrographs of surface type 6 . . . 104
3.16 Estaillades: SEM Overlay 1 . . . . . 106
3.17 Estaillades: SEM Overlay 2 . . . . . 107
3.18 Estaillades: high magnification SEM micrograph of surface type 1 . 109
3.19 Estaillades: high magnification SEM micrograph of surface type 2 . 109
3.20 Estaillades: high magnification SEM micrographs of surface type 3 . 110
3.21 Estaillades: high magnification SEM micrograph of surface type 4 . 111
3.22 Indiana: SEM Overlay 1 . . . . . 113
3.23 Indiana: SEM Overlay 2 . . . . . 114
3.24 Indiana: high magnification SEM micrograph of surface type 1 . . . 114

3.25 Indiana: high magnification SEM micrographs of surface type 2 . . 116

3.26 Indiana surface type 2a and Estaillades surface type 3b . . . . . 116

3.27 Indiana surface types 3 and 4 and Estaillades surface types 2 and 3a 117

3.28 Indiana: high magnification SEM micrographs of surface type 5 . . 119

3.29 Indiana surface type 5a and Estaillades surface type 4 . . . . . 119

3.30 Calcite: 10 × 10 $\mu$m SICM image of surface type 2 . . . . . 124

3.31 Calcite: two SICM images of the same region of surface type 2 . . . 125

3.32 Calcite: height profiles across two SICM images of surface type 2 . . 126

3.33 Calcite: height profile across an SICM image of surface type 2 . . . 127

3.34 Calcite: 2 × 2 $\mu$m SICM image of surface type 3 or 4 . . . . . 128

3.35 Calcite: two SICM images of surface type 3 or 4 . . . . . 129

3.36 Height distribution plots for SICM images of surface type 3 or 4 . . 130

3.37 Ketton: 3 × 3 $\mu$m SICM image of surface type 1 . . . . . 133

3.38 Ketton: 10 × 10 $\mu$m SICM image of surface type 2 . . . . . 134

3.39 Ketton: Three 2 × 2 $\mu$m SICM images of surface type 3, 4 or 6 . . . 135

3.40 Ketton: two SICM images of surface type 3, 4 or 6 . . . . . 137

3.41 Estaillades: 2 × 2 $\mu$m SICM image of surface type 1 . . . . . 140

3.42 Estaillades: two 2 × 2 $\mu$m SICM images of surface type 2 . . . . . 141

3.43 Estaillades: height distributions of surface type 2 . . . . . 142

3.44 Estaillades: two 5 × 5 $\mu$m SICM images of surface types 2 and 3 . . 144

3.45 Estaillades: height profiles of surface types 2 and 3 . . . . . 145

3.46 Estaillades: four SICM images of surface type 3 . . . . . 146

3.47 Estaillades: crystallite measurement of surface type 3 . . . . . 148

3.48 Estaillades: 5 × 5 $\mu$m SICM image of surface type 4 . . . . . 149

3.49 Indiana: 2 × 2 $\mu$m SICM image of surface type 1 . . . . . 152

3.50 Indiana: height profiles of surface types 1 and 2 . . . . . 153

3.51 Indiana: 10 × 10 $\mu$m SICM image of surface type 2 . . . . . 155

3.52 Indiana: SICM images of surface type 3 . . . . . 156

3.53 Indiana: SEM micrograph of surface type 3 . . . . . 157

3.54 Indiana: 2 × 2 $\mu$m SICM image of surface type 5 . . . . . 158

3.55 Indiana: 5 × 5 $\mu$m SICM image of surface type 5 . . . . . 159

3.56 Ketton: Three AFM images of surface type 3 or 4 . . . . . 163

3.57 Ketton: AFM and SICM images compared . . . . . 165

3.58 Estaillades: AFM images of surface type 2 . . . . . 167

3.59 Estaillades: AFM images of surface type 3 . . . . . 169

3.60 Indiana: Two AFM image of surface type 3 . . . . . 170

3.61 Indiana: Three AFM images of surface type 3 . . . . . 171

3.62 Indiana: SICM image height histogram . . . . . 172

4.1 Kaolinite booklets . . . . . 181

4.2 The low-salinity flooding effect on clay . . . . . 183

4.3 Indiana: 17.4 × 17.4 $\mu$m SICM image in acetonitrile . . . . . 189

4.4 Indiana: An incomplete 20 × 20 $\mu$m SICM image in acetonitrile . . 189

4.5 Polystyrene on glass: SEM Overlay . . . . . 192

4.6 Polystyrene on glass: high magnification SEM 1 . . . . . 193

4.7 Polystyrene on glass: high magnification SEM 2 . . . . . 193

4.8 Polystyrene on glass: high magnification SEM 3 . . . . . 194

4.9 Polystyrene on glass: AFM area 1 . . . . . 196

4.10 Polystyrene on glass: AFM area 1 - small dent profile . . . . . 198

4.11 Polystyrene on glass: AFM area 1 - larger dent profiles . . . . . 199

4.12 Polystyrene on glass: AFM area 2 . . . . . 200

4.13 Polystyrene on glass: AFM area 2 - 1 × 1 $\mu$m AFM image . . . . . 201

4.14 Polystyrene on glass: AFM area 2 - 5 × 5 $\mu$m AFM image . . . . . 204

4.15 Polystyrene on glass: SICM topographical maps . . . . . 206

4.16 Polystyrene on glass: SICM topography - 20 × 20 $\mu$m map . . . . . 208

4.17 Polystyrene on glass: SICM height profiles - dent . . . . . 209

4.18 Polystyrene on glass: SICM height profiles - raised features . . . . . 210

4.19 Polystyrene on glass: SICM current response . . . . . 212

5.1 Aged Calcite 1: SEM Overlay . . . . . 222

5.2 Aged Calcite 2: SEM Overlay . . . . . 223

5.3 Calcite: high magnification SEM micrograph of an unaltered surface 224

5.4 Aged Calcite 1: SEM micrograph with labelled areas of interest . . 224

5.5 Aged Calcite 1: high magnification SEM micrographs of area A . . 225

5.6 Aged Calcite 1: high magnification SEM micrograph of area A - zoomed in . . . . . 226

5.7 Aged Calcite 1: high magnification SEM micrograph of area B . . . 226

5.8 Aged Calcite 1: high magnification SEM micrograph of area C . . . 227

5.9 Aged Calcite 2: high magnification SEM micrographs of surface type 4 . . . . . 228
5.10 Calcite: EDX results for surface type 4a . . . . . 229
5.11 Aged Calcite 2: EDX results . . . . . 231
5.12 Aged Calcite post-SICM: SEM Overlay . . . . . 233
5.13 Aged Calcite post-SICM: SEM micrographs of surface type 1 . . . . 234
5.14 Aged Calcite post-SICM: SEM micrograph of surface types 1 and 2 235
5.15 Aged Calcite post-SICM: EDX result for area A . . . . . 237
5.16 "Old" Aged Calcite: SEM Overlay . . . . . 239
5.17 "Old" Aged Calcite: high magnification SEM micrograph of area 1 . 240
5.18 "Old" Aged Calcite: high magnification SEM micrograph of area 2 . 240
5.19 "Old" Aged Calcite: EDX results for area 2 . . . . . 242
5.20 "Old" Aged Calcite: EDX results for area 3 . . . . . 243
5.21 Aged Estaillades 1: SEM Overlay . . . . . 246
5.22 Aged Estaillades 2: SEM Overlay . . . . . 247
5.23 Aged Estaillades 1: high magnification SEM micrographs . . . . . 249
5.24 Aged Estaillades 2: high magnification SEM micrographs . . . . . 249
5.25 Estaillades: locations of EDX Areas A and B . . . . . 250
5.26 Estaillades: EDX results for area A . . . . . 251
5.27 Estaillades: EDX results for area B . . . . . 252
5.28 Aged Estaillades: EDX element maps for area 1 . . . . . 254
5.29 Aged Estaillades: EDX element maps for area 2 . . . . . 255
5.30 Aged Estaillades: EDX X-ray energy spectrum for area 1 . . . . . 256

5.31 Aged Estaillades: EDX X-ray energy spectrum for area 2 . . . . . 256

5.32 Aged Estaillades post-SICM: SEM Overlay . . . . . 257

5.33 Aged Estaillades post-SICM: high magnification SEM micrographs . 258

5.34 Aged Estaillades post-SICM: high magnification SEM micrograph . 258

5.35 Aged Estaillades post-SICM: EDX X-ray energy spectrum . . . . . 260

5.36 Aged Estaillades post-SICM: EDX element maps . . . . . 261

5.37 Aged Calcite: Two AFM images of surface type 1 . . . . . 263

5.38 Aged Calcite: Four AFM images of surface type 1 . . . . . 264

5.39 Aged Calcite: overlay of AFM images of surface type 1 . . . . . 265

5.40 Aged Calcite: Two AFM images of surface type 2 . . . . . 266

5.41 Aged Estaillades: Two AFM images . . . . . 268

5.42 Aged Estaillades: low-vacuum SEM micrograph for comparison . . . 268

5.43 Aged Estaillades: Three AFM images . . . . . 270

5.44 Aged Calcite: SICM images of surface types 1 and 2 . . . . . 273

5.45 Aged Calcite: Two SICM images of surface type 1 . . . . . 275

5.46 Aged Calcite: Histogram of pixel heights for SICM image in Figure 5.45c . . . . . 276

5.47 Aged Estaillades: 5 × 5 $\mu$m SICM image . . . . . 278

5.48 Aged Estaillades: 10 × 10 $\mu$m SICM image . . . . . 278

6.1 Bandera Brown 1: SEM Overlay . . . . . 284

6.2 Bandera Brown 1: high magnification SEM micrograph of area 1 . . 285

6.3 Crystal structure of $\alpha$-Quartz . . . . . 286

6.4 Bandera Brown 1: high magnification SEM micrograph of area 2 . . 287

6.5 Chemical structure of mica and vermiculite . . . . . 287
6.6 Bandera Brown 1: high magnification SEM micrograph of area 3 . . 289
6.7 Calcite crystallites: examples from Estaillades and Indiana . . . . . 289
6.8 Bandera Brown 1: high magnification SEM micrograph of area 4 . . 290
6.9 Bandera Brown 1: high magnification SEM micrograph of area 5 . . 290
6.10 Bandera Brown 2: low magnification SEM micrograph . . . . . 292
6.11 Bandera Brown 2: high magnification SEM micrograph of area 1 . . 293
6.12 Bandera Brown 2: high magnification SEM micrograph of area 2 . . 293
6.13 Crystal structure of hematite . . . . . 294
6.14 Bandera Brown 3: SEM Overlay with EDX locations . . . . . 295
6.15 Bandera Brown 3: high magnification SEM micrograph of area 1 . . 296
6.16 Bandera Brown 3: EDX results for area 1, part 1 . . . . . 297
6.17 Bandera Brown 3: EDX results for area 1, part 2 . . . . . 298
6.18 Bandera Brown 3: high magnification SEM micrograph of area 2 . . 299
6.19 Bandera Brown 3: EDX results for area 2, part 1 . . . . . 300
6.20 Bandera Brown 3: EDX results for area 2, part 2 . . . . . 301
6.21 Bandera Brown 3: high magnification SEM micrograph of area 3 . . 302
6.22 Bandera Brown 3: EDX results for area 3, part 1 . . . . . 303
6.23 Bandera Brown 3: EDX results for area 3, part 2 . . . . . 304
6.24 Bandera Brown 3: high magnification SEM micrograph of area 4 . . 306
6.25 Bandera Brown 3: EDX results for area 4, part 1 . . . . . 307
6.26 Bandera Brown 3: EDX results for area 4, part 2 . . . . . 308
6.27 Bandera Brown 3: EDX results for area 4, part 3 . . . . . 309

6.28 Chemical structure of albite . . . . . 310
6.29 Bandera Brown 3: high magnification SEM micrograph of area 5 . . 311
6.30 Bandera Brown 3: EDX results for area 5, part 1 . . . . . 312
6.31 Bandera Brown 3: EDX results for area 5, part 2 . . . . . 313
6.32 Bandera Brown 3: EDX results for area 5, part 3 . . . . . 314
6.33 Bandera Brown 3: high magnification SEM micrograph of area 6 . . 315
6.34 Bandera Brown 3: EDX results for area 6, part 1 . . . . . 316
6.35 Bandera Brown 3: EDX results for area 6, part 2 . . . . . 317
6.36 Bandera Brown: 5 × 5 $\mu$m SICM image of vermiculite/mica . . . . 319
6.37 Bandera Brown: SEM micrograph of vermiculite/mica "side-on" . . 319
6.38 Bandera Brown: height profiles for the SICM image in Figure 6.36 . 320
6.39 Bandera Brown: SEM micrograph of vermiculite/mica "face-on" . . 321
6.40 Bandera Brown: three SICM images of vermiculite/mica . . . . . 323
6.41 Bandera Brown: two SICM images of smectite clay . . . . . 324
6.42 Bandera Brown: 6.7 × 6.7 $\mu$m SICM image of smectite clay . . . . 325
6.43 Bandera Brown: high magnification SEM micrograph of smectite . . 325
6.44 Bandera Brown: Feature size comparison for smectite clay . . . . . 326
6.45 Aged Bandera Brown 1: SEM Overlay . . . . . 331
6.46 Aged Bandera Brown 1: high magnification SEM micrograph of area 1332
6.47 Aged Bandera Brown 1: high magnification SEM micrograph of area 2332
6.48 Aged Bandera Brown 1: high magnification SEM micrograph of area 3333
6.49 Aged Bandera Brown 1: high magnification SEM micrograph of area 5334
6.50 Aged Bandera Brown 1: SEM micrograph of area 5 with labels . . . 334

6.51 Aged Bandera Brown 2: SEM Overlay . . . . . 336
6.52 Bandera Brown: example of an unaltered Bandera Brown EDX spectrum . . . . . 337
6.53 Aged Bandera Brown 1: EDX results for area 4 . . . . . 338
6.54 Aged Bandera Brown: 2.8 × 2.8 $\mu$m SICM image . . . . . 340
6.55 Aged Bandera Brown: 10 × 10 $\mu$m SICM image . . . . . 340
6.56 Aged Bandera Brown: Height profiles for the SICM image in Figure 6.55b . . . . . 341
6.57 Aged Bandera Brown: SEM micrograph with measurements . . . . 343
6.58 Aged Bandera Brown post-SICM: SEM Overlay . . . . . 345
6.59 Aged Bandera Brown post-SICM: SEM micrograph of area 1 . . . . 346
6.60 Aged Bandera Brown post-SICM: EDX element maps for area 1 . . 347
6.61 Aged Bandera Brown post-SICM: EDX X-ray energy spectrum for area 1 . . . . . 348
6.62 Aged Bandera Brown post-SICM: SEM micrograph of area 2 . . . . 349
6.63 Aged Bandera Brown post-SICM: EDX element maps for area 2 . . 350
6.64 Aged Bandera Brown post-SICM: EDX X-ray energy spectrum for area 2 . . . . . 351
6.65 Aged Bandera Brown post-SICM: SEM micrograph of area 3 . . . . 352

6.66 Aged Bandera Brown post-SICM: EDX X-ray energy spectrum for area 3 . . . 352

6.67 Aged Bandera Brown post-SICM: EDX element maps for area 3 . . 353

7.1 Ketton: ooid grain shell perspectives . . . 359

7.2 Optical microscopy image of a nanopipette tip . . . 367

7.3 Sharp height changes in Estaillades surface type 3 . . . 371

7.4 Step-like structures in Indiana and Estaillades . . . 374

7.5 Positioning of Indiana surface types 3 and 4 . . . 376

7.6 Bandera Brown: Quartz locations . . . 381

7.7 Bandera Brown: Mica/vermiculite, smectite and kaolinite . . . 384

7.8 Bandera Brown: Smectite . . . 385

7.9 Bandera Brown: Calcite . . . 386

7.10 Hematite evidence in EDX results . . . 388

7.11 Bandera Brown: Albite and apatite locations - SEM micrograph . . 389

7.12 Bandera Brown: Albite and apatite locations - EDX results . . . . . 390
7.13 Reproducibility of ageing on Estaillades . . . . . 409
7.14 Reproducibility of ageing on calcite . . . . . 410
7.15 Surface alteration of aged calcite . . . . . 414
7.16 Surface alteration of aged Bandera Brown: SEM . . . . . 415
7.17 Surface alteration of aged Bandera Brown: EDX . . . . . 416
7.18 SICM images of aged materials . . . . . 419
7.19 Polystyrene on glass: SICM pulsed-potential attempt . . . . . 421
7.20 Polystyrene on glass: current response variations - Part 1 . . . . . 423
7.21 Polystyrene on glass: current response variations - Part 2 . . . . . 424

8.1 Bandera Brown: Kaolinite . . . . . 429
8.2 Kaolinite surface charge pH-dependency . . . . . 430
8.3 Chemical structure of erythorbic acid . . . . . 432
8.4 Bandera Brown: Hematite . . . . . 433
8.5 Petri dish design for swapping electrolytes between scans . . . . . 435
8.6 Asymmetrical pulls on nanopipettes . . . . . 438
8.7 Bandera Brown: EDX results showing hidden heterogeneity . . . . . 441

A.1 Calibration Sample: SICM image and height profile . . . . . 463
A.2 Calibration Sample: low-vacuum SEM micrograph . . . . . 464
A.3 Nanopipette cyclic voltammogram example . . . . . 466

B.1 Low-vacuum SEM: Micrograph 1 of a calcite crystal from Figure 3.2 469
B.2 Low-vacuum SEM: Micrograph 2 of a calcite crystal from Figure 3.2 469

B.3 Low-vacuum SEM: Micrograph 3 of a calcite crystal from Figure 3.2 470

B.4 Low-vacuum SEM: Micrograph 4 of a calcite crystal from Figure 3.2 470

B.5 Low-vacuum SEM: Micrograph 1 of a calcite crystal from Figure 3.3 471

B.6 Low-vacuum SEM: Micrograph 2 of a calcite crystal from Figure 3.3 471

B.7 Low-vacuum SEM: Micrograph 3 of a calcite crystal from Figure 3.3 472

B.8 Low-vacuum SEM: Micrograph 4 of a calcite crystal from Figure 3.3 472

B.9 Low-vacuum SEM: Micrograph 1 of the aged calcite surface shown in Figure 5.1 . . . . . 473

B.10 Low-vacuum SEM: Micrograph 2 of the aged calcite surface shown in Figure 5.1 . . . . . 474

B.11 Low-vacuum SEM: Micrograph 3 of the aged calcite surface shown in Figure 5.1 . . . . . 474

B.12 Low-vacuum SEM: Micrograph 4 of the aged calcite surface shown in Figure 5.1 . . . . . 475

B.13 Low-vacuum SEM: Micrograph 1 of the aged calcite surface shown in Figure 5.2 . . . . . 475

B.14 Low-vacuum SEM: Micrograph 2 of the aged calcite surface shown in Figure 5.2 . . . . . 476

B.15 Low-vacuum SEM: Micrograph 3 of the aged calcite surface shown in Figure 5.2 . . . . . 476

B.16 Low-vacuum SEM: Micrograph 4 of the aged calcite surface shown in Figure 5.2 . . . . . 477

B.17 Low-vacuum SEM: Micrograph 5 of the aged calcite surface shown in Figure 5.2 . . . . . 477
B.18 Low-vacuum SEM: Micrograph 1 of the aged calcite surface after SICM measurements shown in Figure 5.12 . . . . . 478
B.19 Low-vacuum SEM: Micrograph 2 of the aged calcite surface after SICM measurements shown in Figure 5.12 . . . . . 479
B.20 Low-vacuum SEM: Micrograph 3 of the aged calcite surface after SICM measurements shown in Figure 5.12 . . . . . 479
B.21 Low-vacuum SEM: Micrograph 4 of the aged calcite surface after SICM measurements shown in Figure 5.12 . . . . . 480
B.22 Low-vacuum SEM: Micrograph 5 of the aged calcite surface after SICM measurements shown in Figure 5.12 . . . . . 480
B.23 Low-vacuum SEM: Micrograph 6 of the aged calcite surface after SICM measurements shown in Figure 5.12 . . . . . 481
B.24 Low-vacuum SEM: Micrograph 7 of the aged calcite surface after SICM measurements shown in Figure 5.12 . . . . . 481
B.25 Low-vacuum SEM: Micrograph 8 of the aged calcite surface after SICM measurements shown in Figure 5.12 . . . . . 482
B.26 Low-vacuum SEM: Micrograph 9 of the aged calcite surface after SICM measurements shown in Figure 5.12 . . . . . 482
B.27 Low-vacuum SEM: Micrograph 1 of the old aged calcite surface . . . 483
B.28 Low-vacuum SEM: Micrograph 2 of the old aged calcite surface . . . 484
B.29 Low-vacuum SEM: Micrograph 3 of the old aged calcite surface . . . 484

B.30 Low-vacuum SEM: Micrograph 4 of the old aged calcite surface . . . 485

B.31 Low-vacuum SEM: Micrograph 5 of the old aged calcite surface . . . 485

B.32 EDX: Calcite Surface Type 4b . . . . . 487

B.33 Aged Calcite 2: EDX Area 2 . . . . . 488

B.34 Aged Calcite 2: EDX Area 3 . . . . . 489

B.35 Aged Calcite post-SICM: EDX Area B . . . . . 490

B.36 Aged Calcite post-SICM: EDX Area C . . . . . 491

B.37 Low-vacuum SEM: Micrograph 1 of Ketton from Figure 3.7 . . . . . 492

B.38 Low-vacuum SEM: Micrograph 2 of Ketton from Figure 3.7 . . . . . 492

B.39 Low-vacuum SEM: Micrograph 3 of Ketton from Figure 3.7 . . . . . 493

B.40 Low-vacuum SEM: Micrograph 4 of Ketton from Figure 3.7 . . . . . 493

B.41 Low-vacuum SEM: Micrograph 5 of Ketton from Figure 3.7 . . . . . 494

B.42 Low-vacuum SEM: Micrograph 6 of Ketton from Figure 3.7 . . . . . 494

B.43 Low-vacuum SEM: Micrograph 1 of Ketton from Figure 3.8 . . . . . 495

B.44 Low-vacuum SEM: Micrograph 2 of Ketton from Figure 3.8 . . . . . 495

B.45 Low-vacuum SEM: Micrograph 3 of Ketton from Figure 3.8 . . . . . 496

B.46 Low-vacuum SEM: Micrograph 4 of Ketton from Figure 3.8 . . . . . 496

B.47 Low-vacuum SEM: Micrograph 5 of Ketton from Figure 3.8 . . . . . 497

B.48 Low-vacuum SEM: Micrograph 6 of Ketton from Figure 3.8 . . . . . 497

B.49 Low-vacuum SEM: Micrograph 7 of Ketton from Figure 3.8 . . . . . 498

B.50 Low-vacuum SEM: Micrograph 1 of Estaillades from Figure 3.16 . . 499

B.51 Low-vacuum SEM: Micrograph 2 of Estaillades from Figure 3.16 . . 500

B.52 Low-vacuum SEM: Micrograph 3 of Estaillades from Figure 3.16 . . 500

B.53 Low-vacuum SEM: Micrograph 4 of Estaillades from Figure 3.16 . . 501
B.54 Low-vacuum SEM: Micrograph 5 of Estaillades from Figure 3.16 . . 501
B.55 Low-vacuum SEM: Micrograph 6 of Estaillades from Figure 3.16 . . 502
B.56 Low-vacuum SEM: Micrograph 1 of Estaillades from Figure 3.17 . . 502
B.57 Low-vacuum SEM: Micrograph 2 of Estaillades from Figure 3.17 . . 503
B.58 Low-vacuum SEM: Micrograph 1 of the aged Estaillades surface from Figure 5.21 . . . . . 504
B.59 Low-vacuum SEM: Micrograph 2 of the aged Estaillades surface from Figure 5.21 . . . . . 505
B.60 Low-vacuum SEM: Micrograph 3 of the aged Estaillades surface from Figure 5.21 . . . . . 505
B.61 Low-vacuum SEM: Micrograph 4 of the aged Estaillades surface from Figure 5.21 . . . . . 506
B.62 Low-vacuum SEM: Micrograph 5 of the aged Estaillades surface from Figure 5.21 . . . . . 506
B.63 Low-vacuum SEM: Micrograph 6 of the aged Estaillades surface from Figure 5.21 . . . . . 507
B.64 Low-vacuum SEM: Micrograph 1 of the aged Estaillades surface from Figure 5.22 . . . . . 507
B.65 Low-vacuum SEM: Micrograph 2 of the aged Estaillades surface from Figure 5.22 . . . . . 508
B.66 Low-vacuum SEM: Micrograph 3 of the aged Estaillades surface from Figure 5.22 . . . . . 508

B.67 Low-vacuum SEM: Micrograph 4 of the aged Estaillades surface from Figure 5.22 . . . 509
B.68 Low-vacuum SEM: Micrograph 5 of the aged Estaillades surface from Figure 5.22 . . . 509
B.69 Low-vacuum SEM: Micrograph 1 of the aged Estaillades surface from Figure 5.32 . . . 510
B.70 Low-vacuum SEM: Micrograph 2 of the aged Estaillades surface from Figure 5.32 . . . 511
B.71 Low-vacuum SEM: Micrograph 3 of the aged Estaillades surface from Figure 5.32 . . . 511
B.72 Low-vacuum SEM: Micrograph 4 of the aged Estaillades surface from Figure 5.32 . . . 512
B.73 Low-vacuum SEM: Micrograph 5 of the aged Estaillades surface from Figure 5.32 . . . 512
B.74 Low-vacuum SEM: Micrograph 6 of the aged Estaillades surface from Figure 5.32 . . . 513
B.75 Estaillades: SEM overview, EDX Area C . . . 514
B.76 Estaillades: EDX Area C . . . 515
B.77 Low-vacuum SEM: Micrograph 1 of Indiana from Figure 3.22 . . . 516
B.78 Low-vacuum SEM: Micrograph 2 of Indiana from Figure 3.22 . . . 517
B.79 Low-vacuum SEM: Micrograph 3 of Indiana from Figure 3.22 . . . 517
B.80 Low-vacuum SEM: Micrograph 4 of Indiana from Figure 3.22 . . . 518
B.81 Low-vacuum SEM: Micrograph 5 of Indiana from Figure 3.22 . . . 518

B.82 Low-vacuum SEM: Micrograph 6 of Indiana from Figure 3.22 . . . . 519

B.83 Low-vacuum SEM: The micrograph of Indiana shown in Figure 3.23, without numbers. . . . . 519

C.1 Low-vacuum SEM: Micrograph 1 of Bandera Brown from Figure 6.1 521

C.2 Low-vacuum SEM: Micrograph 2 of Bandera Brown from Figure 6.1 521

C.3 Low-vacuum SEM: Micrograph 3 of Bandera Brown from Figure 6.1 522

C.4 Low-vacuum SEM: Micrograph 4 of Bandera Brown from Figure 6.1 522

C.5 Low-vacuum SEM: Micrograph 1 of Bandera Brown from Figure 6.14523

C.6 Low-vacuum SEM: Micrograph 2 of Bandera Brown from Figure 6.14523

C.7 Low-vacuum SEM: Micrograph 1 of Aged Bandera Brown from Figure 6.45 . . . . . 524

C.8 Low-vacuum SEM: Micrograph 2 of Aged Bandera Brown from Figure 6.45 . . . . . 524

C.9 Low-vacuum SEM: Micrograph 3 of Aged Bandera Brown from Figure 6.45 . . . . . 525

C.10 Low-vacuum SEM: Micrograph 4 of Aged Bandera Brown from Figure 6.45 . . . . . 525

C.11 Low-vacuum SEM: Micrograph 5 of Aged Bandera Brown from Figure 6.45 . . . . . 526

C.12 Low-vacuum SEM: Micrograph 6 of Aged Bandera Brown from Figure 6.45 . . . . . 526

C.13 Low-vacuum SEM: Micrograph 7 of Aged Bandera Brown shown in Figure 6.45 . . . . . 527

C.14 Low-vacuum SEM: Micrograph 1 of Aged Bandera Brown from Figure 6.51 . . . 527
C.15 Low-vacuum SEM: Micrograph 2 of Aged Bandera Brown from Figure 6.51 . . . 528
C.16 Low-vacuum SEM: Micrograph 3 of Aged Bandera Brown from Figure 6.51 . . . 528
C.17 Low-vacuum SEM: Micrograph 4 of Aged Bandera Brown from Figure 6.51 . . . 529
C.18 Low-vacuum SEM: Micrograph 1 of Aged Bandera Brown post SICM from Figure 6.58 . . . 530
C.19 Low-vacuum SEM: Micrograph 2 of Aged Bandera Brown post SICM from Figure 6.58 . . . 531
C.20 Low-vacuum SEM: Micrograph 3 of Aged Bandera Brown post SICM from Figure 6.58 . . . 531

D.1 Low-vacuum SEM: Micrograph 1 of a glass slide dip-coated in polystyrene from Figure 4.5 . . . 532
D.2 Low-vacuum SEM: Micrograph 2 of a glass slide dip-coated in polystyrene from Figure 4.5 . . . 533
D.3 Low-vacuum SEM: Micrograph 3 of a glass slide dip-coated in polystyrene from Figure 4.5 . . . 533
D.4 Low-vacuum SEM: Micrograph 4 of a glass slide dip-coated in polystyrene from Figure 4.5 . . . 534

# List of Tables

1.1 Mineral compositions of Ketton, Estaillades and Indiana . . . . . 73

2.1 Crude Oil Organic Composition . . . . . 80

2.2 Crude Oil Trace Elements . . . . . 81

3.1 Summary of the calcite surface types . . . . . 96

3.2 Summary of the Ketton surface types . . . . . 105

3.3 Summary of the Estaillades surface types . . . . . 111

3.4 Summary of the Indiana surface types . . . . . 121

3.5 RMS roughnesses for Figures 3.39 and 3.40 . . . . . 137

3.6 RMS roughnesses for Figures 3.41 and 3.42 . . . . . 143

3.7 Carbonate surface types identified by SICM . . . . . 161

3.8 Carbonate surface types identified by AFM . . . . . 174

3.9 Summary of the carbonate rock surface types and SICM and AFM identification . . . . . 177

5.1 Aged Calcite Surface Types . . . . . 244

6.1 Summary of Bandera Brown minerals identified . . . . . 328

7.1 Summary of the carbonate rock surface types . . . . . 360

7.2 Carbonate surface types identified by SICM or AFM . . . . . 361

7.3 Summary of Bandera Brown minerals identified . . . . . 382

7.4 Bandera Brown minerals identified in SEM data compared to literature analyses . . . . . 393

7.5 Summary of Aged Carbonate Surface Types . . . . . 404

7.6 Summary of Aged Bandera Brown Surface Types . . . . . 405

7.7 Aged material surface types identified by SICM or AFM . . . . . 406

A.1 Polynomial fit details for the cyclic voltammogram in Figure A.2.2 . . 467

# Acronyms

**AES** Auger electron spectroscopy

**AFM** atomic force microscopy

**AFM-IR** AFM-based infrared spectroscopy

**BET** Brunauer–Emmett–Teller

**BSE** backscattered electron

**CCS** carbon capture and storage

**CE** counter electrode

**CV** cyclic voltammetry

**DDL** diffuse double layer

**EBSD** electron backscatter diffraction

**EDX** energy-dispersive X-ray spectroscopy

**EOR** enhanced oil recovery

**HOMO** highest occupied molecular orbital

**HPAM** partially hydrolyzed polyacrylamide

**IR** infrared

**micro-CT** micro-computed tomography

**FEM** finite element modelling

**FM-AFM** frequency-modulated atomic force microscopy

**LSF** low-salinity flooding

**OIIP** oil initially in place

**PNM** pore network modelling

**PoG** polystyrene on glass

**QRCE** quasi-reference counter electrode

**RE** reference electrode

**RMS** root mean square

**SCAL** special core analysis

**SDRP** Shell Digital Rocks Programme

**SE** secondary electron

**SICM** scanning ion conductance microscopy

**SEM** scanning electron microscopy

**SPM** scanning probe microscopy

**STM** scanning tunnelling microscopy

**TXM** transmission x-ray spectroscopy

**WE** working electrode

**XPS** x-ray photoelectron spectroscopy

**XRD** x-ray diffraction

**XRF** x-ray fluorescence

# Chapter 1

# Introduction

## 1.1 Motivation and context

Recent progressions have moved the world towards more renewable energies, but oil and gas still remain the world's largest sources of primary energy, providing a total of 57.3 % of the global demand in 2019, with oil being the largest single source at 33.1 %.[1] To continue to meet this demand, whilst spreading out the environmental and financial costs of drilling into new areas, it is necessary to more efficiently utilise sub-surface resources and obtain high recovery yields.

### 1.1.1 Oil and Gas Extraction Processes

Primary oil recoveries from oil reservoirs will typically yield between 10 - 20 % of the original oil content of a reservoir, or oil initially in place (OIIP), which is further increased through secondary and tertiary recovery stages to up to 60 - 70 % of the OIIP.[2] The initial phase will typically make use of the natural gas pressure in

the reservoir to extract the first batch of oil, and will typically be the stage with highest production rate.[3] The subsequent stages, and on occasion, even the primary stage, will employ enhanced oil recovery (EOR) strategies to deliver the increased yield of 60 - 70 % of the OIIP, which can range in type from chemical or microbial additives, to thermal and miscible gas injection projects.[2,4,5] A diagram of a typical arrangement for a section of a reservoir employing EOR is shown in Figure 1.1; here two wells are depicted, an *Injection Well* and a *Production Well*. The *Injection Well* injects fluid down into the oil reservoir, which is then continuously pushed through the reservoir, in the direction of the arrows, using the pressure of further injections until it reaches the *Production Well*, where it can be extracted. These wells are usually spaced 200 - 300 m apart for optimal pressure and thus recovery yields.[6,7] The *Injected Fluid* in this diagram can represent any of the EOR injections mentioned above.[2,4,5,8] In some EOR techniques, multiple fronts of fluid will be injected, e.g. a polymer-containing solution may be followed by a water front, under which circumstances there would be multiple bands within the faded section of the diagram, all pushing the crude oil towards the *Production Well*.[8,9] The most effective EOR technology to use for a particular reservoir will depend on numerous considerations such as the composition of the crude oil, the tortuosity of the pore network and the chemical composition of the porous rock in which it sits.[10] Constructing reliable numerical models which take these factors into account, and obtaining accurate physical and chemical information from reservoirs as inputs for these models, is therefore of key importance to best utilise our available reservoirs.

Improving the modelling of oil reservoir behaviour for the progression of EOR

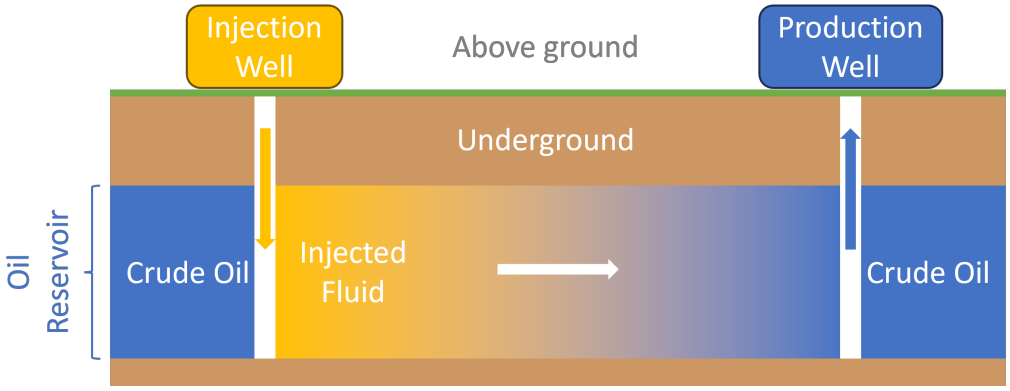



Figure 1.1: Diagram of the typical set up for enhanced oil recovery
A diagram of the set up of a typical oil reservoir set up for enhanced oil recovery. EOR fluids are injected via the Injection Well to push crude oil through the reservoir along the direction of the arrows, so that it can be extracted at the Production Well. Drawn with inspiration from Ahmadi *et al.*.[8]

technology through improved understanding of these systems has the direct consequence of improving carbon capture and storage (CCS) technology in spent oil reservoirs. An increased understanding of fluid flow in oil reservoirs, and new characterisation methods with which to probe them, would not only allow for an improved understanding of CCS behaviour, but by removing more crude oil from reservoirs there will also be a greater available volume for CCS once oil extraction has ceased.

### 1.1.2 Special Core Analysis

Special core analysis (SCAL) is currently the standard characterisation workflow used for obtaining the required input properties, such as remaining oil saturations and relative permeabilities, for numerical simulations of different EOR scenarios.[11,12] It is however not without its shortcomings; one of the more important of these being that SCAL can take over a year to complete, and as such oil extraction processes have often commenced before SCAL results have been collected or analysed.[12] As SCAL is predominantly required for EOR, and EOR is used only once initial oil extraction

process yields are in decline, this is not of immediate importance.[2] However, understanding the infrastructural and financial requirements of the EOR technique(s) a reservoir will ultimately require prior to commencing any extraction would be of significant commercial benefit. McPhee also argued in 2012 that up to 70 % of SCAL data at the time of publishing should be deemed unusable due to inconsistencies in experimental design and interpretation, and inadequate assessment of the sensitivity of certain rock properties to small changes in methodology.[13] Looking into new characterisation methods for determining key system properties is therefore of interest, primarily due to the clear need for faster results, but also due to the questions around SCAL's consistency.

### 1.1.3 Wettability

The term "wettability" is used in petrophysics to describe whether a system of interest is more hydrophylic or hydrophobic, often described as "water-wet" or "oil-wet" respectively. The established way of determining whether a system is water-wet or oil-wet is to look at the contact angle of a water or oil droplet on the surface of interest in the presence of the other immiscible fluid.[14–16] As described in Figure 1.2, which is re-drawn from Schön, if the contact angle of a water droplet on a surface in the presence of oil is $< 90$ °, then the rock is said to be water-wet, whereas if this contact angle exceeds 90°, then the rock is said to be oil-wet.[15]

Contact angles of immiscible fluids on rock surfaces are typically measured using optical tensiometers.[17–19] However, recent progressions have seen contact angles being determined microscopically and *in situ* from micro–computed tomog-

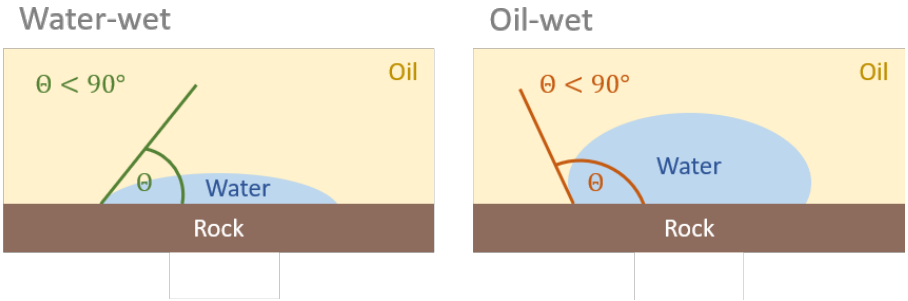



Figure 1.2: Wettability determination from a contact angle measurement
A diagram of how wettability is determined from a contact angle measurement. A water droplet on a rock surface surrounded by oil will have a $\theta < 90°$ if the surface is *water-wet* and a $\theta > 90°$ if the surface is *oil-wet*. Redrawn from reference 15.

raphy (micro-CT) images by Andrew *et al.* (2014) and subsequently automated by Scanziani *et al.* (2017).[20,21] Contact angles have also been measured at the nanoscale using atomic force microscopy (AFM) by Savulescu *et al.* (2021),[22] and predicted with molecular dynamics simulations of fluids on solid surfaces re-constructed from AFM images by Zheng *et al.* (2020).[23]

Although measuring the contact angle is a relatively simple way of determining the wettability of a surface, this contact angle is itself impacted by a number of factors. Some of the more obvious factors are the chemical compositions and oxidation states of any of the three phases: the water, crude oil and rock surface. These chemical properties will have a direct impact on the surface charges and thus how the fluid and solid phases interact; the hydrocarbon composition of crude oils varies from reservoir to reservoir, the water phase can have a range of salt or polymer surfactant concentrations and pHs, and of course the reservoir rock can contain a range of minerals. Physical factors such as the roughness or topography of the pore walls will also have a sizeable impact on the wettability of a rock, which is the core focus of this thesis.

### 1.1.4 Digital Rock

*Digital rock*, or *digital rock physics*, are terms used to describe the numerical modelling of pore-scale fluid flow processes in porous rock, typically for oil extraction applicatons.[12] The results from these models can be fed into SCAL in lieu of experimental results, as they can be generated much faster; if reliable, this would save a considerable amount of time.[24,25] The process does not however have to exclude experimental results altogether; pore network modelling (PNM), a commonly used numerical method for digital rock, will often use pore network systems reconstructed from experimental imaging results, such as 3D images obtained *via* micro-CT; a good example of which is presented by Bultreys *et al.* (2016).[10,12,26,27]. More recently, Tembely *et al.* (2021) developed a workflow for the estimation of the permeability of a core, a key SCAL input, by using machine learning to look at micro-CT images.[25] These models are however not yet fully able to predict the behaviour of two-phase fluid flow through these complex networks when compared to experimental results. The digital rock workflow therefore, in addition to advancements in our understanding of the fundamental physics governing these systems, requires advances in characterisation techniques such as micro-CT and opens up the potential for the integration of new ones. These new techniques would not necessarily be used instead of micro-CT, but alongside it, to create a multi-model workflow for digital rock. As previously mentioned, the wettability of a surface is not purely determined by the topography of the surface or pore structure, and so accurately predicting fluid flow through these rocks requires more than geometrical inputs. As such, in a multi-model workflow, experimental techniques providing additional in-

formation such as chemical composition or surface charge distribution would add to the structural information provided by micro-CT, and could in turn improve the accuracy of PNM simulations.

The project described in this thesis was carried out under the the wider *Shell Digital Rocks Programme* (SDRP) funded by Shell Global Solutions International BV, in collaboration with Imperial College London, the University of Cambridge and Rice University. The SDRP sought to address all aspects of the digital rock workflow, with projects ranging in focus from the pore-scale to the nanoscale in both modelling and experimental work. All results collected could therefore later be fed upwards into PNM, with the aim to improve their predictions of reservoir behaviour. In this project specifically, a range of microscopies were used to map carbonate and sandstone rocks, among other samples, at the nanoscale. The focus was to establish the novel use of scanning ion conductance microscopy (SICM), an electrochemical scanning probe microscopy (SPM), for use in this application. This technique was used alongside the more widely established AFM and scanning electron microscopy (SEM), which both provided verification for the SICM images whilst yielding interesting results in themselves.

## 1.2 Scanning Ion Conductance Microscopy

SICM is an electrochemical SPM which was first reported in 1989 by Hansma *et al.* to provide a means to map the topography of delicate and non-conductive samples, such as living cells, as the sharp probe itself does not come into contact with the sample being investigated.[28] Since its invention, SICM has been used for numerous biological applications,[29–35] as well as a handful of studies in materials and chemistry applications, such as the visualisation of how a catalyst or battery electrode surface can alter with use.[36–39]

### 1.2.1 SICM setup

A typical SICM setup (Figure 1.3) will involve the sample surface of interest being immersed in an electrolyte, along with two quasi-reference counter electrodes (QRCEs), typically both Ag/AgCl, which are held at a constant bias, instead of the more traditional three-electrode setup used in most electrochemical experiments.[40–43] The move towards two-electrode setups in nano-electrochemical experiments in general has arisen from a need to keep the setups small when measuring nanoscale phenomena.[42] QRCEs fulfill this need for smaller setups, as traditional reference electrodes (RE) are bulky and require to be set up adjacent to the experiment, and counter electrodes (CE) should ideally be placed further away from the working electrode (WE) than nano-electrochemical experiments can accommodate.[43] The use of two QRCEs instead of the typical WE/RE/CE setup has therefore been widely reported in the literature in SICM experiments.[41,43,44] QRCE setups are not stable for as long as thermodynamic electrode setups, however the time-frame

of QRCE stability is sufficient for the typical duration of a set of experiments on the SICM; the Ag/AgCl electrodes used in the experiments described in this thesis have been shown to be suitable due to the low currents in nano-electrochemical experiments, and have been shown to be stable over many hours of measurements.[42,43] As such, there is a clear net benefit of using QCREs in nano-electrochemical experiments such as SICM imaging.

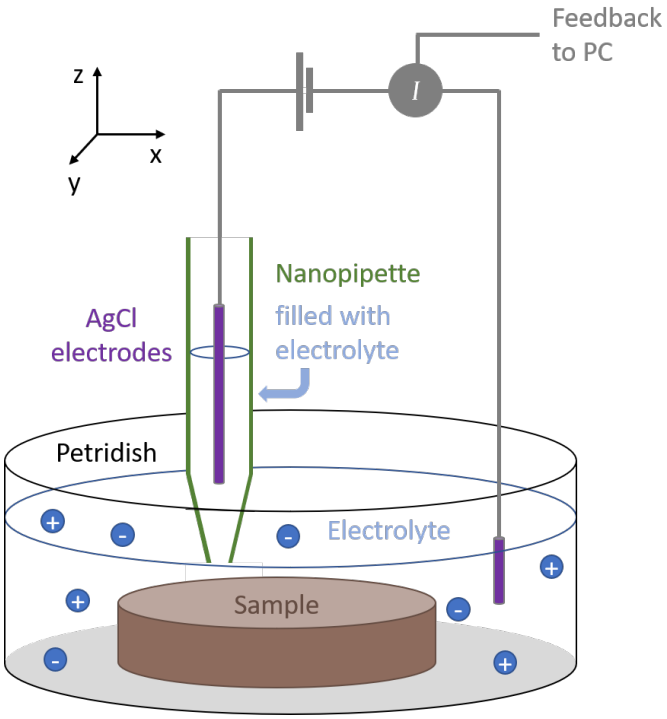



Figure 1.3: A representation of a typical SICM set up.
The typical configuration of an SICM set up; the sample sits within a petri dish, fully immersed in an electrolyte. The probe, a QRCE fitted within a nanopipette sits perpendicular to the sample, above it in solution, with the second QRCE sitting free in solution. Drawn with inspiration from reference 40.

One of the two QRCEs in solution above the sample is fitted inside of a nanopipette, which is also filled with electrolyte, with an opening diameter on the order of tens of nm, so that all ion flow between the two electrodes must pass via this narrow opening; this forms the probe.[29,40,45] This nanopipette probe sits perpendicular to the sample surface, its exact position in $x$, $y$ and $z$ typically being controlled with

piezo actuators. The surface is detected by allowing the probe to slowly approach the sample surface, until a current drop of around 1 % takes place.[40,46] This current drop is the consequence of the nanopipette being close enough to the surface such that the surface itself impedes the flow of ions into the nanopipette. The exact distance required between the nanopipette and the surface to achieve this current reduction is dependent on the size of the nanopipette opening and electrolyte concentration.[46]

### 1.2.2 Tip-sample distance approximation

Rheinlaender and Schäffer recently developed a new model for estimating approach curves, and as such the tip-sample distance at the end of an approach, by looking at the approach curves for a range of pipette sizes, and demonstrated it to be an improvement on previous models.[46–48] The current measured, $I(d)$, at a given tip-sample distance, $d$, during approach was shown to be related to the resistance inside the nanopipette, $R_P$, and the access resistance of the nanopipette opening $R_a$ by equation 1.1:[46]

$$I(d) = \frac{V_0}{R_P + R_a^{(r_0/r_i)}(d)} = \frac{R_P + R_a^{(r_0/r_i)}(d \to \infty)}{R_P + R_a^{(r_0/r_i)}(d)} I_0 \tag{1.1}$$

where $V_0$ is the applied bias, $R_a$ is a function of $r_0/r_i$, the ratio between the outer, $r_0$, and inner, $r_i$, radii of the nanopipette tip opening (see Figure 1.4), and the tip-sample distance, and where $I_0$ is the saturation current when $d \to \infty$. Rheinlaender and Schäffer showed that the other sources of resistances in the system such as the electrodes and wires could be neglected whilst still showing a good fit with the experimental data.[46] To determine $I(d)$ from equation 1.1, experimentally determined

$R_a$ values were used, and $R_P$ was calculated using equation 1.2, originally from Nitz *et al.*:[46,47]

$$R_P = \frac{1}{\pi \sigma r_i \tan \alpha} \tag{1.2}$$

where $\sigma$ is the electrolyte conductivity and $\alpha$ is the pipette cone angle (Figure 1.4). The implications of this model are that, for what Rheinlaender and Schäffer describe as a typical SICM nanopipette with a $r_0/r_i \approx 1.5$ and an $\alpha \approx 3°$, when $d \approx 10r_i$, $d \approx 1r_i$ and $d \approx 0.1r_i$, the observed ion current drop is 0.1, 1 and 10 % respectively. So, for a typical scan described in this thesis, assuming that the nanopipettes have an $\alpha$ around 3°, where the detection threshold is set to 1 %, with $r_i \approx 15$ nm, it is expected that $d \approx 15$ nm.[46]

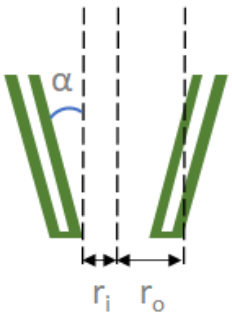



Figure 1.4: Diagram of a nanopipette tip
A representation of the nanopipette tip, with labels for the pipette cone angle, $\alpha$, the outer radius, $r_0$, and inner radius, $r_i$, of the nanopipette tip opening as used in equations 1.1 and 1.2. Redrawn from reference 46.

### 1.2.3 Topographical mapping

In order to collect an image using the SICM set up, multiple scanning modes have been developed to suit different morphologies and scan time requirements, with a particular focus in recent years towards developing faster scan times.[40,49–53] The

push towards faster scan times is driven by SICM imaging being slow in comparison to other SPMs; generating an image of 80 × 80 or 100 × 100 points can take 1 - 2 hours depending on the sample's roughness, which does not allow for many maps to be captured during a working day, particularly when lost time from probe blockages and crashes are taken into account. When compared to AFM mapping, which can take closer to 5 - 10 minutes per scan, it is clear that the longer time requirements for SICM mapping need to be addressed before widespread adoption of the technique will occur. Some of the key progressions in SICM scanning modes are discussed below, but this is far from an exhaustive list.

#### 1.2.3.1 Non-modulated mode

The original method of scanning the surface, as described in Hansma *et al.*'s paper, saw the pipette being brought sufficiently close to the sample surface in order to observe a reduction in current, and then scanned in $x$ and $y$, whilst the $z$ position was adjusted in order to maintain a constant current signal, and thus a constant distance from the surface.[28] The $z$ positions required at the different $x$ and $y$ coordinates were recorded, and from this a topographical map constructed.[28] This mode is now often referred to as non-modulated or DC feedback mode.[40,50,51]

Non-modulated mode is however not without its limitations; most notably, all changes in measured current during a scan are attributed to a change in surface feature height, and there is no way to distinguish these from changes caused by local pockets of higher or lower ion strength or DC drift.[40] Additionally, as the tip is being moved across the surface and only changing height in response to current changes, sudden changes in surface feature height may not be detected in time,

causing the tip to crash into the sample. Due to the tip's fragility, this type of crash will normally cause the the nanopipette to break, requiring it to be replaced before imaging can resume.[40,49] Crashes can also cause damage to certain samples, and so these incidents should be minimised where possible.

#### 1.2.3.2 Distance-modulated mode

To address some of the issues posed by non-modulated mode, distance-modulated mode was first developed in 2001 by Shevchuk *et al.*.[50] Distance-modulated, or AC feedback mode uses a small oscillation of the nanopipette tip close to the sample surface during a scan to generate an oscillating current feedback. This oscillation in the current can be used to differentiate erroneous sources of current change, such as DC drift or small pockets of different ion strength, from those caused by the changing topography of the sample, as they will be out of phase with the oscillation, and those caused by the topography will be in phase.[40,50] In a DC feedback mode scan therefore, any changes which are out of phase with the oscillation are ignored by the feedback loop and do not affect the nanopipette position.[40]

#### 1.2.3.3 Hopping mode

Hopping mode was developed by Novak *et al.* in 2009 in an attempt to solve the problem of how to map rougher surfaces with large and more immediate changes in height.[49] In this mode an individual z-approach is made for each point in the $x$,$y$ grid, halting when the measured current drops by a pre-defined percentage, typically around 1 %. Once this detection threshold has been met, the $z$-position is recorded and the nanopipette retracted, before moving to the next $x$,$y$ position.[49] A

timeline of how the nanopipette position in z and the measured ion current change during the course of a scan is shown in Figure 1.5 below. Although much slower than the non-modulated and distance modulated modes, as the nanopipette must be constantly retracting from and approaching the surface, this method allows for the imaging of surfaces with relatively steep surface features; features that the tip would normally crash into the side of in scanning modes such as non-modulated or distance-modulated mode where the pipette tip remains close to the surface, and has gained popularity in the literature, particularly for commercial systems.[33,54,55]

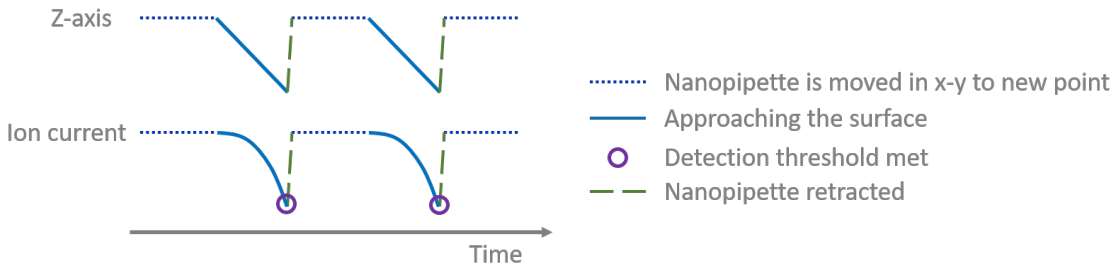



Figure 1.5: Hopping mode
A timeline of the nanopipette position and ion current during a hopping mode scan. Drawn with inspiration from reference 29.

Given the roughness of the outcrop rocks studied in this thesis, hopping mode was deemed to be the best choice for performing topographical measurements on the SICM. This choice came at the expense of time per image, each image typically taking 1 - 2 hours to capture, compared to the 10 - 20 minutes expected of non-modulated and distance-modulated modes. However, when taking into account the time that would be lost to failed measurements caused by pipette crashes if distance-modulated or non-modulated modes were used, this choice was ultimately expected to yield better results.

#### 1.2.3.4 Resolution limits of SICM

There is some debate in the literature as to the absolute lateral resolution limit of SICM with respect to probe size.[49,56–58] Generally, reports on computational modelling predict lower resolution limits than reports on experimental work which have investigated practical resolution limits. Finite element modelling (FEM) simulations performed by Rheinlaender and Schäffer in 2009 and Del Linz *et al.* in 2014 both predicted in the range of $2r_i$ - $3r_i$ as the lateral resolution limit for SICM.[56,57] However, experimental contemporaries such as Novak *et al.* in 2009 and Weber and Baker in 2014 both reported resolutions down to $0.5r_i$ from their experimental work, which were carried out in hopping and distanced modulated modes respectively.[49,58]

Although experimental resolutions have been reported as low as $0.5r_i$, it was decided that for the purpose of the experiments reported in this thesis, the predicted value of $2r_i$ was treated as the accepted resolution limit for each nanopipette, to allow for any errors in characterisation, and to ensure that no artifacts were introduced into the images due to overlapping pixel information.[49,58] The nanopipettes used in this work had an $r_i$ in the range of 10 - 20 nm, so individual pixel information was typically gathered at points 25 - 100 nm apart; see Chapter 2: *Methods*, page 84 for further information. This approach was selected to minimise the risk of having overlapping information in adjacent pixels whilst also seeking to image the samples at the highest possible resolution.

### 1.2.4 Surface charge mapping

When a topographical map is recorded using SICM, a high ionic strength electrolyte is used, such as 0.1 M $KCl_{(aq)}$, to ensure that the diffuse double layer (DDL) at the sample surface does not extend far enough into solution to interfere with the measurement.[59] This can however be looked at in a different way; in order to probe the DDL, and thereby visualise the impact of local sample surface charge distributions on the surrounding electrolyte, a lower ionic strength solution, such as 0.01 - 0.05 M $KCl_{(aq)}$, can be used, as the DDL will extend sufficiently far into solution to be probed with the nanopipette.[29,59] SICM can therefore be employed to observe local surface charge distributions in addition to providing nanoscale topographical maps.

#### 1.2.4.1 Distance-modulated mode for surface charge

A number of methods have been reported to successfully estimate local surface charges using SICM; the first of which being reported by McKelvey *et al.* in 2014, where they described how the distance-modulated mode could be utilised to also record a current response from local surface charge effects.[29,41,59,60] It was found that the phase shift between the oscillation of the nanopipette and the AC current itself was related to the surface charge on the sample locally to the nanopipette, and the applied bias. By mapping the phase of ion current with respect to the nanopipette oscillation, a heat map of differently charged regions could be generated.[59] Additionally, when a negatively charged surface is approached by a nanopipette held at a negative bias, or for a positive surface and positive bias, the measured ion current will increase when the probe in close proximity to the surface, due to interactions

between the DDL at the sample surface and the DDL at the probe tip. Although McKelvey *et al.* did not present a means to deliver a quantitative map of surface charge, this was indeed a leap to show that positive and negative surfaces could be identified using SICM, and map their qualitative charge distributions simultaneously to topographical mapping.[59]

#### 1.2.4.2 Hopping mode for surface charge

More recently, in 2016, Page *et al.* demonstrated how a hopping mode scan for topographical mapping could be adapted to include bias pulses to probe the surface charge local to the probe, which they named pulsed-potential SICM.[29] This adaptation features two identical pulses of the bias which are different to the approach bias. These two pulses happen at the top and the bottom of the hopping regime, the x, y and z-movement being paused during these pulses, and the electrolyte ionic strength is chosen such that the bias pulse at the bottom of the hop is inside of the DDL, and the bias pulse at the retracted position is outside of the DDL, based on FEM simulations prior to imaging.[29] Figure 1.6 describes how the z-position, ion current and bias can change over time in a pulsed-potential SICM scan. The example bias profile shows a pulse to a higher bias, but this can be to a lower one, depending on the nature of the sample under observation. The ion current response inside of and outside of the DDL is recorded in response to this bias pulse, and the difference between these two responses is plotted relative to position in x and y as a current response map. A surface charge map can then be extrapolated from this current response map using FEM simulations of the SICM set up in proximity to surfaces of a range of charges as a calibration.[29]

Since pulsed-potential SICM still contains all the components of a topographical hopping mode scan, the topography and ion current response maps can be collected simultaneously.[29] This adapted hopping mode is the surface charge mapping method with which the SICM in our laboratory is equipped.

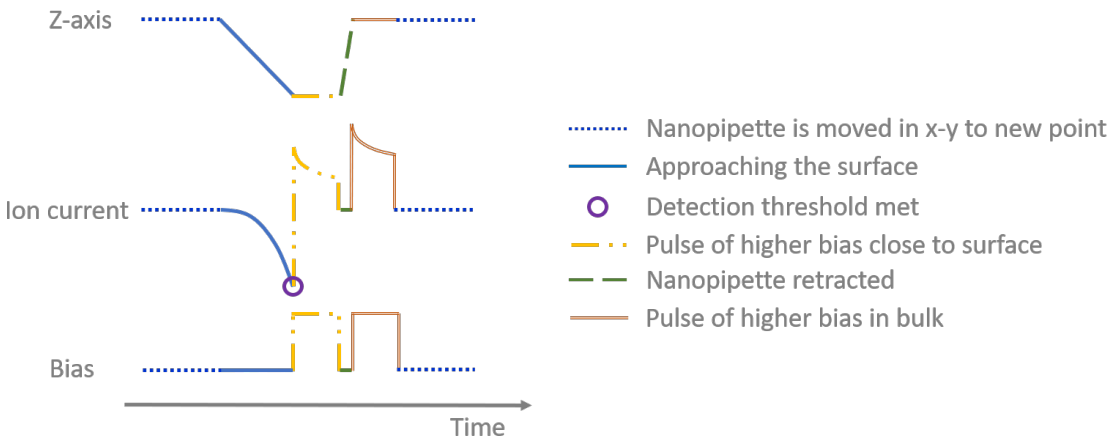



Figure 1.6: Surface charge hopping mode
A timeline of how the nanopipette position, ion current and applied bias can change during an adapted hopping mode scan which incorporates double layer probe steps for estimation of local surface charge. The bias pulses shown are to a higher bias, but lower bias pulses can be used too, depending on the nature of the sample. Drawn with inspiration from reference 29.

## 1.3 Atomic Force Microscopy

Atomic force microscopy (AFM) is another SPM and a contemporary of SICM, being developed just 3 years earlier in 1986 by Binnig *et al.*.[61] The development of the atomic force microscope was a progression from the scanning tunneling microscope (STM), allowing for the nanoscale imaging of non-conductive substrates; which is not to say that the development of STM in itself wasn't a ground-breaking achievement, earning Gerd Binnig, inventor of the AFM, and Heinrich Rohrer the Nobel Prize in Physics in 1986.[61,62]

### 1.3.1 AFM setup

Despite both being SPMs, the working principle of AFM differs considerably from SICM. In a typical AFM set up, shown in Figure 1.7, a cantilever is positioned parallel to the surface under investigation, with a sharp tip sitting on the underside at the end of the cantilever, perpendicular to the surface. This cantilever can either come directly into contact with the sample during a scan, or can approach the surface sufficiently to detect the van der Waals forces but not make contact, for example in non-contact mode.[63]

The cantilever is itself slightly flexible, and will bend towards or away from the sample depending on the van der Waals forces which this sharp tip is experiencing. The cantilever will increasingly bend away from the surface as the probe approaches the surface in the "contact mode" section of Figure 1.8, and will bend increasingly towards the surface as the probe approaches the surface in the "non-contact mode" section of the figure.[63,65] In order to monitor this bending of the cantilever, the

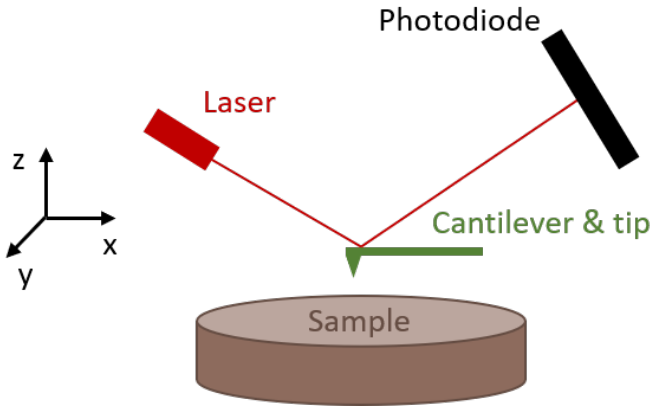



Figure 1.7: Atomic force microscope setup
A diagram of a typical AFM setup, showing the cantilever positioned such that the tip is perpendicular to the sample, with a laser positioned to track the bending of the cantilever as the tip comes in to contact with the surface. Drawn with inspiration from reference 64.

back of the cantilever will typically have a reflective surface at which a laser can be shone, with a photodiode detector positioned to pick up the deflected beam. As the cantilever bends, the deflected beam will move to a different section of the detector, and thus the tip's position relative to the surface can be mapped. The sharp tip on the underside of the cantilever can be produced to be atomically sharp, and as such atomic resolutions have been achieved by numerous groups, even when imaging in liquid.[66–69]

### 1.3.2 Topographical scanning modes

Over the years, numerous topographical image mapping modes have been developed for the AFM.[63] Two of these modes, the contact and tapping modes, are not dissimilar conceptually to SICM's non-modulated and distanced-modulated modes respectively, described above in Section 1.2.3.

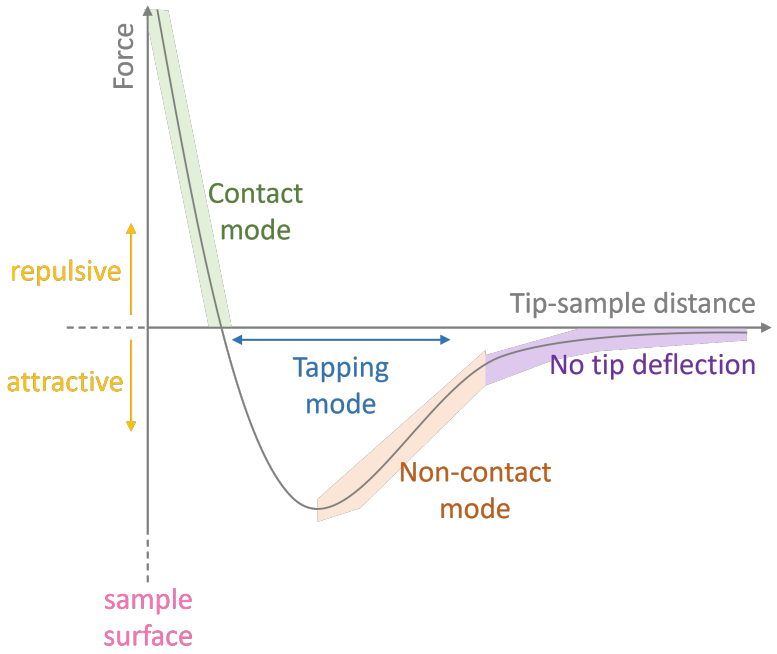



Figure 1.8: Sketch of the force-distance curve of an AFM tip
The force distance curve experienced by the AFM tip as it approaches the sample surface. The highlighted regions show the distances from the sample and associated attractive/repulsive forces where the different AFM scanning modes operate. Drawn with inspiration from Eaton and West.[65]

#### 1.3.2.1 Contact mode

In contact mode, the AFM tip is brought into close contact with the surface, as shown in Figure 1.8, and then moved along in $x$ and $y$. As the tip is moved across the sample, raised or dropped features will result in a change in the van der Waals forces the tip experiences, which will cause the cantilever to bend, and thus the deflected laser beam to move on the detector. In response to these changes, the cantilever's position perpendicular to the surface is adjusted to return the deflected laser beam to its set position and thus the tip's position relative to the surface; similarly to how the ion current is maintained in non-modulated mode in SICM.[63] These adjustments in perpendicular cantilever position are recorded and mapped to generate a topographical image.

#### 1.3.2.2 Tapping mode

During a tapping mode scan, the cantilever is oscillated either at its resonance frequency, or close to it, and at a set amplitude relevant to the roughness of the sample, where the tip is coming in and out of contact with the surface, as shown in Figure 1.8. As the tip is moved across the sample, the change in van der Waals forces arising from changes in feature heights will affect the amplitude of this vibration. The height of the cantilever is adjusted in order to maintain the vibration's amplitude at the set value, and these height adjustments relative to the x,y position on the surface are recorded to generate a topographical map.

Tapping mode on the AFM is more suitable for the mapping of rougher surfaces when compared to contact mode. In contact mode, the cantilever is traced along the surface, responding only to changes in sample height as they occur. In tapping mode, the amplitude of the oscillation is set such that larger height changes across the sample are anticipated, and are therefore better accommodated. In contact mode, there is the risk that if a sudden height change were to occur due to a large raised feature, the AFM tip would come into contact with the side of the feature, and not the top of it, which could lead to the feature being misrepresented in the scan or the tip being knocked out of alignment relative to the laser. The tapping mode on the AFM was therefore employed for all AFM studies described in this thesis, due to the roughness of the outcrop rock surfaces.

### 1.3.3 Surface charge mapping

A number of methods have been developed over the years in order to map surface charge densities using the AFM in a range of applications.[70–72] Two such examples of these developments are outlined briefly here; similarly to the surface charge mapping on the SICM described in Section 1.2.4, these methods make use of the DDL in electrolytes to indirectly map the surface charge distribution on a surface.[29,59,70,72]

#### 1.3.3.1 D-D Mapping

One method for surface charge mapping on the AFM was devised by Heinz and Hoh in 1999, who showed that surface charge maps could be derived by performing iso-force mapping of the same surface in two different electrolytes, and then subtracting them from each other to remove the topographical information; the resulting information being the result of local surface charge heterogeneities creating different DDL environments.[70] This way, relative surface charge density maps could be determined for a surface, without the prior need to characterise the cantilever tip.[70]

#### 1.3.3.2 Frequency Modulation AFM

More recently, in 2015, Umeda *et al.* devised a method for quantitative surface charge determination on the AFM utilizing frequency modulation atomic force microscopy (FM-AFM).[72] FM-AFM is a type of non-contact AFM where the frequency of oscillation of the tip is constantly adjusted to maintain the resonance frequency of the cantilever during a scan. The frequency shift experienced during a scan will change depending on the electrolyte that the sample is immersed in, and so imag-

ing the same sample in two different electrolyte and comparing the frequency shift allows for surface charge maps to be generated.[72]

## 1.4 Comparison of AFM and SICM

There are clear benefits to both AFM and SICM for nanoscale topographical mapping of surfaces. Although SICM can achieve resolutions on the order of tens of nanometres,[58] AFM can achieve atomic resolution, on the order of tens of picometres, which is incredibly powerful.[66,67] The nature of SICM's working principle means that it is highly unlikely that SICM will ever achieve the same resolution limit as AFM; a discussion of the hypothetical resolution limit of SICM compared to results achieved in AFM is presented below.

To achieve atomic resolution in an SICM setup, a nanopipette would first have to be made with an opening diameter on the order of 100s of pm, which in itself has yet to be achieved; at the time of writing, the smallest nanopipette reported in the literature had an opening diameter of 7 nm.[73] If this obstacle was overcome, and technology develops such that nanopipettes can be produced with sub-nanometre opening diameters, limitations imposed by the electrolyte would still need to be considered. During a SICM scan, hydrated ions, typically $K^+$ and $Cl^-$, in the electrolyte are required to pass through the nanopipette opening to reach the electrode within. The hydration radii of $K^+$ and $Cl^-$ have been predicted to be 138 - 146 and 320 pm respectively in the literature,[74,75] and as such SICM with the typical $KCl_{(aq)}$ electrolyte is theoretically limited to using nanopipettes with opening diameters large enough to accommodate the transport of these ions, which in this case

would be $> 640$ pm. If the 0.5 $r_i$ resolution which Shevchuk *et al.* reported with their nanopipettes of 12.5 nm internal diameters proved to be possible with even smaller nanopipettes,[76] and a nanopipette with an opening diameter of approximately 650 - 750 pm was producible, then the hypothetical absolute lateral resolution limit of SICM would be 162 - 187 pm. At this resolution some atoms might be resolved; the atomically smooth silver surface studied by Orisaka *et al.* and the mica surface studied by Fukuma *et al.* showed inter-atomic separations of 280 and 300 pm respectively,[67,69] however as these atoms are only 2× the pixel size, the features would not be expected to be clear.

Despite the resolution limits for SICM imaging, for some surfaces the SICM is a more suitable tool than AFM, and the lower resolution is an acceptable exchange for the other benefits gained from SICM imaging. The interactions required between the AFM tip and the sample surface during a contact mode or tapping mode scan mean that delicate surfaces can become damaged by AFM imaging, and any loose components on the surface could be removed. One of the strengths of the SICM is that the process does not require contact between the probe and the sample, and therefore the scan itself does not damage more fragile samples. This is particularly important for the biological applications for which SICM has been used extensively,[29–35,76] but is also of benefit for the imaging of samples with organic components loosely adhered to a surface, which is relevant to this thesis for the imaging of outcrop rocks coated with crude oil films.

## 1.5 Limitations of Scanning Probe Microscopies

SPMs such as SICM and AFM are incredibly useful for determining relative feature heights at nanoscale resolutions, however they will often incorrectly estimate the width of certain features on a surface, particularly when the probe width is similar in magnitude to the feature itself.[77,78] A discussion of why these errors in feature size determination can occur in SPMs such as AFM and SICM is presented below.

Figure 1.9 illustrates how SICM in hopping mode and AFM in tapping mode might both inaccurately describe the width of the same feature, whilst both accurately describing the depth; in both cases, the recorded profile is shown in black above the "real" surface in brown. When an SPM topographical map is generated, it is assumed that only the surface directly below the centre of the probe is influencing the tip position, however the probe will be influenced by features adjacent to the tip as well. In an SICM scan, if the nanopipette opening is next to a steep surface feature, this can impede the flow of ions sufficiently for the detection threshold to be met. In AFM, the side of the tip might be interacting with an adjacent surface, even if the the end of the tip is not, and could provide sufficient Van der Waals forces to bend the cantilever such that the computer interprets it as being in contact with the surface.[77] The third position from the left in both the SICM and AFM trajectories in Figure 1.9 show examples of such scenarios.

SPMs can also inaccurately measure the height of a surface feature; if a recessed feature were narrower than the width of the the SPM probe, the probe would not be able to descend fully, instead detecting the walls of the feature and retracting prematurely. When interpreting SPM images it is therefore important to bare in

mind that recessed features which are fewer than a couple of pixels wide on the image may not have had their height determined correctly, and the width of any feature may be under or overestimated by a number of pixel widths.

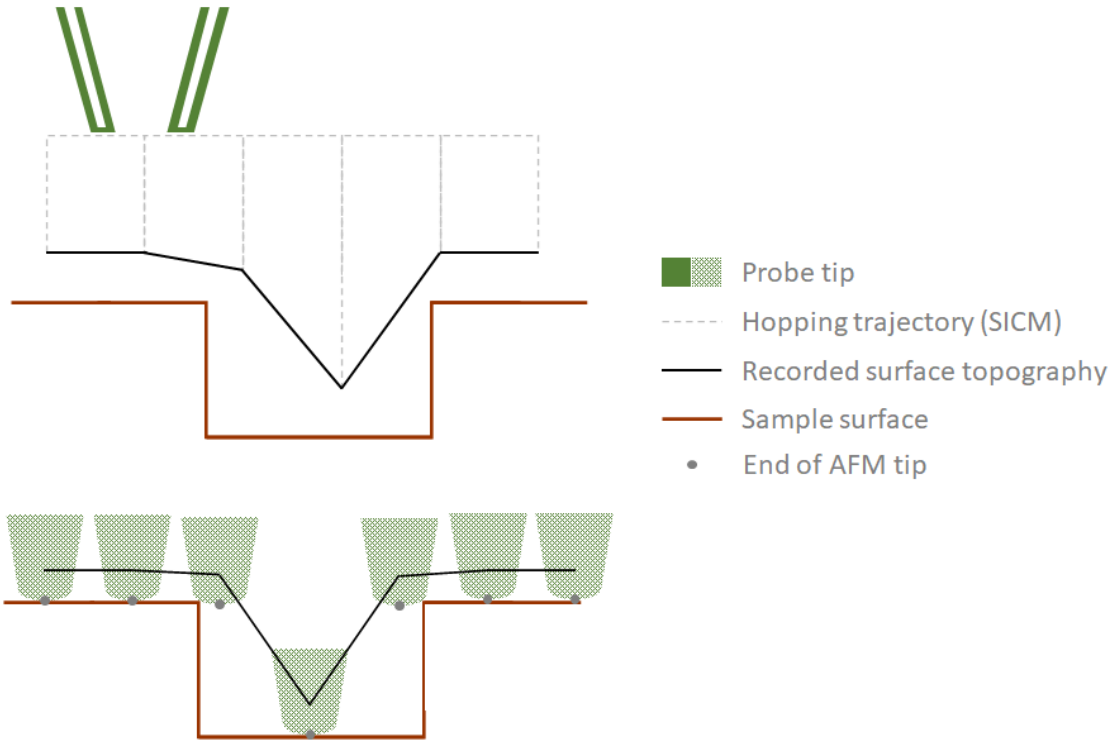



Figure 1.9: Scanning probe microscopy inaccuracies
A diagram of how SICM (top) and AFM (bottom) could inaccurately estimate the width of a similar feature, whilst both accurately describing the depth. Drawn with inspiration from Tognoni *et al.*.[77]

## 1.6 Scanning Electron Microscopy

In SEM, an electron beam is used as the probe with which to map the surface of interest. When this electron beam interacts with the surface, numerous interactions can take place, resulting in a variety of emissions (see Figure 1.10). The electrons in the beam itself can be reflected by the surface; these are called back-scattered electrons (BSE). The beam can also knock electrons out of the sample surface, generating what are referred to as secondary electrons (SEs), which typically have much lower energies than BSEs. If these SEs were originally below the highest occupied molecular orbital (HOMO), then an electron from the HOMO can drop down into this lower orbital, emitting a characteristic X-ray.

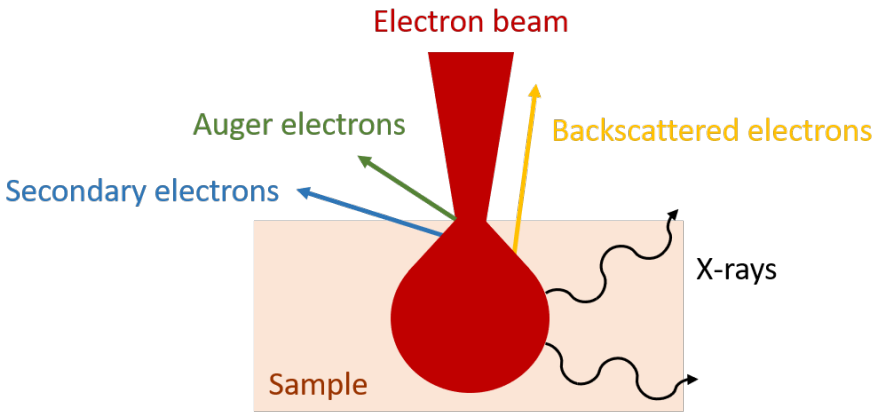



Figure 1.10: Electron and X-ray emissions from SEM beam interaction
A diagram of the interaction volume of the electron beam with a sample, and the electrons and X-rays which can be emitted and detected during an SEM scan. Redrawn from reference 79.

If the electron knocked out by the beam is two or more levels below the HOMO, then a multi-step process called the Auger effect can take place, which is illustrated in Figure 1.11 below. As can be seen in the first diagram, once the electron is removed, an electron from a higher level, but lower than the HOMO, will drop down into the hole that has been generated, shown in the second diagram of Figure 1.11. Instead

of generating an X-ray, the energy generated from this drop, ΔE, can be transferred internally to an electron in a higher level, removing it and ionising the sample. This second removed electron is referred to as an Auger electron.[80]

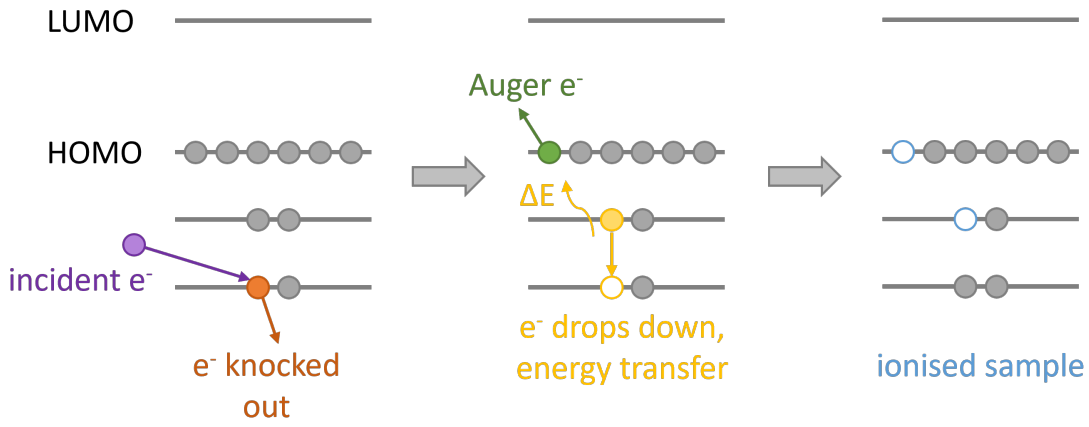



Figure 1.11: Auger Electron Generation
A schematic explanation of how Auger electrons are generated, drawn with inspiration from Ilyin.[80]

During an SEM scan, the electron beam is raster scanned across the surface to build up a map point-by-point, during which time it can make use of all four of the emissions described in Figure 1.10. Morphological mapping on the SEM typically uses the SE signal intensity, often referred to as secondary electron imaging (SEI); SEs do not permeate through the sample very well, so the ones detected during SEI are only from the top approximately 10 nm of the surface.[81] BSEs can be reflected by atoms much deeper into the sample surface than SEs, so BSEs tend to be made use of in electron backscatter diffraction (EBSD) for crystallographic characterisation, due to their interactions deeper into the lattice of crystalline materials.[79,82] The information depth of EBSD varies between experiments, as the BSE penetration is dependent on the atomic weight and density of the material, and the energy of the electron beam.[82] Elemental analysis can be performed via analysis of the X-rays

which can be emitted after SE generation, using a technique known as energy-dispersive X-ray spectroscopy (EDX). X-rays can permeate even further through samples than SEs or BSEs, so EDX gives an idea of the elemental composition down to approximately 2 $\mu m$ into the surface.[83] Finally, Auger electrons can be made use of in Auger electron spectroscopy (AES) another elemental analysis technique, as their kinetic energies are characteristic of certain elements. Unlike EDX, AES is sensitive to just the top 2 - 5 nm of of the sample, as the Auger electrons have a low escape depth.[84]

### 1.6.1 Scanning Electron Microscope Setup

A typical setup for a SEM column is shown in Figure 1.12; to generate the electron beam probe for imaging, there are multiple stages of refinement the beam must go through first. The entirety of the chamber and column are typically under high vacuum to avoid gas particles interfering with the electron beam.

Starting from the top of the column, an electron source, commonly a W filament or $LaB_6$ cathode, will generate electrons which can only escape through the small hole in the Wehnelt cap, the beam being narrowed again through a second aperture. Next the beam passes through a set of condenser lenses; these control the *spot size*, which is a term used to indicate the size of the circular area of sample which is targeted with the electron beam at any one time. Next, the beam passes through the stigmator, which controls the shape of the beam, making sure that when the beam meets the sample the area is circular and not elliptical. The beam then passes through a set of deflection coils which are responsible for controlling the raster

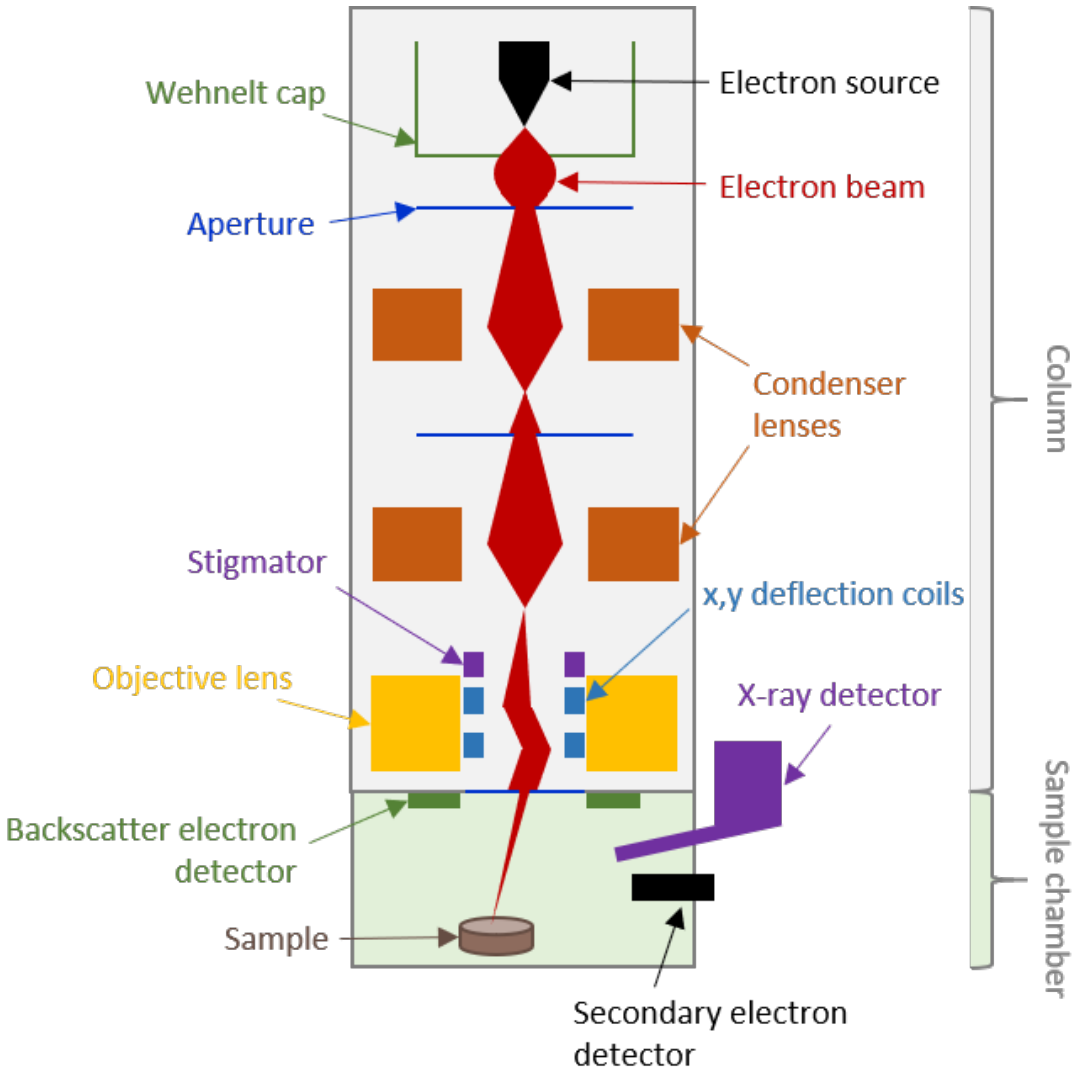



Figure 1.12: Scanning electron microscope column and sample chamber
A diagram of the inside of an SEM column and sample chamber, with the electron beam shown in red. All rectangles either side of the electron beam represent cross-sections of cylindrical objects. Redrawn from reference 85.

scanning of the beam. Simultaneously, the beam passes through the objective lens, which adjusts where the beam comes to a point in the sample chamber, such that the beam is the correct size on the sample surface; this lens thus controls the focus of the image, and requires adjustment for changes in sample height and sample stage position. The beam then passes through the final aperture into the sample chamber, where it can interact with the sample.

The detectors present in the sample chamber will vary between setups, however in any setup the BSE detector will be above the sample, either side of the aperture into the column, as BSEs will commonly come off the sample almost perpendicularly. X-rays, SEs and Auger electrons will come off at a greater angle, and are lower energy, so the detectors for these emissions are positioned towards the edges of the chamber.

### 1.6.2 Low-vacuum scanning

When a sample is imaged using SEM, electrons will become trapped in the material, whether they are from the incident beam, SEs, BSEs or Auger electrons. It is therefore normally a requirement that the sample is conductive, such that these electrons can pass through the material and into the grounded sample stage. If a non-conductive sample is used, then these electrons will simply build up in the surface, causing it to become negatively charged. Once this happens, the SE intensity from these areas will become artificially very high, preventing imaging from occurring. The typical approach to overcoming this issue is to coat the non-conductive sample with a thin layer of a conductive material, such as gold, prior to imaging. For some applications this approach is acceptable, however there is an alternative solution which does not require sample surface alteration called low-vacuum SEM.

Low-vacuum SEM, or variable-pressure SEM, enables the mapping of non-conductive samples by introducing a gas such as $N_2$ at very low pressure into the sample chamber; for example, the experiments described in this thesis were typically performed at 60 Pa.[86] Incoming electrons from the beam will ionize the $N_2$ molecules in the chamber to give $N_2^+$; these positively charged molecules can then mop up the negative

charge build up on the surface, preventing the sample from becoming too charged to image.[86] Although this low gas pressure is still sufficiently low to not prevent the mapping of the surface altogether, typically the SE signal intensity will be lower as a result, and so larger spot sizes have to be used for successful imaging. Although the larger spot size requirement means that the resolution limit is lower than for standard "high-vacuum" SEM, this can be an acceptable compromise for certain applications when it allows for the imaging of completely un-altered, un-coated, non-conductive samples.

## 1.7 Outcrop Rocks

It is common practice in oil recovery research to use substitutes, typically referred to as outcrop rocks, in place of actual reservoir rocks.[21,22,26,87–89] This is in part due to the great cost associated with removing reservoir rock from the ground, but also using more easily obtained substitutes allows for comparable data to be generated over the course of multiple projects. The outcrop rocks discussed in this thesis are carbonate and sandstone rocks from above-ground quarries, and were selected as they are all common substitutes for carbonate and sandstone reservoir rocks in oil recovery research, and were also investigated in other projects in the SDRP.

### 1.7.1 Carbonates: Ketton, Estaillades and Indiana

Understanding and modelling fluid flow processes through carbonate rock is of great importance to the oil and gas industry, as carbonate reservoirs account for the majority of the world's oil and gas reservoirs.[90,91] Numerous carbonate reservoir substitutes have been used over the years;[92–94] the SDRP focusing on three of these, being Ketton, Estaillades and Indiana. All three of these carbonate rocks are thought to be composed of predominantly calcite, with a small quartz component. A range of previously reported mineral compositions in weight percent of these rocks are shown in Table 1.1 on page 73.

Despite all being carbonate rocks with $> 90$ % calcite content, Ketton differs in its structure from Estaillades and Indiana in that it is an oolite, made up of a tight-packed structure of spherical ooid grains. The term "ooid" describes a rounded 3D structure, formed from crystallites which are arranged in concentric circles. These

| Mineral | Calcite (%) | Quartz (%) | Other (%) | Reference (#) | Technique used |
|---|---|---|---|---|---|
| **Ketton** | 99.1 | 0.9 | 0 | 93 | XRD |
| | 98.3 | 1.7 | 0 | 92 | XRF |
| | 99.1 | 0.9 | 0 | 96 | XRD |
| **Estaillades** | 97.2 | 2.8 | 0 | 93 | XRD |
| | 99.6 | 0.4 | 0 | 92 | XRF |
| | 97.9 | 2.1 | 0 | 96 | XRD |
| **Indiana** | 93.0 | 3.8 | 3.2[a] | 97 | EDX |
| | 99.2 | 0.8 | 0 | 92 | XRF |
| | 99.0 | 1.0 | 0 | 96 | XRD |

Table 1.1: Mineral compositions of Ketton, Estaillades and Indiana
Mineral compositions in weight percent of the carbonates: Ketton, Estaillades and Indiana, according to Lai *et al.*, Menke *et al.*, Shah *et al.* and Song *et al.*, as determined by x-ray diffraction (XRD), x-ray fluorescence (XRF) and EDX. [92,93,96,97]

[a]reported impurities included $MgCO_3$ (1.0 %), $BaCO_3$ (0.5 %), $Fe_2O_3$ (0.3 %) and $Al_2O_3$ (0.3 %)

structures were formed around a central nucleation site, where layers of crystallites grew progressively, ultimately fusing with other similar ooid structures to form "oolite" materials. The ooids grains in Ketton are typically around 1 - 2 mm in diameter.[95] Ooids themselves have their own nanoporosity, as well as the macroporosity which is generated between the ooid grains themselves. This more open pore structure leads Ketton to have a much higher internal surface area, with Lai *et al.* reporting a Brunauer–Emmett–Teller (BET) surface area of 2.52 $m^2/g$ for Ketton compared to roughly 0.35 $m^2/g$ and 0.46 $m^2/g$ for Indiana and Estaillades respectively.[92]

### 1.7.2 Sandstone: Bandera Brown

Sandstone reservoirs are much more diverse in their mineralogical composition than carbonates; this thesis focuses on a sandstone outcrop rock called Bandera Brown, which is of particular interest due to its Fe redox behaviour.[88,89] The exact composition of Bandera Brown varies between reports. For example, Yesufu-Rufai *et al.* and Gamal *et al.* both report quartz as the single largest component by mass, reporting 58.89 and 59 % respectively, determined by BSE SEM and XRD respectively.[89,98] Yesufu-Rufai *et al.* report illite ($(K,H_3O)(Al,Mg,Fe)_2(Si,Al)_4O_{10}[(OH)_2,(H_2O)]$), plagioclase ($(Na,Ca)(Si,Al)_4O_8$), smectite ($M^+_{0.33}Al_2(Si_{3.67}Al_{0.33})O_{10}(OH)_2$) and calcite ($CaCO_3$) as the next four most common minerals, however Gamal *et al.* report dolomite ($CaMg(CO_3)_2$), albite ($NaAlSi_3O_8$), illite and kaolinite ($Al_2Si_2O_5(OH)_4$) as the next four most common. This significant difference in reported mineralogy would suggest that Bandera Brown is a reasonably heterogeneous rock, despite the

elements present in the minerals in both cases being the same. This heterogeneity, and mineral-assignment disparities in the literature, are discussed in more depth in the Discussion, Section 7.3, alongside the results obtained in this work.

It was shown by Southwick *et al.* in 2018 that if a Bandera Brown core is flooded with water containing partially hydrolyzed polyacrylamide (HPAM), a polymer surfactant, a large pressure increase across the core occurs.[88] However, if a reducing agent such as erythorbic acid is used to flood the core first, this large pressure increase is not observed.[88] Southwick *et al.* hypothesize in this case that the erythorbic acid reduces the Fe in the Bandera Brown from the +3 to the +2 oxidation state. They further hypothesize that, as the HPAM is negatively charged, the lower magnitude of positive surface charge on the pore walls after reduction means that the HPAM no longer gets stuck in the pores, and is able to instead flow through. There is therefore evidence that the wettability of the rock has been altered through the introduction of a reducing agent.[88] This behaviour is of interest as reservoirs are appreciated to be a reducing environment, given the presence of crude oil; however the majority of studies until now have been carried out in oxidising environments, or samples have been exposed to them without any corrections being made, and so this calls into question the validity of a number of these results.[88,89]

Dr. Yesufu-Rufai, a PhD student in the SDRP, investigated Bandera Brown's proposed redox behaviour and its impact on wettability, with a focus on the use of AFM for the generation of topographical maps. This thesis provides additional insight through the use of SICM and SEM, some images already published by Yesufu-Rufai *et al.*,[99] and by discussing how EDX and the potential for surface charge

mapping on the SICM could provide new insights into this observed redox behaviour, which can not be visualised from the topographical maps generated by AFM.

## 1.8 Thesis Outline

This thesis aims to answer four key questions: 1) Can the SICM be used to map outcrop rocks? 2) How can these experiments be validated? 3) What additional information can be gained from the SICM which was not previously obtainable through other means? and 4) Can the SICM map crude oil-covered surfaces? To this end, this thesis focuses on the investigation of four outcrop rocks; Ketton, Estaillades, Indiana and Bandera Brown. These materials were imaged using low-vacuum SEM, AFM and SICM; the first time SICM has been used in oil and gas recovery research. The suitability of SICM for mapping these materials is assessed, using AFM and low-vacuum SEM as controls, as both techniques have both previously been used to investigate these materials in the literature. The discussion then proceeds to surface charge mapping mode on the SICM, and what avenues this would open up for the study of these materials. Finally, low-vacuum SEM, AFM and SICM images of outcrop rocks which have been artificially aged in crude oil are presented and discussed.

# Chapter 2

# Methods

## 2.1 Samples

### 2.1.1 Outcrop Rocks

A variety of outcrop rocks were investigated. Three carbonates: Ketton (provided by Prof. Paul Luckham, Department of Chemical Engineering), Estaillades (provided by Dr. Branko Bijeljic, Department of Earth Science and Engineering) and Indiana (provided by Dr. John Crawshaw, Department of Chemical Engineering), and one sandstone: Bandera Brown (provided by Prof. Paul Luckham, Department of Chemical Engineering) were selected for this project. Pure calcite crystals (provided by Prof. Paul Luckham, Department of Chemical Engineering) were studied as a simple system to compare to the more topographically complex carbonate rocks. Compositions of these four rocks are discussed in the Introduction in Sections 1.7.1 and 1.7.2, with further discussion of Bandera Brown's mineralogy in the Discussion, Section 7.3.2.

#### 2.1.1.1 Sample Cutting and Cleavage

The majority of the rock samples studied were received as cylinders of typically 0.5 cm in length and 1 cm in diameter, which fit inside all of the instruments used; see Figure 2.1 for a photograph of Estaillades and Indiana cylinders affixed in the SICM holders. However, some of the Estaillades studied was received in a large block which was cut into smaller, not necessarily cylindrical pieces by Dr. John Crawshaw. The Estaillades sample initially used for SICM measurements was originally cut as a micro-CT core, which is a cylinder approximately 1 cm in length and 0.5 cm in diameter, and so was imaged on its side. Large calcite crystals obtained from Dr. Rücker were cleaved in air using a guillotine and a mallet to generate sufficiently small samples for the microscopes.




Figure 2.1: Photograph of examples of Estaillades and Indiana samples
Estaillades (left) and Indiana (right) affixed in 3 cm diameter petri dishes for imaging with SICM.

#### 2.1.1.2 Sample cleaning procedure

Prior to any imaging, samples were immersed in distilled water (Direct-Q 3 UV Water Purification System, Merck KGaA, Germany) and sonicated for 10 minutes before being rinsed, re-immersed in distilled water and sonicated for a further 10 minutes to remove any excess powder from their pores (a side effect of the drilling processes), before being left to dry in air. This cleaning process was required as it

was observed that without prior cleaning, the powder inside the pores would emerge when immersed in the 0.1 M $KCl_{(aq)}$ during SICM measurements, which interfered with the measurement and occasionally led to blockage of the nanopipette. Despite the calcite not requiring this cleaning step, as it does not have pores, it was none the less cleaned in this manner for consistency.

### 2.1.2 Ageing Protocol

Calcite, Estaillades and Bandera Brown samples were artificially aged in crude oil, primarily to investigate SICM's suitability in mapping oil-covered samples, but also to probe the interaction of the different surfaces with the crude oil. Crude oil for ageing protocols was provided to the SDRP by Shell, via Dr. Maja Rücker and Dr. Edward Bailey. The rock samples were first cleaned and dried according to the sonication cleaning procedure described above in Section 2.1.1.2. Samples were then placed in clean glass vials with sufficient crude oil to fully immerse the sample. The vials were then covered with a lids and placed in an oven at 70 °C for four weeks. Samples were then removed from the crude oil and placed in clean glass vials and once more placed in an oven at 70 °C for at least two days to allow any volatile components to evaporate. Once dry, the samples were then transferred to a vacuum desiccator for at least two days to remove any remaining volatile components prior to imaging. There was no further cleaning step after this protocol prior to imaging, deliberately so as not to impact how or where the crude oil stuck to the sample surface, allowing for the visualisation of any preferential regions for rock-oil adhesion. The justification for this protocol is discussed in Chapter 5, page 215.

#### 2.1.2.1 Crude Oil Composition

The crude oil used in the ageing protocol described above was provided by Shell to researchers at Imperial College London on the SDRP. The exact composition can not be disclosed, however Table 2.1 gives an indication of which classes of organic compounds were present and their relative quantities, and Table 2.2 describes the amounts of trace metals and sulfur.

| Compound Class | Carbon number range | Composition (%) |
|---|---|---|
| Long chain hydrocarbons | 8-35 | 42.5 |
| Naphthenes | 8-35 | 27.2 |
| Monoaromatics | 8-35 | 13.9 |
| Naphthenic Aromatics | 11-35 | 3.4 |
| Naphthalenes | 12-35 | 4.0 |
| Naphthenic Naphthalenes | 17-35 | 2.2 |
| Triaromatics | 17-35 | 2.7 |
| Other | 8-35 | 4.3 |

Table 2.1: Crude Oil Organic Composition
An indication of which classes of organic compounds were present in the crude oil used in the ageing experiments described in this thesis, based on information provided by Shell to SDRP researchers.

| Element | Composition (ppm) |
|---|---|
| Ca | 1.36 |
| Fe | $< 0.25$ |
| Mg | 0.18 |
| Mn | $< 0.03$ |
| Mo | 0.21 |
| Na | 0.73 |
| Ni | 0.12 |
| Si | 0.56 |
| V | $< 0.25$ |
| Hg | $< 0.001$ |
| S | 7,920 |

Table 2.2: Crude Oil Trace Elements
A description of the trace metals and sulfur content of the crude oil used in the ageing experiments described in this thesis, based on information provided by Shell to SDRP researchers.

### 2.1.3 Polystyrene on Glass

In order to repeat previous surface charge mapping work from the literature,[29] polystyrene on glass samples were prepared. Approximately 1 x 1 cm sections were cut from a 76 x 26 mm, 0.8 - 1 mm thick glass microscope slides (Agar Scientific Ltd., UK), immersed in isopropanol (Sigma-Aldrich, USA) and sonicated for 10 minutes before being left to dry. These slides were then fully immersed for 10 seconds in a 1 mg/ml polystyrene (Sigma-Aldrich, USA) in chloroform (Sigma-Aldrich, USA) solution, before being allowed to dry flat. The side facing up during this drying process was the side investigated during imaging.

## 2.2 Scanning Ion Conductance Microscopy

### 2.2.1 Topographical Mapping

SICM measurements were carried out in hopping mode with a SICM Scan Head IC-nano2015 (Ionscope, UK). Coarse positioning motors were controlled with a Micro-Drive (Mad City Labs Inc, Wisconsin USA), piezo actuators for pipette position were controlled with a Nano-Drive (Mad City Labs Inc., USA) and piezo actuators for sample position were controlled with a Nano-Drive 85 (Mad City Labs Inc., Wisconsin USA). Samples were affixed with Blu Tack (Bostik, France) in the center of a 3 cm diameter, 1 cm high-sided petri dish, and fully immersed in a 0.1 M $KCl_{(aq)}$ (Sigma-Aldrich, USA) in distilled water (Direct-Q 3 UV Water Purification System, Merck KGaA, Germany) electrolyte. Samples being affixed with Blu Tack did not cause any issues with thermal drift or stability; this set up was found to be stable over a day of imaging. The working electrode was placed inside of a nanopipette and held at a 0.2 V bias against the counter electrode which was free in solution. The nanopipette approached the sample surface at 5 nm/ms and currents were recorded for 30 ms at each point, with a minimum hop height between points of 1 $\mu$m, up to 5 $\mu$m for rougher samples. Detection thresholds were set between 0.7 - 1.5 %. Images were plotted and analysed using WSxM 5.0 Develop 9.4 (Nanotec Electrónica S.L., Spain),[100] with any height profiles or histograms being plotted in OriginPro 2018b (OriginLab Corporation, MA, USA).

#### 2.2.1.1 Calibration

Each time the SICM scan head was shipped or moved to a new laboratory, a HS-100MG calibration standard (BudgetSensors, Bulgaria) with 100 nm step heights was imaged to ensure that the set up remained calibrated. An example SICM image of this standard with height profiles is shown in Appendix A, Section A.1.

#### 2.2.1.2 Root mean squared roughness calculation

In order to compare certain SICM images, the root mean square (RMS) roughnesses are given. These RMS roughness values were calculated using WSxM 5.0 Develop 9.4 (Nanotec Electrónica S.L., Spain) software.[100] An RMS roughness value, R, is calculated from all of the height values in the image, $z_i$, as described in equation 2.1, adapted from Espitia *et al.*:

$$R = \sqrt{\frac{1}{N}\sum_{i=1}^{N} z_i^2} \tag{2.1}$$

where N is the number of points in the topographical image.[101,102]

### 2.2.2 Surface Charge Mapping

The SICM hopping mode was adapted to incorporate two pulses at a second bias at the bottom and top of each hop, based on the pulsed-potential SICM method reported by Page *et al.* and described in the Introduction, Section 1.2.4.[29] Attempts to perform surface charge mapping for this project therefore followed the parameters described by Page *et al.*.[29] Experiments were conducted in a 0.05 M $KCl_{(aq)}$ (Sigma-Aldrich, USA) in distilled water (Direct-Q 3 UV Water Purification System, Merck KGaA, Germany) electrolyte. The working electrode was held at a 0.02 V bias

against the counter electrode whilst the nanopipette moved, and pulsed to -0.4 V for 50 ms at the top and bottom of each hop, when the nanopipette was stationary. The minimum hop height was 1 $\mu$m, and the detection thresholds were set between 2.5 - 6.0 %. Images were plotted and analysed using Gwyddion 2.55.

### 2.2.3 Nanopipettes

#### 2.2.3.1 Nanopipette Pulling

Nanopipettes were pulled from 7.5 cm quartz capillaries of 1 mm external diameter and 0.5 mm internal diameter (Sutter Intstrument, California, USA) on a P-2000 Laser-Based Micropipette Puller System (Sutter Instrument, California, USA), using the following parameters: Line 1: Heat 880, Fil 4, Vel 30, Del 185, Pul 100; Line 2: Heat 900, Fil 1, Vel 15, Del 170, Pul 160. Nanopipettes were found to typically have internal diameters of 20 - 40 nm by conductance measurements as described below.

#### 2.2.3.2 Nanopipette Characterisation

Steinbock *et al.* gave the conductance of a nanopipette as:[103]

$$G = \frac{d_i D_i \pi g(c)}{4(l + \frac{\pi}{8}(d_i + D_i))} \tag{2.2}$$

where $G$ is the conductance of the nanopipette, $d_i$ is the internal diameter of the nanopipette opening, $D_i$ is the internal diameter of the capillary from which the nanopipette was pulled, g(c) is the specific conductance of the electrolyte and $l$ is the taper length of the nanopipette.

Equation 2.2 can be rearranged for $d_i$ to give equation 2.3. The full rearrangement resulting in equation 2.3 from the original equation 2.2 can be found in Appendix A, Section A.2.1.

$$d_i = \frac{4Gl + \frac{\pi}{2}GD_i}{D_i\pi g(c) - \frac{\pi}{2}G} \tag{2.3}$$

$D_i$ is a constant, being 0.5 mm for all nanopipettes. $g(c)$ was in the range of 1.16 - 1.28 $\mathrm{Sm}^{-1}$, as all experiments were conducted between 20 - 25 °C.[104] $d_i$ was thus determined for any given nanopipette by measuring $G$ and $l$.

Images of the nanopipettes were taken at 5× magnification on either an Olympus BX51 microscope (Olympus Europa SE & CO. KG, Japan) or on an Olympus BX53M microscope (Olympus Europa SE & CO. KG, Japan). $l$ was measured from these images using either analySIS docu software (Olympus Europa SE & CO. KG, Japan) or OLYMPUS Stream software (Olympus Europa SE & CO. KG, Japan).

Cyclic voltammetry (CV) was carried out in a 0.1 M $\mathrm{KCl}_{(\mathrm{aq})}$ (Sigma-Aldrich, USA) in distilled water (Direct-Q 3 UV Water Purification System, Merck KGaA, Germany) electrolyte, with Ag/AgCl working and counter electrodes to measure $G$. The working electrode was fitted inside the nanopipette and the counter electrode was free in solution. CV experiments were carried out using either a Reference 600 Potentiostat (Gamry Instruments, USA) or a CompactStat.e Potentiostat (Alvatek, UK). Scans were carried out at 100 $\mathrm{mVs}^{-1}$ with a step size of 1 mV from 0.5 to -0.5 V. $G$ was taken as the slope of tangent of the CV plot when the bias was 0 V. A worked example of the estimation of the size of a nanopipette opening is given in Appendix A, Section A.2.2.

At the beginning of the project, each nanopipette was characterised before use. Once the first 30 nanopipettes had been made using the same settings, it was found that all nanopipettes had internal diameters 15 - 40 nm, with the majority sitting between 20 - 40 nm; see Figure 2.2. After this repeatability was established, one nanopipette would be characterised from each batch to ensure that $< 40$ nm internal diameters were still being obtained reliably. If a nanopipette of 20 - 25 nm was specifically required for a high resolution scan, then multiple nanopipettes from a batch would be characterised until a sufficiently narrow nanopipette was found.

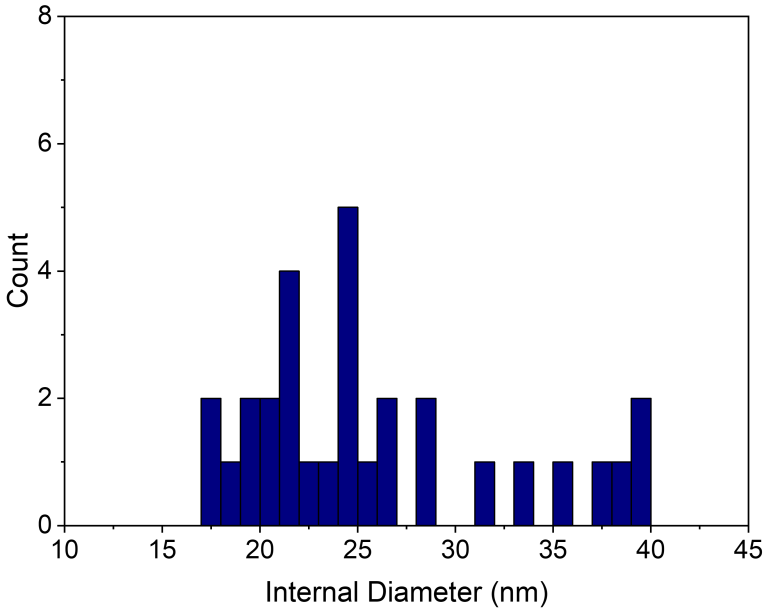



Figure 2.2: Histogram of nanopipette diameters
A histogram showing the internal diameters of the first 30 nanopipettes to be made at the start of the project.

### 2.2.4 Ag/AgCl Electrode Preparation

Electrodes for use on the SICM or for nanopipette characterisation were made in house as needed. For the working electrodes, an approximately 4.3 cm long, 0.25 mm diameter Ag wire (World Precision Instruments, USA) was first immersed in 50 % $HNO_3$ (VWR International, USA) for 30 seconds to remove any contamination or oxide layer from the surface and rinsed in distilled water (Direct-Q 3 UV Water Purification System, Merck KGaA, Germany). AgCl was deposited onto the clean Ag wire in a 1 M $KCl_{(aq)}$ (Sigma-Aldrich, USA) distilled water (Direct-Q 3 UV Water Purification System, Merck KGaA, Germany) solution at room temperature at 0.5 mA for 15 minutes against a second silver counter electrode, using either a Reference 600 Potentiostat (Gamry Instruments, USA) or a CompactStat.e Potentiostat (Alvatek, UK). Equations 2.4 and 2.5 show the redox reactions happening at the anode and cathode respectively during electroplating.

$$Ag_{(s)} + Cl^-_{(aq)} \rightleftharpoons AgCl_{(s)} + e^- \tag{2.4}$$

$$2H^+_{(aq)} + 2e^- \rightleftharpoons H_{2(g)} \tag{2.5}$$

Electrodes were stored at room temperature in air and were used for up to two weeks. If any visible damage to the AgCl coating could be observed the electrode was discarded. For the reference electrode, a 6 cm long, 0.5 mm diameter Ag wire (World Precision Instruments, USA) was electroplated as above.

## 2.3 Atomic Force Microscopy

AFM measurements were carried out to obtain topographical images of the samples prior to testing on the SICM. Four atomic force microscopes were used in total over the course of the project.

During the first year, an Agilent 5500 AFM (Agilent Technologies, USA) was used in tapping mode at room temperature, equipped with a 90 $\mu$m scanner (Keysight Technologies, USA). Silicon cantilevers (NANOSENSORS, Switzerland) 125 $\mu$m long and 30 $\mu$m wide with a tip radius of curvature $<$ 10 nm were oscillated at 327 kHz and scanned at 0.5 - 1 lines $s^{-1}$ to capture images at 1028 lines per frame.

For the majority of the rest of the project, an Innova AFM (Bruker, MA, USA), was used. The Innova AFM broke during the last few months of the project, so an Asylum Research MFP-3D AFM (Oxford Instruments, UK) and a NaioAFM (nanosurf, Switzerland) were used to conclude experiments. The Innova AFM and NaioAFM microscopes were used in tapping mode at room temperature with silicon cantilevers (BudgetSensors, Bulgaria) with an aluminium reflex coating, a resonant frequency of 300 kHz and a force constant of 40 $Nm^{-1}$. The Asylum Research MFP-3D AFM was used in tapping mode at room temperature with silicon cantilevers (Nu Nano Ltd, UK) with an aluminium reflex coating, a resonant frequency of 350 kHz and a spring constant of 42 $Nm^{-1}$. Surfaces were scanned between 0.5 - 2 lines $s^{-1}$, capturing images at either 128 or 256 lines per frame.

## 2.4 Low-Vacuum Scanning Electron Microscopy

Low-vacuum SEM micrographs were collected on a Quanta 650 FEG (FEI, Thermo Fisher Scientific, USA) fitted with a low-field detector and x-ray cone. The pressure was set between 60 - 90 Pa, with an accelerating voltage of 3 - 5 kV; 60 Pa and 5 kV were the defaults which were altered if charging was observed on the surface. All materials were placed in a vacuum desiccator for at least one week prior to imaging.

The Quanta 650 FEG was fitted with an XFlash 6-60 detector (Bruker, USA) for EDX analysis. EDX analysis was performed in continuous capture mode using Esprit 2.1 software (Bruker, USA) until a sufficient signal had been captured for the area, typically 10 - 15 minutes.

# Chapter 3

# Carbonates

## 3.1 Overview

Carbonate reservoirs are of particular interest as they hold the majority of the world's oil and gas reserves.[90,91] Three carbonate outcrop rocks are investigated in this Chapter; Ketton, Estaillades and Indiana, each having a calcite content $> 90$ %, but with morphological and other chemical[a] differences.[92,93,96,97] A pure calcite crystal has also been included in these studies for reference and comparison. In this work these morphological differences have been studied with low-vacuum SEM, SICM and AFM. Starting with the SEM micrographs, distinct surface types on each rock surface will be characterised, such that areas of similar descriptions can be identified from the SICM and AFM images. This approach provides a means to confirm SICM's suitability for these materials, and places the smaller SPM images from SICM and AFM into the wider field of view which low-vacuum SEM provides.

[a] a more detailed description of their chemical compositions was given in Chapter 1: *Introduction*, in Table 1.1 on page 73

## 3.2 Low-Vacuum Scanning Electron Microscopy

Low-vacuum SEM was used to gain an overview of the range of visible surface types across the different carbonates studied. The benefit of performing these experiments in low-vacuum instead of the standard "high-vacuum", was so that these non-conductive materials did not require coating prior to investigation, leaving the surface structure un-altered. Previous SEM work in the literature on Ketton, Estaillades and Indiana has been scarce; the literature predominantly focusing on micro-CT studies to provide images of the pore space.[21,25,105,106] Additionally, the SEM work which has been presented has either been at comparatively low magnification,[92,107,108] altered through conductive-layer coating, polishing and/or setting in a resin,[107,108] or has only shown one or *sometimes* two surface types, not providing the full picture of the heterogeneity present.[20,92,94,107,108] The work presented in this thesis provides new insights compared to previous SEM studies, as imaging is performed at high magnification, showcasing the heterogeneity of these materials, and is performed on minimally altered surfaces; the only alteration was the cutting of the cores, effects of which are accounted for during analysis of the micrographs.

### 3.2.1 Calcite

Calcite was studied as a model system to compare with the more "complex" carbonate rocks: Ketton, Estaillades and Indiana, as calcite is the main component in each. Calcite has trigonal symmetry, space group $R\bar{3}c$: a diagram of the calcite unit cell is shown in Figure 3.1.[109] The unit cell can be understood as a stack of four trigonal structures, shown on the right of Figure 3.1, where in each structure

the molecules or atoms in lattice position A are all the same, but different to the molecules or atoms in lattice position B, which are also all the same as each other. In each case, the $CO_3$ molecule which is on the diagonal dotted line is orientated in the opposite direction to the $CO_3$ molecule in the plane above or below. When a calcite crystal is cleaved it will produce a flat surface if cleaved parallel to a Ca plane, but will reveal a rougher surface if cleaved otherwise.

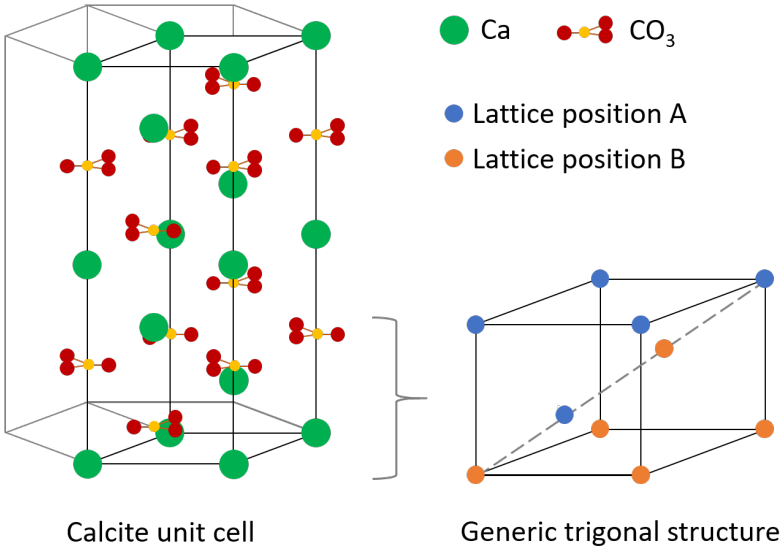



Figure 3.1: Crystal structure of calcite
The calcite unit cell (left) is made up of four trigonal structures (right). These unit cells stack together along the grey lines shown. Redrawn from 109

Figures 3.2 and 3.3 show two sets of four low-vacuum SEM micrographs overlain to create a wider field of view, of two different cleaved calcite crystal surfaces. The calcite crystal in Figure 3.2 has a few different surface types visible on the surface, labelled 1 - 3 on the image, and are all likely to be the result of different cleavage angles. The second calcite crystal studied, shown in Figure 3.3, has a much flatter surface than the crystal surface shown in Figure 3.2, but with some imperfections. These imperfection features are assigned as surface type 4, with two such areas labelled A and B on the overlay.

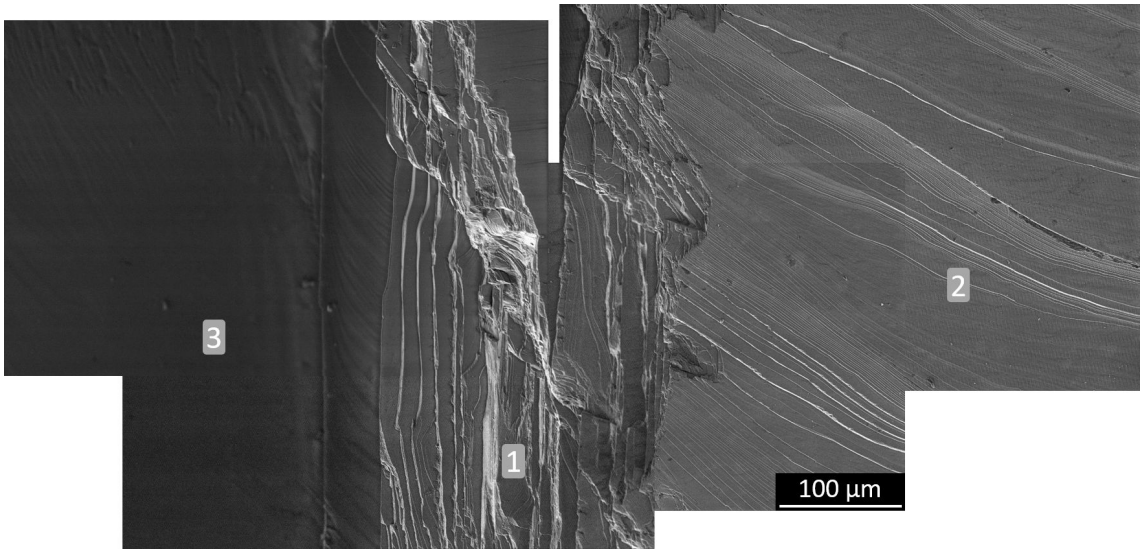



Figure 3.2: Calcite: SEM Overlay 1
An overlay of four low-vacuum SEM micrographs of a cleaved calcite crystal, with numbers labelling different surface types of interest. The individual micrographs which make up this overlay can be found in Appendix B, Figures B.1 - B.4.

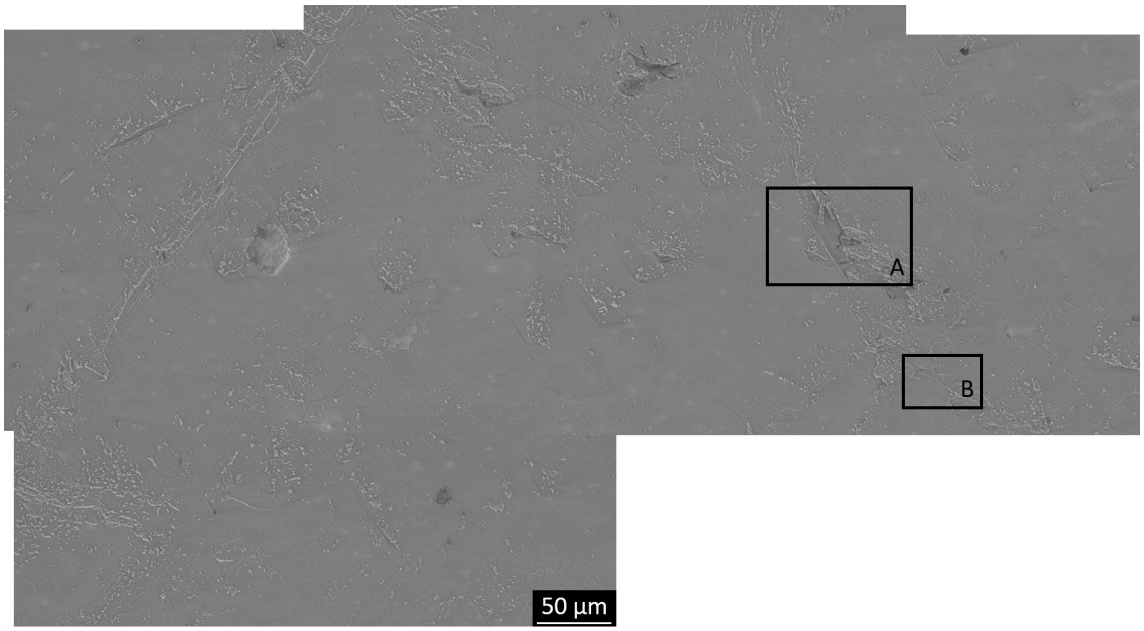



Figure 3.3: Calcite: SEM Overlay 2
A second overlay of four low-vacuum SEM micrographs of a cleaved calcite crystal, with A and B labelling different surfaces of interest. The individual micrographs which make up this overlay can be found in Appendix B, Figures B.5 - B.8.

Calcite surface type 1, as labelled on Figure 3.2, is shown at higher magnification in Figure 3.4 and is visually the roughest surface type captured in Figure 3.2. Surface type 1 likely represents section of calcite which has likely been cleaved almost

perpendicularly to the Ca planes, revealing numerous layers of calcite with irregular edges. When calcite is cleaved parallel to the Ca planes, near entirely smooth surfaces can be obtained; an AFM image of one such example was reported in the literature by Savulescu *et al.*, for comparison.[22] However, this fractured structure is not unlikely to appear in calcite structures in reservoirs, where the rocks have been subjected to damage during drilling or extraction, as fractures will not have exclusively occurred along the Ca planes in the crystal structure.

The second labelled area in 3.2, calcite surface type 2, is shown at higher magnification in Figure 3.5. This section of the calcite surface appears to have been cleaved at a shallower angle relative to the Ca planes than those in calcite surface type 1; individual layers are visible but a reasonably flat surface appears to have been produced. The third labelled area visible in Figure 3.2 is an almost perfectly flat surface; the calcite in this area appears to have been cleaved parallel to the Ca plane, producing a smooth layer underneath.

Calcite surface types 4a and 4b, shown in Figures 3.6a and 3.6b respectively, do not present the same large areas of step-like structures visible in calcite surface types 1 and 2. However, in calcite surface type 4a there appears to have been some damage to the surface resulting in a small dent, exposing an area with a step-like structure, likely due to a few layers of calcite being removed close to the surface. In calcite surface type 4b the damage to the surface is even shallower, with no clear step-like structures at all; small dents and raised areas on the surface are visible where chunks of calcite layers have been removed, or remained after cleavage.

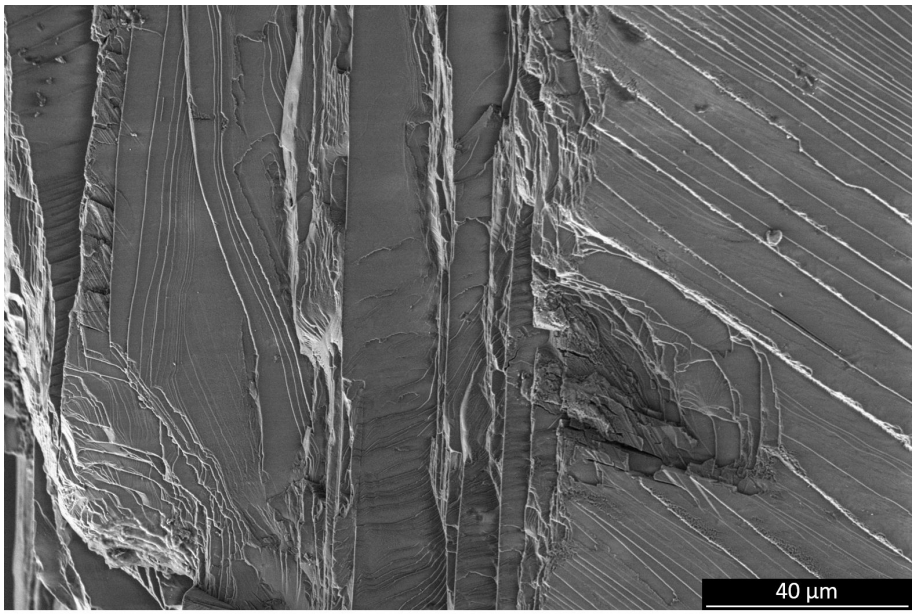



Figure 3.4: Calcite: high magnification SEM micrograph of surface type 1
A higher magnification low-vacuum SEM micrograph of surface type 1 as labelled in the overlay in Figure 3.2

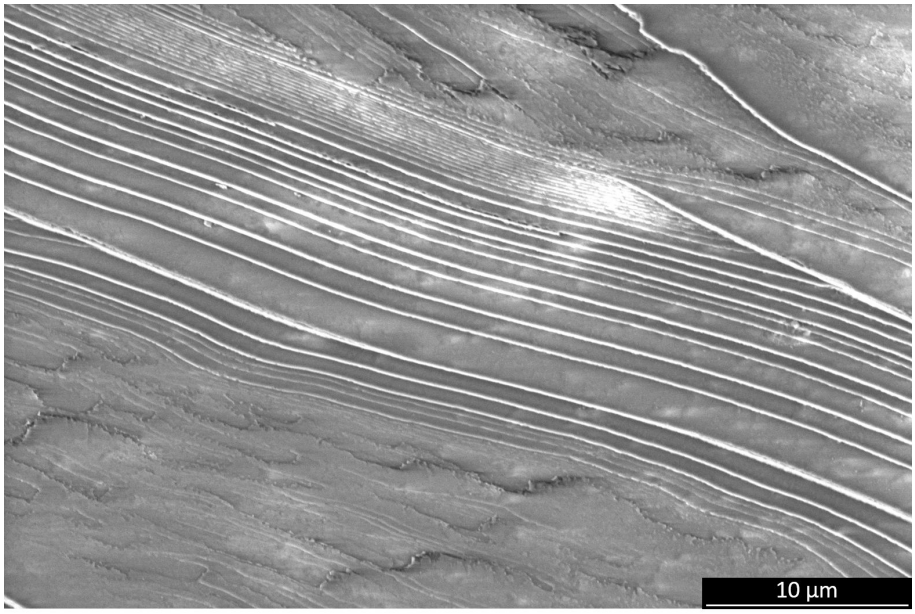
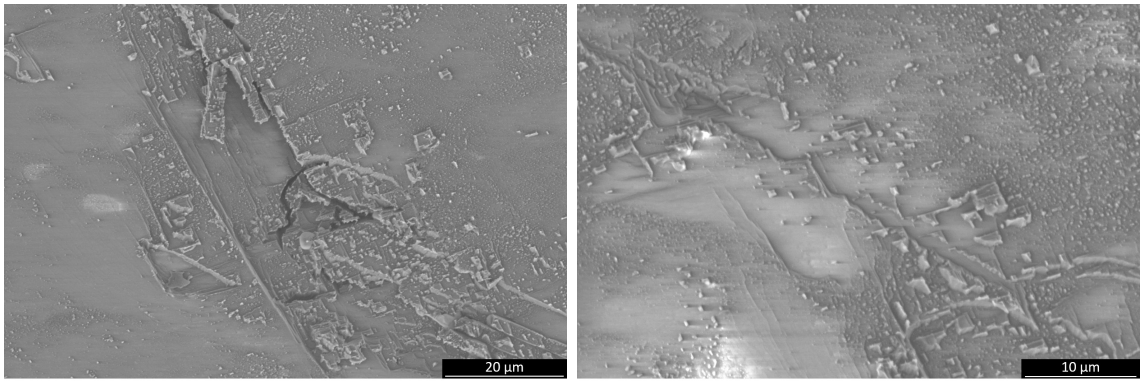



Figure 3.5: Calcite: high magnification SEM micrograph of surface type 2
A higher magnification low-vacuum SEM micrograph of surface type 2 as labelled in the overlay in Figure 3.2




(a) Calcite surface type 4a (b) Calcite surface type 4b

Figure 3.6: Calcite: high magnification SEM micrographs of surface type 4
Two higher magnification low-vacuum SEM micrograph of surface type 4, (a) showing A and (b) showing B as labelled in the overlay in Figure 3.3.

A summary of the four calcite surface types observed across the surfaces in Figures 3.2 and 3.3 is given in Table 3.1. Areas similar to all these surface types are anticipated to be found on calcite surfaces in carbonate reservoirs, and indeed served as a guide in this Chapter when proceeding to the investigation of the more complex carbonate surfaces of Ketton, Estaillades and Indiana.

| Type | Description | Feature size range |
|---|---|---|
| 1 | Deep step-like structures caused by cleavage diagonal to crystal planes | $> 10$ $\mu$m |
| 2 | Shallow step-like structures caused by cleavage diagonal to crystal planes | $< 10$ $\mu$m |
| 3 | Flat regions from cleavage parallel to crystal planes | N/A |
| 4 | Dent from cleavage almost parallel to crystal planes | 5 - 16 $\mu$m |

Table 3.1: Summary of the calcite surface types
A summary of the different surface types identified on the calcite samples: qualitative descriptions of the surfaces and estimated feature size ranges are given based on information from the low-vacuum SEM micrographs.

### 3.2.2 Ketton

Ketton's ooid structure is well-established in the literature,[20,92] and can be clearly seen in the low-vacuum SEM micrograph overlays in Figures 3.7 and 3.8, where a selection of low-vacuum SEM micrographs have been stitched together to form larger fields of view of two different areas on the surface of this material. Figures 3.9 - 3.15 present a set of higher magnification images from these two overlays, showcasing a number of different surface types which have been labelled 1-5 in Figure 3.7, with a further surface type 6 identified in Figure 3.8.

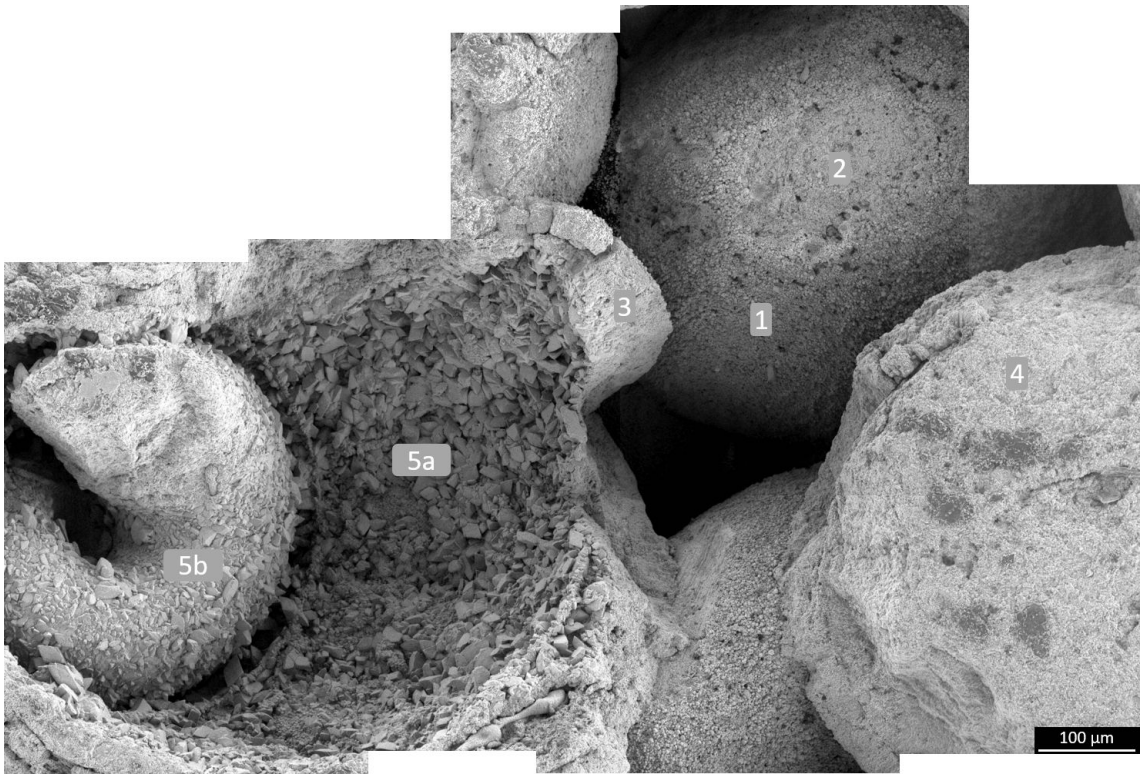



Figure 3.7: Ketton: SEM Overlay 1
An overlay of selected low-vacuum SEM micrographs of Ketton rock, with numbers labelling the different surface types of interest. Individual images can be found in Appendix B, Figures B.37 - B.42.

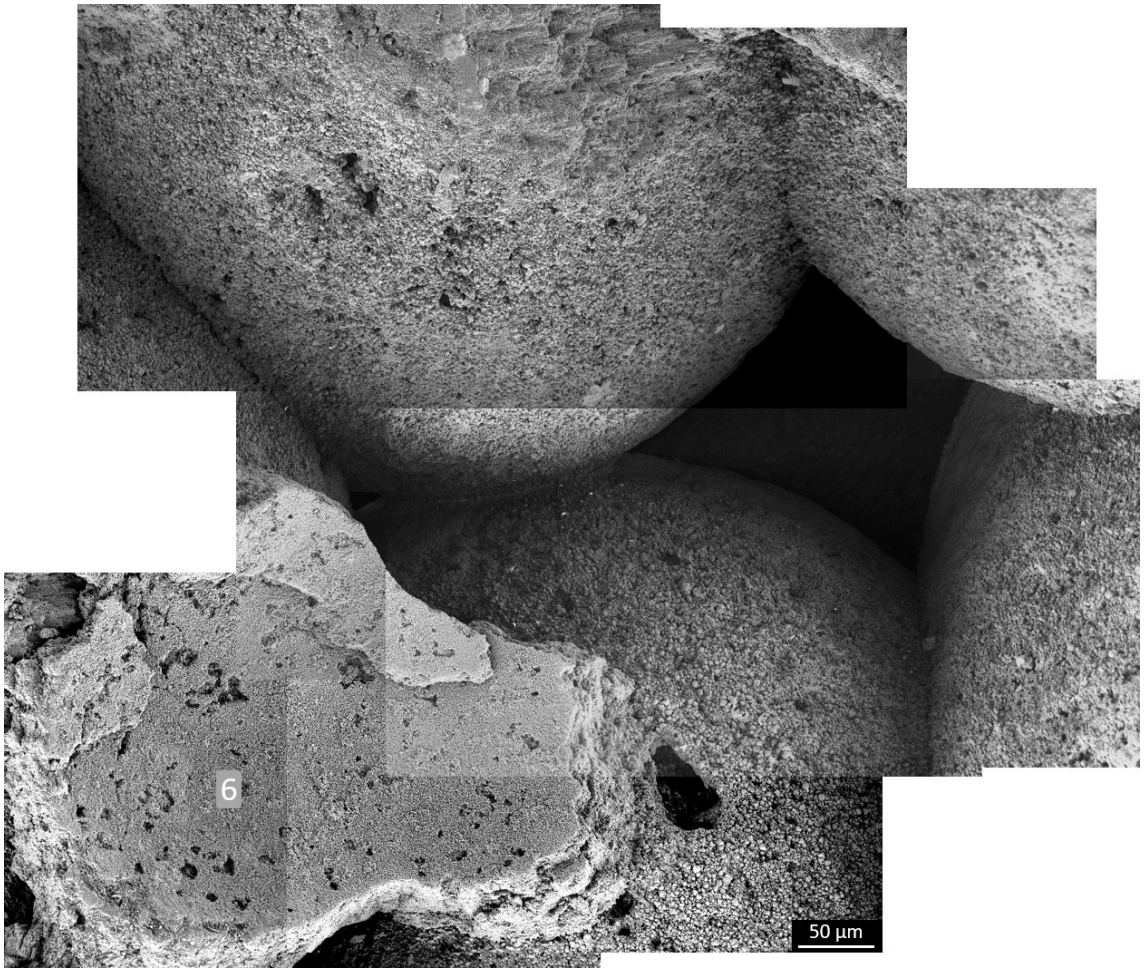



Figure 3.8: Ketton: SEM Overlay 2
An overlay of low-vacuum SEM micrographs of Ketton rock; an additional Ketton surface type not observable in Figure 3.7 is labelled "6" in this Figure. Individual images can be found in Appendix B, Figures B.43 - B.49.

In both of the low-vacuum SEM Ketton overlays shown in Figures 3.7 and 3.8, gaps between the grains can be observed as being on the order of magnitude of 50 - 100 $\mu$m across, which represents the larger pore space in these materials. In addition to this pore network, the grains themselves also have a nanoporosity which becomes more evident in the higher magnification images presented in Figures 3.9 - 3.15. This dual-porosity has also been reported in the literature by Menke *et al.*, who showed their Ketton sample had two common size ranges of pore throat radii via Mercury injection tests; one around 10 - 100 nm and the other around 10 - 50 $\mu$m.[106]

Surface type 1 in Figure 3.7 appears to be the surface of an intact Ketton ooid grain, sitting deep enough into the surface that it has not been affected in the cutting processes involved in sample preparation. Figure 3.9 shows a micrograph of this surface type at higher magnification and its intersection with surface type 2. This second Ketton surface type visible towards the right of Figure 3.9, labelled "2" in Figure 3.7, is proposed to be the result of where another ooid grain previously sat, presumably snapped off during the cutting stage of sample preparation. Figure 3.10 shows a micrograph of this cleaved area at higher magnification than Figure 3.7, where it can be seen that surface type 2 is much rougher than surface type 1. It appears that sharper structures have formed between the two ooid grains, covering the smoother crystallites underneath.

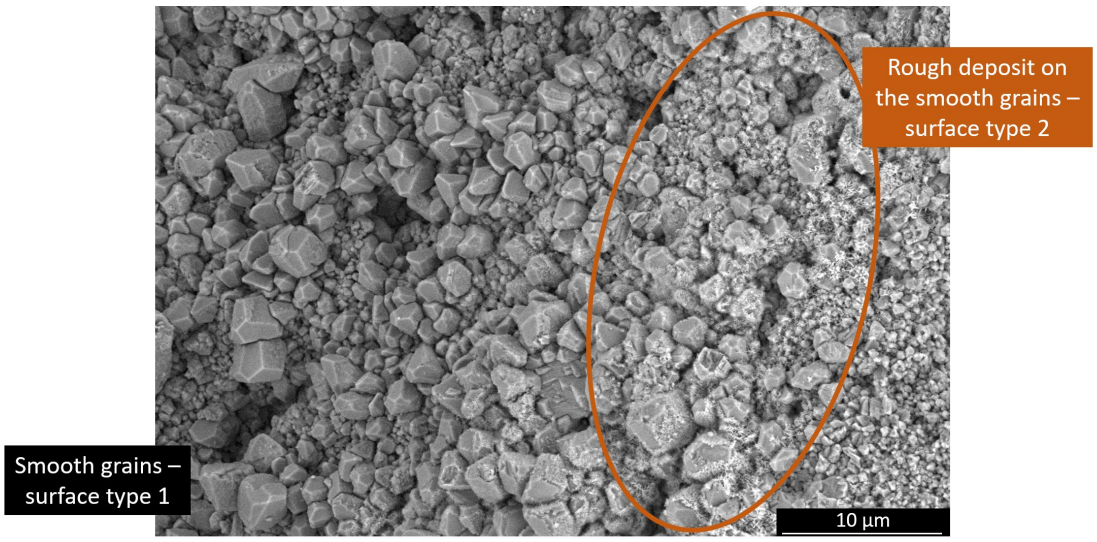



Figure 3.9: Ketton: high magnification SEM micrograph of surface types 1 and 2
A high magnification low-vacuum SEM micrograph of the intersection between Ketton surface types 1 and 2 as defined in Figure 3.7; the intact ooid grain surface towards the left, and the rougher area resulting from where a second grain used to sit towards the right.

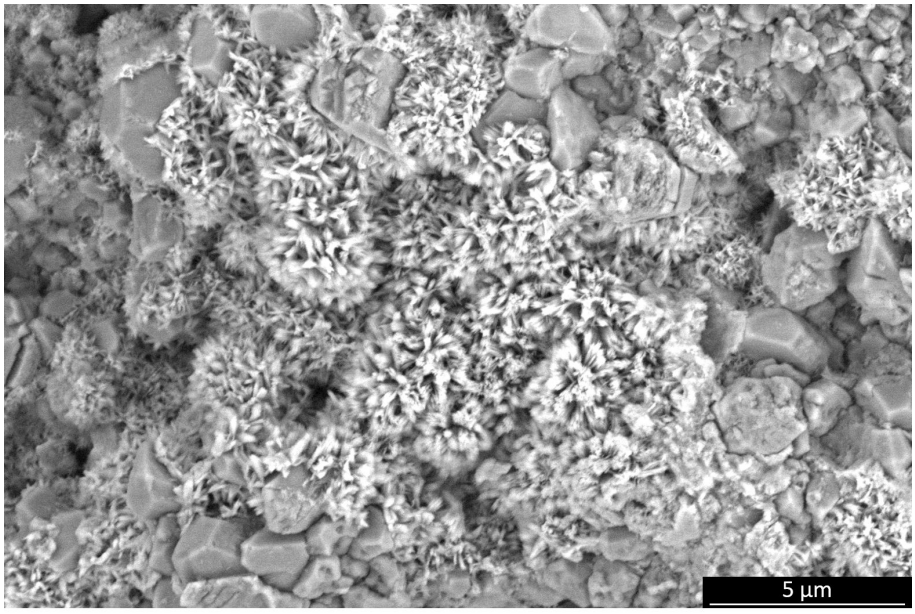
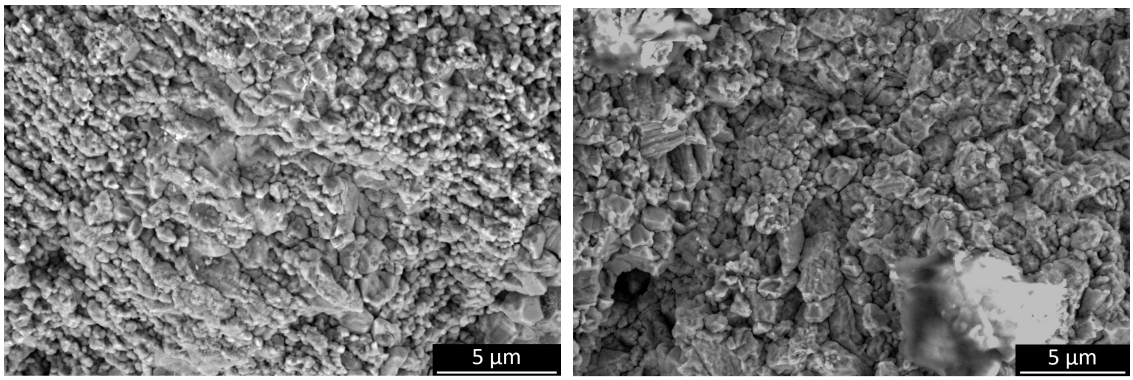



Figure 3.10: Ketton: high magnification SEM micrograph of surface type 2
A high magnification micrograph of Ketton surface type 2 as defined in Figure 3.7; the structures which formed upon contact with another grain, which is assumed to have been removed during the cutting stage of sample preparation.

Ketton surface types 3 and 4, as labelled in Figure 3.7, appear to be fractured ooid grain shell surfaces, but fractured from different angles, as they appear to be similar to each other in structure, with smooth crystallites approximately 1 $\mu$m across. This similarity is illustrated in Figure 3.11 where high magnification low-vacuum SEM micrographs of the two surface types are presented side by side. Figure 3.12 shows surface type 3 at a lower magnification than in Figure 3.11, such that the full cross-section of the fractured ooid grain shell can be clearly seen. What was previously the external surface of the ooid grain can be seen towards the right hand side of the image, where larger crystallites are present, similar those observed in surface type 1 (Figure 3.9), whilst the exposed inside of the grain can be seen in the top left. Concentric lines can be seen in this outer shell, which aligns with how these structures are understood to have formed, with layers of small calcite crystals

depositing over years to progressively grow the spherical ooid structure outwards, as described in Section 1.7.1 of Chapter 1: *Introduction.*[95] Surface type 4 appears to be a "face on" view of a fractured ooid grain shell, shown at higher magnification in Figure 3.13. It is likely that surface type 4 was generated by cutting the outer grain surface, removing surface type 1, to reveal the smaller crystallites underneath. Surface type 4 is thus only showing a handful of layers, whereas surface type 3 is showing tens of layers which make up the ooid shell.




(a) Ketton surface type 3 (b) Ketton surface type 4

Figure 3.11: Ketton: high magnification SEM micrographs of surface types 3 and 4
High magnification low-vacuum SEM micrographs of Ketton surface types 3 and 4, as defined in Figure 3.7, proposed to be exposed ooid grain shell surfaces.

Ketton surface types 5a and 5b sit inside of the fractured ooid grain shown in the lower left hand corner of the first overlay (Figure 3.7, page 97), and have similar structures. Both show larger crystallite sizes than seen in the shell cross-section or on the surface of the ooid, as can be seen from the high magnification micrograph in Figure 3.14. The crystallites inside this grain are quite varied in size, the largest in view measuring 15 $\mu$m across, whilst the smallest only measuring 1 $\mu$m. This is in contrast to the surface of the ooid grain where the crystallites are more regular in size and shape, commonly 0.5 - 4 $\mu$m across, and the shell itself comprised of

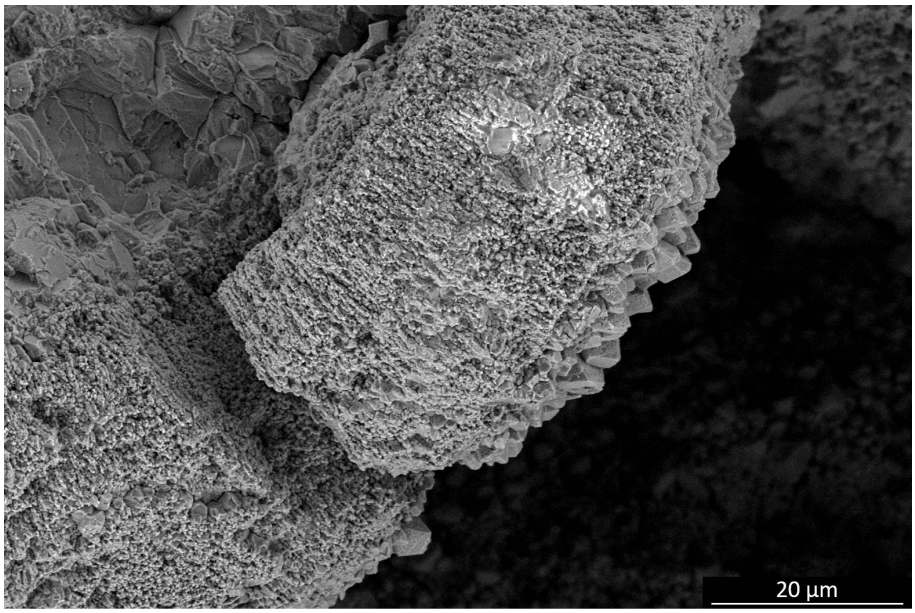



Figure 3.12: Ketton: high magnification SEM micrograph of surface type 3
A high magnification low-vacuum SEM micrograph of Ketton surface type 3 as defined in Figure 3.7; the cross-section of the outer shell of a fractured Ketton grain. This image is rotated 90° clockwise relative to Figure 3.7.

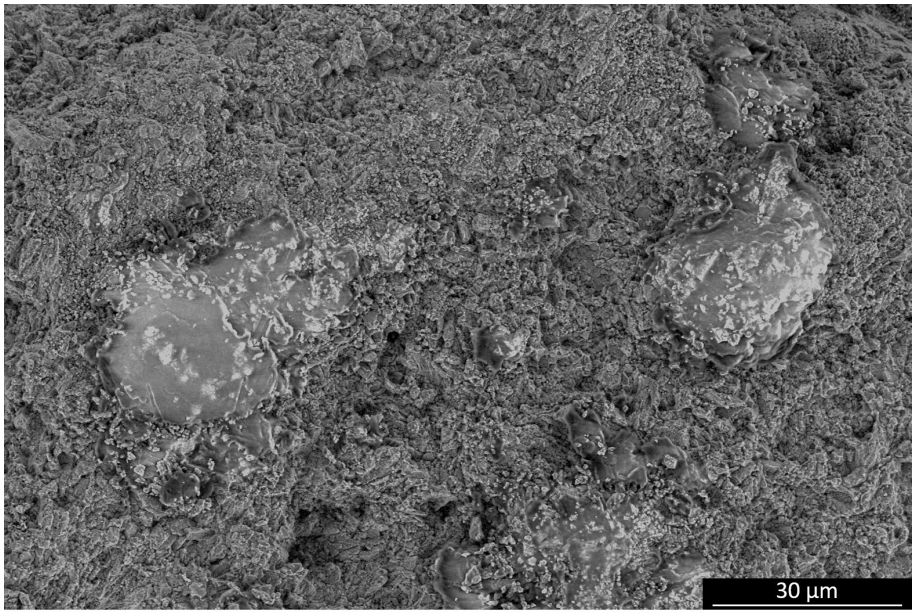



Figure 3.13: Ketton: high magnification SEM micrograph of surface type 4
A high magnification low-vacuum SEM micrograph of Ketton surface type 4 as defined in Figure 3.7; the surface of a fractured ooid grain shell.

crystallites $< 1$ $\mu$m across. The labelled surface type 5b is not particularly different to surface type 5a in terms of surface structure, but the bulk structure itself seems to have grown in a spiral shape, not a sphere as expected in ooids. There is a small gap between surface type 5b and the rest of the ooid; it is hypothesized that this spiral structure formed inside the shell of a microscopic organism, the shell then dissolving to leave this gap. It is also possible that this shell was the nucleus for this particular ooid's growth.

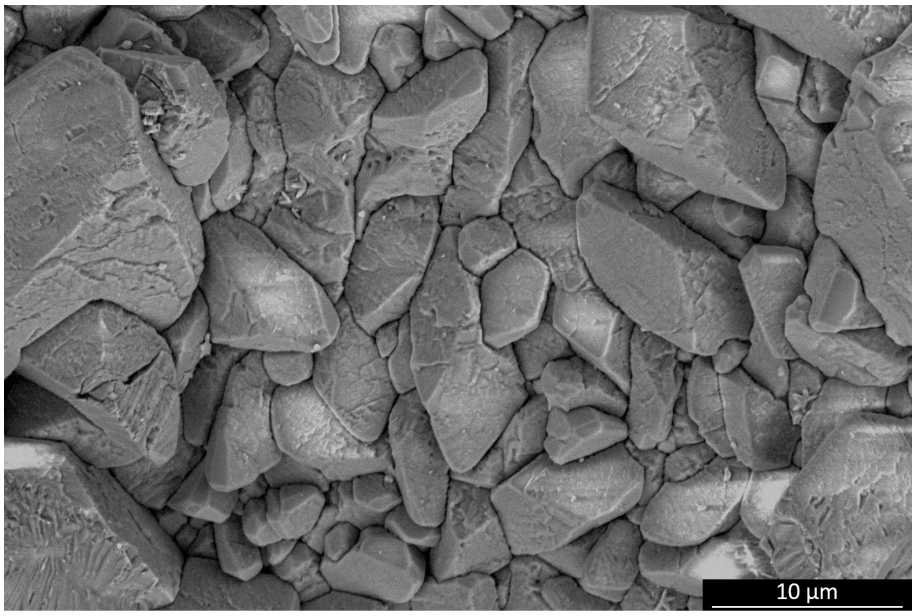
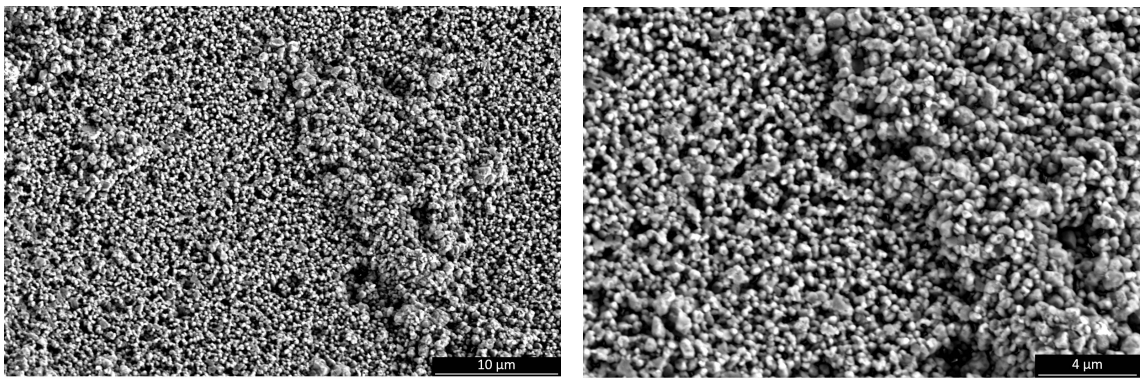



Figure 3.14: Ketton: high magnification SEM micrograph of surface type 5
A high magnification low-vacuum SEM micrograph depicting an example of surface type 5 as defined in Figure 3.7; the inside of the ooid grain shell.

The second low-vacuum SEM micrograph overlay for the Ketton sample, Figure 3.8 (page 98), shows a sixth surface type. In the first overlay in Figure 3.7 (page 97), the open ooid grain present has large crystallites inside, which make up surface types 5a and 5b. Figure 3.8 also shows an open ooid grain structure, however this larger crystallite layer of surface type 5 is missing. From the higher magnification images of this region, shown in Figure 3.15, the structure appears to be similar to that seen

in surface types 3 and 4, with crystallite sizes $< 1$ $\mu$m. This suggests that this is an internal view of an ooid grain shell, as opposed to the cross section, surface type 3 (Figure 3.12) or the outer view, surface type 4 (Figure 3.13), which perhaps used to have a larger crystallite layer on top, such as surface type 5, which would have then been removed during sample preparation.




(a) (b)

Figure 3.15: Ketton: high magnification SEM micrographs of surface type 6
High magnification low-vacuum SEM micrographs of Ketton surface type 6, as defined in Figure 3.8; the inside of the ooid grain shell, as perhaps one might find underneath surface type 5.

Overall, Ketton presented six distinct surface types, a summary of which can be found in Table 3.2. The largest pores in these ooid structures occur from the network of gaps between the grains, and so this is where the majority of the fluid flow will likely be during oil extraction through these types of materials. The most important fluid-solid interactions to understand for predicting fluid flow will therefore occur with the external surfaces of these ooid grains, so predominantly surface type 1, but also the damaged external surface type 2 and fractured surface type 4. Given that Ketton grains themselves are also porous, there will also be flow across surface types 3, 5 and 6, so understanding the fluid-solid interactions with these surfaces will also be of use in predicting reservoir behaviour, even if they play a lesser role due to

the pore sizes being much smaller. The heterogeneity shown here on the surfaces of these grains, in addition to the complex pore geometries which form between the ooid grains, demonstrates the clear need for characterisation of this material across multiple length scales in order to fully understand fluid flow behaviour within its structure.

| Type | Description | Feature size range |
|---|---|---|
| 1 | Intact ooid grain surface, covered with smooth crystallites | 0.5 - 4 $\mu$m |
| 2 | Ooid grain surface with spikey structures on top | 0.5 - 4 $\mu$m with $< 1$ $\mu$m spikes |
| 3 | Ooid grain shell cross-section, irregular crystallites | $< 1$ $\mu$m |
| 4 | Fractured ooid grain shell exterior, irregular crystallites | $< 1$ $\mu$m |
| 5 | Large crystallites inside of ooid grain | 1 - 15 $\mu$m |
| 6 | Fractured ooid grain shell interior, irregular crystallites | $< 1$ $\mu$m |

Table 3.2: Summary of the Ketton surface types
A summary of the different surface types identified on the Ketton sample: qualitative descriptions of the surfaces and estimated feature size ranges are given based on the information provided by the low-vacuum SEM micrographs.

### 3.2.3 Estaillades

Low-vacuum SEM micrographs were collected of two areas on an Estaillades surface, with a selection of these micrographs overlain to create two larger images, shown in Figures 3.16 and 3.17. These overlays give wider fields of view of the rock surface, where four different surface types have been identified and labelled in both Figures.

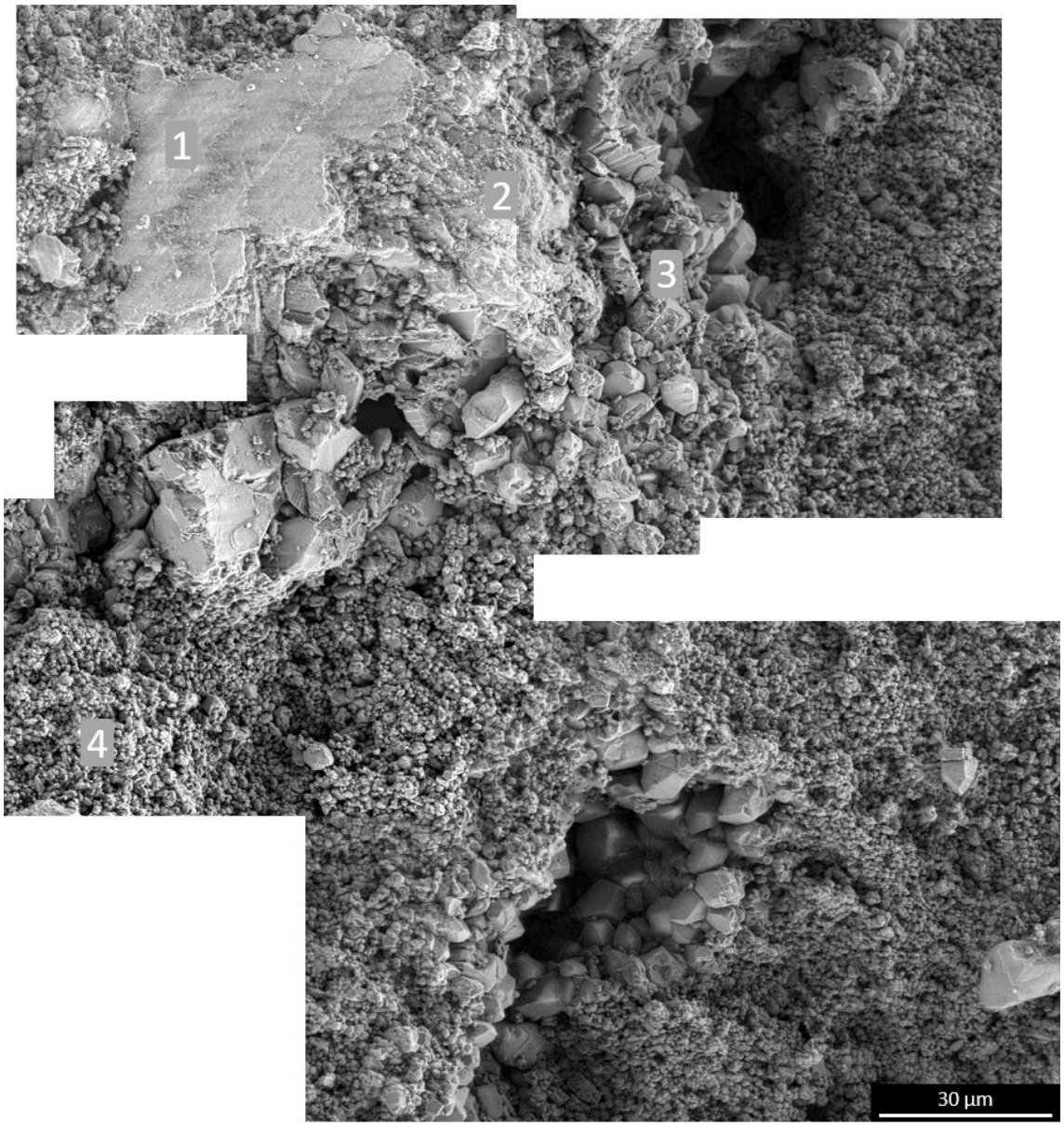



Figure 3.16: Estaillades: SEM Overlay 1
An overlay of low-vacuum SEM micrographs of Estaillades rock. Numbers label examples of the different surface types observed on the surface. Individual images can be found in Appendix B, Figures B.50 - B.55.

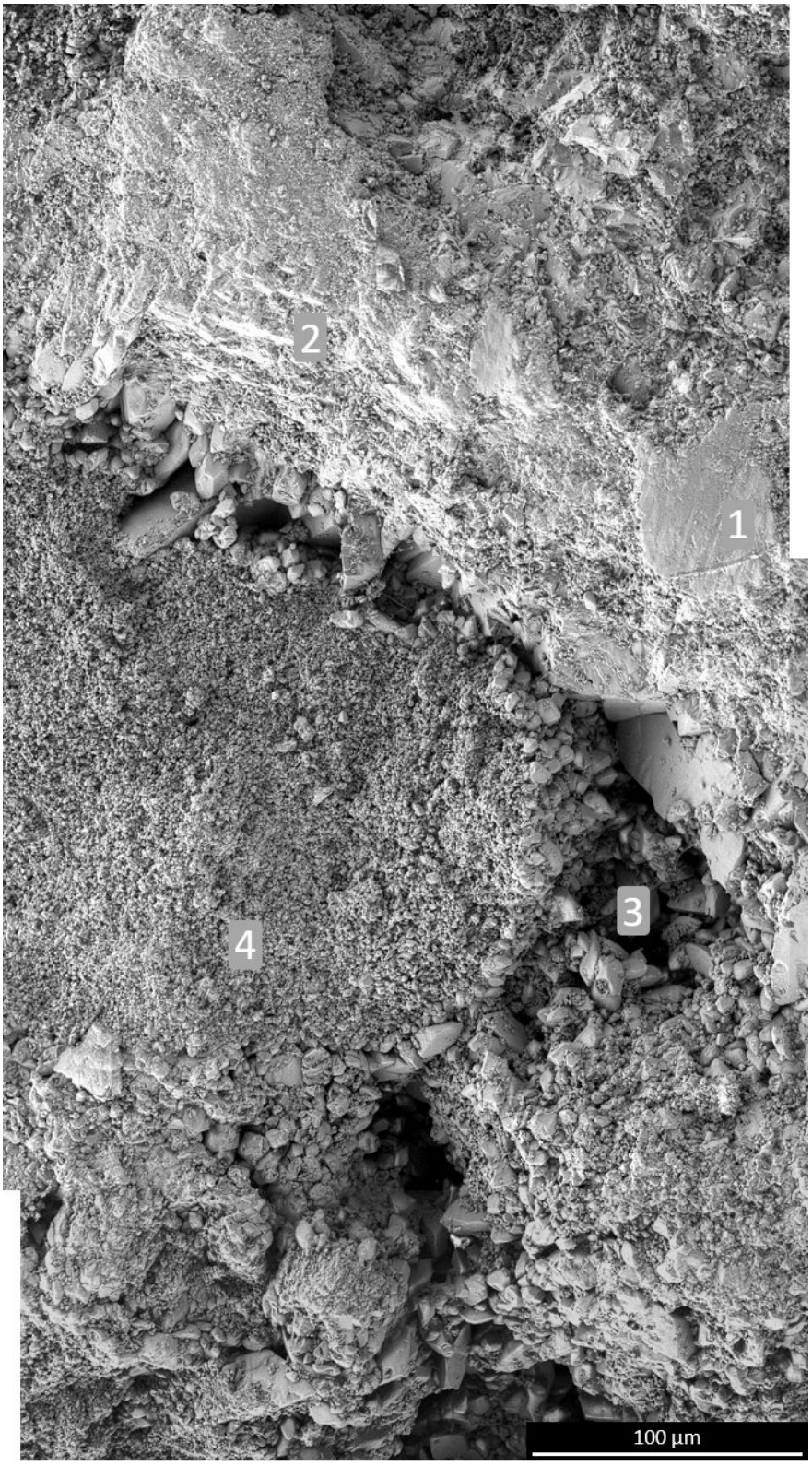



Figure 3.17: Estaillades: SEM Overlay 2
An additional overlay of two low-vacuum SEM micrographs of Estaillades rock, with numbers equivalent to those in 3.16 labelling examples of the different surface types observed on the surface. Individual images can be found in Appendix B, Figures B.56 and B.57.

Upon initial observation of Figures 3.16 and 3.17, surface types 1 and 2 are hypothesized to be artificially generated surfaces. Surface type 1 is much flatter and smoother than the rest of the visible surface of the material, as shown at higher magnification in Figure 3.18. It is proposed that this surface type 1 was generated during the cutting stage of sample preparation, which is supported by it appearing to be the most elevated section of the visible surfaces in both overlays. Surface type 2, shown in greater detail in Figure 3.19, which is found adjacent to surface type 1 in both overlays, is proposed to be a rougher product of the cutting process, where the surface structures have shattered next to the cleaved area, surface type 1, to produce a sort of calcite "rubble".

Estaillades surface types 3 and 4 are shown in greater detail in Figures 3.20 and 3.21 respectively, and both represent surfaces containing crystallites of similar sizes with smooth faces and edges. The distinction between surface types 3 and 4 comes from the crystallite sizes present in each region. Surface type 4 exclusively shows the smaller crystallites, on the order of 1 - 2 $\mu$m in size, whereas surface type 3 contains larger crystallites, 5 - 10 $\mu$m across, in addition to the smaller crystallites. Figure 3.20 shows two sub-types present in surface type 3; the larger crystallites in sub-type 3a (Figure 3.20a) are similar in shape to the crystallites seen in surface type 4, whereas sub-type 3b (Figure 3.20b), shows an almost step-like formation on some of the crystallite surfaces. These "steps" could be similar to the calcite surface type 1 previously observed (Figure 3.4, page 95), and would therefore be the result of the calcite crystallite being cleaved such that the crystal plains become visible.

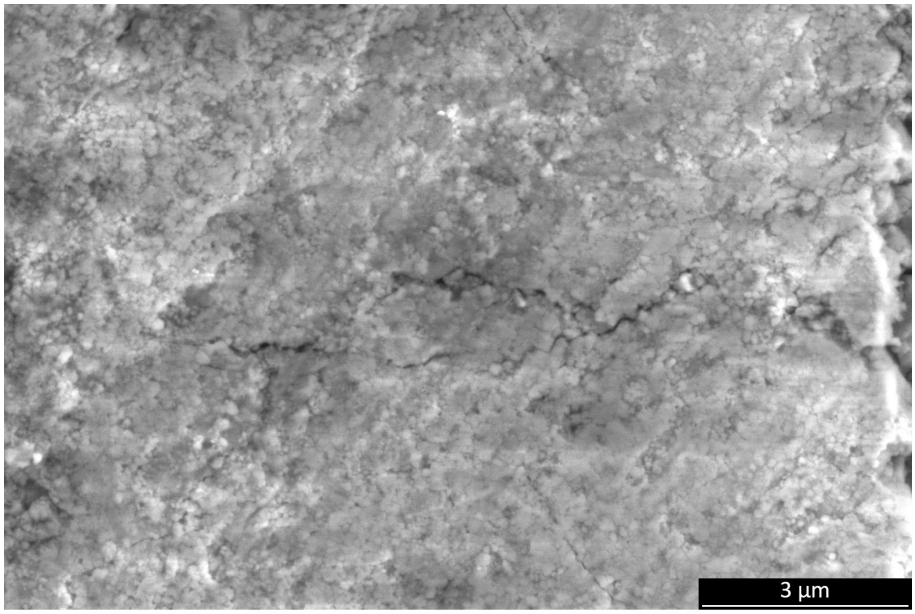



Figure 3.18: Estaillades: high magnification SEM micrograph of surface type 1
A high magnification low-vacuum SEM micrograph of Estaillades surface type 1 as defined in Figures 3.16 and 3.17; a cleaved surface likely generated during the cutting stage of sample preparation.

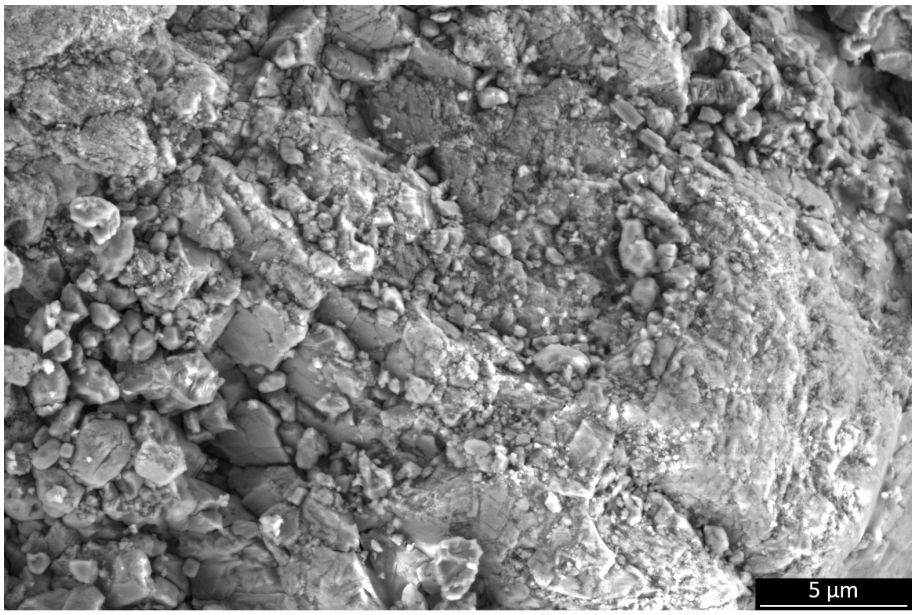
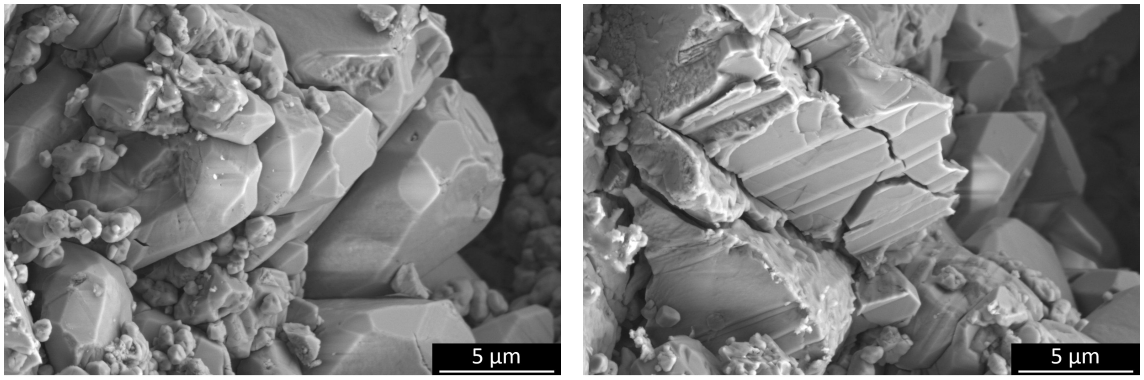



Figure 3.19: Estaillades: high magnification SEM micrograph of surface type 2
A high magnification low-vacuum SEM micrograph of Estaillades surface type 2 as defined in Figures 3.16 and 3.17, which is proposed to be a residue produced during cutting, sitting adjacent to the cleanly cleaved sites making up Estaillades surface type 1.




(a) (b)

Figure 3.20: Estaillades: high magnification SEM micrographs of surface type 3
Two high magnification low-vacuum SEM micrograph of Estaillades of the two sub-types within surface type 3. (a) Represents sub-type 3a, the larger crystallites being similar in shape to the smaller crystallites. (b) Represents sub-type 3b which has a "step" formation visible on the surface

Table 3.3 summarises the four surface types identified for the Estaillades surface. Surface types 3 and 4 are likely to be "natural" areas, left un-altered by the cutting process due to their being deeper into the structure. Since these surface types are assumed to be un-altered, they are therefore likely to be the more representative and relevant surfaces when compared to the "real" surfaces in reservoirs for oil recovery applications. Surface types 1 and 2, despite being proposed to be artificially generated, are still of interest for fluid flow predictions, as similar surfaces may form in reservoirs when rocks are fractured. In addition to their role in fluid-flow modelling, all of these surface types are important to identify, such that the topographical images generated in the SICM and AFM could be appropriately assessed in Sections 3.3.3 and 3.4.2 later in this chapter.

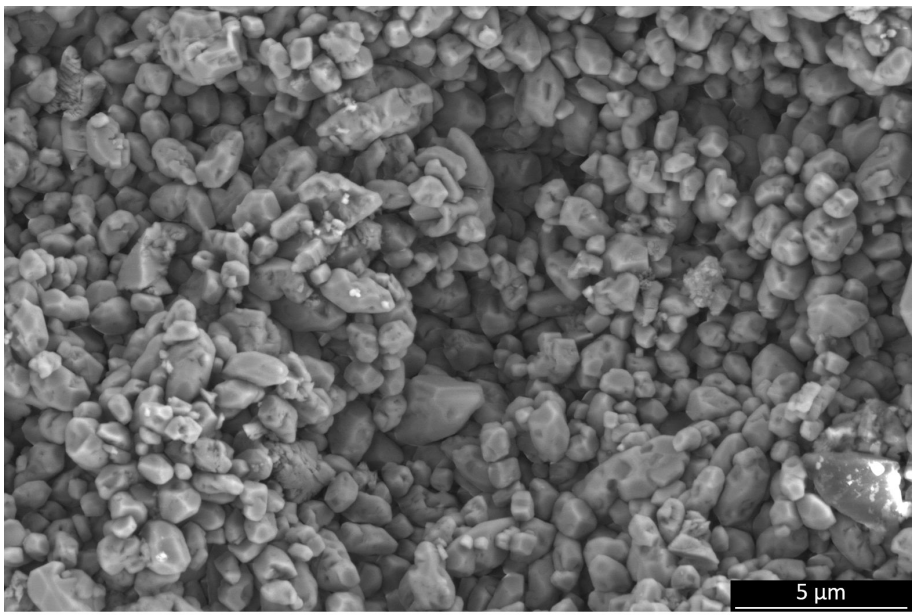



Figure 3.21: Estaillades: high magnification SEM micrograph of surface type 4
A high magnification low-vacuum SEM micrograph of Estaillades surface type 4, showing small crystallites similar in shape to those seen in surface type 3a (Figure 3.20a).

| Type | Description | Feature size range |
|---|---|---|
| 1 | Flat regions caused by cutting during sample preparation | N/A |
| 2 | Fractured regions adjacent to flat regions, result of cutting | 0.5 - 2 $\mu$m |
| 3a | Large, intact crystallites | 5 - 10 $\mu$m |
| 3b | Large crystallites, fractured to reveal a step-like structure | |
| 4 | Small, intact crystallites | 1 - 2 $\mu$m |

Table 3.3: Summary of the Estaillades surface types
A summary of the different surface types identified on the Estaillades sample: qualitative descriptions of the surfaces and estimated feature size ranges are given based on the information provided by the low-vacuum SEM micrographs.

### 3.2.4 Indiana

Indiana, the third carbonate outcrop rock investigated, was also studied using low-vacuum SEM. Figure 3.22 shows an overlay of a selection of the SEM micrographs collected, where five surface types of interest have been identified and labelled. Figure 3.23 shows a low magnification micrograph of a second region on the surface of Indiana where these five surface types can also be observed, and are labelled once more for clarity.

As was observed on the Ketton and Estaillades surfaces, the more elevated regions on the surface of Indiana appear to have been cleaved during the cutting stage of sample preparation. These areas are not as flat on the Indiana surface as were seen in Ketton surface type 3 (Figure 3.12, page 102) or Estaillades surface type 1 (Figure 3.18, page 109), however as can be seen more clearly from the higher magnification SEM micrograph in Figure 3.24, Indiana surface type 1 is one of the flatter areas visible on the surface of the Indiana sample. The small criss-crossing straight lines are proposed to be edges of calcite crystal planes, although they could also be a result of the cutting process.

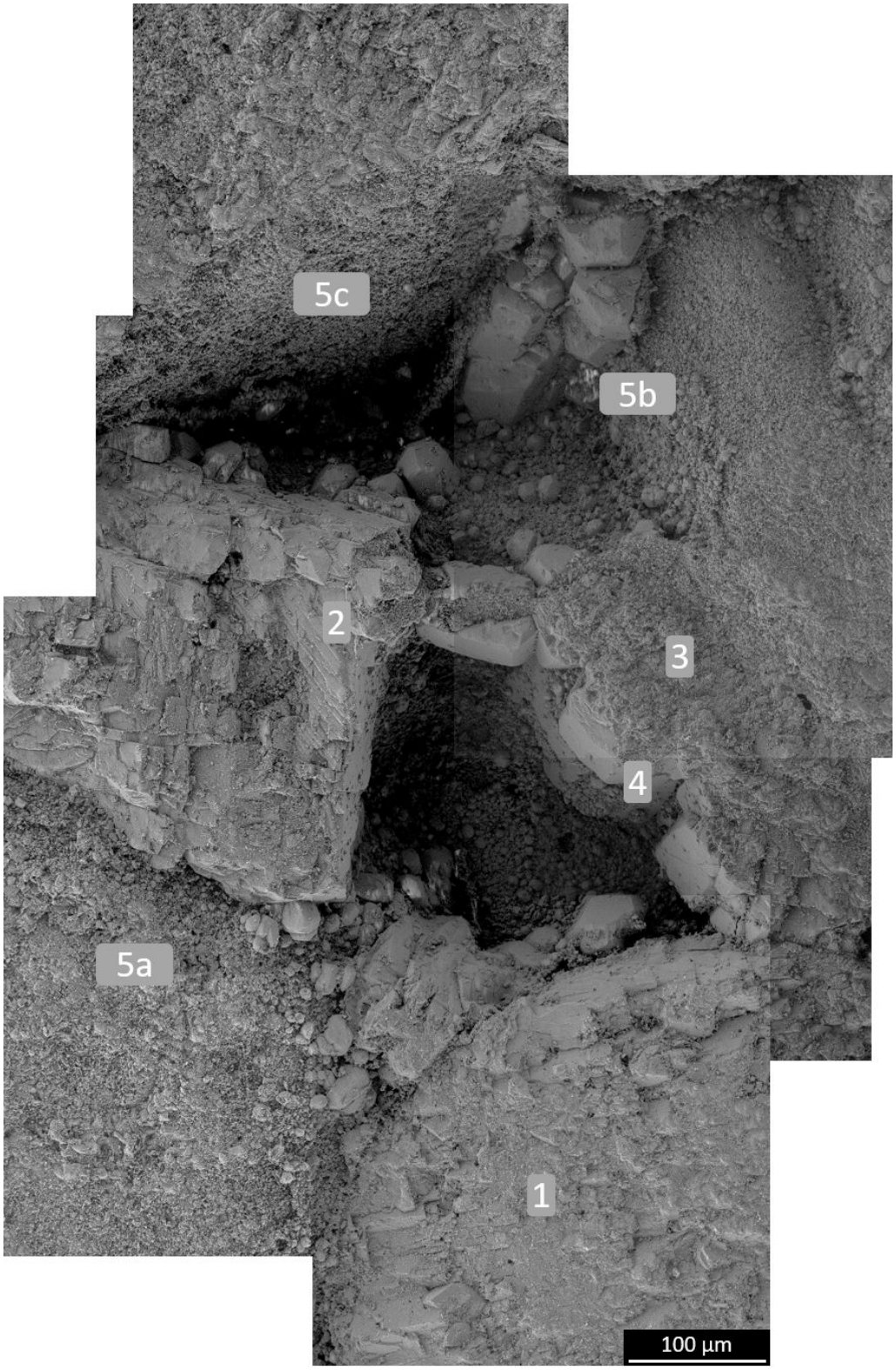



Figure 3.22: Indiana: SEM Overlay 1
An overlay of low-vacuum SEM micrographs of Indiana rock. Different surface types of interest are labelled 1-5 on the Figure. Individual images can be found in Appendix B, Figures B.77 - B.82.

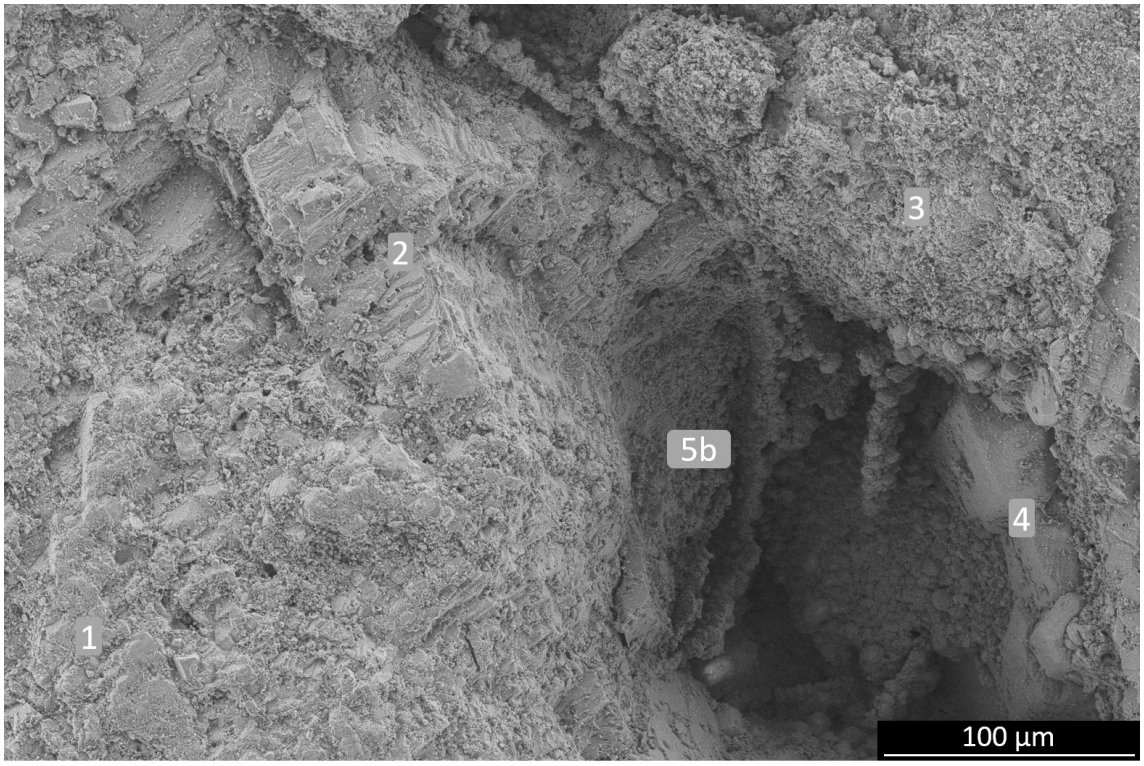



Figure 3.23: Indiana: SEM Overlay 2
A low-vacuum SEM micrograph of Indiana, showing surface types 1-5 as defined in Figure 3.22. The micrograph without numbers overlain can be found in Appendix B, Figure B.83.

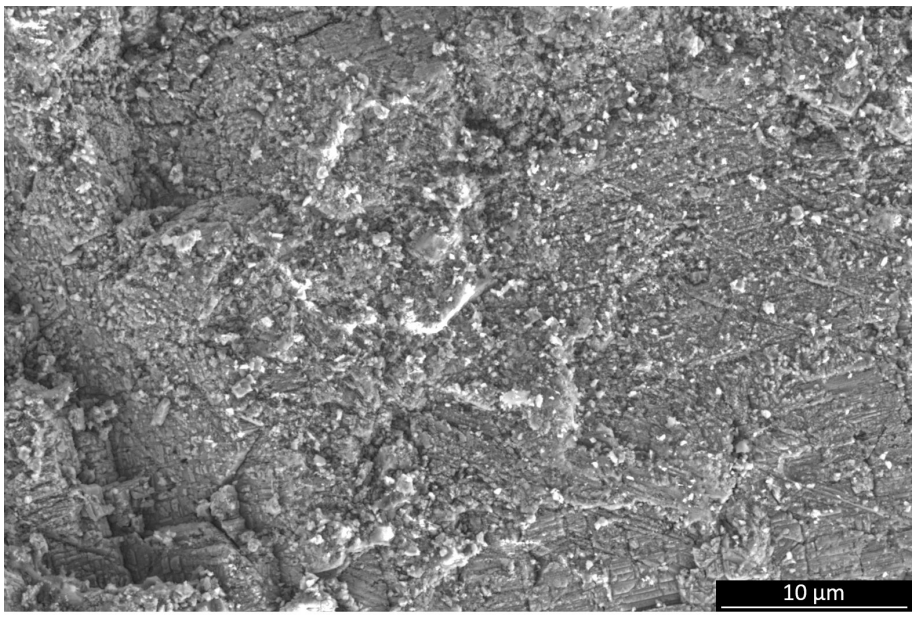
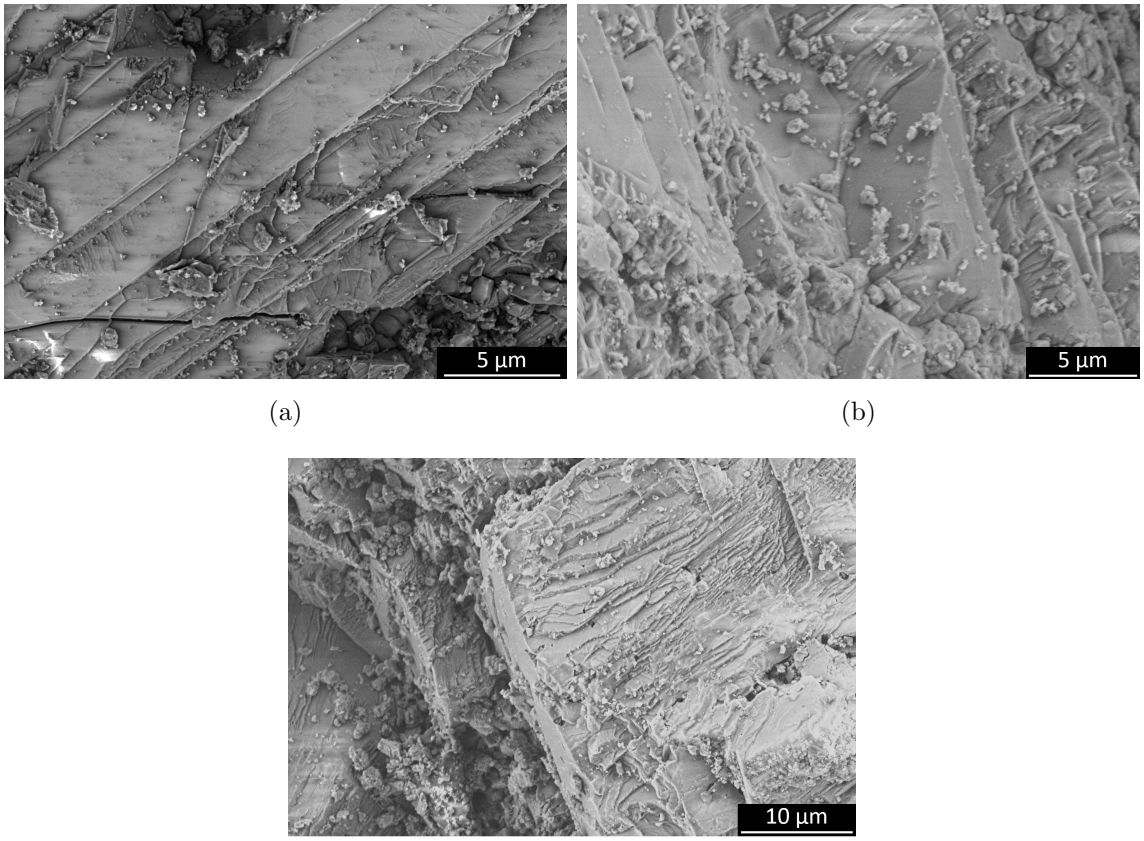



Figure 3.24: Indiana: high magnification SEM micrograph of surface type 1
A high magnification low-vacuum SEM micrograph of Indiana surface type 1, as defined in Figure 3.22, proposed to be a result of the cutting process during sample preparation.

Indiana surface type 2, examples of which are shown at greater magnification in Figure 3.25, appears to be composed of exposed crystal planes in a calcite crystallite. These structures are similar to what was observed for calcite surface type 1 and 2 on pages 95-95, and Estaillades surface sub-type 3b, an example of which is presented next to the low-vacuum SEM micrograph of Indiana from Figure 3.25a in Figure 3.26. Across Figures 3.22 and 3.23, some variation is seen within Indiana surface type 2, which is captured in the selection of high-magnification SEM micrographs shown in Figure 3.25. These differences could have occurred for a number of reasons. The edges of the crystal planes are much straighter in Figures 3.25a and 3.25b than in Figure 3.25c, which could indicate that the cleavage did not occur cleanly, along one crystal plane edge, in this region of the sample. The differences in step heights on different regions of the surface could be due to differences in crystal plane orientation relative to the cleavage plane. The shallower steps in Figure 3.25a and 3.25b could indicate that the crystal planes were near-parallel to the cleavage plane, while the deeper steps in Figure 3.25c could be the result of the crystal planes sitting more perpendicular to the cleavage plane.

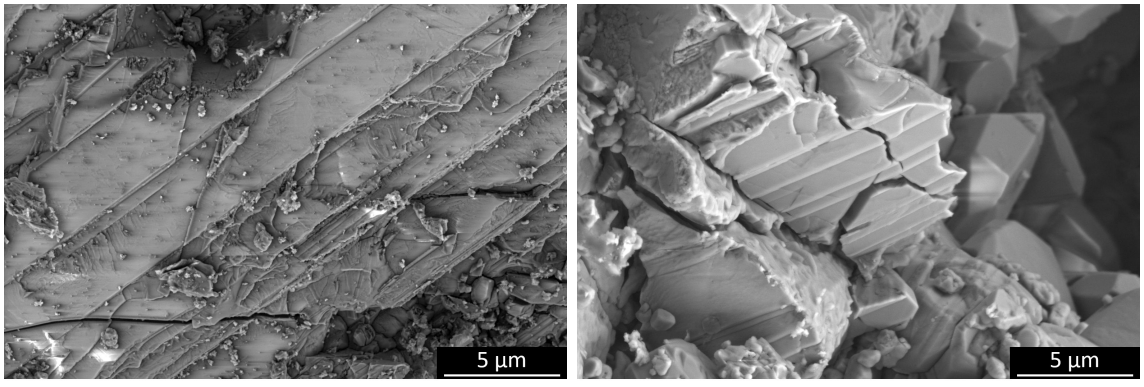
Indiana surface types 3 and 4 as identified in Figures 3.22 and 3.23 are shown at higher magnification in Figure 3.27. Figure 3.27 also shows the Estaillades surfaces which most resemble Indiana surface types 3 and 4. Indiana surface type 3, which is made up of small irregular crystallites, is similar in appearance to Estaillades surface type 2; examples of both surfaces captured via low-vacuum SEM are presented side by side in Figures 3.27a and 3.27b. Indiana surface type 3 and Estaillades surface type 2 are proposed to be a result of fracturing during cutting, particularly in the




(a) (b)

(c)

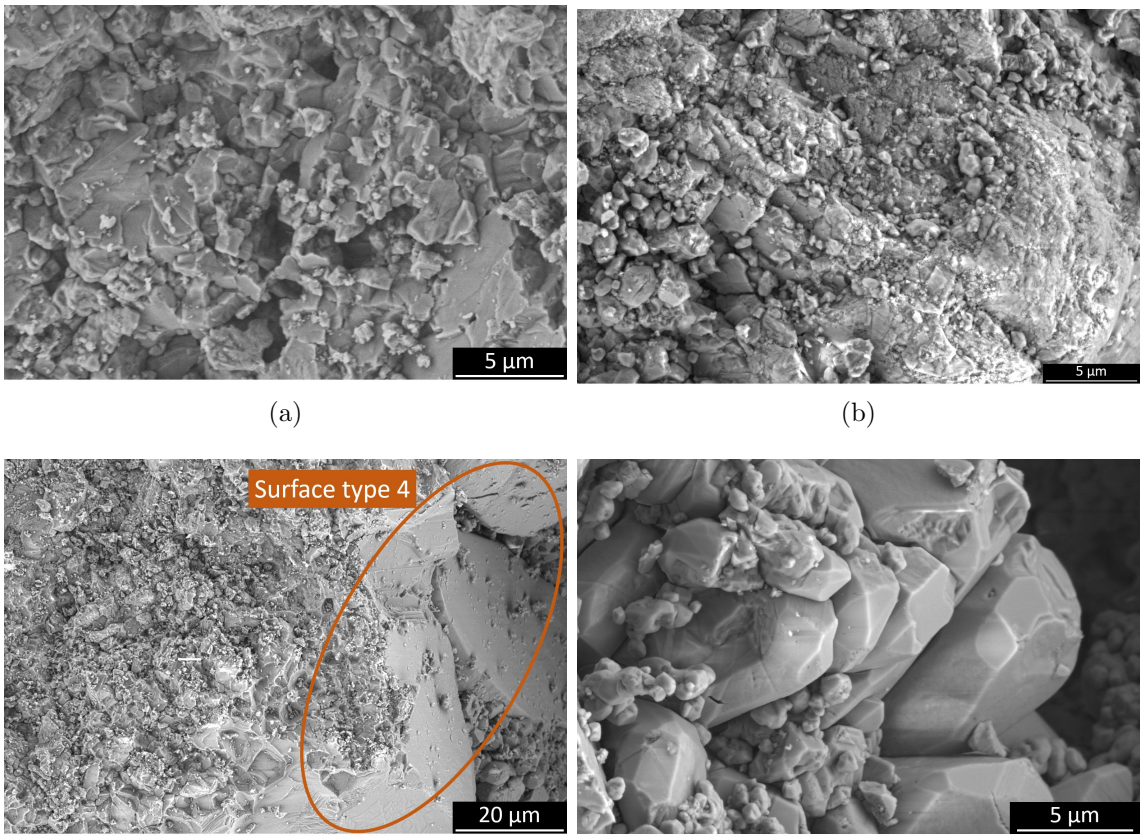
Figure 3.25: Indiana: high magnification SEM micrographs of surface type 2
Three high magnification low-vacuum SEM micrographs of Indiana surface type 2, depicting the variations of step-like formations on the surface proposed to be the result of different calcite cleavages, as observed in Figures 3.22 and 3.23.




(a) (b)

Figure 3.26: Indiana surface type 2a and Estaillades surface type 3b
Two high magnification low-vacuum SEM micrographs showing repeats of a) Indiana surface type 2a, which is similar to b) Estaillades surface type 3b.

case of Estaillades, as surface type 2 is found adjacent to the regions which appear to have been cut cleanly, referred to as Estaillades surface type 1. This correlation is not quite so evident from the images of Indiana in Figures 3.22 and 3.23, however Indiana surface type 3 is exclusively observed on the more elevated regions, so it is still possible that this is indeed a surface type generated during sample preparation, rougher than Indiana surface types 1 and 2, and not a naturally occurring surface.




(a) (b)

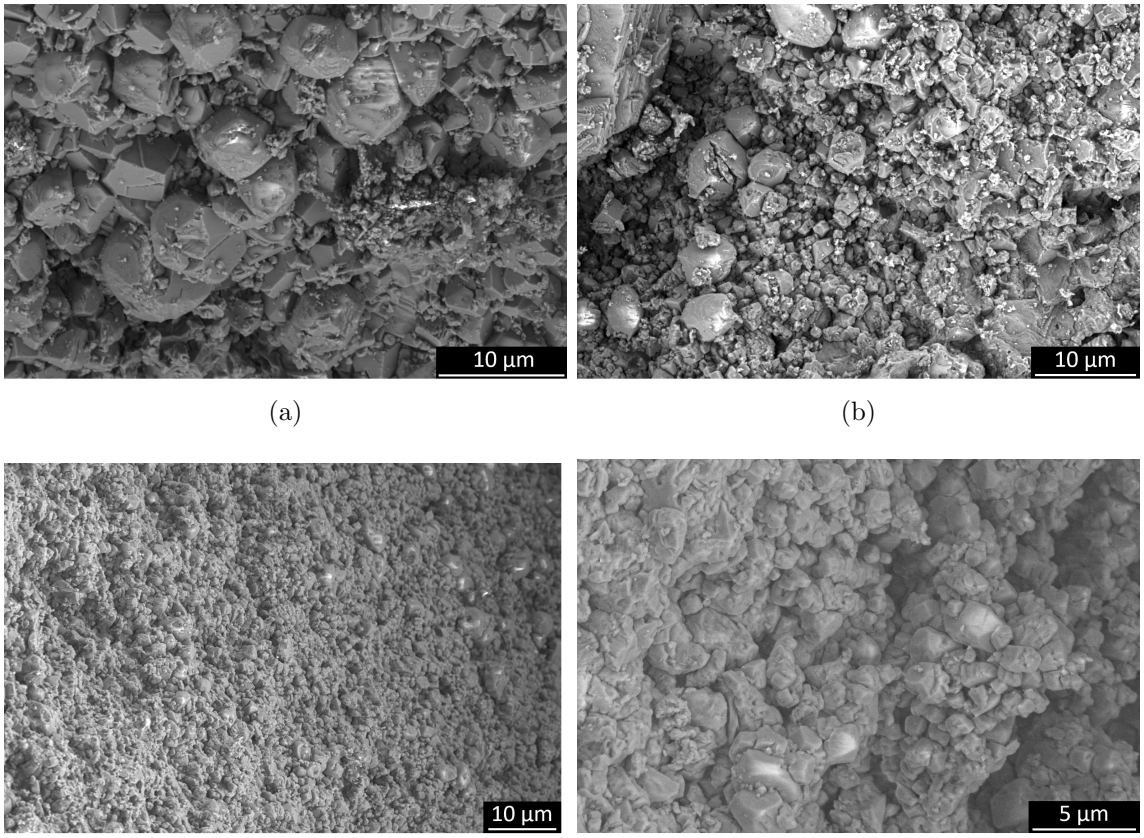
(c) (d)

Figure 3.27: Indiana surface types 3 and 4 and Estaillades surface types 2 and 3a
Four high magnification low-vacuum SEM micrographs showing repeats of a) Indiana surface type 3, which is similar to b) Estaillades surface type 2, and c) Indiana surface type 4 which is similar to d) Estaillades surface type 3a.

Indiana surface type 4 is made up of large, intact crystallites with smooth faces and are visible in patches across both Figures 3.22 and 3.23. This surface type is highlighted in the high magnification low-vacuum SEM micrograph in Figure 3.27c, underneath surface type 3. These larger intact crystallites of Indiana's surface type 4 are similar to Estaillades surface sub-type 3a, which was also made up of large, intact calcite crystallites, as shown in Figure 3.27d.

Indiana surface type 5, as defined across Figures 3.22 and 3.23, is characterised as being comprised of small, smooth-sided crystallites, and is divided into three sub-types, 5a, 5b and 5c, based on the size distributions of the crystallites in each region. Four high-magnification low-vacuum SEM micrographs of these three sub-types are shown in Figure 3.28. This Indiana surface is most similar to Estaillades surface type 4, which was also composed of small, smooth-sided crystallites. As was the case for Estaillades surface type 4, Indiana surface type 5 is proposed to represent naturally occurring surfaces, as they appear in the more recessed sections of the surfaces under investigation. Indiana surface type 5a is shown side by side with Estaillades surface type 4 in Figure 3.29 for comparison.

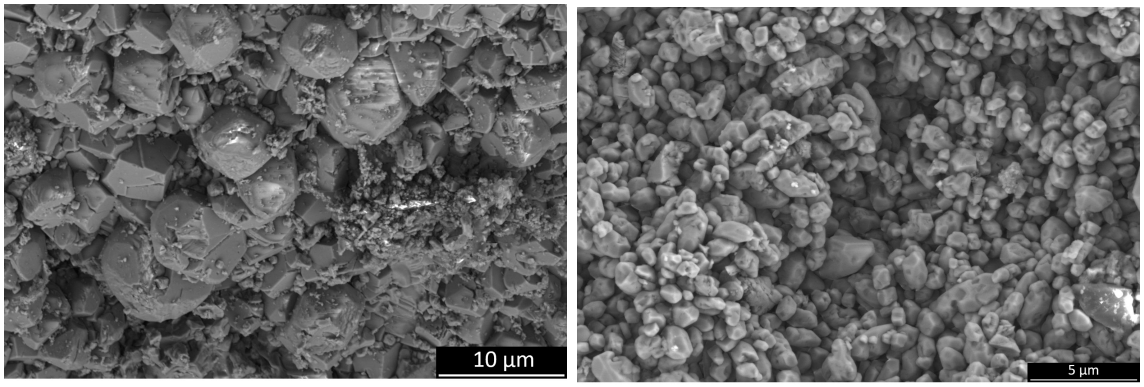
As already noted, surface type 5 is sub-divided into three sub-types: 5a, 5b and 5c, and labelled as such on the wider field of view overlays of the low-magnification micrographs in Figures 3.22 and 3.23. All surface type 5 sub-types are made up of crystallites of $< 10$ $\mu$m. Surface type 5a (Figure 3.28a) is predominantly made up of 5 - 10 $\mu$m crystallites, with some smaller crystallites $< 1$ $\mu$m. Surface type 5b (Figures 3.28b and 3.28d) has comparatively fewer crystallites exceeding 5 $\mu$m, with the majority of the crystallites being on the order of 1 $\mu$m. Surface type 5c




(a) (b)

(c) (d)

Figure 3.28: Indiana: high magnification SEM micrographs of surface type 5
The three sub-types present in surface type 5; 5a shown in (a), 5b shown in (b) and (d) and 5c in (c). (a), (b) (c) are high magnification low-vacuum SEM micrographs from the region depicted in Figure 3.22, and (d) from the region depicted in Figure 3.23.




(a) (b)

Figure 3.29: Indiana surface type 5a and Estaillades surface type 4
Two high magnification low-vacuum SEM micrographs showing repeats of a) Indiana surface type 5a, which is similar to b) Estaillades surface type 4.

(Figure 3.28c) is comprised of entirely $< 5$ $\mu$m crystallites, the majority being 1 - 2 $\mu$m in size. These are perhaps minor differences when looking at the surfaces from a wider field of view, however these differences could be more noticeable during SICM and AFM measurements. Image sizes acquired with these SPMs range from $2 \times 2$ - $10 \times 10$ $\mu$m, and so these sub-types have been assigned for the benefit of integration with the topographical measurements, found later on in this chapter in Sections 3.3.4 and 3.4.3.

The five surface types which were identified across the low-vacuum SEM micrographs of Indiana are summarised in Table 3.4. In terms of areas of interest for understanding fluid flow in these rock systems, surface types 4 and 5 appear to have been unaffected by sample preparation, and represent smooth-sided, reasonably rounded crystallites of a variety of sizes, ranging from approximately 100 $\mu$m in surface type 4 down to $< 1$ $\mu$m in surface type 5. As was concluded with the similar surface types 1 and 2 in Estaillades, even though Indiana surface types 1 - 3 are proposed to be artificially generated, these fractured surfaces could also occur in the context of an oil and gas reservoir, so they are still of interest to study for reservoir modelling applications.

| Type | Description | Feature size range |
|---|---|---|
| 1 | Flat regions caused by cutting during sample preparation | N/A |
| 2 | Large crystallites fractured to reveal a step-like structure | 0.2 - 3 $\mu$m |
| 3 | Fractured regions adjacent to flat regions, result of cutting | 1 - 2 $\mu$m |
| 4 | Intact, large crystallites | $>$ 10 $\mu$m |
| 5a | | 5 - 10 $\mu$m |
| 5b | (a-c) Intact, small crystallites | Mostly 1 - 2 $\mu$m, minority $>$ 5 $\mu$m |
| 5c | | Mostly 1 - 2 $\mu$m, entirely $<$ 5 $\mu$m |

Table 3.4: Summary of the Indiana surface types
A summary of the different surface types identified on the Indiana sample: qualitative descriptions of the surfaces and estimated feature size ranges are given based on the information provided by the low-vacuum SEM micrographs.

## 3.3 Scanning Ion Conductance Microscopy

SICM has been used for the first time in oil and gas applications to determine whether rock samples were compatible with the technique, and what information could be gained from incorporating its use into a digital rock workflow. Topographical maps were acquired of the calcite, Ketton, Estaillades and Indiana surfaces, and a correlative approach was used to assign each image to one, or a narrowed-down shortlist, of the surface types defined in Section 3.2. Summaries of these assigned types are given in the relevant sections below, but can also be found in Tables 3.1, 3.2, 3.3 and 3.4 on pages 96, 105, 111 and 121 for calcite, Ketton, Estaillades and Indiana respectively.

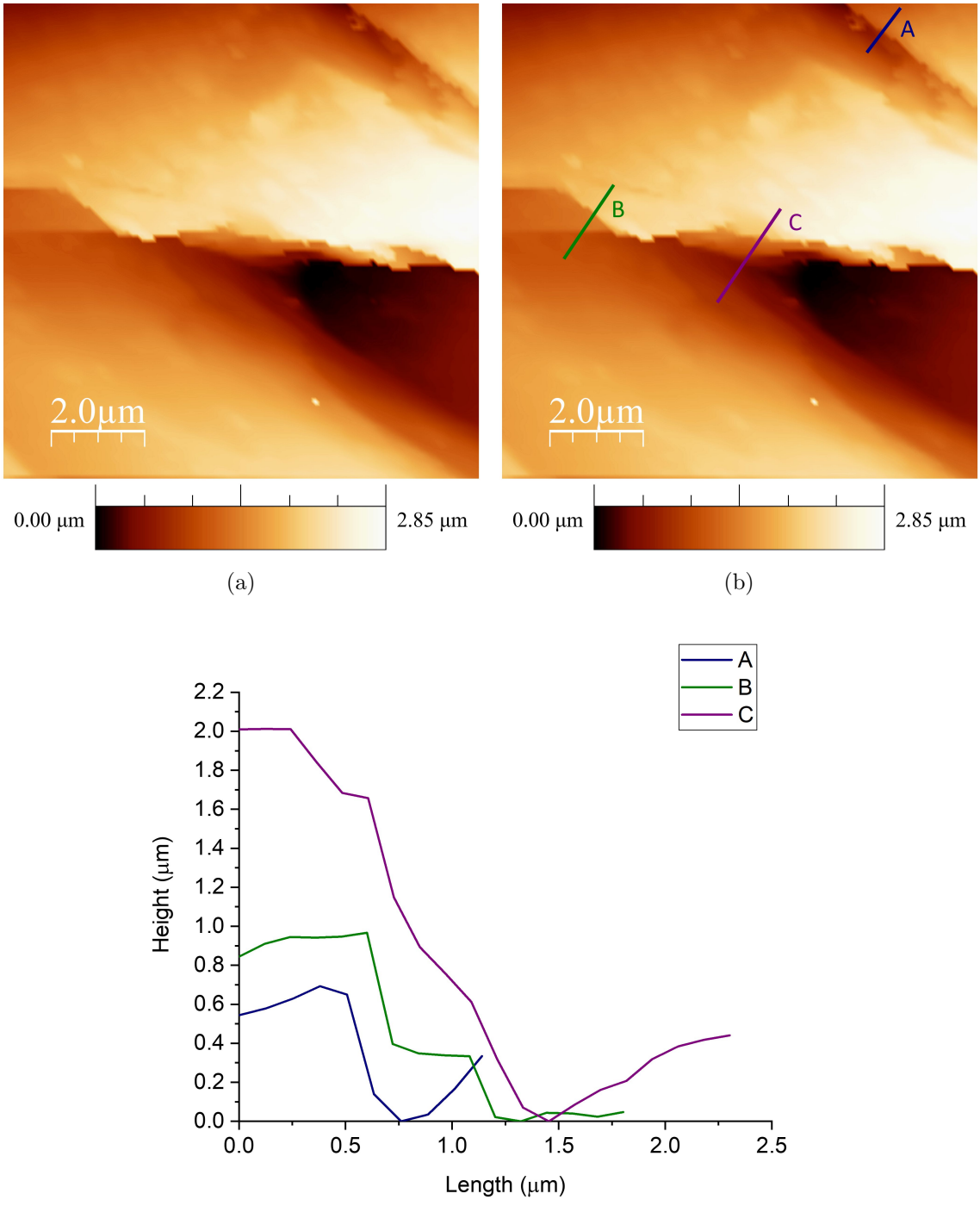
### 3.3.1 Calcite

A calcite crystal was imaged using SICM to provide a reference for the calcite step heights and feature sizes observed in the more complex outcrop rocks: Ketton, Estaillades and Indiana. As summarised in Table 3.1 on page 96, the calcite surfaces investigated by low-vacuum SEM highlighted four distinct surface types: 1 and 2 showed step-like structures, presumed from where cleavage had occurred diagonally to the calcite crystal planes; the former represented deep steps of $> 10$ $\mu$m, where the latter showed shallower steps of $< 10$ $\mu$m. It is not possible from these low-vacuum SEM micrographs to determine the height of the steps across these two surface types. Surface types 3 and 4 showed predominantly flat crystal planes of calcite, surface type 4 representing the areas in the flat surface were small dents can be found, revealing multiple layers of calcite crystal planes beneath. Calcite surface

type 1 contains features too large, $> 10$ $\mu$m, to capture within the largest field of view used in SICM imaging, $10 \times 10$ $\mu$m, and so no examples were identified in the SICM images presented below, however examples of surface types 2 - 4 were identified and are presented in Figures 3.30 - 3.35.

The SICM image shown in Figure 3.30 has been assigned as belonging to calcite surface type 2 due to the presence of step-like structures, and these steps being $< 10$ $\mu$m deep. Three height profiles along the lines A - C labelled in Figure 3.30b are shown in Figure 3.30c. These profiles demonstrate the variation in step heights on this surface type, ranging from 0.6 - 2 $\mu$m. Two other SICM images of surface type 2 are shown in Figure 3.31; these SICM images are of the same region as each other, the smaller $5 \times 5$ $\mu$m image shown in Figure 3.31b providing a higher resolution view of the centre of the $10 \times 10$ $\mu$m image in Figure 3.31a. The image shown in Figure 3.31c is the same SICM image as Figure 3.31b, but with an equalisation function applied to compensate for the, presumed erroneous, bright spot in the top right hand corner of the image. Use of this equalisation allows for improved visual comparison with the larger field of view SICM image presented in Figure 3.31a.

Excellent agreement in feature heights between the two images shown in Figure 3.31 is shown in Figure 3.32 by profiles A and B which sit across what appears to be the same region in Figures 3.32a and 3.32b respectively. A third profile, shown in Figure 3.33, displays the height changes across the line labelled C in Figure 3.32b, highlighting two other step-like structures in this region approximately 1 and 1.25 $\mu$m high. This is in agreement with the previous SICM image of calcite surface type 2 (Figure 3.30), which showed step heights ranging from 0.6 - 2 $\mu$m.




(a) (b)

(c)

Figure 3.30: Calcite: 10 × 10 $\mu$m SICM image of surface type 2
(a) shows a 10 × 10 $\mu$m SICM topographical image with a pixel size of 100 × 100 nm of what is proposed to be calcite surface type 2 as defined in Section 3.2.1. (b) shows the same SICM images with three lines labelled A - C, height profiles along which are shown in (c), each profile depicted from the top right to bottom left of their lines in (b).

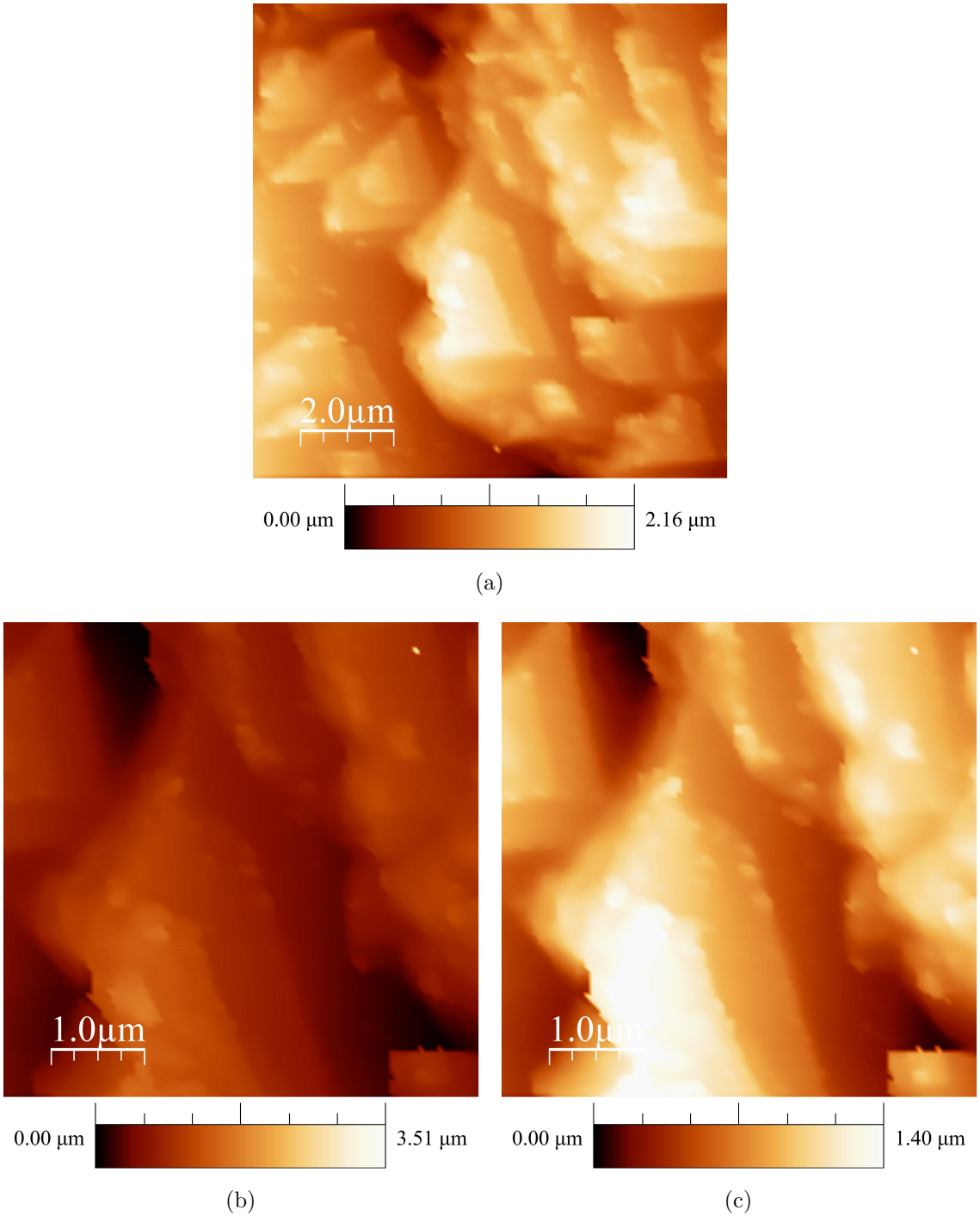



Figure 3.31: Calcite: two SICM images of the same region of surface type 2
Two SICM topographical images of the same region, proposed to be part of calcite surface type 2 as defined in Section 3.2.1. (a) shows a 10 × 10 $\mu$m SICM topographical image with a pixel size of 100 × 100 nm. (b) shows a 5 × 5 $\mu$m SICM topographical image with a pixel size of 50 × 50 nm; (c) shows image (b) with an equalization function applied. The area shown across figures (b) and (c) shows the region in the centre of figure (a) at higher magnification.

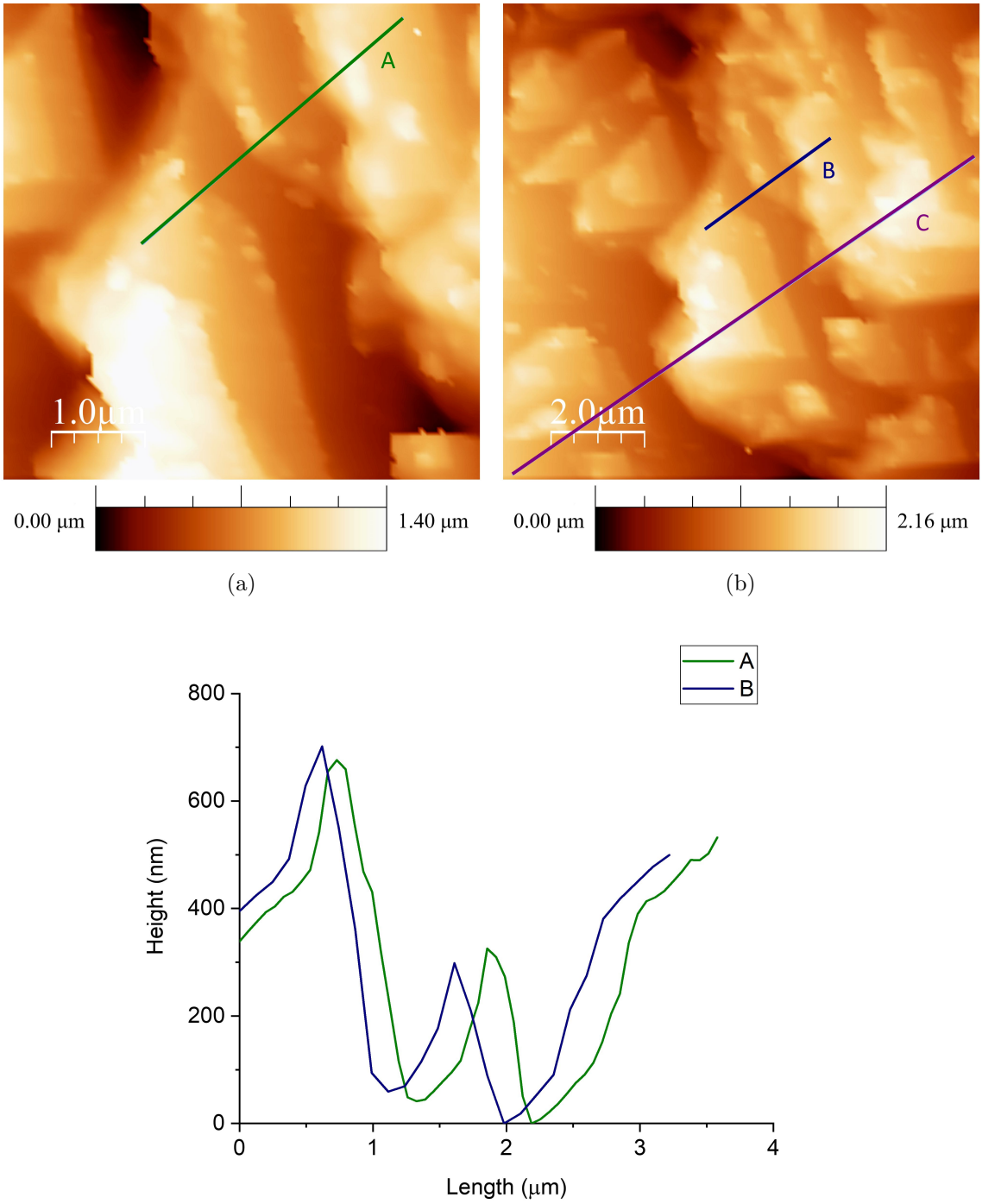



Figure 3.32: Calcite: height profiles across two SICM images of surface type 2 (a) and (b) show two SICM images from Figure 3.31, with three lines, *A* - *C*, labelled. (c) Shows the height profiles along lines *A* and *B*, from top right to bottom left, which appear to be of the same region. The height profile labelled C in (b) is shown in Figure 3.33.

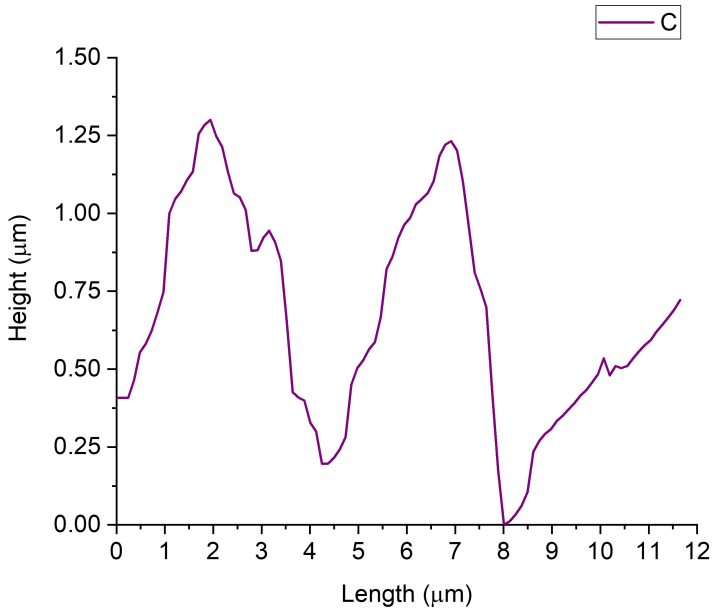



Figure 3.33: Calcite: height profile across an SICM image of surface type 2
A height profile along the line $C$ shown in Figure 3.32b from the top right to the bottom left of the line.

The region of the surface shown in Figure 3.31 does not have as clean a step-like structure as was seen in Figure 3.30, with smaller, $< 2$ $\mu$m, features present being reminiscent of calcite surface type 4. However, from the low-vacuum SEM micrographs in Section 3.2.1, calcite surface type 4 appears to present as quite shallow dents in the surface; given the $> 2$ $\mu$m scale bar on Figure 3.31a, and numerous step heights of $> 1$ $\mu$m being shown in Figure 3.33, this region is therefore proposed to be best assigned as belonging to calcite surface type 2.

The SICM images across Figures 3.34 and 3.35 show regions which are thought to be of surface type 3 or 4, as they are predominantly flat with small raised features present on the surface and $< 1$ $\mu$m scale bars. The SICM images in Figures 3.35a and 3.35c both show small, bright spots on them which mask the topography beneath. These bright spots are presumed to be erroneous, caused by temporary, partial blocking of the nanopipette tip, as there were no vertical structures 5 - 7 $\mu$m high

and $< 50$ nm deep observed on the calcite surface when imaged under low-vacuum SEM, nor were such structures observed in the literature at the time of writing. As such, an equalisation was applied to both, producing the images presented in Figures 3.35b and 3.35d respectively. Height distribution plots for Figures 3.35a and 3.35c are shown in Figure 3.36 to illustrate the justification for using an equalisation function on these two images. As labelled on the graphs, both regions show the vast majority of their pixels below 1 or 1.1 $\mu$m, with a handful of bright pixels around 5 - 8 $\mu$m, and as such there is clear justification to manually narrow the colour scale to focus in on the information of interest.

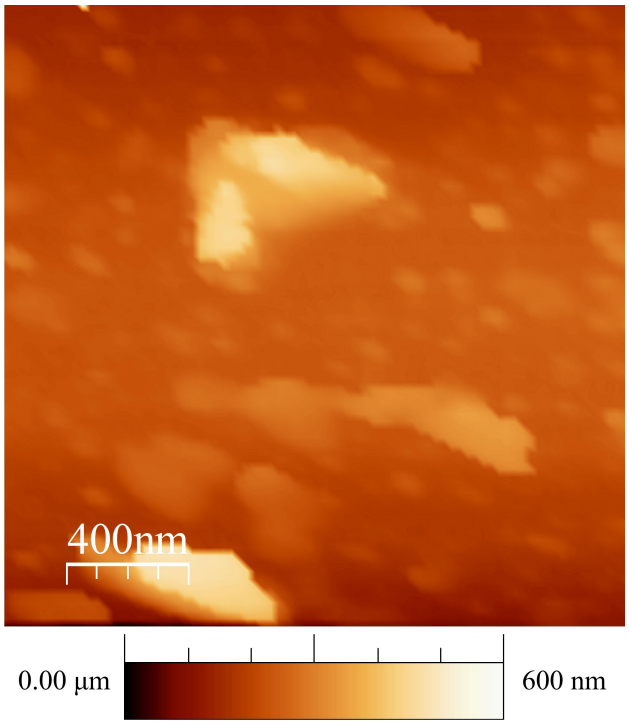



Figure 3.34: Calcite: 2 $\times$ 2 $\mu$m SICM image of surface type 3 or 4
A 2 $\times$ 2 $\mu$m SICM topographical image with a pixel size of 25 $\times$ 25 nm of what is proposed to be calcite surface type 3 or 4 as defined in Section 3.2.1.

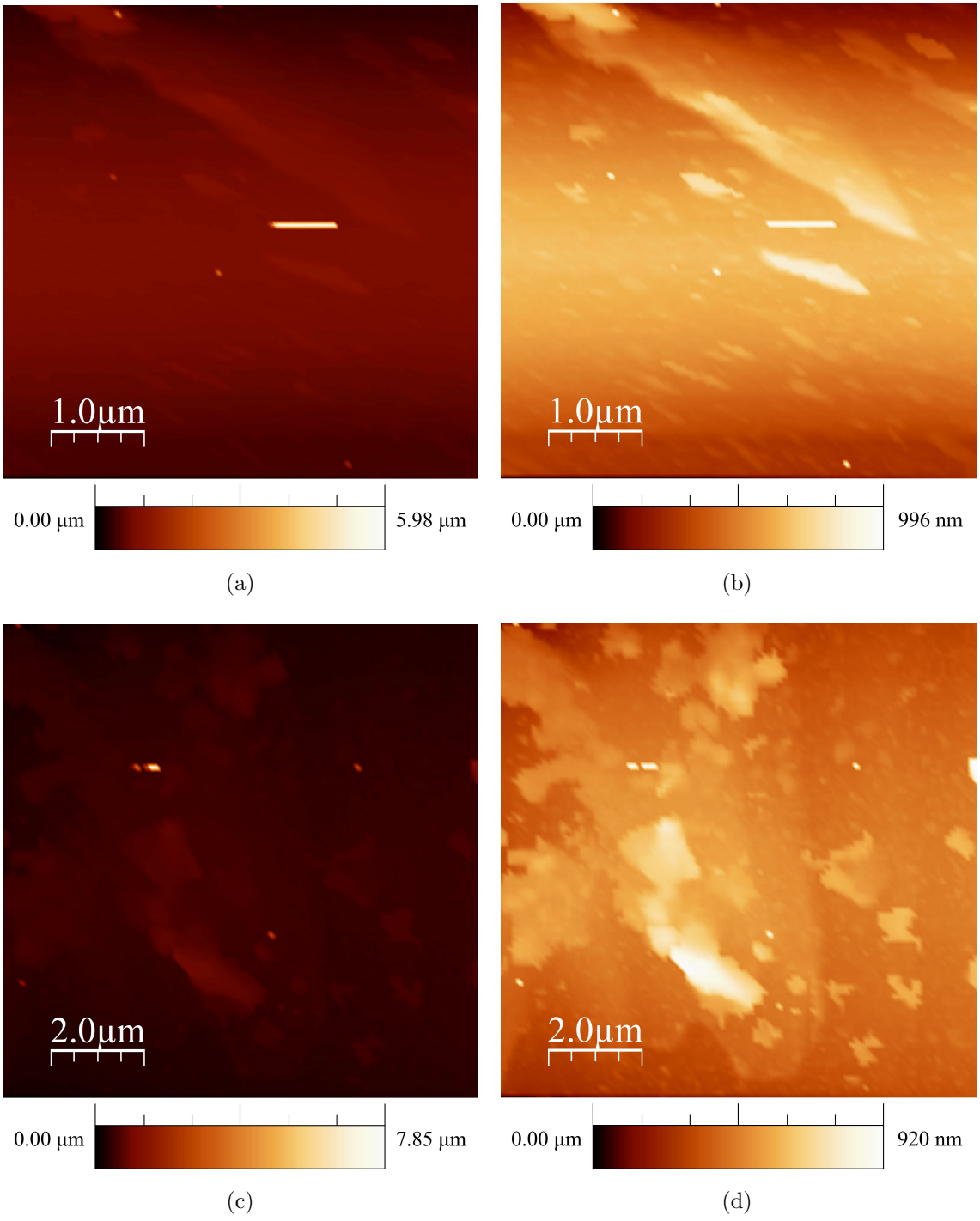
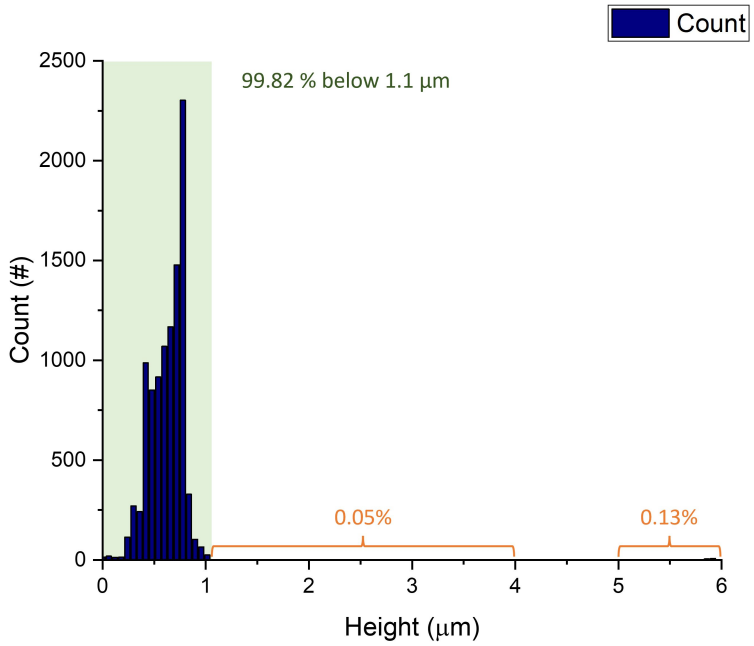
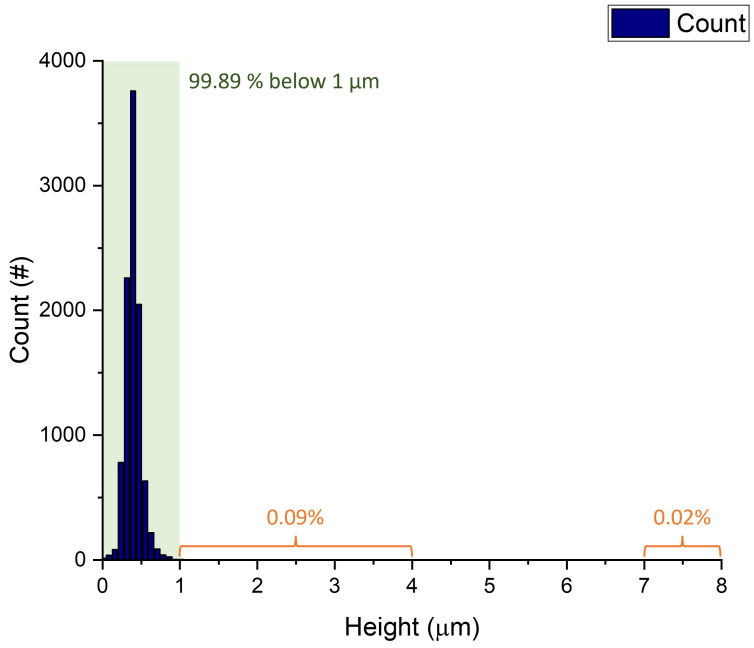



Figure 3.35: Calcite: two SICM images of surface type 3 or 4
Two SICM topographical images of what is proposed to be calcite surface type 3 or 4 as defined in Section 3.2.1. (a) shows a 5 × 5 $\mu$m SICM image with a 50 × 50 nm pixel size and (c) shows a 10 × 10 $\mu$m SICM image with a 100 × 100 nm pixel size. (b) and (d) show the SICM images from (a) and (c) with an equalisation function applied respectively.




(a)




(b)

Figure 3.36: Height distribution plots for SICM images of surface type 3 or 4
The height distribution plots for the SICM images in (a) Figure 3.35a and (b) Figure 3.35c. Pixel counts expressed as percentages are given for certain height ranges of interest.

Overall, three out of the four surface types identified in the low-vacuum SEM micrographs of the calcite surface were assigned to the SICM images presented here. In particular, the step-heights found across surface type 2 were useful for comparison with some of the structures observed on the carbonate outcrop rock samples presented later in this chapter. The surface type not assigned, surface type 1, would not have been possible to identify due to its distinctive features being larger than the largest SICM scans used, $10 \times 10$ $\mu$m, and as such was not anticipated to be identified.

### 3.3.2 Ketton

In Section 3.2.2, six Ketton surface types were defined from the low-vacuum SEM micrographs shown in the overlays in Figures 3.7 and 3.8 (pages 97 and 98 respectively). These were defined as 1) the intact Ketton grain surface, 2) the effect on a Ketton grain surface where a second grain used to be in contact, 3) the cross section of a fractured grain shell, 4) the surface of a fractured grain shell, 5) the larger crystallites present on the inside of the grain and 6) the inside of a fractured grain shell, without larger crystallites. A summary of the feature shapes and sizes associated with these surface types was shown in Table 3.2, page 105. These categories, and the feature sizes observed, served as a guide when looking at the SICM images presented below, providing a means to place these smaller field of view images within the wider context of the outcrop rock surface observed in the low-vacuum SEM micrographs.

Figure 3.37 below shows a 3 $\times$ 3 $\mu$m SICM topographical image with a pixel size of 30 $\times$ 30 nm, and is proposed to belong to surface type 1, as the features are on the order of 1 $\mu$m across, and the individual surfaces of the visible grains are themselves quite smooth. The features are more elongated in shape than was seen for surface type 1 in the low-vacuum SEM micrographs, and are instead closer in shape to the crystallites observed in surface type 5. However, the shapes are not identical to what was observed for surface type 5, and the crystallite sizes are much smaller, which were on the order of 1 - 15 $\mu$m for surface type 5, so this region was ultimately assigned as being of the outside of a Ketton ooid grain, surface type 1.

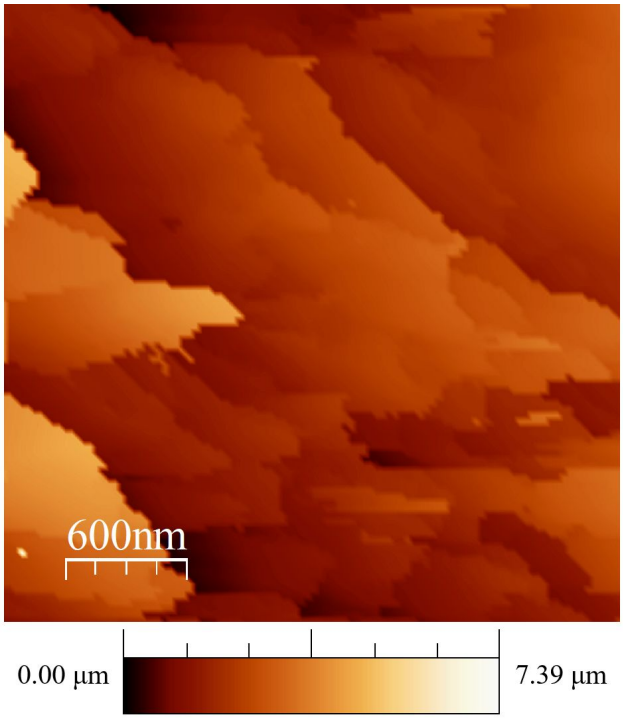



Figure 3.37: Ketton: 3 × 3 $\mu$m SICM image of surface type 1
A 3 × 3 $\mu$m SICM topographical image with a pixel size of 30 × 30 nm of what is proposed to be Ketton surface type 1 as defined in Section 3.2.2.

Ketton surface type 2 is the rough ooid grain surface left behind after a grain is removed, creating a spikey surface on top of the smooth crystallites. Figure 3.38 shows a 10 × 10 $\mu$m SICM topographical image with a pixel size of 100 × 100 nm, which depicts crystallites 1 - 2 $\mu$m in size but with a rougher surface texture than those seen in Figure 3.37. It is therefore proposed that this image captures a section of Ketton surface type 2, the rough shape of the crystallites on the ooid grain surface still visible with a "spikey" texture on top.

Ketton surface types 3, 4 and 6 are difficult to distinguish from one another when looking at the SICM topographical images due to their narrower field of view. As all three areas show fractured shell surfaces, but from different perspectives, they have similar crystallite sizes and shapes, which make them very similar at this

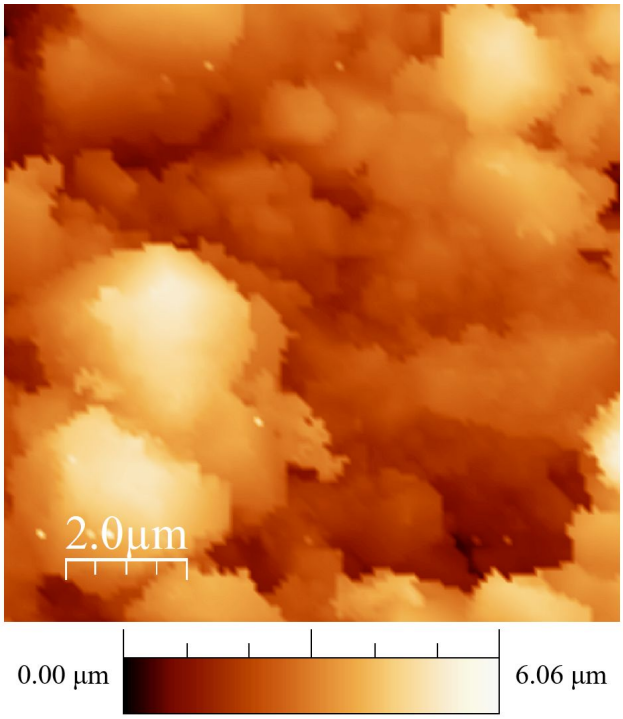



Figure 3.38: Ketton: 10 × 10 $\mu$m SICM image of surface type 2
A 10 × 10 $\mu$m SICM topographical image with a pixel size of 100 × 100 nm of what is proposed to be Ketton surface type 2, as defined in Section 3.2.2.

high magnification. The trio of 2 × 2 $\mu$m SICM topographical images presented in Figure 3.39 are proposed to depict one of Ketton surface types 3, 4 or 6, due to the crystallite size being on the order of 100 nm. The regions captured in the SICM image in Figure 3.39 are also much flatter than those previously attributed to Ketton surface types 1 and 2, with the largest height range being only 2.29 $\mu$m, compared to those seen in Figures 3.37 and 3.38, which have height ranges of 6.06 and 7.39 $\mu$m. This assessment aligns with how Ketton surface types 1 and 2 appeared in comparison to surface types 3, 4 and 6 in the SEM micrographs in Section 3.2.2. It should also be noted that the trio of SICM images in Figure 3.39 overlap with one another, and so all belong to only one of the surface types 3, 4 and 6; the bottom left of Figure 3.39a overlaps with the top right of Figure 3.39b, and the top right of Figure 3.39b can be seen in the middle of Figure 3.39c.

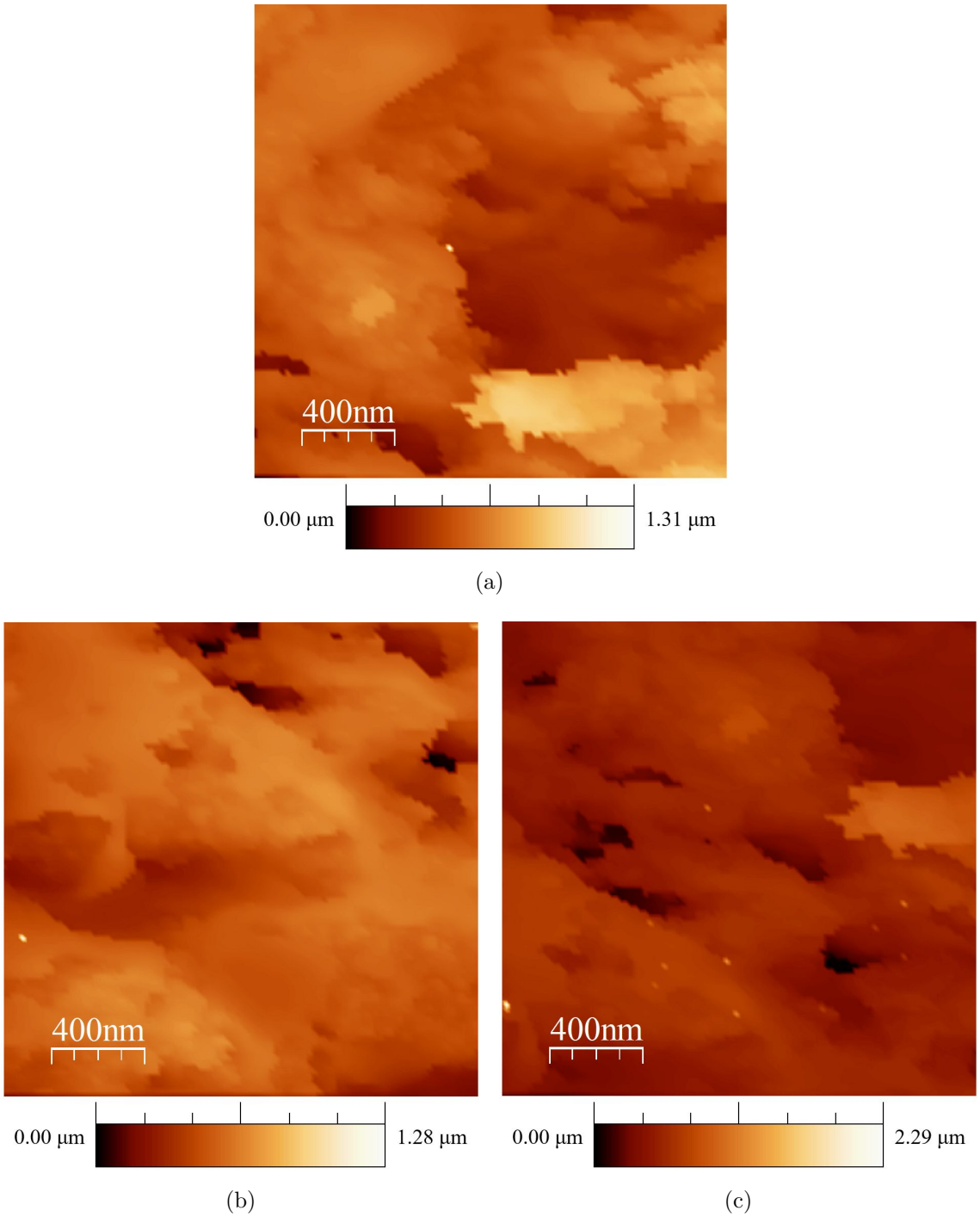
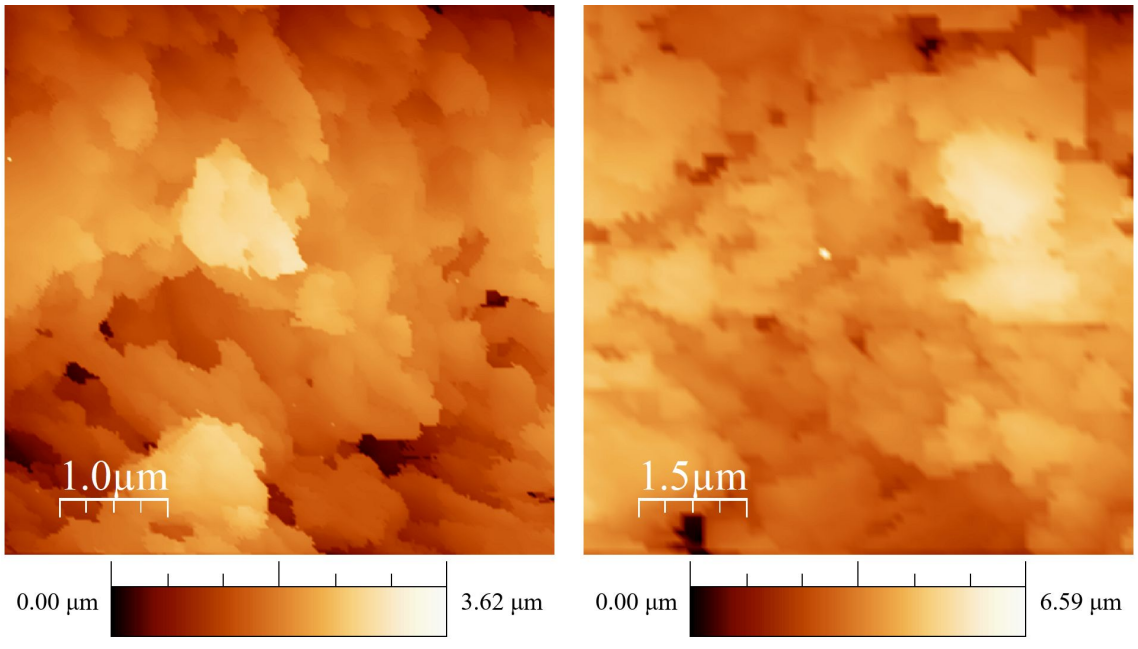



Figure 3.39: Ketton: Three 2 × 2 $\mu$m SICM images of surface type 3, 4 or 6
Three 2 × 2 $\mu$m SICM topographical images taken of overlapping sites with pixel sizes of 20 × 20 nm of what is proposed to be Ketton surface type 3, 4 or 6 as defined in Section 3.2.2.

Two additional SICM topographical images are shown in Figure 3.40 which are also proposed to belong to a fractured ooid shell surface; surface types 3, 4 or 6. The regions in Figure 3.40 are rougher than those shown in Figure 3.39; root mean square (RMS) roughnesses for each SICM image are given in Table 3.5 for comparison. Given the increased roughness observed in Figure 3.40, it is possible that Figure 3.39 shows three images of Ketton surface type 6, a smoother surface made up of one ooid shell layer, and Figure 3.40 shows two images from Ketton surface types 3 or 4, which are likely to be rougher due to multiple ooid shell layers being exposed. Additionally, the pores visible on the surface in Figures 3.39b and 3.39c are similar in size to those observed in the high magnification low-vacuum SEM micrograph for Ketton surface type 6, shown in Figure 3.15b (page 104), both techniques showing pores estimated to be on the order of 200 - 400 nm across. Although these roughness measurements could be indicative of an assignment towards one of the three fractured ooid shell surface types 3, 4 or 6, it is not possible to categorically state which of the Ketton types these five SICM images belong to.

| Proposed Surface Type | Figure # | RMS Roughness |
|---|---|---|
| 6 | 3.39a | 0.1466 |
| | 3.39b | 0.1160 |
| | 3.39c | 0.1439 |
| 3 or 4 | 3.40a | 0.4948 |
| | 3.40b | 0.8061 |

Table 3.5: RMS roughnesses for Figures 3.39 and 3.40
RMS roughnesses and proposed surface type assignments for the five SICM images shown across Figures 3.39 and 3.40. It can be observed that SICM images shown in Figure 3.39 have considerably lower roughnesses than those shown in Figure 3.40.




(a) (b)

Figure 3.40: Ketton: two SICM images of surface type 3, 4 or 6
(a) 5 × 5 $\mu$m and (b) 7.6 × 7.6 $\mu$m SICM topographical images with pixel sizes of (a) 25 × 25 nm and (b) 100 × 100 nm of what is proposed to be Ketton surface type 3, 4 or 6 as defined in Section 3.2.2.

Overall, SICM has been used to map the majority of the different Ketton surface types identified from the low-vacuum SEM micrographs in Section 3.2.2. The ability to provide RMS roughness values from these topographical maps provides additional insight into these surface types, which can not be derived from the low-vacuum SEM micrographs alone.

No examples of surface type 5 were found across the SICM images of Ketton which were collected during this study. Given the size of the crystallites in the regions labelled as surface type 5, many being $> 10$ $\mu$m across (Figure 3.14, page 103), it is possible that these regions present a sizeable challenge in terms of SICM mapping, as the notable and sudden height changes would likely lead the pipette tip to crash into the surface and break. Additionally, surface type 5 was only found in one ooid grain within the two regions shown in the overlays in Figures 3.7 and 3.8 (pages 97 and 98), so it is possible that this surface type is rarer than the the others, reducing its likelihood of being imaged with the SICM.

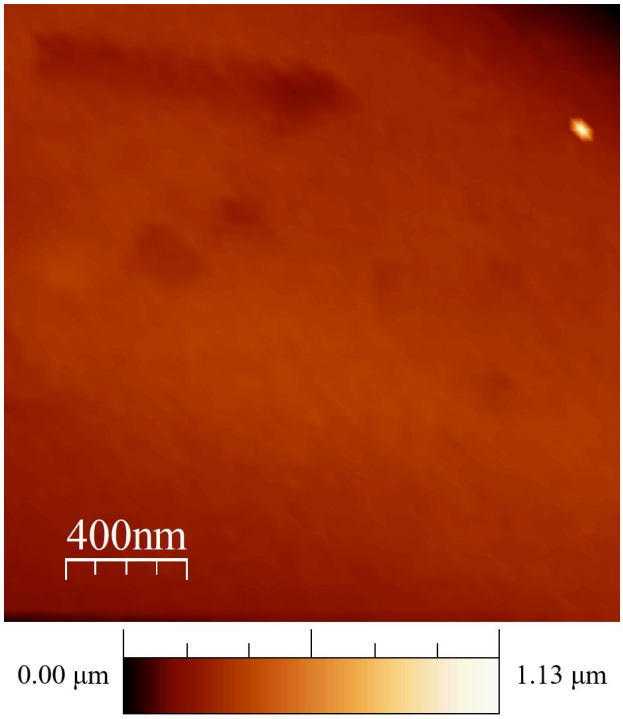
Despite the potential limitations associated with the mapping of surface type 5, examples of all of the other surface types were found in the SICM images of Ketton. The range of surface types successfully imaged by the SICM shows promise for the technique being used in further studies of this outcrop rock.

### 3.3.3 Estaillades

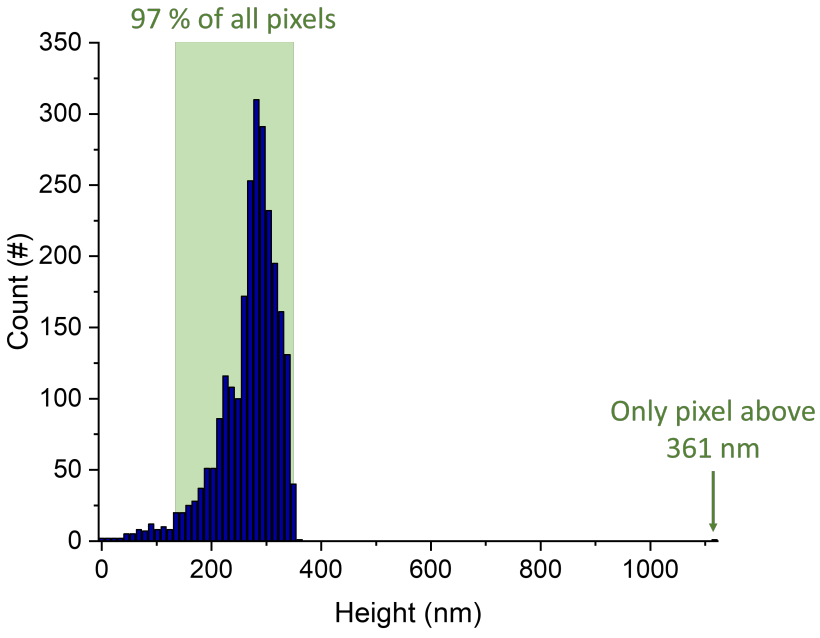
Estaillades showed four distinct surface types in Section 3.2.3, labelled on the SEM micrographs in Figures 3.16 and 3.17 on pages 106-107. These surface types can be summarised as: 1) the flatter areas caused directly by the cutting procedure used to prepare the samples, 2) the fractured areas next to surface type 1, likely a by-product of the cutting, 3) the intact areas with larger crystallite sizes, 5 - 10 $\mu$m across and 4) the intact areas with smaller crystallite sizes, 1 - 2 $\mu$m across.

Figure 3.41 shows a 2 $\times$ 2 $\mu$m SICM topographical image of a region which is proposed to belong to Estaillades surface type 1. A height distribution plot in Figure 3.41b, showing the numbers of pixels per recorded heights, shows a narrow height distribution, where approximately 97 % of pixels can be seen to be within the range of 135 - 350 nm, and 99.96 % of points sit below 361 nm high relative to the lowest point. The bright pixel in the top right of Figure 3.41a therefore, at approximately 1.1 $\mu$m above the lowest point can probably be disregarded as erroneous. This height distribution, combined with a relatively low RMS roughness of 0.0580, indicates that this image was taken of a reasonably flat surface, possibly one generated during sample preparation, and is therefore assigned as a region belonging to surface type 1.

Two 2 $\times$ 2 $\mu$m SICM topographical images of what are proposed to be from Estaillades surface type 2 are shown in Figure 3.42. These images show areas with $\leq$ 1 $\mu$m crystallite sizes, smaller than those observed in Estaillades surface type 4, but larger than the texture in Estaillades surface type 1. They are also rougher than the area in Figure 3.41, with RMS roughnesses of 0.2596 and 0.6158 for Figures 3.42a



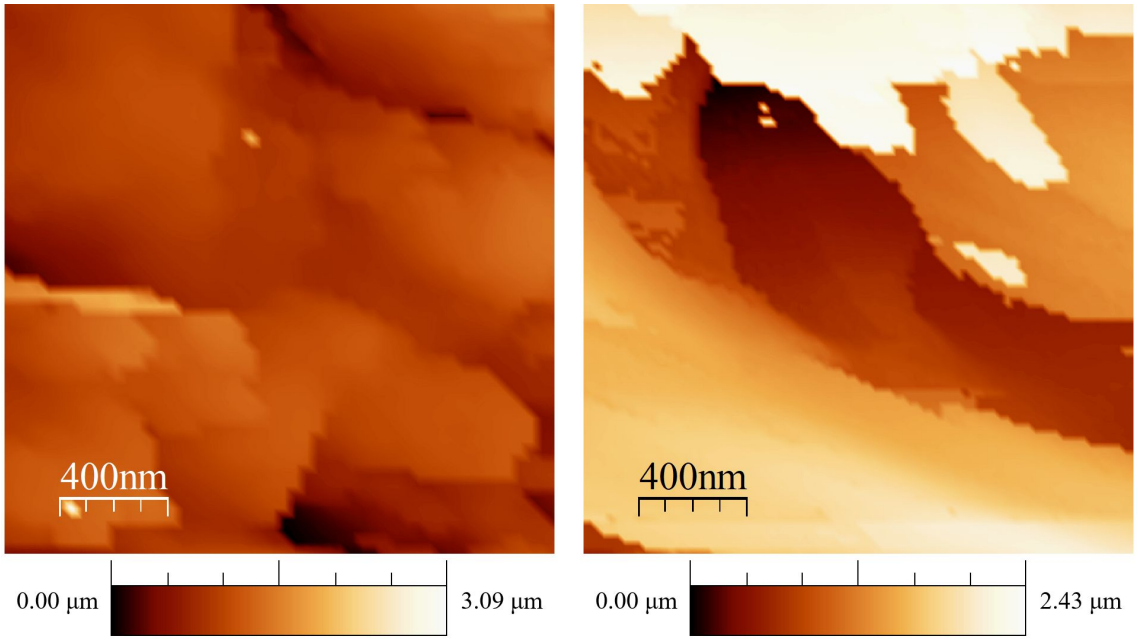

(a)




(b)

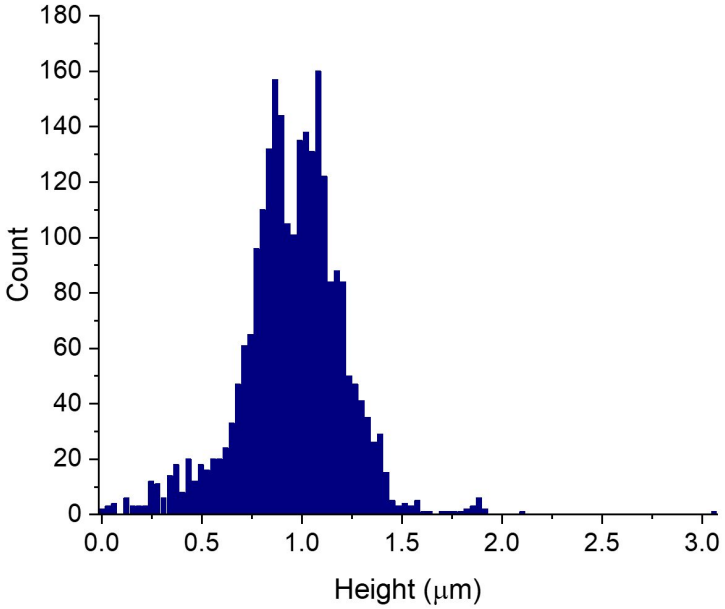
Figure 3.41: Estaillades: 2 × 2 $\mu$m SICM image of surface type 1
a) A 2 × 2 $\mu$m SICM topographical image with a pixel size of 40 × 40 nm of what is proposed to be Estaillades surface type 1 as defined in Section 3.2.3. b) Annotated height distribution plot of the topographical image in (a).

and 3.42b respectively, with wider relative height distributions which can be seen in Figure 3.43. In comparison to the SICM capture of surface type 1, which showed 90 % of points in a 200 nm wide range from 200 - 400 nm high relative to the lowest point, 3.42a has 93 % of points spread across a 1 $\mu$m range, between 0.5 - 1.5 $\mu$m high relative to the lowest point, and 3.42b has 90 % of points spread across a 2 $\mu$m range, from 0.5 - 2.5 $\mu$m high relative to the lowest point. Due to this greater roughness than Estaillades surface type 1 (Figure 3.41), yet smaller crystallite sizes than Estaillades surface types 3 and 4, the areas shown in Figure 3.42 are assigned as part of Estaillades surface type 2.

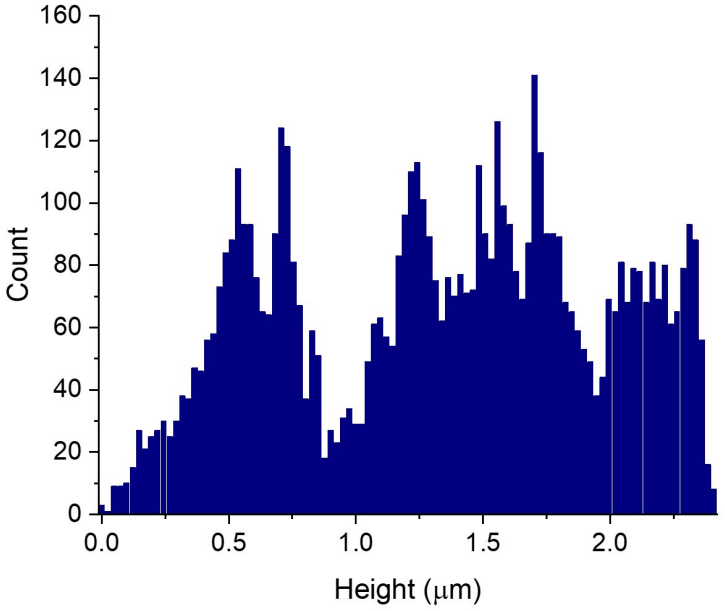



(a) (b)

Figure 3.42: Estaillades: two 2 × 2 $\mu$m SICM images of surface type 2
Two 2 × 2 $\mu$m SICM topographical images with pixel sizes of (a) 40 × 40 nm and (b) 25 × 25 nm of what is proposed to be Estaillades surface type 2 as defined in Section 3.2.3.




(a)



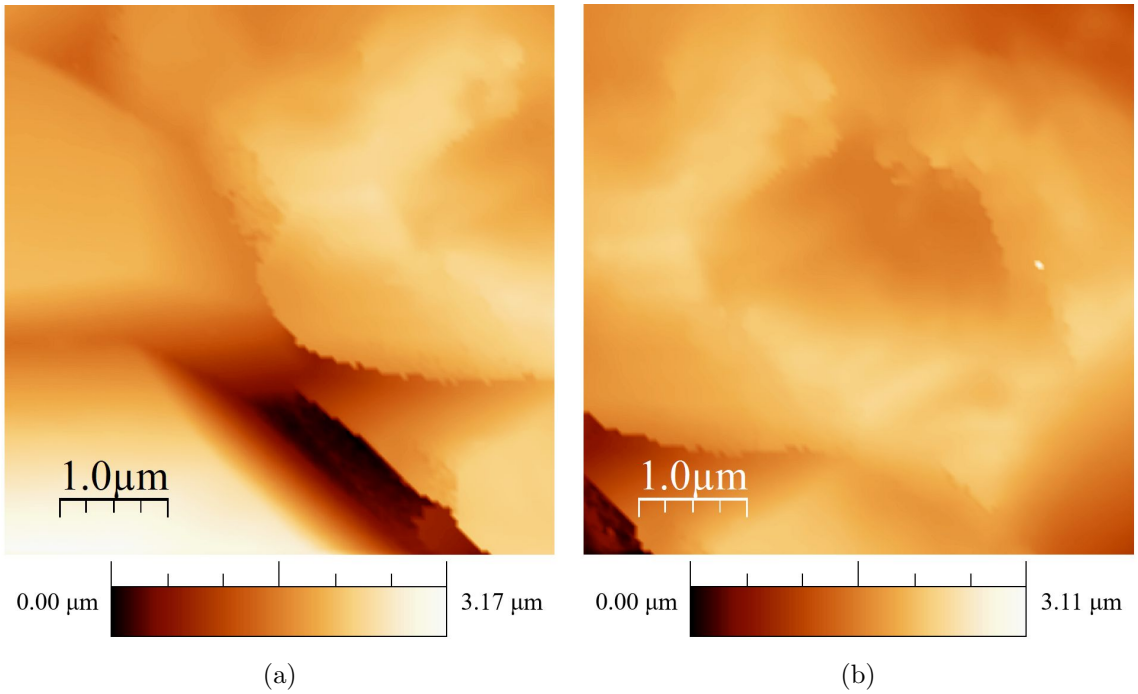

(b)

Figure 3.43: Estaillades: height distributions of surface type 2
Height distribution plots for the SICM topographical images of Estaillades surface type 2 shown in a) Figure 3.42a and b) Figure 3.42b.

| Proposed Surface Type | Figure # | RMS Roughness |
|---|---|---|
| 1 | 3.41a | 0.0580 |
| 2 | 3.42a | 0.2596 |
| | 3.42b | 0.6158 |

Table 3.6: RMS roughnesses for Figures 3.41 and 3.42
RMS roughnesses and proposed surface type assignments for the three SICM images shown across Figures 3.41 and 3.42.

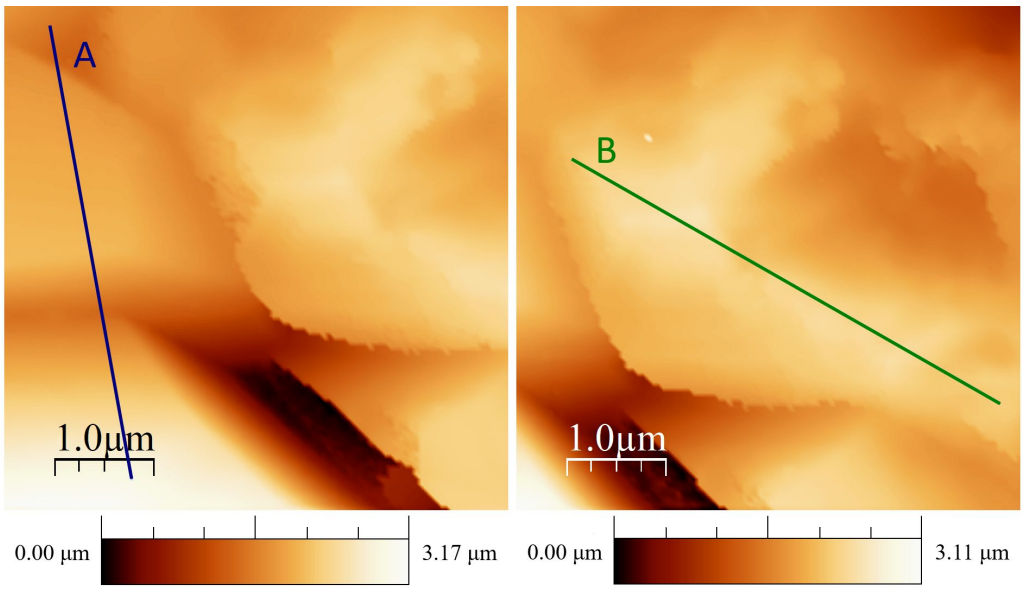
There are of course intersections between surface types, which is possibly captured in Figure 3.44. The areas depicted in Figures 3.44a and 3.44b overlap with each other, the right hand side of Figure 3.44a visible on the left hand side of Figure 3.44b. Towards the left of Figure 3.44a the edges of a few large, smooth crystallites can be seen. Their exact sizes are unknown, as no one crystallite is visible in its entirety, however the sides that can be seen are larger than the crystallites in Estaillades surface type 4, 1 - 2 $\mu$m across, so are proposed to be part of Estaillades surface type 3, which has crystallite sizes typically 5 - 10 $\mu$m. Towards the right of Figure 3.44a, and filling almost the entirety of Figure 3.44b is a rougher, grainier surface than the smooth structures in the bottom left of 3.44a. The contrast between these surfaces in shown in Figure 3.45, where two height profiles are overlain; one profile taken across the surface type 3 section visible in Figure 3.44a, labelled "A", and one taken across the are type 2 section visible in Figure 3.44b, labelled "B". Figure 3.45b shows the two height profiles overlain so that the difference between the smooth and rough crystallites can be readily visualised. The surfaces shown across profile A are much smoother than those across profile B, which is in agreement with assignment of the region which profile A traverses belonging to Estaillades surface type 3 and the region which B traverses belonging to Estaillades surface type 2.



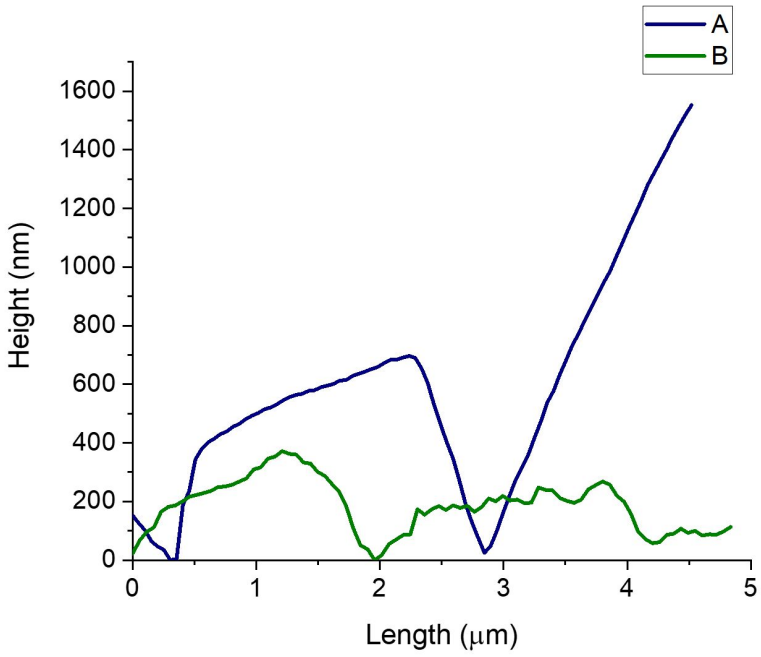

(a) (b)

Figure 3.44: Estaillades: two 5 × 5 $\mu$m SICM images of surface types 2 and 3
Two 5 × 5 $\mu$m SICM topographical images taken of overlapping sites with pixel sizes of 50 × 50 nm of what is possibly the intersection between Estaillades surface types 2 and 3 as defined in Section 3.2.3.

Examples of Estaillades surface type 3, composed of the larger, smooth crystallites approximately 5 - 10 $\mu$m across, are shown in Figure 3.46. Figures 3.46a, 3.46b and 3.46c show 5 × 5 $\mu$m SICM topographical images, and Figure 3.46d shows a 10 × 10 $\mu$m SICM topographical image. The three 5 × 5 $\mu$m images show crystallites too large to be fully captured in this image size, but they are clearly much larger than the 1 - 2 $\mu$m crystallites of surface type 4, so are assigned as surface type 3. The 10 × 10 $\mu$m image has a wide enough field of view to capture a few full lengths of some of the crystallites, which measure 8.1 $\mu$m ± 0.1 $\mu$m, 5.4 $\mu$m ± 0.1 $\mu$m and 3.9 $\mu$m ± 0.1 $\mu$m across (Figure 3.47), which confirms that this area belongs to Estaillades surface type 3, but also demonstrates the diversity of this surface type, even in such a small sample size.




(a)




(b)

Figure 3.45: Estaillades: height profiles of surface types 2 and 3
Height profiles from the SICM topographical images shown in Figure 3.44 of the two Estaillades surface types visible; 2 and 3. a) shows the lines across which the profiles were taken, and b) shows the height profiles themselves, profiles "A" and "B" referring to the images in Figures 3.44a and 3.44b respectively; "A" an example of a surface type 3 profile, and "B" an example of a surface type 2 profile.

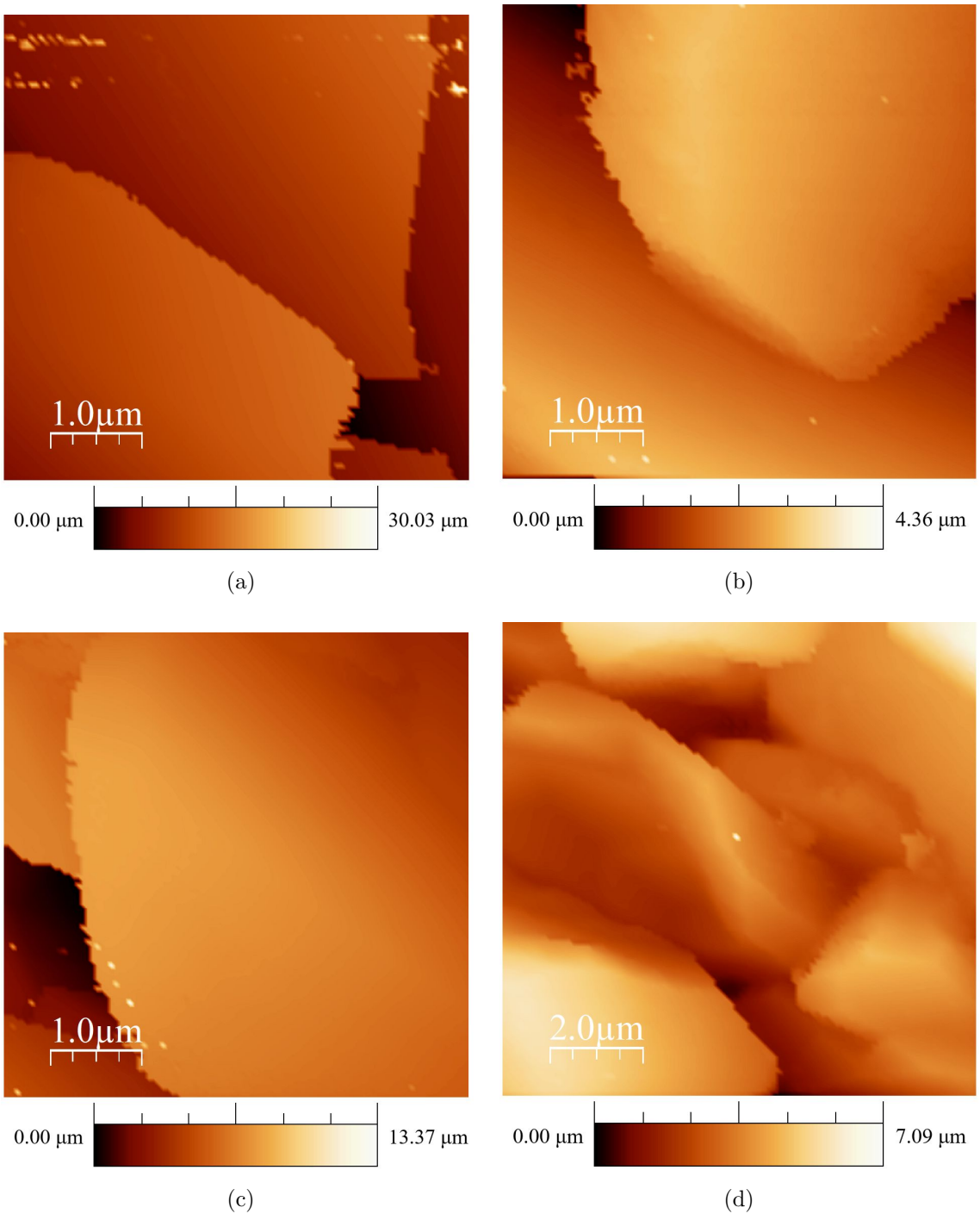



Figure 3.46: Estaillades: four SICM images of surface type 3
Four SICM topographical images of what is proposed to be Estaillades surface type 4 as defined in Section 3.2.3. (a), (b) and (c) are 5 × 5 $\mu$m images with a pixel size of 50 × 50 nm, and (d) is a 10 × 10 $\mu$m image with a pixel size of 100 × 100 nm.

Figure 3.48 shows a 5 × 5 $\mu$m SICM topographical image which is proposed to be an image of Estaillades surface type 4, alongside a low-vacuum SEM micrograph of surface type 4, originally shown in Figure 3.21 on page 111 for comparison. This area is composed of smaller crystallites than were seen in the images of surface type 3 in Figure 3.46, yet they still have smooth surfaces so are not presumed to be part of surface type 2. Some example crystallite sizes have been labelled in Figure 3.48b, showing crystallites of 2.7 $\mu$m ± 0.05 $\mu$m, 1.8 $\mu$m ± 0.05 $\mu$m and 1.5 $\mu$m ± 0.05 $\mu$m across. The crystallite which has been measured as 2.7 $\mu$m ± 0.05 $\mu$m is partially hidden by the crystallites above it, so it is possible that it is much larger than visible from this image. Figure 3.48 could therefore be depicting an intersection between Estaillades surface types 3 and 4, with smaller crystallites hiding the larger crystallites below.

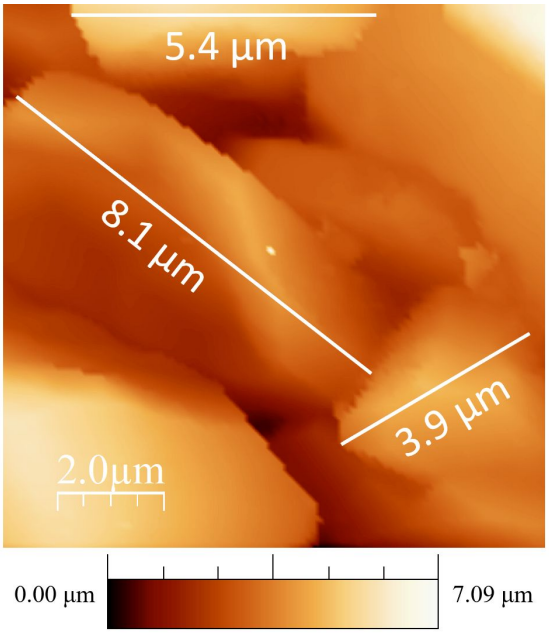
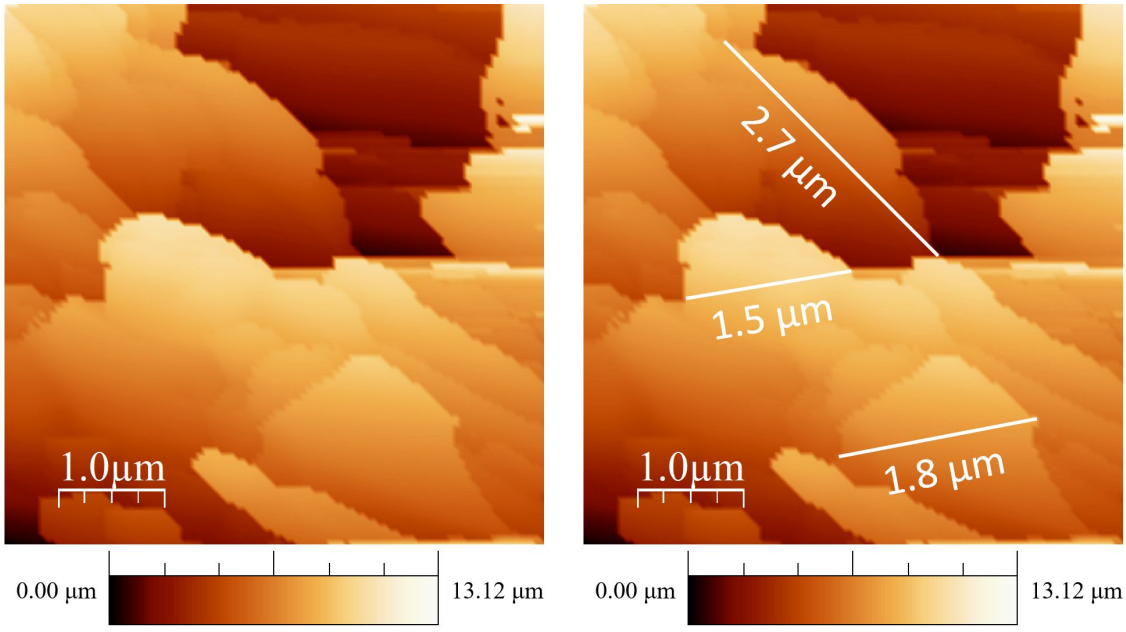
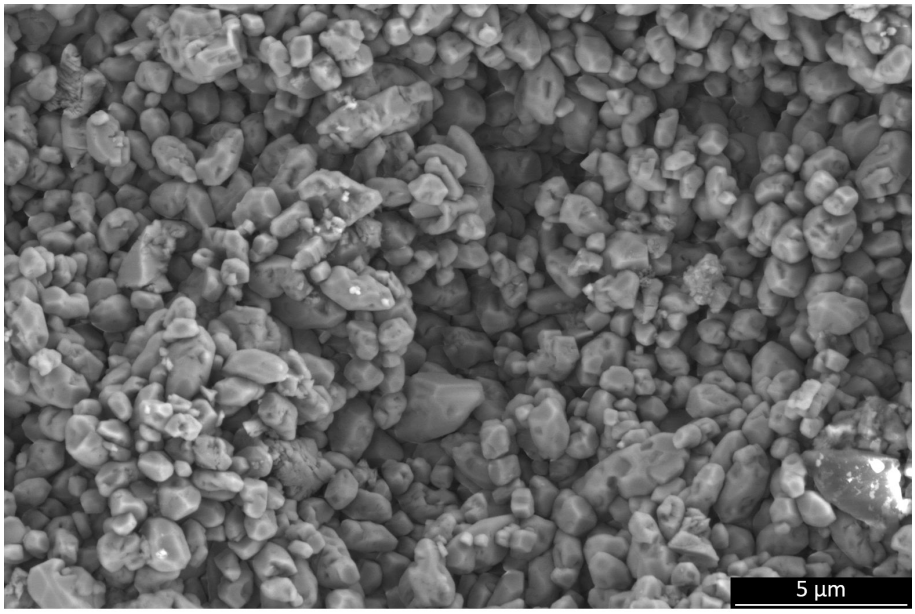



Figure 3.47: Estaillades: crystallite measurement of surface type 3
The 10 × 10 $\mu$m SICM topographical image with a pixel size of 100 × 100 nm previously shown in Figure 3.46d, with measured crystallite lengths.

The SICM has overall found success in mapping the range of regions on the Estaillades surface, capturing examples of all four surface types. This is encouraging not only as it shows SICM's suitability for the topographical mapping of this sample, but also going forward as it lays the groundwork for surface charge mapping using SICM of all Estaillades surface types in future work.




(a) (b)




(c)

Figure 3.48: Estaillades: 5 × 5 $\mu$m SICM image of surface type 4
a) A 5 × 5 $\mu$m SICM topographical image with a pixel size of 50 × 50 nm of what is proposed to be Estaillades surface type 4 as defined in Section 3.2.3. b) shows the same image with a selection of measured crystallite widths labelled. c) A low-vacuum SEM micrograph of an region belonging to Estaillades surface type 4, originally shown in Figure 3.21, page 111, for comparison.

### 3.3.4 Indiana

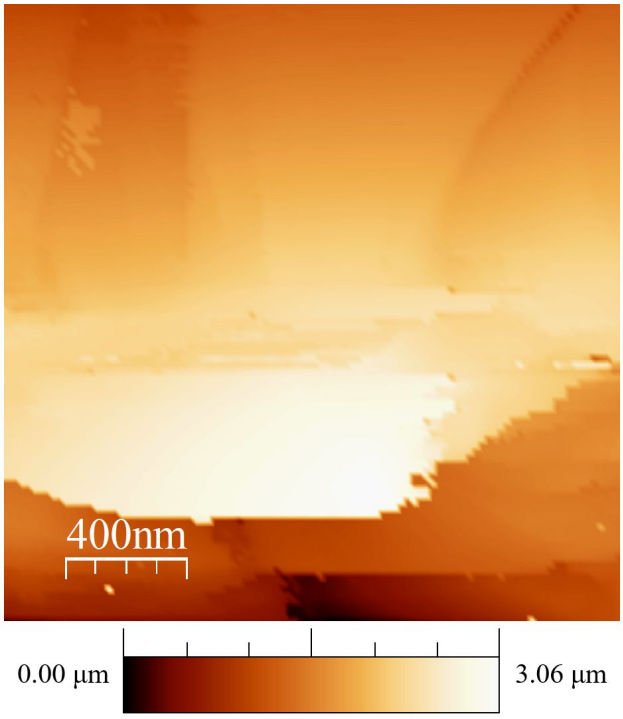
The SEM micrographs of the Indiana surface in Section 3.2.4 showed five different surface types: 1) the flatter areas proposed to be generated during sample preparation, 2) large calcite crystallites which have been cleaved during sample preparation to generate "steps", 3) small irregular crystallites, possibly a fractured surface resulting from sample preparation akin to Estaillades surface type 2, 4) large, intact crystallites similar to Estaillades surface type 3, and 5) smaller crystallites up to 10 $\mu$m in width, split into three sub-types; 5a being made up entirely of crystallites 5 - 10 $\mu$m across, 5b being a mixture of a few crystallites $>$ 5 $\mu$m but mostly 1 - 2 $\mu$m across, and 5c being entirely crystallites $<$ 5 $\mu$m, with the majority between 1 - 2 $\mu$m across. From the two regions imaged by low-vacuum SEM, it appears that surface types 1, 2 and 5 are the most commonly occurring on the surface, and were expected to be the easier to image with SPM techniques as they appear to be present on the more elevated regions of the sample. Surface types 3 and 4 were seen across both low-vacuum SEM micrograph overlays (Figures 3.22 and 3.23, pages 113 and 114), but covered comparatively less of the imaged regions than the other three surface types, and were observed on the more recessed areas of the surface, so were expected to be more challenging to image with SPM techniques.

Figure 3.49 shows a 2 $\times$ 2 $\mu$m SICM topographical image which is proposed to be an example of Indiana surface type 1. There are shallow grooves visible in an otherwise reasonably flat surface towards the top of the image, which as can be seen from the height profile line shown in Figure 3.50, are around 100 - 200 nm in depth. This could be expected from the criss-crossing texture visible in the low-vacuum

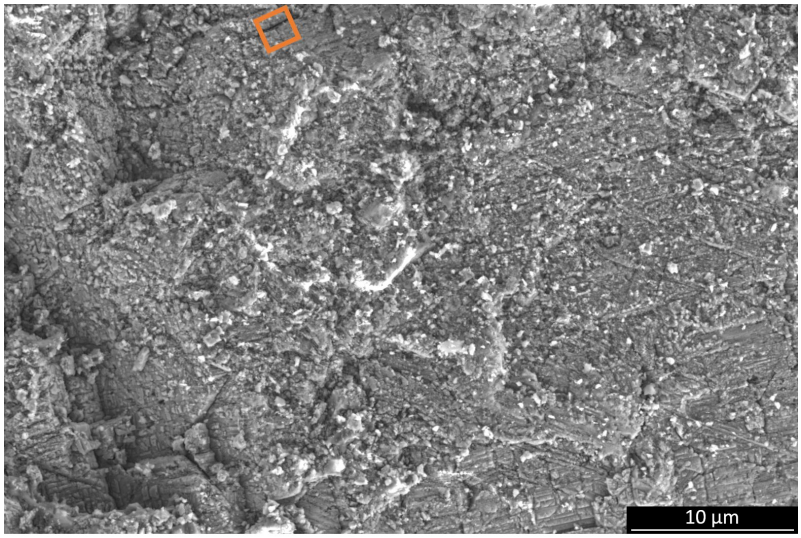
SEM micrograph for surface type 1, which re-shown in Figure 3.49b for ease of comparison with the SICM image.

Towards the bottom of the SICM image of Indiana surface type 1 in Figure 3.49, there is an approximately 3 $\mu$m drop from this flat surface, however this is not incompatible with what was previously observed in the SEM images for Indiana surface type 1. Figure 3.49b shows the high magnification low-vacuum SEM micrograph of Indiana surface type 1 previously shown in Section 3.2.4, Figure 3.24 (page 114), with an orange square representing an approximately 2 $\times$ 2 $\mu$m area on the micrograph. This square has been placed over an area which looks similar to the one shown in the SICM topographical image in Figure 3.49, where a flat area is visible next to a small drop to another flat area. A challenge of using low-vacuum SEM in a workflow alongside an SPM like SICM is the inability to image the exact same area sequentially with each technique. As such it is not proposed that this square on the low-vacuum SEM micrograph indicates the exact area imaged with SICM, but serves as a visual guide to understanding the type of region within Indiana surface type 1 which the SICM topographical image in Figure 3.49 could represent.

Indiana surface type 2 shows large crystallites which have been cleaved to generate a step-like structure. The SICM topographical image in Figure 3.51 covers a 10 $\times$ 10 $\mu$m area and appears to show an example of Indiana surface type 2. A low-vacuum SEM micrograph of Indiana surface type 2 is also re-shown in Figure 3.51 as a reference. The original SICM image is shown in Figure 3.51a, and the equalized version of the same SICM image shown in Figure 3.51b. An equalization function was applied to the image to better highlight the height changes in the image

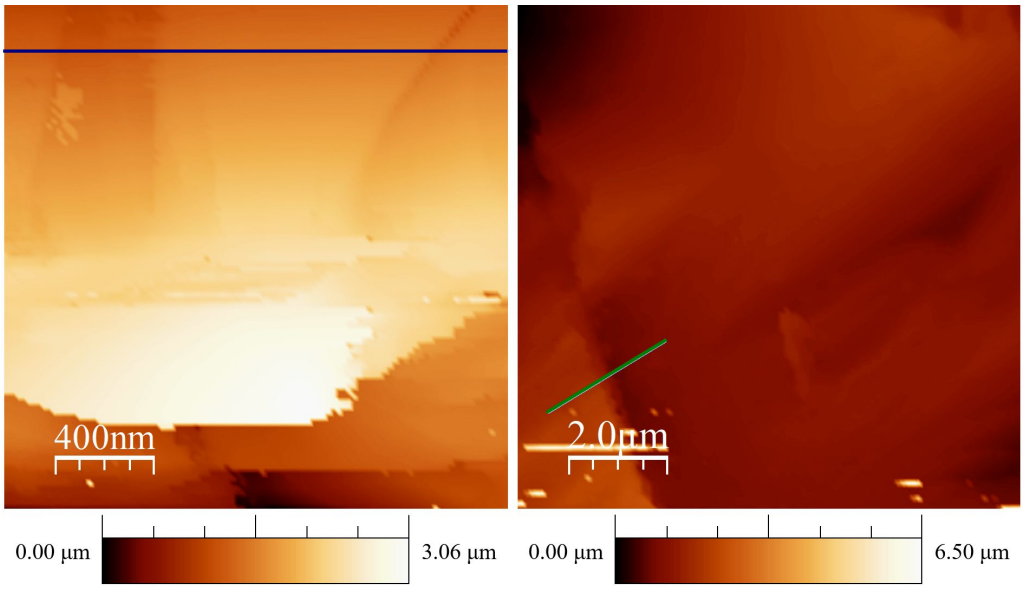



(a)

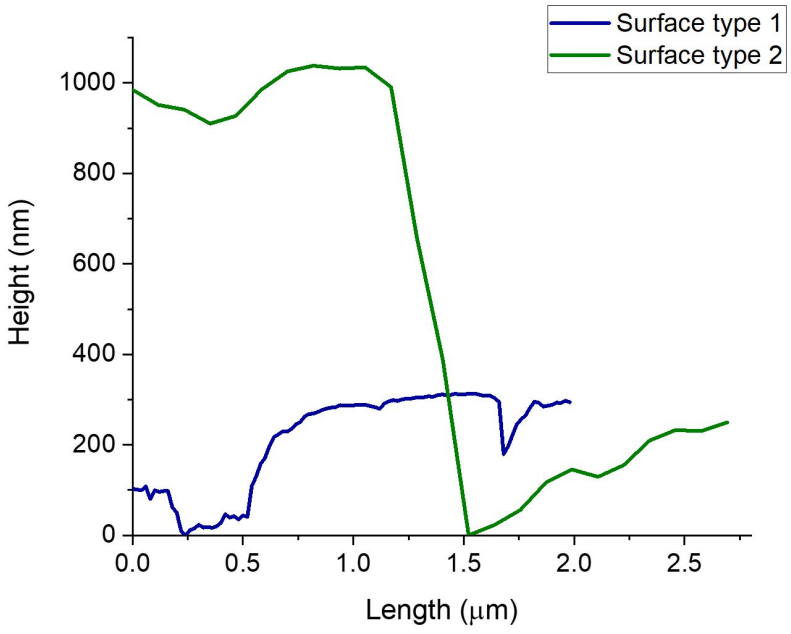



(b)

Figure 3.49: Indiana: 2 × 2 $\mu$m SICM image of surface type 1
(a) A 2 × 2 $\mu$m SICM topographical image with a pixel size of 20 × 20 nm of what is proposed to be Indiana surface type 1 as defined in Section 3.2.4. (b) The high magnification low vacuum SEM micrograph previously shown in Figure 3.24 (page 114), with a 2 × 2 $\mu$m-sized orange square illustrating an example section of what type of region in Indiana surface type 1 the SICM topographical image in Figure 3.49a might be depicting.




(a)

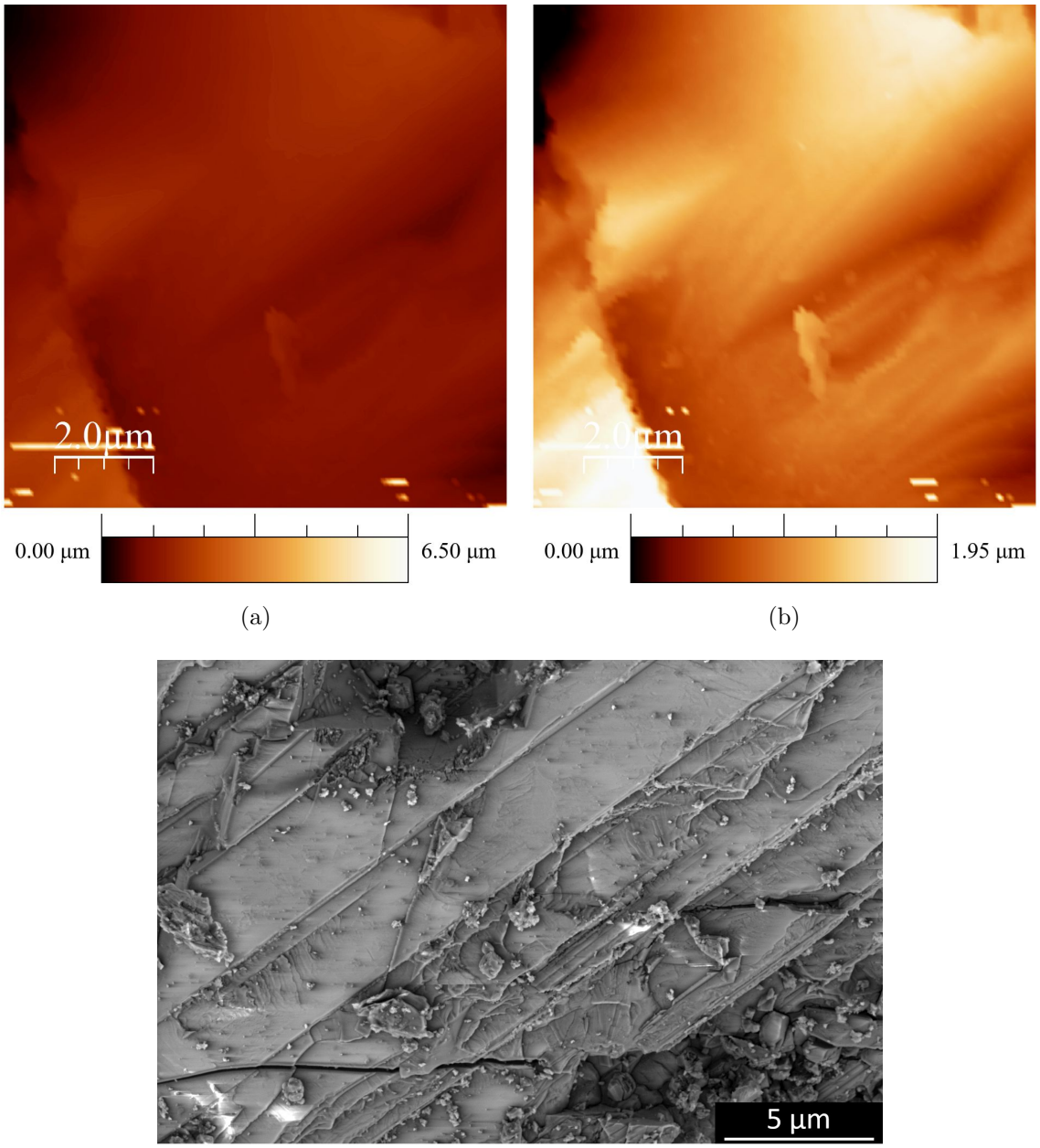



(b)

Figure 3.50: Indiana: height profiles of surface types 1 and 2
A comparison of the step heights visible on the otherwise flat surfaces of the SICM topographical images shown for Indiana surface types 1 and 2 in Figures 3.49 and 3.51 respectively. (a) shows the topographical images with lines indicating where each profile was taken, and (b) shows the height profiles along those lines, each profile running from left to right of the lines depicted in (a).

which were at first less evident due to the noise towards the bottom of the image in Figure 3.51a. The sharp change in height of this step can be seen in the height profile shown in Figure 3.50, with a drop of approximately 1 $\mu$m. This step height is similar to that of the calcite surface type 2 steps measured from SICM images in Section 3.3.1, which showed step heights ranging from 0.6 - 2 $\mu$m; this correlation implies that these surfaces might have been generated in a similar manner, and that the SICM imaging has captured the feature height successfully.

Figure 3.52 shows four SICM images of what are possibly different regions within Indiana surface type 3, which was proposed to have occurred as a consequence of cutting during sample preparation. The rougher crystallites present in these images are similar to those shown in the low-vacuum SEM image of surface type 3 (re-shown in Figure 3.53), all being approximately 1 - 2 $\mu$m across, none of which having the smooth, straight edges seen in Indiana surface types 2, 4 or 5. As the height scale bar ranges in the SICM images in Figure 3.52 sit between 6.91 $\mu$m and 14.30 $\mu$m, these SICM images do not appear to represent Indiana surface type 1 either; the SICM image proposed to belong to surface type 1 in Figure 3.49 having a height scale bar range of 3.06 $\mu$m.




(a) (b)

(c)

Figure 3.51: Indiana: 10 × 10 $\mu$m SICM image of surface type 2
A 10 × 10 $\mu$m SICM topographical image with a pixel size of 100 × 100 nm of what is proposed to be a region of Indiana surface type 2 as defined in Section 3.2.4. (a) and (b) show the same image before and after an equalizing function was applied respectively. (c) shows the high magnification SEM image of Indiana surface type 2 previously shown in Figure 3.25a on page 116 for comparison.

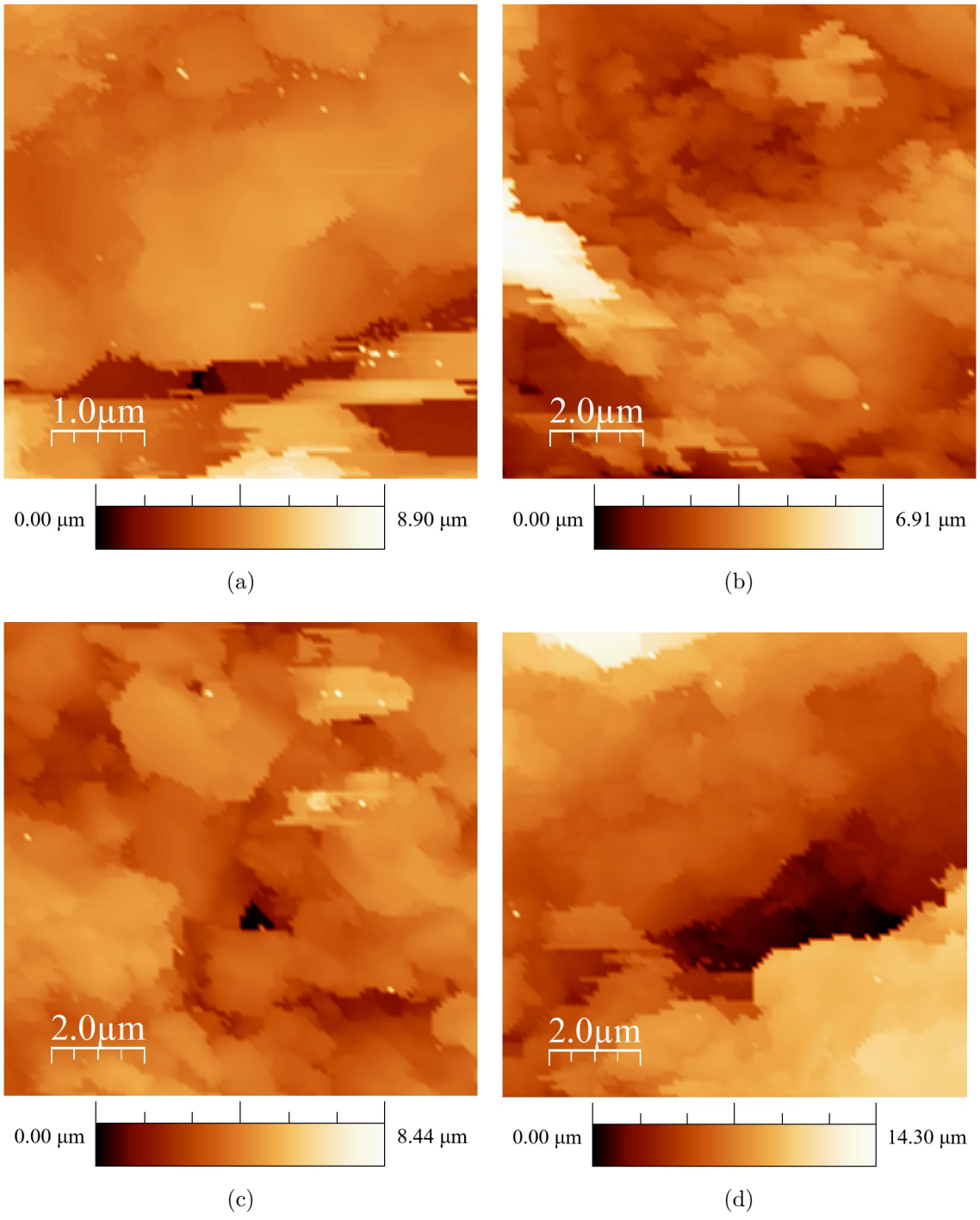



Figure 3.52: Indiana: SICM images of surface type 3
Four SICM topographical images of what is proposed to be Indiana surface type 3 as defined in Section 3.2.4. (a) is a 5 × 5 $\mu$m image with 50 × 50 nm pixels and (b), (c) and (d) are 10 × 10 $\mu$m images with 100 × 100 nm pixels.

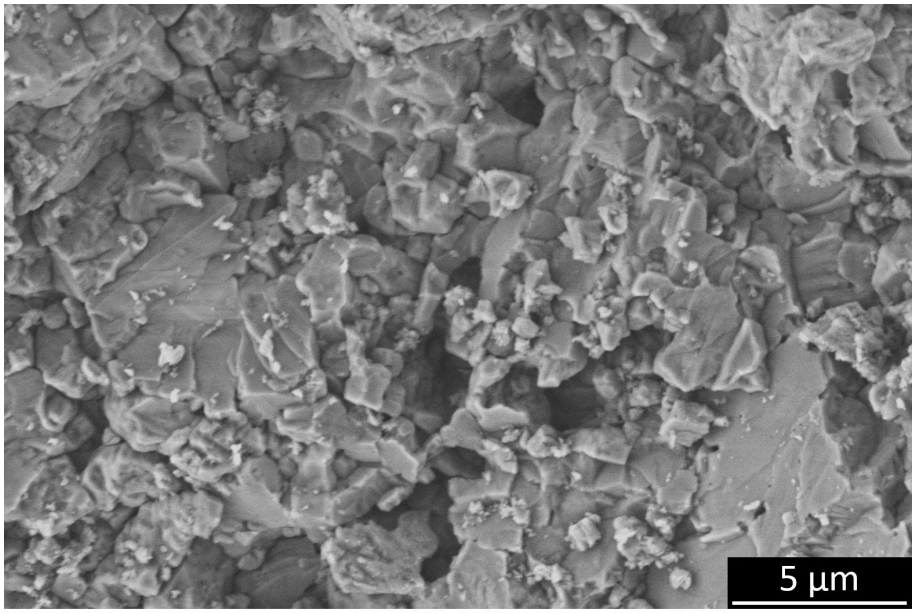



Figure 3.53: Indiana: SEM micrograph of surface type 3
The high magnification low-vacuum SEM micrograph which was originally shown in Figure 3.27 on page 117.

Indiana surface type 5 was characterised by areas of smooth, rounded crystallites, with different sizes present across the three sub-groups 5a, 5b and 5c. Figures 3.54 and 3.55 below show SICM images of two areas which appear to belong to Indiana surface type 5. A range of crystallite sizes are visible in Figure 3.54, with some $< 1$ $\mu$m in diameter, whilst others likely exceeding 2 $\mu$m; their exact size unclear as the image itself is only $2 \times 2$ $\mu$m in size. The size of this SICM image thus makes determining the sub-group of surface type 5 to which it belongs impossible. Figure 3.55 on the other hand depicts two crystallites for which widths can be estimated, as shown by the lines in Figure 3.55b. The height profiles along these lines are shown in Figure 3.55c, which show both crystallites have smooth surfaces, a key characteristic of surface type 5. Both crystallites have diameters of approximately 3.5 $\mu$m, which would suggest that this area belongs to surface type 5b, as most crystallites in 5a and 5c are 5 - 10 $\mu$m and 1 - 2 $\mu$m across respectively.

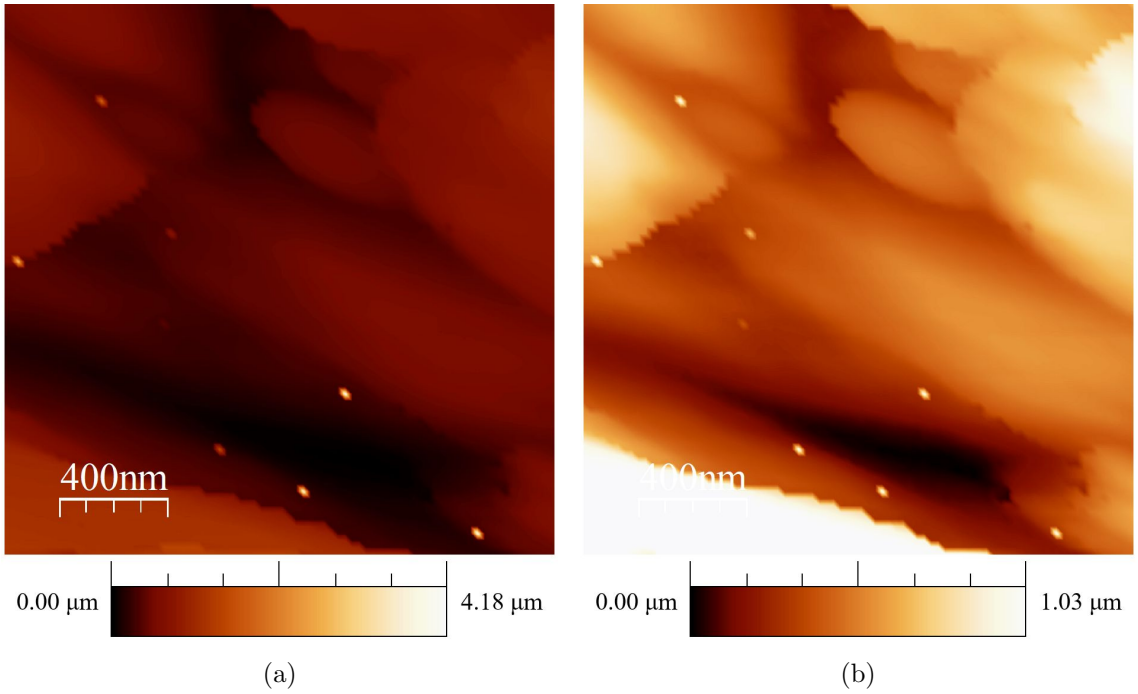
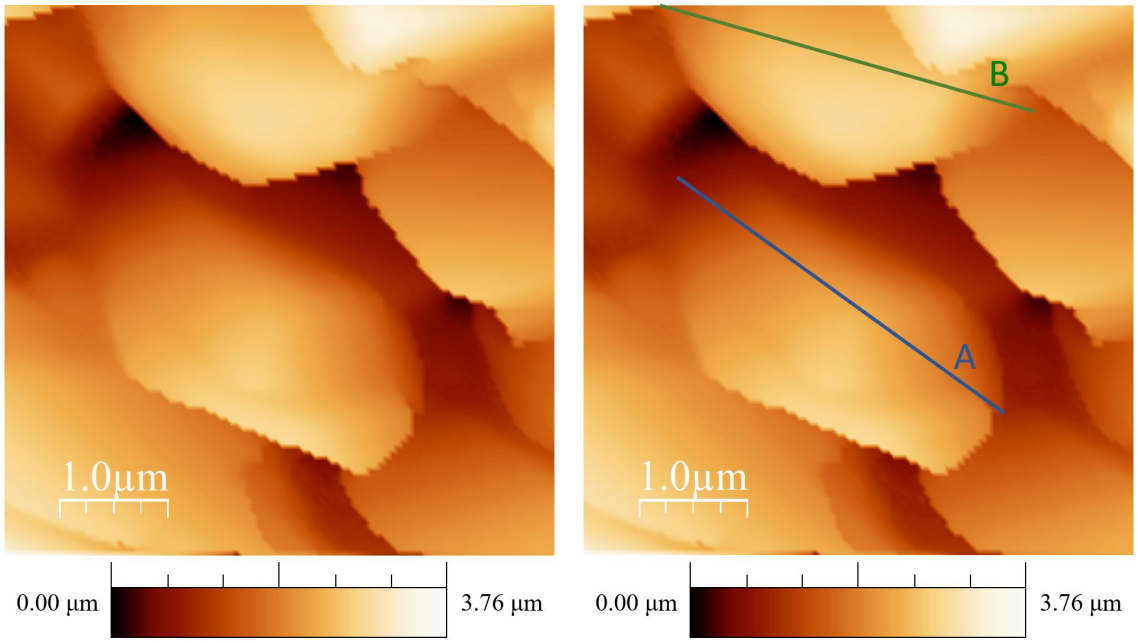
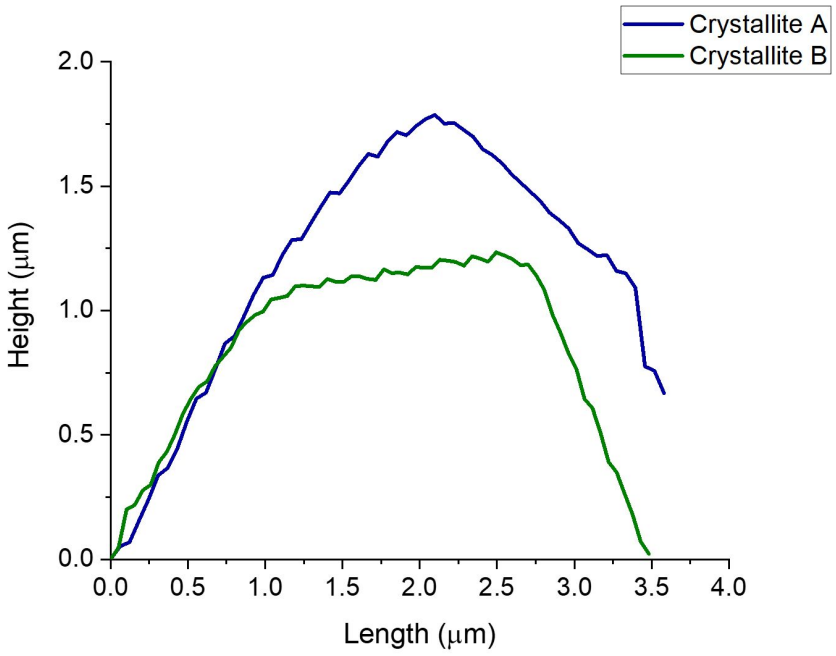



Figure 3.54: Indiana: 2 × 2 $\mu$m SICM image of surface type 5
A 2 × 2 $\mu$m SICM topographical image with a pixel size of 25 × 25 nm of what is proposed to be Indiana surface type 5 as defined in Section 3.2.4. (a) and (b) show the same image before and after an equalizing function was applied respectively.




(a) (b)




(c)

Figure 3.55: Indiana: 5 × 5 $\mu$m SICM image of surface type 5
(a) A 5 × 5 $\mu$m SICM topographical image with a pixel size of 50 × 50 nm of what is proposed to be Indiana surface type 5 as defined in Section 3.2.4. (b) Shows the same image but with lines describing what the two height profiles in (c) are describing.

### 3.3.5 Summary of SICM imaging

Overall the SICM has been shown to be a suitable tool for imaging three carbonate outcrop rocks: Ketton, Estaillades and Indiana. Table 3.7 highlights which of the surface types identified using low-vacuum SEM were subsequently identified in the SICM images. "✓"s indicate where a surface type was identified with some certainty, which was the case for two out of six, four out of five and four out of seven of the surface types and sub-types of Ketton, Estaillades and Indiana respectively. "?"s indicate where an SICM image was too small to provide sufficient information to categorically identify, but where the surface type or sub-type in question was a contender.

Only one surface type/sub-type of each of the carbonates was not identified to any extent; Ketton surface type 5, Estaillades surface type 3b and Indiana surface type 4. In the case of Ketton surface type 5 and Estaillades surface type 3b, these two surfaces types were the least commonly observed surface types in the low-vacuum SEM micrographs, so their absence from the SICM images is possibly due to rarity. Indiana surface type 4 was anticipated to be the least likely to be successfully mapped by SICM due to its large feature sizes, and predominantly occurring on vertical surfaces, so again is unsurprising that it was absent from the SICM images.

| Sample | Type | SICM |
|---|---|---|
| Ketton | 1 | ✓ |
| | 2 | ✓ |
| | 3 | ? |
| | 4 | ? |
| | 5 | |
| | 6 | ? |
| Estaillades | 1 | ✓ |
| | 2 | ✓ |
| | 3a | ✓ |
| | 3b | |
| | 4 | ✓ |
| Indiana | 1 | ✓ |
| | 2 | ✓ |
| | 3 | ✓ |
| | 4 | |
| | 5a | ? |
| | 5b | ✓ |
| | 5c | ? |

Table 3.7: Carbonate surface types identified by SICM
A summary of the carbonate surface types which were identified in the SICM topographical images. "✓" signifies that the surface type was identified in at least one image, no symbol signifies that no examples of that surface type were identified, and "?" signifies that the surface type was a contender for at least one image which did not ultimately provide sufficient information for a definitive identification.

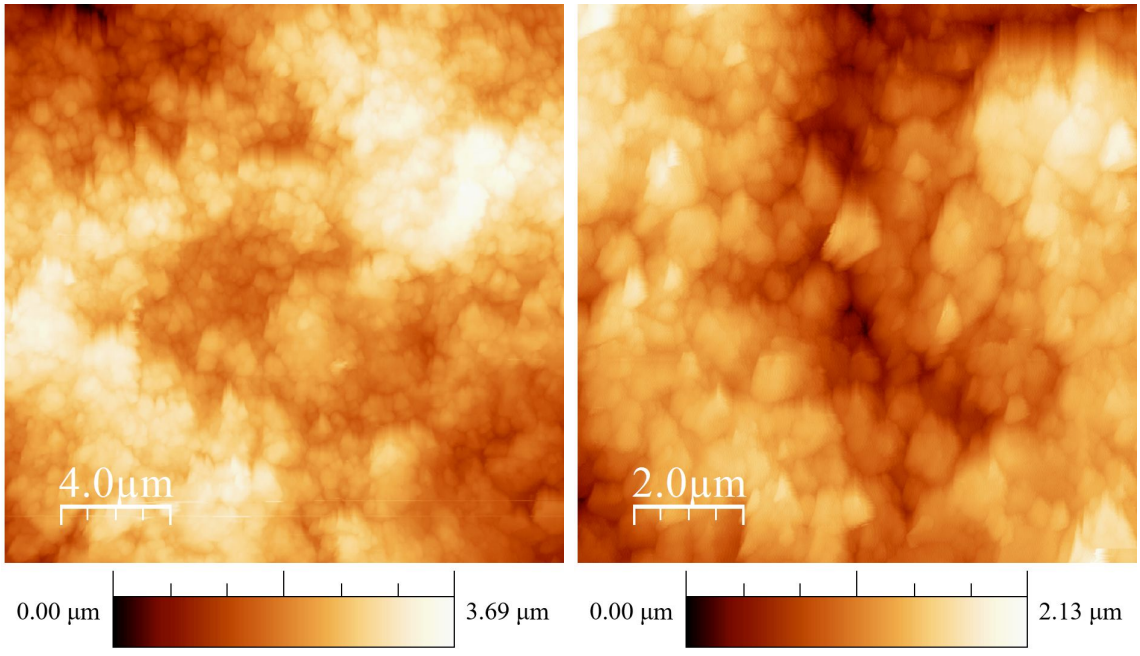
## 3.4 Atomic force microscopy

As a scanning probe microscopy which had already been used in the field of oil and gas recovery for generating topographical images of outcrop rocks,[110–113] AFM was used to collect images of Ketton, Estaillades and Indiana primarily to validate those collected on the SICM in terms of the shapes, heights and widths of the features recorded. In doing so, a correlative approach is used once more to assign the AFM images to one of the surface types defined in Section 3.2.

### 3.4.1 Ketton

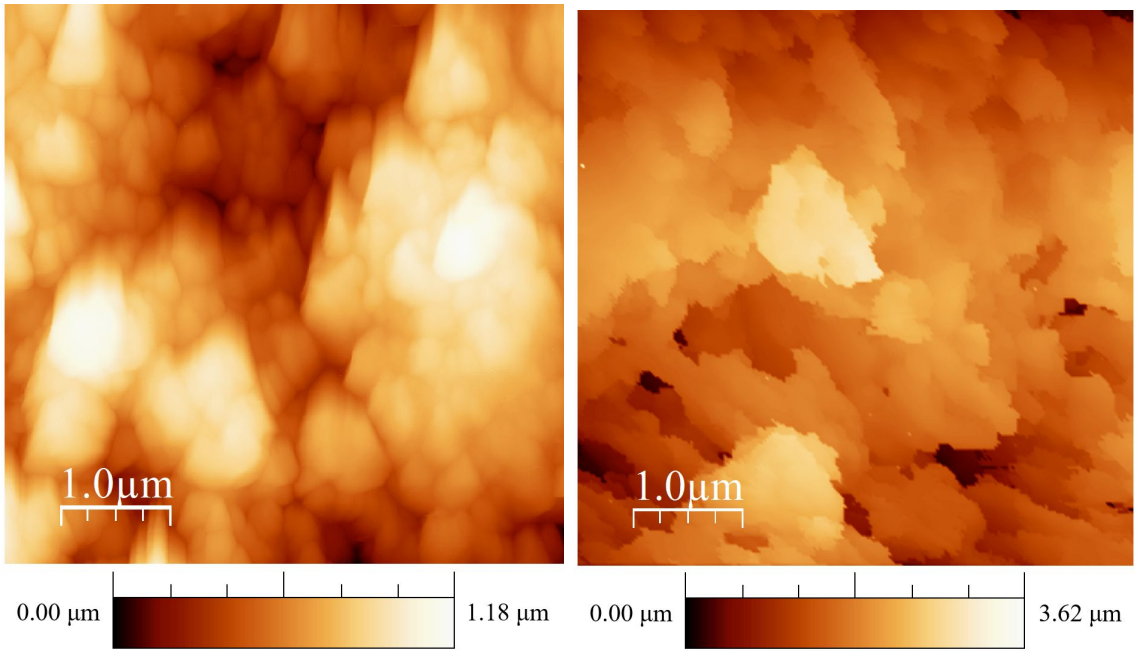
Three AFM images of Ketton which appear to be of Ketton surface type 3, 4 or 6 are presented in Figure 3.56 alongside an SICM image originally shown in Figure 3.40a (page 137) which was also proposed to be from surface type 3 or 4 for comparison. All three AFM images show small crystallites $< 1$ $\mu$m, similar to the surfaces observed by low-vacuum SEM in Section 3.2.2 and the SICM image re-shown in Figure 3.56d.

Height profiles from the $5 \times 5$ $\mu$m AFM and SICM images in Figures 3.56c and 3.56d are presented in Figure 3.57 to compare typical feature sizes and shapes recorded by the two SPMs. In the graph of the height profiles in Figure 3.57c, the positions of the profiles relative to one another on the $y$-axis have been changed in order to more clearly see all traces, and the SICM traces have been displaced 6 $\mu$m across the $x$-axis such that the traces for each SPM are displayed beneath the relevant image. From these traces, it can be seen that most of the raised features are on the order of 0.5 $\mu$m across, with the larger features closer to 1 $\mu$m across, which is consistent with what was observed in surface types 3 and 4 in the low-




(a) 20 × 20 $\mu$m AFM image

(b) 10 × 10 $\mu$m AFM image



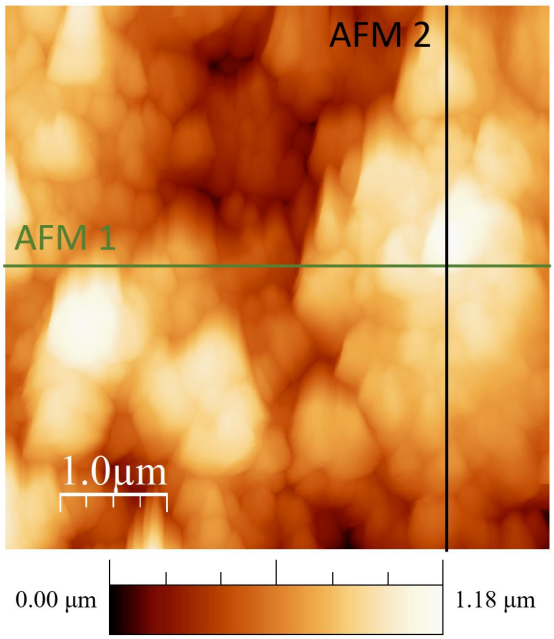

(c) 5 × 5 $\mu$m AFM image

(d) 5 × 5 $\mu$m SICM image

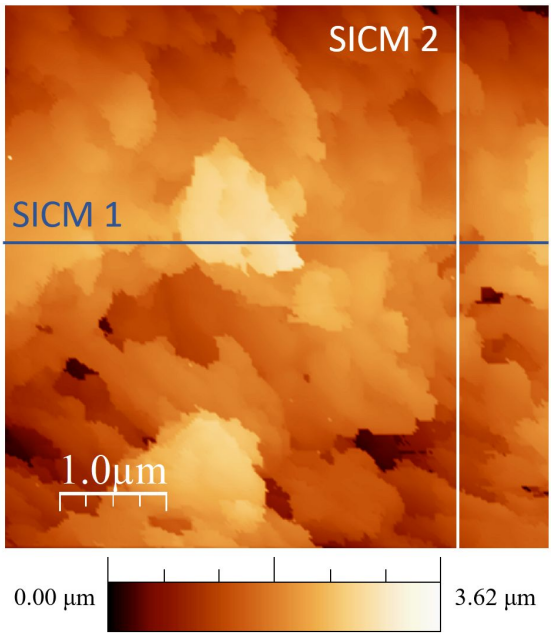
Figure 3.56: Ketton: Three AFM images of surface type 3 or 4
Three AFM images of Ketton: (a) a 20 × 20 $\mu$m image with approximately 20 × 20 nm pixels (1024 × 1024 points), (b) a 10 × 10 $\mu$m image with approximately 10 × 10 nm pixels (1024 × 1024 points) and (c) a 5 × 5 $\mu$m image with approximately 5 × 5 nm pixels (1024 × 1024 points). (d) Shows a the 5 × 5 $\mu$m SICM image proposed to be from either surface type 3 or 4, which was originally shown in Figure 3.40a (page 137) for comparison.

vacuum SEM micrographs. The majority of these features are around 250 nm high relative to their adjacent features, with the exception of a few features in the SICM image, as the SICM image appears to be of a slightly rougher region. The key difference between the two SPM's traces however, is the sharpness of the edges of each feature in the SICM image compared to the AFM image. This possibly due to the comparatively higher pixel density in the AFM image, which contains over $1 \times 10^6$ pixels, whereas the SICM image only contains $1 \times 10^4$ pixels, and as such, height changes are observed more abruptly in the SICM image.

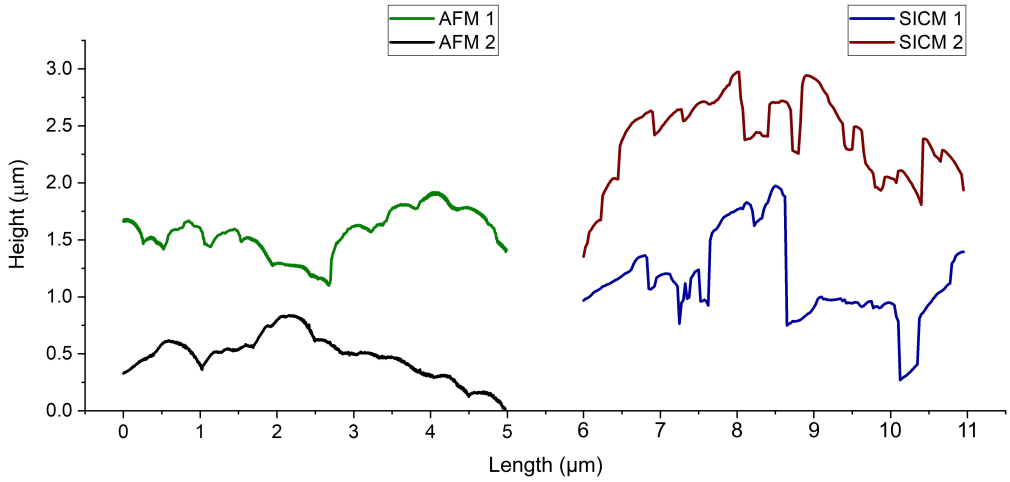
The AFM images of Ketton have a blurred quality to them, with a ghosting effect observed adjacent to the majority of the crystallites on the surface. This is most likely due to the roughness of the surfaces compared to typical candidates for AFM imaging, and possibly due to less time being dedicated to the AFM, for scan parameters to be fully optimised; the SICM image on the other hand is much clearer, and allows for more accurate crystallite size measurements to be made. The relative ease in obtaining clear images of these materials is likely due to the differences between hopping mode on the SICM and tapping mode in the AFM. Whilst carrying out the SICM imaging the hop height of the probe between points is much higher, 1 - 5 $\mu$m in this work, than the amplitude of cantilever oscillation in AFM tapping mode, which is typically 10 - 100 nm.[114,115] This smaller amplitude in AFM therefore might not be fully accommodating the sharp height changes observed in these samples. AFM images are also typically much faster to acquire; AFM imaging of these materials takes around 10-20 minutes, whereas each SICM image takes around 2 hours to collect.




(a) 5 × 5 $\mu$m AFM image




(b) 5 × 5 $\mu$m SICM image

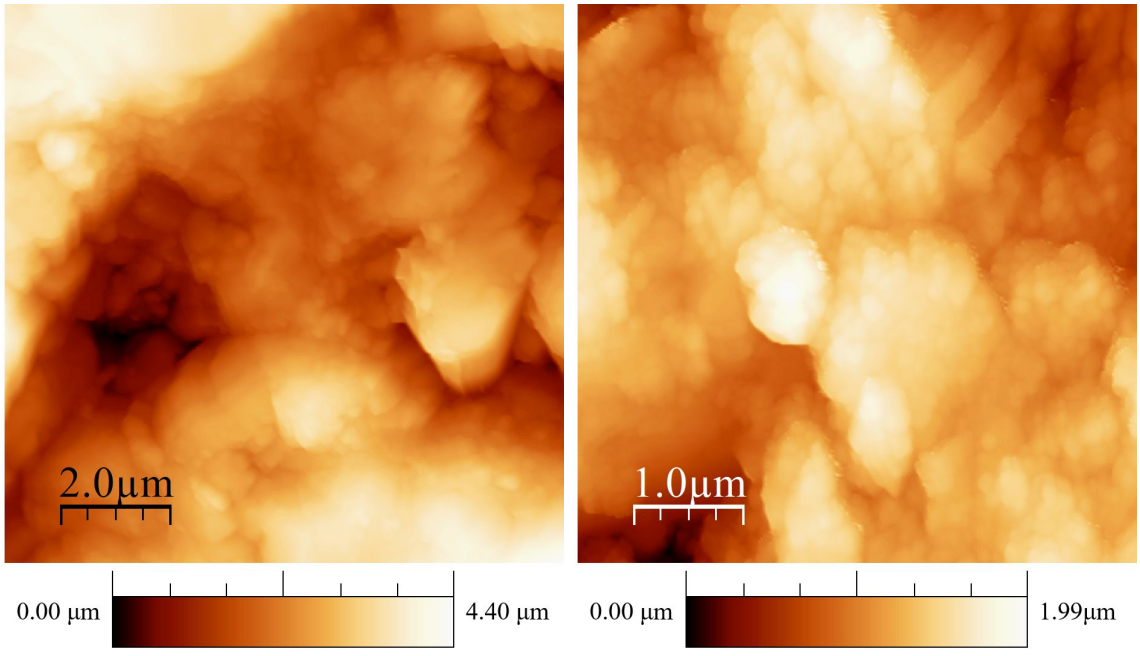



(c) Height profiles

Figure 3.57: Ketton: AFM and SICM images compared
The 5 × 5 $\mu$m (a) AFM and (b) SICM images from Figure 3.56, with height profiles labelled and shown in (c) for comparison of feature widths and heights.

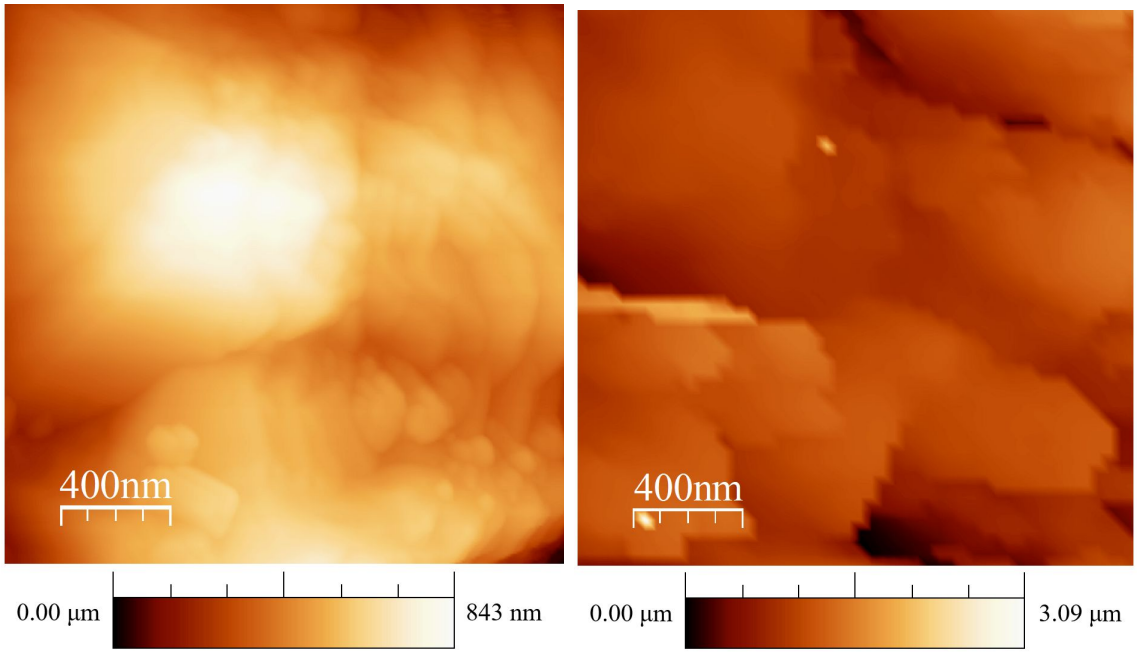
### 3.4.2 Estaillades

AFM images were collected of Estaillades surface area types 2 and 3, shown below in Figures 3.58 and 3.59 respectively. Estaillades surface type 2 is an amorphous area of broken crystallites, deemed as most likely to be the result of the cutting of the cores, whereas surface type 3 represents the area of smooth crystallites, with a size range of 5 - 10 $\mu$m across. Given the roughness of surface type 2, topographical images of these areas will have a range of height scale bar ranges, in the AFM images in Figure 3.58 these range from 843 nm - 4.40 $\mu$m, and the crystallite sizes will also vary. Surface type 2 is however distinct from the other areas in that it is not flat like surface type 1, and is not made up of the smooth crystallites which are seen in surface types 3 and 4. Therefore, despite the crystallites observed in the AFM images in Figure 3.58 being smaller than those in the SICM image re-shown in Figure 3.58d, they are proposed to all belong to the same surface type. As was the case with the AFM images on Ketton, the AFM images in Figure 3.58 appeared blurred when compared to the SICM image in Figure 3.58d. It is hypothesized that this is due to the same factors as were discussed for the Ketton images; that the AFM tapping mode did not respond quickly enough at the scan speed chosen, as such the feature edges are not clearly resolved.




(a) 10 × 10 $\mu$m AFM image

(b) 5 × 5 $\mu$m AFM image



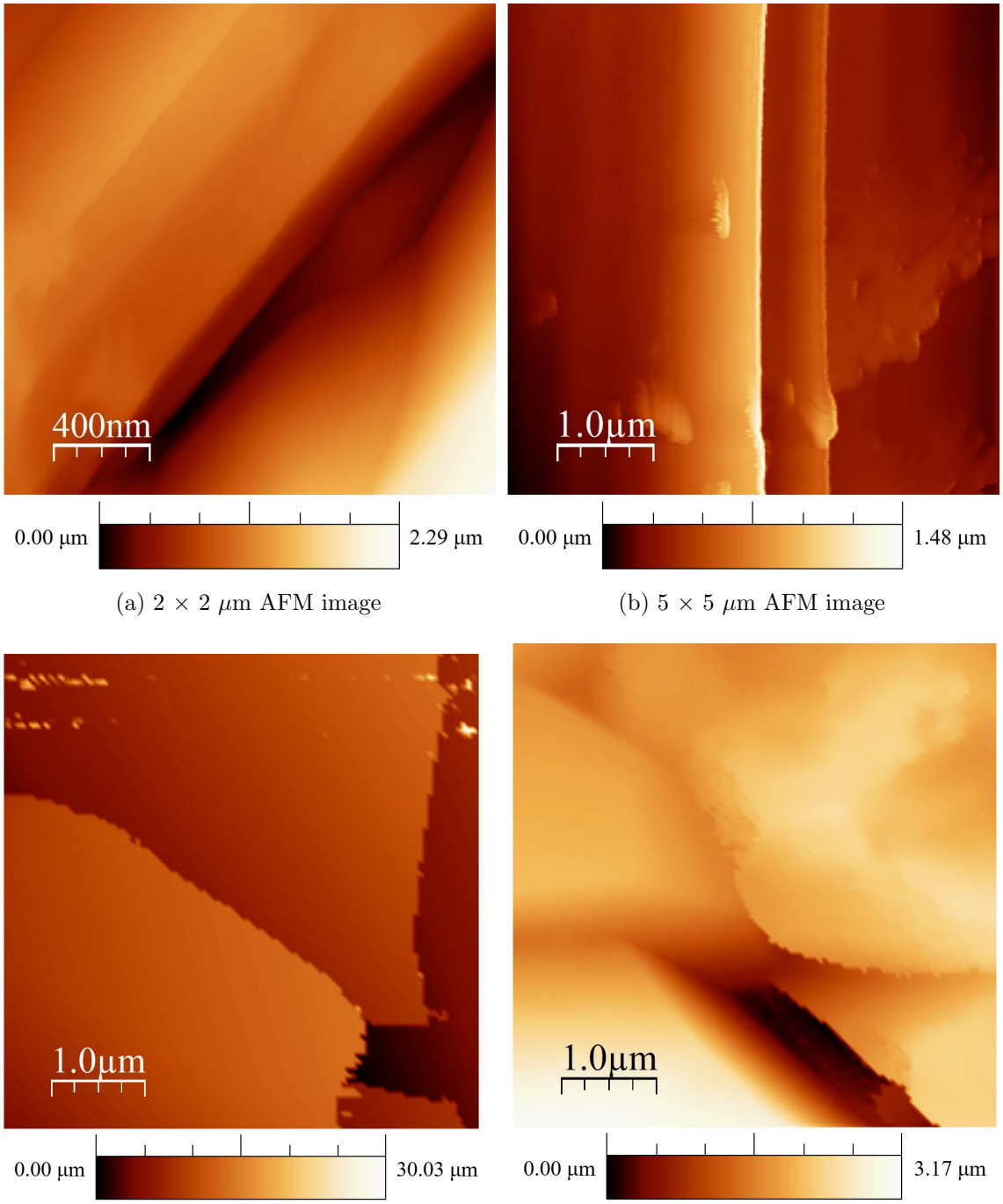

(c) 2 × 2 $\mu$m AFM image

(d) 2 × 2 $\mu$m SICM image

Figure 3.58: Estaillades: AFM images of surface type 2
Three AFM images of surface type 2, (a) being a 10 × 10 $\mu$m image with a pixel size of approximately 40 × 40 nm (256 × 256 points), (b) being a 5 × 5 $\mu$m image with a pixel size of approximately 20 × 20 nm (256 × 256 points) and (c) being a 2 × 2 $\mu$m image with a pixel size of approx 8 × 8 nm (256 × 256 points). The 2 × 2 $\mu$m SICM image of surface type 2 originally shown in Figure 3.42a (page 141) is re-shown in (d) for comparison.

The AFM images in Figures 3.59a and 3.59b appear to be of Estaillades surface type 3. Given that they are 2 × 2 $\mu$m and 5 × 5 $\mu$m in size, the large 5 - 10 $\mu$m crystallites of surface type 3 can not be fully mapped, however in both images it is clear that the smooth crystallites which are partly in view exceed 1 - 2 $\mu$m, and so do not belong to surface type 4, and so are assigned as belonging to surface type 3. The AFM image in Figure 3.59a appears to show the gap between two of these crystallites, which is similar to the SICM image re-shown in 3.59c for ease of comparison. In Figure 3.59b a rough-edged feature, possibly indicative of a more amorphous region, can be seen to the right of the image, with small rough-edged crystallites visible on the larger, smoother surfaces to the left. This image is therefore proposed to map an intersection between surface types 2 and 3, such as that observed in the SICM image re-shown in Figure 3.59d, where again a rougher area is seen to the right of the image, being surface type 2, with large, smooth crystallites seen towards the left of the image, being surface type 3.

The AFM images of surface type 3 presented in Figure 3.59 are much clearer than those of surface type 2 presented in Figure 3.58. This is possibly due to the differences between the surface types being mapped; the regions shown in Figure 3.59 are much smoother than Figure 3.58, and so the AFM is not having to accommodate for repeated height changes as regularly, leading to a clearer image. This is further underpinned by there being blurring around the rougher areas mapped in Figure 3.59b, and the rest of the image, of the smoother surface, being sharper.




(a) 2 × 2 $\mu$m AFM image

(b) 5 × 5 $\mu$m AFM image

(c) 5 × 5 $\mu$m SICM image

(d) 5 × 5 $\mu$m SICM image

Figure 3.59: Estaillades: AFM images of surface type 3
Two AFM images of surface type 3, (a) being a 2 × 2 $\mu$m image with a pixel size of approx 8 × 8 nm (256 × 256 points) and (b) being a 5 × 5 $\mu$m image with a pixel size of approximately 20 × 20 nm (256 × 256 points). Two 5 × 5 $\mu$m SICM images of surface type 3, originally shown in Figures 3.46a and 3.44a (on pages 146 and 144 respectively) are re-shown in (c) and (d) respectively for comparison.

### 3.4.3 Indiana

Five AFM images of Indiana are shown across Figures 3.60 and 3.61, and appear to all belong to surface type 3. Briefly, the Indiana surface types are 1) the flatter areas created during sample preparation, with calcite crystal lines visible, 2) step-like structures formed during cutting, exposing the calcite crystal planes, 3) the rough-textured area which is proposed to be generated during cutting, made up of fractured calcite grains with a wide range of sizes, 4) the large, smooth, un-damaged calcite crystallites, on the order of 10 - 100 $\mu$m across, and 5) the smaller, smooth, un-damaged crystallites, ranging from 1 - 10 $\mu$m across.

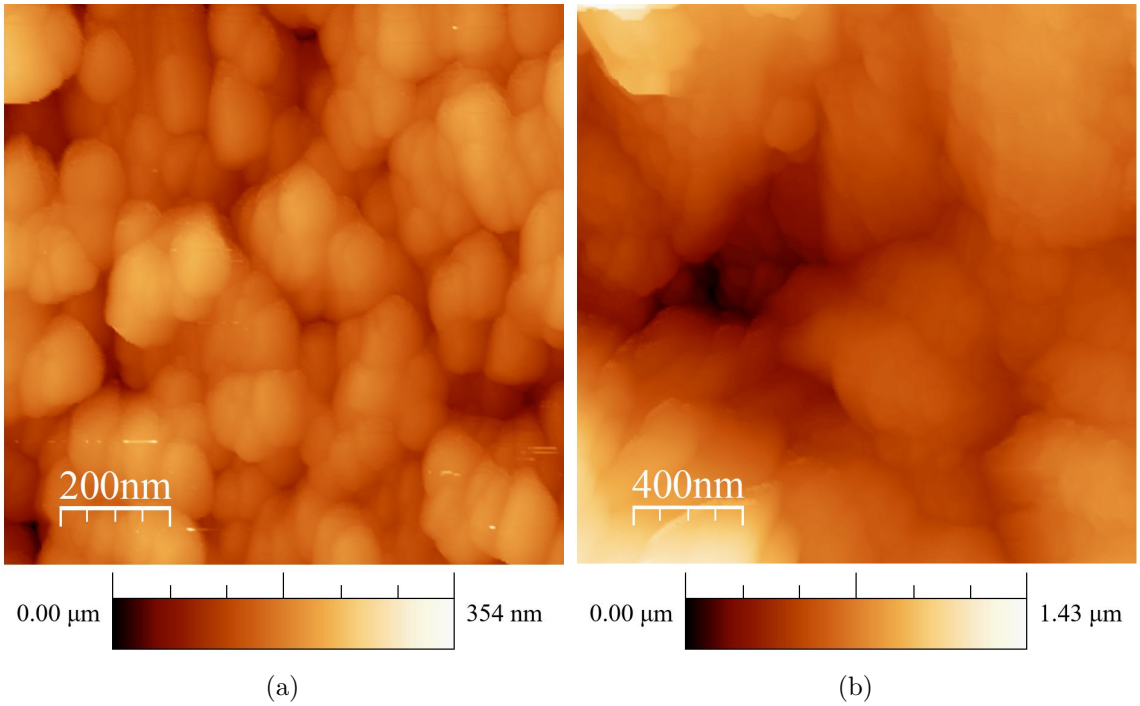
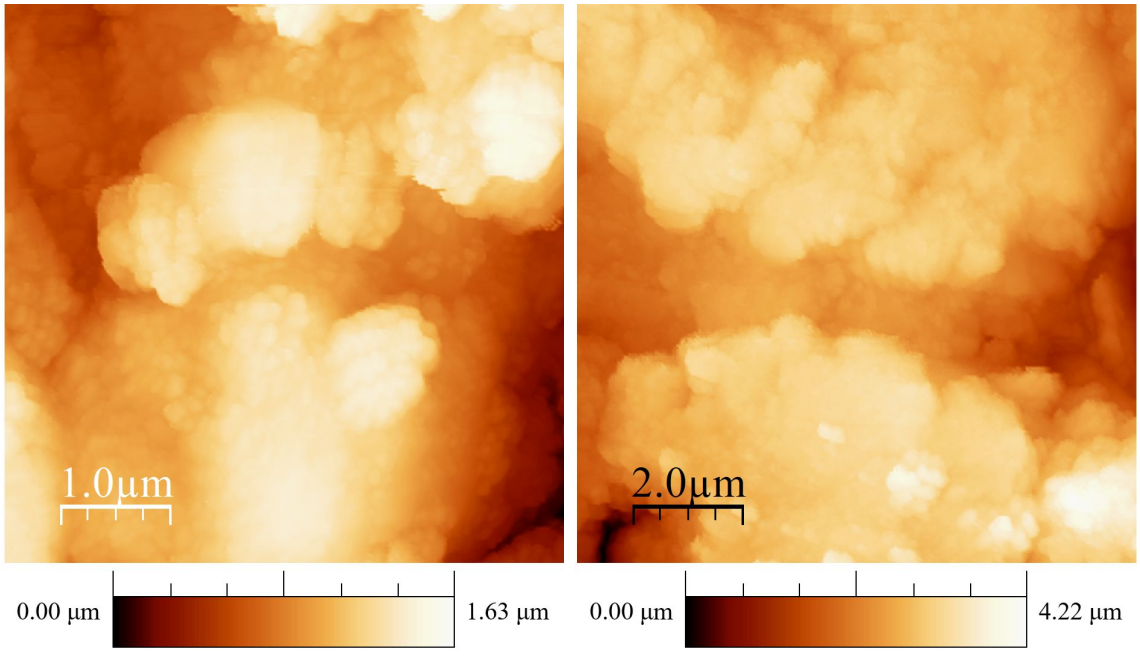


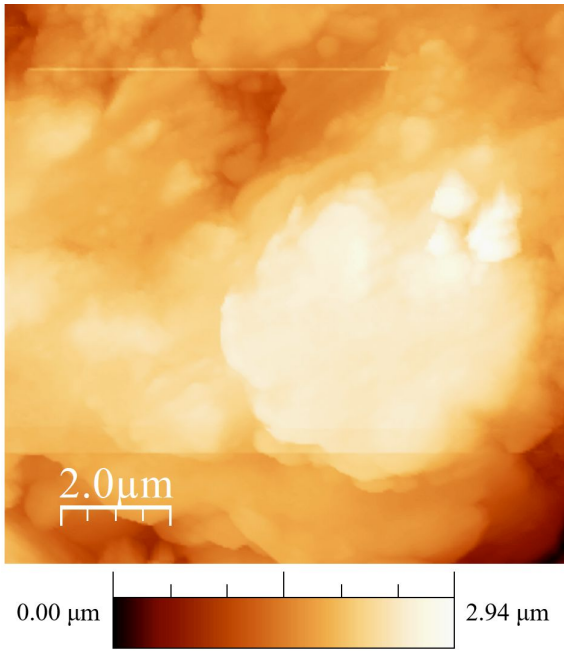

Figure 3.60: Indiana: Two AFM image of surface type 3
Two AFM images of Indiana surface type 3, (a) being a 1 × 1 $\mu$m AFM image with a pixel size of approx 4 × 4 nm (256 × 256 points) and (b) being a 2 × 2 $\mu$m image with a pixel size of approx 8 × 8 nm (256 × 256 points).



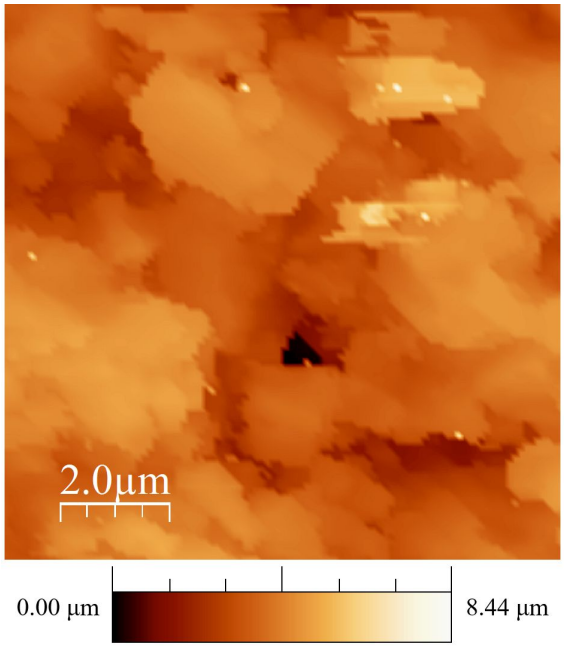

(a) 5 × 5 $\mu$m AFM image




(b) 10 × 10 $\mu$m AFM image




(c) 10 × 10 $\mu$m AFM image




(d) 10 × 10 $\mu$m SICM image

Figure 3.61: Indiana: Three AFM images of surface type 3
Three AFM images of surface type 3, (a) being a 5 × 5 $\mu$m image with a pixel size of approximately 20 × 20 nm (256 × 256 points) and (b) and (c) being 10 × 10 $\mu$m images with a pixel size of approximately 40 × 40 nm (256 × 256 points). (d) Shows the 10 × 10 $\mu$m SICM image of Indiana surface type 3 originally shown in Figure 3.52c (page 156) for ease of comparison.

All of the crystallites imaged across Figures 3.60 and 3.61 are $< 1$ $\mu$m across, and as such are too small to belong to any of the surface type 5 sub-types, and they all appear to have rough edges, so are therefore all assigned as belonging to surface type 3. A SICM image which was assigned to surface type 3, originally shown in Figure 3.52c on page 156, is re-shown in Figure 3.61d for ease of comparison to the AFM images. Visually, this SICM image is very similar to the other AFM images in Figure 3.61, the surface made up of clusters of smaller rough-edged crystallites. The height scale bar range is much higher in the SICM map, at 8.44 $\mu$m, than the AFM maps, between 1.63 and 4.22 $\mu$m; however, this is due to the difference between the deep pore in the center of the SICM image, and the few, assumed erroneously, bright pixels.

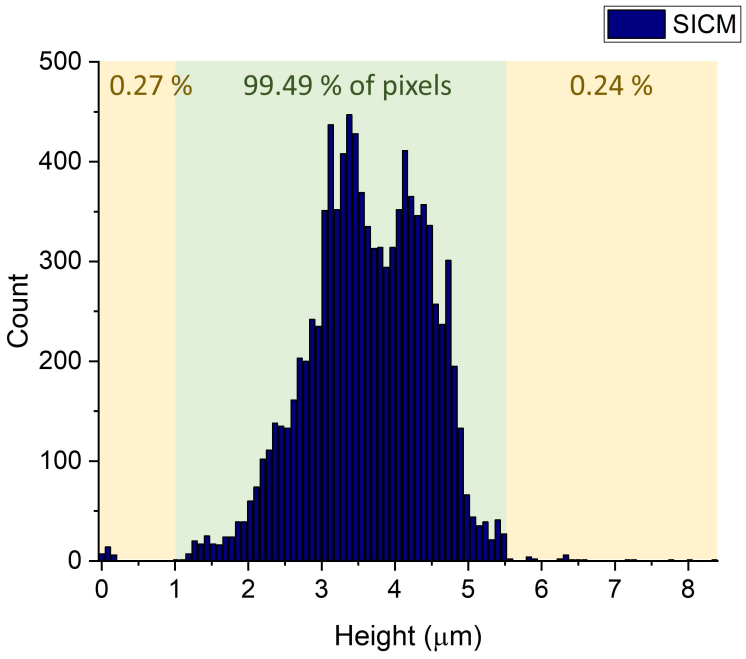



Figure 3.62: Indiana: SICM image height histogram
A histogram of the pixel height values in the SICM image represented in Figure 3.52c, and again in Figure 3.61d, showing that the majority of the pixel values sit in a 4.5 $\mu$m range between 1 and 5.5 $\mu$m.

As can be seen from the histogram presented in Figure 3.62, 99.5 % of the pixels in the SICM map sit within an approximately 4.5 $\mu$m range between 1 - 5.5 $\mu$m, highlighted in green, which is much closer to the 4.22 $\mu$m range observed in the AFM image shown in Figure 3.61b. As observed previously when looking at the Ketton and Estaillades AFM images, the AFM images collected of the Indiana surface are blurry in comparison to the SICM image, which is expected to be due to the same factors previously discussed.

### 3.4.4 Summary of AFM imaging

Overall, AFM has been shown to have validated the SICM images shown in Section 3.3. On some of the rock surface types, it was found that the SICM images were clearer. This is possibly due to an insufficient optimisation of AFM scan parameters, or could indicate that SICM may be a better tool for investigating these materials than AFM; further studies would be required to make a definitive assessment. Table 3.8 shows which of the surface types identified in the low-vacuum SEM micrographs of Ketton, Estaillades and Indiana were also identified in the AFM images. Fewer surfaces were identified in the AFM images than in the SICM images (Table 3.7, page 161), which is possibly to be, at least in part, due to fewer sessions being devoted to AFM imaging than SICM imaging.

| Sample | Type | AFM |
|---|---|---|
| Ketton | 1 | |
| | 2 | |
| | 3 | ? |
| | 4 | ? |
| | 5 | |
| | 6 | ? |
| Estaillades | 1 | |
| | 2 | ✓ |
| | 3a | ✓ |
| | 3b | |
| | 4 | |
| Indiana | 1 | |
| | 2 | |
| | 3 | ✓ |
| | 4 | |
| | 5a | |
| | 5b | |
| | 5c | |

Table 3.8: Carbonate surface types identified by AFM
A summary of the carbonate surface types which were identified in the AFM topographical images. "✓" signifies that the surface type was identified in at least one image, no symbol signifies that no examples of that surface type were identified, and "?" signifies that the surface type was a contender for at least one image which did not ultimately provide sufficient information for a definitive identification.

## 3.5 Summary and conclusions

It has been demonstrated that low-vacuum SEM and SICM can be used in tandem to better understand the surfaces of carbonate outcrop rocks. From the SEM micrographs it was possible to determine six individual surface types of interest on Ketton, four on Estaillades and five on Indiana. The SICM images which were subsequently collected of these materials appear to show four or five out of six of these types on Ketton, all four on Estaillades and four out of five on Indiana. Without the low-vacuum SEM micrographs for reference, understanding the context of each of the SICM topographical images would have been significantly more challenging. Using the low-vacuum SEM micrographs for reference also demonstrated that SICM is a suitable tool for imaging a wide range of the surface types found on these materials.

Comparison of the SICM and AFM images demonstrated that the SICM could not only image similar areas, but generate clearer, sharper images than the AFM, particularly on the rougher surface types, highlighted in particular when looking at Ketton surface type 3 or 4 and Estaillades surface type 2. Despite the SICM providing better images than the AFM of these carbonates, the trade-off is time; AFM can be used to generate images 6 - 12× faster than the SICM, which is of consideration if this technique were to be more widely used by the industry for routine sample analysis. Coupled with the surface charge mapping potential of SICM however, these clearer images could provide even greater value and tip the balance in favour of SICM over AFM for topographical analysis of these samples.

Table 3.9 on page 177 presents the qualitative descriptions of the carbonate reservoir rock surface types from Tables 3.2, 3.3 and 3.4 (pages 105, 111 and 121

respectively), alongside the data from the SICM and AFM summary tables, Tables 3.7 and 3.8 (pages 161 and 174 respectively), in order to best summarise the information collected in this Chapter.

Overall, it has been shown that SICM is a suitable tool for topographical mapping of these carbonate outcrop rocks. There is also evidence to suggest that the SICM has an advantage over AFM for mapping of the range of surface types on these rough surfaces. Further insight can be gained from the SPM techniques when coupled with low-vacuum SEM, as the smaller field of view SPM images can be placed into context within the wider surface heterogeneity.

| Sample | Type | Description | SICM | AFM |
|---|---|---|---|---|
| Ketton | 1 | Intact ooid grain surface, covered with smooth crystallites | ✓ | |
| | 2 | Ooid grain surface with spikey structures on top | ✓ | |
| | 3 | Ooid grain shell cross-section, irregular crystallites | ? | ? |
| | 4 | Fractured ooid grain shell exterior, irregular crystallites | ? | ? |
| | 5 | Large crystallites inside of ooid grain | | |
| | 6 | Fractured ooid grain shell interior, irregular crystallites | ? | ? |
| Estaillades | 1 | Flat regions caused by cutting during sample preparation | ✓ | |
| | 2 | Fractured regions adjacent to flat regions, result of cutting | ✓ | ✓ |
| | 3a | Large, intact crystallites | ✓ | ✓ |
| | 3b | Large crystallites, fractured to reveal a step-like structure | | |
| | 4 | Small, intact crystallites | ✓ | |
| Indiana | 1 | Flat regions caused by cutting during sample preparation | ✓ | |
| | 2 | Large crystallites, fractured to reveal a step-like structure | ✓ | |
| | 3 | Fractured regions adjacent to flat regions, result of cutting | ✓ | ✓ |
| | 4 | Large, intact crystallites | | |
| | 5a | | ? | |
| | 5b | (a-c) Small, intact crystallites | ✓ | |
| | 5c | | ? | |

Table 3.9: Summary of the carbonate rock surface types and SICM and AFM identification
A summary of the different surface types identified on the Ketton, Estaillades and Indiana samples. Qualitative descriptions are taken from the individual summary tables 3.2, 3.3 and 3.4 on pages 105, 111 and 121 respectively, and are shown alongside details of whether a surface type was identified in the SICM or AFM images. "✓" signifies that the surface type was identified in at least one image, no symbol signifies that no examples of that surface type were identified, and "?" signifies that the surface type was a contender for at least one image which did not ultimately provide sufficient information for a definitive identification.

# Chapter 4

# Surface Charge Mapping

## 4.1 Overview

Numerous methods have been developed to perform surface charge mapping using SICM, details of which were given in Chapter 1: *Introduction*, Section 1.2.4.[29,59,60] Although AFM has also been shown in the literature to be able to provide maps of surface charge densities, discussed in Chapter 1: *Introduction*, Section 1.3.3,[70–72] the SICM was chosen for the analysis of these samples. As was discussed in Chapter 3: *Carbonates*, SICM produced clearer images of the rough surfaces of three carbonate outcrop rocks, and so appears to be better suited to the analysis of these materials than AFM. The greater suitability of SICM compared to AFM for the mapping of equivalent surfaces on these materials is proposed to predominantly be the result of the SICM hop height, 1 - 5 $\mu$m, being much larger than the 10 - 100 nm oscillation amplitude which was typically used in this work during AFM mapping.[114,115] SICM also appeared to be able to map a greater range of the surface types found across

the carbonate outcrop rocks in Chapter 3: *Carbonates*, due to the SICM having a considerably longer probe which can map surfaces within pores that the AFM probe can not reach. This chapter discusses the potential uses for surface charge mapping using SICM in the context of oil and gas recovery, and the experiments which were carried out in efforts to establish the surface charge mapping mode in the laboratory at Imperial.

## 4.2 Relevance for Digital Rock

For a given pair of fluids and imposed conditions, the key properties of a porous rock surface that will impact the wettability of the system are the surface topography and its chemical composition. Although SEM EDX can provide simultaneous imaging with elemental analysis, the x-rays used to determine elemental composition can originate from up to 2 $\mu m$ deep into the sample,[83] and as such the technique is not specifically surface-sensitive. The topography of a given surface can be captured at the nanoscale using SICM, as was previously shown in Chapter 3: *Carbonates* for the three carbonate outcrop rocks. The recent progressions in surface charge mapping modes in SICM opens up an additional avenue for wettability characterisation,[29,59,60] as the chemical composition and nanoscale distribution of minerals is expected to have a direct impact on the local surface charges. Zheng *et al.* in 2020 demonstrated how a real 3D surface of Ketton, generated with AFM, was recreated and used in molecular modelling to predict contact angles.[23] It is proposed that providing simultaneous topographical and surface charge maps on the SICM of these materials would enable more accurate simulations of fluid interactions with outcrop rocks,

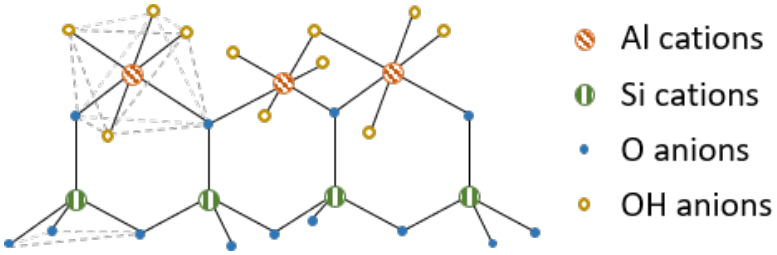
building on the method laid out by Zheng *et al.*, outputs from which could then be fed upwards into PNM simulations and ultimately provide the basis for more accurate reservoir simulations.

Over the years numerous wettability-altering effects have been observed on a variety of minerals commonly found on reservoir rock surfaces, which although have been proposed to be due to local surface charge alteration, have not been directly mapped and demonstrated.[116–119] A few such examples are discussed below, with suggestions for how surface charge mapping on the SICM could contribute to increased understanding of these phenomena.

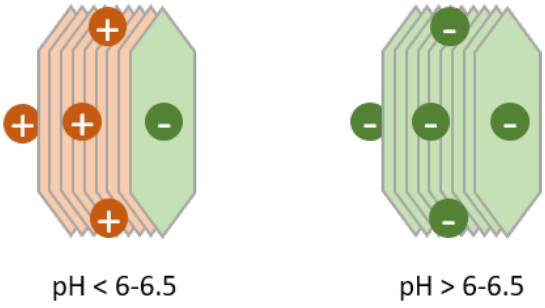
### 4.2.1 pH-dependent crude oil adhesion to clay surfaces

Clays are known to have a pH-dependent behaviour in terms of their affinity to crude oil.[120,121] A clay known as kaolinite, with an ideal chemical formula of $Al_2Si_2O_5(OH)_4$, composed of sheets of tetrahedral silica and octahedral alumina layers sharing oxygen atoms, is one such mineral of interest.[118,122–124] A diagram of kaolinite's crystal structure is shown in Figure 4.1a, with dotted lines to highlight the tetrahedral silicon and octahedral aluminium configurations.[123] These aluminosilicate layers stack together to form what are described as "booklets", and by default have a negative charge due to the unbound oxygen ions on the edges. This "default" negative charge is however thought to change when exposed to environments of acidic pH (Figure 4.1b).[118] Wan and Tokunaga in 2002 showed that under acidic conditions, the kaolinite particles in a colloidal kaolinite suspension were attracted to the negatively charged air-water interface, and that under basic pH this was not the case.[125]

The accepted explanation for this observation is that under acidic pH, the protons in solution will attach to the $O^-$ anions on the edges and Si faces of the kaolinite booklet, creating positively charged surfaces, as shown on the left hand side of Figure 4.1b.[118,125] This build up of positive charge leads the booklet to be drawn to the negative air-water interface.[125] Under basic pH, the negative charge-shielding effect is not observed as there are fewer protons in solution to be drawn to these negatively charged surfaces, and the booklet remains a net negatively-charged particle.[118] As one might expect, this pH-dependent behaviour, which is observed in numerous clay minerals, has implications for the wettability of clay-containing surfaces.[120,121]




(a)




(b)

Figure 4.1: Kaolinite booklets
(a) The crystal structure of a kaolinite sheet redrawn from Hu *et al.*,[123] and (b) a diagram of the proposed kaolinite booklet surface charge distributions and how they change with pH, redrawn from Tombàcz and Szekeres.[118]

Clays have been observed to have a strong attraction to crude oil, which is negatively charged, in low pH brines, but a preference for the water phase instead of the crude oil phase when under high pH brines.[120,121] This switch of preference from the crude oil to the water phase was observed by Lebedeva and Fogden to be around pH 6, which aligns well with the kaolinite booklet behaviour proposed in the literature.[118,121,125] Although this pH-dependent surface charge altering behaviour has been inferred from experiments,[118,125] it has yet to be directly mapped. Surface charge mapping with SICM could provide the opportunity to map this effect directly. For example, a kaolinite booklet could be located on a sandstone surface with SICM topographical mapping, and once found, simultaneous topographical and surface charge mapping of the area could be performed under a high and low pH electrolyte.

### 4.2.2 Low-salinity flooding

Low-salinity flooding (LSF) is a well-reported EOR approach which uses lower-concentration aqueous salt solutions to alter the effective wettability of a reservoir rock from oil-wet to water-wet, and thus facilitates the displacement of oil and provides higher recovery yields.[119,120,126,127] In sandstones, this effect is thought to be due to a change in the interaction of the oil with the clays present in the rock, however there have been numerous explanations over the years as to the exact mechanism.[127,128] One such explanation recently published by Mahani *et al.* discusses the impact of thin water films on the surface.[120] Crude oils and clays both tend to have negatively charged surfaces, and so should repel one another, however when in the presence of a high-salinity brine, these clay surfaces are found to behave oil-wet.

This is thought to be due to a thin high-salinity water film forming between the oil droplet and clay surface, which provides a "shield" as the DDLs of the oil and clay are compressed sufficiently that they do not repel each other, as shown at the top of Figure 4.2.[120] The two negative surfaces are attracted to the positive ions present in the brine, holding the oil droplet against the rock surface. When a low-salinity brine displaces this high-salinity brine during LSF however, the new lower-salinity water film does not suppress the DDLs sufficiently, allowing the negative surfaces of the crude oil and clay to repel one another, and the oil droplet is thus removed from the surface, as shown at the bottom of Figure 4.2.[120,127]

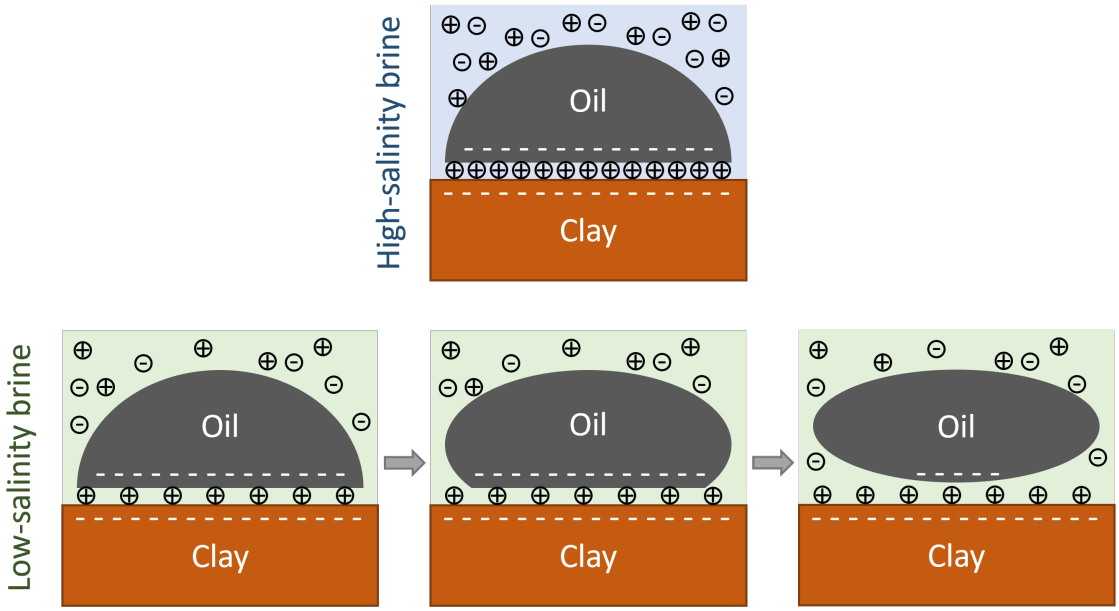



Figure 4.2: The low-salinity flooding effect on clay
Top: diagram depicting the DDL shielding between the negative surfaces of the crude oil and clay by the positive ions in a high-salinity brine. Bottom: diagram depicting the insufficient DDL shielding between the negatively charged surfaces by the positive ions in a low-salinity brine and the consequential removal of the crude oil droplet from the clay surface due to electrostatic repulsion. Inspired by multiple figures in reference 120.

In carbonate reservoir and outcrop rocks however, there is little to no clay, the majority of the surface being calcium carbonate,[92,93,96,97] and so a different explanation is required for a mechanism of LSF, as increased oil recovery yields are still

observed in these systems.[119,126,127] Alotaibi *et al.* showed through zeta potential measurements that calcite surfaces become more negatively charged in the presence of low-salinity brines, thereby increasing the extent to which the DDL extends into solution.[119,129] Although this was not directly presented as an explanation in their paper for how LSF might function in carbonate materials, it is possible that the behaviour of calcite in low-salinity brine is analogous to the behaviour of clays presented by Mahani *et al.*.[119,120,129]

Low-salinity flooding has over the years been shown to vary in effectiveness depending on the brine composition itself, not just the salt concentration. The literature seems to point towards a requirement for the presence of divalent cations such as $Ca^{2+}$ and $Mg^{2+}$, with less success reported when using exclusively monovalent cations such as $Na^{+}$ or $K^{+}$.[119,120,127] This makes sense from a theoretical perspective, as divalent cations are more charge-dense than monovalent cations, and will therefore be more effective in providing the DDL shield proposed by Mahani *et al.*.[120] It would therefore be of interest for surface charge mapping experiments of outcrop rocks on the SICM to map the same surface under different brine compositions and different concentrations, whilst maintaining the concentration low enough to perform surface charge mapping, to see if increases or decreases in charge magnitude are observed locally. Conveniently, the salt concentration range for "low-salinity" brines, Mahani *et al.* using brines between approximately 1.6 - 6.5 g/L salt concentrations, overlaps with the salt concentration ranges used in the literature for surface charge mapping on the SICM, McKelvey *et al.* and Page *et al.* using approximately 0.7 and 3.7 g/L $KCl_{(aq)}$ solutions respectively.[29,59,120]

### 4.2.3 Redox activity in iron-bearing minerals

As touched upon in Chapter 1: *Introduction*, Section 1.7.2, Bandera Brown, a sandstone outcrop rock, was chosen for study in the SDRP due to evidence in the literature that the iron present in some of the minerals on the surface is redox active, and can exist in the Fe +2 or +3 oxidation state, depending on the external conditions.[88,89] Briefly, one such example of this behaviour was shown by Southwick *et al.* where a polymer, HPAM, stuck to the pore walls of a Bandera Brown sample in an EOR core flood experiment, causing a significant back-pressure.[88] However, this back-pressure did not build up when the core was flooded with a reducing agent prior to the experiment. The proposed explanation for this behaviour is that the negatively-charged HPAM has a greater affinity for Fe +3 surfaces than Fe +2 surfaces, so if the Fe present in the pores has been reduced to the 2+ oxidation state, HPAM is able to flow more freely without sticking to the Fe sites and blocking the pores.[88] This impact of oxidising or reducing conditions on wettability in reservoir and outcrop rocks raises questions around the usefulness of data collected in oxidising environments. Reservoirs are generally accepted to be reducing environments due to the presence of crude oil and the low oxygen levels present beneath the earth's surface, so a thorough understanding of this reducing effect is necessary to evaluate how to proceed in future experiments on similar surfaces. It is proposed that this redox effect could be directly visualised with surface charge mapping on the SICM, by mapping an Fe-bearing region on a Bandera Brown surface twice; once before and once after the addition of a reducing agent, such as the erythorbic acid used by Southwick *et al.*[88] to the electrolyte, and observing whether a change in local

surface charges takes place in certain, presumed Fe-bearing, regions of the sample.

### 4.2.4 Organic and aqueous environments

It has already been discussed that the presence of oil will contribute to the reducing environment in reservoirs, and how the brine and oil components in a reservoir will have different charges, impacting their wetting of rock surfaces. A next step therefore, after observing surfaces in aqueous electrolytes with and without the addition of a reducing agent, is to look at a given surface under both aqueous and organic electrolytes to see if any changes in behaviour and local surface charges can be observed.

To date there have been few reports in the literature of the use of SICM with organic electrolytes. Two papers report the mapping of battery materials under a 1 M $LiPF_6$ in 1:1 by volume ethylene carbonate to dimethyl carbonate electrolyte,[38,39] however this work required the experiment be carried out in a glovebox under an inert atmosphere, which is much less practical than the typical aqueous experiments, which can be performed in air. No other examples of organic electrolyte use in the SICM were found in the literature at the time of writing. Due to this lack of previous work in organic electrolytes, prior to establishing surface charge mapping of outcrop rocks under organic electrolytes, it was important to provide a precedent of topographical mapping of these materials using SICM with an organic electrolyte, and, for practical considerations, for these to take place in air.

## 4.3 Surface Charge Mapping Progress

### 4.3.1 Organic Electrolytes in the SICM

In order to select an organic electrolyte for attempts to map outcrop rocks on the SICM in air, fields such as organic electronics were examined. For example, cyclic voltammetry experiments on acceptor and donor materials for organic solar cells are commonly performed in organic electrolytes in air.[130–132] An electrolyte that has been used extensively in this application and others, 0.1 M tetrabutylammonium hexafluorophosphate ($NBu_4PF_6$) in acetonitrile was therefore chosen for SICM experiments.[130–136]

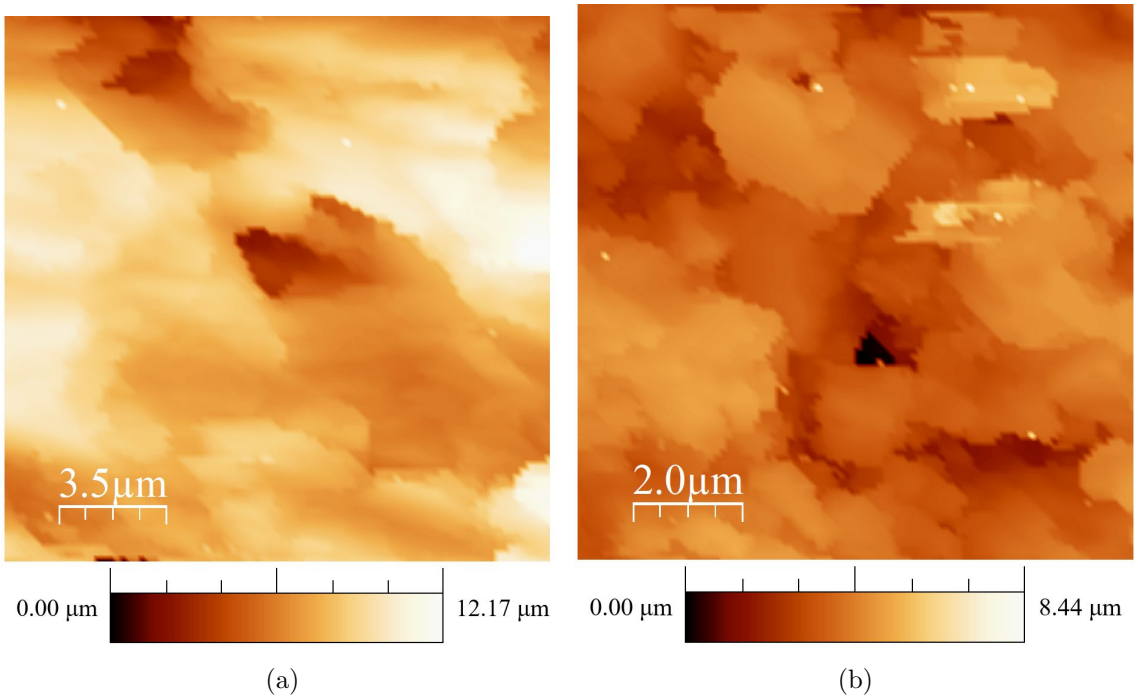
The 0.1 M $NBu_4PF_6$ in acetonitrile electrolyte yielded images of Indiana in one of the first sessions in which it was tested, which was somewhat unexpected, but there were challenges which needed to be overcome before successful imaging took place. Acetonitrile was not compatible with the plastic syringes and petri dishes which were used for the $KCl_{(aq)}$ electrolyte, as it started to partially dissolve the plastic; glass alternatives therefore had to be sourced to use this new electrolyte. Additionally, acetonitrile has a lower boiling point than water of around 82 °C,[137] so it evaporated more readily over the course of a day of SICM imaging, and as such had to be topped up 1-2 times per day between scans, otherwise the sample became exposed, and imaging was interrupted.

Despite the issues initially encountered when using 0.1 M $NBu_4PF_6$ in acetonitrile on the SICM, topographical mapping of Indiana in this organic electrolyte was successful. A 17.4 × 17.4 $\mu$m map gathered in these experiments is shown in

Figure 4.3; this area appears to belong to the Indiana surface type 3 defined in Section 3.2.4, characterised as being composed of rough-edged crystallites approximately 1 - 2 $\mu$m across. For comparison, a SICM image of Indiana surface type 3 collected in 0.1 M $KCl_{(aq)}$ and previously presented in Chapter 3: *Carbonates*, Figure 3.52, page 156, is shown alongside in Figure 4.3b.

A second map of Indiana taken under 0.1 M $NBu_4PF_6$ in acetonitrile is presented in Figure 4.4, where a section of a 20 $\times$ 20 $\mu$m area was successfully mapped prior to a nanopipette blockage. Nanopipette blockage is a common occurrence in SICM mapping in aqueous electrolytes, so this is not necessarily an indication of an issue with the organic electrolyte. The two larger, smooth crystallites visible in this second image, $>$ 5 $\mu$m across, could indicate that this map is from Indiana surface type 5, although it is difficult to say with any certainty given the restricted field of view.

These two topographical maps give precedence for topographical mapping on the SICM under organic electrolytes in air, which is relevant for the potential future surface charge mapping experiments on these materials in organic electrolytes in the SICM, as discussed previously in Section 4.2.4.




(a) (b)

Figure 4.3: Indiana: 17.4 × 17.4 $\mu$m SICM image in acetonitrile
(a) A 17.4 × 17.4 $\mu$m SICM topographical image with a pixel size of 200 × 200 nm taken in a 0.1 M $NBu_4PF_6$ in acetonitrile electrolyte. (b) re-shows the 10 × 10 $\mu$m SICM image taken in 0.1 M $KCl_{(aq)}$ originally shown in Chapter 3: *Carbonates*, Figure 3.52, page 156. Both areas imaged are proposed to belong to Indiana surface type 3 as defined in Section 3.2.4.

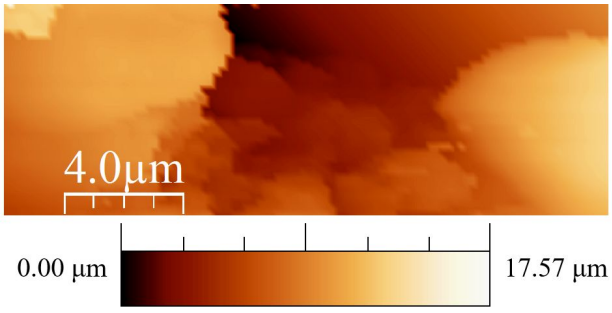



Figure 4.4: Indiana: An incomplete 20 × 20 $\mu$m SICM image in acetonitrile
An incomplete 20 × 20 $\mu$m SICM topographical image with a pixel size of 200 × 200 nm taken in a 0.1 M $NBu_4PF_6$ in acetonitrile electrolyte. Nanopipette blockage prevented the rest of the region from being mapped.

### 4.3.2 Polystyrene on Glass

Prior to any attempt to map the surface charge distributions on outcrop rock surfaces, a model surface was used in efforts to establish surface charge mapping in the laboratory. Page *et al.* carried out their initial experiments on a relatively simple sample with distinct surface charge differences; a negatively charged glass surface which had been dip-coated with charge-neutral polystyrene.[29] Efforts were made to reproduce Page *et al.*'s experiments, to ensure that the setup was fully functional, prior to attempts on more complex surfaces. Unfortunately, surface charge maps of this material were not successfully collected prior to the conclusion of the project time, however the progress which was made towards this end is described.

As touched upon in Chapter 1: *Introduction*, the surface charge mapping mode installed on the scanning ion conductance microscope in our laboratory was based on the the pulsed-potential SICM mode described by Page *et al.*.[29] This mode is an adapted hopping mode, where a pause in the hopping regime takes place at the bottom and the top of each hop. During these pauses the applied bias is changed to a different bias from the approach bias, and the current response during this pulse is recorded.[29] If the electrolyte has a sufficiently low ionic strength, then the current responses at the bottom and top of the hop should represent responses inside and outside of the DDL for a given point on the surface. The difference between these current responses can then be plotted, providing a heat map of surface charge heterogeneities, and through computational simulations a quantitative surface charge map can be generated alongside the topographical map.[29]

#### 4.3.2.1 Low-Vacuum Scanning Electron Microscopy

To ensure that the sample preparation of the glass slide dip-coated in polystyrene (polystyrene on glass, PoG) was successful, the PoG sample was first imaged using low-vacuum SEM. Although imaging was successfully achieved with low-vacuum SEM, if one area of the polystyrene film was imaged for longer than approximately 10 minutes at high magnification, the charge build up caused the film to change its structure, becoming warped, and so care was taken to move to new areas frequently during imaging. Indications of this tendency towards charge build up can be seen in all of the low-vacuum SEM micrographs of the polystyrene film presented in this chapter; at the edges of the film, where the glass slide is presumed to be revealed, the film is considerably brighter than the rest of the surrounding film.

Figure 4.5 shows an overlay of four low-vacuum SEM micrographs of the PoG surface. From this overlay it can be observed that the polystyrene film has formed with gaps revealing what is possibly the glass surface underneath, as was produced by Page *et al.* in their experiments.[29] There are however a range of gap sizes, which are shown at higher magnification in Figures 4.6 - 4.8.

Figure 4.6 shows a high magnification low-vacuum SEM micrograph of an example of PoG surface type 1, which is of a region near the area labelled "1" on the PoG surface shown in Figure 4.5. PoG surface type 1 has gaps in the polystyrene film $< 1$ $\mu$m across at their widest point, which are similar to the gaps shown in the SICM image in Page *et al.*'s paper. Figure 4.7 shows a high magnification low-vacuum SEM micrograph of PoG surface type 2, taken near the area labelled "2" in Figure 4.5, where the majority of the gaps in the polystyrene film are $> 1$ $\mu$m

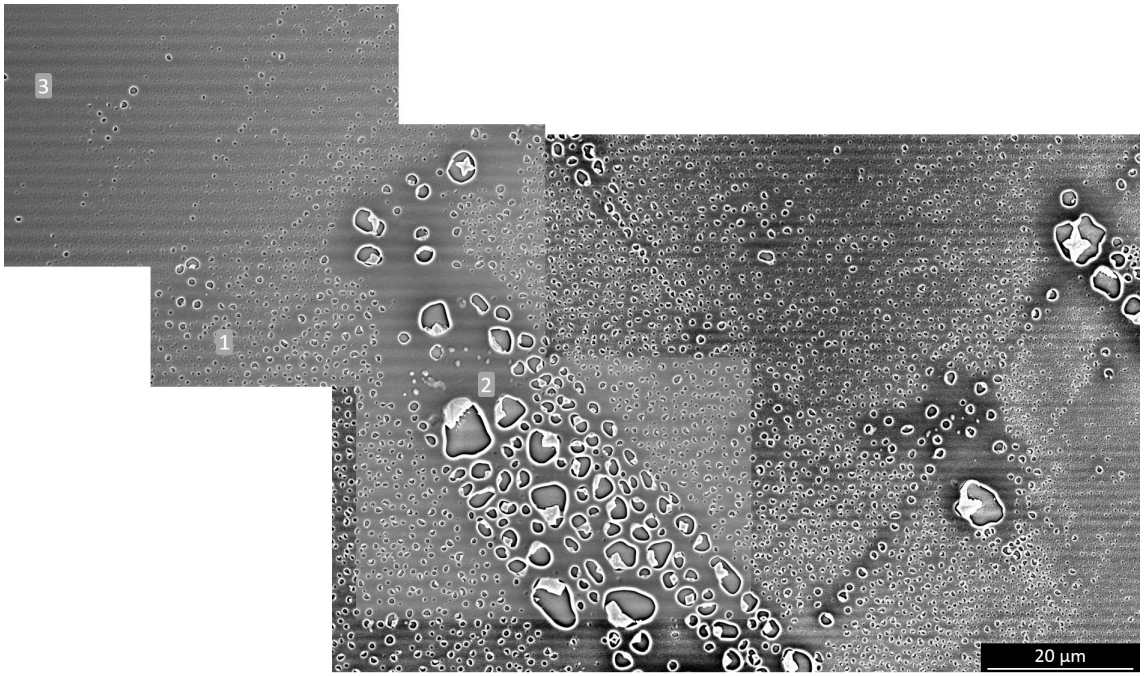



Figure 4.5: Polystyrene on glass: SEM Overlay
An overlay of four low-vacuum SEM micrographs of a glass slide dip-coated in polystyrene, with three different area types labelled. The individual micrographs which make up this overlay wihtout numbers overlain can be found in Appendix D, Figures D.1 - D.4.

across at their widest point, mostly sitting between 1 - 5 $\mu$m. One of the gaps in the Page *et al.* paper is on the order of 3 $\mu$m at its widest point, so this is still in line with their results.

PoG surface type 3 is shown in the high magnification low-vacuum SEM micrograph in Figure 4.8, which was taken close to the area labelled "3" in Figure 4.5. PoG surface type 3 is an area where there are numerous dents in the polystyrene surface which do not appear to be deep enough to reveal the glass surface underneath. Although this is unconfirmed by the low-vacuum SEM micrograph in Figure 4.8, this hypothesis is re-visited during the analyses of the AFM and SICM images in Sections 4.3.2.2 and 4.3.2.3. For the purposes of attempting to repeat Page *et al.*'s surface charge mapping experiments with SICM, based on these low-vacuum SEM

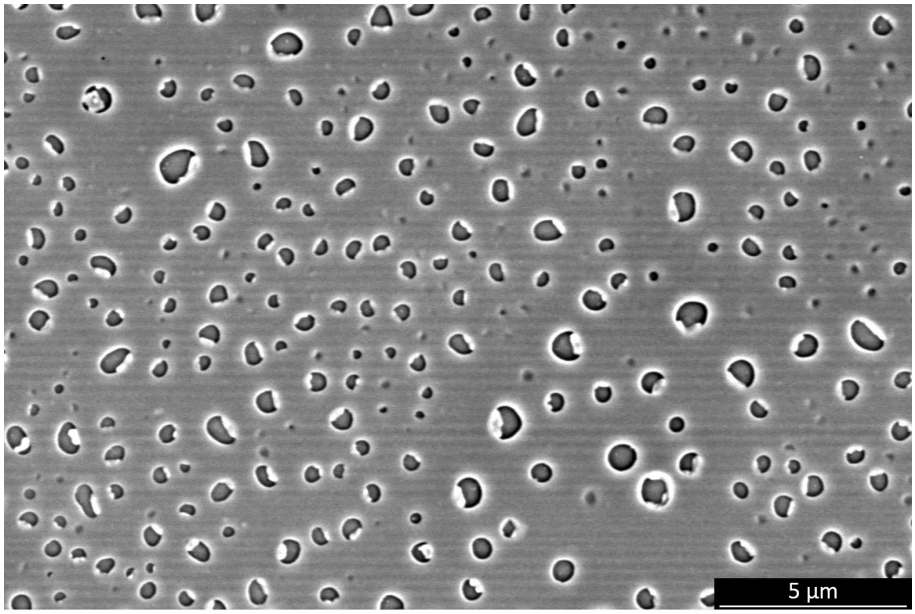



Figure 4.6: Polystyrene on glass: high magnification SEM 1
A higher magnification low-vacuum SEM micrograph of a glass slide dip-coated in polystyrene, from the area type 1 as labelled in Figure 4.5.

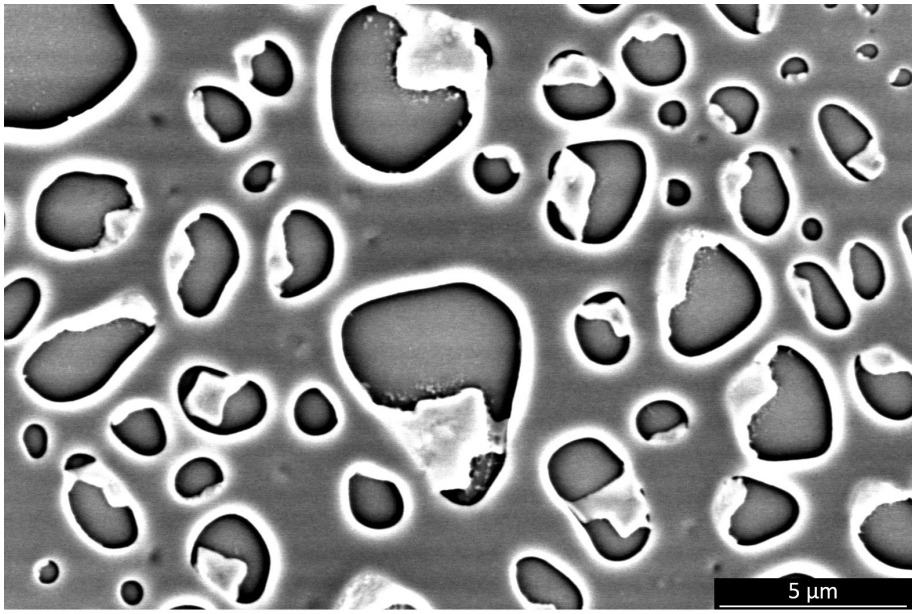



Figure 4.7: Polystyrene on glass: high magnification SEM 2
A higher magnification low-vacuum SEM micrograph of a glass slide dip-coated in polystyrene, from the area type 2 as labelled in Figure 4.5.

micrographs, larger areas such as 10 × 10 or 20 × 20 $\mu$m should be mapped with the SICM in order to establish which area type has been approached and to increase the chances of locating an appropriate region of the PoG film. PoG surface type 3 is not of use for surface charge mapping validation if it indeed does not reveal the glass underneath, so surface types 1 and 2 are of particular interest. Once a region has been approached with the SICM probe, and is identified as either surface type 1 or 2, higher resolution images can then be carried out and attempts at surface charge mapping can be made.

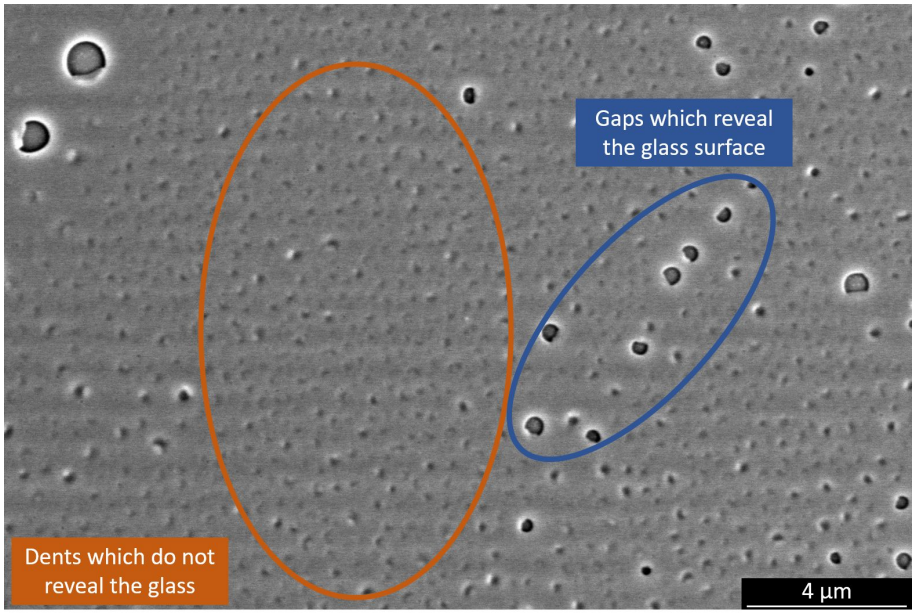



Figure 4.8: Polystyrene on glass: high magnification SEM 3
A higher magnification low-vacuum SEM micrograph of a glass slide dip-coated in polystyrene, from the area type 3 as labelled in Figure 4.5.

#### 4.3.2.2 Atomic Force Microscopy

Atomic force microscopy was used to investigate the PoG surface to provide an additional frame of reference with which to assess the SICM images, and served as an additional checking process to assess whether the samples used by Page *et al.* had been replicated correctly.[29] Page *et al.* show a SICM image of the PoG sample where the majority of the polymer appears to sit in approximately 100 nm thick film on the glass, with a few sections up to 200 nm thick around the larger gaps.[29] Given this information, a gap in the film on these surfaces was only assumed to reveal the glass underneath if the height of the edge of the film relative to the bottom of the dent is around 100 nm or higher.

Figure 4.9 shows four AFM images which overlap in their field of view of the same larger area. The top right of Figure 4.9a overlaps with the bottom left of Figure 4.9b, with the same $< 1$ $\mu$m gap in the polystyrene film visible in both images indicated with a green square. These $5 \times 5$ $\mu$m images are fully encompassed by the $10 \times 10$ $\mu$m image shown in Figure 4.9c, with the same gap indicated with a green square once more. The top of this third image overlaps with the bottom of the fourth image shown in Figure 4.9d, with a purple square indicating the same 1 $\mu$m across gap which appears in both fields of view.

In Figures 4.9a and 4.9b, the largest gap in the polymer film, indicated by the green square, is approximately 100 - 200 nm across, and only 30 nm deep, as can be seen in the height profile in Figure 4.10. This area is therefore likely to belong to the PoG surface type 3 classification described from the low-vacuum SEM micrographs in Section 4.3.2.1, as the dents in the polystyrene film are too narrow to allow for

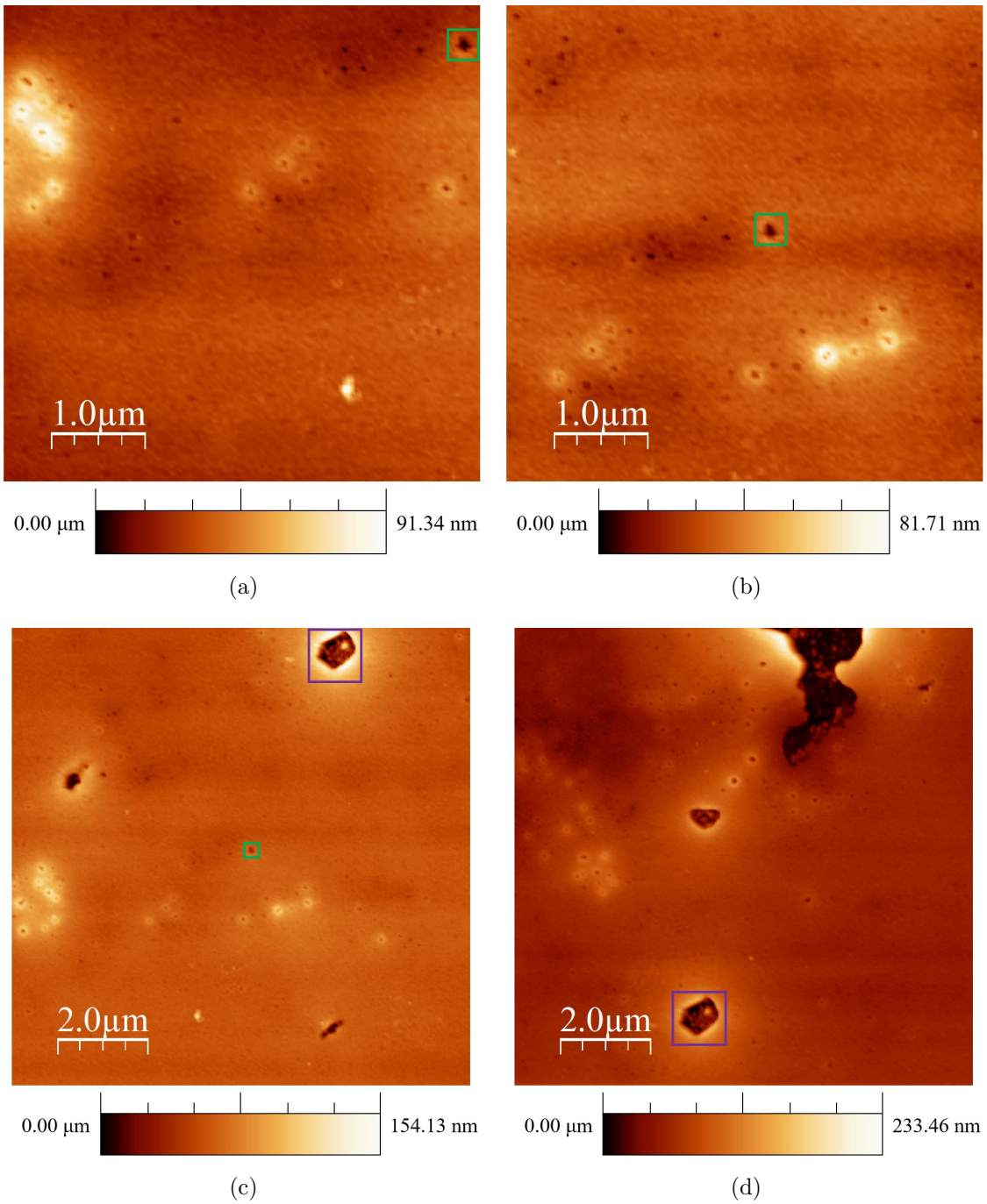
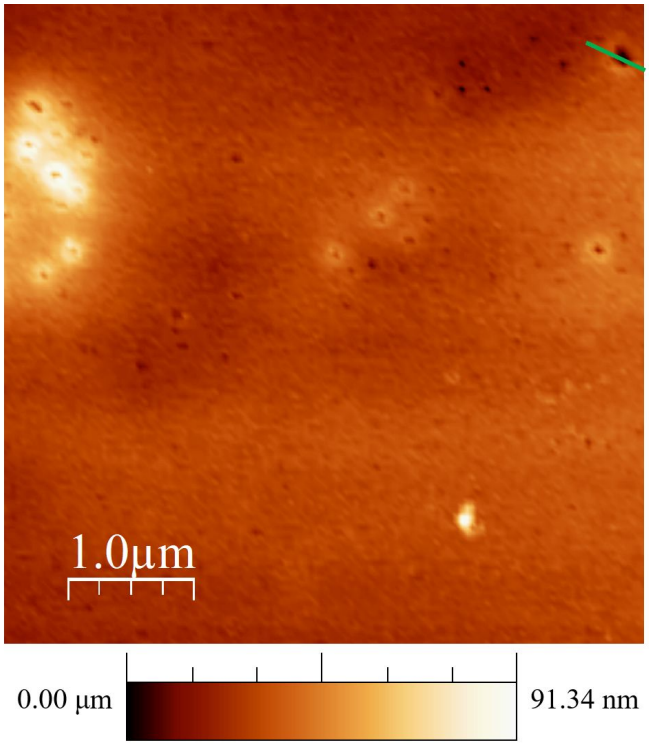
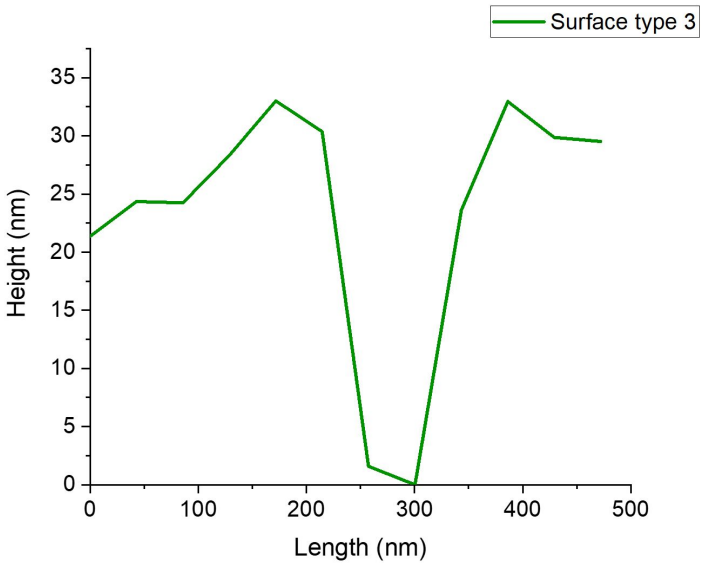



Figure 4.9: Polystyrene on glass: AFM area 1
Four AFM images which overlap in fields of view of the same area. The top right corner of (a) overlaps with the bottom left corner of (b); both (a) and (b) are fully captured within image (c), and the top right corner of (c) overlaps with the bottom right corner of (d). (a) and (b) are 5 × 5 $\mu$m AFM images and (c) and (d) are 10 × 10 $\mu$m AFM images, all having a pixel size of approximately 40 × 40 nm (128 × 128 and 256 × 256 points respectively).

the glass underneath to be exposed. In Figures 4.9c and 4.9d however, larger gaps in the polymer film are visible. Height profiles across two of these gaps are shown in Figure 4.11, where it can be seen that these gaps are much larger, approximately 1 - 2 $\mu$m across, and the dents themselves are 100 - 200 nm in depth, similar to the gaps in the polymer film reported by Page *et al.*.[29] This is not only further indication that these samples have been replicated successfully, but due to their depth, as proposed in Section 4.3.2.1 they are assumed to reveal the glass underneath. Figures 4.9c and 4.9d are therefore proposed to show the edge of a PoG surface type 2 area, at the intersection with PoG surface type 3 area, as highlighted by Figures 4.9a and 4.9b.

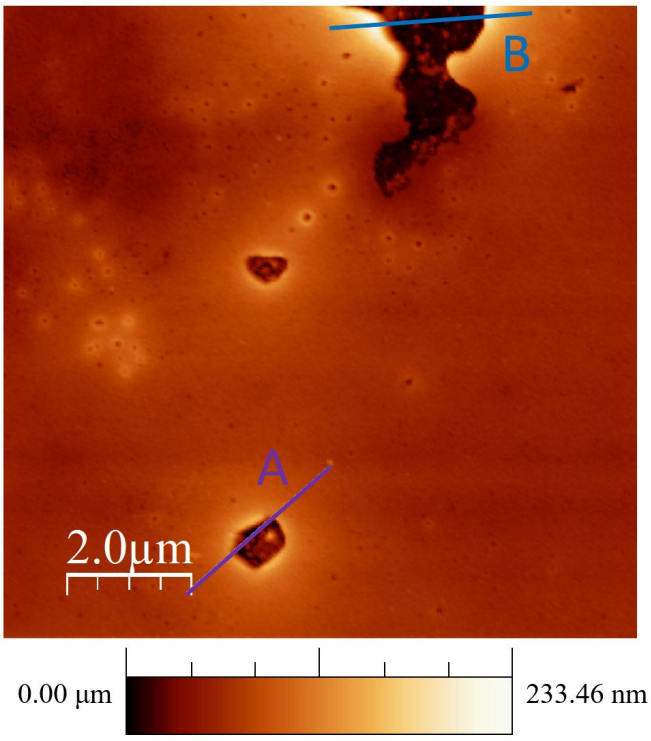



(a)

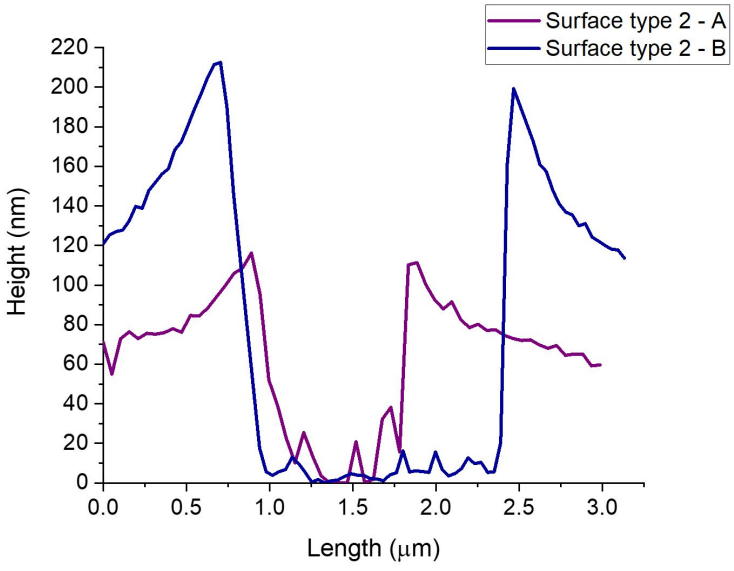



(b)

Figure 4.10: Polystyrene on glass: AFM area 1 - small dent profile
(a) The 5 × 5 $\mu$m AFM image previously shown in 4.9a, with a green line indicating the position of the height profile shown in (b).




(a)




(b)

Figure 4.11: Polystyrene on glass: AFM area 1 - larger dent profiles
(a) the 10 × 10 $\mu$m AFM image previously shown in 4.9d, with lines labelled "A" and "B" showing the positions of the two height profiles "A" and "B" shown in (b).

A fourth surface type, PoG surface type 4, was observed during AFM measurements, but had not been observed in the low-vacuum SEM measurements. An area of what appear to be small, circular structures standing proud on an otherwise reasonably flat surface was imaged at two different magnifications and is presented in Figure 4.12. The height profiles shown in Figures 4.13 and 4.14 show that these structures are between 75 - 90 ± 2 nm across and 14 - 17 ± 0.5 nm high (Figure 4.13), and 100 ± 10 nm across and 11 - 12 ± 0.5 nm high (Figure 4.14). Although it is not immediately clear what these structures are, polystyrene nanospheres have been reported in the literature as small as 50 nm across, so it is possible that small polystyrene structures have formed and are embedded in the otherwise flat polystyrene film.[138]

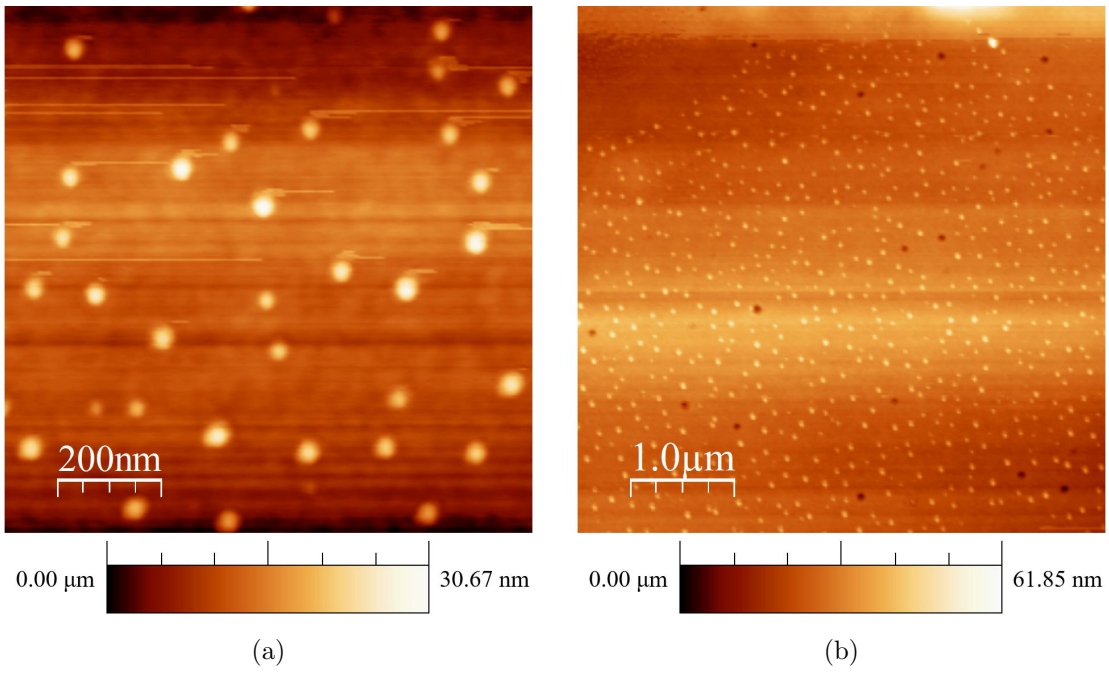
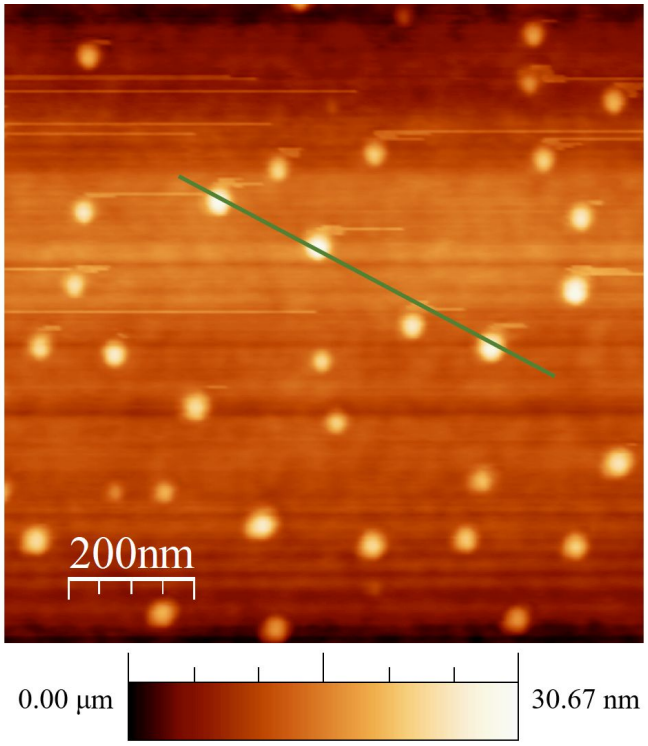
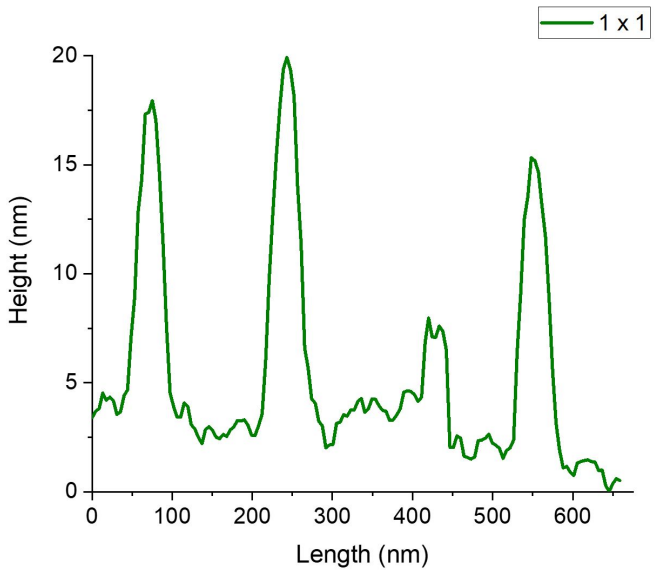



Figure 4.12: Polystyrene on glass: AFM area 2
Two AFM images at different magnifications of the same area on the PoG surface. (a) is a 1 × 1 $\mu$m AFM image with a pixel size of approximately 4 × 4 nm (256 × 256 points) and (b) is a 5 × 5 $\mu$m AFM images with a pixel size of approximately 20 × 20 nm (256 × 256 points).




(a)




(b)

Figure 4.13: Polystyrene on glass: AFM area 2 - 1 × 1 $\mu$m AFM image
(a) The 1 × 1 $\mu$m AFM image previously shown in Figure 4.12a, with a green line indicating the position of the height profile shown in (b).

In addition to the raised structures on the film, there are also small dents visible in the surface shown in Figure 4.12b, with similar proportions to the structures which stand proud of the surface, being 100 ± 10 nm across and 13 ± 0.5 nm deep; a height profile across two raised and two recessed features is shown in Figure 4.14 for illustration. Due to the dimensions of these dents being remarkably similar to the dimensions of the raised features on the surface, it is perhaps possible that a polystyrene nano-structure which was embedded in the surface at these points had since been removed, revealing a dent. Being considerably shallower than 100 nm however, it is proposed that these dents do not reveal the glass surface underneath. Although this fourth surface type does not show any dents proposed to be deep enough to reveal the glass surface underneath, and therefore may not have relevance for surface charge measurements, it is still worthy of note, in case similar structures are observed during mapping with SICM.

The polystyrene used in these experiments is approximated below to be small enough to have formed these structures. When polymers are dissolved in solution, they will adopt random orientations, folded around on themselves; how large the resulting coiled structure is will depend on the molecular weight of the polymer, as well as the bulkiness of the side chains. The radius of gyration can be used as a measure of the resulting size of this random orientation in solution, as it is the average distance between each monomer and the centre of gravity of the polymer.[139,140] Equation 4.1 shows an empirical equation from Teraoka, determined for polystyrene in toluene and benzene solutions, as an approximation for the polystyrene in chloroform used in these experiments,[141] the radius of gyration in nm, $R_g$, can be estimated

from the molecular weight in g/mol, $M$:

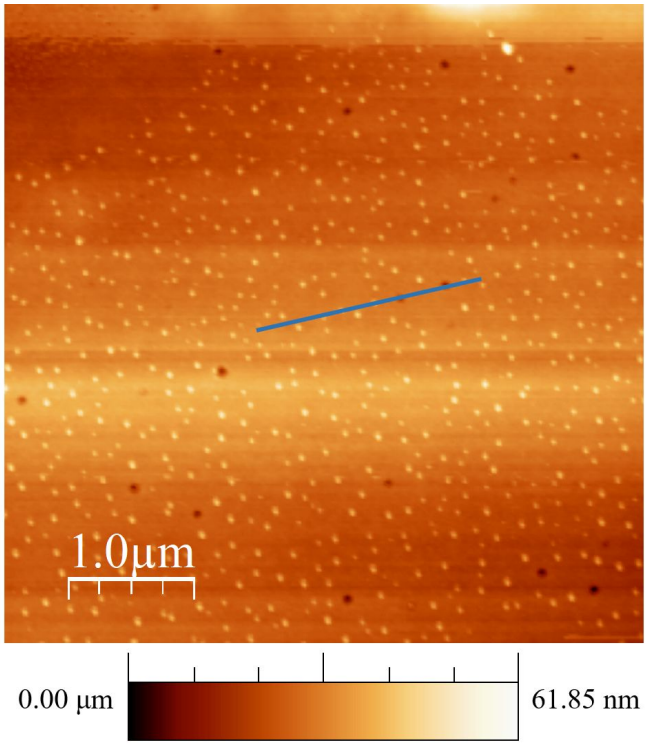
$$R_g = 0.01234 \times M^{0.5936} \tag{4.1}$$

The polystyrene used in these experiments had an average $M$ of 35,000 g/mol, so $R_g$ can be estimated as:

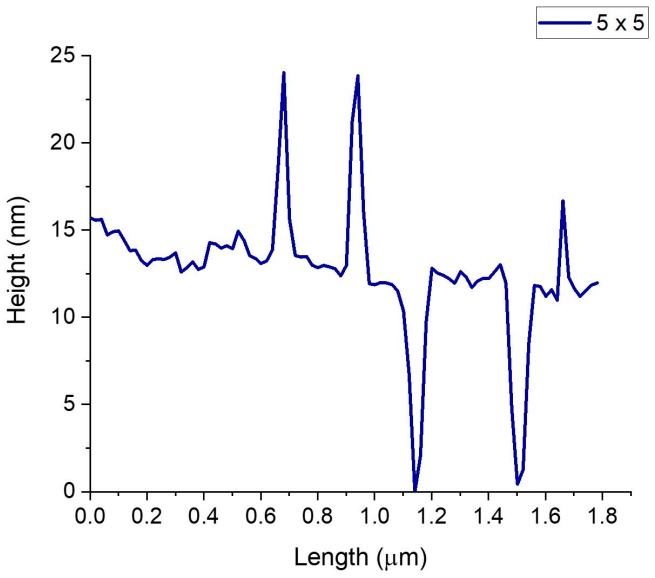
$$R_g = 0.01234 \times (35,000)^{0.5936} = 6.15\ nm$$

As this $R_g$ is around half the depth and height of the recessed and raised features in the polymer film, it is possible that the polystyrene used in these experiments agglomerated to form these larger structures on and in the polymer film. This estimated $R_g$ of around 6 nm also implies that the film is multi-layered and not a monolayer, as some sections of the film in Figure 4.11 were found to have dents of up to 100 - 200 nm deep.

Although images were obtained for the PoG sample with AFM, and the same features observed in the low-vacuum SEM micrographs are also shown in the AFM images, the features across these images are not well resolved, which had not been anticipated for such a relatively flat surface. It is proposed that this lack of clarity in the images is due to the polystyrene film not actually being adhered to the glass surface. As the AFM tip traced across the surface, it is possible that it disturbed or moved the film slightly, creating a blurring of the feature edges in the images, as the surface was not entirely static.




(a)




(b)

Figure 4.14: Polystyrene on glass: AFM area 2 - 5 × 5 $\mu$m AFM image (a) The 5 × 5 $\mu$m AFM image previously shown in Figure 4.12b, with a blue line indicating the position of the height profile shown in (b).

#### 4.3.2.3 Scanning Ion Conductance Microscopy

Replicating the surface charge mapping experiments reported by Page *et al.* proved more challenging than initally anticipated.[29] A selection of topographical images obtained using SICM for the PoG surface are shown in Figure 4.15 below. All three SICM images show raised structures similar to those in the PoG surface type 4 which was observed using AFM (Figure 4.12, page 200), but not in the low-vacuum SEM micrographs. The raised structures in these SICM images appear blurred around the edges, possibly indicating that they are not fully static on the surface, and are partially dissolved in the electrolyte. Beneath the raised structures in Figure 4.15a, two raised ridges can be seen running horizontally across the image; these are thought to be due to imperfections in the glass. The third SICM image shown in Figure 4.15c shows a predominantly flat surface with large raised features, however unlike Figures 4.15a and 4.15b, shows one small dent in the surface, which as can be seen in Figure 4.17 is approximately 100 nm deep. This dent fulfills the criterion determined from the AFM images and low-vacuum SEM micrographs for a PoG surface type 2 dent, and was therefore selected for surface charge mapping in case the dent was deep enough to reveal the glass surface underneath.

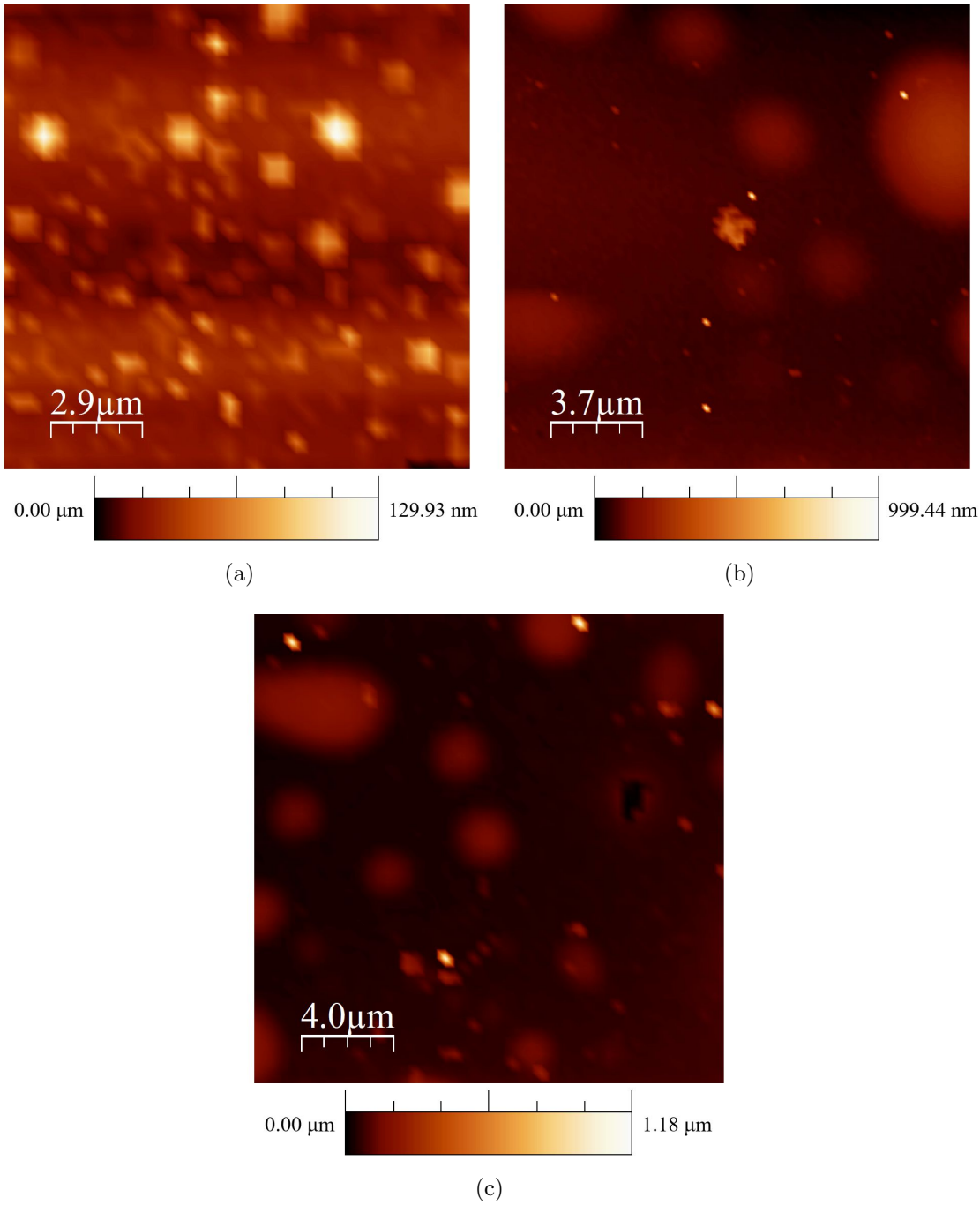



Figure 4.15: Polystyrene on glass: SICM topographical maps
Three SICM topographical maps of the PoG surface, (a) being a 14.4 × 14.4 $\mu$m SICM image with a pixel size of 400 × 400 nm, (b) being a 18.6 × 18.6 $\mu$m SICM image with a pixel size of 200 × 200 nm and (c) being a 20 × 20 $\mu$m SICM image with a pixel size of 400 × 400 nm.

Figure 4.16a shows the 20 $\times$ 20 $\mu$m topographical image originally shown in Figure 4.15c alongside a topographical map of the same area which was obtained during a subsequent surface charge mapping mode scan (Figure 4.16b). These two images are also shown with an equalization function applied in Figures 4.16c and 4.16d respectively to better visualise the structures on the surface. Three features which appear in both of these images are compared across Figures 4.17 and 4.18, and show good repeatability in terms of heights and widths of features across the two images. The 100 nm deep dent previously identified as a good contender for surface charge mapping in Figure 4.15c is also observed in Figure 4.16b, and as can be seen in Figure 4.17, both dents are approximately 100 nm deep, and $>$ 1 $\mu$m across. The two SICM images portray the shape of the dent slightly differently, but this is assumed to be due to the dent being only a few pixels wide, and thus falling prey to the issues surrounding feature shape determination accuracy for SPMs discussed in Chapter 1: *Introduction*, Section 1.5.

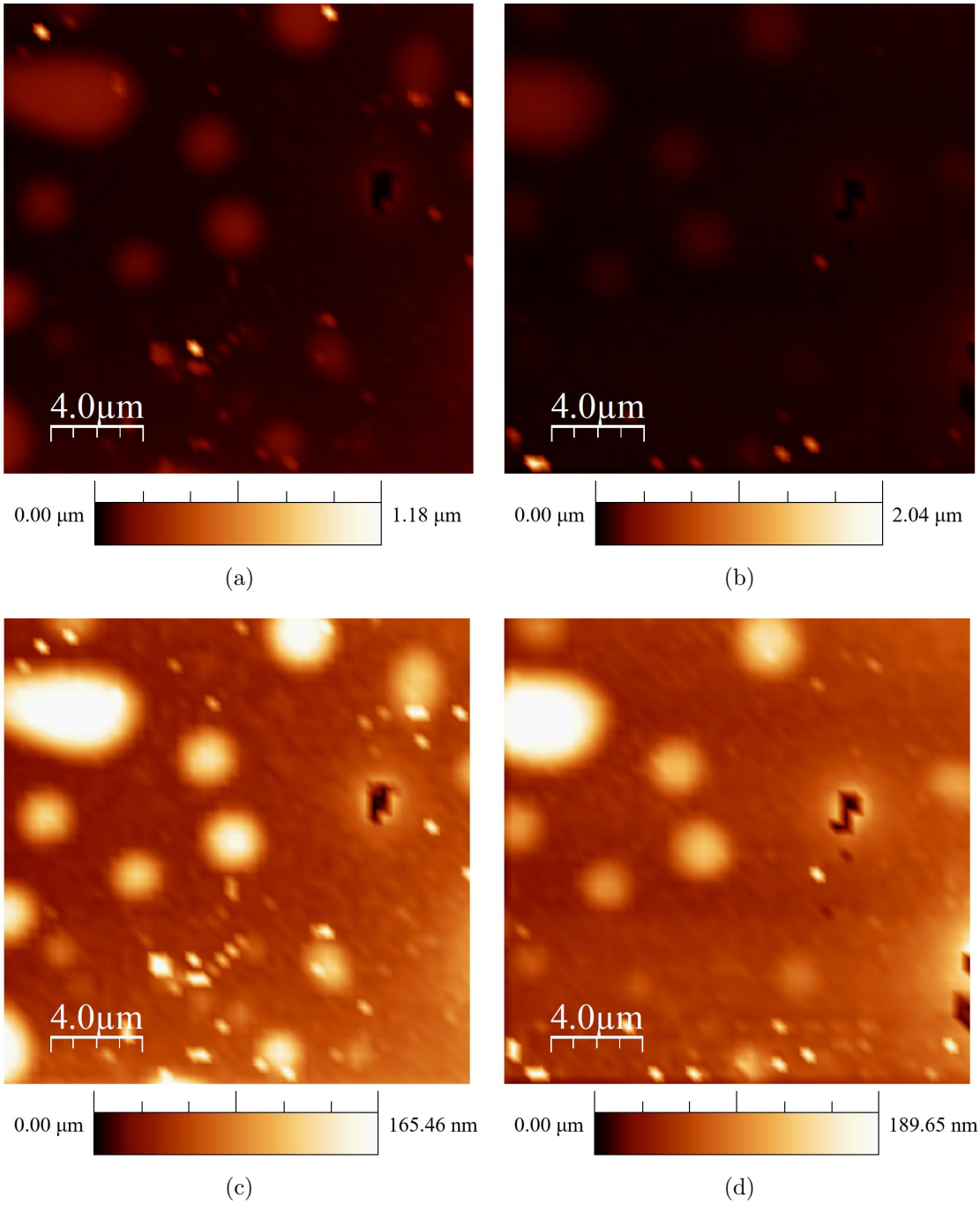



Figure 4.16: Polystyrene on glass: SICM topography - 20 × 20 $\mu$m map
Two SICM topographical images obtained on the same area of a PoG surface. (a) Shows the 20 × 20 $\mu$m SICM topographical map originally shown in Figure 4.15c, which was obtained using a normal SICM hopping mode. (b) shows a 20 × 20 $\mu$m SICM topographical map with a pixel size of 400 × 400 nm of the same area, but obtained during a surface charge mapping mode scan. (c) and (d) show the same maps from (a) and (b) respectively, with equalization functions applied to better see the features by ignoring the bright spots in the original images.

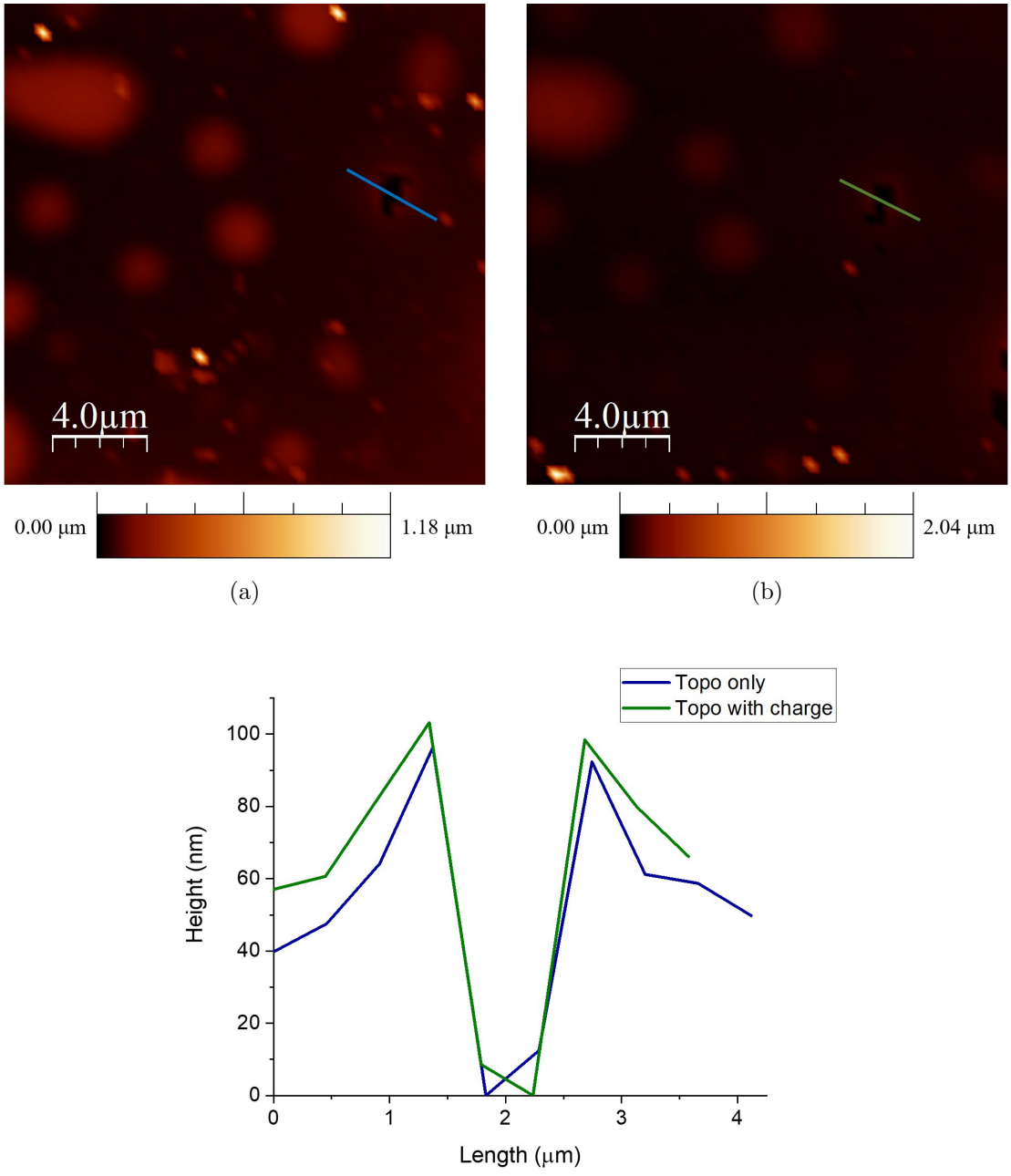



Figure 4.17: Polystyrene on glass: SICM height profiles - dent
(a) and (b) show the two SICM topographical images originally shown in Figures 4.15c and 4.16b respectively, with blue and green lines showing the positions of the height profile traces across a dent in the surface which are displayed in (c).

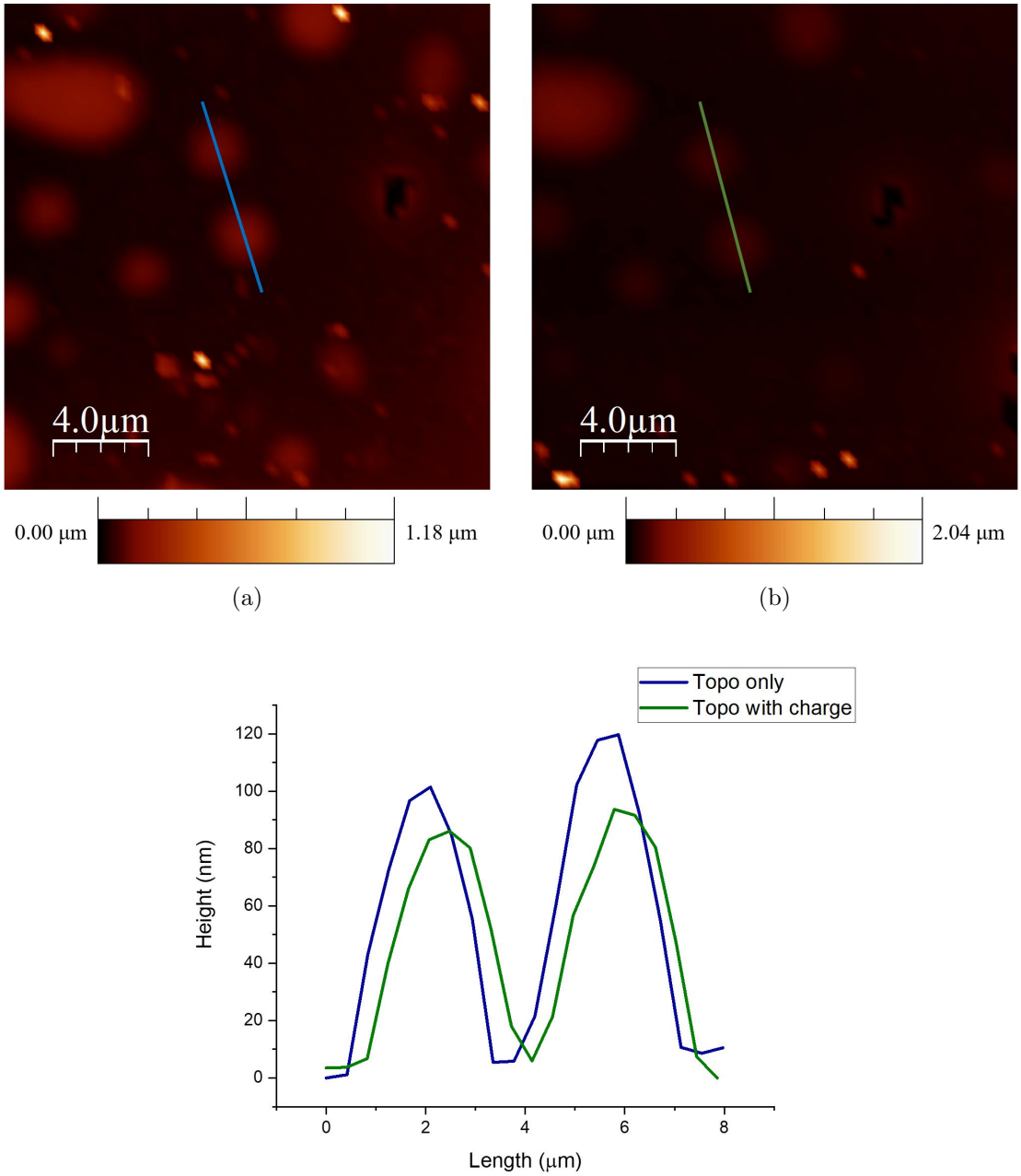
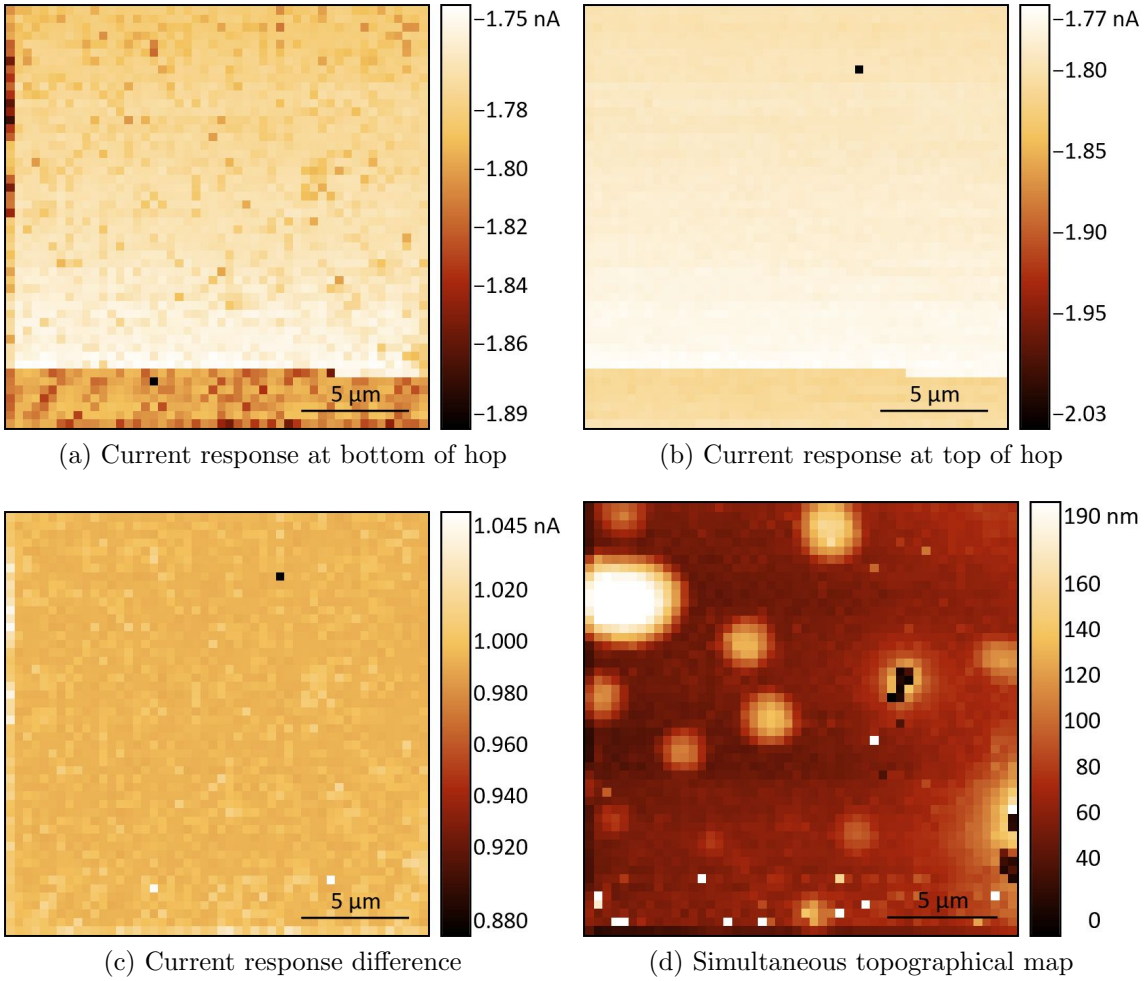



Figure 4.18: Polystyrene on glass: SICM height profiles - raised features
(a) and (b) show the two SICM topographical images originally shown in Figures 4.15c and 4.16b respectively, with blue and green lines showing the positions of the height profile traces across two raised features on the surface which are displayed in (c).

The current response maps for the area shown in Figure 4.16b unfortunately did not indicate any significant surface charge heterogeneities. Figure 4.19 shows the two maps for the current responses at the bottom and top of each hop (Figures 4.19a and 4.19b respectively) and the difference between the two, the net current response map for each point, is shown in Figure 4.19c. The equalized version of the simultaneously obtained topographical map, previously shown in Figure 4.16d, was re-plotted in Gwyddion 2.55,[a] and re-shown in Figure 4.19d for ease of comparison. When the net current response map (Figure 4.19c) and topographical map (Figure 4.19d) are compared side by side, it can be seen that there is no correlation of topographical features with current response signal. A discussion of why these experiments may have failed to yield the expected results is included later on in Chapter 7: *Discussion*, Section 7.5.

[a] the original, Figure 4.16d, was plotted in WSxM 5.0 Develop 9.4




(a) Current response at bottom of hop

(b) Current response at top of hop

(c) Current response difference

(d) Simultaneous topographical map

Figure 4.19: Polystyrene on glass: SICM current response
Outputs from the surface charge mapping mode scan carried out on the area shown in Figure 4.16. (a) Shows the current responses recorded at the bottom of each hop in the topographical image, (b) shows the current response recorded at the top of each hop in the topographical image, (c) shows a plot of the differences between the current responses at the top and bottom of each hop, and (d) is a re-plotting in Gwyddion of the topographical map originally shown in Figure 4.16b.

## 4.4 Summary and conclusions

Overall, surface charge mapping using SICM is expected to have great potential in the field of oil and gas recovery, as well as other geological applications such as CCS, with numerous wetting behaviours thus far being attributed to surface charge manipulation and distribution in the literature, yet none directly mapped at the time of writing.[88,89,118–120,125] The behaviours of interest discussed here were the pH-dependency of the charge on clay particles,[118,125] the LSF effect, and how this behaviour is potentially explained by changes in the DDLs of the rock surface and the crude oil,[119,120] and the impact of reducing or oxidising environments on the wettability of surfaces, such as the redox-active Fe in sandstones such as Bandera Brown.[88,89] All of these effects can have an impact on the wettability of rock surfaces, and thus the oil recovery yields from reservoirs; increased understanding of these behaviours are therefore of great interest to the oil industry, such that EOR techniques can be selected and tailored more effectively to best make use of each reservoir.

In anticipation of the establishment of surface charge mapping on the SICM of outcrop rocks, SICM topographical mapping of Estaillades in an organic electrolyte in air was successfully achieved; this is of importance as no reports in the literature of using organic electrolytes in air on the SICM had been reported at the time of writing.

The scanning ion conductance microscope used in this work was equipped with a surface charge mapping mode based on the pulsed-potential SICM mode described by Page *et al.* in 2016.[29] Replication of Page *et al.*'s work on a polystyrene film on

glass was of limited success. Imaging using AFM and low-vacuum SEM indicates that the samples themselves were replicated successfully, and although topographical maps of this samples were successfully acquired using SICM, surface charge heterogeneity mapping by probing the current response remained elusive.

Although numerous attempts were made to find a suitable area of the PoG surface for surface charge mapping using SICM, none located a section with clear surface charge heterogeneities before the conclusion of the project. Further work to this end is however underway as part of an extension of the SDRP, due to the range of pertinent topics it has the ability to contribute to in the field of oil and gas recovery.

# Chapter 5

# Carbonate Ageing Studies

## 5.1 Overview

In core flood experiments, it is common to take measurements before and after an "ageing" process has been performed on the outcrop rock under investigation.[142–144] An ageing process aims to simulate the wettability-altering effects of exposing a reservoir rock to crude oil over 1000s of years, typically by exposing the outcrop rock to crude oil at elevated temperatures and pressures for an extended period of time.[142–144] In the experiments described in this chapter, samples were placed in crude oil in sealed glass jars at 70 °C for 28 days; although a pressure cell was not employed, it is expected that within the sealed glass jar, the elevated temperature would have caused the pressure inside the jar to increase - see Section 5.2 for an estimation of this pressure.[142] Samples in this section referred to as "aged" will have undergone this artificial ageing procedure, and samples referred to as "unaltered" have been imaged without prior crude oil exposure.

The common ageing approach taken in the literature required an additional step to be included in order to produce samples suitable for low-vacuum SEM. After a typical ageing procedure, the excess crude oil is dabbed off the outside of the sample before being used directly in core flood experiments.[142–144] Instead, here, after the sample was removed from the crude oil, it was placed inside a clean glass jar and heated once more to 70 °C, allowing any volatile compounds to evaporate, leaving the surface dry. The samples were then placed inside a vacuum desiccator prior to SEM imaging, to ensure that no volatile components remained on the surface.

Samples were imaged with three techniques: low-vacuum SEM, AFM and SICM. For all samples, low-vacuum SEM imaging was performed first, then AFM imaging, and finally SICM imaging. This order was selected as although low-vacuum SEM locally, very slightly, damages the area which was directly imaged with the electron beam, the majority of the sample remains unaltered, and it is also the most sensitive technique in terms of sample preparation. SICM on the other hand was deemed the most likely out of the three techniques to alter the crude oil film on the sample surface, due to the requirement to submerge the sample in an aqueous salt solution.

To investigate the suitability of SICM for mapping aged carbonate samples, a pure calcite crystal and an Estaillades sample were selected. The calcite crystal was chosen as sample of relatively simple topography and homogeneous mineral composition, while the Estaillades sample was selected as a more complex surface topographically and mineralogically, whilst still being deemed to have the most simple surface out of the carbonate outcrop rocks studied in Chapter 3: *Carbonates*, with the fewest individual surface types.

## 5.2 Estimated Cell Pressure During Ageing

Table 2.1 in Chapter 2: *Methods* summarised the 100s of organic components in the crude oil used in the experiments described in this thesis; due to the complexity of the system, and as exact chemical information was not provided by Shell, it is not possible to calculate the exact contribution from the crude oil to the pressure inside the cell during ageing, but it can be approximated as follows. Roughly 50 mL crude oil was used in each experiment; the crude oil used had a density of 0.8339 g/mL, giving a mass of 41.70 g crude oil. 10.4 wt% of the crude oil was composed of $C_8$ organics, 6.71 wt% of $C_9$ and 7.30 wt% of $C_{10}$ organics. It therefore follows that the masses of the $C_8$, $C_9$ and $C_{10}$ organics present were 4.34, 2.80 and 3.04 g respectively, from the wt%s and the mass of the crude oil.

An estimation of the contribution from the crude oil to the pressure inside the glass jar during ageing can be achieved by treating all $C_8$ organics as n-octane, all $C_9$s as n-nonane and $C_{10}$s as n-decane; the heavier organics can be ignored, as they are assumed to have a negligible effect on the pressure, as the boiling points of alkanes with carbon chains longer than $C_{11}$ are $> 200°C$.[145] The molar masses of n-octane, n-nonane and n-decane are 114.23, 128.26 and 142.28 g/mol respectively, so the number of moles present of each of the components under consideration are:

$$number\ of\ moles = mass/molar\ mass$$

$$number\ of\ moles\ octane = 4.34/114.23 = 0.038\ mol$$

$$number\ of\ moles\ nonane = 2.80/128.26 = 0.022\ mol$$

$$number\ of\ moles\ decane = 3.04/142.28 = 0.021\ mol$$

In order to estimate whether the crude oil itself had a significant impact on the

pressure inside the vessel at elevated temperatures, it can be assumed that under these conditions, the entirety of the octane, nonane and decane components have evaporated, and are all gases. For the purposes of this hypothetical estimation, these gases can be treated as ideal gases, and thus the ideal gas law in Equation 5.1 can be used:

$$PV = nRT \tag{5.1}$$

where P is the pressure, V is the volume, n is the number of moles, R is the ideal gas constant, and T is the temperature. The jar used would have had approximately 200 mL air space remaining after the crude oil was added, so rearranging for P, the pressures of octane, nonane and decane, $P_{octane}$, $P_{nonane}$ and $P_{decane}$ respectively, can be estimated as:

$$P_{octane} = \frac{0.038 \times 8.314 \times 343.15}{0.2} = 542\ Pa$$

$$P_{nonane} = \frac{0.022 \times 8.314 \times 343.15}{0.2} = 314\ Pa$$

$$P_{decane} = \frac{0.021 \times 8.314 \times 343.15}{0.2} = 300\ Pa$$

The contribution from the air above the crude oil to the total pressure experienced inside the vessel can then also be estimated. Treating the air above the crude oil within the sealed vessel as an ideal gas, we can use the ideal gas law in Equation 5.1 once more. Since V, n and R were constant as the temperature increased within the sealed vessel, we can write the following, where $P_{\mathrm{x}}$ is the pressure at T = $x$ K, and $P_{\mathrm{y}}$ is the pressure at T = $y$ K respectively:

$$\frac{P_x}{x} = \frac{nR}{V} = \frac{P_y}{y}$$

Using the values for standard temperature and pressure, $x = 273.15\ K$ and $P_x = 100\ kPa$,[146] we can predict $P_y$, the air pressure inside the vessel during ageing conditions at $y = 343.15\ K$:

$$P_y = \frac{P_x y}{x} = \frac{100 \times 343.15}{273.15} = 126\ kPa$$

The cumulative contribution of the three most volatile components in the crude oil, making up a total of 24.41 wt% of the crude oil, was only 1.156 kPa, with the assumption that the entirety of each component had fully evaporated. It therefore is clear that the contribution of the crude oil to the pressure within the ageing vessel is negligible for the experiments described in this thesis, and that the pressure can be estimated as around 126 kPa, or 1.24 atm.

## 5.3 Low-Vacuum Scanning Electron Microscopy

The SEM work in the literature for the unaltered carbonates, as discussed in Chapter 3: *Carbonates*, was predominantly carried out on samples which had been polished, coated and/or set in resin, recorded at fairly low magnification, and/or did not showcase the full heterogeneity of the rock.[20,92,94,107,108] At the time of writing, limited work had been carried out using SEM to image aged carbonate outcrop rocks.[147–150] Similarly to the unaltered surfaces, SEM work in the literature has either been carried out at a comparatively low magnification,[147] on polished samples,[148–150] and/or only presents one or two images of one surface type,[147–149] not showcasing the heterogeneity present on the surface. This work therefore adds to previous work by imaging aged carbonates which have not been polished, at high magnification, to showcase any heterogeneity present on the surfaces. It is of particular importance for these studies that the work was not carried out on polished surfaces, such that any impact of the natural underlying topography on the crude oil film can be observed.

### 5.3.1 Calcite

Low-vacuum SEM micrographs of aged calcite were collected for a range of different post-ageing conditions. Low-vacuum SEM micrographs were collected immediately post-ageing, but were also collected for the surface after AFM and SICM imaging had taken place, to observe whether the use of SICM had altered the surface in any way. A second aged calcite sample, Aged Calcite 2, was also imaged using low-vacuum SEM immediately post-ageing but then left in air for 2 months prior to low-vacuum

SEM imaging once more. This second sample provides a comparison for the first sample, Aged Calcite 1, which had undergone the full set of characterisations, to ensure that any observed surface alterations were the result of AFM and SICM imaging, and not just deterioration due to age.

#### 5.3.1.1 Post-Ageing

An overlay of four low magnification low-vacuum SEM micrographs of one area of the Aged Calcite 1 surface is shown in Figure 5.1, and a second overlay of five low magnification low-vacuum SEM micrographs from the Aged Calcite 2 surface is shown in Figure 5.2. Aged Calcite 1, pictured in Figure 5.1, was used for subsequent AFM and SICM imaging, before being imaged once more using low-vacuum SEM to determine if any surface alterations at taken place. Aged Calcite 2, imaged in Figure 5.2, was kept in air after imaging with SEM, then re-imaged 2 months later as a comparison for the Aged Calcite 1 after AFM and SICM imaging, to determine whether any surface alterations had occurred as a result of the age of the sample, or as the direct consequence of SPM imaging. The results from these subsequent SEM experiments are discussed later in this chapter, in Sections 5.3.1.2 and 5.3.1.3.

A low-vacuum SEM micrograph of an unaltered calcite surface, originally shown in Chapter 3: *Carbonates*, Figure 3.4, is re-shown in Figure 5.3. When compared to the aged surfaces shown in the overlays in Figures 5.1 and 5.2, it appears that during the ageing process, the crude oil has formed a film covering the majority of the calcite surface. The low-vacuum SEM micrograph at the bottom of Figure 5.1 is shown by itself, rotated 90°, in Figure 5.4. Aged calcite areas A - C are labelled on Figure 5.4, and shown at higher magnification in Figures 5.5 - 5.8 respectively.




Figure 5.1: Aged Calcite 1: SEM Overlay
An overlay of four low-vacuum SEM micrographs of Aged Calcite 1. The individual micrographs which make up this overlay can be found in Appendix B, Figures B.9 - B.12.

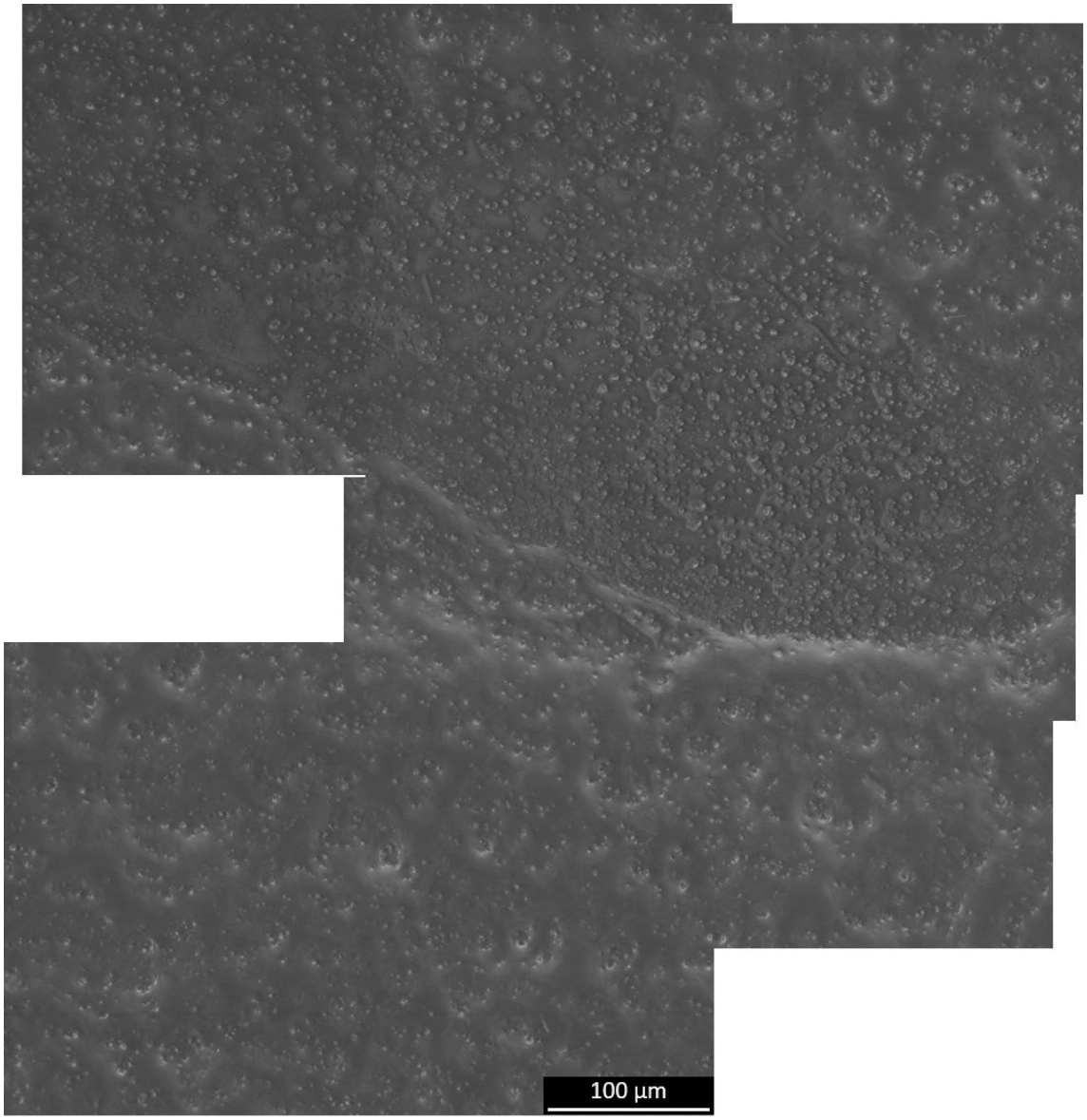



Figure 5.2: Aged Calcite 2: SEM Overlay
An overlay of five low-vacuum SEM micrographs of Aged Calcite 2. The individual micrographs which make up this overlay can be found in Appendix B, Figures B.13 - B.17.

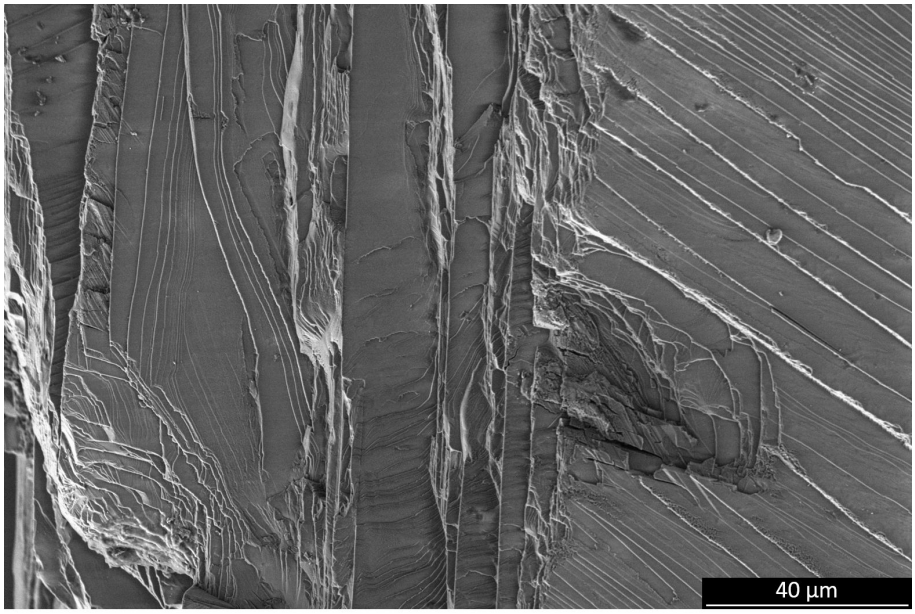
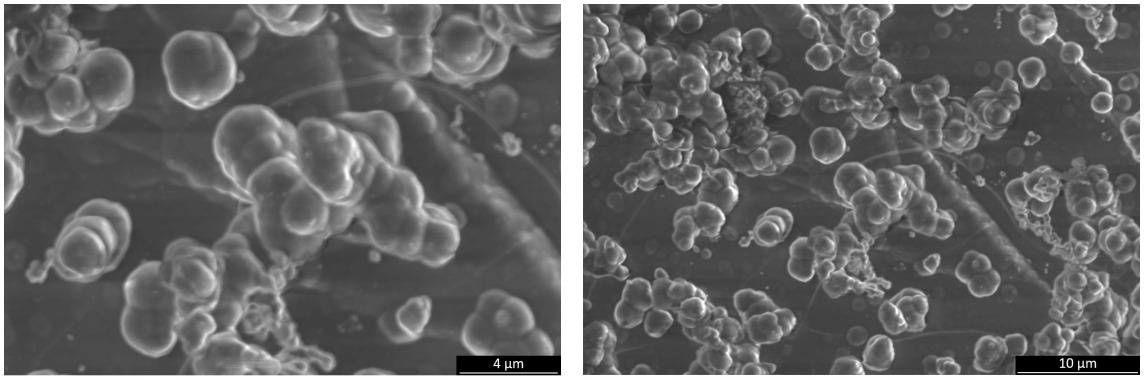



Figure 5.3: Calcite: high magnification SEM micrograph of an unaltered surface
The higher magnification low-vacuum SEM micrograph of an unaltered calcite surface previously shown in Chapter 3: *Carbonates*, Figure 3.4, page 95.




Figure 5.4: Aged Calcite 1: SEM micrograph with labelled areas of interest
The right-hand low-vacuum SEM micrograph from the overlay in Figure 5.1 showing the fields of view for the three higher-magnification low-vacuum SEM micrographs, A-C, presented in Figures 5.5 - 5.8 below respectively.

Figure 5.5 shows aged calcite area A at higher magnification. From these micrographs it can be seen that smooth, raised crude oil agglomerates of a few $\mu$m across, made up of almost spherical oil droplets are present across the surface, creating a much rougher surface than was observed for unaltered calcite in Chapter 3: *Carbonates*. A straighter structure, which could be the edge of a calcite plane, appears to be visible underneath the agglomerates, which as can be seen at the increased size in Figure 5.6, is itself also coated in smaller agglomerates. Areas similar to the one shown in Figure 5.5 are classified as aged calcite surface type 1.




(a) (b)

Figure 5.5: Aged Calcite 1: high magnification SEM micrographs of area A
Two higher magnification low-vacuum SEM micrographs of the area labelled "A" on the aged calcite surface shown in Figure 5.4. Both depict aged calcite surface type 1.

Figure 5.7 shows a high magnification low-vacuum SEM micrograph of aged calcite area B. The right hand side of the image appears to show a region of aged calcite surface type 1, however towards the left a rougher section is present. This rougher area does not show the same smooth agglomerates as surface type 1, instead showing a larger agglomerate of smaller droplets. This agglomerate is 10s of $\mu$m across and appears to also sit thicker on the calcite surface than surface type 1. These characteristics are classified as aged calcite surface type 2.

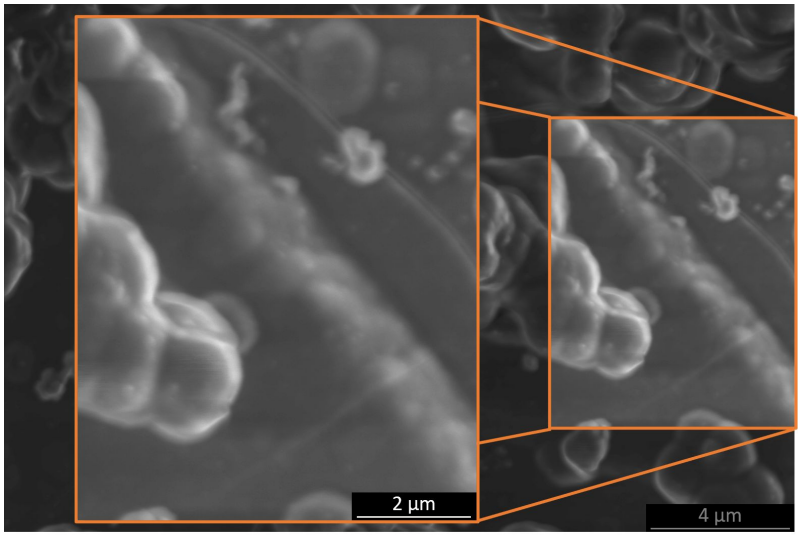



Figure 5.6: Aged Calcite 1: high magnification SEM micrograph of area A - zoomed in
A zoom in of the area of Figure 5.5a which appears to be a calcite crystal plane edge coated with small crude oil agglomerates.

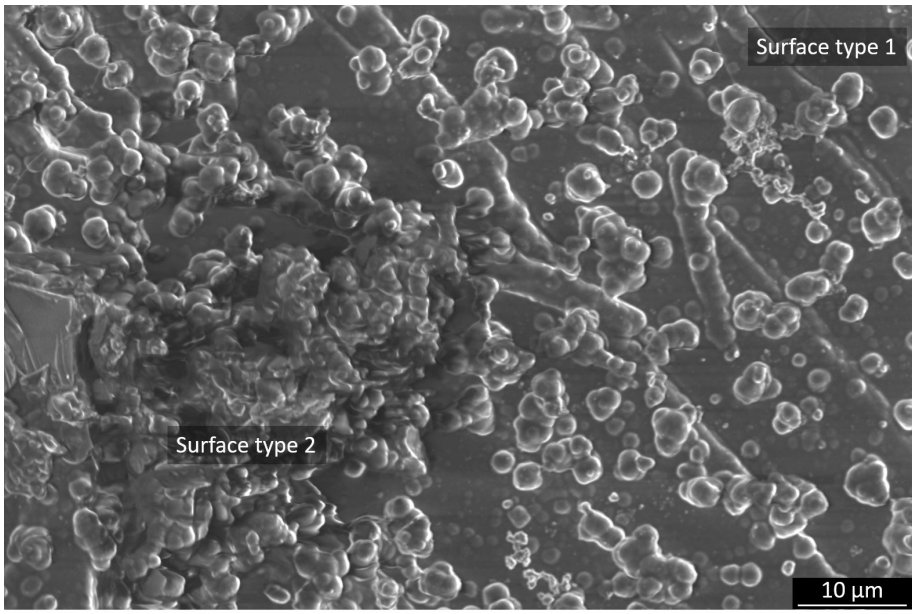



Figure 5.7: Aged Calcite 1: high magnification SEM micrograph of area B
A higher magnification low-vacuum SEM micrograph of the area labelled "B" on the aged calcite surface shown in Figure 5.4, depicting aged calcite surface types 1 and 2.

Aged calcite surface type 3 is labelled in Figure 5.8, which is a higher magnification low-vacuum SEM micrograph of the area labelled "C" in Figure 5.4. This third surface type represents an area of the calcite surface which does not appear to have been coated with crude oil, with the unaltered calcite surface apparently

visible. In this case, this un-coated surface is unaltered calcite surface type 2, as defined in Chapter 3: *Carbonates*, Section 3.2.1,[a] which can also be seen towards the right hand side of Figure 5.3 in this chapter. Aged calcite surface types 1 and 2 are also present in Figure 5.8, and are annotated on the micrograph.

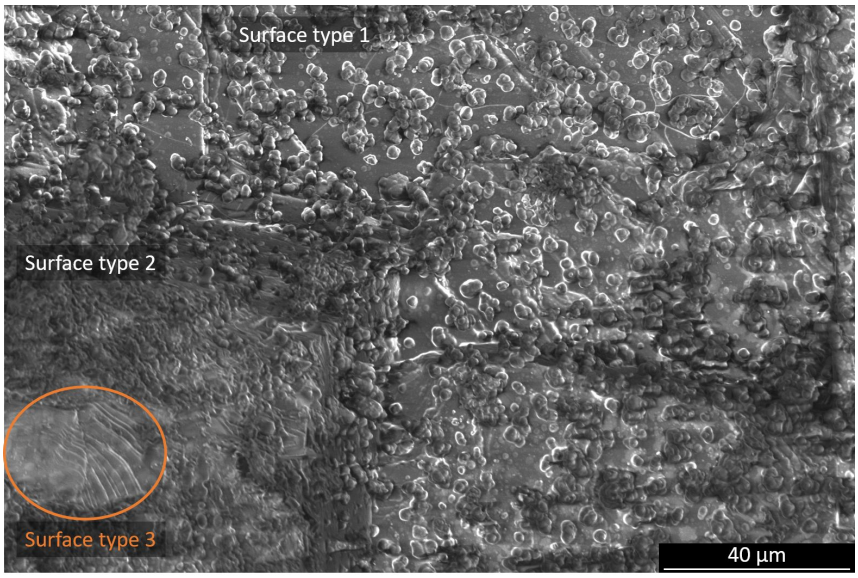
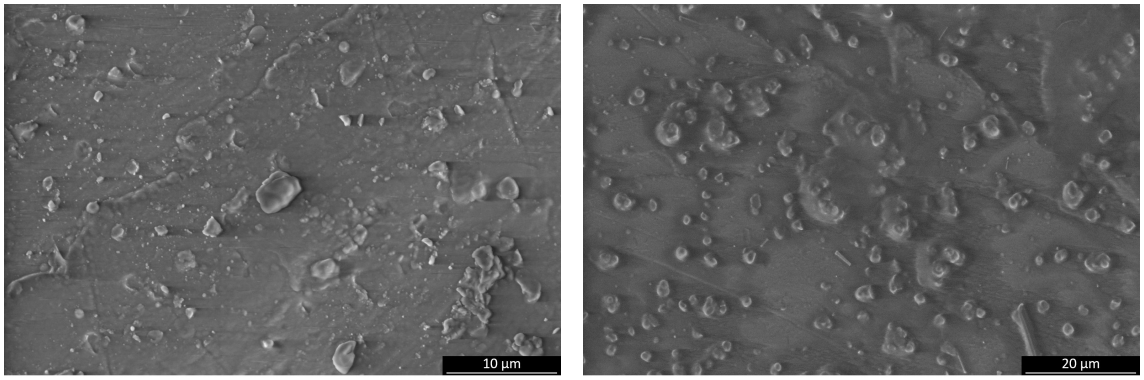


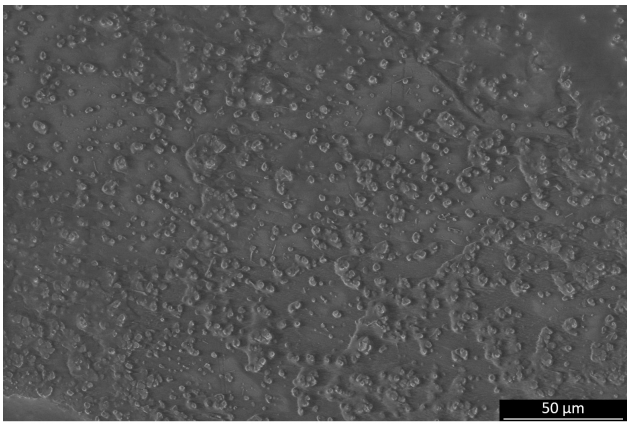

Figure 5.8: Aged Calcite 1: high magnification SEM micrograph of area C
A higher magnification low-vacuum SEM micrograph of the area labelled "C" on the aged calcite surface shown in Figure 5.4, depicting aged calcite surface types 1, 2 and 3.

Figure 5.2 on page 223 showed an overlay of five low-vacuum SEM micrographs of the Aged Calcite 2 surface. Three higher magnification images of this surface are presented in Figure 5.9. The oil film's surface coverage over this sample is much more uniform than observed for Aged Calcite 1 in Figure 5.1. There is also an absence of the smooth agglomerates present in aged calcite surface type 1, the entirety of the surface being made up of irregular oil droplets similar to those observed in surface type 2, but more evenly distributed across the flat surface. As this surface type was not observed in Figure 5.1, the surface shown in Figure 5.2 and in greater detail in Figure 5.9, is classified as aged calcite surface type 4.

[a] a summary of unaltered calcite surface types can be found in Table 3.1, page 96



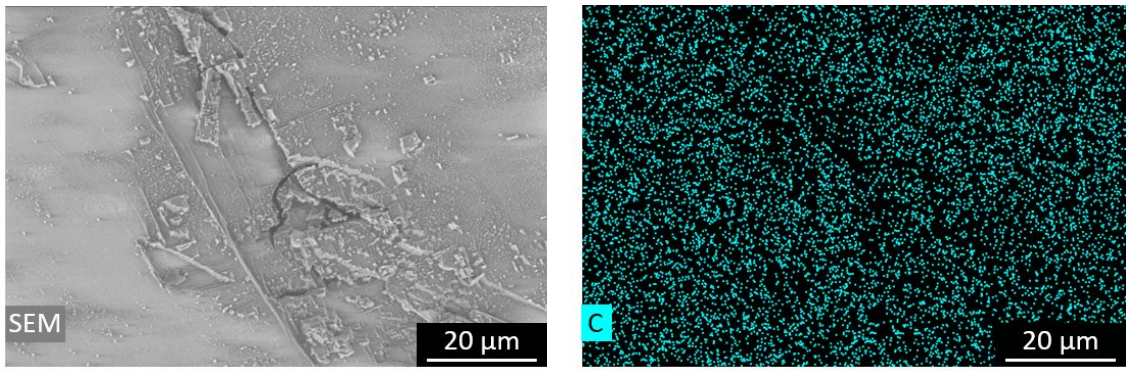

(a) (b)




(c)

Figure 5.9: Aged Calcite 2: high magnification SEM micrographs of surface type 4 Three higher magnification low-vacuum SEM micrographs of the aged calcite surface shown in Figure 5.2.

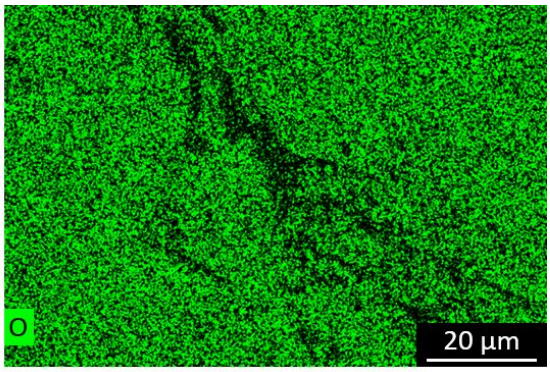
To serve as a comparison for the aged calcite samples, EDX data for the unaltered calcite surface type 4a, as defined in Chapter 3: *Carbonates*, Section 3.2.1, was collected and is shown below in Figure 5.10. As was expected from a pure calcite crystal, the elements present on the calcite surface were Ca, C and O, and were evenly distributed across the surface. A further EDX scan was carried out on calcite area 4b, data from which can be found in Appendix B, Figure B.32, which showed identical elements present and similar distributions.



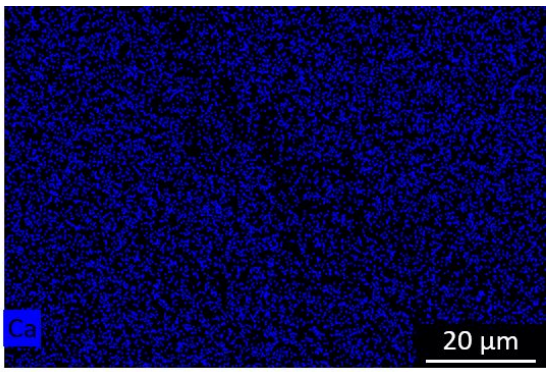

(a)



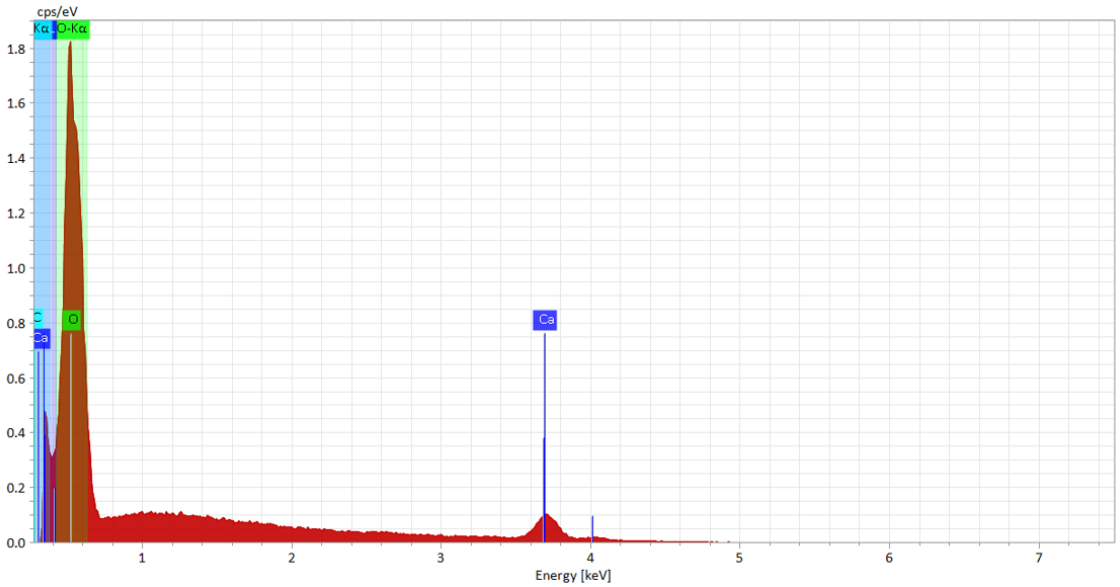

(b)




(c)




(d)




(e)

Figure 5.10: Calcite: EDX results for surface type 4a
EDX results for area 4a of the calcite surface defined and labelled in Figure 3.6a in Section 3.2.1. (a) Shows the low-vacuum SEM micrograph of the area, (b), (c) and (d) show the C, O and Ca distribution maps for the area respectively, and (e) shows the X-ray energy spectrum for the image, with element assignments labelled.

EDX was carried out on a few areas of the Aged Calcite 2 surface during low-vacuum SEM imaging, to give a reference for the studies later conducted on Aged Calcite 1 after AFM and SICM imaging. Element distribution maps from the region towards the center of the Aged Calcite 2 overlay in Figure 5.2 (page 223) are shown in Figure 5.11, alongside the associated micrograph. The X-ray energy spectrum for this scan is shown in Figure 5.11e; the characteristic Ca peak at 3.69 keV, clearly visible in the unaltered calcite spectrum in Figure 5.10e, is marked to highlight its absence from the spectrum. The elements present in the spectrum are predominantly C with a small amount of O and S, and can be seen to be evenly distributed across the surface. This to be expected from a crude oil film, as crude oil is predominantly made up of a wide range of hydrocarbons, with small amount of S-containing compounds;[151] as stated in Chapter 2: *Methods*, Table 2.1, the crude oil used in these studies contained 0.792 % S. The lack of any Ca signal would indicate that the oil film fully covers the investigated surface and likely exceeds 2 $\mu$m thick, as this is the sensitivity depth of EDX.[83]

It is generally accepted that using EDX for quantitative measurements of the wt% compositions of light elements is not advisable, as their low energy characteristic X-rays are readily absorbed by other elements.[152] Despite this, the relative heights of the O and C peaks in the X-ray energy spectra can still be compared qualitatively. In the unaltered calcite EDX spectrum in Figure 5.10e, the O peak is substantially higher than the C peak, which is expected, as the formula for calcite is $CaCO_3$. In the aged sample however, the O peak in Figure 5.11e is very small, and the C peak comparatively much larger. Again, this is expected from a crude

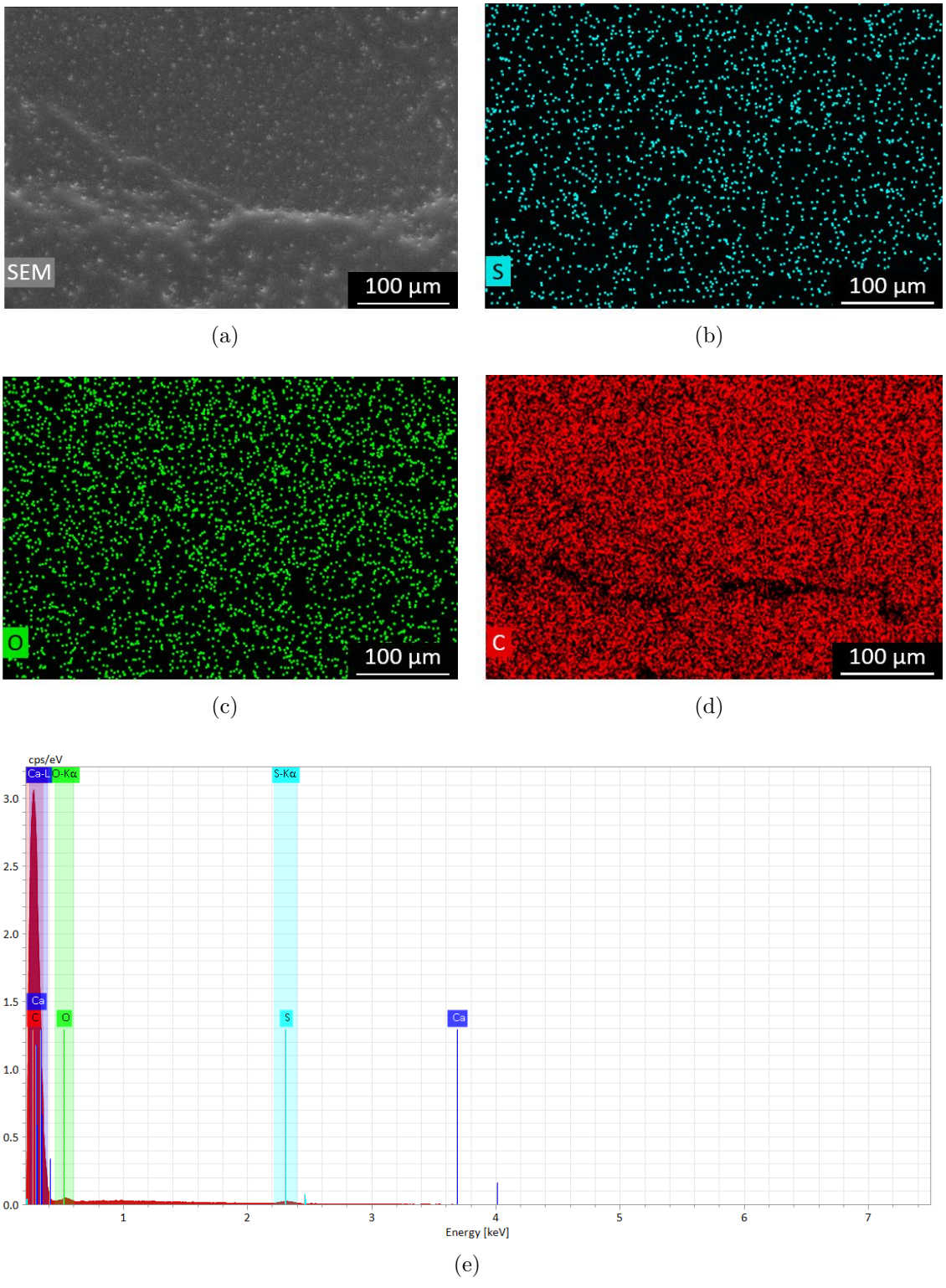



Figure 5.11: Aged Calcite 2: EDX results
EDX results for Aged Calcite 2, from the section at the center of Figure 5.2. (a) Shows the low-vacuum SEM micrograph of the area, (b), (c) and (d) show the S, O and C distribution maps for the area respectively, and (e) shows the X-ray energy spectrum for the image, with element assignments labelled.

oil hydrocarbon film, which is predominantly made up of alkanes, cycloalkanes and aromatics of varying weights, and thus this surface is expected to be more C-rich.[153]

Two further EDX scans were carried out on other areas of the Aged Calcite 2 surface, data from which is shown in Appendix B, Figures B.33 and B.34, both showing the same elements and similar distributions to those shown in Figure 5.11.

#### 5.3.1.2 Post-Ageing, post-SICM Measurements

After SICM imaging, visual inspection of the aged calcite surface showed areas which had lightened compared to the freshly aged sample, and indeed compared to the sample surface after low-vacuum SEM and AFM imaging. The sample was therefore once again imaged with low-vacuum SEM to gain an insight into the possible surface alterations which may have occurred during SICM topographical mapping. Figure 5.12 shows an overlay of nine low-vacuum SEM micrographs of the Aged Calcite 1 surface after SICM measurements had taken place. When compared back to the relatively homogeneous aged calcite surfaces presented in Section 5.3.1.1, surface alterations, possibly due to exposure to the electrolyte, have clearly occurred.

Aged calcite post-SICM surface type 1 is shown in the higher magnification low-vacuum SEM micrographs in Figure 5.13, from the region labelled "B" on Figure 5.12. These micrographs show an example of one of the darker, rougher regions of the aged calcite surface visible in Figure 5.12, which are similar to aged calcite surface type 4. It is assumed that these regions are the crude oil film which has remained attached to the calcite surface.

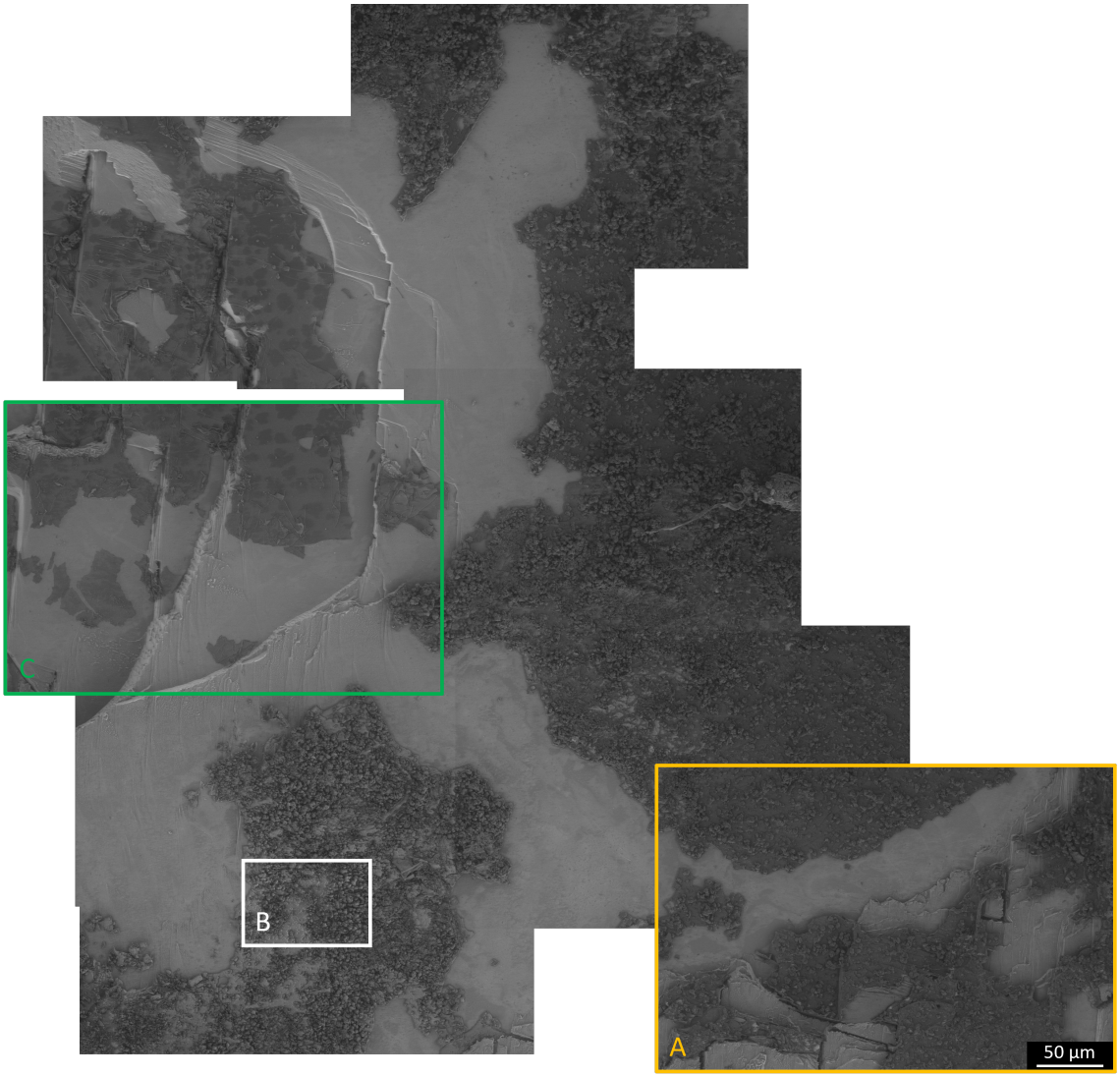
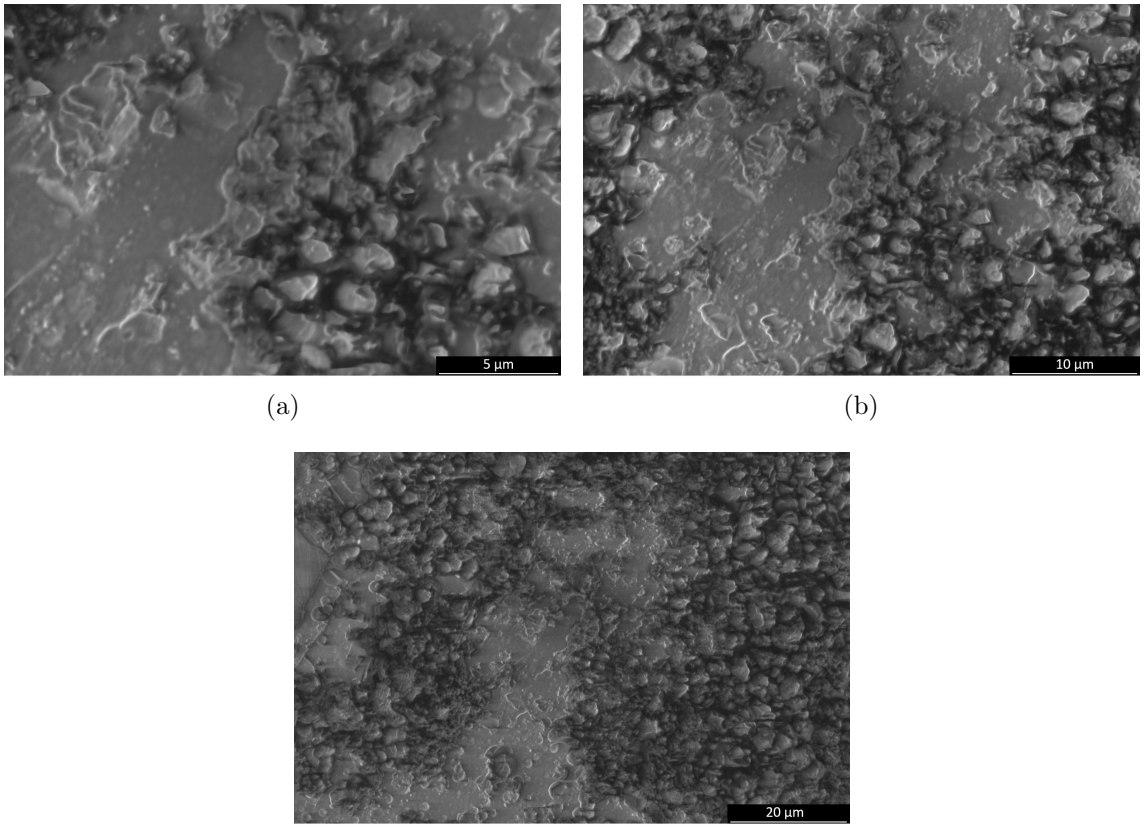



Figure 5.12: Aged Calcite post-SICM: SEM Overlay
An overlay of nine low-vacuum SEM micrographs of an aged calcite crystal after SICM measurements had been performed. Labelled boxes A-C indicate the three areas where EDX measurements were performed. The individual micrographs which make up this overlay can be found in Appendix B, Figures B.18 - B.26.




(a) (b)

(c)

Figure 5.13: Aged Calcite post-SICM: SEM micrographs of surface type 1
A set of higher magnification low-vacuum SEM micrograph of surface type 1 of the post-SICM Aged Calcite 1 surface. (c) shows the area labelled "B" in Figure 5.12, with (a) and (b) being higher magnification images of the same area.

A low-vacuum SEM micrograph of aged calcite post-SICM surface type 2 is shown in Figure 5.14, which is the micrograph labelled "A" in the overlay in Figure 5.12. This surface type represents the paler, smoother regions of the post-SICM aged calcite surface, and upon first inspection appear to be the re-exposed calcite surface, due to its similarity to the unaltered calcite images from Chapter 3: *Carbonates*. Aged calcite post-SICM surface types 1 and 2 are annotated on Figure 5.14 for clarity.

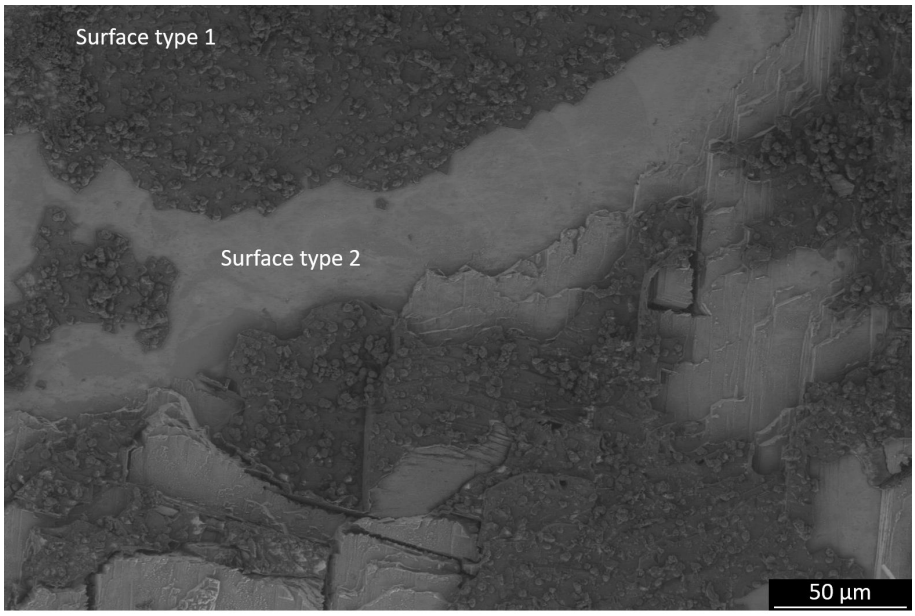



Figure 5.14: Aged Calcite post-SICM: SEM micrograph of surface types 1 and 2
A low-vacuum SEM micrograph of surface types 1 and 2 of the region of post-SICM Aged Calcite 1 surface labelled "A" in Figure 5.12.

An EDX scan was performed on the area labelled "A" in Figure 5.12, results from which are shown in Figure 5.15. Comparing the O distribution map with the SEM micrograph, side by side in Figures 5.15a and 5.15b, the paler areas, defined as surface type 2, appeared to contain considerably more O than the darker, rougher areas, defined as surface type 1, which would align with the hypothesis that these regions were exposed calcite. However, there is an absence of any Ca peak at 3.69 keV in the spectrum in 5.15d, which would be expected if calcite were exposed. It is therefore proposed that this area is not exposed calcite, but is an area where the crude oil film has become smooth and flat, reflecting the topography of the calcite crystal underneath. The darker, rougher areas are where the crude oil film remains similar to how it was prior to SICM mapping. Although there is insufficient evidence to point towards a clear explanation, it is possible that during exposure to the $KCl_{(aq)}$ electrolyte during SICM imaging, partial separation of the crude oil components has occurred on the calcite surface, with areas of more oxygen-rich organics separated from less oxygen rich material. It remains unclear however why some areas were affected and others were not, given the chemical and relative topographical homogeneity of the surface; this phenomenon is discussed further in Chapter 7: *Discussion*, Section 7.4.3.

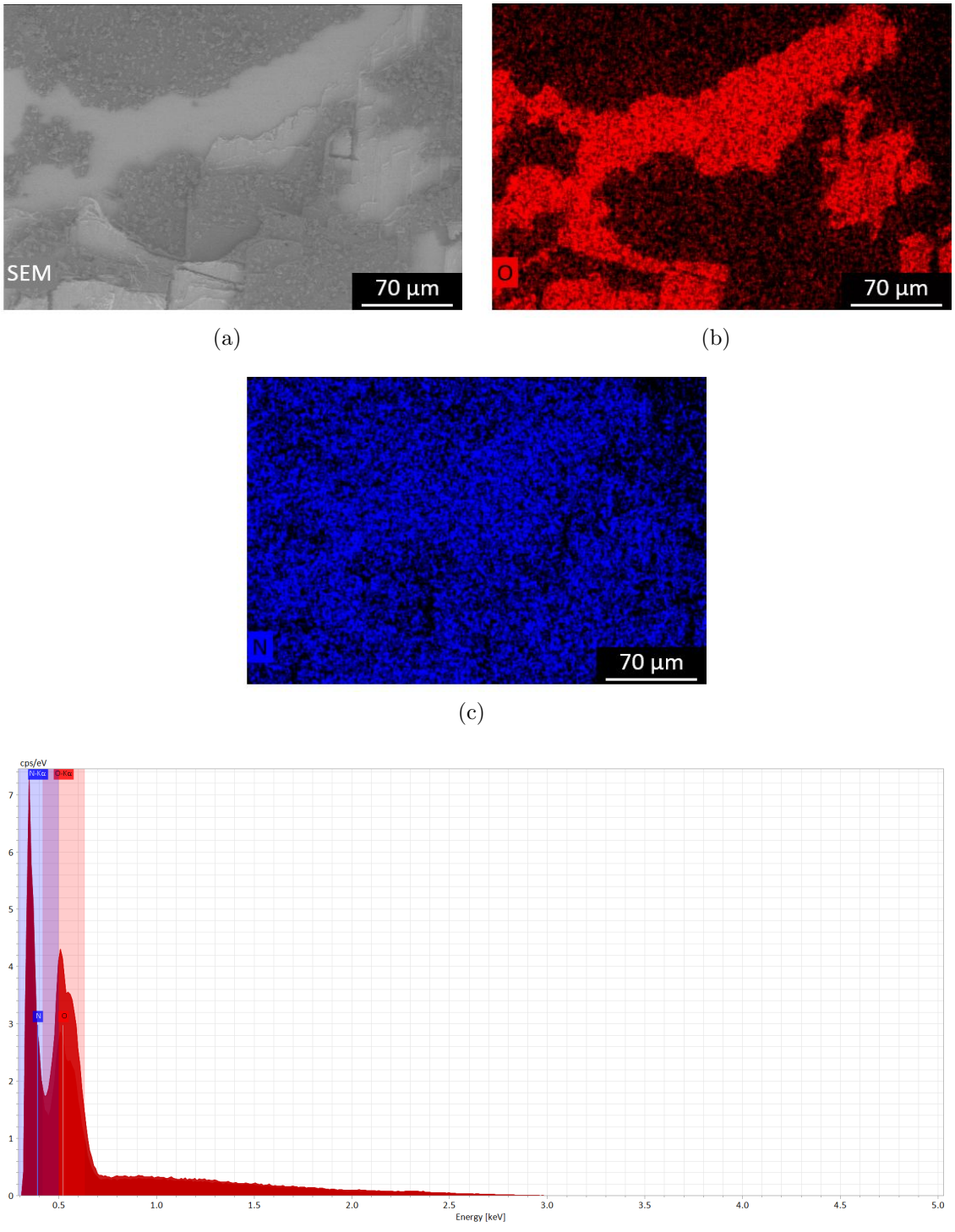



Figure 5.15: Aged Calcite post-SICM: EDX result for area A
EDX results for the post-SICM measurement Aged Calcite 1 surface imaged by SEM shown Figure 5.14. (a) Shows the low-vacuum SEM micrograph of the area, (b) and (c) show the O and N distribution maps for the area respectively, and (d) shows the X-ray energy spectrum for the image, with element assignments labelled.

EDX results for the two other areas of interest on the post-SICM Aged Calcite 1 surface, labelled "B" and "C" in Figure 5.12, are shown in Appendix B, Figures B.35 and B.36, as they show the same elemental compositions, with similar distributions across the two surface types as the data shown in Figure 5.15.

#### 5.3.1.3 Post-Ageing, Stored in Air

Aged Calcite 2, instead of being characterised by AFM and SICM, was left in air for months before being re-imaged with low-vacuum SEM. This sample was investigated to determine whether the changes observed post-SICM on the aged calcite surface in Section 5.3.1.2 were the impact of SICM imaging or simply age. Five low-vacuum SEM micrographs of this "old" Aged Calcite 2 surface are overlain in Figure 5.16, where it can be seen that the surface is similar to the low-vacuum SEM results immediately after ageing, with a crude oil film covering the whole surface. The regions of the surface towards the bottom of Figure 5.16 is most similar to the aged calcite surface type 4, identified on Aged Calcite 2 immediately after ageing. This can be seen clearly in the high magnification low-vacuum SEM micrograph of the area labelled "1", shown in Figure 5.17. Towards the top of 5.16 however, smoother, rounded structures appear to have formed on the surface of the crude oil film, which can be observed more clearly in the high magnification low-vacuum SEM micrograph of the area labelled "2" shown in Figure 5.18. Due to the observation of these new structures, the two areas labelled 2 and 3 on the overlay in Figure 5.16 were selected for further investigation with EDX.

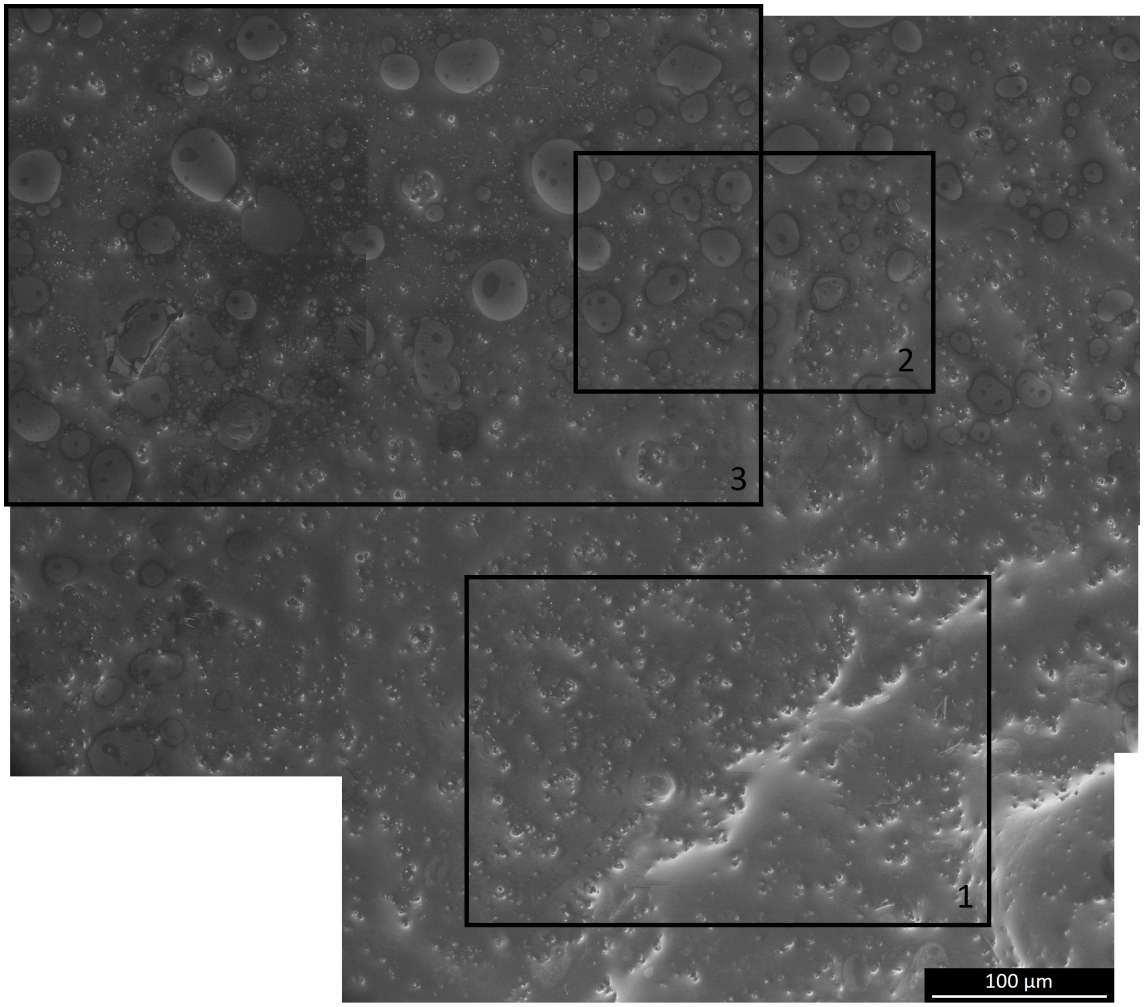



Figure 5.16: "Old" Aged Calcite: SEM Overlay
An overlay of five low-vacuum SEM micrographs of an aged calcite crystal after it had been stored in air for two months. Three areas of interest are labelled 1 - 3; 2 and 3 were selected for EDX analysis. The individual micrographs which make up this overlay can be found in Appendix B, Figures B.27 - B.31.

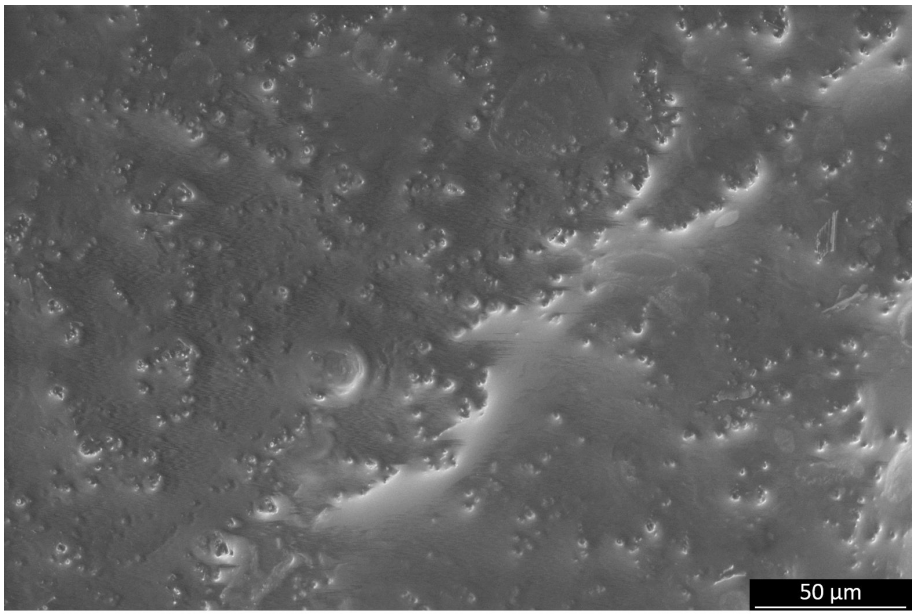



Figure 5.17: "Old" Aged Calcite: high magnification SEM micrograph of area 1
A higher magnification low-vacuum SEM micrograph of the area labelled "1" on the old aged calcite surface shown in Figure 5.16.

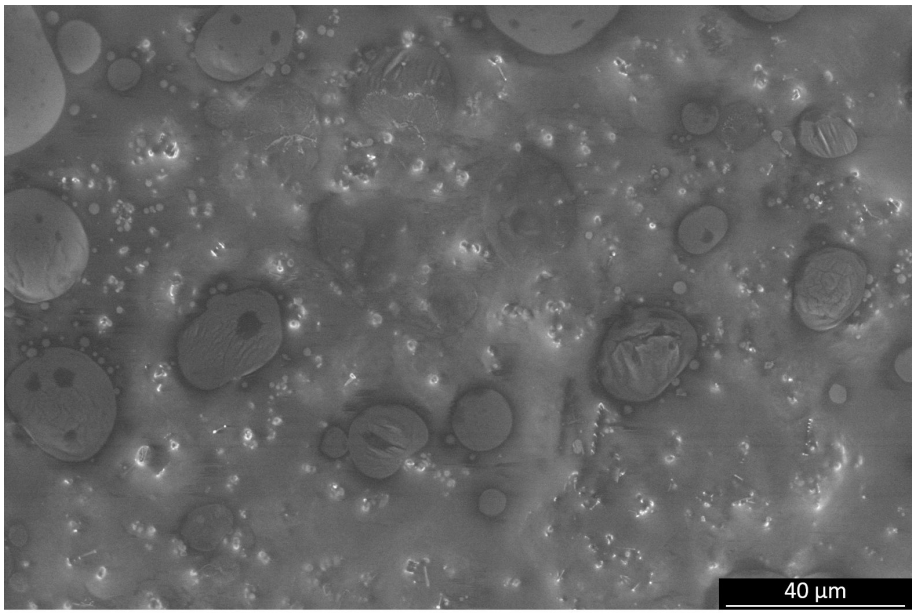



Figure 5.18: "Old" Aged Calcite: high magnification SEM micrograph of area 2
A higher magnification low-vacuum SEM micrograph of the area labelled "2" on the old aged calcite surface shown in Figure 5.16.

Figures 5.19 and 5.20 show the EDX results for the two areas labelled 2 and 3 in Figure 5.16 respectively. When comparing Figures 5.19a and 5.19c and Figures 5.20a and 5.20c for areas 2 and 3 respectively, a clear correlation between the smooth, rounded structures and a higher concentration of oxygen being present can be observed. These smooth structures were not necessarily caused by the same effects as the smooth areas observed in post-SICM aged calcite surface type 2 (Figure 5.14, page 235), but there are common characteristics. Both surfaces are smoother than the freshly aged rough surfaces, and both surfaces appear to be oxygen-rich in comparison to the rougher areas. The oxygen-rich areas are larger in the post-SICM Aged Calcite 1 sample than those observed on the old Aged Calcite 2 sample. It is possible that the process that caused the formation of the smooth oxygen-rich areas, which was hypothesised in Section 5.3.1.2 to be due to the partial separation of the crude oil film into oxygen-rich and less-oxygen-rich components, was accelerated by the exposure to the $KCl_{(aq)}$ electrolyte, and that the old Aged Calcite sample demonstrated a less progressed segregation of the film. Unfortunately, there is insufficient evidence to make any conclusive remarks on these results, and further studies would be necessary to fully understand the observed behaviour.

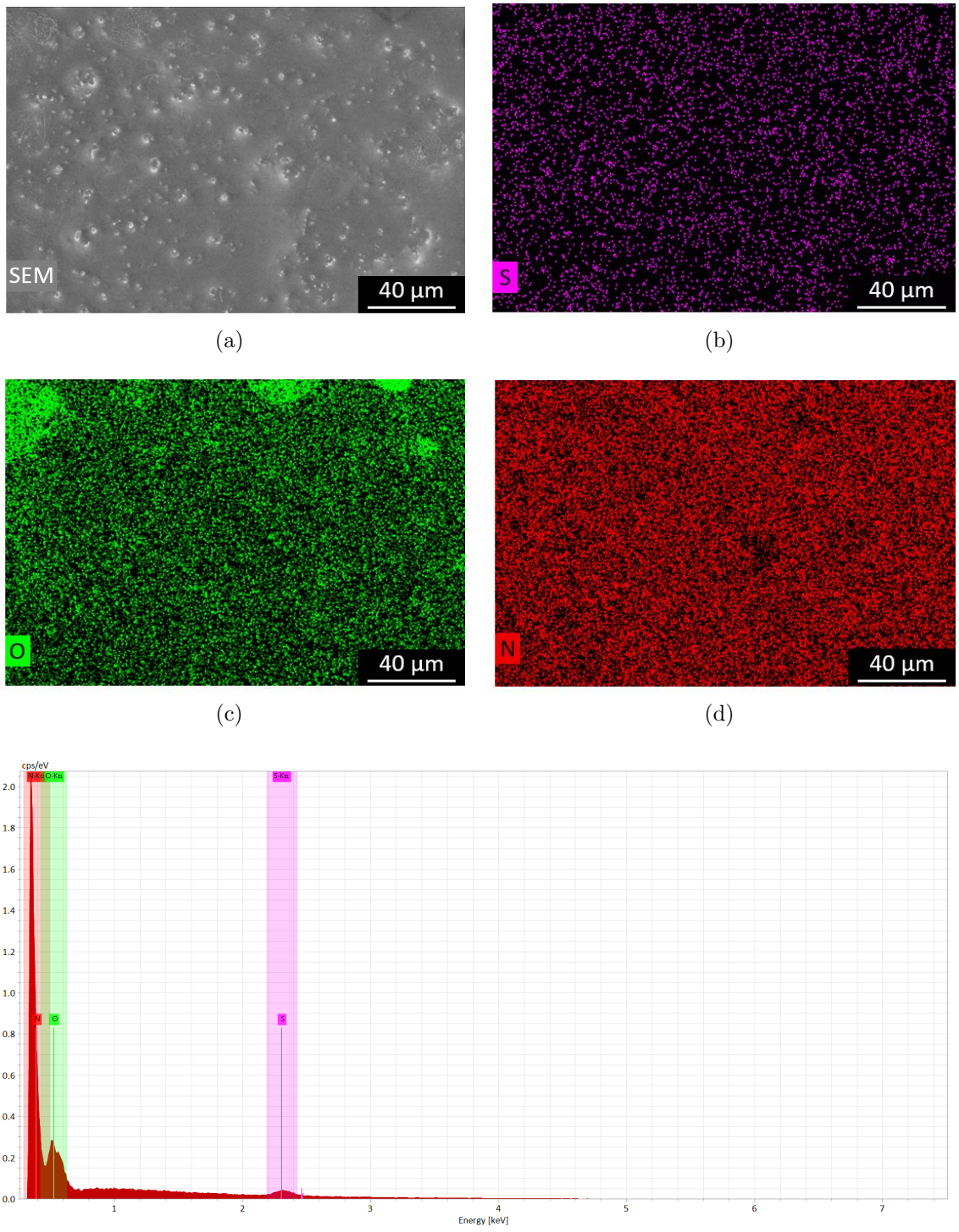



Figure 5.19: "Old" Aged Calcite: EDX results for area 2
EDX results for area 2 of the "old" aged calcite 2 surface shown and labelled in Figure 5.16. (a) Shows the low-vacuum SEM micrograph of the area, (b), (c) and (d) show the S, O and N distribution maps for the area respectively, and (e) shows the X-ray energy spectrum for the image, with element assignments labelled.

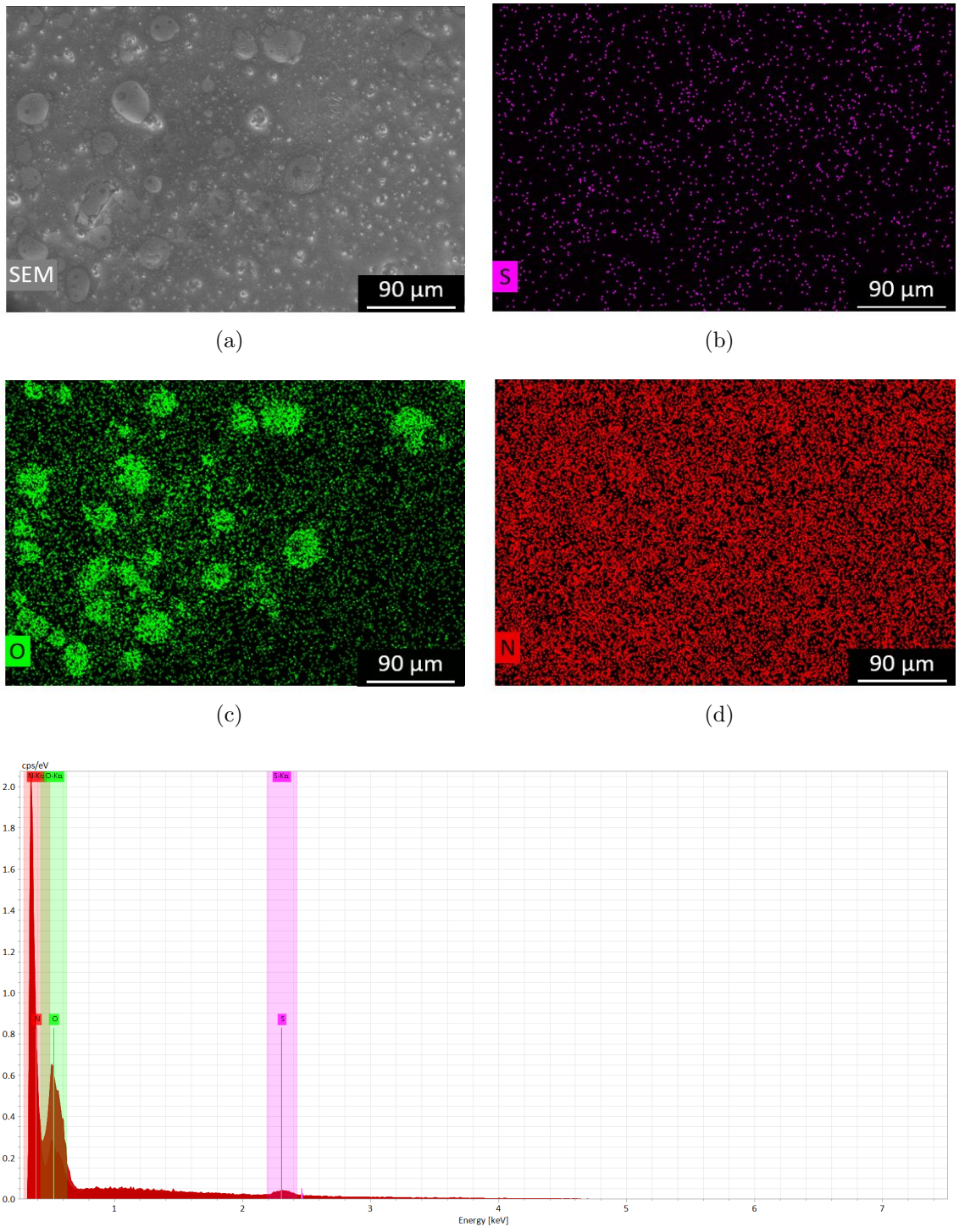



Figure 5.20: "Old" Aged Calcite: EDX results for area 3
EDX results for area 3 of the "old" aged calcite 2 surface shown and labelled in Figure 5.16. (a) Shows the low-vacuum SEM micrograph of the area, (b), (c) and (d) show the S, O and N distribution maps for the area respectively, and (e) shows the X-ray energy spectrum for the image, with element assignments labelled.

#### 5.3.1.4 Summary

Overall, four surface types were identified across the freshly aged calcite samples, two on the aged calcite sample after SICM imaging and two on the old aged calcite sample. Mostly qualitative descriptions, with some semi-quantitative information, of these surface types are summarised in Table 5.1, alongside lists of elements picked up in the EDX, if carried out for that surface type. This table helps to visualise not only the heterogeneity of these crude-oil covered surfaces, but also the alterations the crude-oil film appears to undergo.

| Aged Calcite | Surface Type | Description | EDX Signals |
|---|---|---|---|
| Aged 1 | 1 | Spherical droplets of 1-2 $\mu$m across on an otherwise smooth crude oil film | N/A |
| | 2 | Agglomerates 10s of $\mu$m across of the smaller droplets | |
| | 3 | Regions which do not have any droplet structures present | |
| Aged 2 | 4 | Irregular deposits on an otherwise smooth crude oil film | C, O and S |
| Post-SICM | 1 | Irregular deposits on an otherwise smooth crude oil film | N, little O |
| | 2 | Smooth surface without any droplets or deposits | N, lots O |
| Old aged | 1 | Irregular deposits on an otherwise smooth crude oil film | N, little O and S |
| | 2 | Smooth, raised, rounded structures within the irregular droplet film | N, little S, lots O |

Table 5.1: Aged Calcite Surface Types
A summary of the different surface types identified on the aged calcite samples: qualitative descriptions based on low-vacuum SEM micrographs and summaries of relevant EDX data.

### 5.3.2 Estaillades

Two Estaillades samples were aged and mapped with low-vacuum SEM in order to gain an insight into the crude oil film coverage on a more structurally complex surface than the calcite surface previously described. Due to the observed differences in the aged calcite's crude oil film before and after characterisation with SICM, Estaillades was also imaged with low-vacuum SEM after characterisation with SICM.

#### 5.3.2.1 Post-Ageing

The first Estaillades sample which was aged and imaged under low-vacuum SEM was unfortunately not imaged with SICM prior to the COVID-19 lockdown in March 2020. A second Estaillades sample was therefore aged later in the year when laboratories re-opened, so that SICM measurements could be carried out whilst the sample was still new. Overlays of low-vacuum SEM micrographs of both of these aged Estaillades samples are shown in Figures 5.21 and 5.22.

Four higher-magnification low-vacuum SEM micrographs from the region in the first overlay (Figure 5.21) are shown in Figure 5.23. All four of these micrographs show similar surfaces, and display characteristics similar to aged calcite surface types 1 and 2. These areas are covered with a film of smooth oil droplets on the order of 1 $\mu$m across, forming a continuous agglomerate film across the surface. The similarity with aged calcite surface type 1 is that the oil droplets are smooth, and larger than those in aged calcite surface type 2. However, the extensive agglomeration of these droplets is closer in appearance to aged calcite surface type 2, and unlike aged calcite surface type 1, which has flatter sections between each droplet or small

agglomeration of droplets. This appearance of a continuous agglomerate film could be in part due to Estaillades being a rougher surface that calcite. As the unaltered Estaillades surface is itself made up of numerous raised features, it is perhaps not possible to tell the difference between sections of the surface where the crude oil is forming agglomerates of droplets and where it is simply coating the surface with an even film. It is also likely that the droplets are more likely to form on the edges of surface features, similarly to how droplets were visible on the aged calcite crystal plane edge in Figure 5.6 on page 226, which would play more of a role in Estaillades.

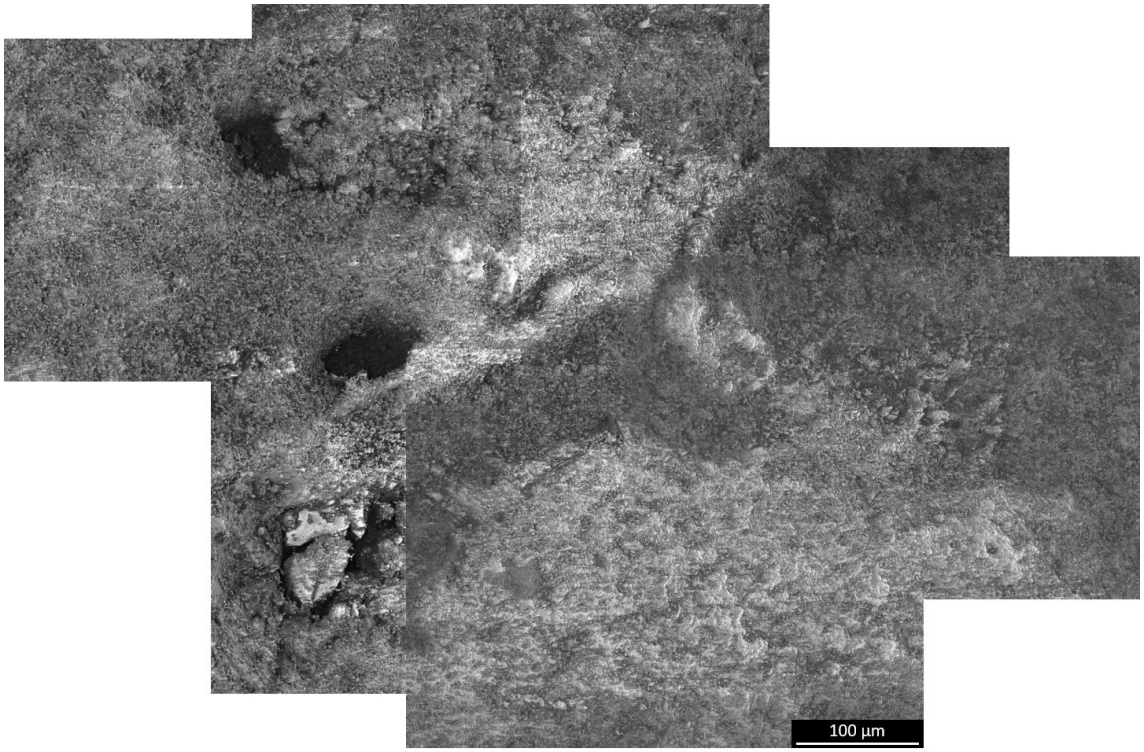



Figure 5.21: Aged Estaillades 1: SEM Overlay
An overlay of six low-vacuum SEM micrographs of an aged Estaillades sample. The individual micrographs which make up this overlay can be found in Appendix B, Figures B.58 - B.63.

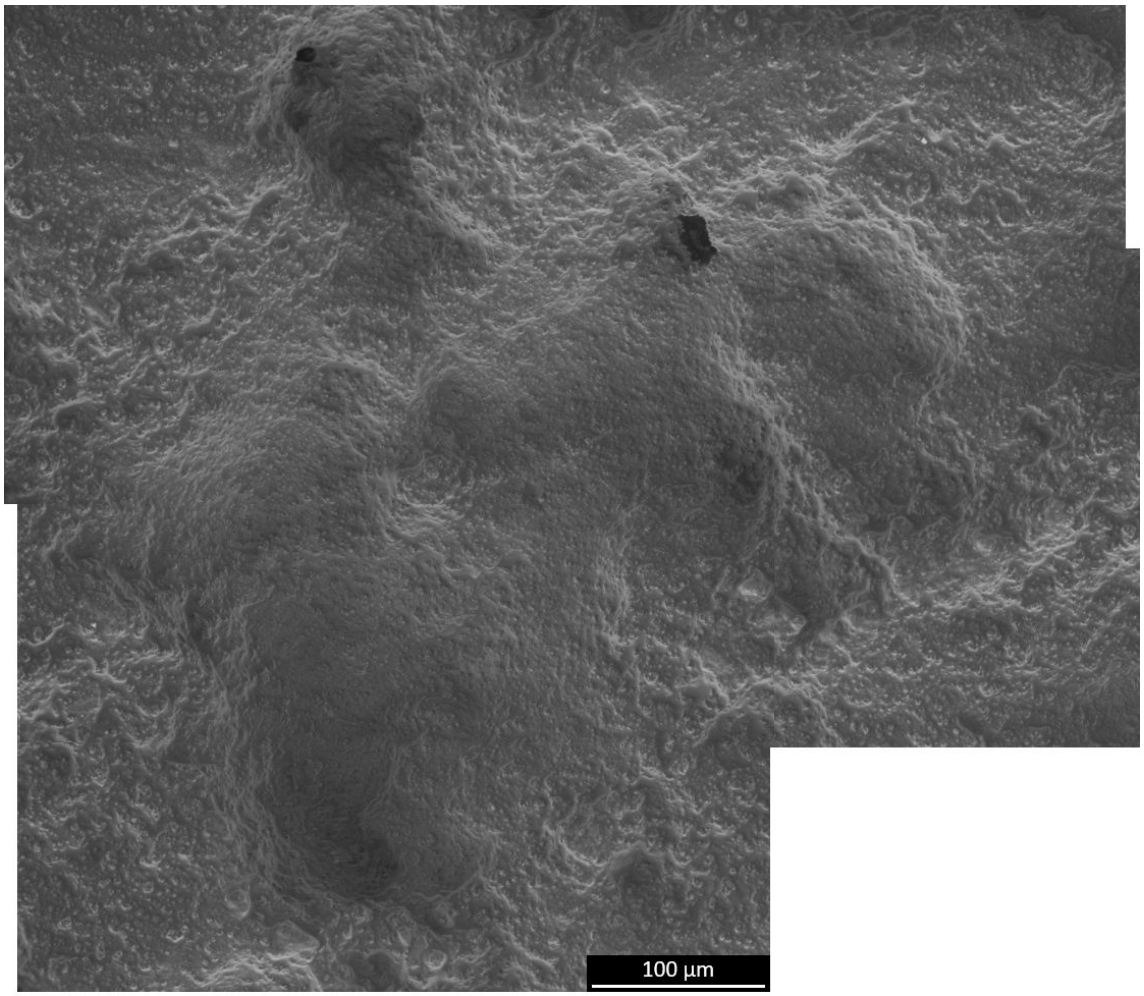
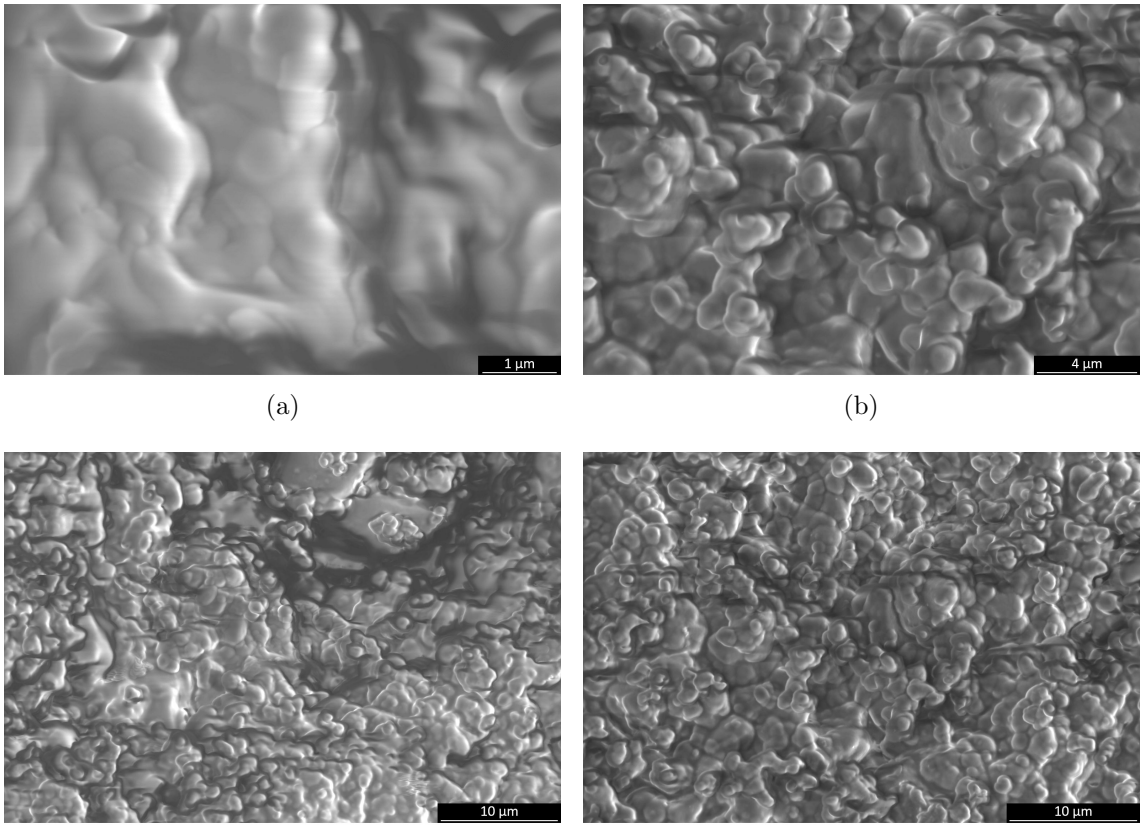



Figure 5.22: Aged Estaillades 2: SEM Overlay
An overlay of five low-vacuum SEM micrographs of an aged Estaillades sample. The individual micrographs which make up this overlay can be found in Appendix B, Figures B.64 - B.68.

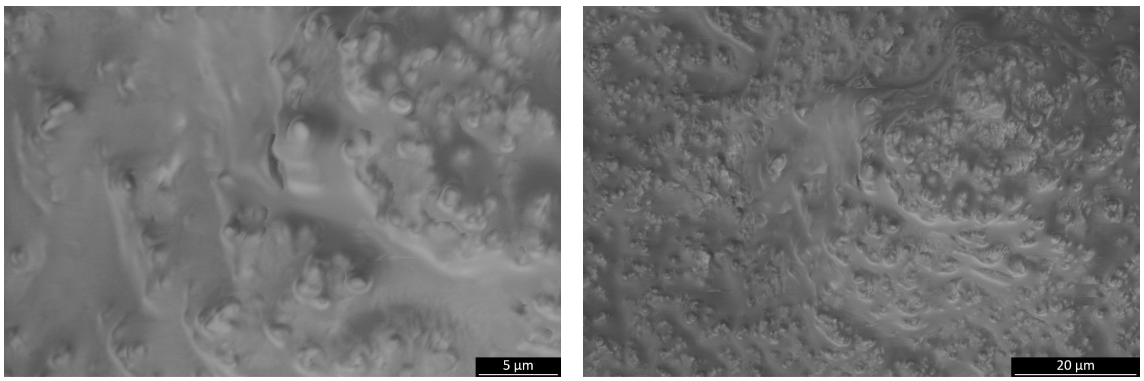
An overlay of low magnification low-vacuum SEM micrographs from the second aged Estaillades sample surface is shown in Figure 5.22, with two high magnification low-vacuum SEM micrographs from this region shown in Figure 5.24, all showing similar surfaces to those observed on the first aged Estaillades sample. The agglomerates visible in 5.24 are not as smooth as those on the first sample (Figure 5.23), the crude oil film on this second sample being similar to that of aged calcite surface type 4. There are also sections of smoother film, without raised agglomerate structures, particularly towards the left of Figure 5.24a, which were not observed in the low-vacuum SEM micrographs of the first aged Estaillades sample. These smooth sections perhaps indicate a thicker crude oil film masking the topography underneath, or could simply be a smooth crude oil film covering a flat section of Estaillades surface type 3, which was defined as being made up of larger, smooth-faced calcite crystallites.




(a) (b)

(c) (d)

Figure 5.23: Aged Estaillades 1: high magnification SEM micrographs
Four higher magnification low-vacuum SEM micrographs of the aged Estaillades surface shown in Figure 5.21.




(a) (b)

Figure 5.24: Aged Estaillades 2: high magnification SEM micrographs
Two higher magnification low-vacuum SEM micrographs of the aged Estaillades surface shown in Figure 5.22.

EDX scans of Estaillades prior to ageing were performed to provide a comparison for EDX scans post-ageing. Two regions which were selected for EDX mapping are labelled on Figure 5.25 as A and B. A third area, C, is shown in Appendix B but is not discussed here as the results are similar. The EDX data from areas A and B are shown in Figures 5.26 and 5.27; area A is an example of Estaillades surface type 4 and area B is an example of Estaillades surface type 3, as defined in Chapter 3: *Carbonates*, Section 3.2.3.

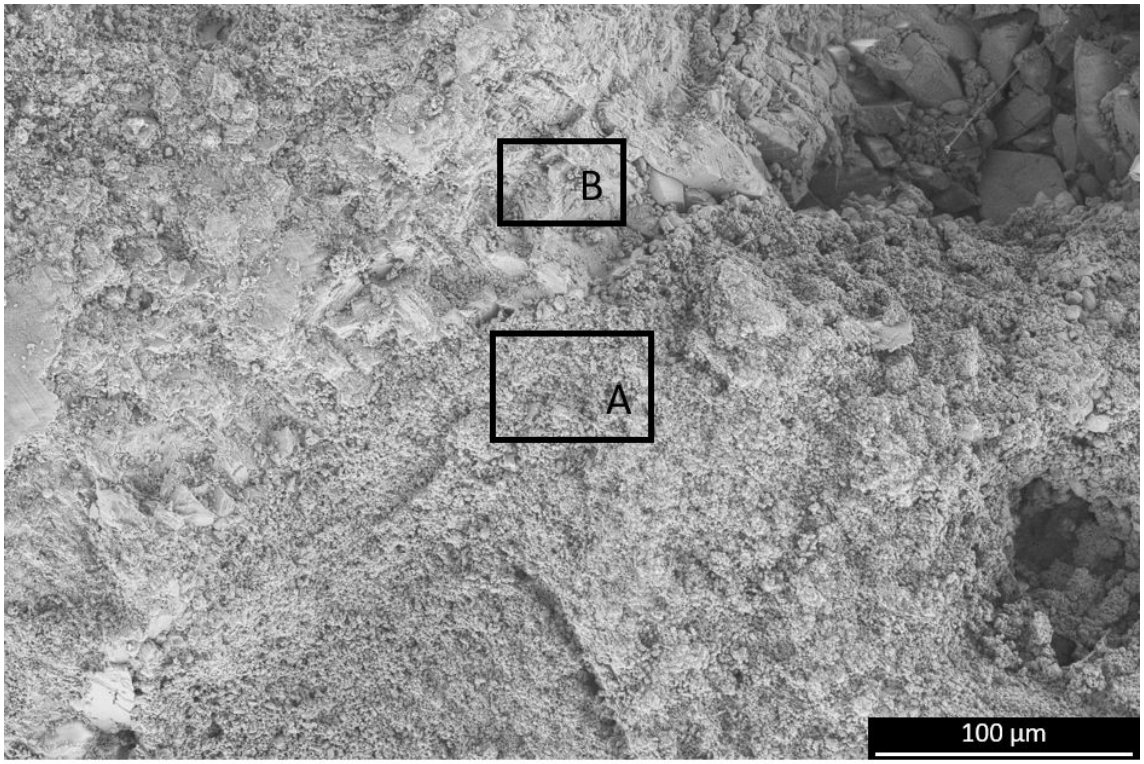
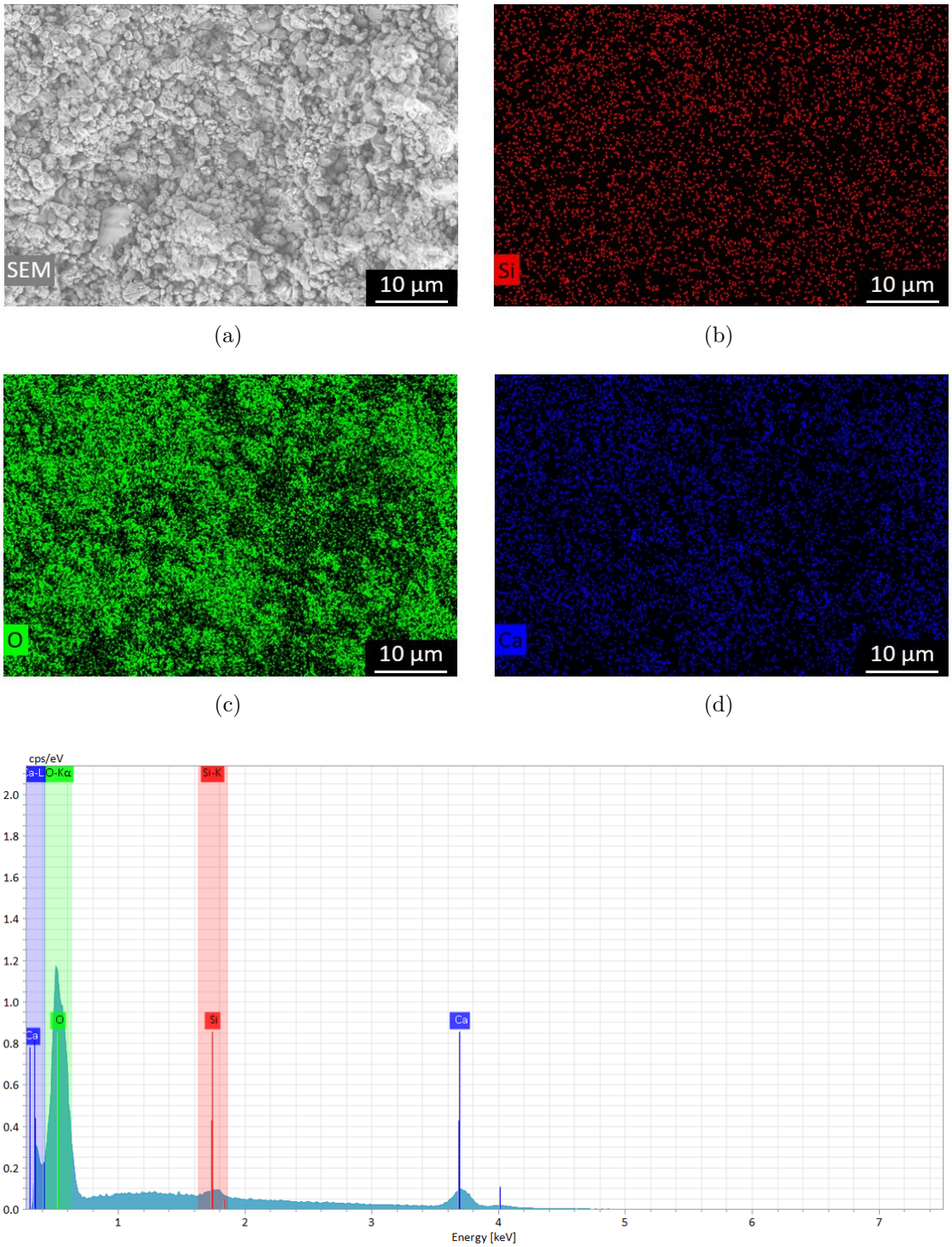



Figure 5.25: Estaillades: locations of EDX Areas A and B
A low-vacuum SEM micrograph of Estaillades, with the areas studied by EDX below in Figures 5.26 and 5.27 labelled A and B respectively.




(a) (b) (c) (d) (e)

Figure 5.26: Estaillades: EDX results for area A
EDX results for area A of the Estaillades surface imaged by SEM shown and labelled in Figure 5.25. (a) Shows the low-vacuum SEM micrograph of the area, (b), (c) and (d) show the Si, O and Ca distribution maps for the area respectively, and (e) shows the X-ray energy spectrum for the image, with element assignments labelled.

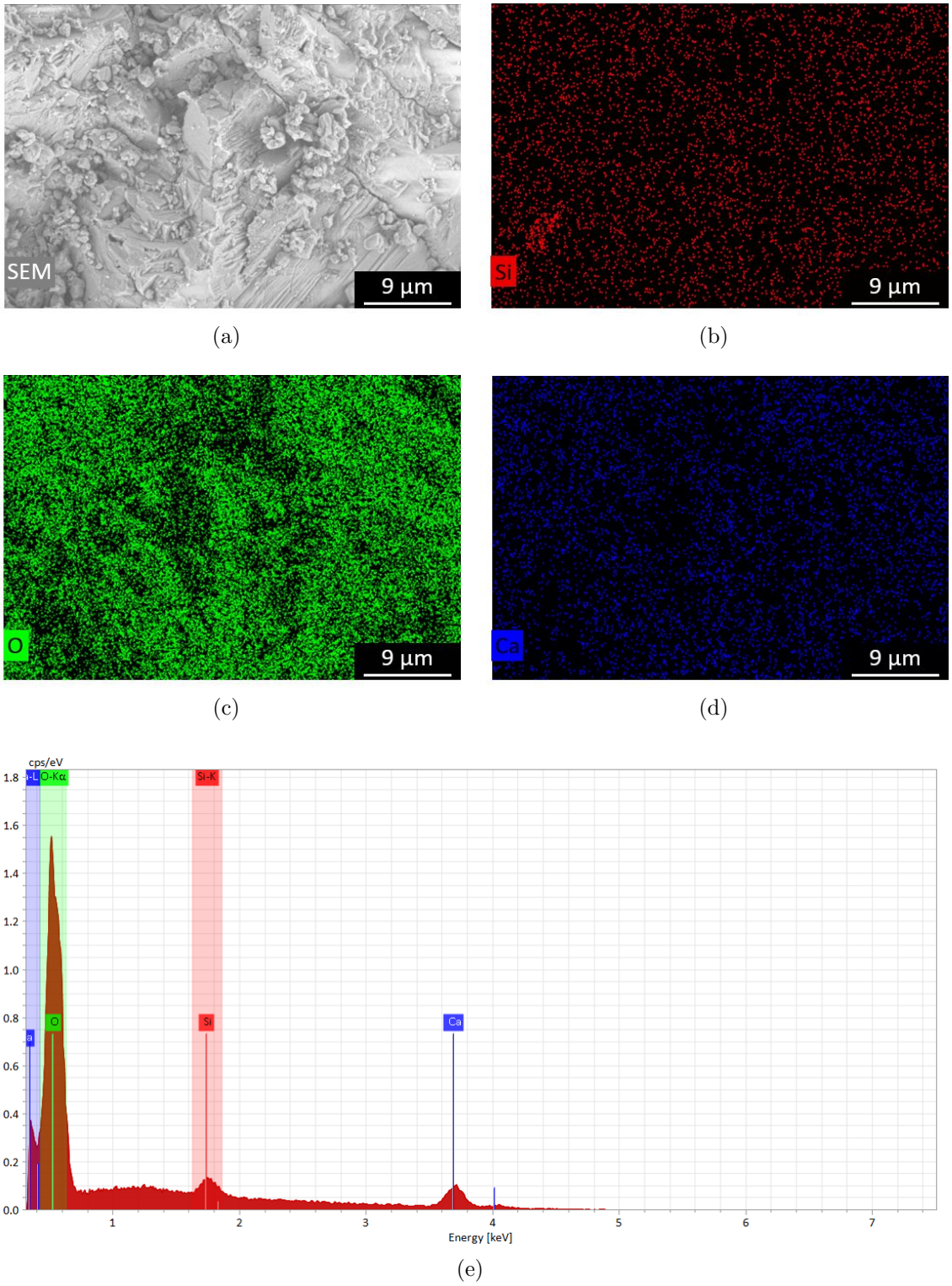
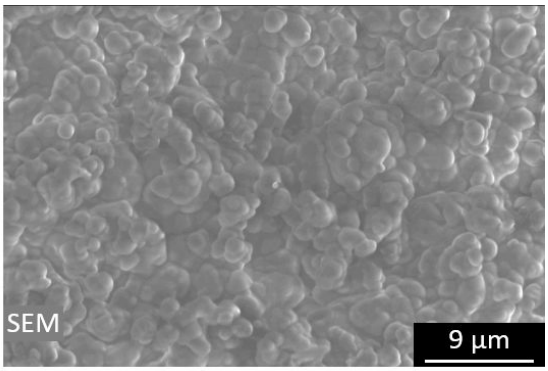


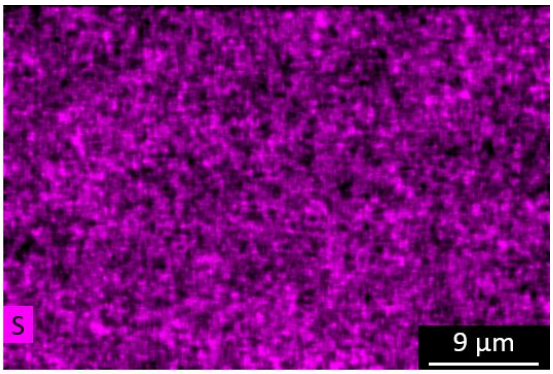

Figure 5.27: Estaillades: EDX results for area B
EDX results for area B of the Estaillades surface imaged by SEM shown and labelled in Figure 5.25. (a) Shows the low-vacuum SEM micrograph of the area, (b), (c) and (d) show the Si, O and Ca distribution maps for the area respectively, and (e) shows the X-ray energy spectrum for the image, with element assignments labelled.

As expected, the EDX scans for areas A and B of the Estaillades surface showed the presence of Ca, Si and O, as Estaillades is primarily (97.2 - 99.6 %) composed of calcite ($CaCO_3$) with a small (0.4 - 2.8 %) quartz ($SiO_2$) component, as summarised in Table 1.1 in Chapter 1: *Introduction.*[92,93,96] The distributions of these elements in Figures 5.26b - 5.26d and 5.27b - 5.27d are relatively even, with the exception of a small section towards the left of the Si map for area B in Figure 5.27b. This region of area B's Si map shows a localised higher concentration of Si, probably indicating a higher-than-average concentration of quartz at that location on the surface.

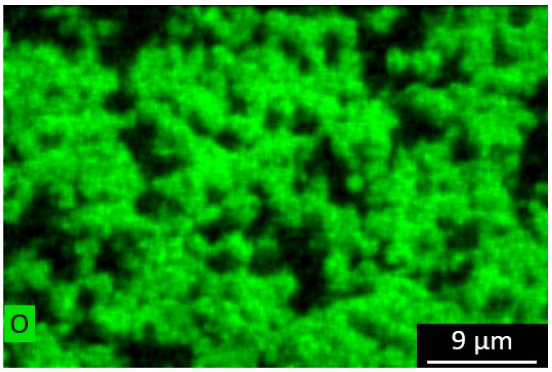
Two regions on the first aged Estaillades sample surface, shown at high magnification in Figures 5.23d and 5.23c (page 249), were mapped with EDX. The element distribution maps for these regions are shown in Figures 5.28 and 5.29 respectively alongside the relevant low-vacuum SEM micrographs. The associated X-ray energy spectra are shown in Figures 5.30 and 5.31 respectively. From these maps and associated spectra, it can be seen that there is no longer a Ca or Si signal present, which were both present in the unaltered Estaillades EDX data in Figures 5.26 and 5.27. The lack of Ca or Si peaks would indicate that the crude oil film has fully covered the Estaillades surface in a film possibly exceeding 2 $\mu$m thick, as 2 $\mu$m is the sensitivity limit for EDX,[83] as was previously observed on the aged calcite surface. The elements which are detected as being present, C, S, O and N, can all be explained by the presence of crude oil, and are all evenly distributed across the aged Estaillades surface.[151,153]



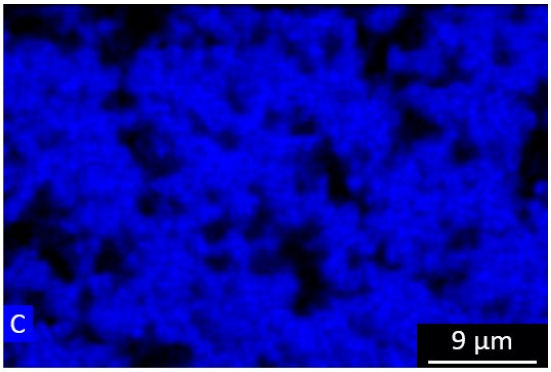

(a)



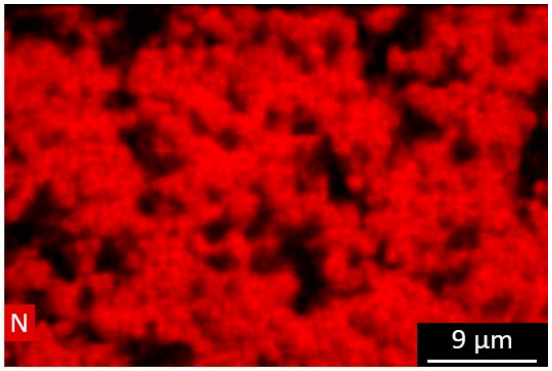

(b)




(c)

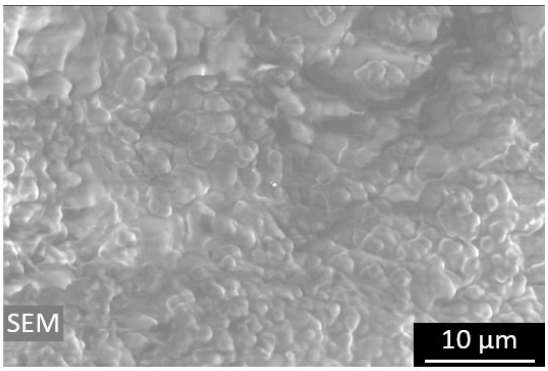



(d)

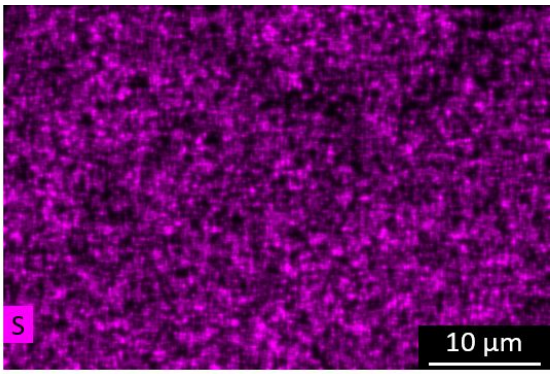



(e)

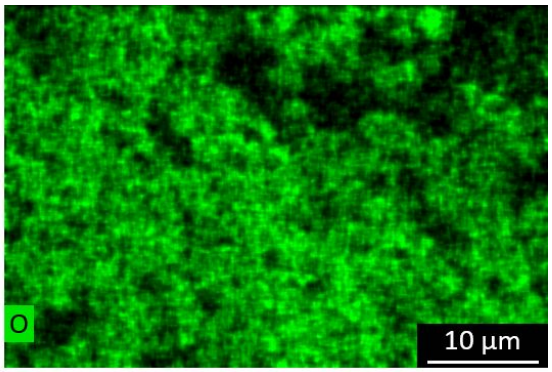
Figure 5.28: Aged Estaillades: EDX element maps for area 1
EDX results for area 1 of the aged Estaillades surface imaged by SEM shown and labelled in Figure 5.21. (a) Shows the low-vacuum SEM micrograph of the area, (b), (c), (d) and (e) show the S, O, C and N distribution maps for the area respectively. The X-ray energy spectrum for this micrograph, with element assignments labelled is shown in Figure 5.30.



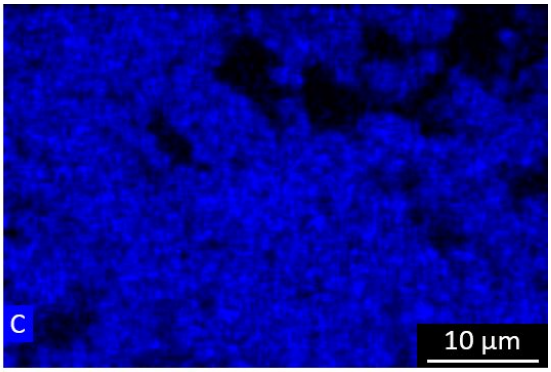

(a)



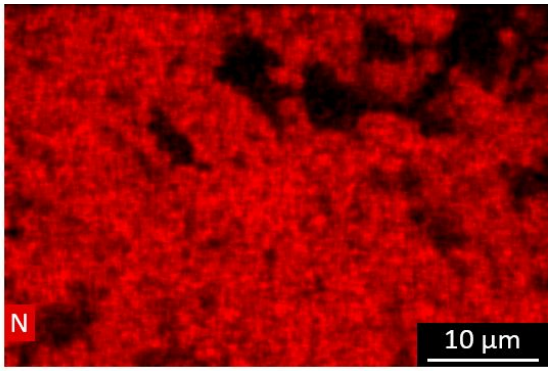

(b)




(c)




(d)




(e)

Figure 5.29: Aged Estaillades: EDX element maps for area 2
EDX results for area 2 of the aged Estaillades surface imaged by SEM shown and labelled in Figure 5.21. (a) Shows the low-vacuum SEM micrograph of the area, (b), (c), (d) and (e) show the S, O, C and N distribution maps for the area respectively. The X-ray energy spectrum for this micrograph, with element assignments labelled is shown in Figure 5.31.

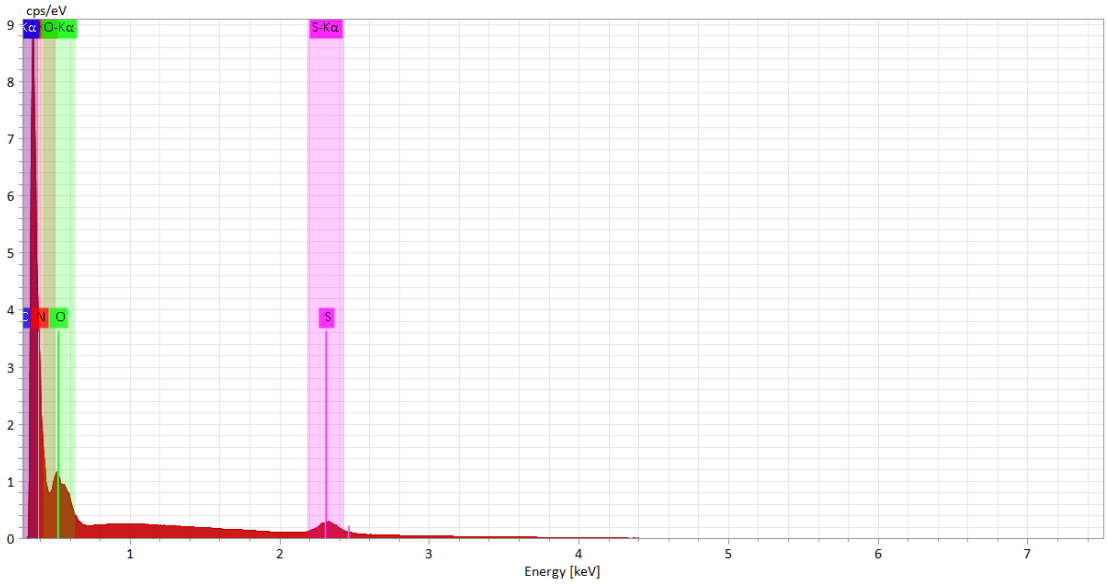



Figure 5.30: Aged Estaillades: EDX X-ray energy spectrum for area 1
The X-ray energy spectrum for the micrograph show in Figure 5.28, with element assignments labelled.

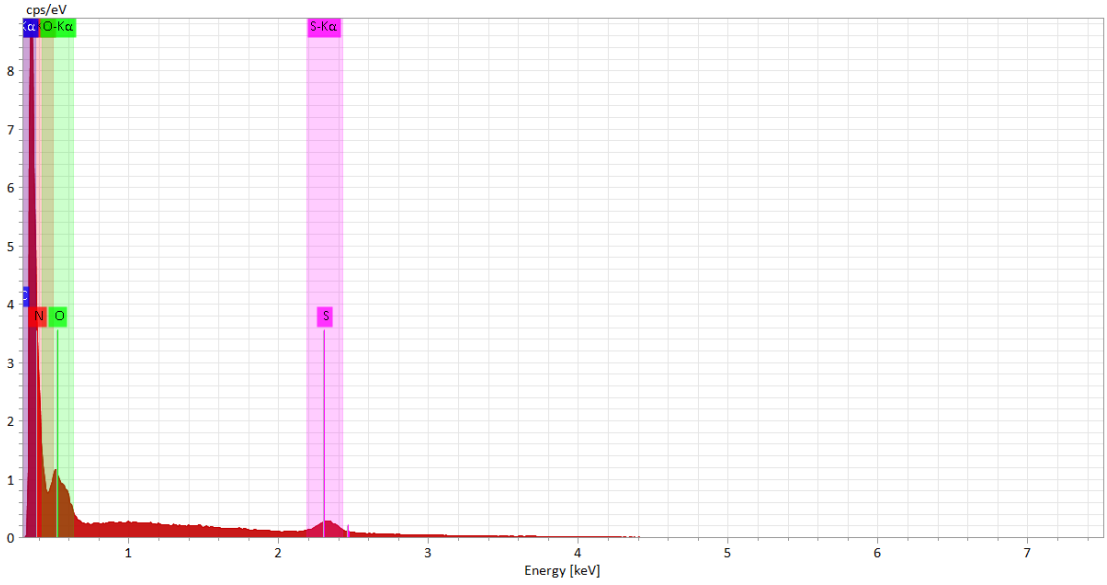



Figure 5.31: Aged Estaillades: EDX X-ray energy spectrum for area 2
The X-ray energy spectrum for the micrograph shown in Figure 5.29, with element assignments labelled.

#### 5.3.2.2 Post Ageing, post-SICM Measurements

Due to the changes to the crude oil film observed on the aged calcite sample after imaging under AFM and SICM, the aged Estaillades sample was also investigated with low-vacuum SEM after characterisation with SICM. An overlay of six low-vacuum SEM micrographs of the post-SICM aged Estaillades surface is presented in Figure 5.32, with a black box indicating where EDX measurements were performed. Higher magnification low-vacuum SEM micrographs from this region are shown across Figures 5.33 and 5.34.

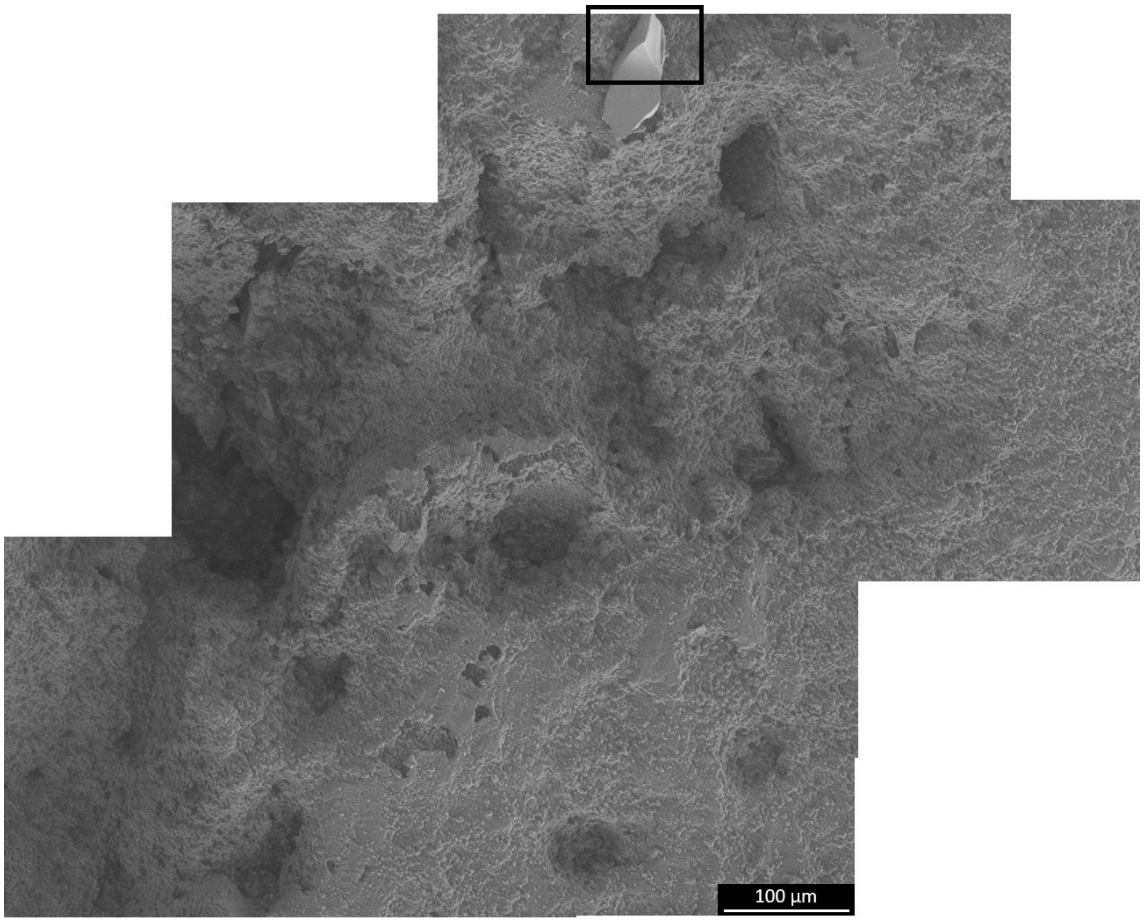
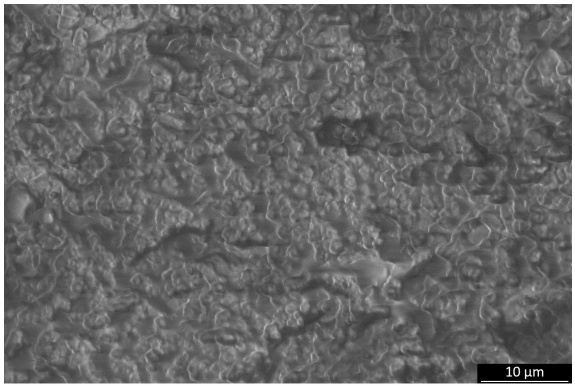
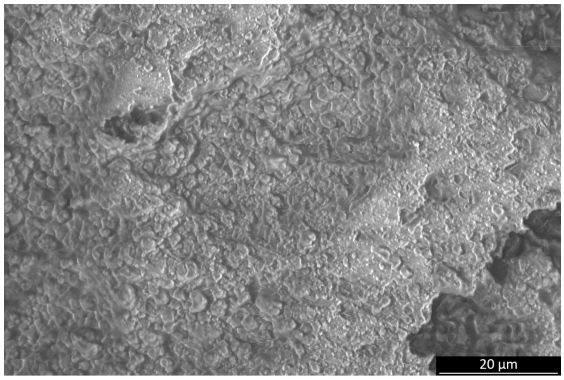


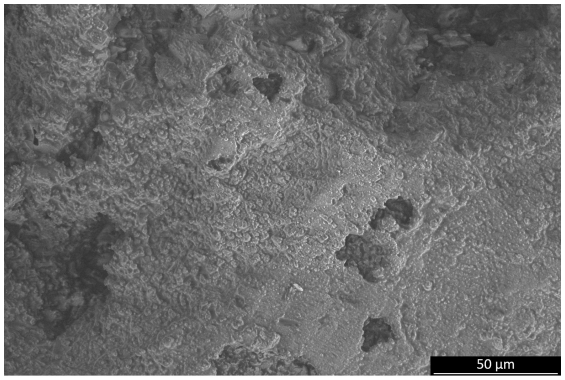

Figure 5.32: Aged Estaillades post-SICM: SEM Overlay
An overlay of six low-vacuum SEM micrographs of an aged Estaillades sample after SICM measurements had been performed. A black box depicts where EDX measurements were performed. The individual micrographs which make up this overlay can be found in Appendix B, Figures B.69 - B.74.




(a)




(b)




(c)

Figure 5.33: Aged Estaillades post-SICM: high magnification SEM micrographs
Three higher magnification low-vacuum SEM micrograph of the aged Estaillades surface after SICM measurements had been performed shown in Figure 5.32.

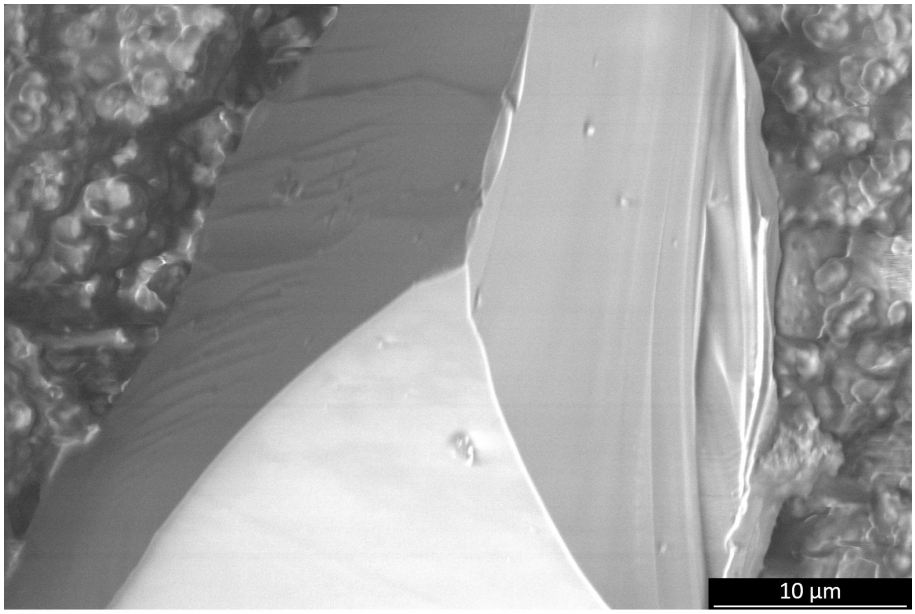



Figure 5.34: Aged Estaillades post-SICM: high magnification SEM micrograph
A higher magnification low-vacuum SEM micrograph of the aged Estaillades surface after SICM measurements had been performed shown in Figure 5.32.

The majority of the surface in Figure 5.32 appears to have remained unchanged by the AFM and SICM mapping. This could possibly be due to a stronger adhesion of the crude oil onto the Estaillades surface, preventing partial removal or segregation of the crude oil film. This enhanced adhesion would likely be a consequence of the rougher Estaillades surfaces compared to calcite, as chemically Estaillades and calcite are almost identical, with the literature reporting Estaillades as being composed of 97.2 - 99.6 % calcite.[92,93,96] Higher magnification images of the surface in Figure 5.33 show the same agglomerate patterns of smooth crude oil droplets which were observed in the freshly aged Estaillades sample in Figure 5.23 (page 249). The aged Estaillades surface does not appear to have changed as a result of the SICM measurements, unlike the aged calcite sample, where smooth oxygen-rich areas appeared on the surface. It is unclear whether this has not occurred due to the crude oil having a higher affinity for the Estaillades surface, or whether this is simply due to the aged Estaillades sample perhaps not spending the same amount of time submerged in $KCl_{(aq)}$ as the aged calcite sample.

Towards the top of the overlay in Figure 5.32 a smooth-sided raised structure can be observed, and is shown at higher magnification in Figure 5.34. In order to determine whether this structure was an exposed Estaillades surface feature, EDX was performed, the results from which are shown across Figures 5.35 and 5.36. From the element distribution maps in Figure 5.36, it appears that the elements present on the smooth structure are Si, N, Na and O, with a little S. The particularly high concentrations of Si and O compared to the surrounding areas could suggest that this is a large, exposed quartz section of Estaillades, as quartz is reported as making

up 0.4 - 2.8 % of Estaillades in the literature.[92,93,96] This could possibly indicate that the crude oil is less strongly adhered to quartz components on the surface. The N and S components can be attributed to the presence of crude oil, as was assigned previously in the freshly aged calcite and Estaillades samples' EDX results. The presence of Na however is peculiar, and could suggest that this structure is not quartz, and is instead a contaminant, such as a small piece of glass, as $Na_2O$ is a common component of borosilicate glass after $SiO_2$.[154] This contamination, if it is indeed a small fragment of glass, could be a chip off the glass vial in which it was stored. The samples were removed from the vials using tweezers, so it is possible that the tweezers may have chipped the mouth of the vessel during sample removal or replacement.

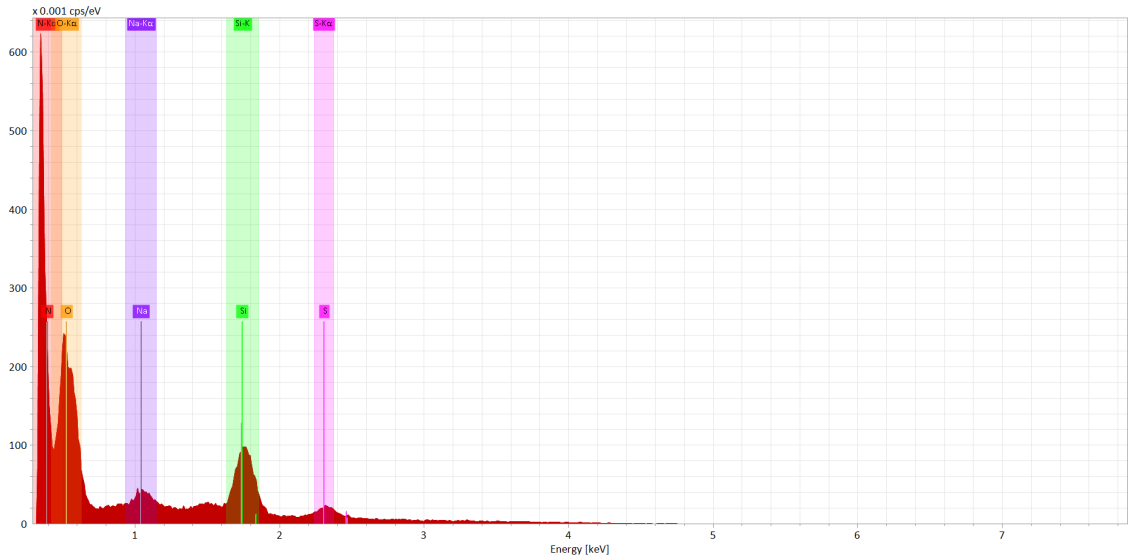



Figure 5.35: Aged Estaillades post-SICM: EDX X-ray energy spectrum
The X-ray energy spectrum for the micrograph of the post-SICM aged Estaillades surface shown in Figure 5.36.

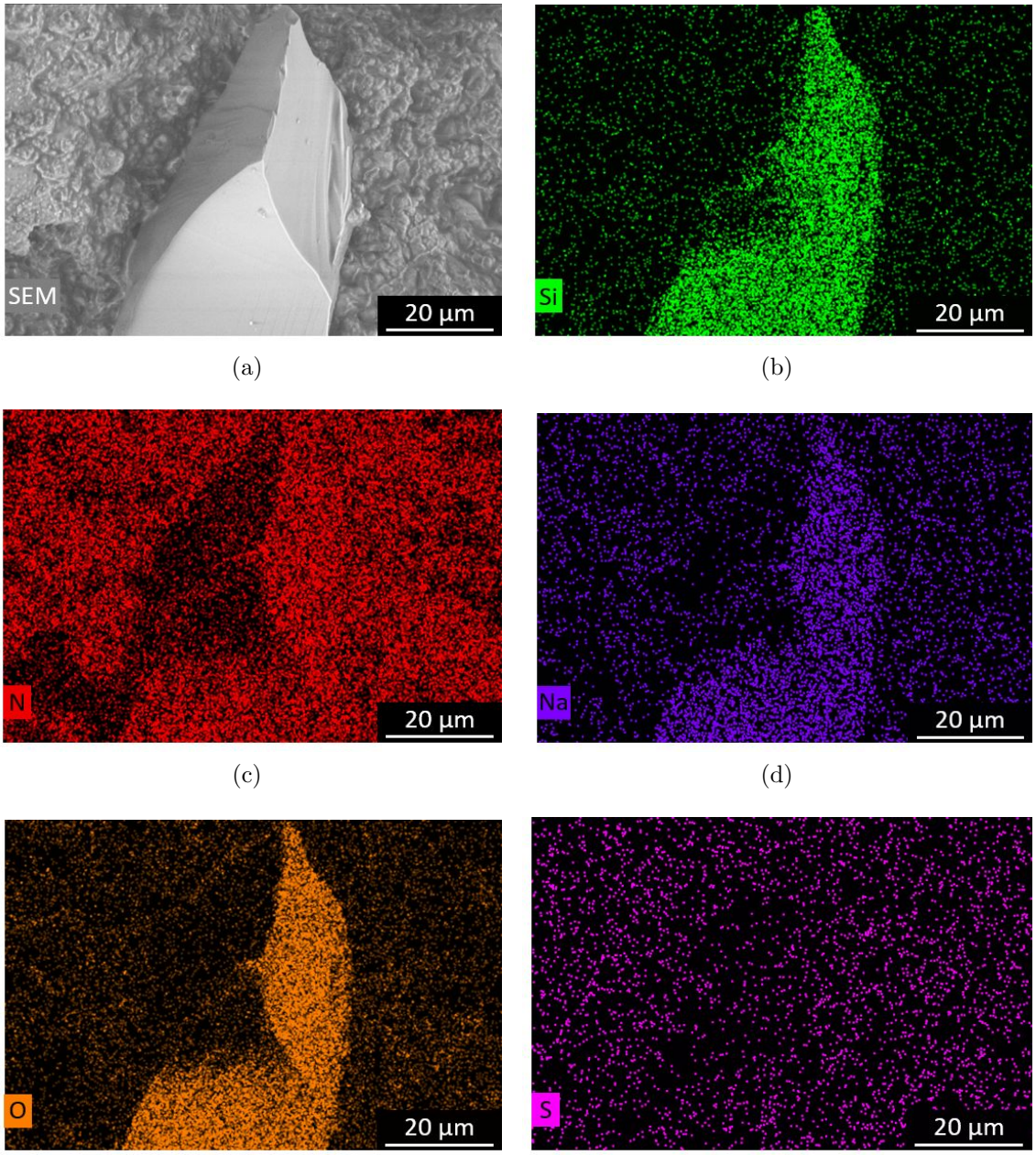



Figure 5.36: Aged Estaillades post-SICM: EDX element maps
EDX results for the area labelled on the post-SICM aged Estaillades surface shown in Figure 5.32. (a) Shows the low-vacuum SEM micrograph of the area, (b), (c), (d) and (e) show the S, O, C and N distribution maps for the area respectively. The X-ray energy spectrum for this micrograph, with element assignments labelled is shown in Figure 5.35.

## 5.4 Atomic Force Microscopy

The use of AFM for the mapping of calcite or mica surfaces with either real crude oils or, more often, model crude oils such as n-decane or asphaltenes have been reported in the literature.[22,110,111,113,155] Due to this precedence, AFM was selected to investigate the aged calcite and Estaillades samples prior to SICM imaging in order to provide comparison and validation.

### 5.4.1 Aged Calcite

Topographical maps of the aged calcite surface were obtained via AFM and are presented in Figures 5.37 - 5.40 below. The first set of images in Figure 5.37 are two 5 × 5 $\mu$m images which have overlapping fields of view. The spherical structure in the top right-hand corner of Figure 5.37a is present towards the right-hand side of Figure 5.37b; this feature is picked out with a green guide square on both images for clarity. These images appear to show a region of the aged calcite surface type 1 identified in Section 5.3.1.1, as smooth crude oil droplets on the order of 1 $\mu$m across forming larger agglomerates are present, with flatter surfaces in between.

A similar region is shown in Figure 5.38, which shows four 10 × 10 $\mu$m images with overlapping fields of view. The raised structure in the top left hand corner of Figure 5.38a is present in the bottom left hand corner of Figure 5.38b. The recessed feature which is present at the top of Figure 5.38b can be seen towards the bottom of Figure 5.38c. Finally the top right hand corner of Figure 5.38c overlaps with the bottom right hand corner of Figure 5.38d. For ease of visualisation, an overlay of the four images is presented in Figure 5.39. All four images are of a relatively flat

surface with crude oil droplets on the order of 1 $\mu$m across forming agglomerates. The recessed feature seen at the top of Figure 5.38b, and the bottom of Figure 5.38c, is possibly a gap in the crude oil film and may reveal the calcite underneath, but may also reflect a dent in the calcite itself, such as the one observed on the unaltered calcite surface type 4 shown in Figure 5.10a, page 229.

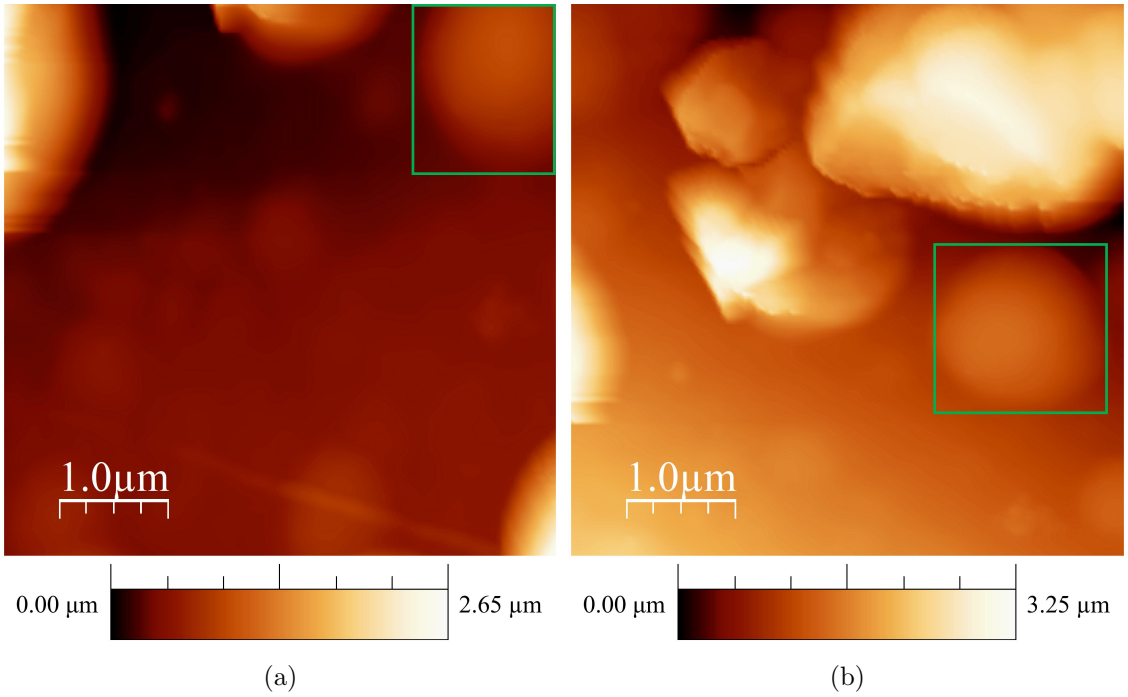



Figure 5.37: Aged Calcite: Two AFM images of surface type 1
Two 5 × 5 $\mu$m AFM images of surface type 1 of an aged calcite surface with pixel sizes of approximately 40 × 40 nm (128 × 128 points). The green guide square highlights a feature which is present across both images, for ease of comparison.

The AFM images presented in Figure 5.40 show a slightly different surface type to the AFM images presented in Figures 5.37 and 5.38. The two regions imaged here are most similar to aged calcite surface type 2, which represents the larger crude oil agglomerates made up of smaller, less rounded droplets. For ease of comparison, the low-vacuum SEM micrograph previously shown in Figure 5.7 on page 226 is re-shown in Figure 5.40c for comparison, with surface types 1 and 2 labelled.

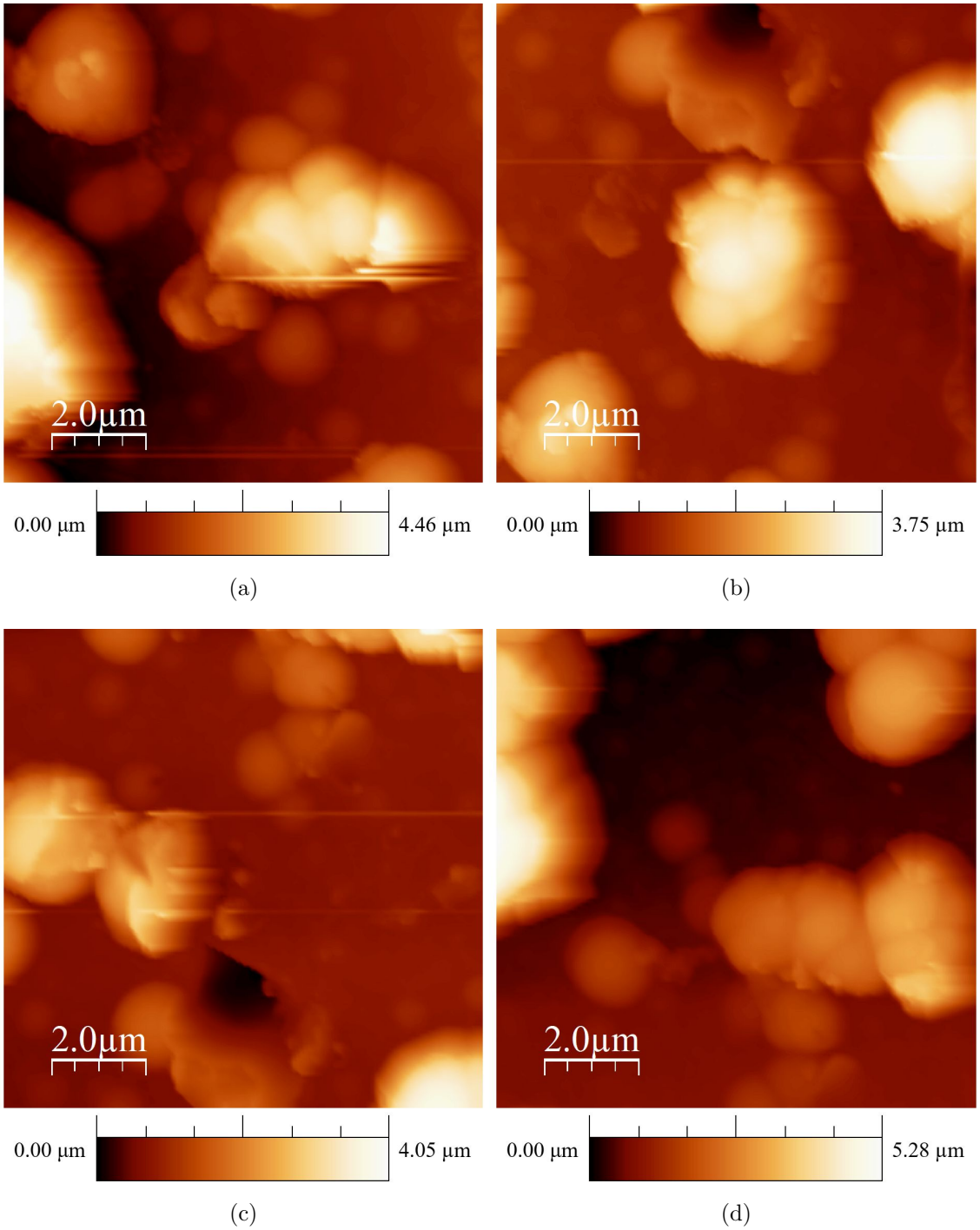



Figure 5.38: Aged Calcite: Four AFM images of surface type 1
Four 10 × 10 $\mu$m AFM images of surface type 1 of an aged calcite surface with pixel sizes of approximately 80 × 80 nm (128 × 128 points).

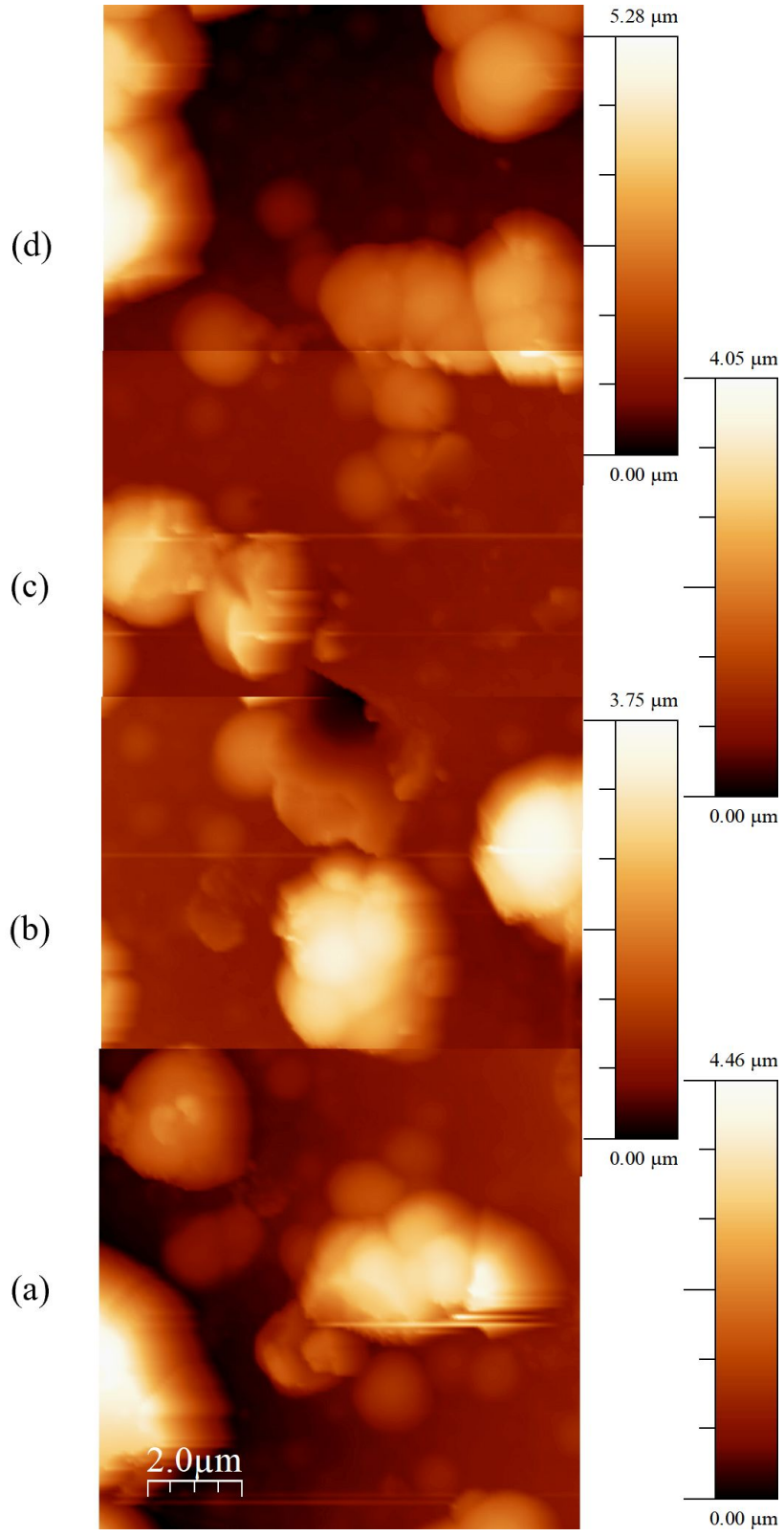
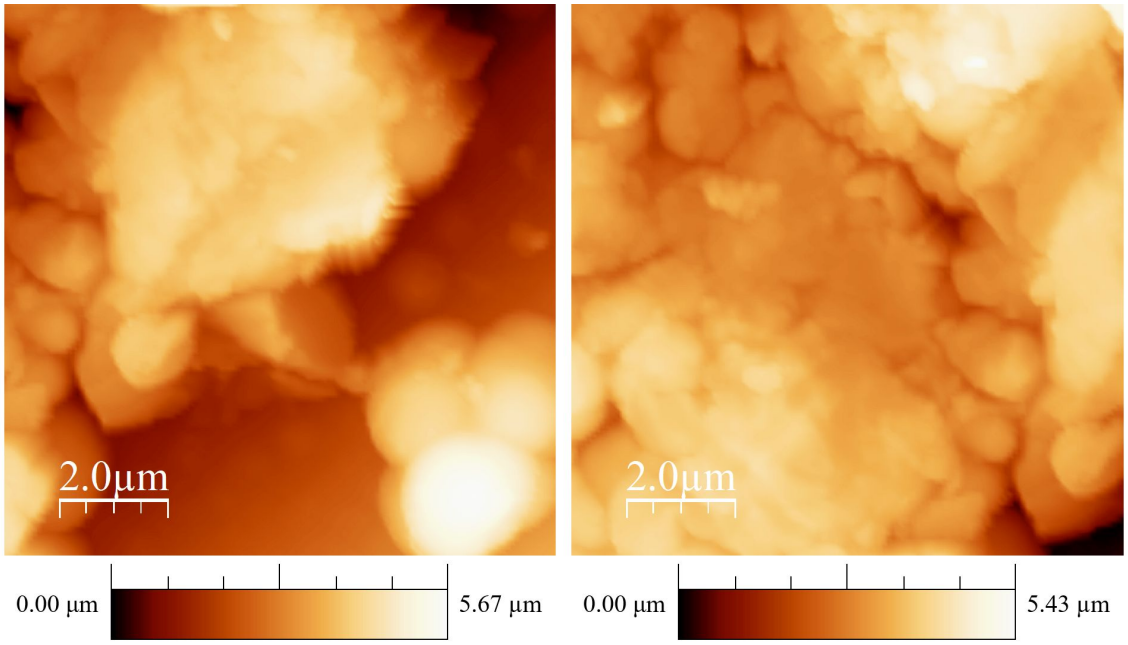
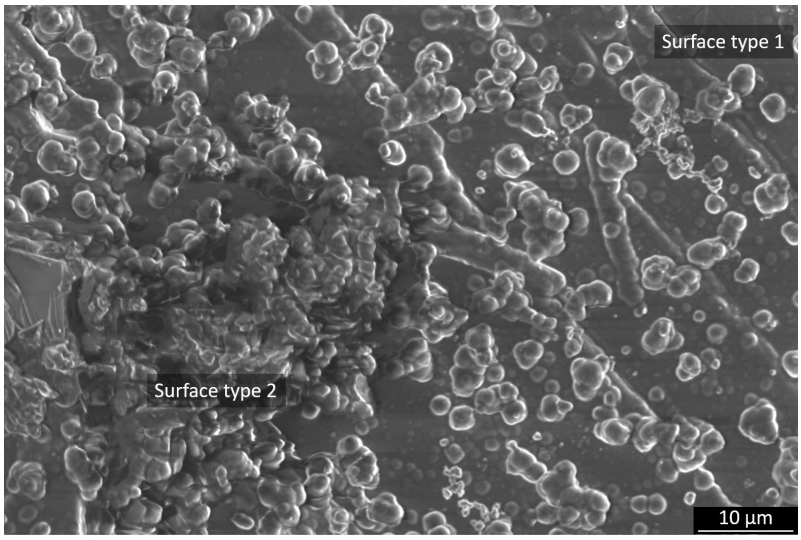



Figure 5.39: Aged Calcite: overlay of AFM images of surface type 1
The four AFM images from Figure 5.38 overlain to aid in the visualisation of how they are connected. Labels (a) - (d) denote which of the images from Figure 5.38 each image corresponds to.




(a) (b)




(c)

Figure 5.40: Aged Calcite: Two AFM images of surface type 2
(a) and (b) show two 10 × 10 $\mu$m AFM images of surface type 2 of an aged calcite surface with pixel sizes of approximately 80 × 80 nm (128 × 128 points). (c) Shows the low-vacuum SEM micrograph of aged calcite surface types 1 and 2 previously shown in Figure 5.7 on page 226 for comparison.

### 5.4.2 Aged Estaillades

Topographical images of aged Estaillades were collected on the AFM and are shown in Figures 5.41 and 5.43. Figure 5.41 shows two 2 $\times$ 2 $\mu$m images which appear to show intersections between oil droplets within the large agglomerate film which was previously observed in Section 5.3.2.1. For ease of comparison, the high magnification low-vacuum SEM micrograph of the aged Estaillades surface previously shown in Figure 5.23a on page 249 is re-shown in Figure 5.42. Due to the size of the field of view of these AFM images being on the same order of magnitude as the sizes of crude oil droplets present on the aged Estaillades surface, the droplet sizes present in these regions can not be estimated.

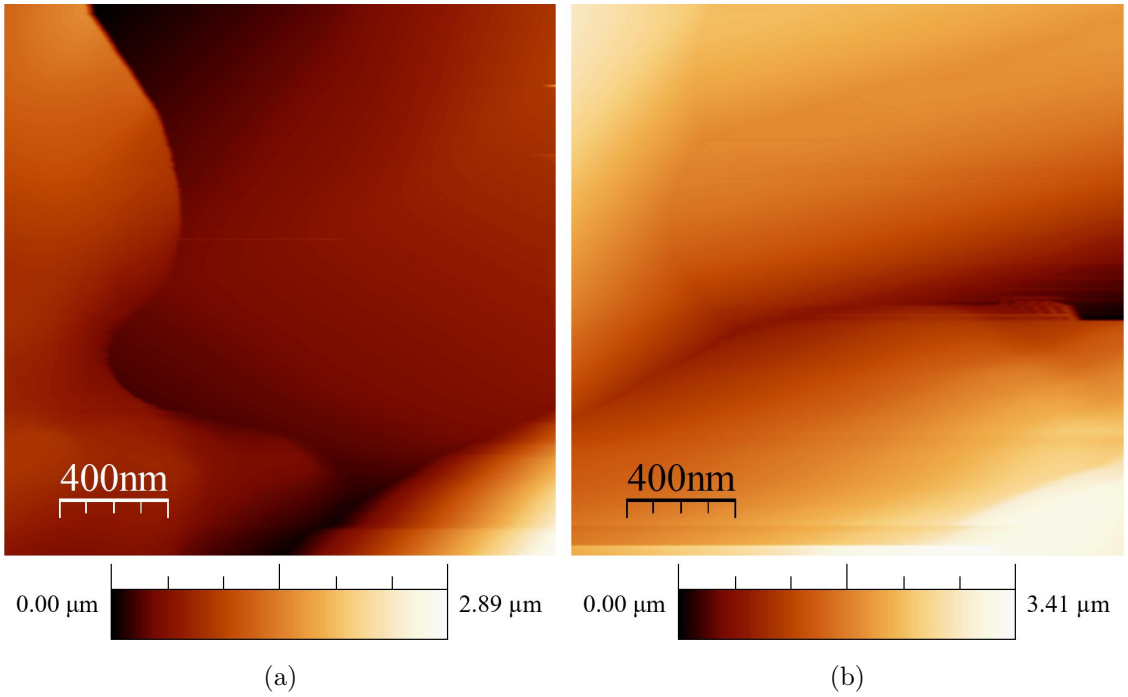



Figure 5.41: Aged Estaillades: Two AFM images
Two 2 × 2 $\mu$m AFM images of an aged Estaillades surface with pixel sizes of approximately 8 × 8 nm (256 × 256 points).

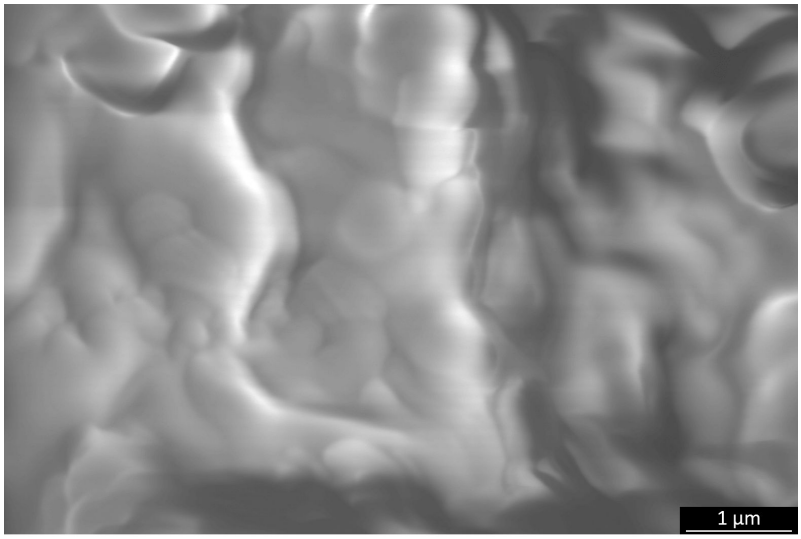



Figure 5.42: Aged Estaillades: low-vacuum SEM micrograph for comparison
The SEM micrograph previously shown in Figure 5.23a on page 249 for comparison with the AFM images presented in Figures 5.41 and 5.43.

Figure 5.43 shows one 5 × 5 $\mu$m and two 10 × 10 $\mu$m images of the aged Estaillades surface, which allow for a greater number of the oil droplets to be seen within each image than the 2 × 2 $\mu$m images presented in Figure 5.41. These are most clear in the 5 × 5 $\mu$m image in Figure 5.43a, where numerous agglomerates of oil droplets approximately 1 $\mu$m across are visible. The larger 10 × 10 $\mu$m AFM images shown in Figures 5.43b and 5.43c provide the ability to visualise a greater number of oil droplets simultaneously. However, due to the greater, more frequent variations in height, and insufficient time being dedicated to the collection of these images, the scan parameters have not been set up for optimal clarity. As such, there is a "ringing" noise effect around the more elevated features, due to the height changes between hops being larger than the selected tapping amplitude, resulting in the cantilever being unable to respond appropriately to the topographical changes, and are therefore less clear than the smaller field of view images presented in Figures 5.41 and 5.43a. These greater and more frequent variations in height are reflected in the scale bars, showing ranges of 0 - 5.16 and 7.95 $\mu$m for Figures 5.43b and 5.43c respectively. The scale bar ranges for the two 2 × 2 $\mu$m images in Figure 5.41 and the 5 × 5 $\mu$m image in Figure 5.43a are 0 - 2.89, 3.41 and 1.52 $\mu$m respectively in comparison. Beneath this noise however, the same agglomerate structures can be seen, with similar oil droplet sizes as were observed in the low-vacuum SEM micrographs and the 5 × 5 $\mu$m image in Figure 5.43a.

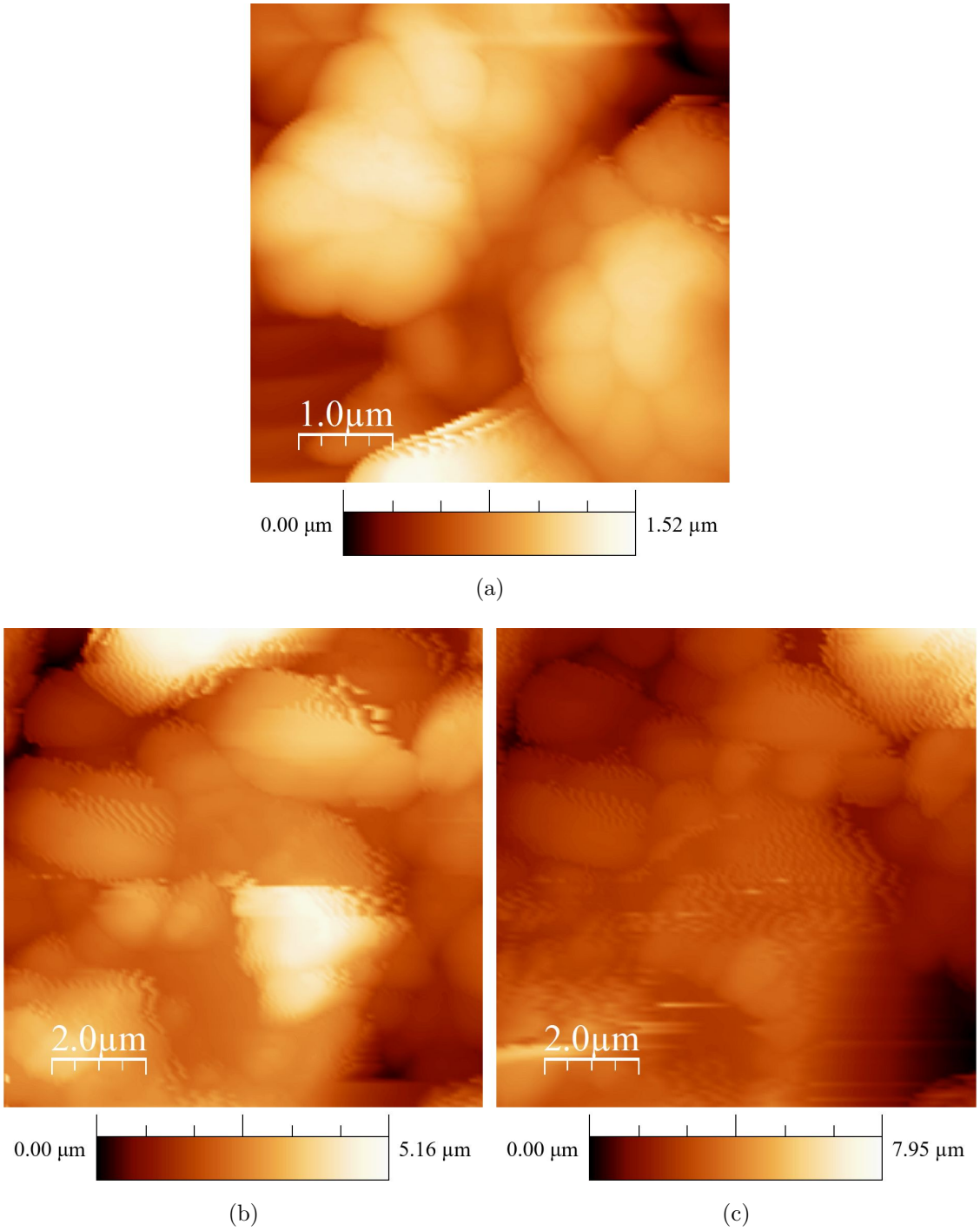



Figure 5.43: Aged Estaillades: Three AFM images
Three AFM image of an aged Estaillades surface, (a) being a 5 × 5 $\mu$m image with a pixel size of approximately 40 × 40 nm (128 × 128 points), and (b) and (c) being 10 × 10 $\mu$m images with pixel sizes of approximately 80 × 80 nm (128 × 128 points).

## 5.5 Scanning Ion Conductance Microscopy

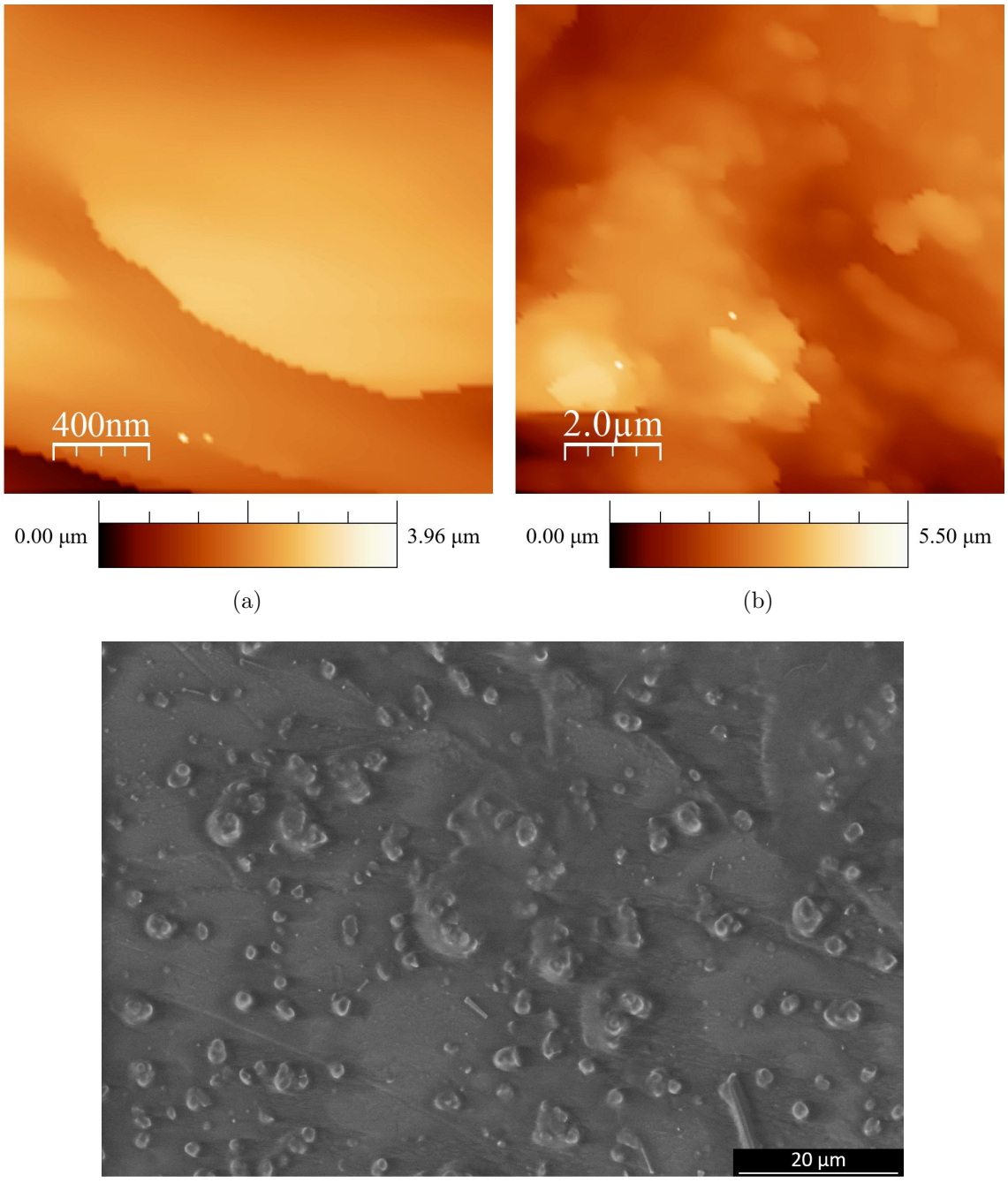
SICM was used to collect images of the aged calcite and Estaillades surfaces. Although the feature sizes present in these images align with those observed in the low-vacuum SEM and AFM images, there is unfortunately a "blurred" quality to them. This blurring effect is proposed to be the result of partial removal of the crude oil film by the electrolyte during mapping. It was also observed during these experiments that the nanopipette became blocked, deemed to be blocked when 0 nA current was recorded, more frequently than in the SICM experiments where unaltered samples were imaged. It is proposed that this is, in part at least, due to crude oil particles blocking the nanopipette opening. Limitations aside, the features which were mapped do still align with the feature sizes and shapes observed in the low-vacuum SEM and AFM work presented previously in this chapter, and so are still deemed to be in part successful.

### 5.5.1 Aged Calcite

Four SICM images of the aged calcite surface are presented below across Figures 5.44 and 5.45. All four areas imaged show the characteristic oil droplets/agglomerates seen previously in the low-vacuum SEM and AFM images of the aged calcite surface, and are proposed to belong to two of the four defined surface types.

The 2 × 2 $\mu$m SICM image in Figure 5.44a shows a large crude oil droplet, exceeding 1 $\mu$m across, which can not be measured properly due to it not being fully captured within the small field of view. The larger size and rounded shape would indicate that this image is most likely to be from a region of aged calcite surface type 1. However, due to the narrow field of view of this image, the surface type can not be assigned with any certainty, as insufficient information about the surrounding area is presented.

The 10 × 10 $\mu$m SICM image in Figure 5.44b appears to be of a reasonably rough region, with sizeable differences between the lowest and highest points; the scale bar range being 0 - 5.50 $\mu$m. The entirety of the area which is in view appears to be completely covered with crude oil droplets approximately 1 $\mu$m across forming one large agglomerate, with no flat areas visible. The lack of flat surface would suggest that the region belongs to calcite surface type 2. The droplets which are in view are not as rounded as were observed in the low-vacuum SEM micrographs of aged calcite surface type 2, and instead more closely resemble those present on aged calcite surface type 4. A low-vacuum SEM micrograph of aged calcite surface type 2 was shown on page 266 (Figure 5.40c), and a low-vacuum SEM micrograph of aged calcite surface type 4, originally shown in Figure 5.9b, page 228, is re-shown




(a) (b)

(c)

Figure 5.44: Aged Calcite: SICM images of surface types 1 and 2
Two SICM images of aged calcite and one low-vacuum SEM image for comparison. (a) Shows a 2 × 2 $\mu$m SICM topographical image with a pixel size of 25 × 25 nm of what appears to be surface type 1, (b) shows a 10 × 10 $\mu$m SICM topographical image with a pixel size of 100 × 100 nm of surface type 2, and (c) shows the low-vacuum SEM micrograph previously shown in Figure 5.9b on page 228 of aged calcite surface type 4.

for comparison in Figure 5.44c. Despite this combination of characteristic features from surface types 2 and 4, this region is assigned as being part of surface type 2 for two reasons; this SICM image is of aged calcite 1, upon which no examples of surface type 4 were observed in the low-vacuum SEM, and the low-vacuum SEM images of aged calcite 2, where surface type 4 was located, did not present any examples of large agglomerations of these raised structures.

Figure 5.45 shows two SICM images in Figures 5.45a and 5.45c which both have a number of bright pixels; pixels where, presumably in error, a much higher height was recorded than for the rest of the surface. To best see what are deemed to be the real surfaces, an equalization function has been applied to both Figures 5.45a and 5.45c, the results from which are shown in Figures 5.45b and 5.45d respectively. Equalization functions shorten the scale bar to encompass the range with the greatest number of points, ignoring the outliers. In the case of the SICM image in Figure 5.45c for example, a histogram of pixel height vs count is shown in Figure 5.46. The new scale bar range used in the equalized image in Figure 5.45d is highlighted by the green shaded area in Figure 5.46, representing 96.5 % of the pixels. The two outlying pixels, at 2.84 and 3.16 $\mu$m, are also highlighted on the histogram.

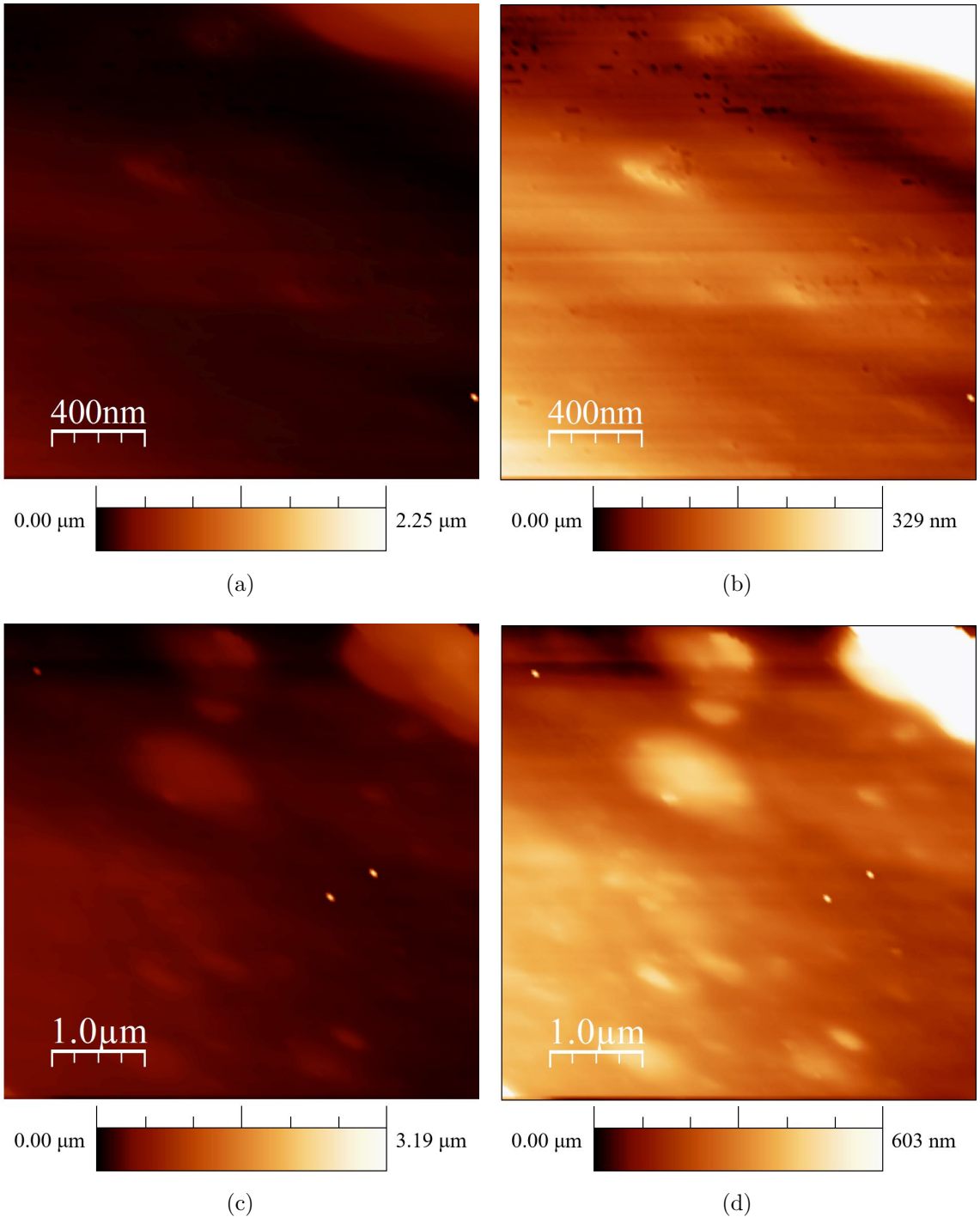



Figure 5.45: Aged Calcite: Two SICM images of surface type 1
(a) and (b) show a 2 × 2 $\mu$m SICM topographical image with a pixel size of 25 × 25 nm of the Aged Calcite 1 sample, and show the same image (a) before and (b) after an equalizing function was applied respectively. (c) and (d) show a 5 × 5 $\mu$m SICM topographical image with a pixel size of 50 × 50 nm of the Aged Calcite 1 sample, and show the same image (c) before and (d) after an equalizing function was applied respectively.

Figures 5.45b and 5.45d show flatter regions than those shown in Figure 5.44, with scale bar ranges of 329 and 603 nm respectively. Raised droplets appear to be present in these regions, with flatter areas between droplets. These flatter surfaces in Figure 5.45 are therefore proposed to be images of aged calcite surface type 1.

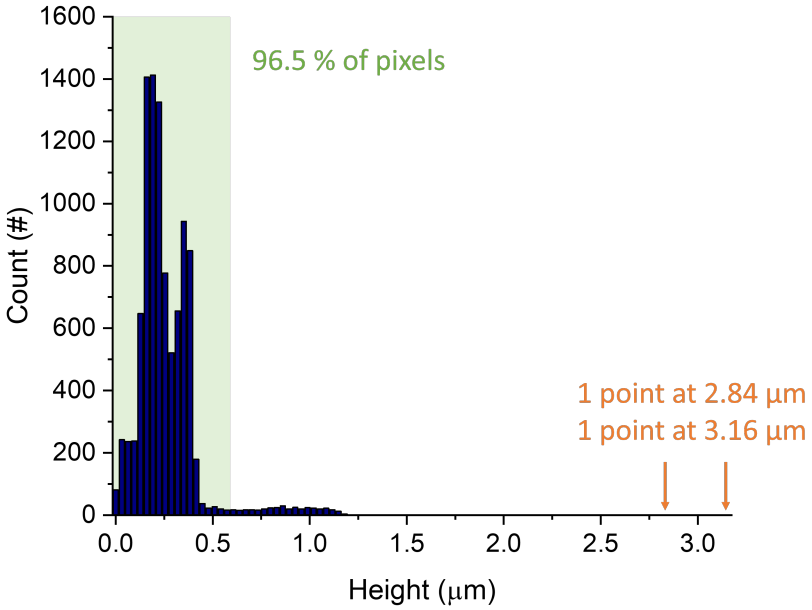



Figure 5.46: Aged Calcite: Histogram of pixel heights for SICM image in Figure 5.45c A histogram of the pixel heights vs count for the SICM image in Figure 5.45c. The shaded green area, which represents 96.5 % of the pixels, highlights the range which is selected in the equalized SICM image in Figure 5.45d. Only 2 pixels have values exceeding 1.18 $\mu$m, which are highlighted with orange arrows at 2.84 and 3.16 $\mu$m.

### 5.5.2 Aged Estaillades

Only the second aged Estaillades sample which was imaged under low-vacuum SEM was investigated with SICM, as laboratories closed for the COVID-19 lockdown in March 2020 prior to the first sample being fully characterised. When laboratories re-opened, the first sample was deemed too old to use for comparative work with AFM and SICM imaging, and so a second Estaillades sample was aged for full characterisation to be performed. Two topographical images of the second aged Estaillades surface were obtained using SICM, shown below in Figures 5.47 and 5.48. The features in these images are not as clearly defined as the unaltered Estaillades surfaces imaged in Chapter 3: *Carbonates*, which is proposed to be the result of partial removal of the crude oil film by the electrolyte close to the sample surface.

Unlike the aged calcite surface, for which four surface types were defined, the aged Estaillades sample did not appear to have any significant variation which could be differentiated into "types". The crude oil coverage on the Estaillades surface when imaged by low-vacuum SEM in Section 5.3.2.1 was instead reasonably uniform, with crude oil droplets on the order of 1 $\mu$m across visible across the surface in a continuous agglomerate film. The raised features visible on the regions shown in the SICM images in Figures 5.47 and 5.48 are also around 1 $\mu$m across, although due to the blurring effect it is difficult to accurately measure the features or determine their shape. The approximate feature sizes being on the order of 1 $\mu$m would however suggest that although difficulties were encountered during the imaging of these surfaces, these are indeed showing the "real" surface.

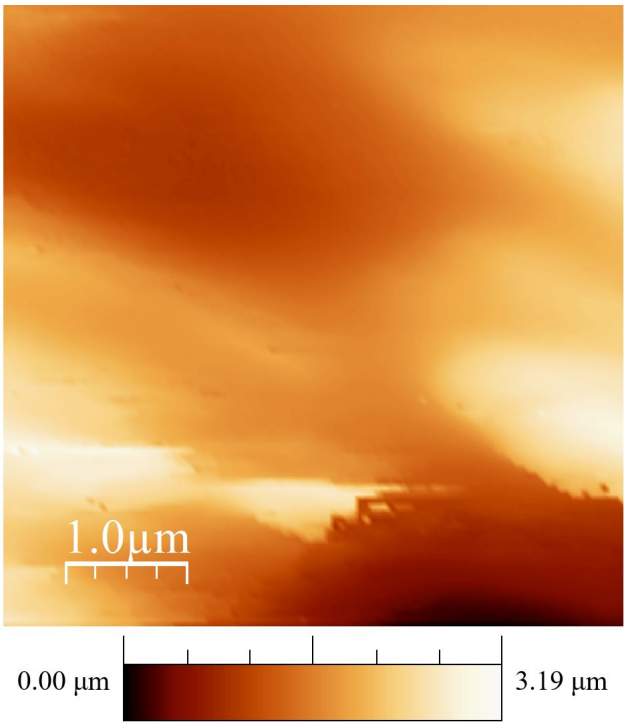



Figure 5.47: Aged Estaillades: 5 × 5 $\mu$m SICM image
A 5 × 5 $\mu$m SICM topographical image with a pixel size of 50 × 50 nm of the second aged Estaillades sample.

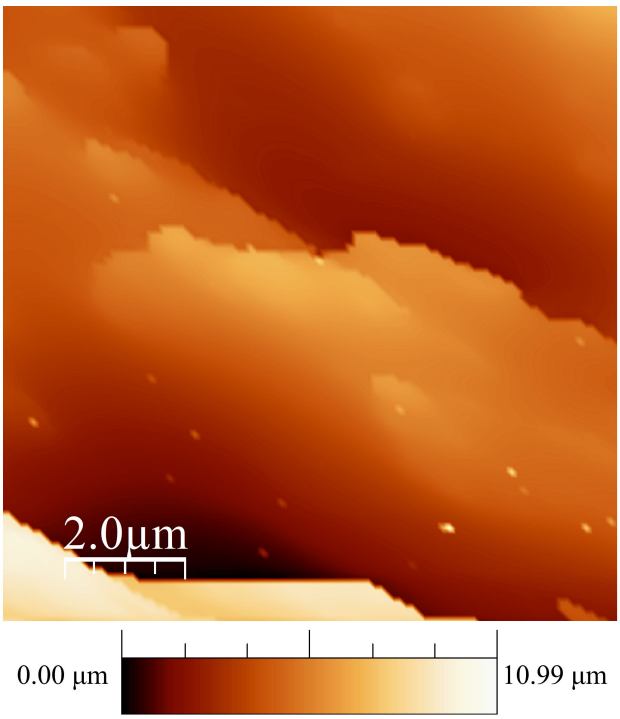



Figure 5.48: Aged Estaillades: 10 × 10 $\mu$m SICM image
A 10 × 10 $\mu$m SICM topographical image with a pixel size of 100 × 100 nm of the second aged Estaillades sample.

## 5.6 Summary and conclusions

In this Chapter it has been shown that SICM can be used to map aged carbonate rocks, which had not been previously shown in the literature. The low-vacuum SEM work has also provided an addition to what had already been published in the literature on these materials, imaging un-polished samples at high magnification and showcasing the multiple topographical surface types which can be present as a result of ageing. As was the case in the two previous chapters, the low-vacuum SEM micrograph overlays were once again used to catalogue different surface type regions, providing a context with which to understand the smaller field of view topographical images captured using AFM and SICM.

Analysis of the aged samples with EDX showed that the calcite and Estaillades surfaces had been fully covered by the crude oil film, the lack of Ca and/or Si peaks, which had been present in the spectra of the unaltered samples, demonstrating that the crude oil film was at least 2 $\mu$m thick. The low-vacuum SEM micrographs themselves showed evidence of strong adhesion between the crude oil and the Estaillades in particular, as the topology beneath was reflected in the film, and not obscured by it.

Further analysis with low-vacuum SEM after SICM measurements were performed revealed alterations to the crude oil film. This is not wholly unexpected, as brines and salt solutions similar to those used in the SICM are commonly used in EOR techniques to aid in the removal of oil from reservoir rocks. The relative stability of the crude oil film under the three different imaging techniques is also potentially indicative of the strength of the adhesion of the crude oil film to the

calcite and Estaillades surfaces. From visual inspection, exposure to low vacuum during SEM imaging did not appear to damage the sample; nor did the interaction with the AFM tip, although any effect would not have necessarily been observed with the naked eye given the fields of view imaged on the surfaces. The low-vacuum SEM micrographs post-SICM imaging however clearly demonstrated the surface alteration which had occurred during SICM imaging on the aged calcite surface, which was not observed on the aged Estaillades surface, indicating a stronger interaction of the crude oil film with the Estaillades surface than on the pure calcite crystal.

During the SICM scans themselves, the images collected of the aged calcite and Estaillades samples had a "blurred" quality to them, which was not the case for the SICM images of the unaltered samples presented in Chapter 3: *Carbonates*. Despite the challenges, the SICM demonstrated an, albeit limited, ability to map crude oil films on carbonate outcrop rocks. The demonstration of SICM's ability to generate topographical maps of these materials also opens up avenues for possible future work into generating surface charge maps on these aged materials.

Overall in this chapter, SICM's promise for use in the analysis of aged carbonate samples has been demonstrated, but some methodological changes may improve image quality in future work. The low-vacuum SEM micrographs and AFM topographical maps helped to verify the feature sizes measured on the SICM maps, and provided the context within which to place these smaller field of view images.

# Chapter 6

# Bandera Brown

## 6.1 Overview

As touched upon in Chapter 1: *Introduction*, Bandera Brown is a commonly used sandstone outcrop rock in oil recovery research, with a complex mineralogical composition.[89,98] One of the interests for digital rock modelling and reservoir behaviour prediction in sandstones such as Bandera Brown lies in the Fe-bearing minerals, some of which are thought to be redox active, existing in either the Fe 2+ or Fe 3+ oxidation state depending on the environment. Reports in the literature have given evidence of wettability alteration in core flood experiments with the addition of a reducing agent, which is thought to reduce this iron from the Fe 3+ to Fe 2+ oxidation state.[88,89] Bandera Brown is also rich in clays, which as discussed in Chapter 4: *Surface Charge Mapping* can exhibit wettability changes with variations in brine pH, composition and concentration which are all thought to be the result of surface charge alterations or DDL shielding.[120,121,127,128] Thorough characterisation of

Bandera Brown is therefore of interest, in particular for laying the groundwork for surface charge mapping of its surfaces using SICM.

This chapter also examines images of Bandera Brown samples which underwent the artificial ageing procedure which some of the carbonate outcrop rocks in Chapter 5: *Carbonate Ageing Studies* were subjected to. As was the case for the carbonate outcrop rocks, Bandera Brown samples which have been exposed to crude oil at high temperatures and pressures are referred to as "aged", and Bandera Brown samples which have not been exposed to crude oil are referred to as "unaltered".

Similarly to previous chapters, low-vacuum SEM was used to catalogue the different areas present on the Bandera Brown surface prior to SICM imaging, to allow for the smaller topographical images to be placed into a wider context. Due to the chemical heterogeneity of Bandera Brown, EDX was also employed as a tool alongside the SEM micrographs to help identify the minerals present on the surface. AFM was not employed in these studies, as it was established in Chapter 3: *Carbonates* that SICM is a suitable tool for mapping similar rock surfaces. Additionally, the Bandera Brown surfaces were found to present greater sudden height changes during mapping the SICM, and so were deemed to be even less suited to AFM mapping than the carbonate materials.

## 6.2 Unaltered Bandera Brown Studies

### 6.2.1 Low Vacuum Scanning Electron Microscopy

Although low-vacuum SEM microscopy is used to catalogue the variety of regions present across the Bandera Brown surface, as was performed for the carbonate materials, the way in which this is performed is changed for Bandera Brown. Due to the chemical heterogeneity of Bandera Brown, for example Yesufu-Rufai *et al.* identifying 15 different minerals,[89] the surfaces imaged here do not lend themselves to the "surface type" categorisation method previously employed for the carbonate surfaces, which were predominantly one mineral, calcite. Instead, attempts were made to identify the compounds present on these surfaces via SEM and EDX imaging, and will therefore be referred to by their proposed mineral assignments. Mineral assignments on these surfaces were performed with significant guidance from Dr. Fons Marcelis[a], whose geological expertise was invaluable in this work.

#### 6.2.1.1 Secondary Electron Imaging

Bandera Brown was imaged using low-vacuum SEM; three regions, labelled 1 - 3, are shown at low magnification across Figures 6.1, 6.10 and 6.14 respectively, each highlighting a number of regions of interest. The first overlay of low-vacuum SEM micrographs, shown in Figure 6.1, has five areas of interest labelled. These areas are shown at higher magnification in Figures 6.2, 6.4, 6.6 - 6.9 below.

[a]Research Geologist at Shell Global Solutions International B.V., Amsterdam, the Netherlands

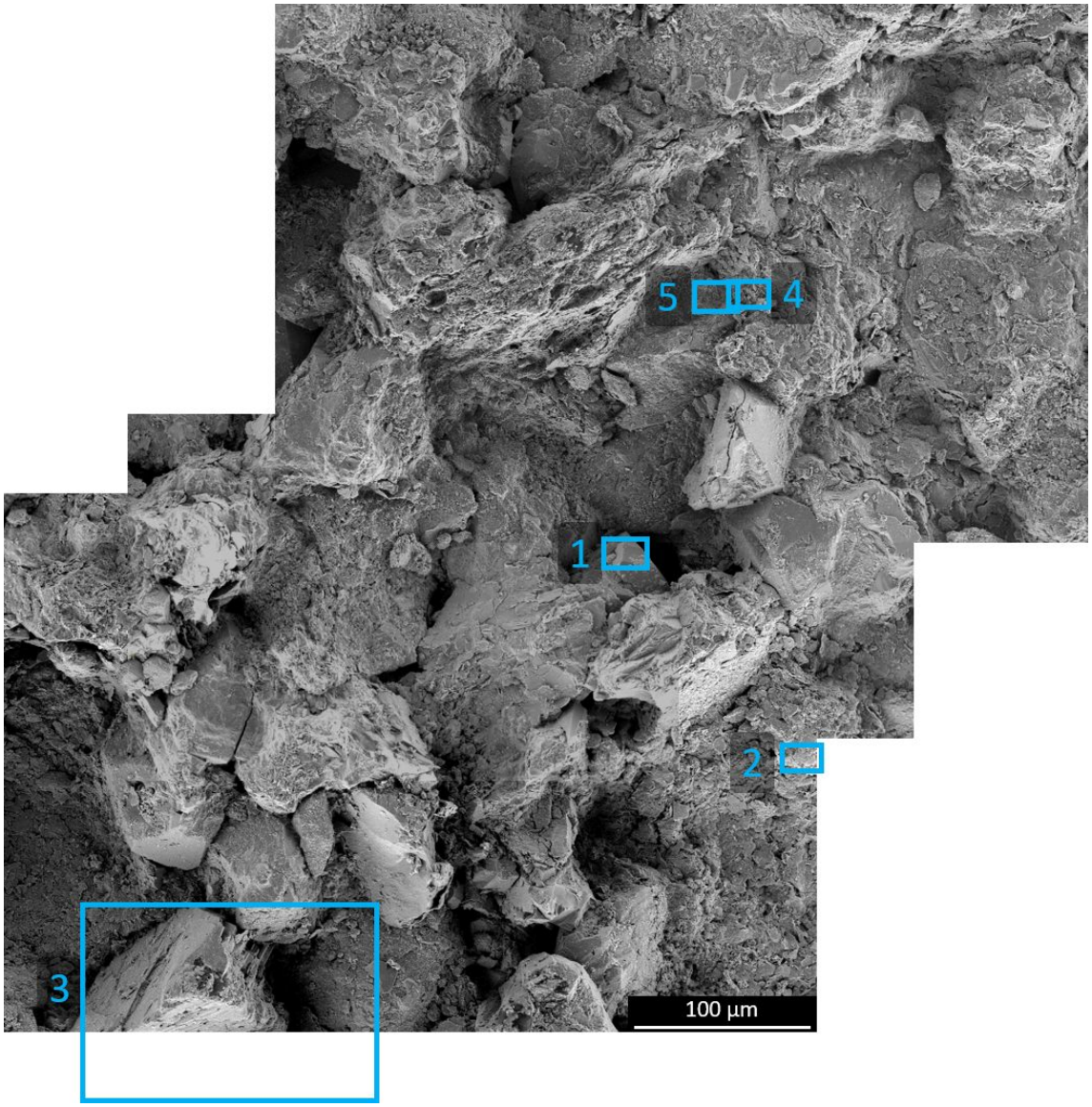



Figure 6.1: Bandera Brown 1: SEM Overlay
An overlay of four low-vacuum SEM micrographs of the Bandera Brown surface. The areas shown at higher magnification in Figures 6.2, 6.4, 6.6 - 6.9 are labelled 1-5 on the figure respectively. The individual micrographs which make up this overlay can be found in Appendix C, Figures C.1 - C.4.

The area labelled "1" on Figure 6.1 and shown at higher magnification in Figure 6.2 shows a structure which appears to be crystalline from the smooth sides and sharp edges. From the list of minerals reportedly present on the Bandera Brown surface given by Yesufu-Rufai *et al.*, quartz and calcite could both produce structures which could fit this description.[89] Due to the relative abundances reported for each, 58.89 % for quartz and 7.00 % for calcite,[89] this structure is more likely to be a quartz crystal than a calcite crystal. Quartz is a trigonal crystalline form of silica which has two enantiomeric forms, $\alpha$- and $\beta$-quartz, the $\alpha$- form being the more commonly occurring form in nature.[156–159] The structure of $\alpha$-quartz is shown in Figure 6.3 below, where it can be seen that each unit cell has three Si atoms and six O atoms, the chemical formula for quartz being $SiO_2$.[160–162]

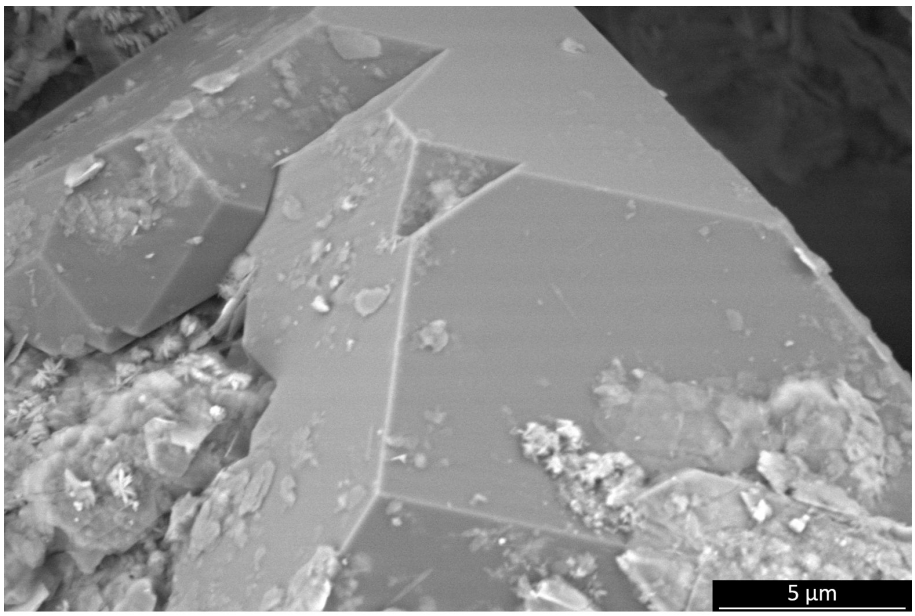



Figure 6.2: Bandera Brown 1: high magnification SEM micrograph of area 1
A high magnification low-vacuum SEM micrograph of the area labelled "1" in Figure 6.1.

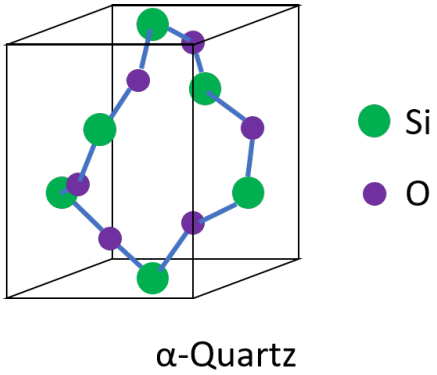



Figure 6.3: Crystal structure of $\alpha$-Quartz
The unit cell for $\alpha$-quartz, redrawn from reference 160 in the crystallographic database described by Mehl *et al.* and Hicks *et al.*.[160–162]

Area "2" on Figure 6.1 is shown at higher magnification in Figure 6.4. This surface can not be classified with certainty, as the appearance is similar to both vermiculite clay and mica. This similarity is unsurprising, as vermiculite materials are typically formed from mica, both being classed as phyllosilicates with chemical structures that follow a pattern of tetrahedral-octahedral-tetrahedral alumina and silica stacks.[124] A diagram of a generic structure for mica and vermiculite is shown in Figure 6.5. Mica has an ideal formula of $KAl_2(AlSi_3)O_{10}(OH)_2$, whilst vermiculite can be expressed as $M^+_{0.75}Al_2(Si_{3.25}Al_{0.75})O_{10}(OH)_2$, where $M^+$ is an interchangeable interlayer cation.[124] These formulae are ideal formulae; *mica* is an umbrella term for a number of minerals, and can have $Mg^{2+}$, $Fe^{2+}$ or $Fe^{3+}$ instead of $Al^{3+}$ in the octahedral sites, and $Ca^{2+}$ or $Na^+$ instead of $K^+$ as interlayer cations. Vermiculites can have $K^+$, $Mg^{2+}$ or $Ca^{2+}$ in their interlayer.[124] In mica, the tetrahedral sites in Figure 6.5 are occupied by $Si^{4+}$ and $Al^{3+}$ in a 3:1 ratio. In vermiculite, the tetrahedral sites are occupied by $Si^{4+}$ and $Al^{3+}$ in a 3.25:0.75 ratio. This altered ratio towards a greater number of $Si^{4+}$ ions in the tetrahedral sites of vermiculite has the consequence of fewer interlayer cations being required between the tetrahedral-octahedral-

tetrahedral sheets to balance the negative charge when compared to mica.[124] SEM micrographs of pure mica and vermiculite clay samples can be found in reports from Au *et al.* and Nguyen *et al.* respectively for comparison.[163,164]

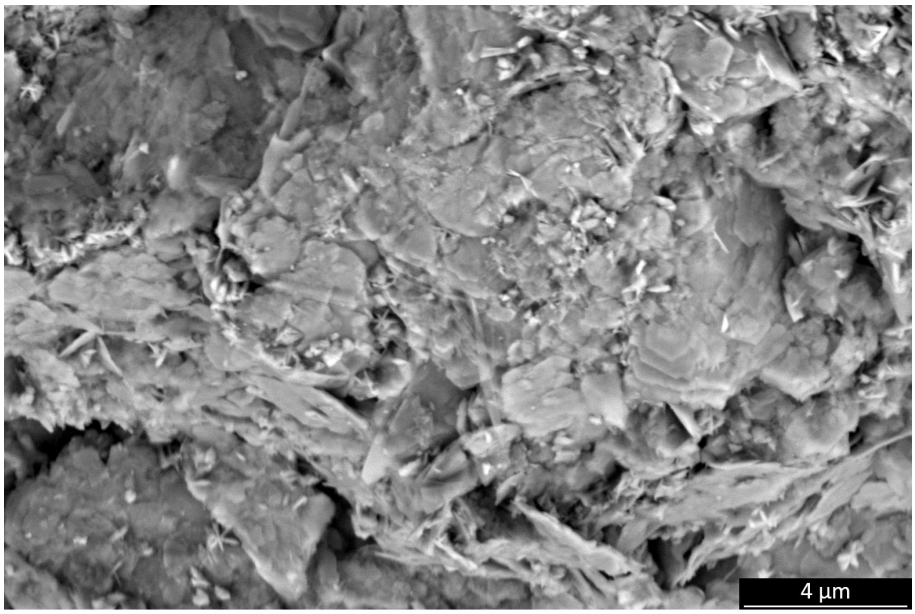



Figure 6.4: Bandera Brown 1: high magnification SEM micrograph of area 2
A high magnification low-vacuum SEM micrograph of the area labelled "2" in Figure 6.1.

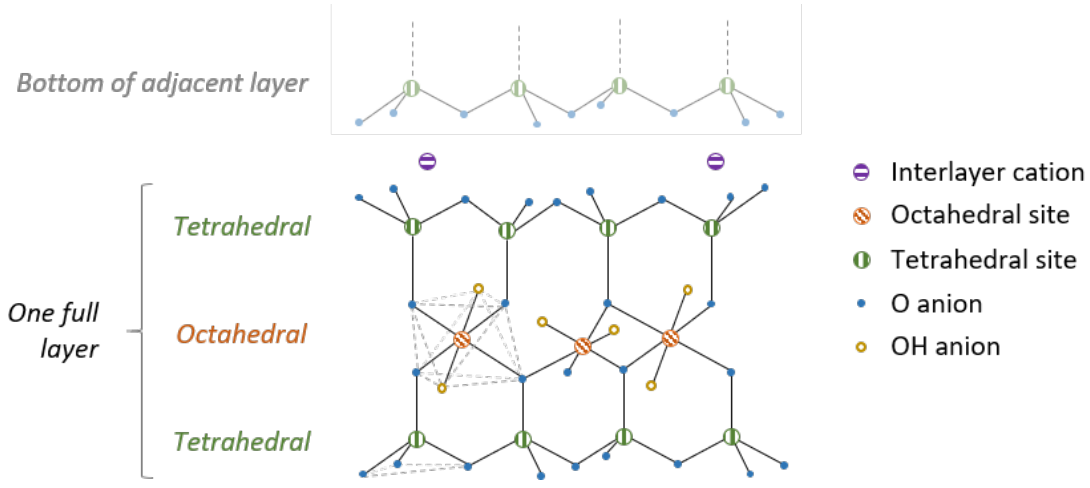



Figure 6.5: Chemical structure of mica and vermiculite
A generic chemical structure for mica and vermiculite. In mica the $Si^{4+}$:$Al^{3+}$ ratio in the tetrahedral sites in 3:1, whereas for vermiculite it is 3.25:0.75. Fewer interlayer cations are therefore required in vermiculite than mica to balance the negative charge in the clay sheets. Structure redrawn from 165.

The third area labelled in Figure 6.1 is shown at higher magnification in Figure 6.6. This features a large smooth-sided structure which is similar to the step-like structures found on some calcite crystallites on Estaillades and Indiana. SEM micrographs of Estaillades surface type 3b (Figure 6.7a) and Indiana surface type 2 (Figure 6.7b) are shown in Figure 6.7 for comparison. Due to the striking similarity, and given that calcite has been reported in the literature as being present in Bandera Brown, it is proposed that Figure 6.6 shows a large calcite crystal.[89]

Area "4" from Figure 6.1 is shown at higher magnification in Figure 6.8. The area appears to be predominantly covered by either mica or vermiculite, similar in appearance to area "2", with what appears to be a small amount of smectite clay in the centre. Smectite clay has a structure similar to that of mica or vermiculite shown in Figure 6.5, being made up of silica and alumina sheets stacked in a tetrahedral-octahedral-tetrahedral arrangement. A generic smectite formula is $M^{+}_{0.33}Al_2(Si_{3.67}Al_{0.33})O_{10}(OH)_2$ where $M^+$ is a cation such as $Mg^{2+}$ or $Ca^{2+}$.[124] The key difference in chemical structure between smectite and mica/vermiculite lies in the $Si^{4+}$:$Al^{3+}$ ratio of 3.67:0.33 in the tetrahedral layers, which sits even further towards $Si^{4+}$ than vermiculite, which is 3.25:0.75. This ultimately means that the number of interlayer cations ($M^+$ ions) required to balance the negative charge in the tetrahedral-octahedral-tetrahedral alumina and silica stacks is even lower for smectite than for vermiculite; 0.33 $M^+$ ions versus 0.75 $M^+$ ions per 2 octahedral $Al^{3+}$ respectively.[124] Some clear SEM micrographs of smectite clay structures were published in 2007 by Fesharaki *et al.*, for comparison.[166]

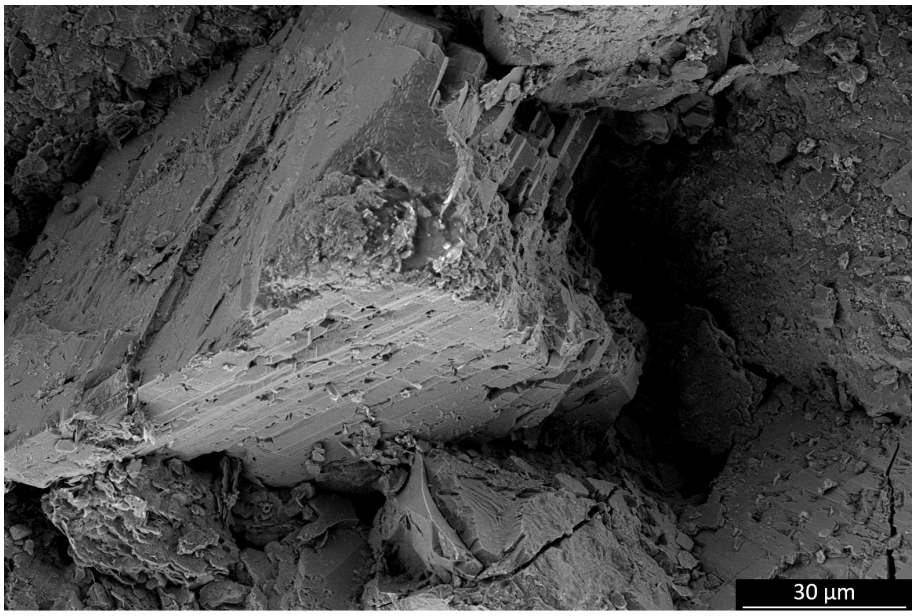
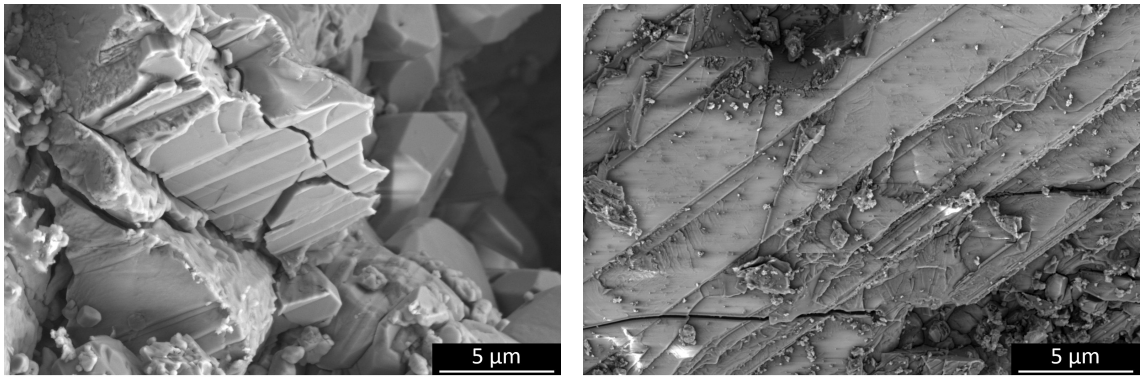



Figure 6.6: Bandera Brown 1: high magnification SEM micrograph of area 3
A high magnification low-vacuum SEM micrograph of the area labelled "3" in Figure 6.1.




(a) (b)

Figure 6.7: Calcite crystallites: examples from Estaillades and Indiana
Micrographs of (a) Estaillades area type 3b and (b) Indiana area type 2 originally shown in Chapter 3: *Carbonates*, Figures 3.20b and 3.25a on pages 110 and 116 respectively. The structures shown here are similar to the structure shown above in Figure 6.6, which is deemed to also be a calcite crystal.

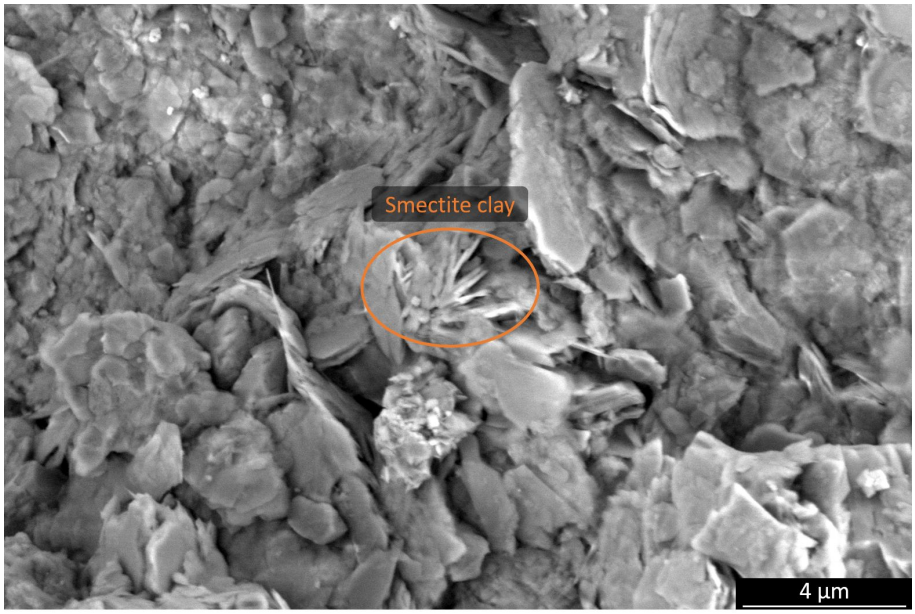



Figure 6.8: Bandera Brown 1: high magnification SEM micrograph of area 4
A high magnification low-vacuum SEM micrograph of the area labelled "4" in Figure 6.1.

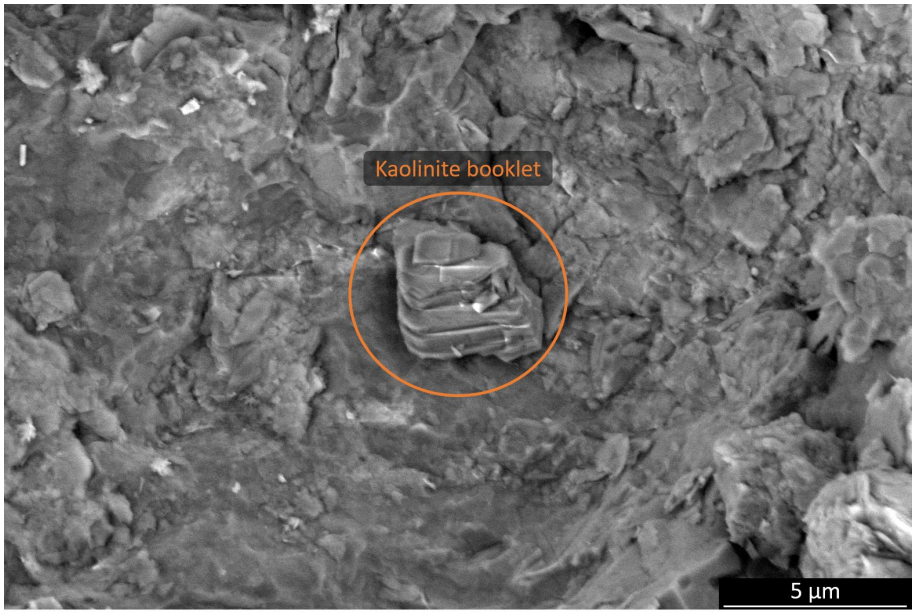



Figure 6.9: Bandera Brown 1: high magnification SEM micrograph of area 5
A high magnification low-vacuum SEM micrograph of the area labelled "5" in Figure 6.1. A section of this low-vacuum SEM micrograph was published in reference 99.

Figure 6.9 shows area "5" from Figure 6.1, at the centre of which a kaolinite booklet structure can be seen. Kaolinite clay, $Al_2Si_2O_5(OH)_4$, which is a phyllosilicate like mica and vermiculite, was discussed in Chapter 4: *Surface Charge Mapping*, where Figure 4.1 showed a diagram of the booklet structure. Kaolinite has an alternating tetrahedral-octahedral crystal structure, unlike mica and vermiculite which have tetrahedral-octahedral-tetrahedral structures, and as such do not require interlayer cations to balance the negative charge. As previously discussed in Chapter 1: *Introduction*, these booklets are of interest for the proposed surface charge mapping studies using SICM due to their pH-dependent surface charge distributions.[118,122,123,125]

A low magnification low-vacuum SEM micrograph of the second Bandera Brown region is presented in Figure 6.10, in which two areas of interest are labelled. These two areas are shown at higher magnification in Figures 6.11 and 6.12. Figure 6.11 shows an area which appears to be covered in smectite clay, which as discussed for Figure 6.8, has an tetrahedral-octahedral-tetrahedral structure of silica (tetrahedral) and alumina (octahedral) sheets.[124]

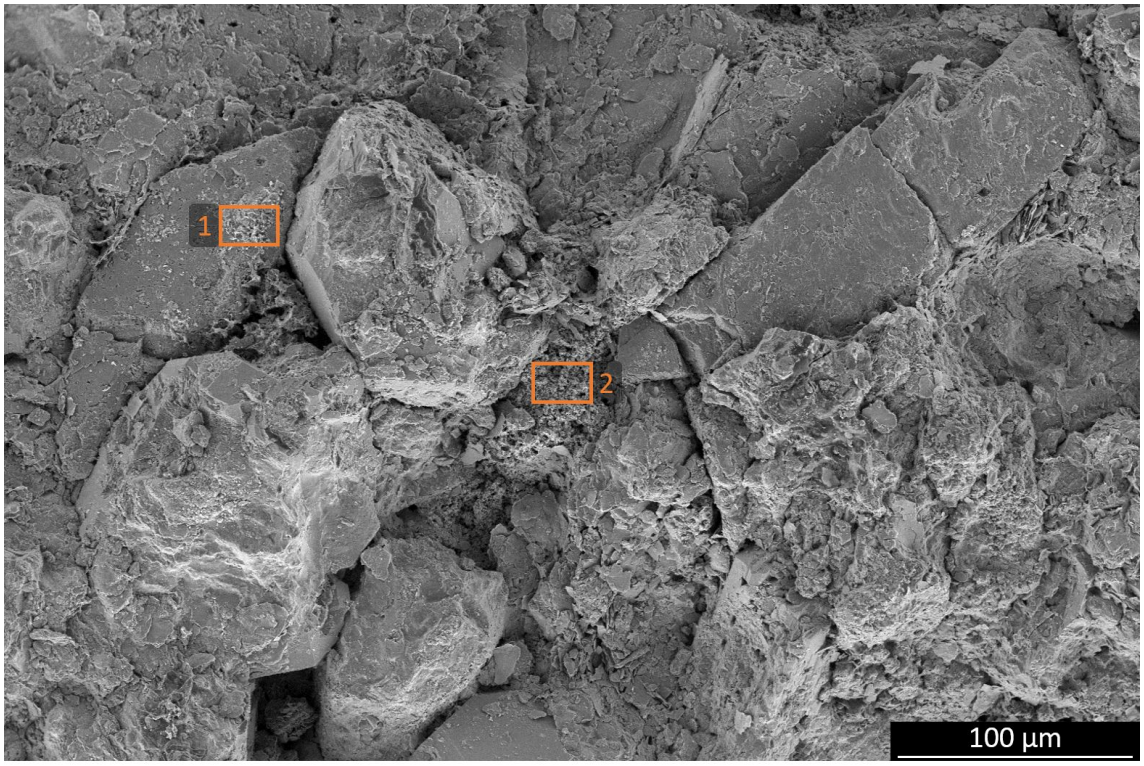



Figure 6.10: Bandera Brown 2: low magnification SEM micrograph
A low magnification low-vacuum SEM micrograph of the Bandera Brown surface. Two areas of interest shown at higher magnification in Figures 6.11 and 6.12 are labelled 1 and 2 on this figure respectively.

Area "2" from Figure 6.10 is shown at higher magnification in Figure 6.12 and features an area covered in what appear to be star-shaped hematite crystals. Hematite has the chemical formula $Fe_2O_3$, and consists of octahedral Fe atoms sharing each of their six O atoms with one other Fe atom inside of a hexagonal unit cell. Figure 6.13 shows the structure of hematite, with two octahedral arrangements of O atoms around Fe atoms shown with dotted lines for clarity.[167,168]

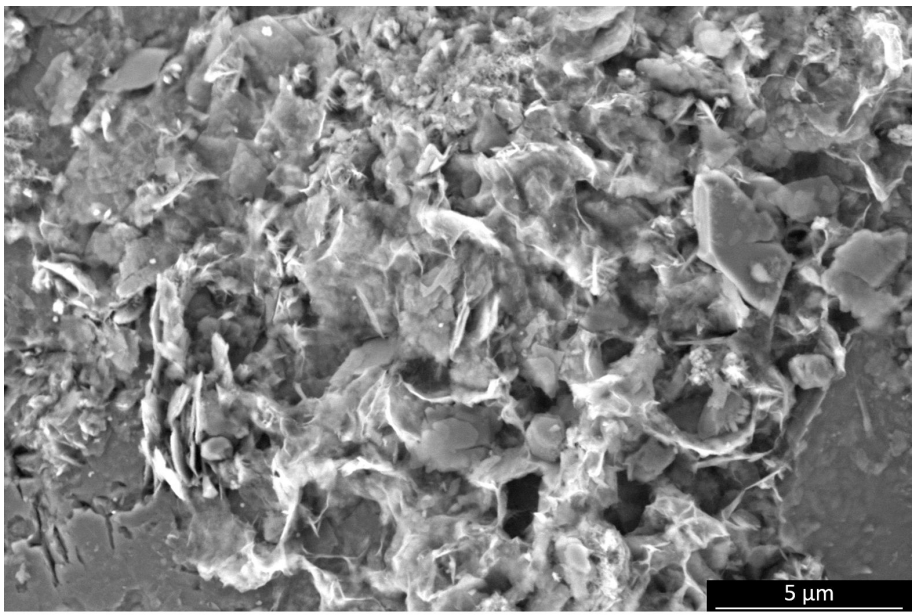



Figure 6.11: Bandera Brown 2: high magnification SEM micrograph of area 1 A high magnification low-vacuum SEM micrograph of the area labelled "1" in Figure 6.10.

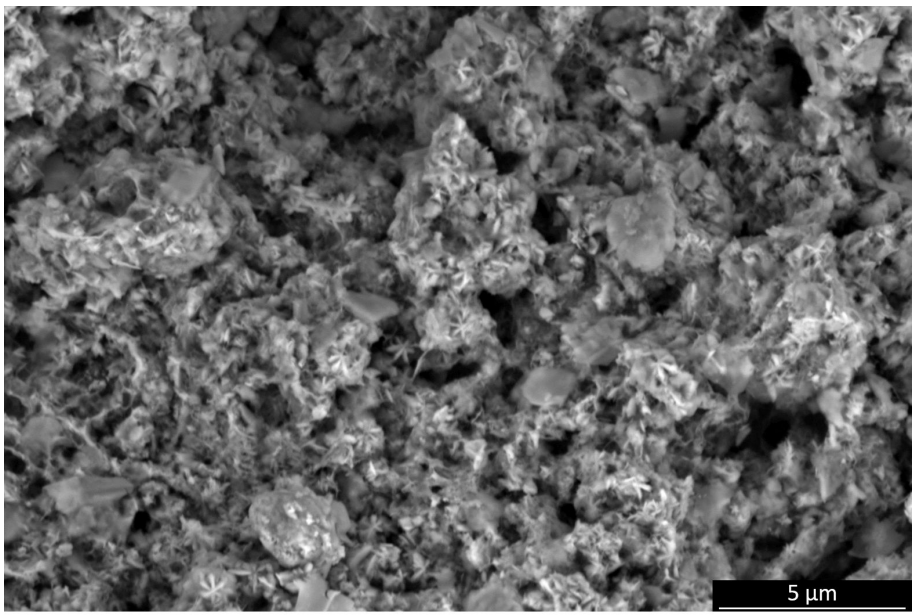



Figure 6.12: Bandera Brown 2: high magnification SEM micrograph of area 2 A high magnification low-vacuum SEM micrograph of the area labelled "2" in Figure 6.10.

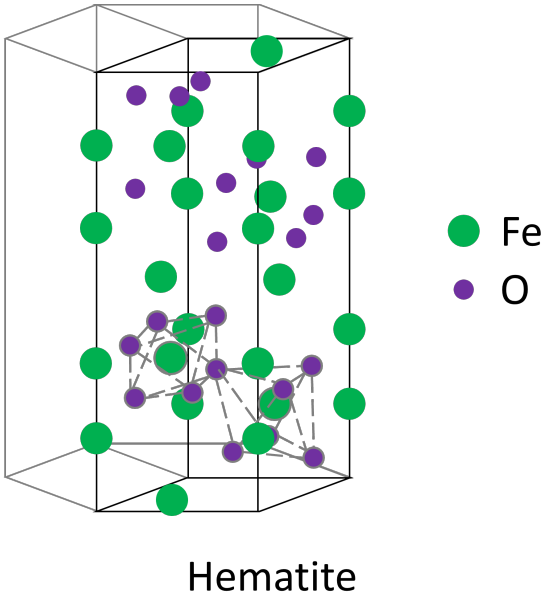



Figure 6.13: Crystal structure of hematite
The hexagonal unit cell of hematite, with two Fe atoms highlighted along with their associated oxygen atoms to show the octahedral arrangement. Redrawn from 168.

#### 6.2.1.2 Energy-Dispersive X-Ray Spectroscopy

EDX was performed on six areas on the Bandera Brown region shown in Figure 6.14, labelled 1 - 6, and shown at higher magnification in Figures 6.15, 6.18, 6.21, 6.24, 6.29 and 6.33 respectively, adjacent to their associated EDX results.

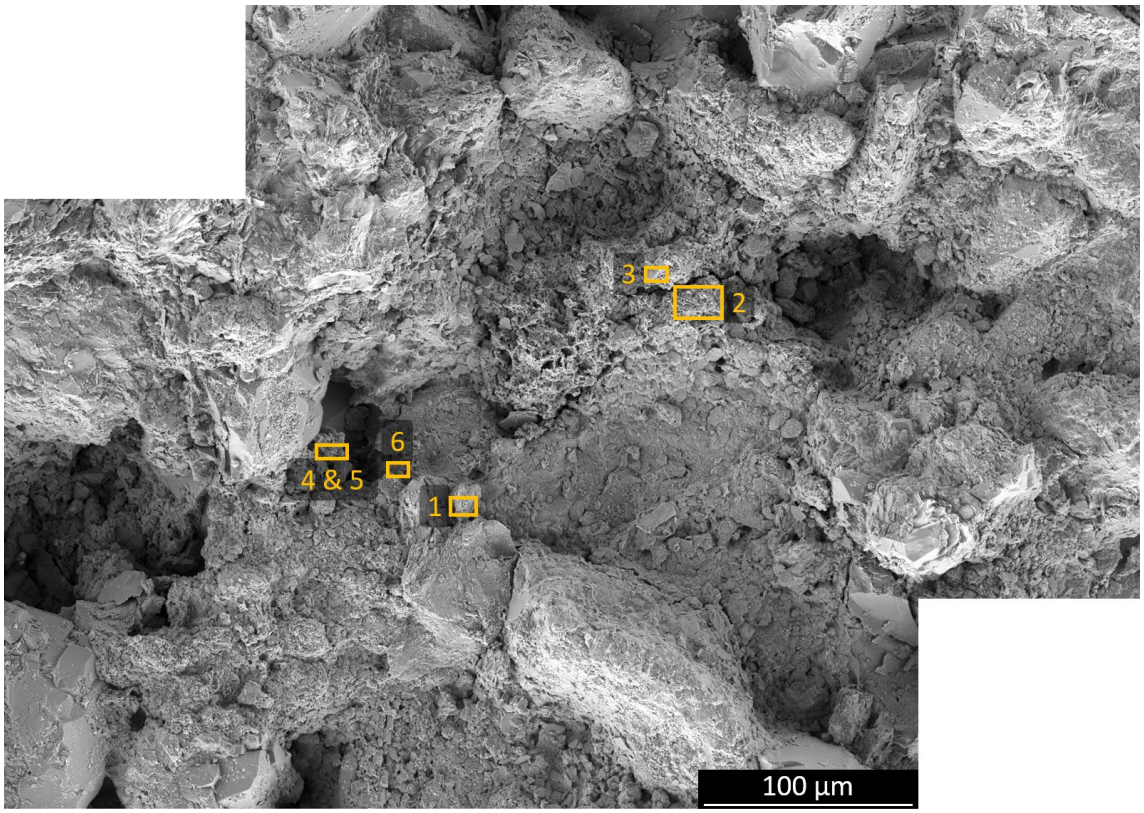



Figure 6.14: Bandera Brown 3: SEM Overlay with EDX locations
An overlay of two low-vacuum SEM micrographs of the Bandera Brown surface. The areas shown at higher magnification in Figures 6.15, 6.18, 6.21, 6.24, 6.29 and 6.33 are labelled 1 - 6 in this figure respectively. The individual micrographs which make up this overlay can be found in Appendix C, Figures C.5 and C.6

A high magnification low-vacuum SEM micrograph of area 1 from Figure 6.14 is presented in Figure 6.15, and shows a surface which, from the topography, is proposed to be vermiculite or mica. EDX results are presented for this area in Figures 6.16 and 6.17, where it can be seen that Al, C, Fe, K, Mg, Na, O and Si are present on the surface. These elements being present agree with the proposed

assignment of vermiculite or mica, which are composed of tetrahedral sheets of either Al or Si and O, octahedral sheets of Fe, Mg or Al and O, and interlayer cations of either Mg, Na or K. The C being present could well be contamination from sample preparation prior to imaging, as this is difficult to avoid.

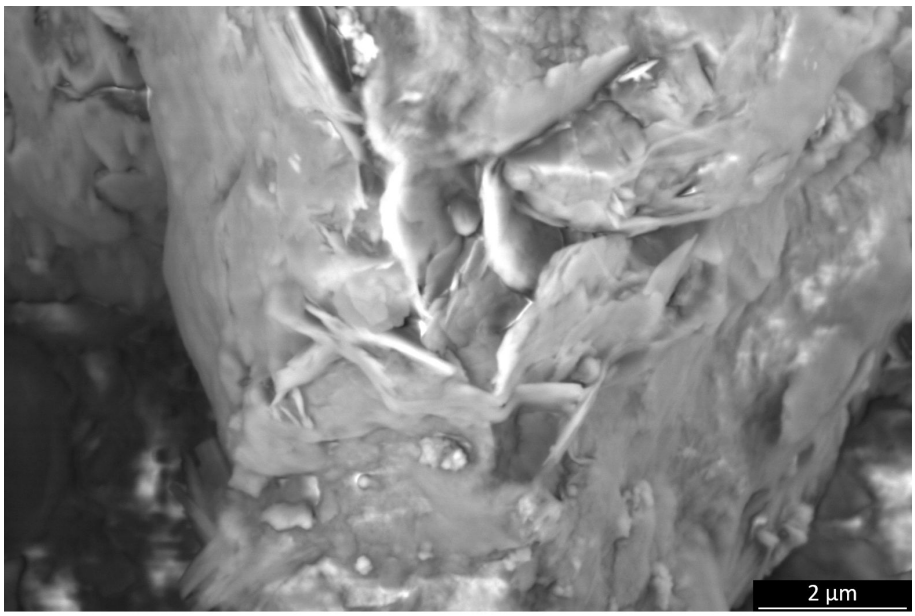



Figure 6.15: Bandera Brown 3: high magnification SEM micrograph of area 1
A high magnification low-vacuum SEM micrograph of the area labelled "1" in Figure 6.14.

Looking more closely at the distributions of these elements across Figures 6.16 and 6.17, some areas of higher or lower concentration point to the possibility of minerals other than mica/vermiculites being present on the surface. The most striking of these is that towards the top of the Si map (Figure 6.16d), a triangular area of higher Si concentration can be seen in the same region as a lower Al concentration area on the Al map (Figure 6.16b), which would not be consistent with this being an entirely clay surface. It is instead proposed that this triangular area is a small section of quartz ($SiO_2$), as there is also a subtly higher concentration of O in this region (Figure 6.16f) than the rest of the map.

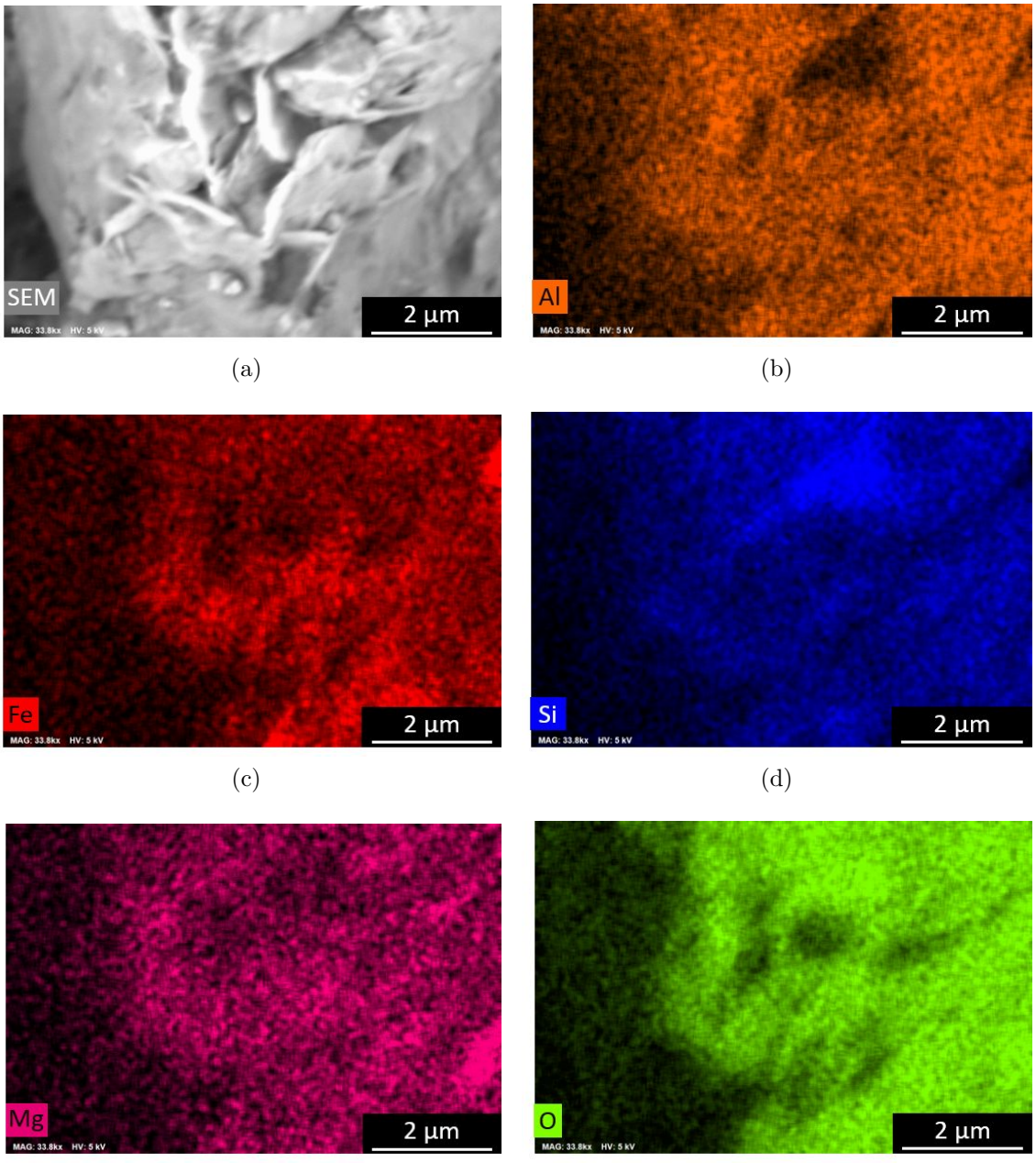
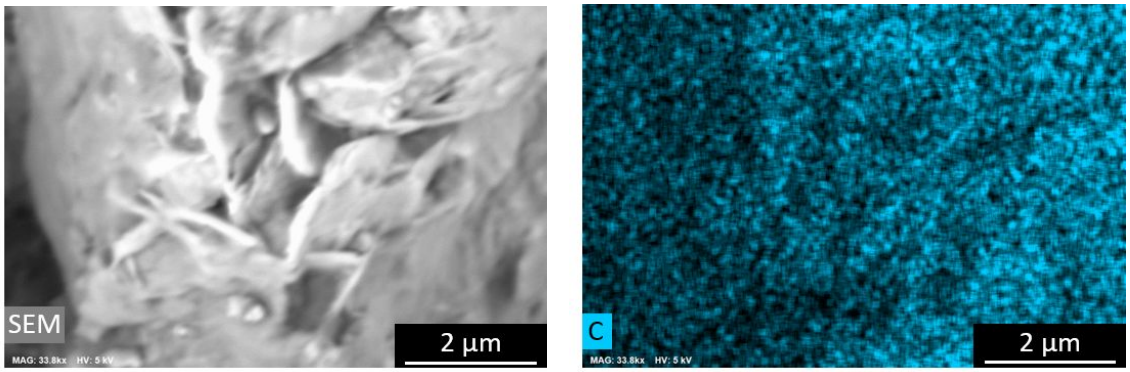
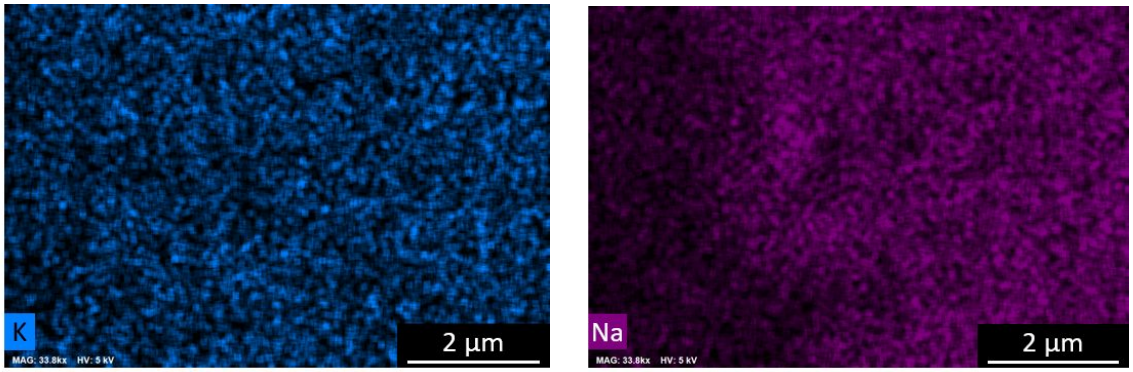


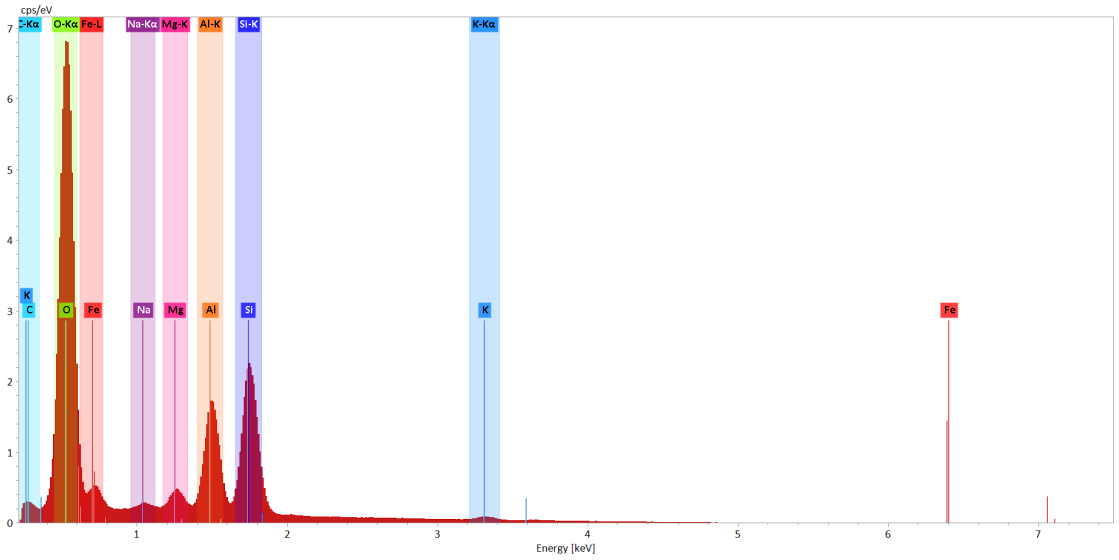

Figure 6.16: Bandera Brown 3: EDX results for area 1, part 1
EDX results for area 1 of the Bandera Brown surface shown and labelled in Figure 6.14. (a) Shows the low-vacuum SEM micrograph of the area and (b) - (f) show the Al, Fe, Si, Mg and O distribution maps for the area respectively.




(a) (b)




(c) (d)




(e)

Figure 6.17: Bandera Brown 3: EDX results for area 1, part 2
EDX results for area 1 of the Bandera Brown surface shown and labelled in Figure 6.14. (a) Shows the low-vacuum SEM micrograph of the area, (b) - (d) show the C, K and Na distribution maps for the area respectively, and (e) shows the X-ray energy spectrum for the image, with element assignments labelled.

The second area labelled in Figure 6.14 is shown at higher magnification in Figure 6.18, with the associated EDX results shown in Figures 6.19 and 6.20. On initial inspection of the SEM micrograph in Figure 6.18, the surface appears to be a mica/vermiculite surface with small, star-shaped hematite structures distributed on top. This assignment is consistent with the EDX results, which show that Al, C, Fe, K, Mg, Na, O and Si are present, as was the case for the mica/vermiculite surface in Figure 6.15. Looking at the X-ray spectrum in Figure 6.20e, the Fe peak is slightly higher compared to the Al and Si peaks than the Fe peak was for area 1 (Figure 6.17e), approximate ratios being 0.29:1 Fe:Al for area 1 and 0.65:1 Fe:Al for area 2. This greater Fe content would be consistent with the assignment of hematite ($Fe_2O_3$) structures being present on top of the clays in area 2 but not in area 1.

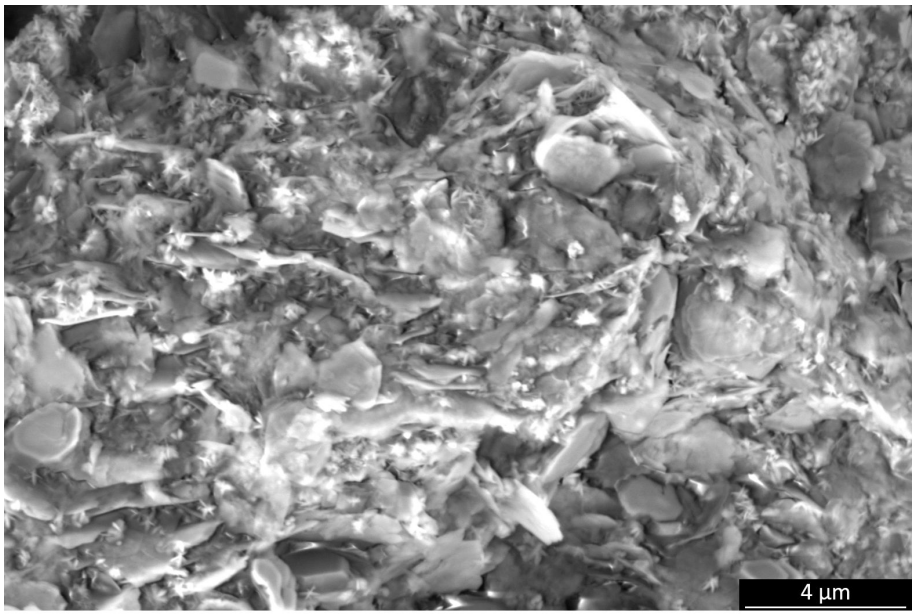



Figure 6.18: Bandera Brown 3: high magnification SEM micrograph of area 2
A high magnification low-vacuum SEM micrograph of the area labelled "2" in Figure 6.14.

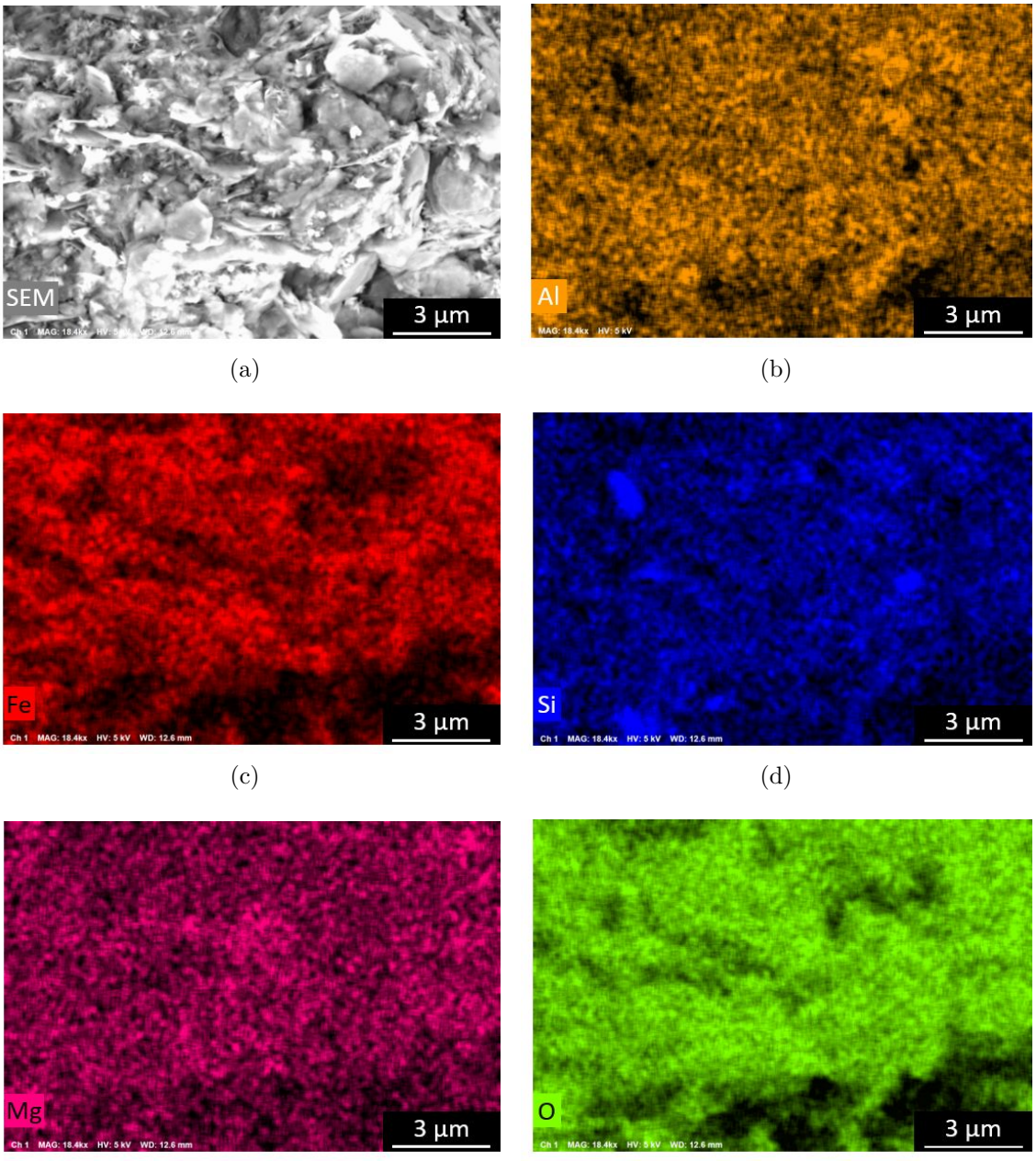
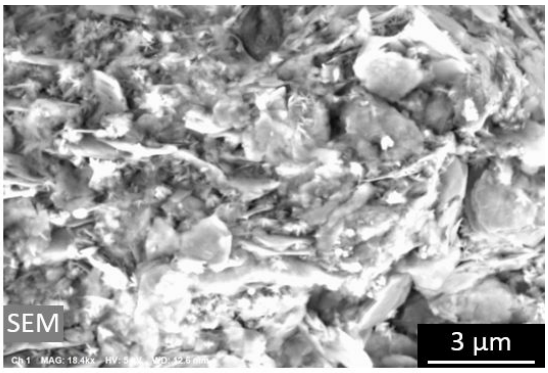
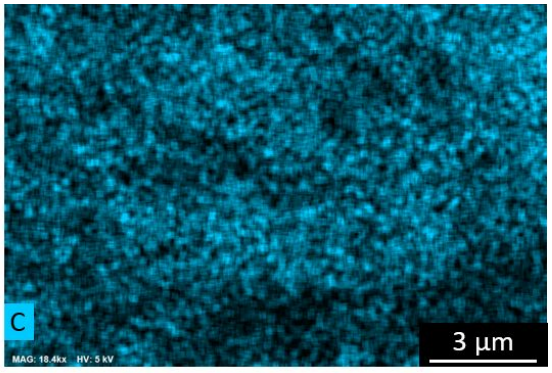


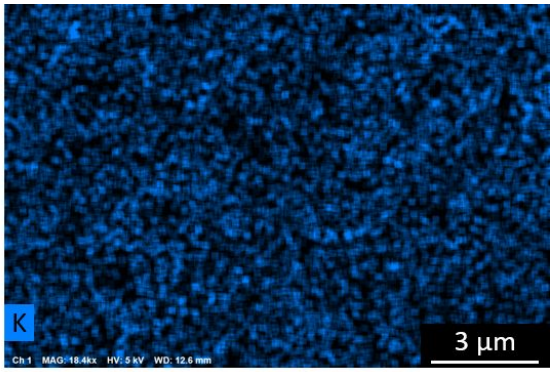

Figure 6.19: Bandera Brown 3: EDX results for area 2, part 1
EDX results for area 2 of the Bandera Brown surface shown and labelled in Figure 6.14. (a) Shows the low-vacuum SEM micrograph of the area and (b) - (f) show the Al, Fe, Si, Mg and O distribution maps for the area respectively.



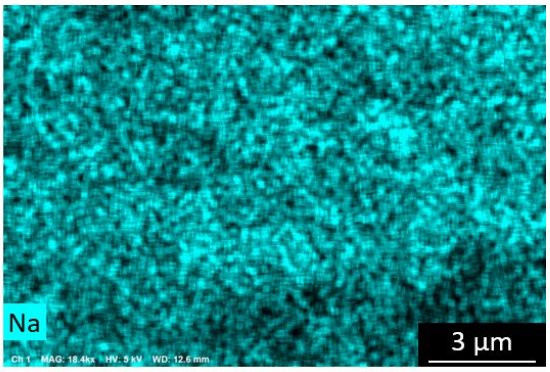

(a)



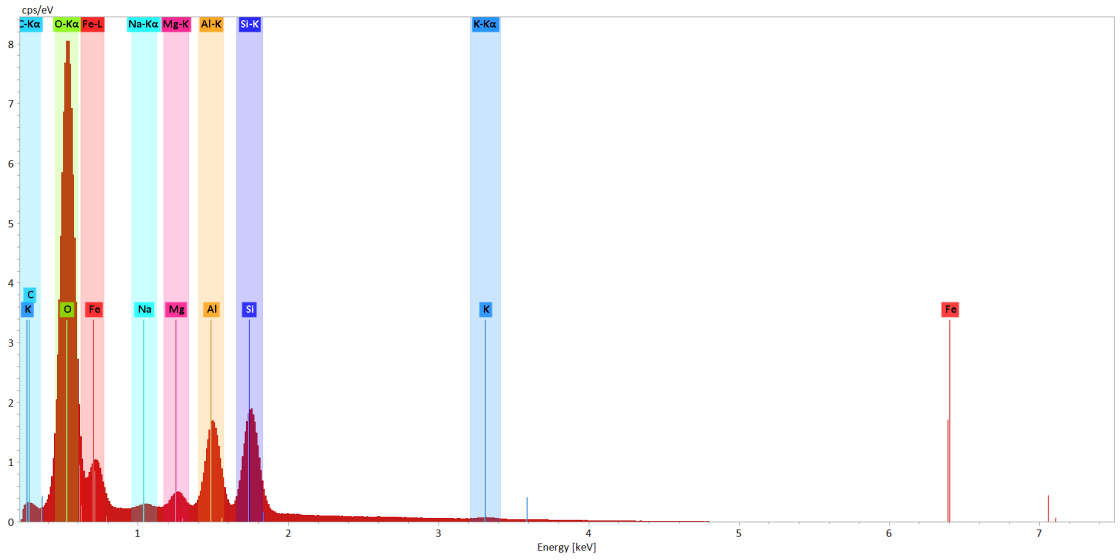

(b)




(c)




(d)




(e)

Figure 6.20: Bandera Brown 3: EDX results for area 2, part 2
EDX results for area 2 of the Bandera Brown surface shown and labelled in Figure 6.14. (a) Shows the low-vacuum SEM micrograph of the area, (b) - (d) show the C, K and Na distribution maps for the area respectively, and (e) shows the X-ray energy spectrum for the image, with element assignments labelled.

The element distribution maps for area 2 show a predominantly even spread for most elements. In the Si distribution map in Figure 6.19d, there are however a few high concentration areas, the largest of these is an oval area in the top left hand corner. The Al map in Figure 6.19b shows a low Al concentration region of the same shape where this high Si concentration region is present in Figure 6.19d. This would suggest, as was the case for the high Si concentration region in area 1, that although this surface is predominantly a mica/vermiculite surface with hematite crystals, this region is a small quartz crystal embedded in the clay.

Figure 6.21 shows a low-vacuum SEM micrograph of area "3" from Figure 6.14 at higher magnification, with associated EDX results given in Figures 6.22 and 6.23. Similarly to area 2, this area appears to have a covering of what are proposed to be star-shaped hematite crystals across the surface, however unlike area 2, these crystals are so densely packed that they obscure the nature of the surface beneath.

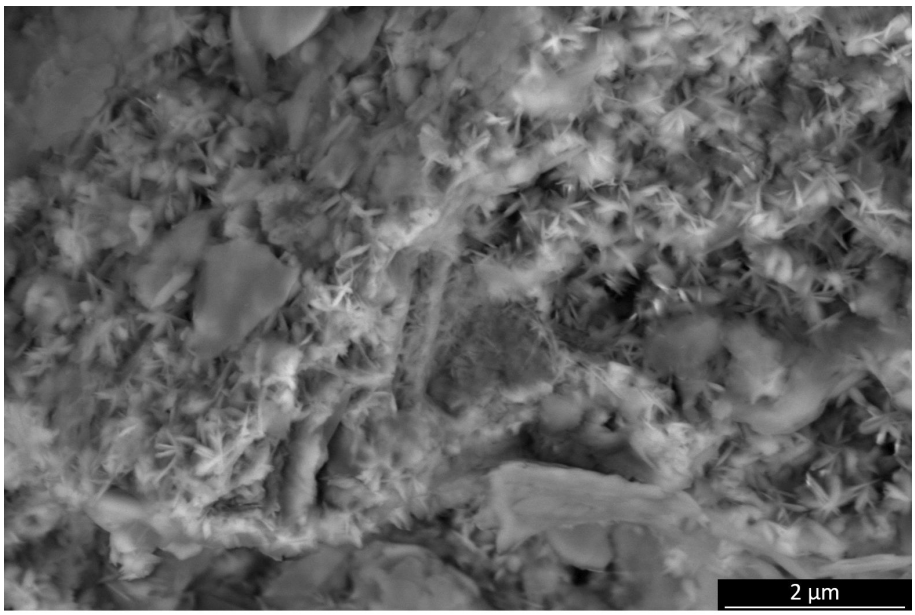



Figure 6.21: Bandera Brown 3: high magnification SEM micrograph of area 3 A high magnification low-vacuum SEM micrograph of the area labelled "3" in Figure 6.14.

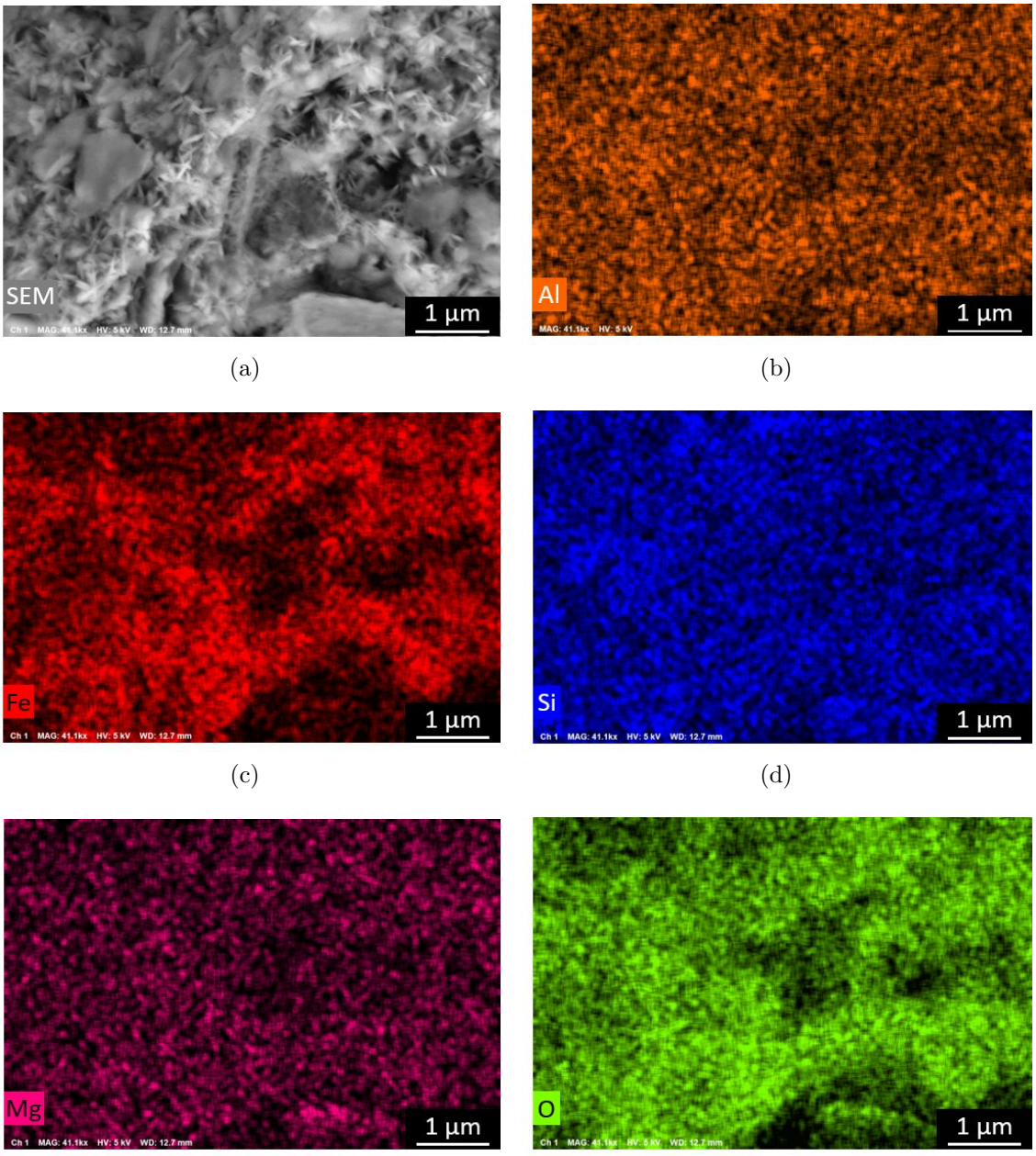
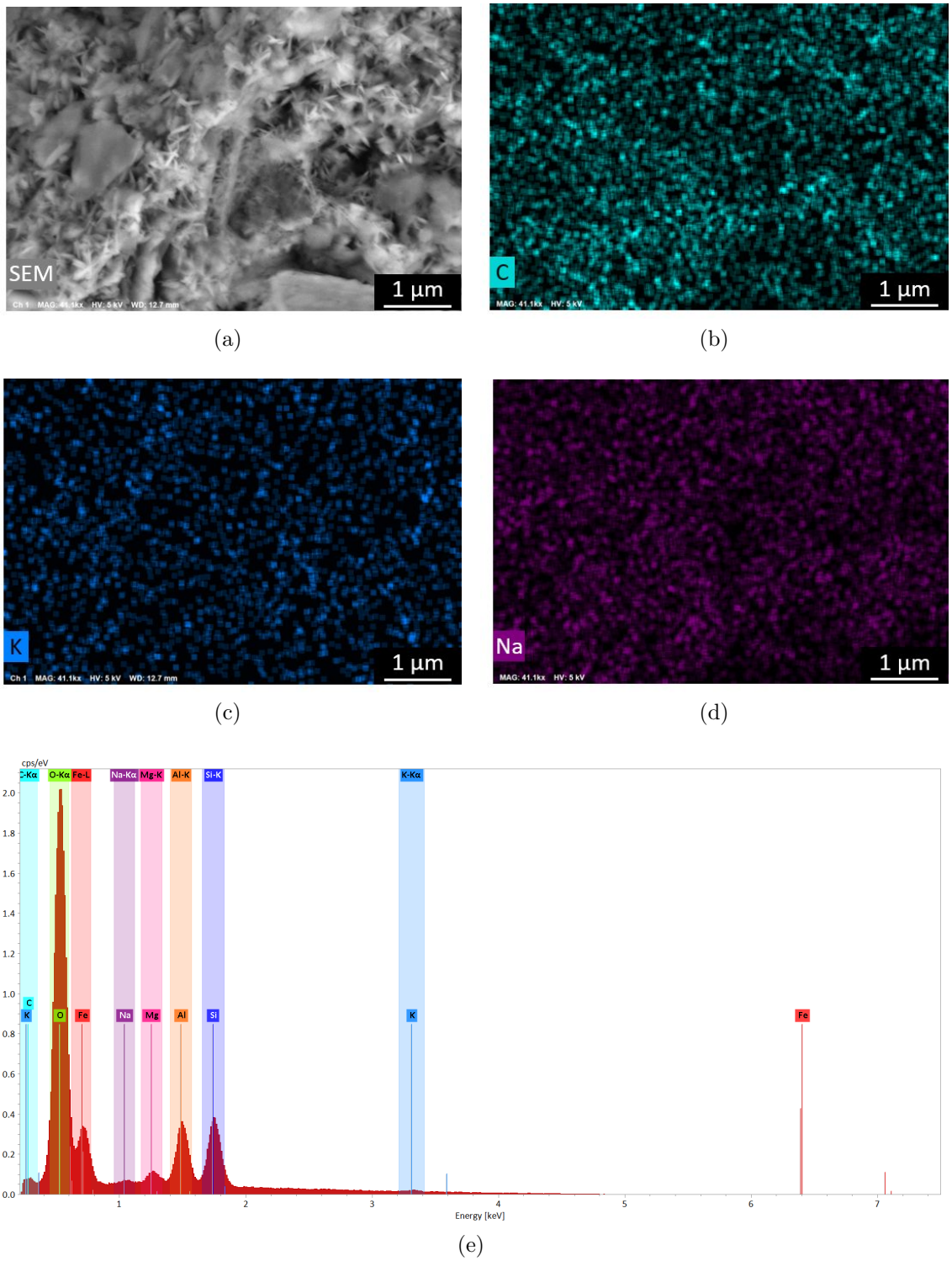



Figure 6.22: Bandera Brown 3: EDX results for area 3, part 1
EDX results for area 3 of the Bandera Brown surface shown and labelled in Figure 6.14. (a) Shows the low-vacuum SEM micrograph of the area and (b) - (f) show the Al, Fe, Si, Mg and O distribution maps for the area respectively.




(a) (b) (c) (d) (e)

Figure 6.23: Bandera Brown 3: EDX results for area 3, part 2
EDX results for area 3 of the Bandera Brown surface shown and labelled in Figure 6.14. (a) Shows the low-vacuum SEM micrograph of the area, (b) - (d) show the C, K and Na distribution maps for the area respectively, and (e) shows the X-ray energy spectrum for the image, with element assignments labelled.

The EDX results for the area "3" are given across Figures 6.22 and 6.23, and similarly to areas 1 and 2, show that the elements Al, C, Fe, K, Mg, Na, O and Si are present, indicating that clays are present. The increased coverage with hematite ($Fe_2O_3$) which is observable in the low-vacuum SEM micrograph compared to area 2 is reflected in the X-ray spectrum in Figure 6.23e, where it can be seen that the Fe:Al ratio is approximately 0.93:1, compared to the 0.65:1 Fe:Al approximated for area 2. The assignment of these star-shaped structures being hematite is reflected in the element distribution maps for Fe and O (Figures 6.22c and 6.22f), where the regions of highest Fe and O concentration are very similar, and when compared to the SEM micrograph in Figure 6.22a appear to be in highest concentration over the regions most densely covered by the star-shaped hematite crystals. The element distribution maps in Figures 6.22 and 6.23 show relatively even distributions of the elements other than Fe and O, which could suggest chemical heterogeneity beneath the hematite crystals.

Figure 6.24 shows a high magnification low-vacuum SEM micrograph of area "4", as labelled on Figure 6.14. Once again, small star-shaped crystals of what are proposed to be hematite can be seen across the surface. As was observed in area 3, the Fe distribution map for area 4 in Figure 6.25c shows regions of higher Fe concentration across the same regions where the star-shaped structures are observed in the SEM for area 4 in 6.25a. The EDX results in Figures 6.25 - 6.27 show that Al, C, Fe, K, Mg, Na, O and Si are all present, similarly to areas 1 - 3, with the addition of a small amount of P. No P-containing compounds were listed by Gamal *et al.* as being present in Bandera Brown, however Yesufu-Rufai *et al.* list one,

apatite ($Ca_5(PO_4)_3F$), and give the low area coverage of 0.08 %.[89,98] Due to this low percentage coverage it is unsurprising that P was not detected on the previous three areas, and that it is present in area 4 at a relatively low concentration, the P:Al ratio being approximately 0.125:1. Given the low concentration of P present on this surface, it is perhaps unsurprising that Ca and F are not detected, however the absence of Ca and F makes conclusive remarks on the exact nature of the P-containing compound present here difficult. Another explanation could be that this peak has been incorrectly assigned as the P $K\alpha$ peak at 2.01 keV, however the only other two characteristic X-rays around 2 keV are the Zr $L\alpha$ and Pt $M\alpha$ peaks at 2.04 and 2.05 keV respectively, and neither element is reported in the literature as being present in Bandera Brown, so it is unlikely to not be P.[89,98,169]

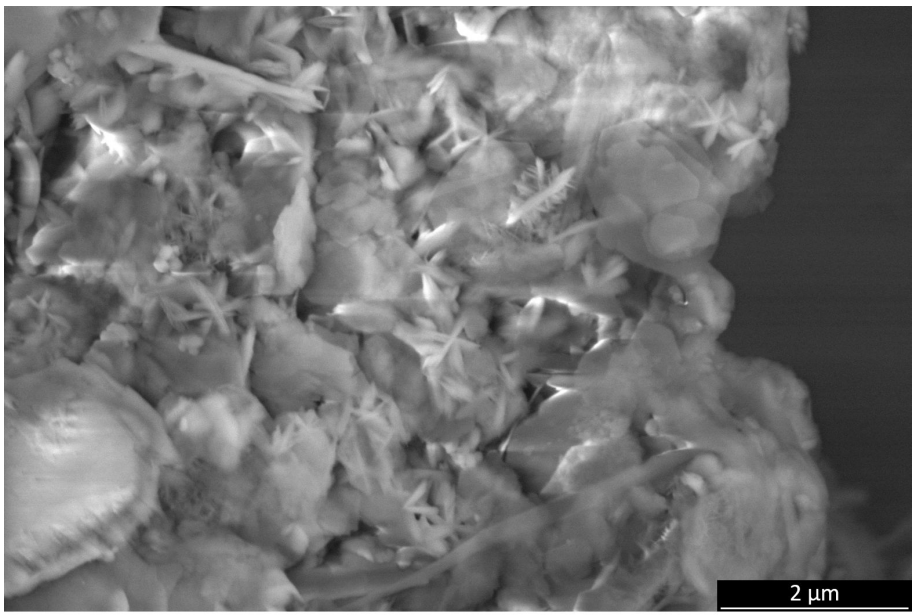
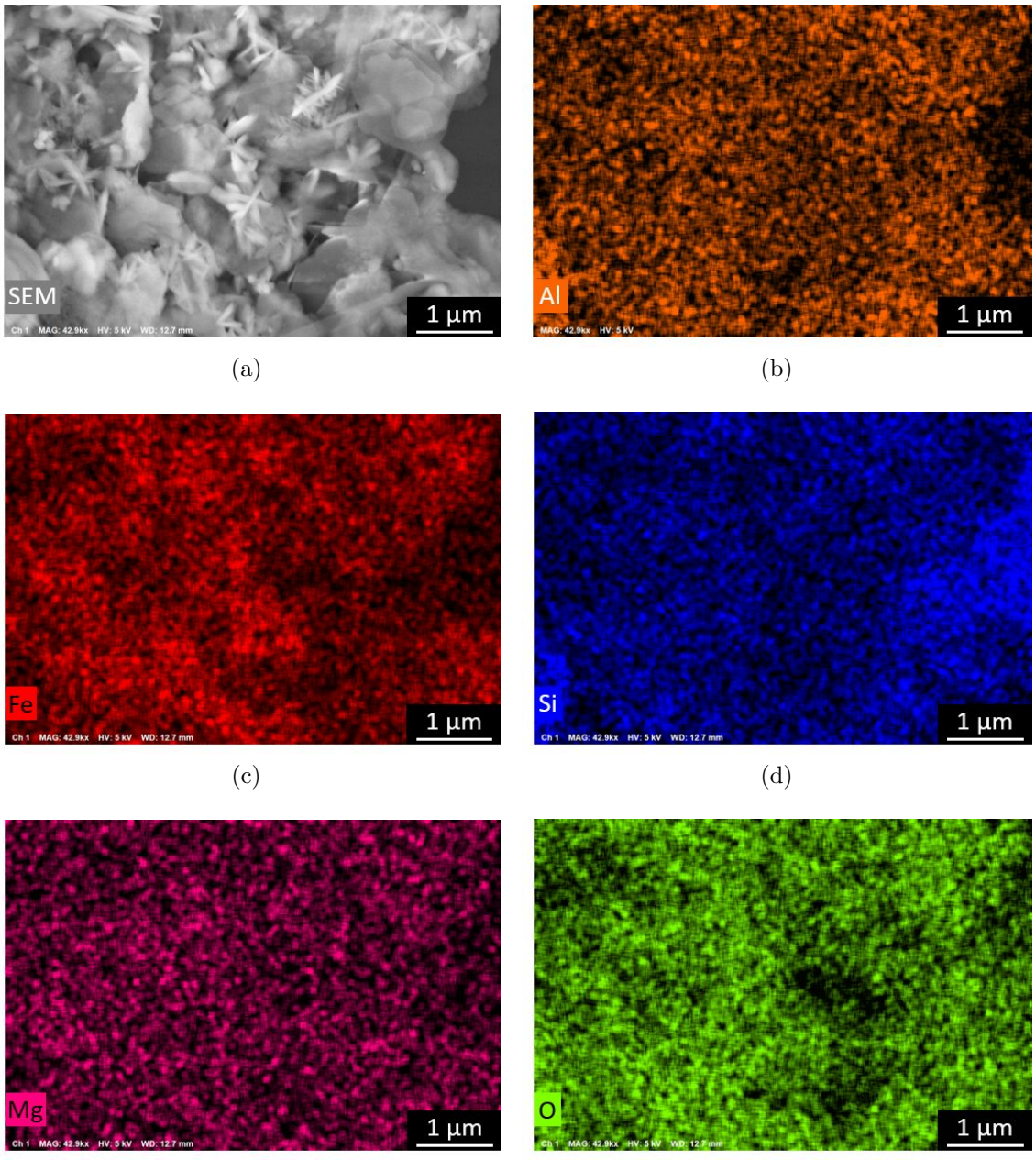



Figure 6.24: Bandera Brown 3: high magnification SEM micrograph of area 4
A high magnification low-vacuum SEM micrograph of the area labelled "4" in Figure 6.14.




(a) (b)

(c) (d)

(e) (f)

Figure 6.25: Bandera Brown 3: EDX results for area 4, part 1
EDX results for area 4 of the Bandera Brown surface shown and labelled in Figure 6.14. (a) Shows the low-vacuum SEM micrograph of the area and (b) - (f) show the Al, Fe, Si, Mg and O distribution maps for the area respectively.

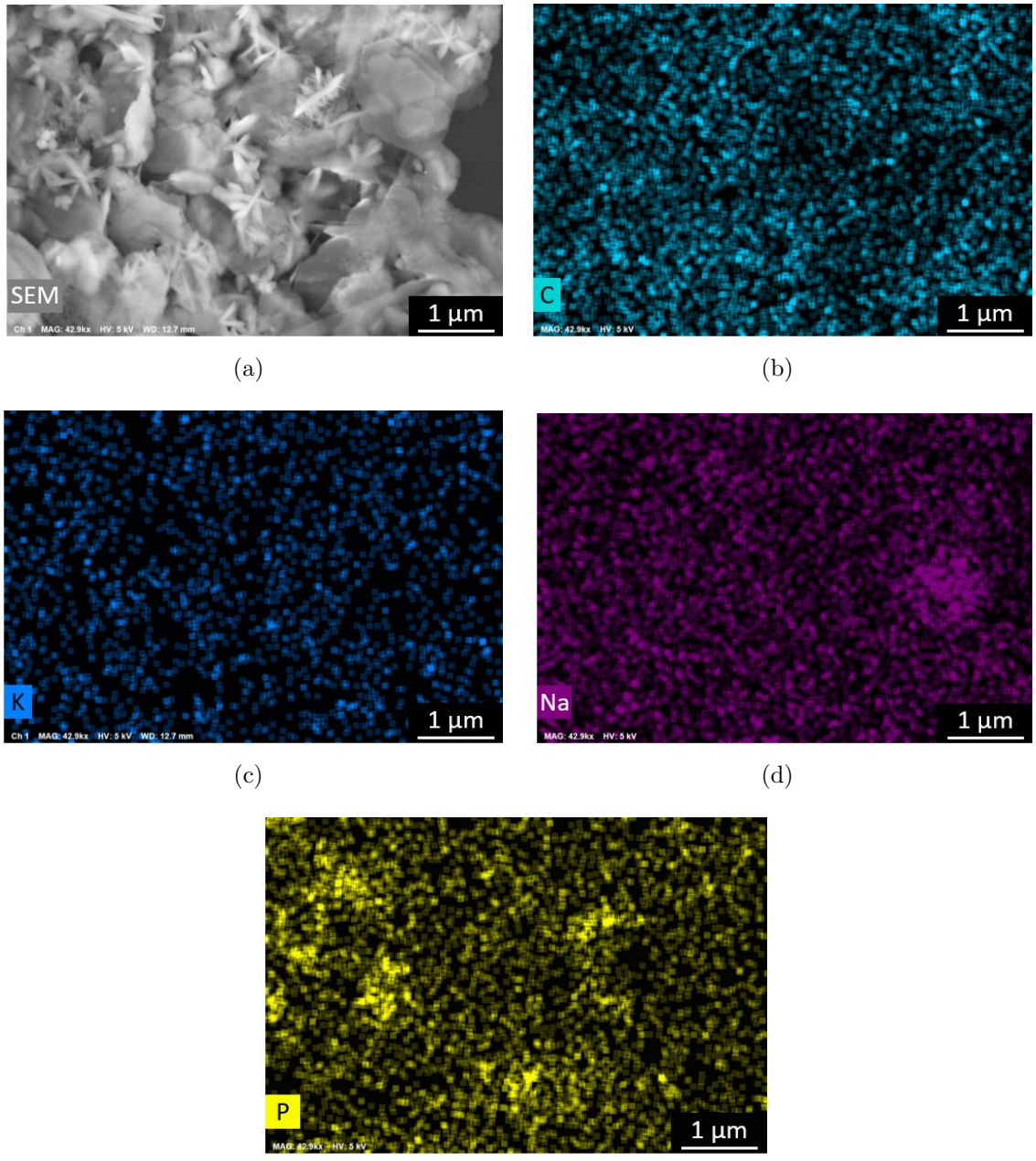



Figure 6.26: Bandera Brown 3: EDX results for area 4, part 2
EDX results for area 4 of the Bandera Brown surface shown and labelled in Figure 6.14. (a) Shows the low-vacuum SEM micrograph of the area and (b) - (e) show the C, K, Na and P distribution maps for the area respectively.

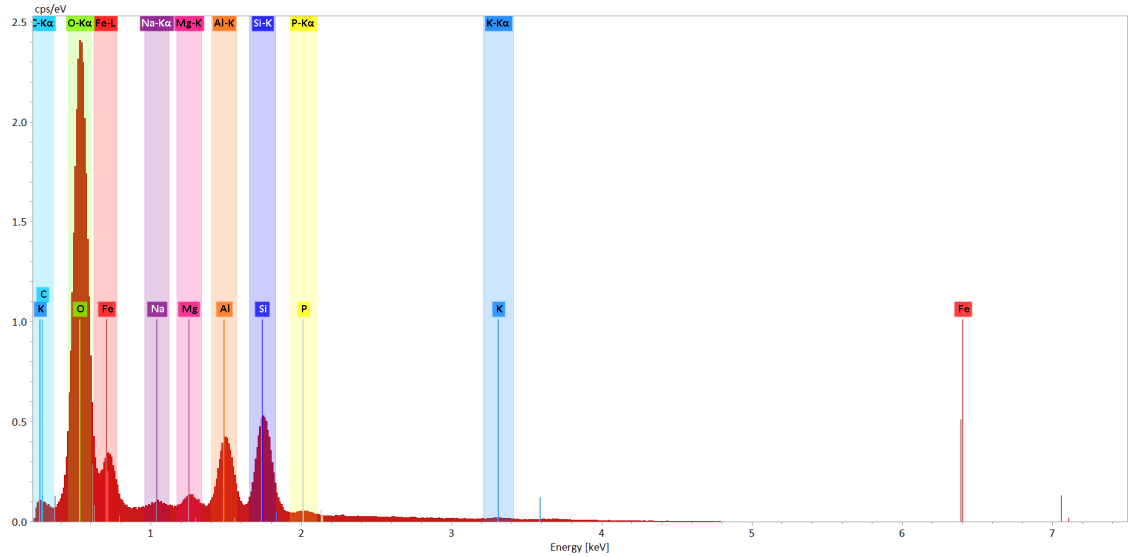



Figure 6.27: Bandera Brown 3: EDX results for area 4, part 3
The X-ray energy spectrum for the EDX results shown in Figures 6.25 and 6.26, with element assignments labelled.

Towards the right hand side of the Na map for area 4 in Figure 6.26d, an approximately 1 $\mu$m diameter section exhibits a higher Na concentration than the rest of area 4. Looking at Figure 6.25d, Si is also present at a higher concentration in this region than other parts of area 4. This might suggest a $Na^+$-containing mica, however the Al distribution map in Figure 6.25b shows a perhaps lower than average concentration in this region, which is not consistent with the overall 1:1 ratio of Si:Al in mica. This region of high concentration Na is therefore proposed to be caused by the presence of albite, a Na-containing plagioclase and alkali feldspar with a chemical formula of $NaAlSi_3O_8$.[170] Plagioclases make up 16.41 % and alkali feldspars make up 1.85 % of the Bandera Brown surface according to Yesufu-Rufai *et al.*, so the presence of albite is not unlikely.[89] Albite is constructed of 4-member rings, each containing on average 3 Si and 1 Al atom, joined together by O atoms. Although quite different to the mica or kaolinite structures previously discussed, cations such

as $Na^+$ are still required to balance out the negative charge on the rings, as shown in Figure 6.28 below.[170–172]

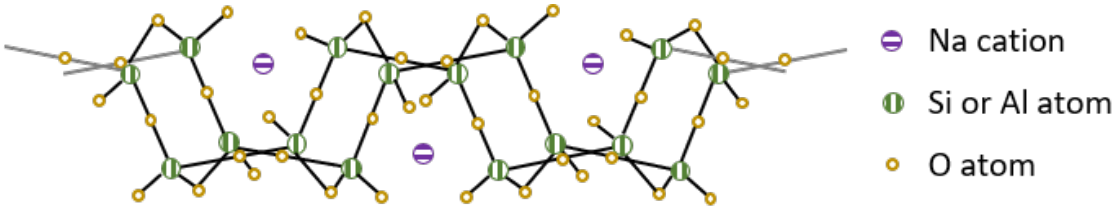



Figure 6.28: Chemical structure of albite
The structure of albite, redrawn from references 170, 171 and 172. The atoms marked "Si or Al atom" are either Si or Al in a 3:1 ratio. Grey bonds on the edges of the structure show where the structure continues in an extended chain.

A high magnification low-vacuum SEM micrograph of area "5" from Figure 6.14 is shown in Figure 6.29, the associated EDX results for this area shown in Figures 6.30 - 6.32. The right-hand side of area 5 overlaps with the left-hand side of area 4, so it is unsurprising that the same nine elements are seen in the EDX spectrum in Figure 6.32. At the center of the SEM micrograph in Figure 6.30a, a 2 - 3 $\mu$m across smooth-sided crystallite can be seen, which from looking at the element distribution maps in Figure 6.30 can be seen to be rich in Si, Al and O. This is proposed to be K-feldspar, a type of alkali feldspar with the chemical formula $KAlSi_3O_8$.[89,171,173] K-feldspar has the same generic structure as albite, as it is also an alkali feldspar, which can be seen in Figure 6.28; the only alteration being that the $Na^+$ cations in the structure are replaced with $K^+$ cations.

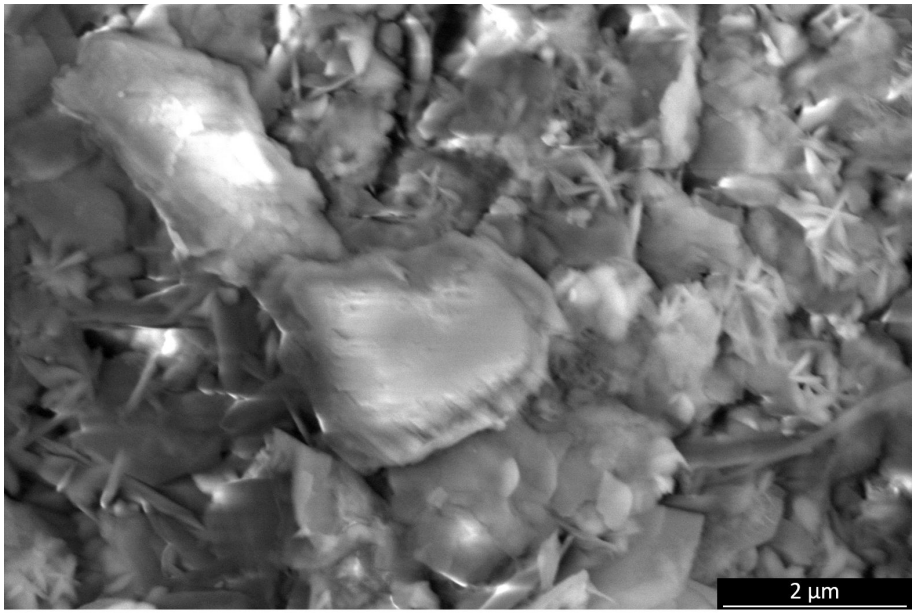



Figure 6.29: Bandera Brown 3: high magnification SEM micrograph of area 5 A high magnification low-vacuum SEM micrograph of the area labelled "5" in Figure 6.14.

Around the outside of the smooth-sided structure in Figure 6.30a, more of the star-shaped hematite ($Fe_2O_3$) structures can be seen, which is reflected in the higher concentration of Fe in these regions in Figure 6.30c. Towards the top of the P distribution map in Figure 6.31e, there are higher concentration areas which are attributed to the presence apatite, $Ca_5(PO_4)_3F$, as they were in area 4. In the top left hand corner of the Mg distribution map in Figure 6.30e there is a higher concentration of Mg than in the rest of area 5, however this does not align with higher concentrations in any element distribution map other than O (Figure 6.30f). Given the number of different Mg-containing compounds that have been reported as being present on the Bandera Brown surface,[89,98] combined with the small visible section in the SEM and the lack of significant signal in any of the other element maps, it is not possible to give a mineral assignment for this area with any certainty.

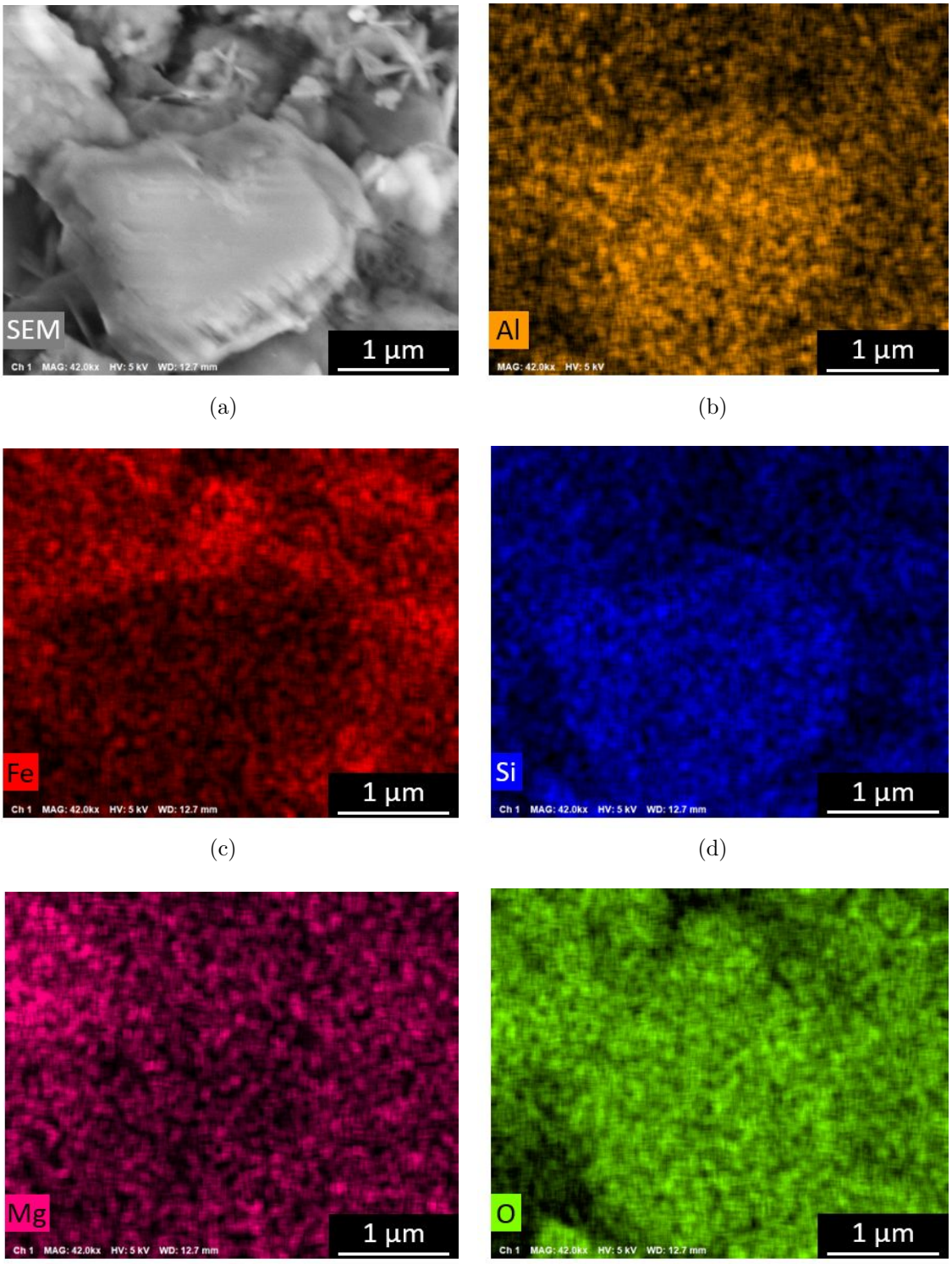
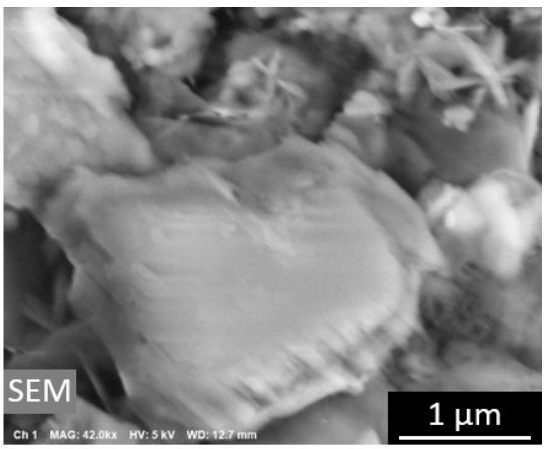
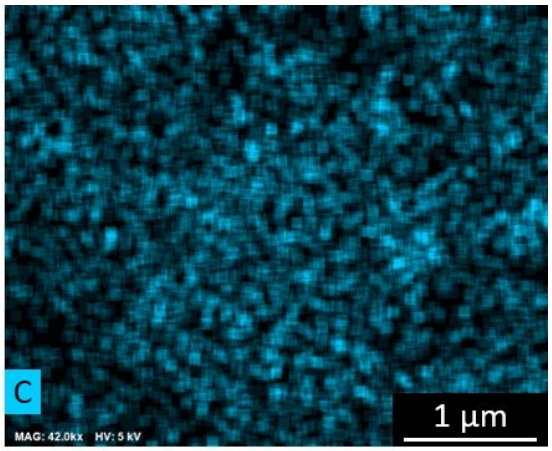


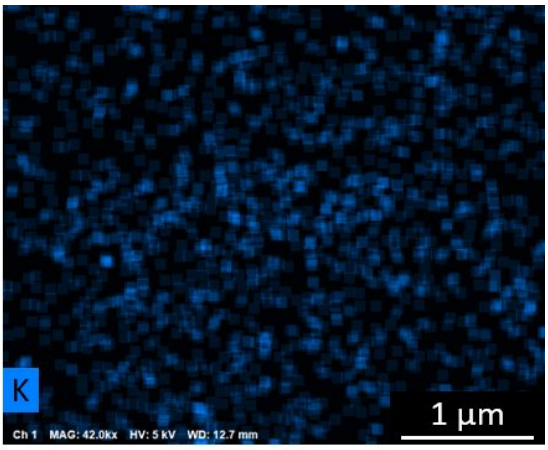

Figure 6.30: Bandera Brown 3: EDX results for area 5, part 1
EDX results for area 5 of the Bandera Brown surface shown and labelled in Figure 6.14. (a) Shows the low-vacuum SEM micrograph of the area and (b) - (f) show the Al, Fe, Si, Mg and O distribution maps for the area respectively.



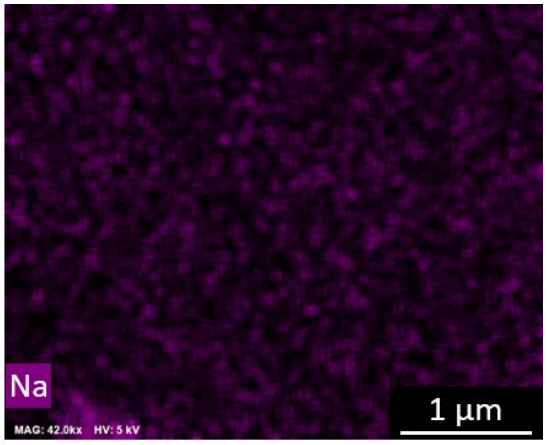

(a)



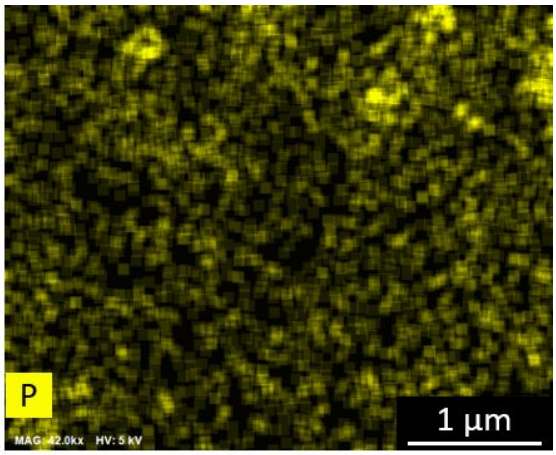

(b)




(c)




(d)




(e)

Figure 6.31: Bandera Brown 3: EDX results for area 5, part 2
EDX results for area 3 of the Bandera Brown surface shown and labelled in Figure 6.14. (a) Shows the low-vacuum SEM micrograph of the area and (b) - (e) show the C, K, Na and P distribution maps for the area respectively.

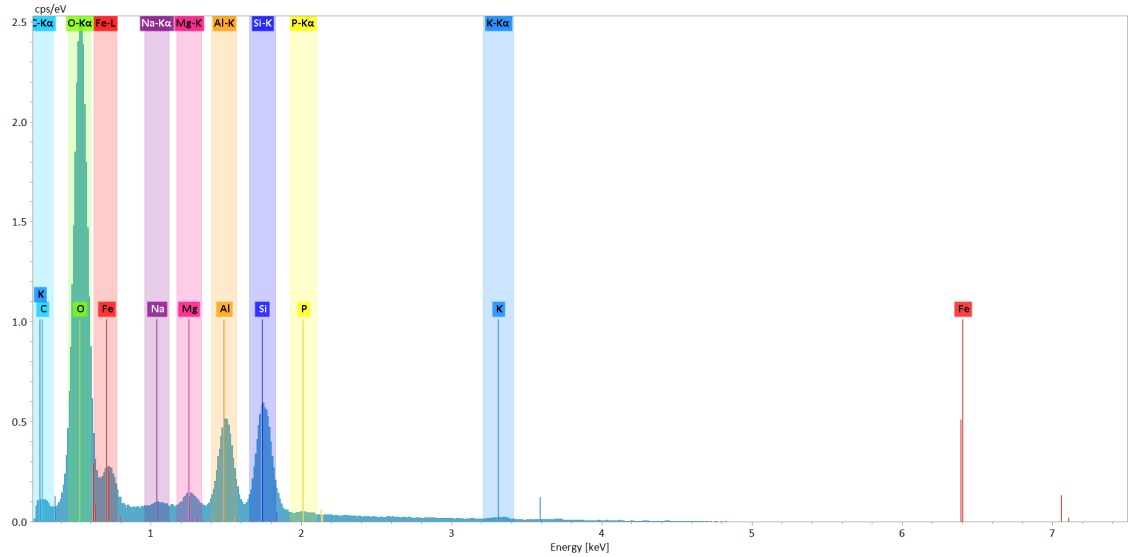



Figure 6.32: Bandera Brown 3: EDX results for area 5, part 3
The X-ray energy spectrum for the EDX results shown in Figures 6.30 and 6.31, with element assignments labelled.

Area "6" as labelled in Figure 6.14 is shown at higher magnification in Figure 6.33. The structures in the centre of this low-vacuum SEM micrograph appear to be a mica or vermiculite clay. The elements present in the EDX spectrum (Figure 6.35e) for this area are Al, C, Fe, K, Mg, Na, O and Si. The element distribution maps across Figures 6.34 and 6.35 do not show any significant patches of higher or lower concentration of any of these elements, which would suggest that this area is homogeneous in terms of its mineralogy. The assignment of this mineral surface being mica or vermiculite can explain the presence of all of the elements shown in the EDX results; the octahedral sites in mica or vermiculite can be occupied by Al, Fe or Mg, the tetrahedral sites can be occupied by Si or Al, O is present throughout both tetrahedral and octahedral layers, and the interlayer cations can be $K^+$, $Na^+$ or $Mg^{2+}$.[124] The C, given its low concentration, is likely to be contamination which occurred during sample preparation.

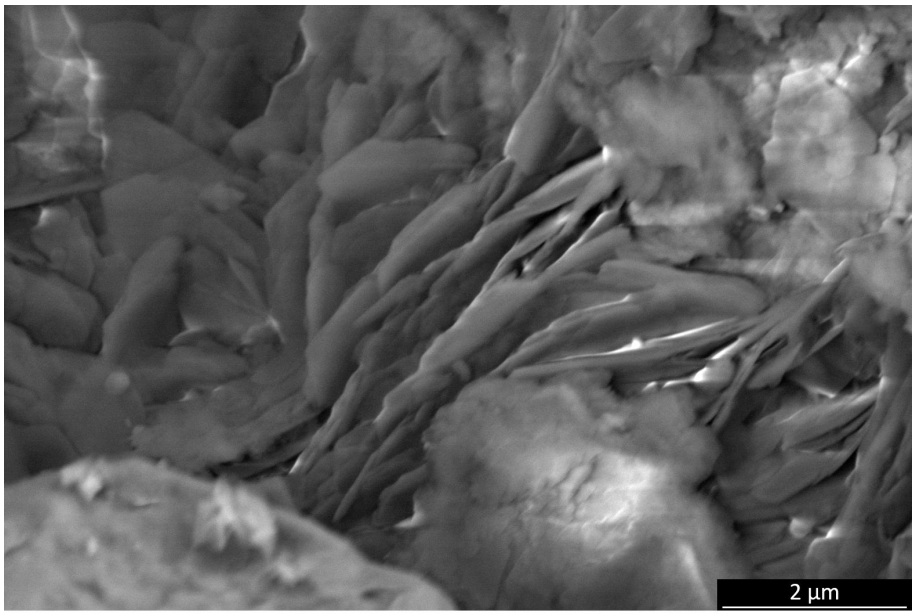



Figure 6.33: Bandera Brown 3: high magnification SEM micrograph of area 6
A high magnification low-vacuum SEM micrograph of the area labelled “6” in Figure 6.14.

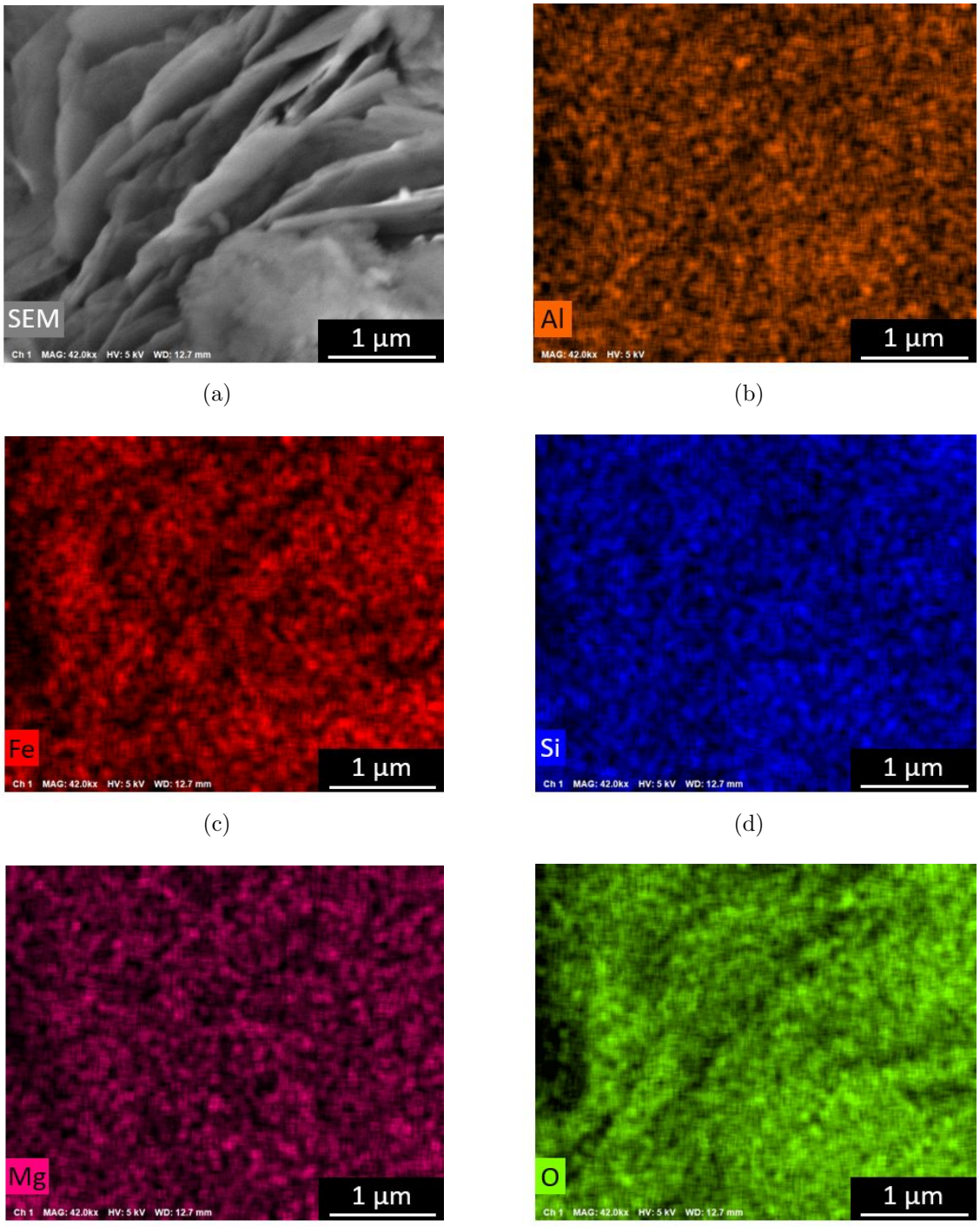



Figure 6.34: Bandera Brown 3: EDX results for area 6, part 1
EDX results for area 6 of the Bandera Brown surface shown and labelled in Figure 6.14. (a) Shows the low-vacuum SEM micrograph of the area and (b) - (f) show the Al, Fe, Si, Mg and O distribution maps for the area respectively.

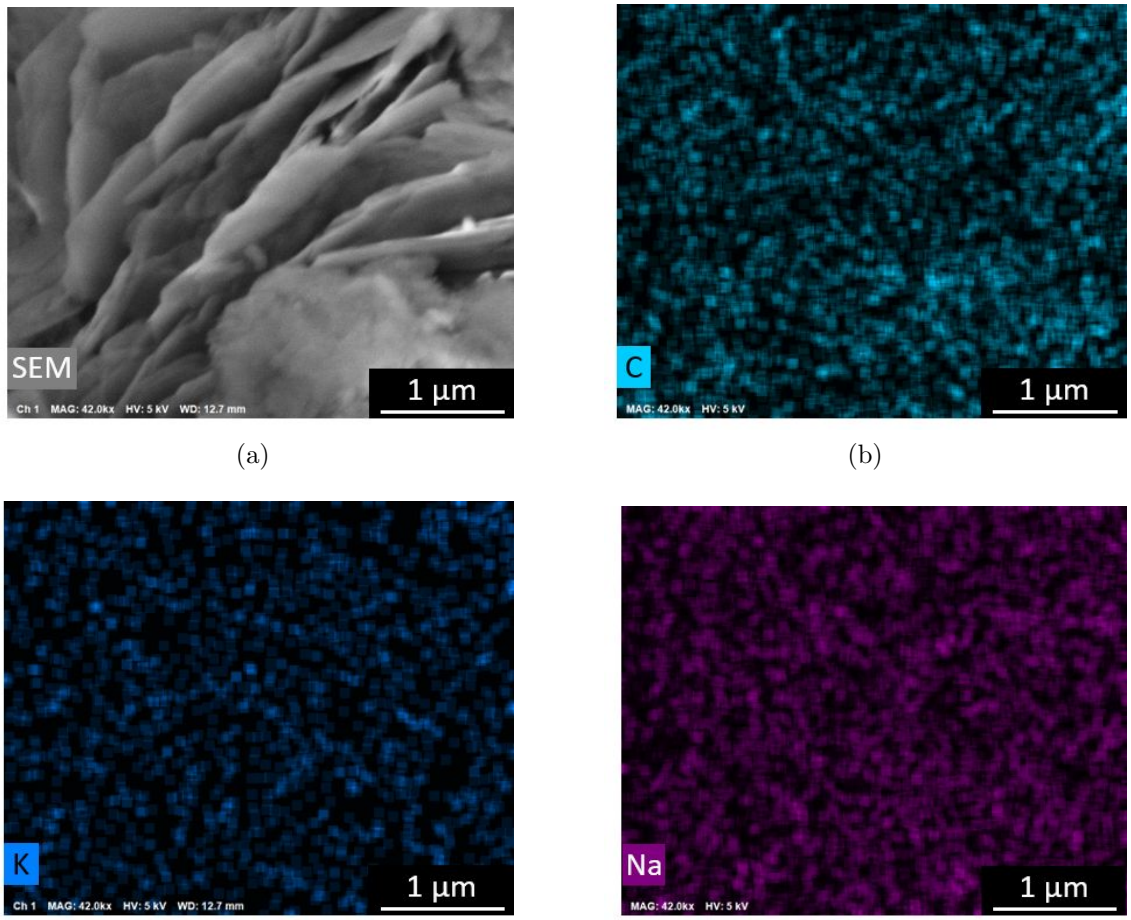



Figure 6.35: Bandera Brown 3: EDX results for area 6, part 2
EDX results for area 6 of the Bandera Brown surface shown and labelled in Figure 6.14. (a) Shows the low-vacuum SEM micrograph of the area, (b) - (d) show the C, K and Na distribution maps for the area respectively, and (e) shows the X-ray energy spectrum for the image, with element assignments labelled.

### 6.2.2 Scanning Ion Conductance Microscopy

SICM topographical imaging was carried out on Bandera Brown to determine whether a range of the minerals present could be mapped, in the same way that multiple surface types were sought from the Ketton, Estaillades and Indiana SICM maps in Chapter 3: *Carbonates*.

Figure 6.36 shows a 5 × 5 $\mu$m SICM topographical map of what appears to be a "side-on" view of vermiculite or mica sheets. Figure 6.37 shows a low-vacuum SEM micrograph of what also appears to depict vermiculite or mica in this orientation for comparison, where sheets of clay can be seen vertically protruding from the surface. Figure 6.38 shows two height profiles across the thin sheets present in the SICM image Figure 6.36. These profiles reveal that each vertical sheet in the structure is around 100 - 200 nm ± 25 nm in width and sit approximately 500 nm apart, which aligns with the thin structures observed on the SEM micrograph of what is proposed to be a vermiculite/mica structure in Figure 6.37. The gaps between the sheets in the SICM image in Figure 6.36, shown in the profiles in Figure 6.38c, and shown as a 3D representation for ease of visualisation in Figure 6.38b, were mostly recorded around 200 - 400 nm, which is not as deep as was anticipated from the low-vacuum SEM micrograph in Figure 6.37; this is possibly due to the narrow channels restricting ion transport, and as such the approach current threshold being met prematurely during SICM imaging when the nanopipette was inserted between the clay sheets.

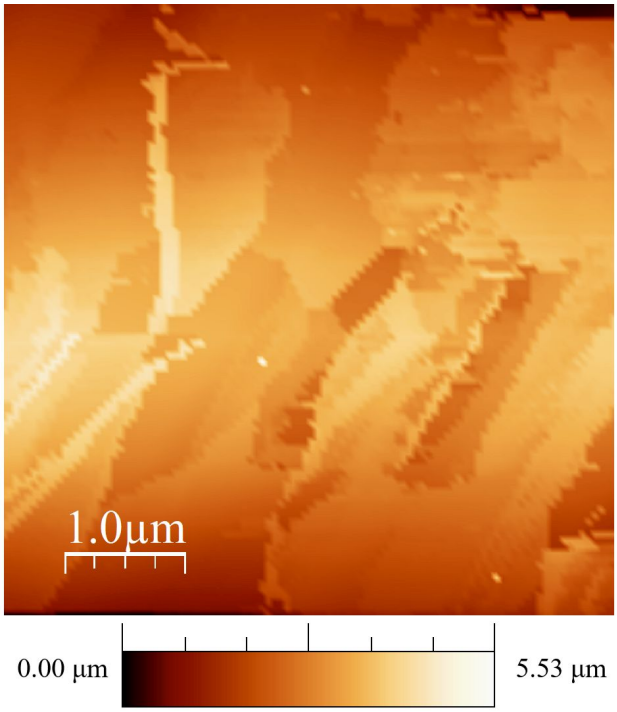



Figure 6.36: Bandera Brown: 5 × 5 $\mu$m SICM image of vermiculite/mica
A 5 × 5 $\mu$m SICM topographical image with a pixel size of 50 × 50 nm of what is proposed to be vermiculite or mica on the Bandera Brown surface. A low-vacuum SEM micrograph which was also assigned as vermiculite or mica is shown in Figure 6.37.

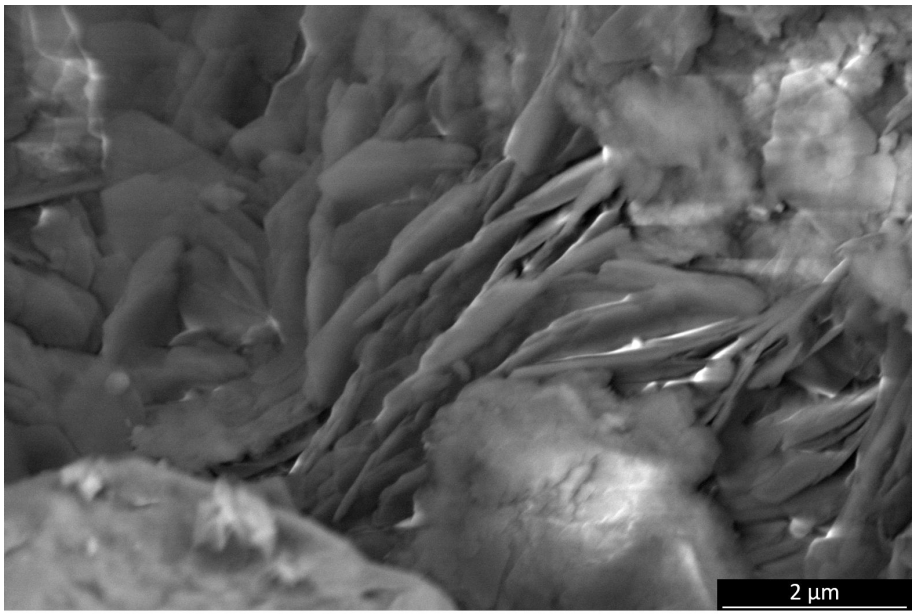
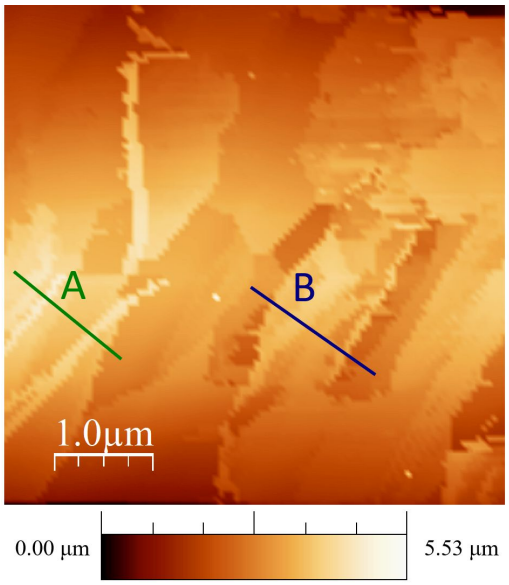
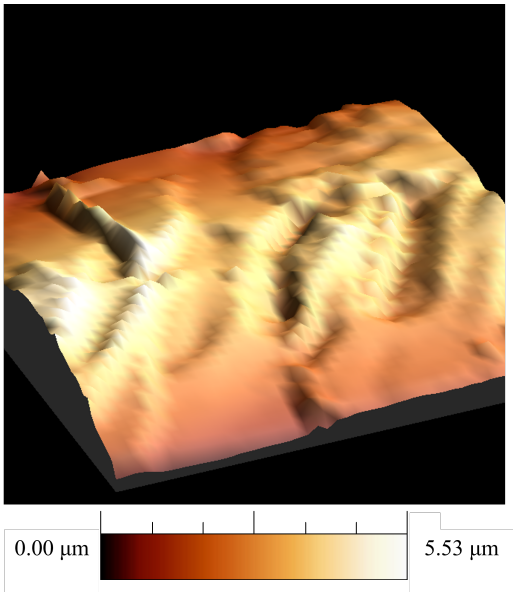


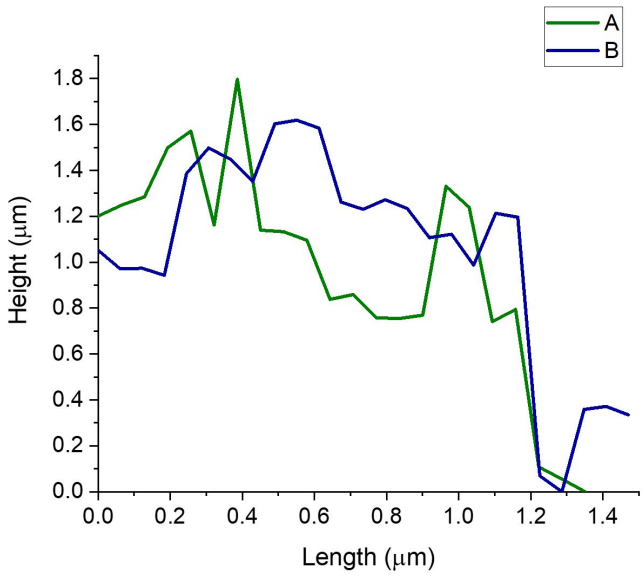

Figure 6.37: Bandera Brown: SEM micrograph of vermiculite/mica "side-on"
A high magnification low-vacuum SEM micrograph of what is proposed to be vermiculite or mica "side-on", revealing individual sheets, originally shown in Figure 6.33 on page 315.




(a)




(b)




(c)

Figure 6.38: Bandera Brown: height profiles for the SICM image in Figure 6.36 Height profiles across two sections of the SICM image shown in Figure 6.36 to shown the thickness of the vertical sheets. (a) shows the SICM image once more, with lines A and B labelled, and (c) shows a plot of the profiles along lines A and B. The same image is represented in 3D in (b) to better visualise the narrow channels between the vertical sheets.

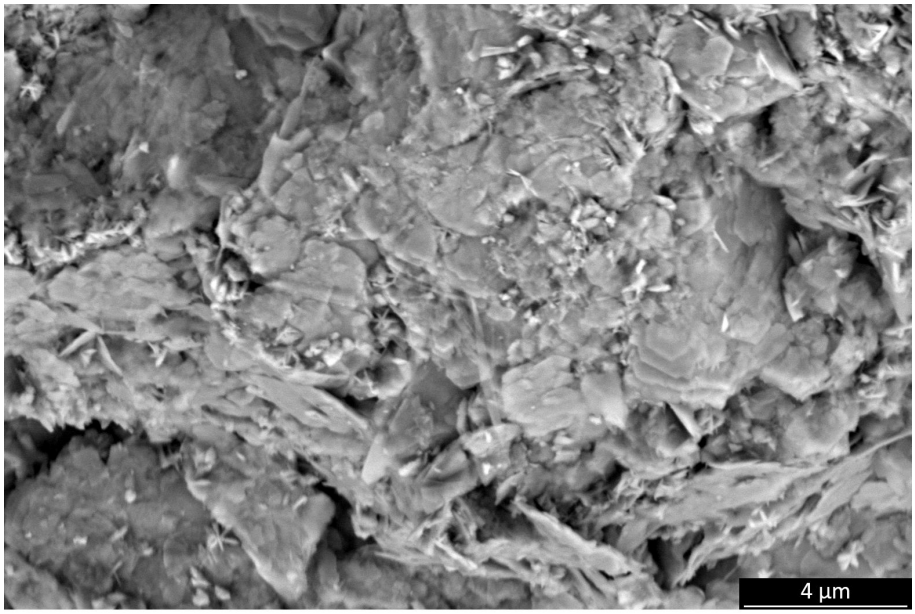



Figure 6.39: Bandera Brown: SEM micrograph of vermiculite/mica "face-on" A high magnification low-vacuum SEM micrograph of what are proposed to be vermiculite/mica sheets "face-on", originally shown in Figure 6.4 on page 287.

Figure 6.40 shows three SICM topographical images, 5.4 × 5.4 $\mu$m, 5.8 × 5.8 $\mu$m and 5 × 5 $\mu$m in size, of what are proposed to be regions of the "face-on" view of vermiculite/mica sheets, similar to what was originally shown in the low-vacuum SEM micrograph in Figure 6.4 (page 287), and re-shown in Figure 6.39 for comparison. This low-vacuum SEM micrograph shows a surface with rough-edged features each $< 1$ $\mu$m across. Similar features are visible across the three SICM topographical images in Figure 6.40, both in terms of their size and rough edges. Some "streaking" effects are observable in these images, which are hypothesised as being due to contaminants in the electrolyte. Particles in the electrolyte which are similar in size to the nanopipette opening, 20 - 40 nm, or larger, if they come into proximity of the nanopipette opening, can restrict the ion current flow sufficiently for the detection threshold to be met, causing the nanopipette to prematurely retract. It is thought that this occurred for many sequential pixels in these images, to create the

"streaking" effect. It is not known whether this contamination is due to powder from the sample which was generated during cutting and unsuccessfully removed during the sonication preparation step,[a] or whether foreign contaminants entered the electrolyte from other sources.

Figures 6.41 and 6.42 show three SICM topographical images, 10 × 10 $\mu$m, 16.4 × 16.4 $\mu$m and 6.7 × 6.7 $\mu$m in size, of two different areas proposed to contain smectite clay. The two SICM topographical images in Figure 6.41 are overlapping images of the same region, Figure 6.41a showing a higher resolution image of the area towards the bottom left corner of Figure 6.41b. A low-vacuum SEM micrograph depicting what was assigned as smectite clay originally shown in Figure 6.8 (page 290) is re-shown in Figure 6.43 for comparison. Across the SICM images in Figures 6.41 and 6.42, the protruding sheets of what are thought to be clay are angled away from each other, similarly to the structure at the center of the low-vacuum SEM micrograph in Figure 6.43. This "fanning" is in contrast to the previous "side-on" vermiculite/mica sheets in Figure 6.36, where thin, straight-edged sheets are protruding perpendicular to the surface and parallel to each other, in line with the vermiculite/mica sheets observed in the low-vacuum SEM micrograph in Figure 6.37.

As the SICM images are presented at different magnifications to the SEM micrograph, feature dimension comparison is not trivial, and so Figure 6.44 shows the images presented in Figures 6.42 and 6.43, with feature dimensions labelled of the regions proposed to be smectite clay. The measurements presented demonstrate that in both imaging methods, the observed fanned sheets themselves are around 2 $\mu$m in length; the measured sheet lengths in Figures 6.44a and 6.44b being 2.17 and

[a]see Chapter 2: *Methods*, Section 2.1.1 for further details

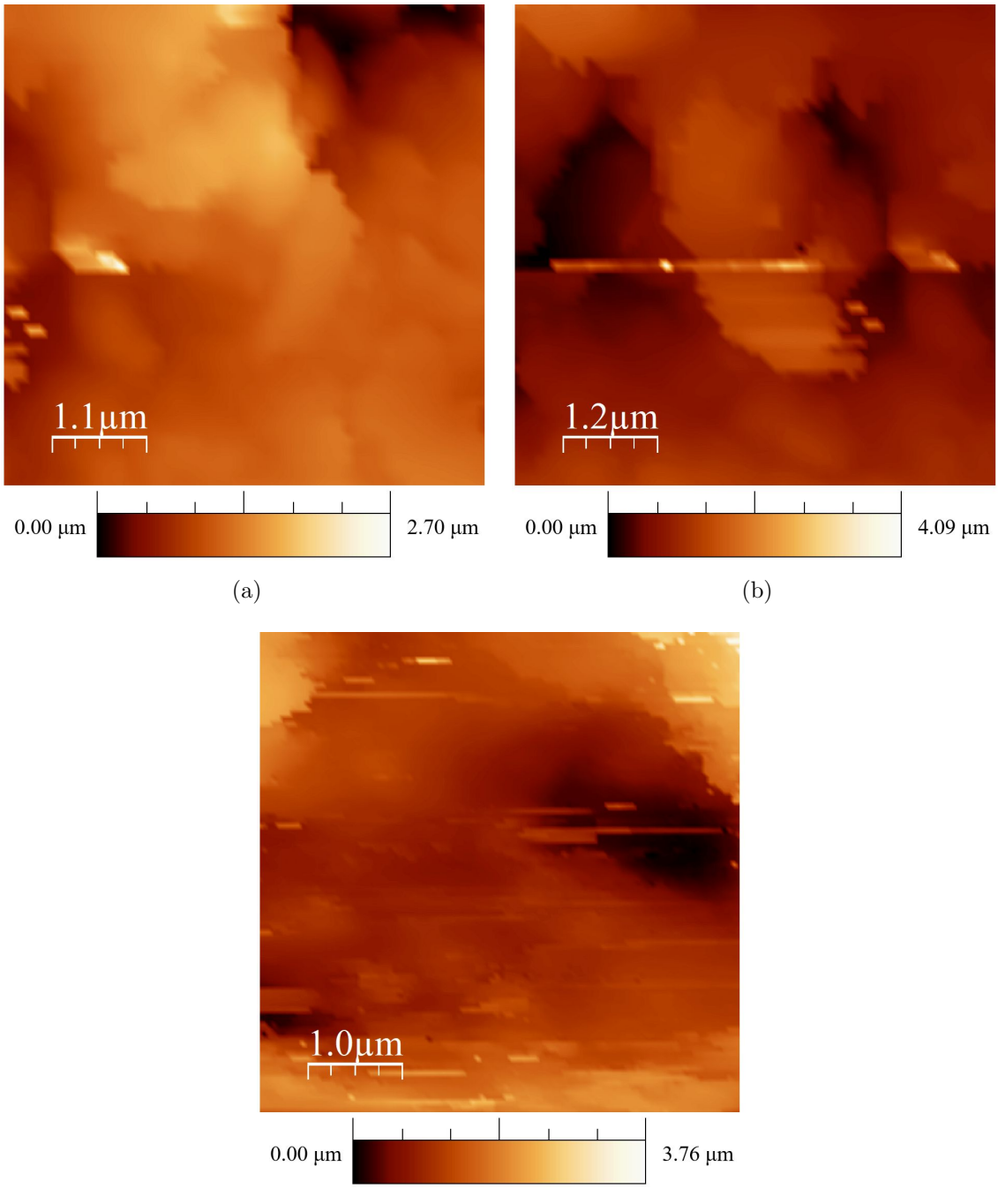



Figure 6.40: Bandera Brown: three SICM images of vermiculite/mica
Three SICM topographical images of Bandera Brown X. (a) shows a 5.4 × 5.4 $\mu$m SICM topographical image with a pixel size of 100 × 100 nm, (b) shows a 5.8 × 5.8 $\mu$m SICM topographical image with a pixel size of 100 × 100 nm and (c) shows a 5 × 5 $\mu$m SICM topographical image with a pixel size of 50 × 50 nm.

1.96 $\mu$m respectively. The edges of these sheets are separated by around 0.5 $\mu$m in both cases; the separations in Figure 6.44a being 0.58, 0.59 and 0.64 $\mu$m and those in Figure 6.44b being 0.42 and 0.46 $\mu$m. These similarities in dimension and orientation would therefore suggest that these features belong to the same mineral, proposed to be smectite clay, imaged using two different techniques.

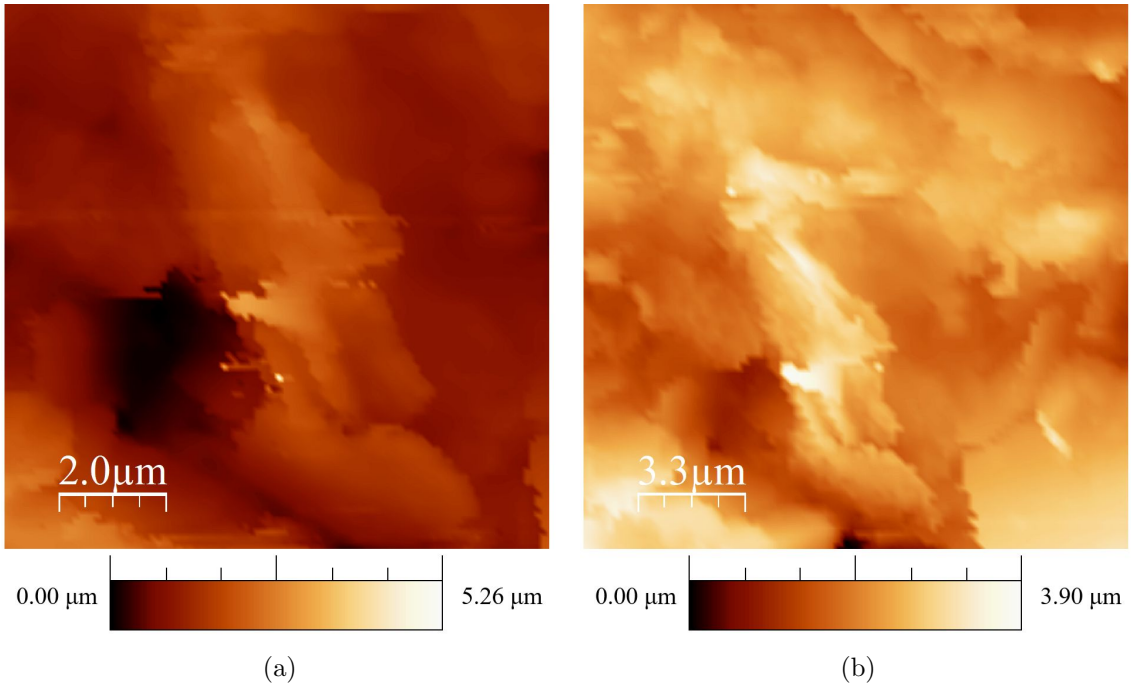



Figure 6.41: Bandera Brown: two SICM images of smectite clay
Two SICM topographical images of the same region, at different resolutions and image sizes; (a) 10 × 10 $\mu$m image with a pixel size of 100 × 100 nm and (b) 16.4 × 16.4 $\mu$m image with a pixel size of 200 × 200 nm, both of which are proposed to be smectite clay.

A final observation to note, which was made during the mapping of Bandera Brown using SICM, is that it was found that the nanopipette tip crashed more frequently during initial attempts compared to the carbonate surfaces discussed in Chapter 3: *Carbonates*. This challenge was overcome by increasing the minimum hop height between points to 5 $\mu$m for Bandera Brown scans, compared to the 3 $\mu$m minimum hop heights typically used for mapping the carbonate samples in

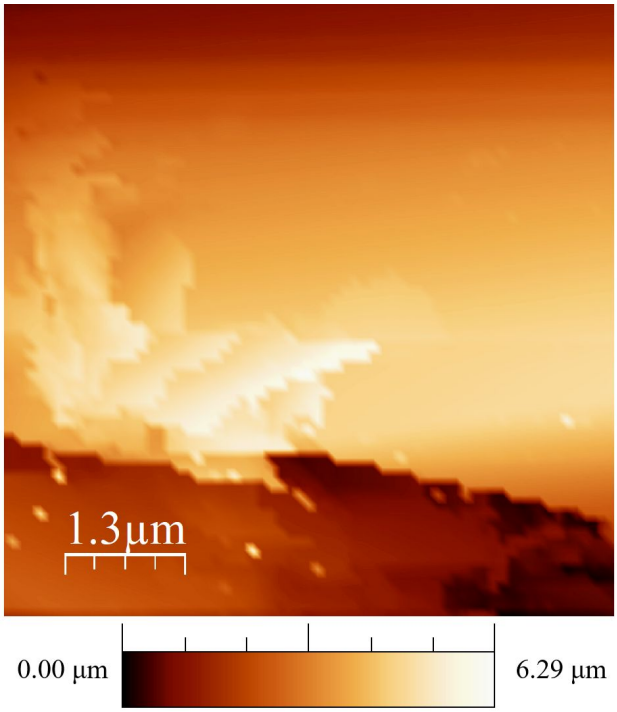



Figure 6.42: Bandera Brown: 6.7 × 6.7 $\mu$m SICM image of smectite clay
A 6.7 × 6.7 $\mu$m SICM topographical image with a pixel size of 100 × 100 nm of what is proposed to be smectite clay.

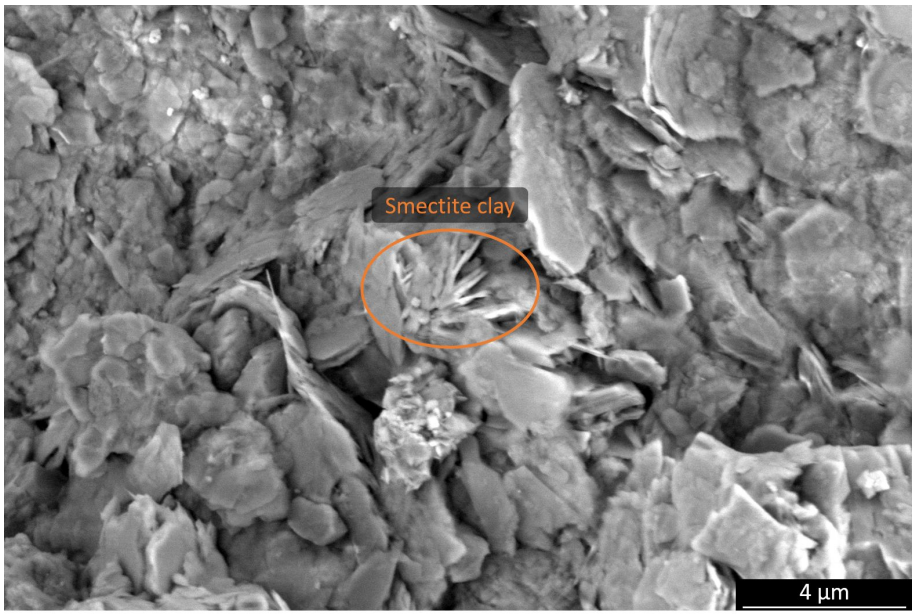
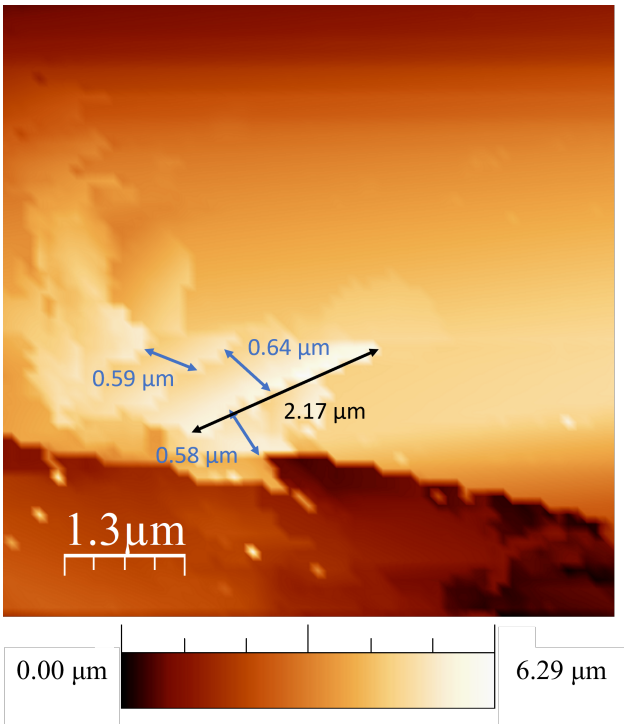
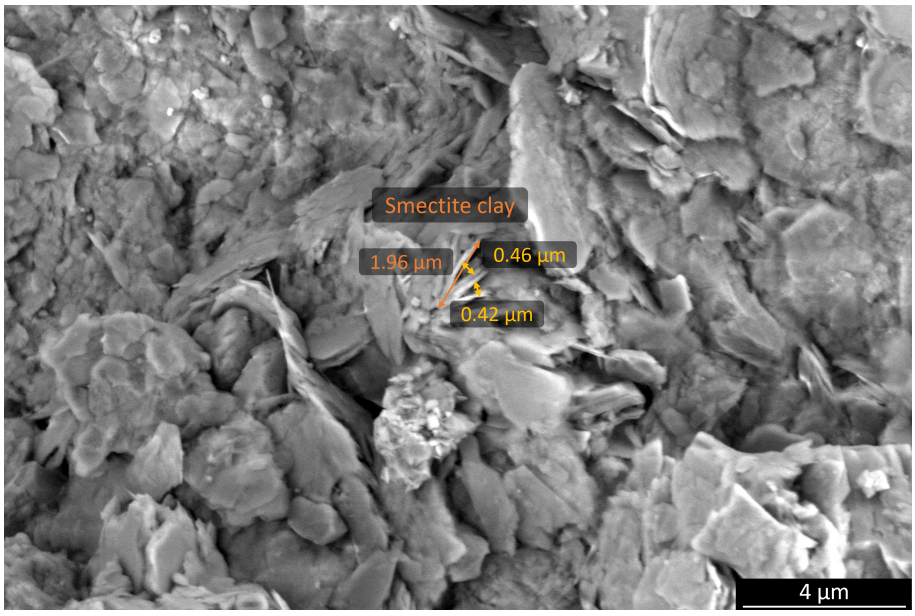



Figure 6.43: Bandera Brown: high magnification SEM micrograph of smectite
A high magnification low-vacuum SEM micrograph of what is proposed to be an area containing smectite clay, originally shown in Figure 6.8 (page 290).




(a)




(b)

Figure 6.44: Bandera Brown: Feature size comparison for smectite clay
(a) The 6.7 × 6.7 $\mu$m SICM image originally presented in Figure 6.42, and (b) the low-vacuum SEM micrograph presented in Figures 6.8 & 6.43, are both re-shown, with feature dimensions labelled of the regions proposed to be smectite clay. Black and orange labels denote the sheet lengths and blue and yellow arrows denote the sheet separation in (a) & (b) respectively.

Chapter 3: *Carbonates*. It is proposed that this increased difficulty in generating topographical maps of these samples using SICM was due to more sudden height changes in the material, possibly due to the diversity of mineral surfaces present. This increase in hop height did however come at the cost of longer imaging times; a typical SICM scan of 100 × 100 points on a carbonate outcrop rock with a 3 $\mu$m minimum hop height took around 2 hours to complete, whereas the same size scan on Bandera Brown with a 5 $\mu$m minimum hop height took closer to 3 hours to complete, and as such, fewer images could be collected in a day's session. Despite the time cost, this was deemed to be of net benefit, as the increase in hop height substantially increased the frequency of successful imaging attempts on Bandera Brown.

### 6.2.3 Summary

Overall, seven minerals were identified on the Bandera Brown surface using low-vacuum SEM: quartz, mica, vermiculite, calcite, smectite, kaolinite and hematite. Two further minerals were proposed from the simultaneous EDX measurements: albite and apatite. Of the seven minerals which were identified from morphology alone, three of these were also tentatively identified in the SICM images presented in Section 6.2.2; mica / vermiculite, which are not possible to distinguish between from morphology alone, and smectite, characterised by its vertical sheets. These identifications are summarised in Table 6.1 below.

| Mineral | Chemical Formula | Description | Feature size | SICM |
|---|---|---|---|---|
| Quartz | $SiO_2$ | Smooth-sided structure with sharp edges | $> 10$ $\mu$m | |
| Mica | $KAl_2(AlSi_3)O_{10}(OH)_2$ | Rough-edged disk-like structures of irregular shape | 1 - 2 $\mu$m | ✓ |
| Vermiculite | $M^+_{0.75}Al_2(Si_{3.25}Al_{0.75})O_{10}(OH)_2$ | | | ✓ |
| Calcite | $CaCO_3$ | Smooth-sided step-like structure with sharp edges | 50 - 90 $\mu$m | |
| Smectite | $M^+_{0.33}Al_2(Si_{3.67}Al_{0.33})O_{10}(OH)_2$ | Thin rough-edged disk-like structures of irregular shape | 1.5 - 2 $\mu$m | ✓ |
| Kaolinite | $Al_2Si_2O_5(OH)_4$ | Booklet structure; stacks of smooth-sided sheets | 3.5 - 4 $\mu$m | |
| Hematite | $Fe_2O_3$ | 6-pointed stars | $< 1$ $\mu$m | |
| Albite | $NaAlSi_3O_8$ | Rough-edged crystallite - identified from EDX | 1 $\mu$m | |
| Apatite | $Ca_5(PO_4)_3F$ | Rough-edged crystallite - identified from EDX | $< 1$ $\mu$m | |

Table 6.1: Summary of Bandera Brown minerals identified

A summary of the different minerals which were identified on the Bandera Brown surface using SEM and EDX. Descriptions and feature size estimates are based on the SEM micrographs of these minerals presented in Chapter 6: *Bandera Brown*. The $M^+$ ions in the vermiculite and smectite chemical formulae represent interlayer cations which can be $K^+$, $Mg^{2+}$ or $Ca^{2+}$, and $Mg^{2+}$ or $Ca^{2+}$ respectively. The "SICM" column denotes whether that sample type was identified in any SICM topographical images of the Bandera Brown surface; "✓" signifies that the surface type was identified in at least one SICM image and no symbol signifies that no examples of that surface type were identified.

## 6.3 Aged Bandera Brown Studies

Bandera Brown was "aged" by the same method as the carbonates in Chapter 5: *Carbonate Ageing Studies*; the clean samples were submerged in crude oil for four weeks at 70 °C, before being removed and dried for at least two days at 70 °C and lastly placed in a vacuum desiccator for at least two days to remove any volatile components prior to low-vacuum SEM imaging. As the process of imaging using the SICM appeared to alter the aged calcite sample surface (Chapter 5: *Carbonate Ageing Studies*, Section 5.3.1.2), the aged Bandera Brown sample was imaged with low-vacuum SEM both before and after SICM imaging, in order to investigate whether similar alterations occurred.

Due to the COVID-19 pandemic, the first aged Bandera Brown sample was only imaged with low-vacuum SEM, as laboratories closed before SICM imaging could be performed. Once laboratories re-opened this sample was deemed too old to continue to use for collecting comparable SICM images, and so a new sample was made. The second aged Bandera Brown sample was imaged with both low-vacuum SEM and SICM once laboratories re-opened later in 2020. All SICM images shown in Section 6.3.2 below are therefore of this second aged surface.

### 6.3.1 Low Vacuum Scanning Electron Microscopy

#### 6.3.1.1 Secondary Electron Imaging

An overlay of seven low-vacuum SEM micrographs of the first aged sample are shown in Figure 6.45; the three areas labelled 1 - 3 are shown at higher magnification in Figures 6.46 - 6.48. The area labelled 4 was selected for EDX analysis, results shown in Figure 6.53 in Section 6.3.1.2. As was the case for the aged Estaillades surfaces shown in Chapter 5: *Carbonate Ageing Studies*, it appears that the crude oil has fully coated the surface, partly obscuring the complex morphology beneath, with some of the larger features still visible. The crude oil also appears to have formed a smooth film across the surface, with raised crude oil droplets forming on top.

Area 1 shown in Figure 6.46 is itself a high-magnification section of the center of area 2, shown in Figure 6.47. This region appears to contain a large smooth-sided structure which has been fully covered with crude oil. From the low-vacuum SEM images of the unaltered Bandera Brown surfaces shown in Section 6.2.1, this could suggest that the surface in question is a quartz or calcite crystal, although it is of course not possible to say with any certainty. The crude oil film may be obscuring finer features, which prevents identification of the mineral beneath.

A low-vacuum SEM micrograph of area "3" from Figure 6.45 is shown in Figure 6.48, depicting a slightly less smooth surface than areas 1 and 2 presented in Figures 6.46 and 6.47, with a higher concentration of raised features protruding from the smooth crude oil film beneath. This could perhaps be due to a rougher surface being present underneath, the raised features being a direct reflection of the surface beneath, or a rougher surface might cause more droplets to form.

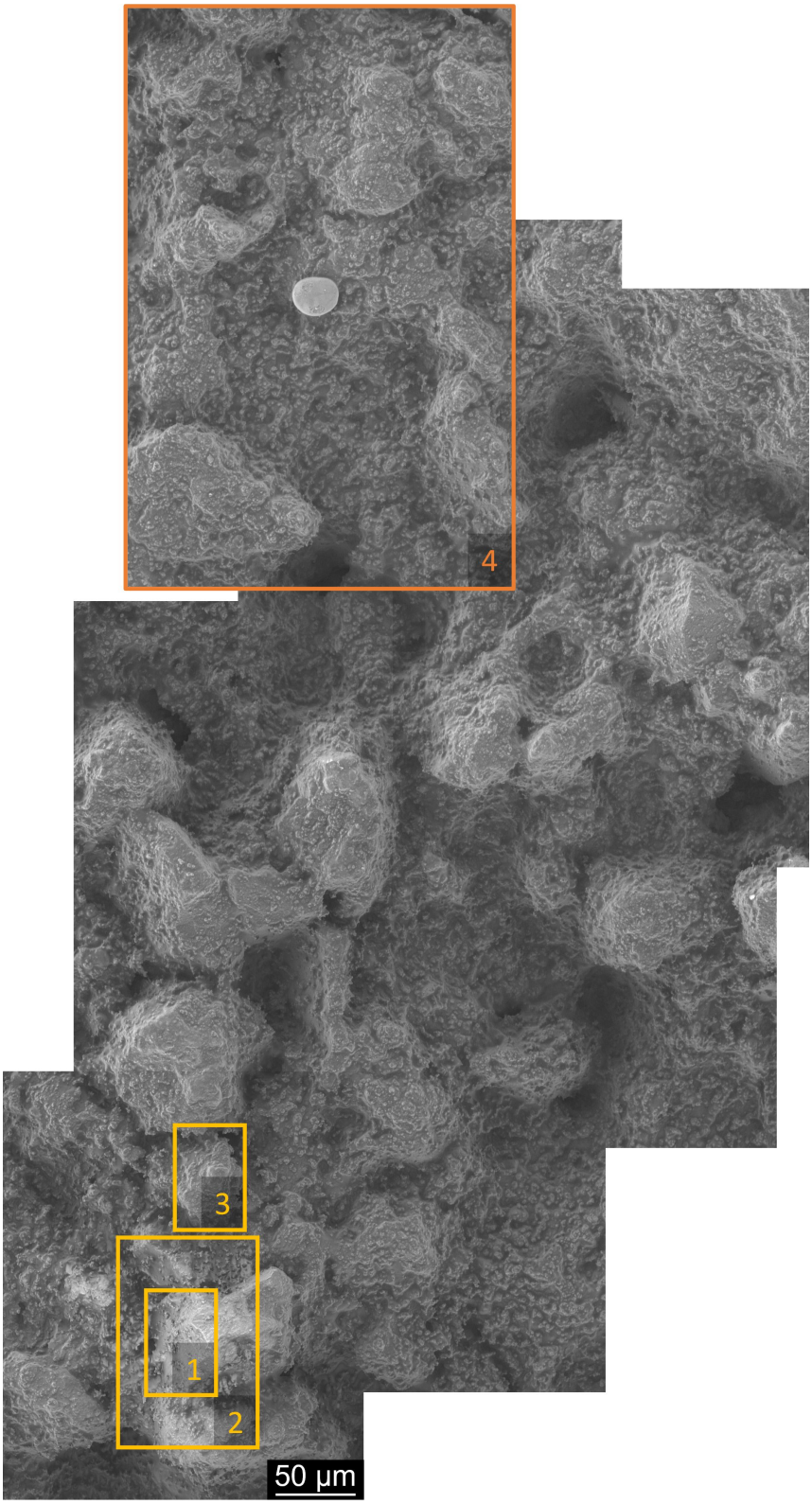



Figure 6.45: Aged Bandera Brown 1: SEM Overlay
An overlay of seven low-vacuum SEM micrographs of the first aged Bandera Brown sample. Areas highlighted in yellow and labelled 1 - 3 are shown at higher magnification in Figures 6.46 - 6.48. The area highlighted in orange and labelled 4 was selected for EDX analysis (see Figure 6.53). The seven micrographs which make up this overlay are shown individually in Appendix C, Figures C.7 - C.13.

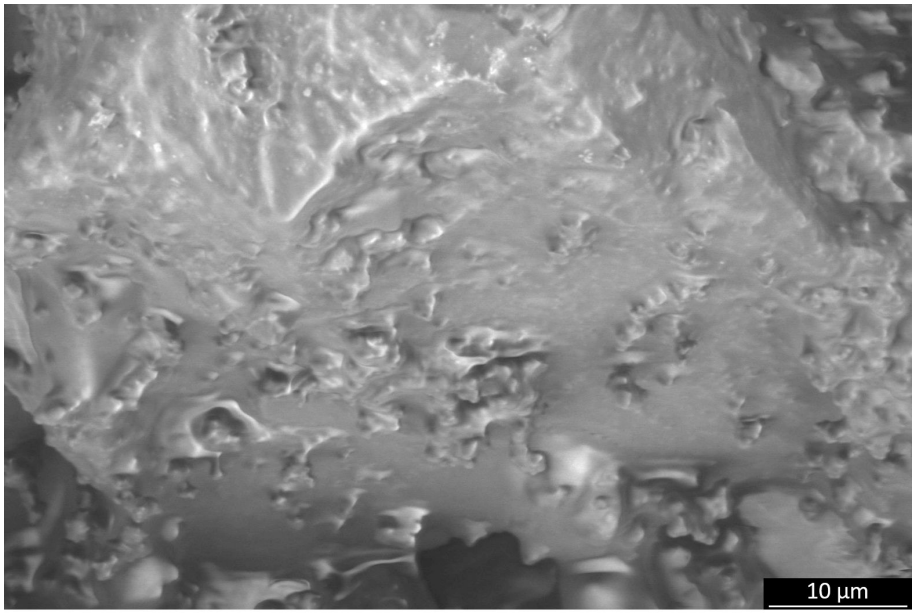



Figure 6.46: Aged Bandera Brown 1: high magnification SEM micrograph of area 1
A high magnification low-vacuum SEM micrograph of the area labelled "1" on the aged Bandera Brown surface shown in Figure 6.45.

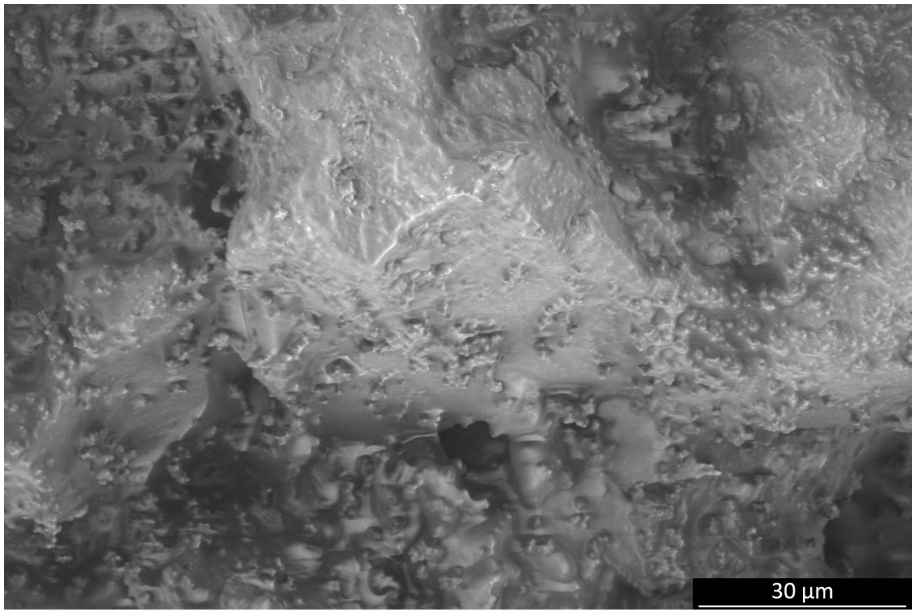



Figure 6.47: Aged Bandera Brown 1: high magnification SEM micrograph of area 2
A high magnification low-vacuum SEM micrograph of the area labelled "2" on the aged Bandera Brown surface shown in Figure 6.45.

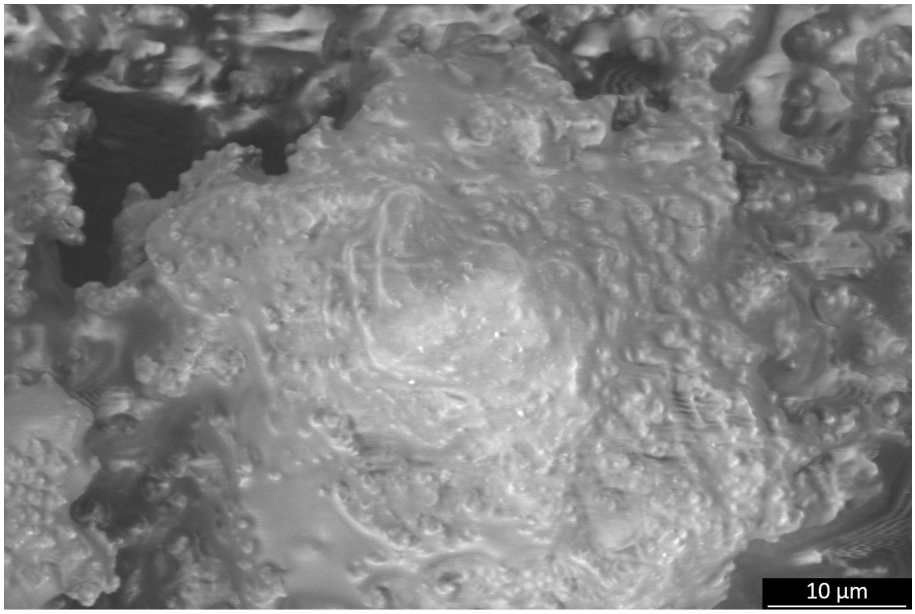



Figure 6.48: Aged Bandera Brown 1: high magnification SEM micrograph of area 3
A high magnification low-vacuum SEM micrograph of the area labelled "3" on the aged Bandera Brown surface shown in Figure 6.45.

Figure 6.49 shows a high-magnification low-vacuum SEM micrograph of a section of the aged Bandera Brown surface outside of the area shown in Figure 6.45, which is dubbed area "5". Both raised sections and small recessed regions in the crude oil film can be seen in this micrograph. It is possible that these recessed regions are a reflection of the topology of the rock underneath, and as such reflect a dent in the Bandera Brown surface. It is also possible that these recessed areas represent areas of localised de-wetting of the substrate by the crude oil film, which would possibly be reflective of the chemical or topographical heterogeneity of the Bandera Brown surface beneath. In some instances these recesses/dents are separate from the raised droplets, whereas in some cases the recesses form structures akin to moats around the crude oil droplets. An example of each of these two cases is picked out and labelled in Figure 6.50.

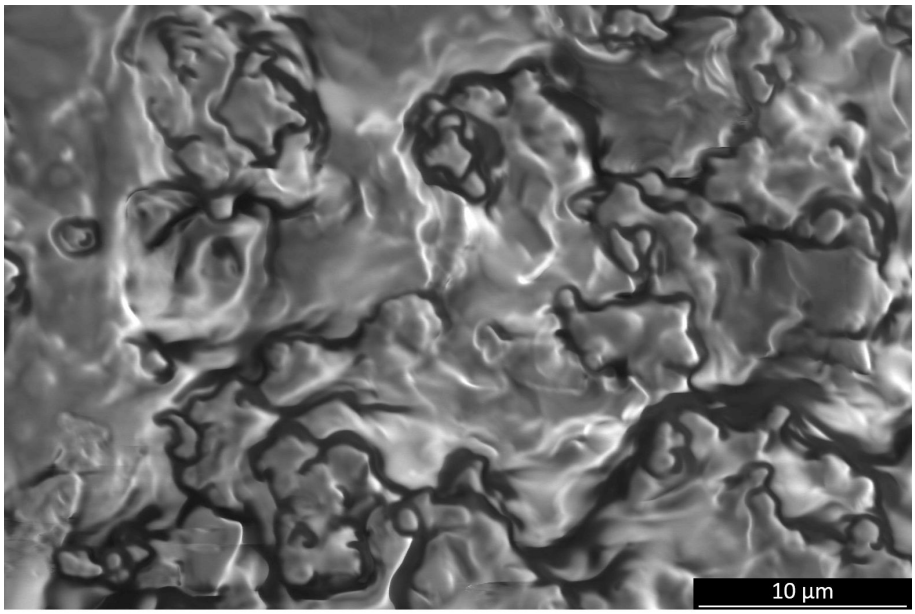



Figure 6.49: Aged Bandera Brown 1: high magnification SEM micrograph of area 5
A high magnification low-vacuum SEM micrograph of a section of the aged Bandera Brown surface outside of the region depicted by the overlay shown in Figure 6.45.

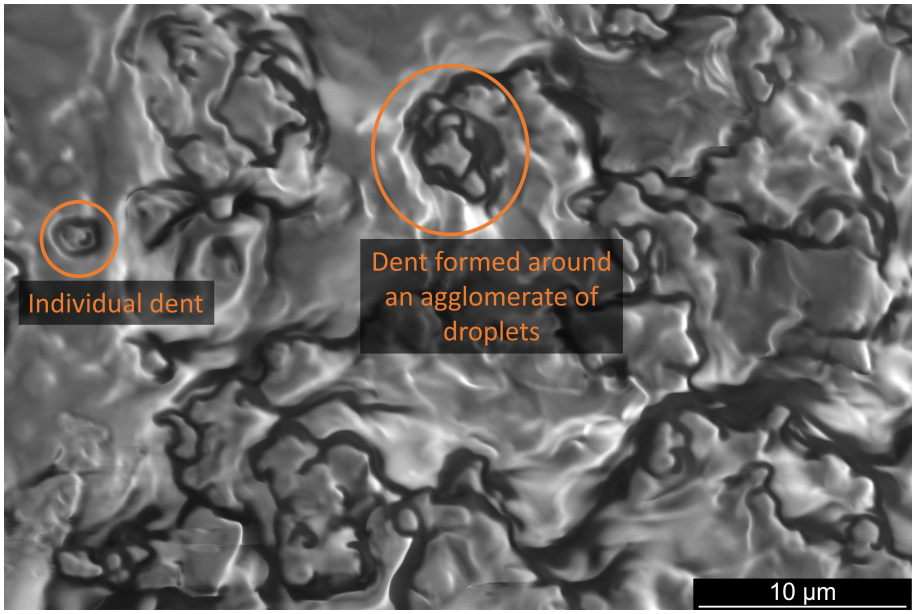



Figure 6.50: Aged Bandera Brown 1: SEM micrograph of area 5 with labels
The high magnification low-vacuum SEM micrograph from Figure 6.49 with different dent types labelled.

The overlay of four low-vacuum SEM micrographs shown in Figure 6.51 is of the second aged Bandera Brown sample. Comparison with the first sample's aged surface shown in Figure 6.45, shows good agreement, indicating that the ageing protocol used is reasonably reproducible on this outcrop rock. The surface appears once more to be entirely covered with a smooth crude oil film, with raised crude oil droplets on top. The bulkier topology with features tens of micrometres across is still visible, but the finer topology underneath is obscured by the film. This surface was later investigated using SICM, results from which are shown in Section 6.3.2.

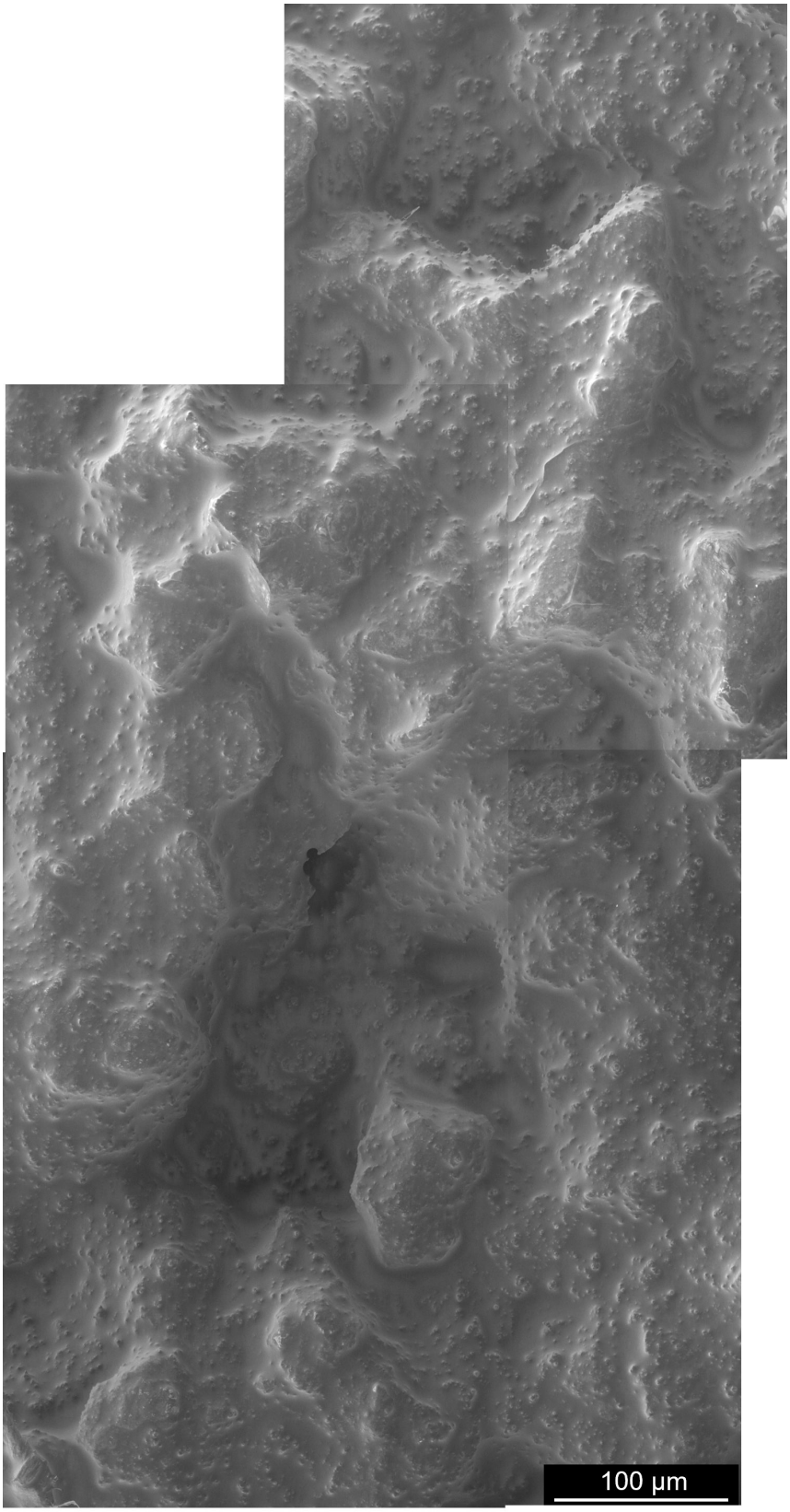



Figure 6.51: Aged Bandera Brown 2: SEM Overlay
An overlay of four low-vacuum SEM micrographs of the second aged Bandera Brown sample. The four micrographs which make up this overlay are shown individually in Appendix C, Figures C.14 - C.17.

#### 6.3.1.2 Energy-Dispersive X-Ray Spectroscopy

EDX was carried out on the area labelled "4" in Figure 6.45, results from which are shown in Figure 6.53 below. As was the case for the aged Estaillades and calcite samples in Chapter 5: *Carbonate Ageing Studies*, the crude oil appears to have fully covered the Bandera Brown surface. An EDX spectrum of the bare Bandera Brown surface is shown in Figure 6.52; when compared to the EDX spectrum for the aged surface shown in Figure 6.53d, it can be seen that the minerals present on the bare surface are completely obscured, from the absence of any Fe, Na, Mg, Al, Si or K peaks. The only elements visible on the aged surface are N and O, suggesting that the crude oil film is at least on the order of $\mu$ms thick, as X-rays detected during EDX scans can typically permeate up to 2 $\mu$m through a sample.[83]

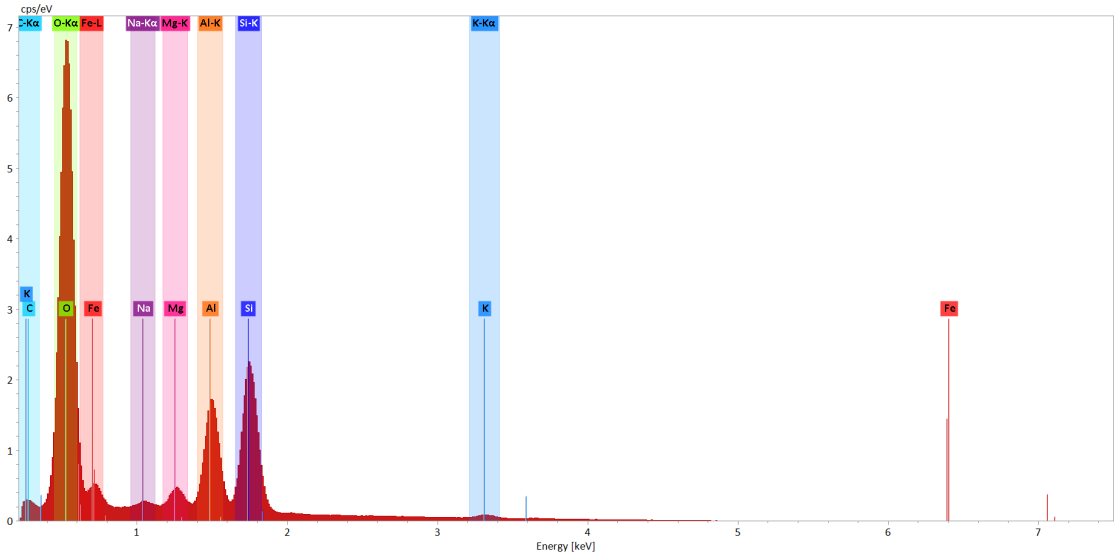
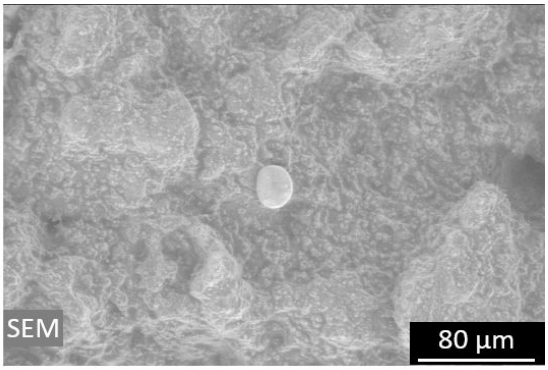
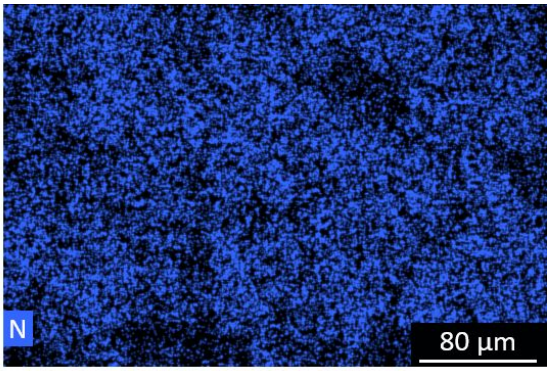


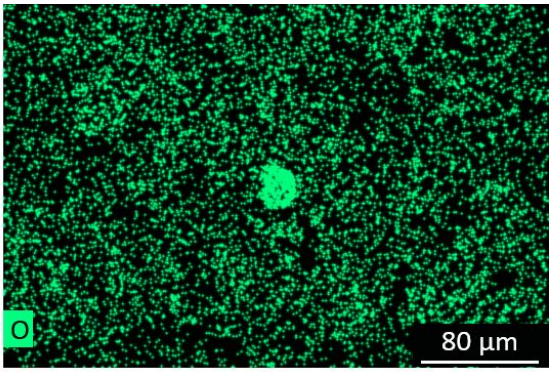

Figure 6.52: Bandera Brown: example of an unaltered Bandera Brown EDX spectrum The EDX spectrum originally shown in Figure 6.17e on page 298 for area 1 of the Bandera Brown surface shown in Figure 6.14 (page 295), for comparison with the spectrum shown in Figure 6.53d.



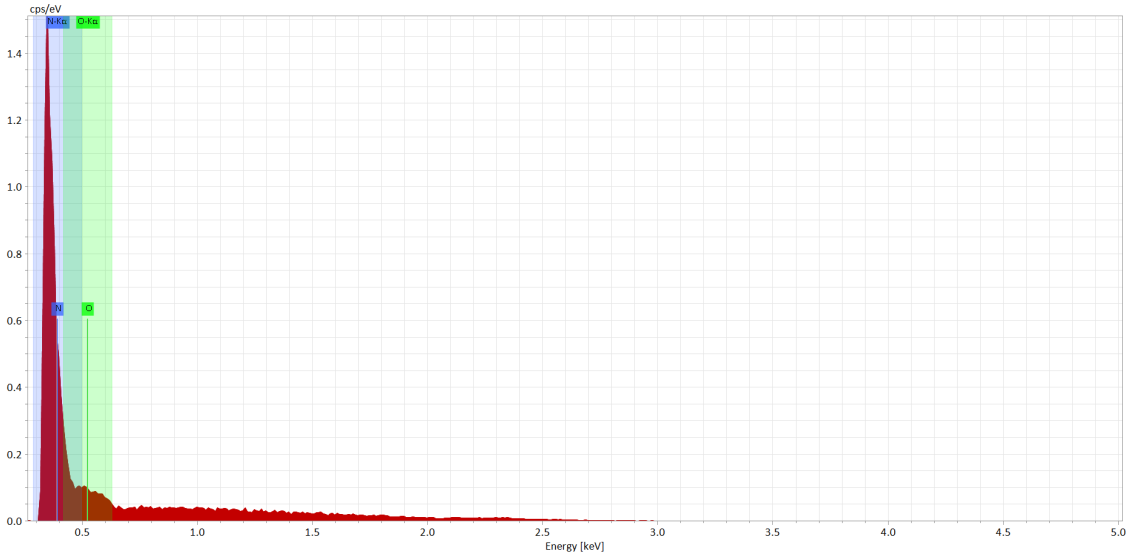

(a)




(b)




(c)




(d)

Figure 6.53: Aged Bandera Brown 1: EDX results for area 4
EDX results for area 4 of the Bandera Brown surface shown and labelled in 6.45. (a) Shows the low-vacuum SEM micrograph of the area, (b) and (c) show the N and O distribution maps for the area respectively, and (d) shows the X-ray energy spectrum for the image, with element assignments labelled.

### 6.3.2 Scanning Ion Conductance Microscopy

Obtaining SICM topographical images of the aged Bandera Brown surface proved challenging, similarly to the studies on the aged calcite and Estaillades samples described in Chapter 5: *Carbonate Ageing Studies*. The SICM images which were obtained have a blurred quality, and the nanopipette became blocked more frequently than when mapping the unaltered surfaces. Sections of the crude oil film also appeared to be damaged upon visual inspection of the sample after imaging. To explain these three observations, as for the Estaillades and calcite samples in Chapter 5: *Carbonate Ageing Studies*, it is proposed that the crude oil was partially removed by the 0.1 M $KCl_{(aq)}$ electrolyte during imaging. Due to the more frequent nanopipette blockages, not many images were successfully obtained; two images of the aged Bandera Brown sample were collected using SICM and are shown below in Figures 6.54 and 6.55a.

The aged Bandera Brown surface in Figure 6.54 appears to show a reasonably smooth section of the Bandera Brown surface, with a raised droplet in the top right hand corner which is at least 0.5 $\mu$m across. As the field of view is only 2.8 $\times$ 2.8 $\mu$m, no other features are visible. The second SICM topographical image of the aged Bandera Brown surface in Figure 6.55 shows a wider field of view of 10 $\times$ 10 $\mu$m, and appears to show a surface with numerous crude oil droplets visible. Lines across some of the features are labelled A-C on Figure 6.55b, height profiles along which can be found in Figure 6.56.

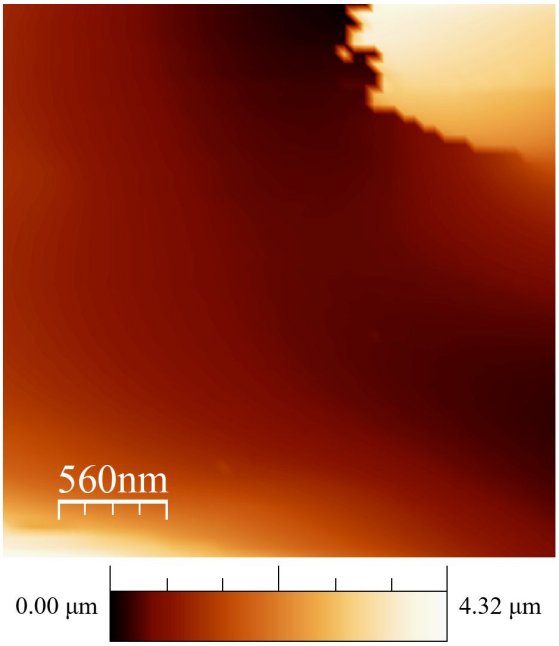
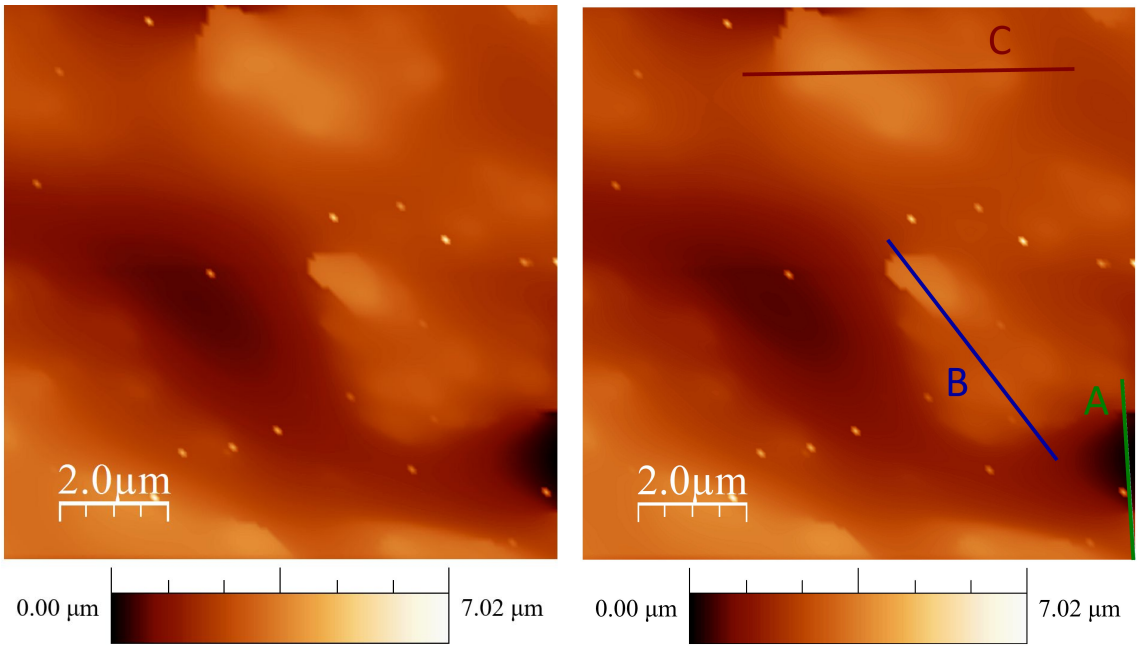
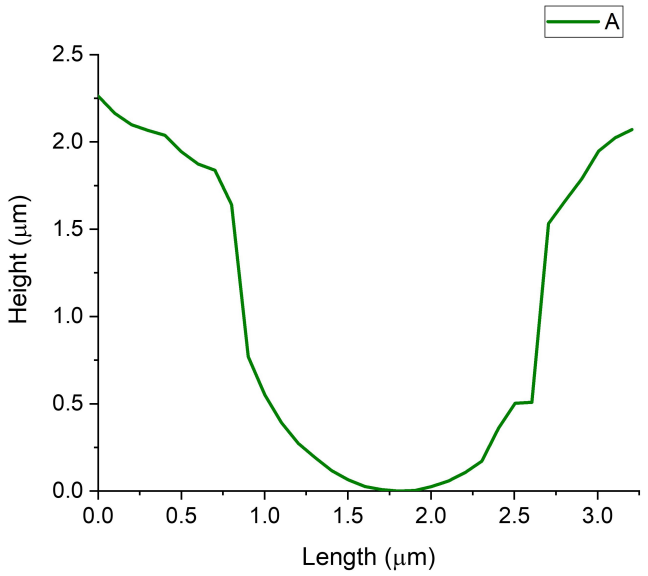



Figure 6.54: Aged Bandera Brown: 2.8 × 2.8 $\mu$m SICM image
A 2.8 × 2.8 $\mu$m SICM topographical image of the aged Bandera Brown surface with a pixel size of 50 × 50 nm.

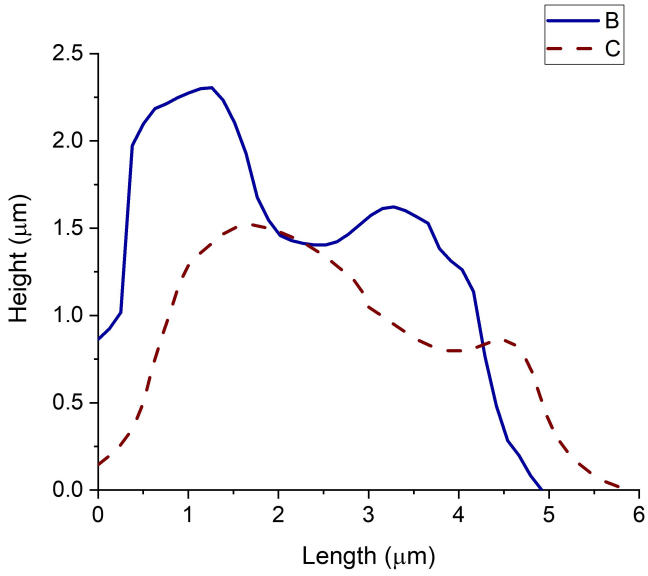



(a) (b)

Figure 6.55: Aged Bandera Brown: 10 × 10 $\mu$m SICM image
A 10 × 10 $\mu$m SICM topographical image of the aged Bandera Brown surface with a pixel size of 100 × 100 nm. (a) shows the image and (b) shows the image with three lines A-C labelled. Height profiles along A-C are shown in Figure 6.56.




(a)




(b)

Figure 6.56: Aged Bandera Brown: Height profiles for the SICM image in Figure 6.55b Height profiles along the lines marked in Figure 6.55b. (a) shows the height profile for line A and (b) shows the height profiles for lines B and C.

Line A crosses a dent in the surface which as can be seen from the profile along it in Figure 6.56a is approximately 2 $\mu$m across. Lines B and C in Figure 6.55b both cross multiple crude oil droplets, the height profiles along which are shown in Figure 6.56b. Both peaks along line B are approximately 2 $\mu$m across. The second peak shows a shoulder on the right hand side, which is proposed to be a partly-obscured droplet sitting beneath the more raised droplet on the left. This second peak is therefore proposed to be an approximately 1 $\mu$m droplet sat on top of a second droplet of unknown diameter. Profile C features a larger droplet approximately 2.5 $\mu$m across with a second smaller droplet approximately 1 $\mu$m across. These droplet and dent sizes align with what was observed in the low-vacuum SEM micrographs, so it is proposed that despite the interference from the crude oil coming off the surface into solution, this is a real image of the surface. The low-vacuum SEM micrograph previously shown in Figure 6.49 (page 334) is shown in Figure 6.57 with a number of droplets and a dent highlighted with approximate measurements alongside. The dent shown on this SEM micrograph is approximately 2.4 $\mu$m across, whilst the raised droplets are in the range of 1.0 - 2.5 $\mu$m across, which compares well with the SICM micrograph in Figure 6.55a where the dent measures approximately 2 $\mu$m across, and the raised droplets measure between 1 - 2.5 $\mu$m across.

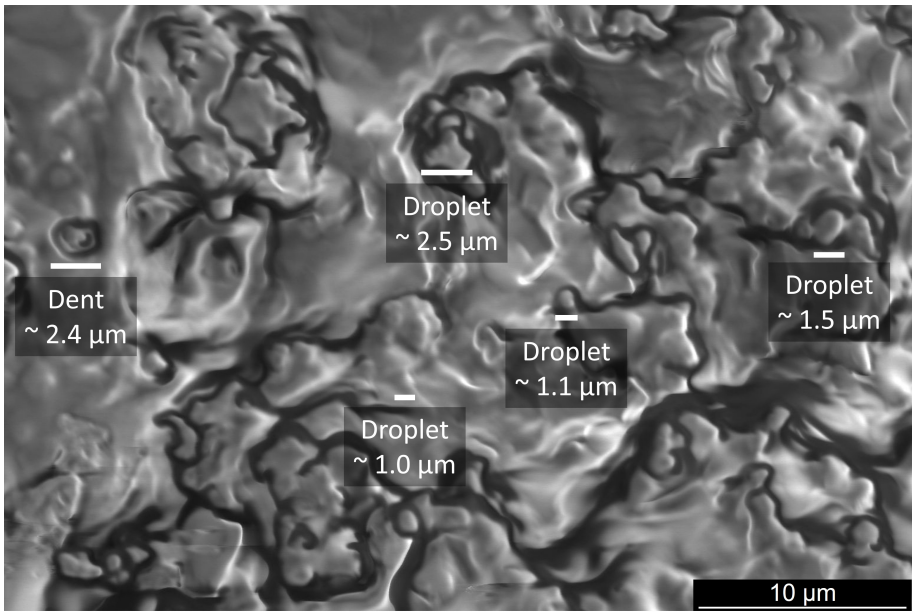



Figure 6.57: Aged Bandera Brown: SEM micrograph with measurements
The high magnification low-vacuum SEM micrograph previously shown in Figure 6.49 with a number of droplets and a dent highlighted, with approximate widths given. For comparison with the feature widths observed in Figure 6.56 for the SICM image in Figure 6.55.

### 6.3.3 Post-Ageing, post-SICM Low Vacuum SEM Studies

Gaps in the crude oil film were observed upon visual inspection of the aged Bandera Brown sample after SICM imaging, which when combined with the blurring of the SICM images, possibly indicated that the crude oil film had been altered. The aged Bandera Brown sample was therefore imaged once more using low-vacuum SEM, in combination with EDX, to elucidate the nature of this alteration.

An overlay of three low-vacuum SEM micrographs of the aged Bandera Brown surface after SICM imaging is shown below in Figure 6.58. The areas labelled 1 - 3 are shown at higher magnification in Figures 6.59, 6.62 and 6.65 respectively, and were also selected for EDX mapping. This wider area captures evidence that the crude oil film still largely remains, with the crude oil droplets previously observed on the freshly aged sample still visible across the sample surface, the majority of the Bandera Brown surface remaining obscured.

Areas 1 - 3 were selected for further investigation, as upon visual inspection, prior to any EDX mapping, they appeared to be examples of where the Bandera Brown surface might have been revealed during SICM imaging. These three areas each have sharp-edged, smooth sided structures protruding from regions with little crude oil droplet coverage. However, it is unclear from these images alone whether the surface has been fully revealed, whether the crude oil film has perhaps thinned to reflect the topology beneath, or whether simply the crude oil droplets have been removed, with the majority of the smooth crude oil film underneath left intact. Due to this uncertainty, EDX mapping was performed on all three areas to help elucidate the nature of these alterations.

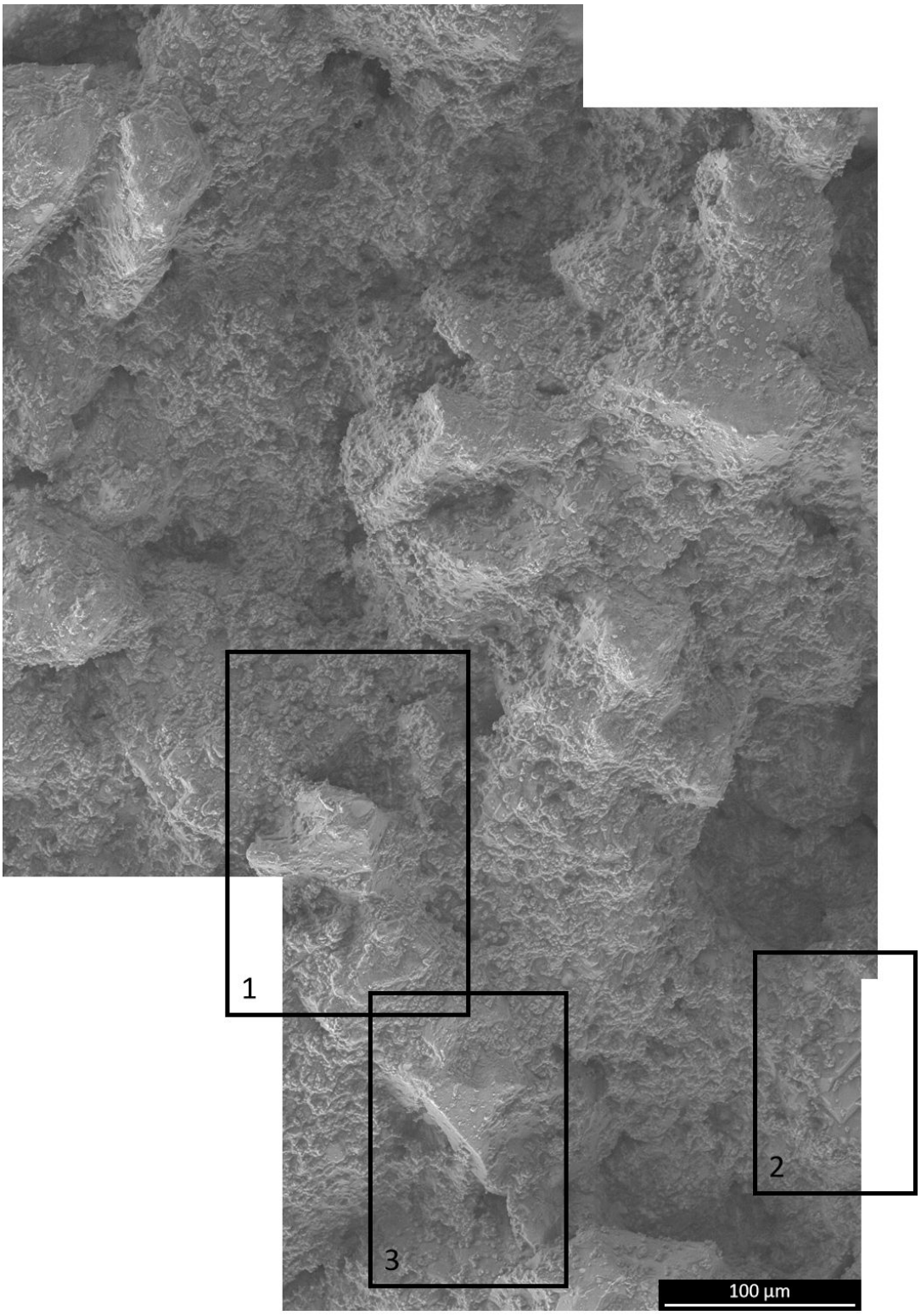



Figure 6.58: Aged Bandera Brown post-SICM: SEM Overlay
An overlay of three low-vacuum SEM micrographs of the aged Bandera Brown post-SICM surface. Labelled boxes indicated the regions which were further analysed with EDX, which are shown at higher magnification in Figures 6.59, 6.62 and 6.65. The individual micrographs which make up this overlay can be found in Appendix C, Figures C.18 - C.20.

The EDX results for areas 1 - 3 of the aged Bandera Brown post SICM surfaces as defined in Figure 6.58 are shown in Figures 6.60 and 6.61, 6.63 and 6.64, and 6.67 6.66 for areas 1, 2 and 3 respectively. In each of the three EDX spectra in Figures 6.61, 6.64 and 6.66, in addition to the N and O peaks which were observed in the freshly aged Bandera Brown spectrum (Figure 6.53, page 338), Si and S peaks can also be observed.

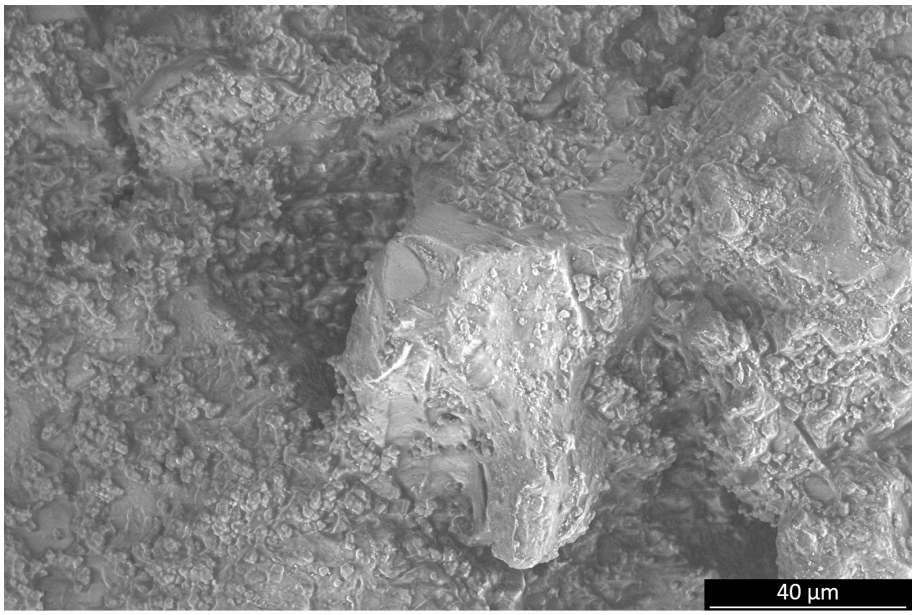
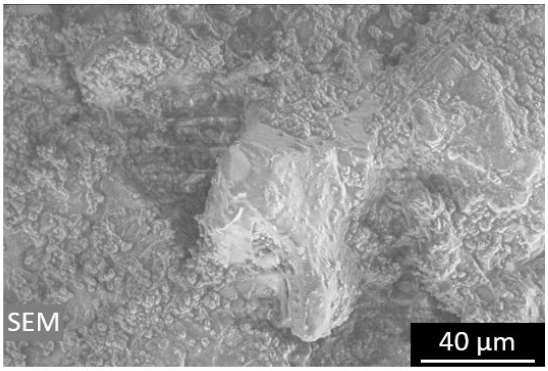
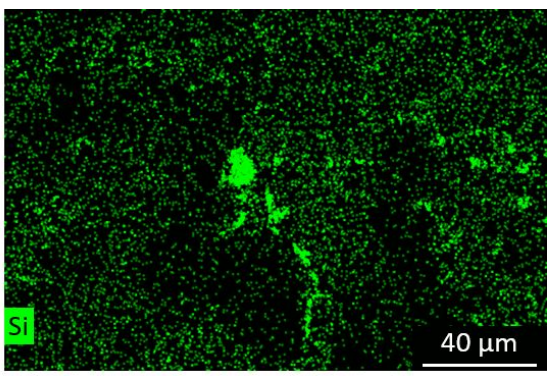



Figure 6.59: Aged Bandera Brown post-SICM: SEM micrograph of area 1
A high magnification low-vacuum SEM micrograph of the area labelled "1" in Figure 6.58.

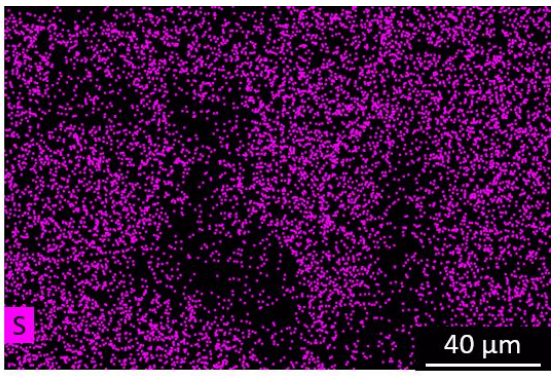
The Si's presence in the spectra could indicate that the Bandera Brown's surface is either being partly exposed, or that the crude oil film is thinning to $< 2$ $\mu$m thick, allowing the detectors to pick up this new signal from the rock beneath.[83] Looking at the Si distribution maps for areas 1 and 2 in Figures 6.60b and 6.63b, the Si distribution is not uniform; the higher concentration areas likely indicate where the surface is either fully exposed, or where the crude oil film is at its thinnest. These regions with higher Si concentrations on areas 1 and 2 correlate with regions of higher



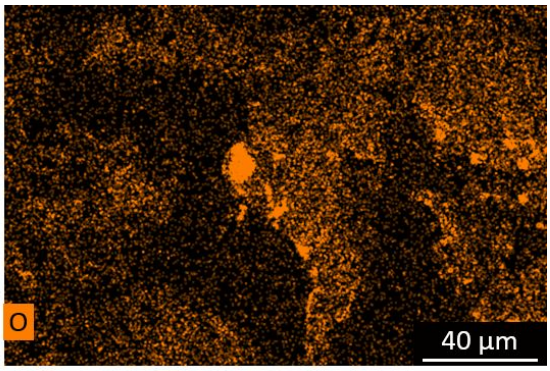

(a)



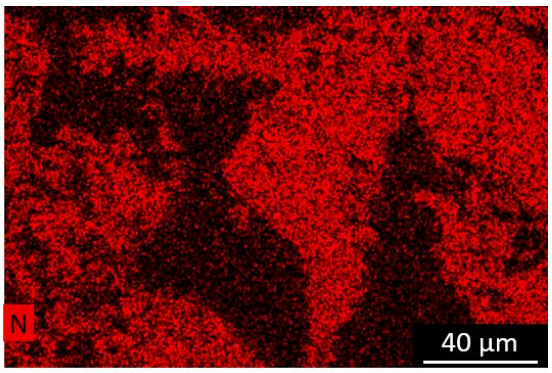

(b)




(c)

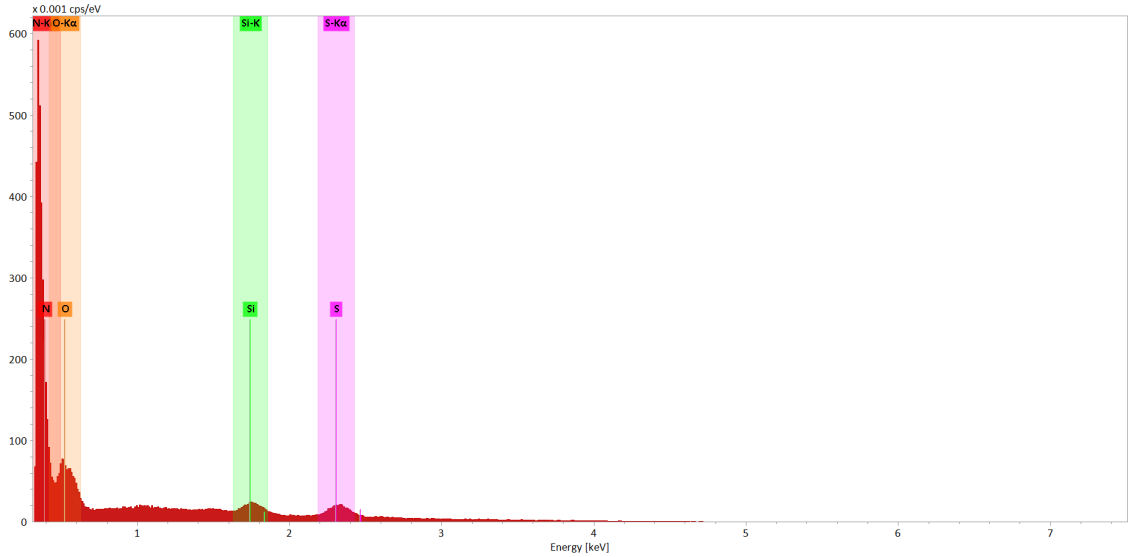



(d)




(e)

Figure 6.60: Aged Bandera Brown post-SICM: EDX element maps for area 1
EDX results for area 1 of the Aged Bandera Brown post-SICM surface shown and labelled in 6.58. (a) Shows the low-vacuum SEM micrograph of the area and (b) - (e) show the Si, S, O and N distribution maps for the area respectively.




(a)

Figure 6.61: Aged Bandera Brown post-SICM: EDX X-ray energy spectrum for area 1 The X-ray energy spectrum for the EDX results in Figure 6.60, with element assignments labelled.

O concentration (Figures 6.60d and 6.63d), which is perhaps indicative of quartz close to the surface. For area 1, these high Si and O concentration regions correlate with what appears to be the most elevated section of the surface, possibly suggesting that the crude oil film is being removed from the most exposed regions first. On area 2, these regions of high Si and O concentrations are seemingly "random" and do not appear to correlate with any significant features in the SEM.

Given this apparent thinning or detachment of the crude oil film, the lack of any Na, Mg or Al signal is peculiar, suggesting that the crude oil film is not thinning evenly across all minerals on the Bandera Brown surface. The exposure of exclusively Si- and O-bearing surfaces, possibly quartz, could suggest that these surfaces are the most water-wet, as the crude oil has been most readily displaced from them. Quartz has been shown in the literature to exhibit both water-wet and oil-wet behaviours depending on pH, temperature and crude oil composition, so it is possible that the

conditions in the experiments performed here lead to a water-wet state on the quartz surfaces, causing them to be more readily exposed by the 0.1 M $KCl_{(aq)}$ electrolyte than the other minerals present on the Bandera Brown surface.[174]

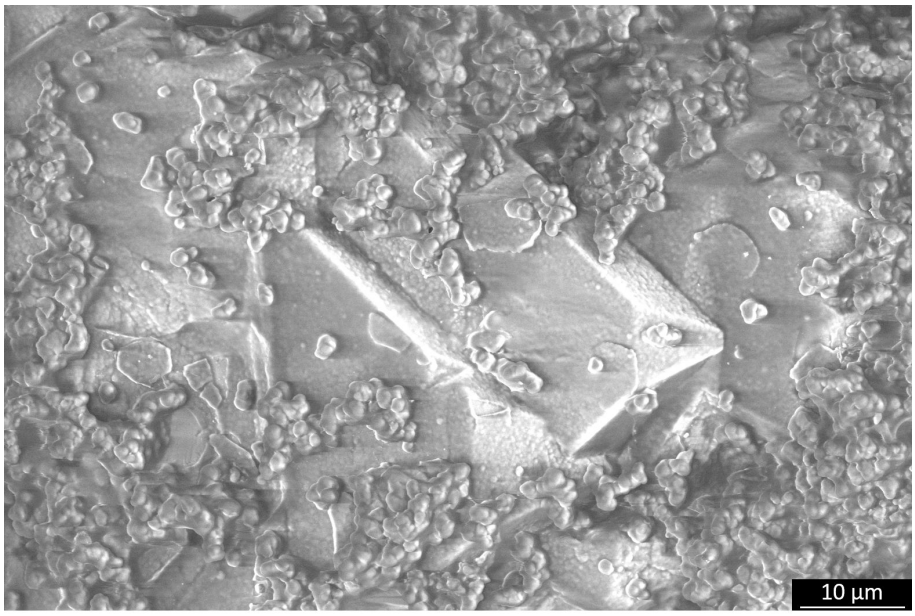
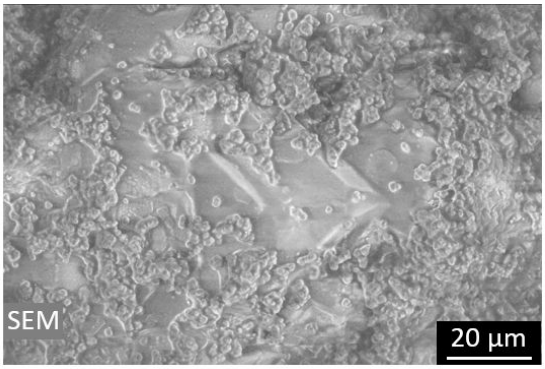
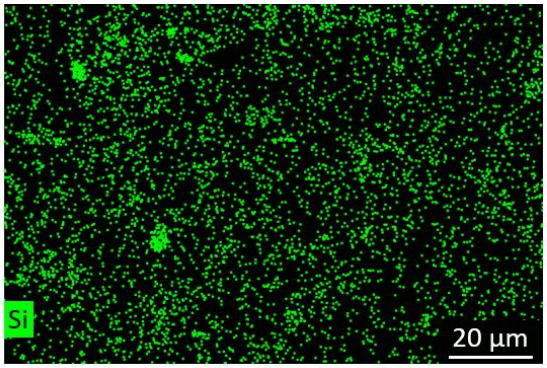



Figure 6.62: Aged Bandera Brown post-SICM: SEM micrograph of area 2
A high magnification low-vacuum SEM micrograph of the area labelled "2" in Figure 6.58.

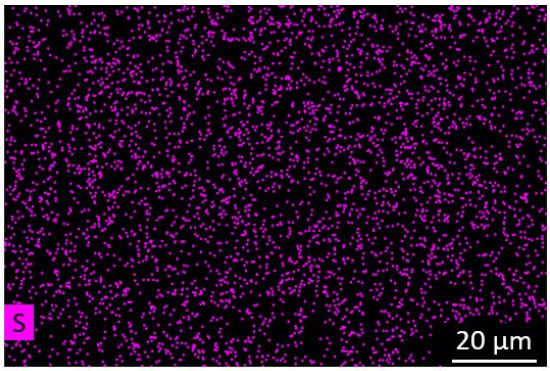
As S was not observed in the EDX spectrum for aged Bandera Brown prior to SICM imaging, or the bare Bandera Brown surface, it is perhaps un-expected that S should show a strong peak in all three EDX spectra for aged Bandera Brown post-SICM. However, S-containing compounds are common in crude oil, and S was observed in both the aged calcite and aged Estaillades EDX spectra; see Figures 5.11 and 5.28 - 5.31 in Chapter 5: *Carbonate Ageing Studies*. It therefore seems most likely that the S signals observed for aged Bandera Brown post-SICM are indeed from the crude oil film, and that perhaps by chance a region with very low S-content was mapped on the freshly aged Bandera Brown surface.



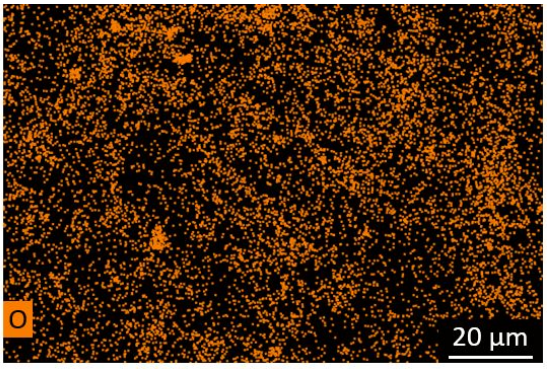

(a)



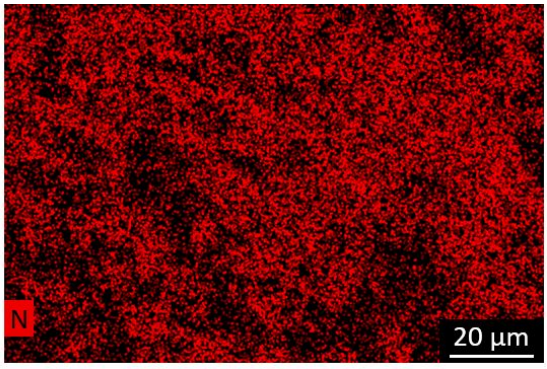

(b)




(c)

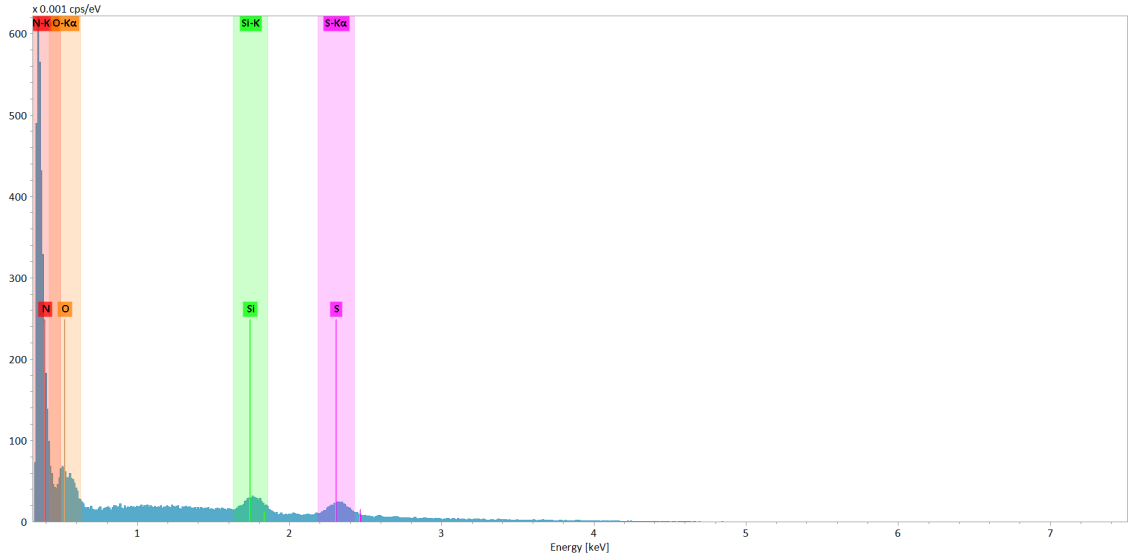



(d)




(e)

Figure 6.63: Aged Bandera Brown post-SICM: EDX element maps for area 2
EDX results for area 2 of the Aged Bandera Brown post-SICM surface shown and labelled in 6.58. (a) Shows the low-vacuum SEM micrograph of the area and (b) - (e) show the Si, S, O and N distribution maps for the area respectively.




(a)

Figure 6.64: Aged Bandera Brown post-SICM: EDX X-ray energy spectrum for area 2 The X-ray energy spectrum for the EDX results in Figure 6.63, with element assignments labelled.

Area "3" on the aged Bandera Brown surface after SICM imaging, defined in Figure 6.58 is shown in Figure 6.65 at higher magnification. This area, although similar in appearance to areas 1 and 2, with a raised region less covered in crude oil droplets than the surrounding regions, does not have any notable heterogeneities in the EDX results (Figures 6.66 and 6.67). Si is present in the X-ray spectrum, however there are no clear regions of high Si content in the Si distribution map (Figure 6.67b), suggesting that area 3's crude oil film has been reasonably uniformly thinned. When compared with areas 1 and 2, the need for EDX analysis for samples such as this is highlighted, as three seemingly similar regions in SEM micrographs alone are in fact subtly different in nature.

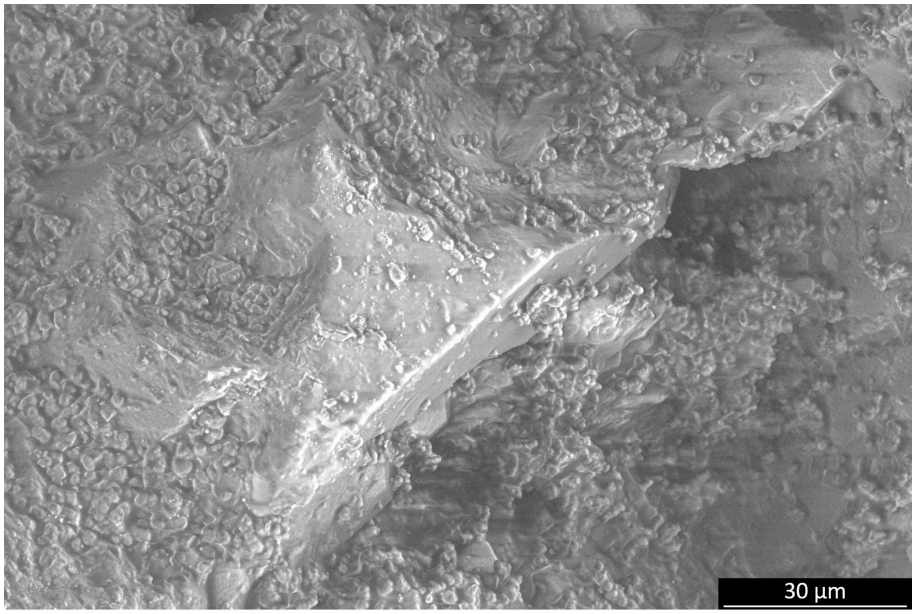
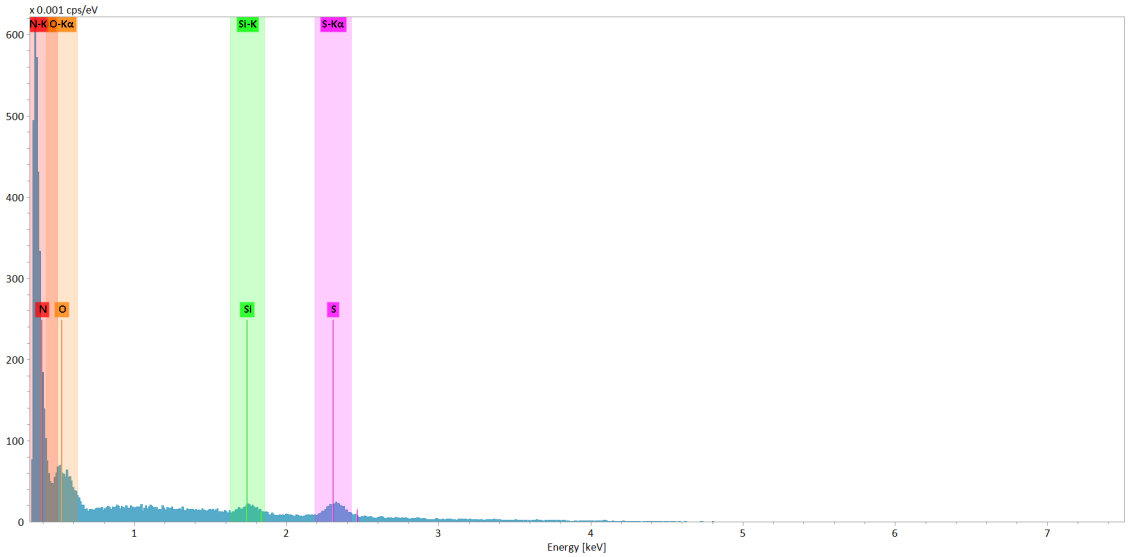
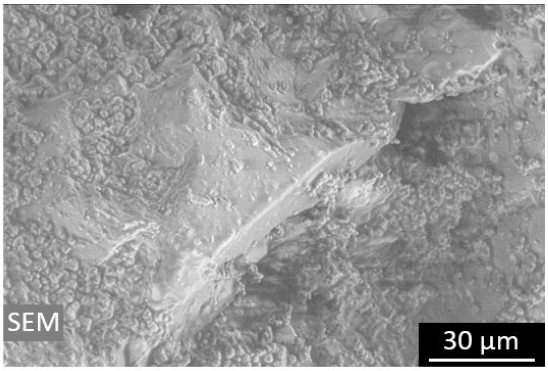



Figure 6.65: Aged Bandera Brown post-SICM: SEM micrograph of area 3
A high magnification low-vacuum SEM micrograph of the area labelled “3” in Figure 6.58.

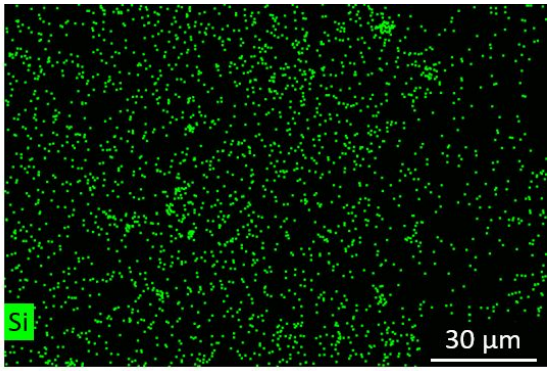



(a)

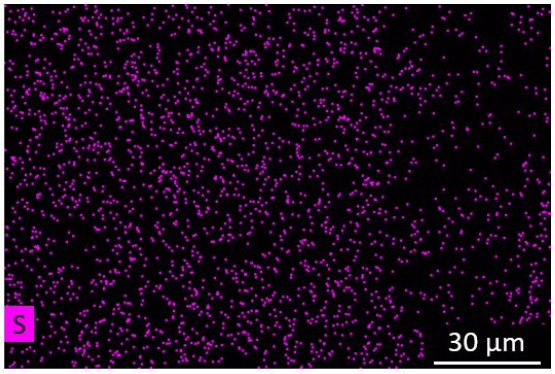
Figure 6.66: Aged Bandera Brown post-SICM: EDX X-ray energy spectrum for area 3
The X-ray energy spectrum for the EDX results in Figure 6.67, with element assignments labelled.



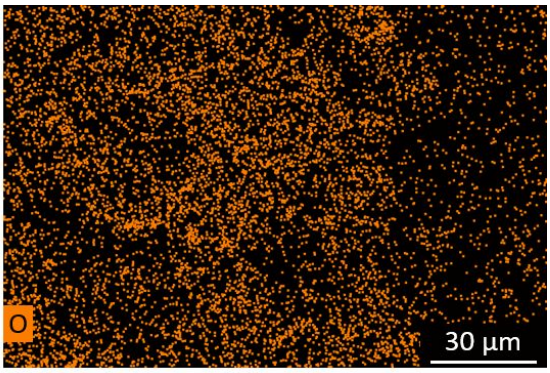

(a)



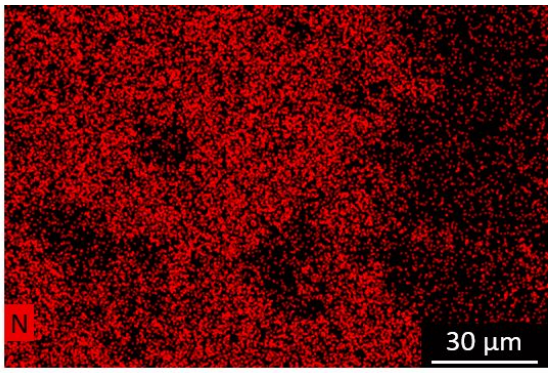

(b)




(c)




(d)




(e)

Figure 6.67: Aged Bandera Brown post-SICM: EDX element maps for area 3 EDX results for area 3 of the Aged Bandera Brown post-SICM surface shown and labelled in 6.58. (a) Shows the low-vacuum SEM micrograph of the area and (b) - (e) show the Si, S, O and N distribution maps for the area respectively.

## 6.4 Summary

In this chapter the diversity of the mineralogy on Bandera Brown was showcased through low-vacuum SEM imaging and EDX mapping. Two of these different minerals were identified from SICM topographical mapping, however it is possible that some of the minerals in the SICM images shown were incorrectly or failed to be identified and that more than two minerals were in fact mapped. Bandera Brown proved to be a more challenging sample than the carbonates to map with the SICM, as it is proposed that changes in feature height on the Bandera Brown surface were larger than for the carbonates. This difficulty was however overcome with a simple change to the minimum hop height to reduce the number of nanopipette probe crashes. This change, of course, came at a cost; imaging takes longer the higher each hop, so each Bandera Brown SICM image took around 1.5× longer to collect than for the carbonate outcrop rocks discussed in this thesis. To significantly increase the chances of recording a successful SICM image, this time cost is proposed to be of net benefit.

As was found with the aged calcite and aged Estaillades samples in Chapter 5: *Carbonate Ageing Studies*, topographical mapping of the aged Bandera Brown sample using the SICM was more challenging than for the unaltered samples. The crude oil film appeared to be partially removed by the electrolyte, blurring the images and causing more frequent blocking of the nanopipette. SEM and EDX mapping was carried out on the aged Bandera Brown sample after SICM imaging, and it was found that this apparent partial removal of the crude oil by the electrolyte resulted in the localised removal/thinning of the crude oil film. This was shown via

SEM, as some of the topology of the Bandera Brown surface beneath was revealed, and a Si signal appeared in all three areas probed with EDX, some revealing local regions of higher Si concentrations, suggesting an uneven film distribution.

# Chapter 7

# Discussion

## 7.1 Digital Rock and SICM

Digital rock, although a term primarily used to refer to the numerical modelling of fluid flow through complex pore geometries in rock, often utilises experimentally-obtained images as a starting point for calculations. Progress has been made in recent years to enhance imaging techniques such as micro-CT in order to gain more detailed information for numerical simulations, however there is still further progress to be made before reservoir behaviour can be fully predicted.[10,12,25–27]

SICM was developed for and has been primarily used for the imaging of soft, delicate samples such as living cells, as it is a non-contact nanoscale topographical mapping technique.[28,35,40] It has also been used in the fields of chemistry and materials science, but not extensively, to investigate surfaces such as battery materials and catalysts,[36–39] brought about by the advent of hopping mode, which has the ability to map samples with more sudden changes in feature height than other SPMs such

as AFM.[35,49] At the time of writing there were no known examples of SICM being used to map any type of rock, for any application, in the literature.

The core focus of this thesis was to investigate the possible uses for SICM in terms of providing inputs for modelling in the field of digital rock. Validation of the topographical maps generated with SICM came from low-vacuum SEM and AFM. Low-vacuum SEM set the scene for interpreting the SICM topographical images, providing a means of categorising the different surface types or minerals present. The micrographs generated also served as useful tools in themselves to gain insights into the heterogeneities present on the variety of mineral surfaces studied. AFM was used as a validation measure for the feature heights and widths measured with SICM, which was chosen as it is a more established technique in the literature for the mapping of reservoir and outcrop rocks.[110–113]

In this thesis, SICM topographical maps were acquired for: three carbonate outcrop rocks: Estaillades, Ketton and Indiana, and their reference, calcite; a sandstone outcrop rock: Bandera Brown; a polystyrene film on glass; and aged surfaces of calcite, Estaillades and Bandera Brown. Validation of these SICM images was provided by low-vacuum SEM micrographs for all surfaces studied, and from AFM images for the Ketton, Estaillades, Indiana, polystyrene film on glass, and aged calcite and Estaillades samples.

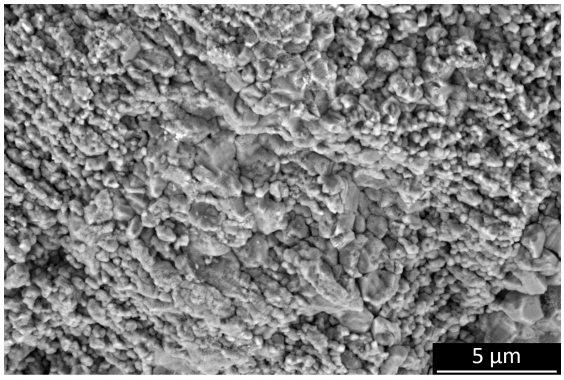
## 7.2 Carbonates

Chapter 3: *Carbonates* presented low-vacuum SEM micrographs, and SICM and AFM images of three carbonate outcrop rocks: Ketton, Estaillades and Indiana, which were chosen as they are commonly used in oil and gas recovery research. All three carbonates each have calcite percentage compositions reported as $> 90$ %.[92,93,96,97] As these surfaces were primarily composed of calcite, a pure calcite crystal was also imaged with low-vacuum SEM and SICM for comparison.

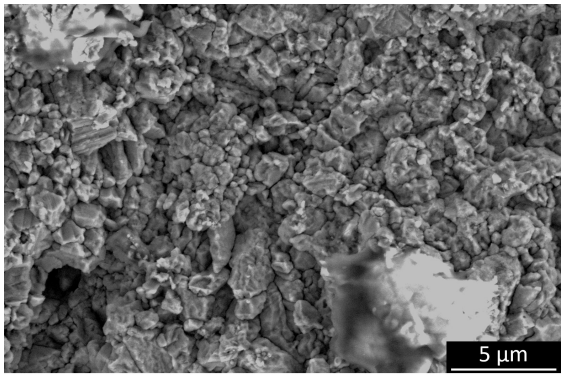
Table 7.1 brings together the four summary tables given in Chapter 3: *Carbonates*, summarising the different area types identified across the three different carbonate outcrop rocks and calcite in the low-vacuum SEM micrographs. Table 7.2 summarises which of the surface types identified in the low-vacuum SEM micrographs were subsequently identified in the SICM and AFM topographical images. In Table 7.2, "✓" signifies that an example of that surface type was identified, no symbol signifies that no examples were identified, and "?" is used to indicate where the surface type was not definitively identified, but that there was an SICM or AFM image for which it was a contender.

In the case of Ketton, surface types 3, 4 and 6 are all marked as "?" for both the SICM and AFM columns. Each of these surface types are different perspectives on a broken ooid grain shell. As they are all ooid grain shell surfaces, they have similar characteristics; they are made up of irregularly shaped crystallites each $< 1$ $\mu$m across. Figure 7.1 shows low-vacuum SEM micrographs of these three surface types at high magnification to best visualise the similarity. The consequence is that in the nanoscopic view of the SICM images it is not possible to differentiate them.

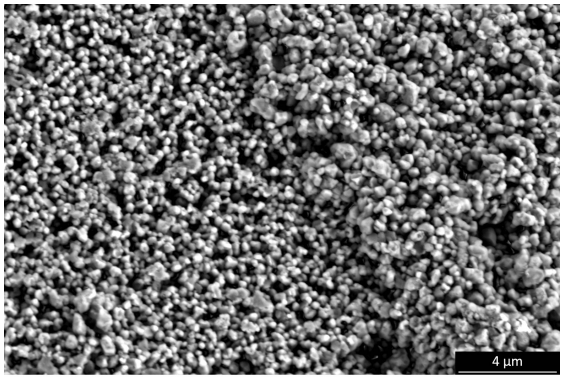
Their distinction becomes apparent in the microscopic view of the low-vacuum SEM micrographs, when it can be easily determined whether a surface is from the outside, inside or cross-section of an ooid grain shell.




(a) Ketton surface type 3




(b) Ketton surface type 4




(c) Ketton surface type 6

Figure 7.1: Ketton: ooid grain shell perspectives
Three low-vacuum SEM micrographs of the Ketton ooid shell from different perspectives; (a) shows surface type 3, the cross-section of the ooid grain shell, (b) shows surface type 4, the fractured exterior of the ooid grain shell, and (c) shows surface type 6, the fractured interior of the ooid grain shell. These micrographs were originally shown in Figures 3.11 and 3.15 in Chapter 3: *Carbonates*.

In the case of Indiana, surface types 5a and 5c have been marked as "?" for the SICM images. Both surface types are made up of smooth-surfaced crystallites which are either either 5 - 10 $\mu$m or 1 - 2 $\mu$m across respectively. Thus when smaller, for example 2 $\times$ 2 $\mu$m, images are taken on the SICM the two surface types can not be differentiated, as no crystallite is captured in its entirety.

| Sample | Type | Description | Feature size range |
|---|---|---|---|
| Calcite | 1 | Deep step-like structures caused by cleavage diagonal to crystal planes | $> 10$ $\mu$m |
| | 2 | Shallow step-like structures caused by cleavage diagonal to crystal planes | $< 10$ $\mu$m |
| | 3 | Flat regions from cleavage parallel to crystal planes | N/A |
| | 4 | Dent from cleavage almost parallel to crystal planes | 5 - 16 $\mu$m |
| Ketton | 1 | Intact ooid grain surface, covered with smooth crystallites | 0.5 - 4 $\mu$m |
| | 2 | Ooid grain surface with spikey structures on top | 0.5 - 4 $\mu$m with $< 1$ $\mu$m spikes |
| | 3 | Ooid grain shell cross-section, irregular crystallites | $< 1$ $\mu$m |
| | 4 | Fractured ooid grain shell exterior, irregular crystallites | $< 1$ $\mu$m |
| | 5 | Large crystallites inside of ooid grain | 1 - 15 $\mu$m |
| | 6 | Fractured ooid grain shell interior, irregular crystallites | $< 1$ $\mu$m |
| Estaillades | 1 | Flat regions caused by cutting during sample preparation | N/A |
| | 2 | Fractured regions adjacent to flat regions, result of cutting | 0.5 - 2 $\mu$m |
| | 3a | Large, intact crystallites | 5 - 10 $\mu$m |
| | 3b | Large crystallites, fractured to reveal a step-like structure | |
| | 4 | Small, intact crystallites | 1 - 2 $\mu$m |
| Indiana | 1 | Flat regions caused by cutting during sample preparation | N/A |
| | 2 | Large crystallites, fractured to reveal a step-like structure | 0.2 - 3 $\mu$m |
| | 3 | Fractured regions adjacent to flat regions, result of cutting | 1 - 2 $\mu$m |
| | 4 | Large, intact crystallites | $> 10$ $\mu$m |
| | 5a | | 5 - 10 $\mu$m |
| | 5b | (a-c) Small, intact crystallites | Mostly 1 - 2 $\mu$m, minority $> 5$ $\mu$m |
| | 5c | | Mostly 1 - 2 $\mu$m, entirely $< 5$ $\mu$m |

Table 7.1: Summary of the carbonate rock surface types
A summary of the different surface types identified on the calcite, Ketton, Estaillades and Indiana samples: qualitative descriptions of the surfaces and estimated feature size ranges are given based on the low-vacuum SEM micrographs shown in Chapter 3: *Carbonates*.

| Sample | Type | SICM | AFM |
|---|---|---|---|
| Ketton | 1 | ✓ | |
| | 2 | ✓ | |
| | 3 | ? | ? |
| | 4 | ? | ? |
| | 5 | | |
| | 6 | ? | ? |
| Estaillades | 1 | ✓ | |
| | 2 | ✓ | ✓ |
| | 3a | ✓ | ✓ |
| | 3b | | |
| | 4 | ✓ | |
| Indiana | 1 | ✓ | |
| | 2 | ✓ | |
| | 3 | ✓ | ✓ |
| | 4 | | |
| | 5a | ? | |
| | 5b | ✓ | |
| | 5c | ? | |

Table 7.2: Carbonate surface types identified by SICM or AFM
A summary of the carbonate surface types which were identified in the SICM and AFM topographical images. "✓" signifies that the surface type was identified in at least one image, no symbol signifies that no examples of that surface type were identified, and "?" signifies that the surface type was a contender for at least one image which did not ultimately provide sufficient information for a definitive identification.

From Table 7.2, it can be seen that for each of the three carbonates, the majority of their surface types were identified in the SICM images, demonstrating the technique's applicability in the field of digital rock. Fewer sessions were devoted to AFM imaging than to SICM imaging, so it is unsurprising that fewer surface types were identified in the AFM images. It should also be noted that for each of the three carbonate outcrop rocks, the more recessed surface types or those with the sharpest height changes such as Ketton surface type 5 and Indiana surface type 4,

were not successfully mapped with either AFM or SICM, probably because these surfaces are the least well-suited to being mapped with an SPM. The stark contrast in the number of surface types identified in the AFM images compared to the SICM images is not likely to be a fair reflection on the AFM in terms of its adequacy in imaging these materials, although the surface types observed in the AFM images reported in the literature were found to broadly align with what was observed in the AFM images reported in this thesis, as touched upon in the relevant sections below.[23,175,176]

For each of the carbonate materials, attempts to assess whether a surface was naturally occurring or whether it had been generated in the sample cutting process were made. From this, combined with considerations of pore throat sizes, it was proposed that certain surfaces were of more relevance for modelling oil extraction processes than others. This was originally discussed in Chapter 3: *Carbonates*, Section 3.2, however these assessments will also be summarised for each outcrop rock below.

### 7.2.1 Ketton

Ketton has a hierarchical structure; the surface of the ooids and the gaps between them forming a micro-porous network, and the porosity of the ooid grains themselves forming a nano-porous network. This agrees with mercury-injection tests performed by Menke *et al.*, which indicated two groupings of pore throat radii, the micro- and nano-porous networks being determined as 10 - 50 $\mu$m and 10 - 100 nm respectively.[106] Although Ketton studies in oil and gas research in the literature have

historically focused on the micro-porosity created by the space between the ooids, as this is what can be visualised using micro-CT imaging of cores,[21,93,96,177] examples from nature such as the lotus leaf effect demonstrate the importance of considering multi-scale roughnesses when understanding the wettability of a surface,[178,179] and as such it is possible that both the micro- and nano-porous networks in Ketton play key roles in its macro-scale fluid flow behaviour. AFM and SICM images were collected of the surface to gain insight into the nanoscale roughnesses inside and outside of the ooids, whilst low-vacuum SEM helped link the two scales, placing the nano-scale topographical images into the context of the micro-scale structure.

#### 7.2.1.1 Low-vacuum Scanning Electron Microscopy

As described in Table 7.1 (page 360), the Ketton surface presented six different surface types in the low-vacuum SEM experiments. Surface type 1 is likely to be the most important Ketton surface to study in molecular modelling for digital rock, as this represents the surface which covers the outside of the ooid grains; the surface which would be encountered in the micro-porous network and therefore the network which fluid will more readily flow through.

The other five surface types on Ketton should not however be fully disregarded. Although surface types 2 - 6 represent areas which are proposed as having been altered or exposed due to the cutting stage of sample preparation, they are not necessarily irrelevant to the real systems in oil reservoirs, as the rock will likely become fractured during oil extraction. Surface type 2 represents areas of ooid grain surface which appear to have been affected by previously being in contact with a second ooid grain, a residue of spikey structures approximately 1 $\mu$m long present

on top of the smooth-sided 0.5 - 4 $\mu$m crystallites beneath. It is not impossible for fracturing to occur in oil reservoirs, leading to individual ooid grains to become dislodged and for these surfaces to be exposed to the crude oil flow within the larger pore network with 10 - 50 $\mu$m pore throat radii.[106]

Surface types 3, 4 and 6 represent the surfaces of the ooid grain shell which sit beneath surface types 1 and 2, made up of $< 1$ $\mu$m crystallites with irregular shapes. Further inside the ooid, larger smooth-sided crystallites were observed making up surface type 5, measuring up to 15 $\mu$m across, which appear to cover the inside of the ooid grain shell. Surface types 3 - 6 are therefore the surfaces which would be encountered within the nano-porous network previously discussed. The narrower radii of these pores does make the crude oil less likely to flow through this narrower pore network, however as was argued for surface type 2's relevance, it is not impossible for fracturing to occur in the reservoir, resulting in the exposure of surface types 3 - 6 within the larger 10 - 50 $\mu$m pore network as well.[106]

It is therefore proposed that although surface type 1 is likely to be the most common surface to which the crude oil is exposed when flowing through carbonate reservoirs made up of ooid structures, the study of surface types 2 - 6 has merit in terms of understanding a full picture of all the surfaces with which the crude oil and water may interact.

#### 7.2.1.2 Scanning ion conductance microscopy

As summarised in Table 7.2 (page 361), Ketton surface types 1-4 and 6 were identified to some regard in the SICM topographical images. It is a good indication of SICM's suitability in mapping carbonates such as Ketton that all bar one of the

surface types were identified in the SICM topographical images. Surface type 5 may not have been successfully mapped for multiple reasons. Surface type 5 contains the largest features of the Ketton surface types, containing crystallites up to 15 $\mu$m across. This is not only larger than the largest area typically mapped in Chapter 3: *Carbonates*, 10 $\times$ 10 $\mu$m, but also brings with it the possibility that large height changes of many microns could occur suddenly when mapping the interface between two such crystallites. Large, sudden height changes will inevitably increase the chances of the nanopipette probe crashing into the surface and breaking, and thus the termination of that image attempt. Another factor which may have influenced why surface type 5 was not observed in the SICM topographical maps, is that surface type 5 is the most "hidden" of the six surface types. Surface type 5 was found *inside* an open ooid, beneath the ooid grain shell in the first low-vacuum SEM micrograph overlay (Chapter 3: *Carbonates*, Figure 3.7, page 97), but was not observed at all in the second (Figure 3.8, page 98), which could suggest that surface type 5 is a rarer surface type to expose. This possible rarity, combined with the expected difficulty of mapping surface type 5 with SICM is why it is hypothesised that surface type 5 was not observed in the SICM topographical maps. Due to it being the most recessed inside the ooid structure, it is also likely to be the least important surface type to map for inputs into modelling, as it is the least likely to see crude oil or impact crude oil flow through the structure. That being said, surface type 5 would likely still be of interest for other reservoir applications such as CCS, as the nano-pores in the Ketton ooid grains are large enough for $CO_2$ to easily penetrate, and as such it is still of interest.

#### 7.2.1.3 Atomic Force Microscopy

The AFM topographical images of Ketton, as summarised in Table 7.2 (page 361), showed surfaces each proposed to belong to one of surface types 3, 4 or 6. It is perhaps not a coincidence that the only surfaces mapped with AFM are the ooid grain surfaces which become exposed during cutting. The AFM tips used in these experiments are listed by the manufacturer as being 15 - 19 $\mu$m in height,[180] whereas the Ketton ooid grains can be seen in the low-vacuum SEM micrograph overlays in Chapter 3: *Carbonates*, Figures 3.7 and 3.8, to be many 100s of $\mu$m in diameter. Although it is not possible to measure accurately from the SEM micrographs, it is quite likely that the majority of the surface types other than 3, 4 and 6 are 10s or 100s of $\mu$m deep into the surface, which would be inaccessible to the 15 - 19 $\mu$m high AFM tips. The perpendicular cantilever sitting 15 - 19 $\mu$m above the AFM probe tip prevents the mapping of surfaces which would be accessible to the SICM nanopipette probe, which remains narrow and vertical for 100s of $\mu$m (Figure 7.2) before widening to accommodate the electrode.

These findings are broadly in agreement with the literature. Two AFM images of Ketton were found in the literature, from Rücker *et al.* and Zheng *et al.*.[23,175] Rücker *et al.* show an AFM image of Ketton with a variety of feature sizes and shapes; a detailed scale bar is not shown, but the features do not appear to exceed 4 - 5 $\mu$m in size, which combined with the smaller structures would suggest that they are showing an image of surface type 2.[175] Although surface type 2 was not successfully mapped in the experiments for this thesis, surface type 2, the exposed surface were two ooids used to be in contact, would not necessarily be a recessed surface type

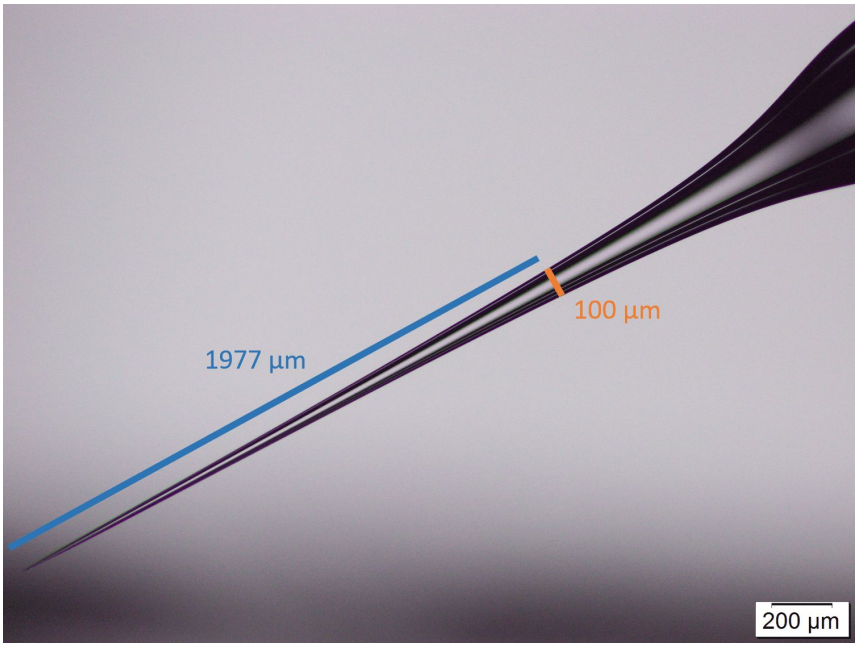



Figure 7.2: Optical microscopy image of a nanopipette tip
An image of a nanopipette tip taken on an optical microscope at x5 magnification. Lengths marked on the image illustrate how the nanopipette is $< 100$ $\mu$m in width for 100s of $\mu$m, allowing it to be used to probe areas recessed in a surface of interest. The wider section, where the electrode would be placed, is not fully visible in this image; the full length of the nanopipettes made for these studies were approximately 3.5 cm long.

depending on where the sample was cut, and so this is not in opposition to the assertion made here that the AFM can not reach more recessed features. Zheng *et al.*'s AFM image of Ketton presents a small field of view, so accurate assignment challenging, but as only sub-micron crystallites can be seen, this is likely to be one of the surface types 3, 4 or 6 which were also mapped successfully by AFM in this thesis.

In addition to the SICM being able to access more recessed features in the sample surface, it was also noted that the AFM images of Ketton had a blurred quality to them, the SICM producing clearer images of the surface. This apparent difference in technique suitability is proposed to be a result of the numerous and significant changes in feature height, which although pose problems for the AFM to resolve in

tapping mode, with tip oscillation amplitudes on the order of 10 - 100 nm,[114,115] are easily accommodated by the SICM hopping mode minimum hop heights of 1 - 5 $\mu$m employed to collect the images presented in this thesis.

### 7.2.2 Estaillades

#### 7.2.2.1 Low-vacuum Scanning Electron Microscopy

Four different surface types were found on the Estaillades surface using low-vacuum SEM in Chapter 3: *Carbonates*, details of which were summarised in Table 7.1 (page 360). Two of these, surface types 1 and 2, are proposed to be surfaces generated during the cutting process of sample preparation. Surface type 1 represents the most elevated sections of the surface, which have been directly caught with the rotating saw during cutting and are flat as a result. Adjacent to regions of surface type 1, regions of surface type 2 can be found. Surface type 2 represents regions of rough-edged crystallites, proposed to be the result of fracturing during the cutting process. Surface types 3 and 4 are proposed to be the regions of the Estaillades surface which were recessed such that they were unaffected by the cutting process. Both surface types 3 and 4 are made up of smooth-sided crystallites, the key difference between the two being size; surface type 3 is made up of larger crystallites, 5 - 10 $\mu$m across, whilst surface type 4 consists of smaller crystallites, typically 1 - 2 $\mu$m across.

As was the case with the Ketton surface types, the surfaces which are interpreted as being un-affected by sample preparation are proposed to be the best candidates for informing molecular or pore network models. In the case of Estaillades, this

would be the surface types 3 and 4, made up of smooth crystallites of varying sizes. The flat surfaces making up surface type 1 are probably unlikely to occur naturally, as it is proposed that they have been artificially made smooth during the cutting process. However, surface type 2 could well be found in reservoirs if any fracturing occurred, possibly producing surfaces similar to these regions. Topographical maps of surface type 2 are therefore likely to be of value for modelling inputs, alongside maps surface type 3 and 4.

#### 7.2.2.2 Scanning Ion Conductance Microscopy

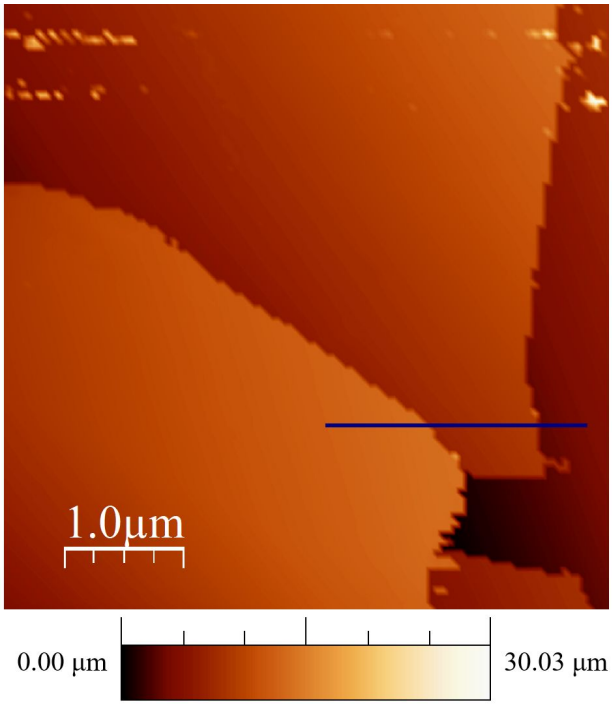
As summarised in Table 7.2 (page 361), all four surface types which were identified in the low-vacuum SEM micrographs of the Estaillades surface were also identified in the SICM topographical maps in Chapter 3: *Carbonates*. The sub-type 3b, which describes regions of the large, smooth crystallites where fracturing has occurred to produce a step-like structure was not found in the SICM topographical images. This is perhaps not surprising, as this sub-type appeared infrequently in the low-vacuum SEM micrographs, and is possibly further indication of its relative rarity.

Surface type 3 was anticipated as being the most difficult of the surface types to map with SICM due to the presence of larger crystallites, and thus larger height changes between adjacent pixels. A 5 $\times$ 5 $\mu$m SICM topographical image which appears to be of Estaillades surface type 3, originally presented in Figure 3.46a in Chapter 3: *Carbonates*, is shown once more in Figure 7.3 below. Sections of the faces of four crystallites are visible, the exact size of them unknown as none are fully captured within the image. Although the exact sizes are unknown, this region is likely to belong to surface type 3, as three of the four crystallites present exceed

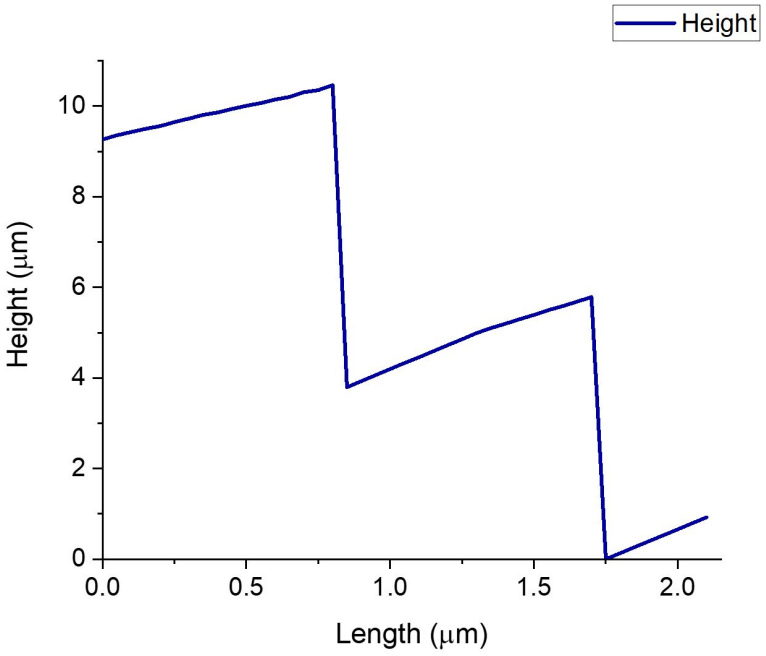
2 $\mu$m across in size. The horizontal blue line shown on Figure 7.3a sits across two crystallite intersections, the height profile along which, from left to right, is shown in Figure 7.3b. The SICM employed for these experiments scans from left to right in horizontal lines, bottom to top relative to the images shown. A horizontal profile was therefore selected as it represents a section of one of the line scans which was taken during image acquisition. From this profile it can be seen that the drops between crystallites is around 6 $\mu$m. It is fortunate that these crystallites were arranged such that the height dropped from left to right, as the minimum hop height which was set for the acquisition of this image was only 1 $\mu$m. If the scan had taken place in the opposite direction, the tip likely would have crashed into the edge of one of these crystallites, and the image would not have been successfully acquired. This highlights the luck which plays a role in imaging some of these surface types, and the importance of selecting appropriate scan parameters.

#### 7.2.2.3 Atomic Force Microscopy

The AFM topographical images collected of the Estaillades sample appeared to show regions of surface types 2 and 3. This is in agreement with the literature, however only one example of AFM imaging of Estaillades was found.[176] Ekanem *et al.* showed an image composed of rough-edged crystallites approximately 1 - 2 $\mu$m across, which fits into the definition of Estaillades surface type 2.[176] It is perhaps unexpected that an example of surface type 1 was not found, as it is the flattest and most elevated of the four surface types, and therefore the best suited for AFM imaging. Surface type 1 did not however account for a large proportion of the surface in the low-vacuum SEM micrograph overlays in Figures 3.16 and 3.17 in Chapter 3: *Carbonates*. The




(a)




(b)

Figure 7.3: Sharp height changes in Estaillades surface type 3
(a) shows the 5 × 5 $\mu$m SICM topographical image of a region of the Estaillades surface proposed to belong to surface type 3, which was originally shown in Figure 3.46a in Chapter 3: *Carbonates*. A blue horizontal line on this topographical map shows the location of the height profile displayed in (b) where the sharp height changes between crystallites can be seen.

lack of surface type 1's presence in the AFM topographical images is therefore likely to be a reflection on the comparatively fewer sessions spent on the atomic force microscope than the scanning ion conductance microscope. Surface type 4 on the other hand was abundant, so its absence from the AFM topographical images can not be explained by rarity. Looking back to the low-vacuum SEM micrograph overlays in Figures 3.16 and 3.17 in Chapter 3: *Carbonates*, surface type 4 is perhaps one of the more recessed surface types on the Estaillades surface, and thus perhaps more difficult to access with the AFM probe tip than the SICM nanopipette.

As was the case for the AFM images collected of the Ketton surface type 3, 4 or 6, the AFM images of Estaillades surface type 2 also appeared blurred in comparison to the images of surface type 2 collected on the scanning ion conductance microscope. This is again proposed to be due to AFM's smaller oscillation of the tip during tapping mode, typically 10 - 100 nm,[114,115] compared to the hopping mode hop heights employed when obtaining SICM images, typically 1 - 5 $\mu$m. This smaller oscillation does not allow the atomic force microscope to fully accommodate the $>$ 100 nm height changes present when imaging these samples.

### 7.2.3 Indiana

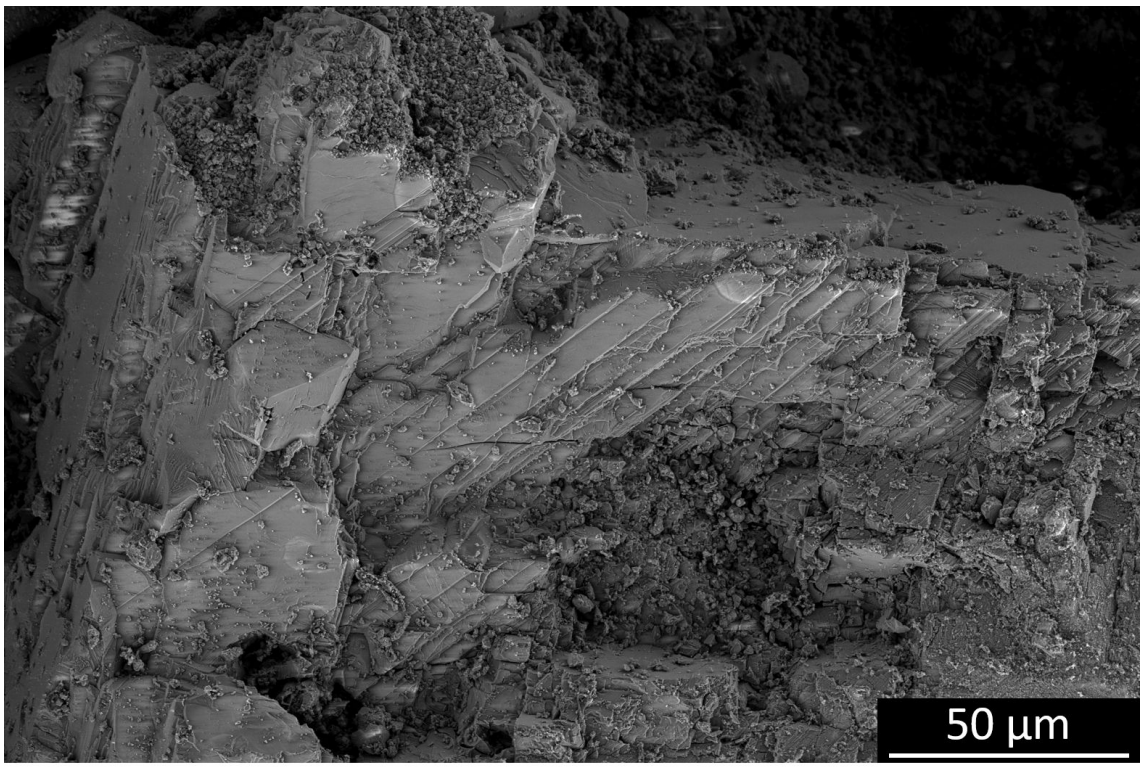
#### 7.2.3.1 Low-vacuum Scanning Electron Microscopy

As described in Table 7.1 (page 360), five different surface types were identified from the low-vacuum SEM micrographs of the Indiana sample. Similarly to Estaillades, two of these surface types are proposed to be the direct result of sample cutting prior to imaging. Indiana surface type 1 represented the most elevated regions which

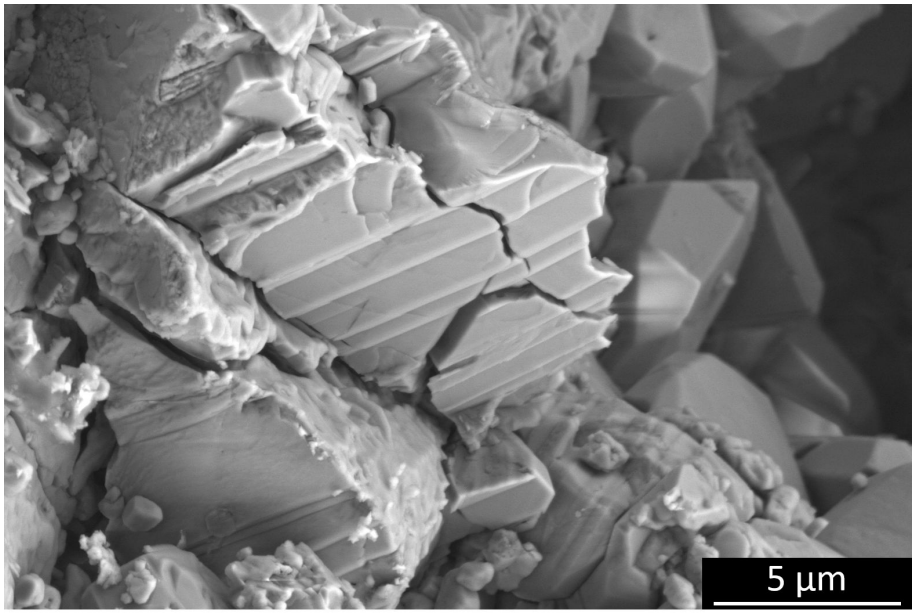
have been made artificially flat, which are similar to Estaillades surface type 1, and Indiana surface type 3 represented the regions adjacent to surface type 1 which consist of small rough-edged crystallites, which are similar to Estaillades surface type 2.

Indiana surface type 2 was similar to Estaillades surface sub-type 3b, in that it represented calcite crystallites which had fractured to reveal step-like structures. These "steps" were however much more abundant on the Indiana surfaces studied compared to the Estaillades sample, and the large crystallites in which the step-like structures formed were much larger on Indiana's surfaces than on Estaillades. Due to the greater abundance and therefore greater perceived importance of Indiana surface type 2 compared to Estaillades surface sub-type 3b, it was assigned its own separate surface type instead of being classed as a sub-type. Two low-vacuum SEM micrographs are shown in Figure 7.4, showing Indiana surface type 2 (Figure 7.4a) and Estaillades surface sub-type 3b (Figure 7.4b) side-by-side for ease of comparison; the step-like structures on Indiana can be seen to be on the order of 100 $\mu$m across compared to Estaillades where the structures are approximately 5 $\mu$m across.

Indiana surface type 4 represented large, intact, smooth-surfaced crystallites, which although similar to Estaillades surface type 3 in shape, were again much larger, being 50 - 100 $\mu$m across. Indiana surface type 5 was made up of smaller smooth-surfaced crystallites, similar in size and shape to Estaillades surface types 3 and 4, and was split into three sub-types. Indiana surface type 5a is similar to Estaillades surface type 3, with smooth-surfaced crystallites on the order of 5 - 10 $\mu$m across. Indiana surface types 5b and c were composed of smooth-sided crystallites




(a) Indiana Surface Type 2




(b) Estaillades Surface Sub-Type 3b

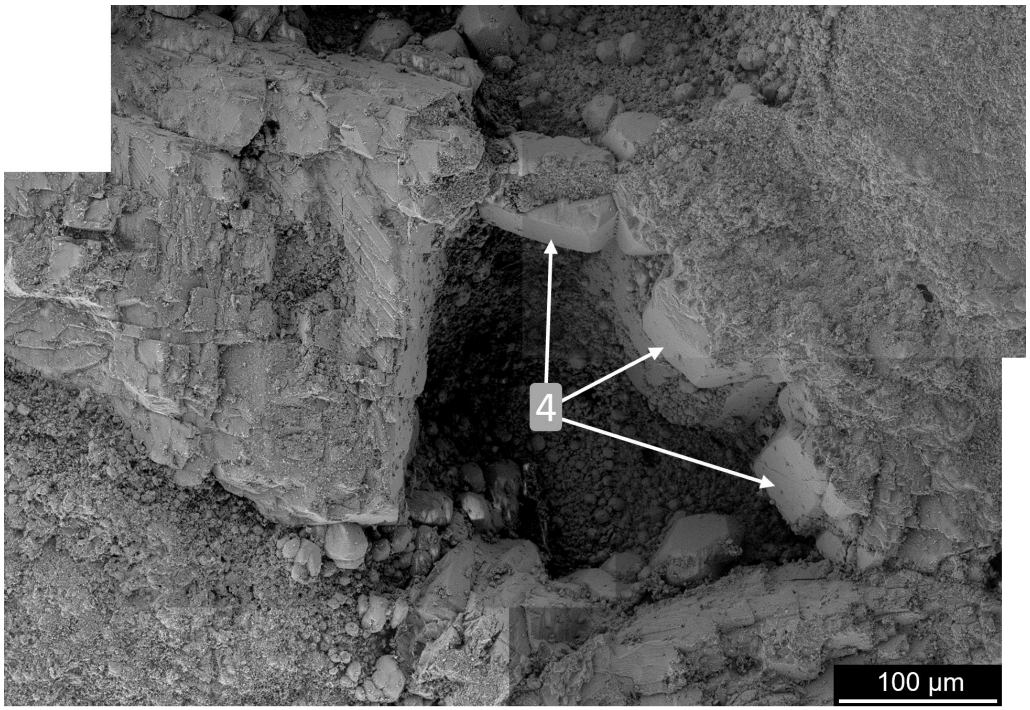
Figure 7.4: Step-like structures in Indiana and Estaillades
Two low-vacuum SEM micrographs originally shown in Chapter 3: *Carbonates* showing (a) Indiana surface type 2 at a lower magnification than the same region was shown in Figure 3.25a, and (b) Estaillades surface type 3b, which was originally shown in Figure 3.20b.

which were predominantly 1 - 2 $\mu$m across, similar to Estaillades surface type 4. The differentiation between 5b and 5c is that in surface type 5b a few $> 5$ $\mu$m crystallites are present, whereas surface type 5c is made up of entirely $< 5$ $\mu$m crystallites.

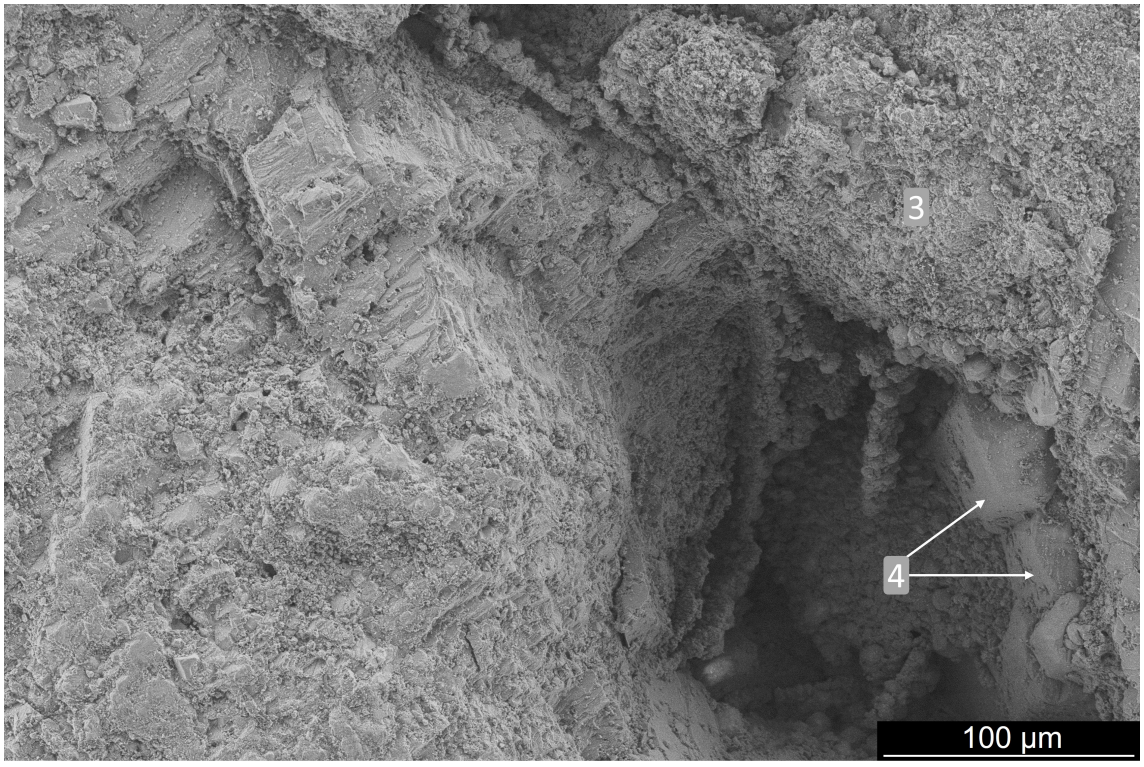
#### 7.2.3.2 Scanning Ion Conductance Microscopy

As described in Table 7.2 (page 361), SICM topographical maps were collected on four of the five Indiana surface types. The surface type which was not identified in the SICM maps was Indiana surface type 4, made up of smooth-sided crystallites 50 - 100 $\mu$m across. There are two possible explanations for why this surface type might not have been identified. The crystallites which make up surface type 4 are significantly larger than the areas typically scanned with the scanning ion conductance microscope; as such, no one full crystallite would have been captured within one image, and so assignment would be challenging. Additionally, surface type 4 is located predominantly on the vertical edges of pore throats or dents, as indicated in Figure 7.5. Due to the nature of image collection on the SICM, where the nanopipette approaches vertically and any information collected is assumed to be the result of the surface directly below the probe, vertical surfaces are not typically imaged. These two factors combined could have both contributed to the resulting lack of Indiana surface type 4 being identified in the SICM images.

Two question marks are also present in Table 7.2 (page 361) next to Indiana surface types 5a and 5c. As previously mentioned, these question marks indicate that a region of the Indiana sample was mapped on the SICM which was too small a field of view to determine the size of the smooth-sided crystallites present. As such, the image could be a region of any of the three Indiana surface type 5 sub-types.




(a)




(b)

Figure 7.5: Positioning of Indiana surface types 3 and 4
SEM micrographs showing the locations of Indiana surface types 3 and 4. (a) shows sections of four of the SEM micrographs in the center of the overlay shown in Figure 3.22, and (b) shows the same SEM micrograph as shown in Figure 3.23, both from Chapter 3: *Carbonates*.

#### 7.2.3.3 Atomic Force Microscopy

The AFM images collected of the Indiana sample exclusively showed what was identified as surface type 3; labelled in Figure 7.5b for reference. Unfortunately, no AFM images of Indiana could be found in the literature at the time of writing with which to compare these findings, so it is possible that these images are in themselves novel. As was the case for the Ketton and Estaillades samples, less time was devoted to imaging Indiana with the AFM than the SICM. The lack of AFM images of surface types other than surface type 3 is therefore not necessarily an indication of the atomic force microscope's inability to map the other surface types present. Indiana surface type 3 is characterised as being made up of small, irregular crystallites, and is proposed to be the result of fracturing caused during cutting, as it is typically observed in the more elevated regions of the surface, adjascent to surface type 1. As it is found on the more elevated regions of the sample, it is therefore also one of the more likely to be successfully approached by the AFM tip. As discussed previously, the AFM probe tip is only 15 - 19 $\mu$m long,[180] so is unlikely to reach the more recessed regions of the Indiana surface.

### 7.2.4 Summary

Overall, the body of work presented in this thesis on the carbonate outcrop rocks demonstrates a robust workflow for future characterisation of outcrop rocks in the field of oil and gas extraction. By following the procedures presented herein from sample preparation to low-vacuum SEM imaging and surface type-determination, to the more detailed AFM imaging and SICM imaging; information which is currently

lacking in literature analyses of these outcrop rocks around their topographical heterogeneity at the sub-micron scale,[92] would be clearly and methodically elucidated. The showcasing of the heterogeneity of these outcrop rocks, and the assessment of the relative significances of their different surface types, has direct implications for molecular modelling and PNM of these systems. If this workflow were used more widely, this would probably uncover sub-micron scale heterogeneity of other outcrop rocks commonly studied in the literature, such as Berea, Bentheimer, Edwards or Guelph.[92,181]

Recently, Zheng *et al.* demonstrated how a topographical map generated using AFM could be directly re-generated within a molecular modelling simulation, and used as an input for the fluid-solid interactions.[23] This paper, although very promising, did not touch upon the relevance of the surface type which was chosen for these simulations.[23] If the workflow presented here were incorporated into a similar study, then the significance of the surface type being modelling would be known, and multiple surface types of differing importances could have be utilized, to see how much of an impact the *real* nanoscale topographical heterogeneities actually have on fluid-solid interactions at the molecular scale. The outputs from these experiments would also have relative weightings of importance when fed up the length scale into PNM simulations, which would be expected to lead to more accurate simulations of these complex rock systems.

## 7.3 Bandera Brown

In Chapter 6: *Bandera Brown*, a Bandera Brown surface was imaged using low-vacuum SEM and SICM. In Chapter 3: *Carbonates*, low-vacuum SEM micrographs were used to define surface types to categorize the SICM images of the carbonate materials. Similarly, in Chapter 6: *Bandera Brown*, low-vacuum SEM micrographs were used to identify a selection of the minerals present on the surface of Bandera Brown, which aided with the identification of the features found in the smaller SICM images. Due to the mineralogical heterogeneity on the Bandera Brown surface, EDX was also used as a complementary method to aid in the identification of the minerals present in some of the low-vacuum SEM micrographs, in addition to expertise provided by Dr. Fons Marcelis.[a] AFM was not employed in the studies of Bandera Brown, as the AFM work on the carbonates in Chapter 3: *Carbonates* had already demonstrated that SICM is a suitable SPM for mapping these types of materials, if not better suited than AFM.

### 7.3.1 Mineral identification with low-vacuum SEM

Table 7.3 on page 382, originally shown in Chapter 6: *Bandera Brown*, page 328, summarises the nine minerals identified on the Bandera Brown surface using low-vacuum SEM and EDX in Chapter 6: *Bandera Brown*, and which of these minerals were proposed to have been identified in the SICM images. Seven of these nine minerals were identified from the SEM micrographs, with the further two minerals being identified from EDX results alone. Although the first seven minerals in Table 7.3

[a]Research Geologist at Shell Global Solutions International B.V., Amsterdam, the Netherlands

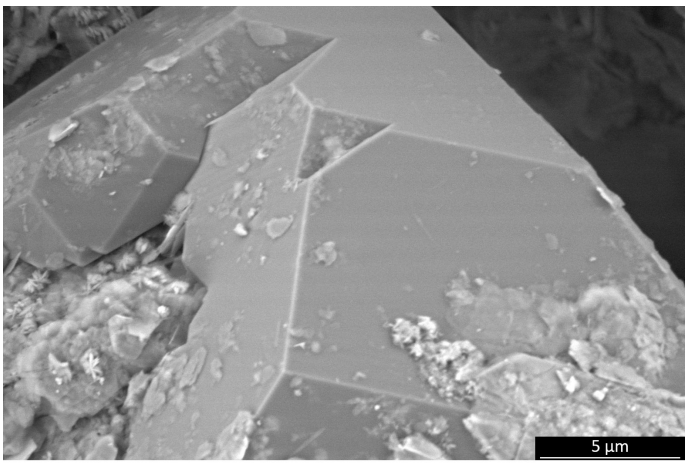
were first identified based on the low-vacuum SEM micrographs alone, subsequent EDX investigations presented additional evidence for the presence of some of these minerals.

#### 7.3.1.1 Quartz

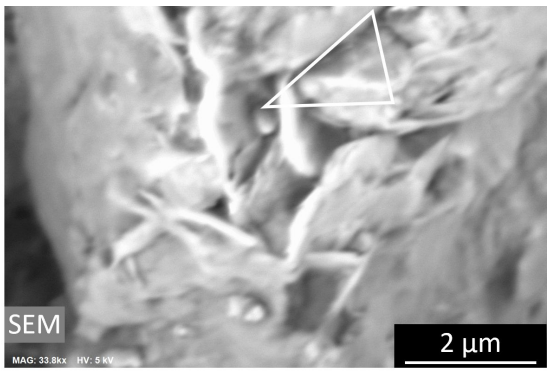
Quartz ($SiO_2$) was first identified as a large crystal in the low-vacuum SEM micrograph re-shown in Figure 7.6a. Quartz was identified again in the EDX, the first example of which is also shown in Figure 7.6; although the majority of this surface is proposed to be vermiculite/mica, the area highlighted by the white triangle in the low-vacuum SEM micrograph (Figure 7.6b) and associated Al, Si and O distribution maps (Figures 7.6c - 7.6e) is proposed to be a small quartz section. The triangular shape of this region is further evidence of the presence of quartz, which, as discussed in Chapter 6: *Bandera Brown* has a trigonal crystalline structure.[156–159] The comparatively low Al concentration in this triangular section would indicate that there is little clay in this region; in contrast, this triangle shows comparatively higher Si and O concentrations, which would suggest that a quartz component is present. C, Fe, K, Mg and Na were also found in the region shown in 7.6b, maps for which were shown in Chapter 6: *Bandera Brown*, across Figures 6.16 and 6.17 on pages 297 and 298.

#### 7.3.1.2 Mica/vermiculite

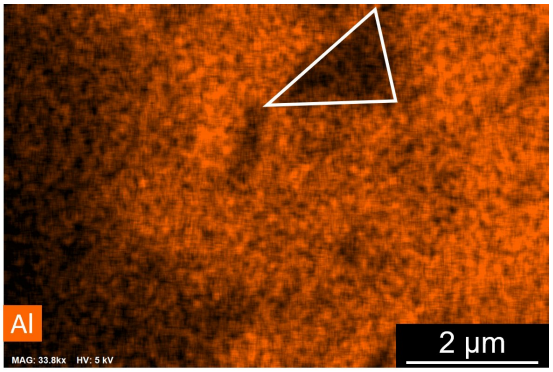
Mica ($KAl_2(AlSi_3)O_{10}(OH)_2$) and vermiculite ($M^+_{0.75}Al_2(Si_{3.25}Al_{0.75})O_{10}(OH)_2$) were identified across numerous low-vacuum SEM micrographs in Chapter 6: *Bandera Brown*. Due to the chemical and morphological similarities between these two ma-



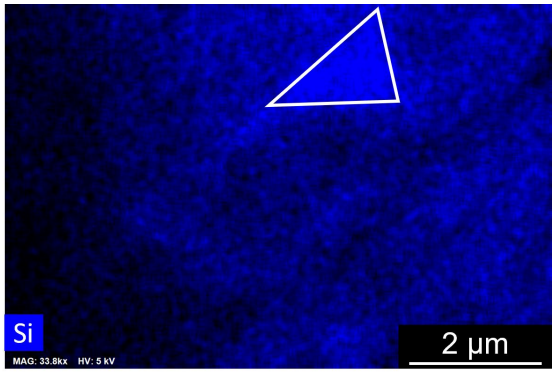

(a)



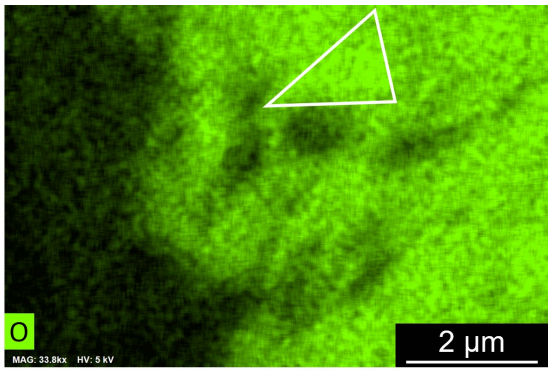

(b)




(c)




(d)




(e)

Figure 7.6: Bandera Brown: Quartz locations
(a) and (b) show two low-vacuum SEM micrographs where quartz was identified. The large smooth-sided structure in (a) is proposed to be entirely quartz; (b) is proposed to be mostly vermiculite/mica, but contains quartz in the highlighted triangular area, based on the element distribution maps in (c), (d) and (e) of Al, Si and O respectively. These images were originally shown in Figures 6.2 and 6.16 in Chapter 6: *Bandera Brown*.

| Mineral | Chemical Formula | Description | Feature size | SICM |
|---|---|---|---|---|
| Quartz | $SiO_2$ | Smooth-sided structure with sharp edges | $> 10$ $\mu$m | |
| Mica | $KAl_2(AlSi_3)O_{10}(OH)_2$ | Rough-edged disk-like structures of irregular shape | 1 - 2 $\mu$m | ✓ |
| Vermiculite | $M^+_{0.75}Al_2(Si_{3.25}Al_{0.75})O_{10}(OH)_2$ | | | ✓ |
| Calcite | $CaCO_3$ | Smooth-sided step-like structure with sharp edges | 50 - 90 $\mu$m | |
| Smectite | $M^+_{0.33}Al_2(Si_{3.67}Al_{0.33})O_{10}(OH)_2$ | Thin rough-edged disk-like structures of irregular shape | 1.5 - 2 $\mu$m | ✓ |
| Kaolinite | $Al_2Si_2O_5(OH)_4$ | Booklet structure; stacks of smooth-sided sheets | 3.5 - 4 $\mu$m | |
| Hematite | $Fe_2O_3$ | 6-pointed stars | $< 1$ $\mu$m | |
| Albite | $NaAlSi_3O_8$ | Rough-edged crystallite - identified from EDX | 1 $\mu$m | |
| Apatite | $Ca_5(PO_4)_3F$ | Rough-edged crystallite - identified from EDX | $< 1$ $\mu$m | |

Table 7.3: Summary of Bandera Brown minerals identified

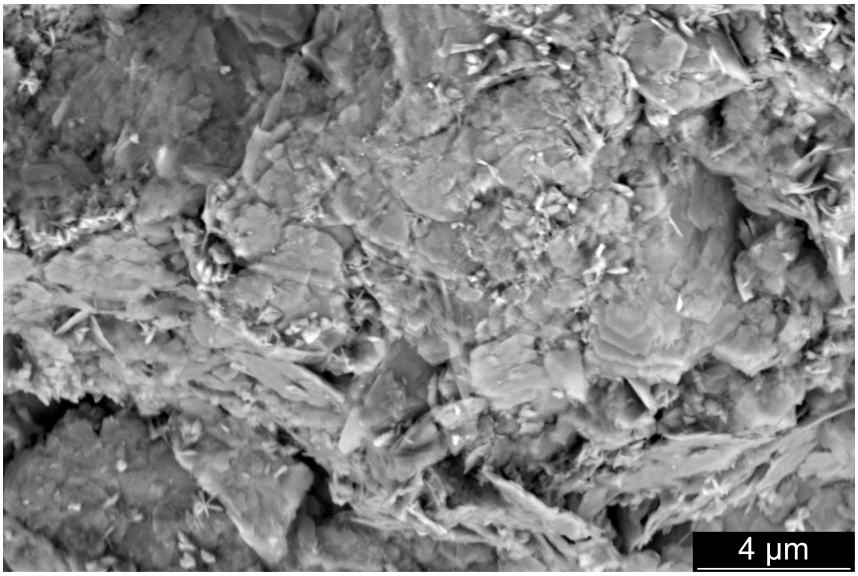
A summary of the different minerals which were identified on the Bandera Brown surface using SEM and EDX. Descriptions and feature size estimates are based on the SEM micrographs of these minerals presented in Chapter 6: *Bandera Brown*. The $M^+$ ions in the vermiculite and smectite chemical formulae represent interlayer cations which can be $K^+$, $Mg^{2+}$ or $Ca^{2+}$, and $Mg^{2+}$ or $Ca^{2+}$ respectively. The "SICM" column denotes whether that sample type was identified in any SICM topographical images of the Bandera Brown surface; "✓" signifies that the surface type was identified in at least one SICM image and no symbol signifies that no examples of that surface type were identified.

terials it is not possible to distinguish them from each other with any certainty from low-vacuum SEM or EDX results, and so they are mostly referred to together. The majority of the region shown in the low-vacuum SEM micrograph in 7.6b is proposed to be a mica or vermiculite surface, with the exception of the outlined triangular area which is likely to be quartz. The assignment of mica/vermiculite for this feature is reinforced by an even distribution of Al, Si and O across the majority of the surface. A few examples of areas where mica/vermiculite were identified in the low-vacuum SEM micrographs alone are presented in Figure 7.7 for comparison. Figure 7.7a appears to show an area which is entirely mica/vermiculite, whereas Figures 7.7b and 7.7c show areas which are predominantly mica/vermiculite with small sections of two other clays, smectite and kaolinite, at their centres.

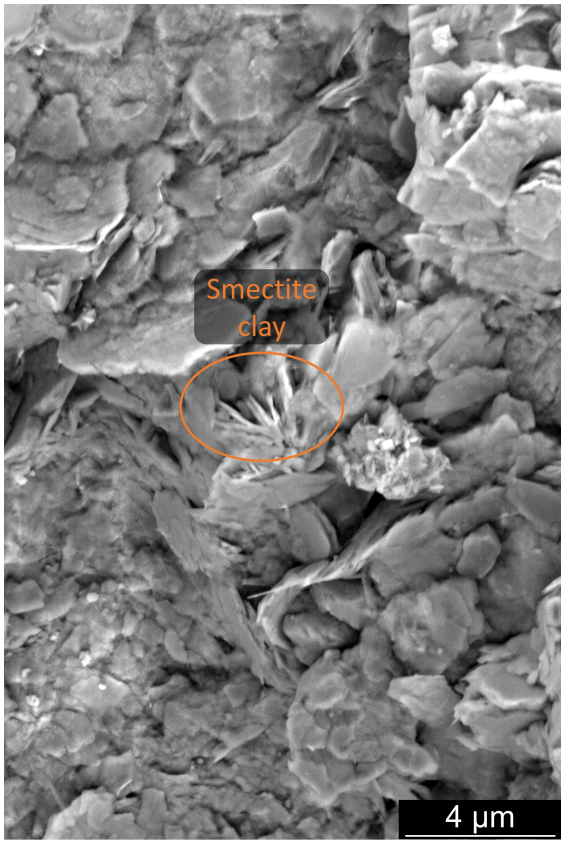
#### 7.3.1.3 Smectite

Smectite ($M^{+}_{0.33}Al_2(Si_{3.67}Al_{0.33})O_{10}(OH)_2$) was first identified in the low-vacuum SEM micrograph which is re-shown in Figure 7.7b, and once more covering a larger area in Figure 7.8. Smectite clay is very similar to mica and vermiculite in terms of chemical structure and as such is very similar in appearance. EDX results can not provide distinction between these three clays, as the same elements can be present in all three structures. The assignment was therefore made through a combination of the guidance of Dr. Fons Marcelis[a], and comparison to the SEM micrographs presented by Fesharaki *et al.*.[166]

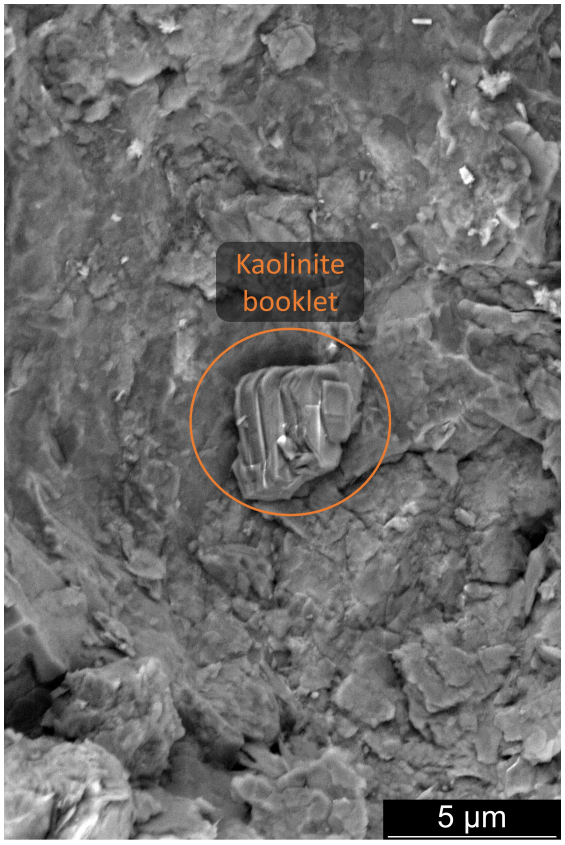
[a]Research Geologist at Shell Global Solutions International B.V., Amsterdam, the Netherlands




(a)




(b)




(c)

Figure 7.7: Bandera Brown: Mica/vermiculite, smectite and kaolinite
Three low-vacuum SEM micrographs of regions which are proposed to predominantly be mica/vermiculite. (a) is proposed to be entirely mica/vermiculite, and (b) and (c) are proposed to be predominantly mica/vermiculite with smectite and kaolinite at their centres respectively. These micrographs were originally shown in Figures 6.4, 6.8 and 6.9 in Chapter 6: *Bandera Brown* on pages 287, 290 and 290 respectively.

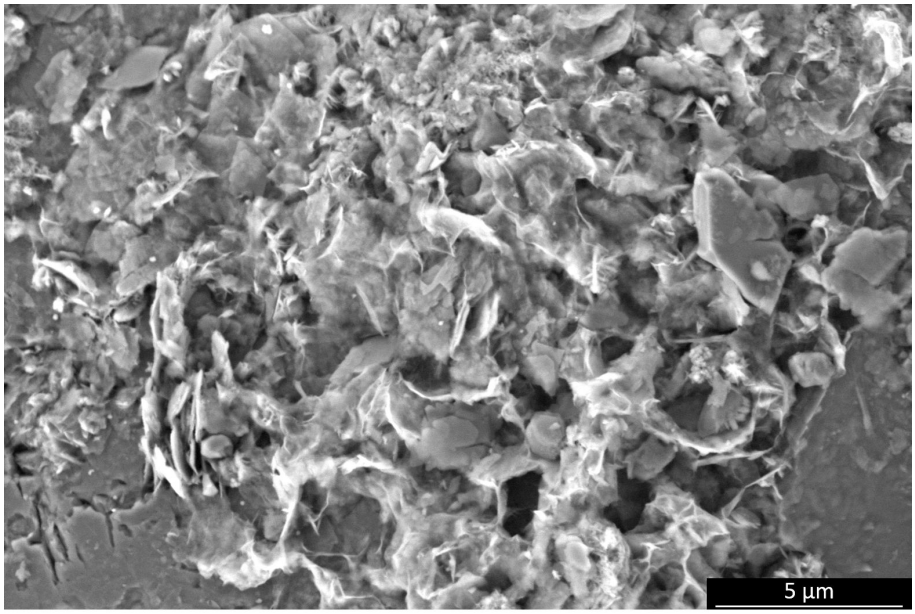



Figure 7.8: Bandera Brown: Smectite
The low-vacuum SEM micrograph of smectite clay which was originally presented in Figure 6.11 in Chapter 6: *Bandera Brown*.

#### 7.3.1.4 Kaolinite

Kaolinite ($Al_2Si_2O_5(OH)_4$) was only observed in one low-vacuum SEM micrograph of the Bandera Brown surface in Chapter 6: *Bandera Brown*, which was re-shown in Figure 7.7c. Kaolinite was identified from this low-vacuum SEM micrograph by its characteristic "booklet" structure shape; good examples of kaolinite booklet structures imaged with SEM were published by Wilson *et al.*,[116] and can be viewed for comparison in reference 116.

#### 7.3.1.5 Calcite

Calcite ($CaCO_3$) was also only identified once in the low-vacuum SEM micrographs of Bandera Brown in Chapter 6: *Bandera Brown*, which is re-shown in Figure 7.9. In this case, the assignment of calcite was given due to the large feature's striking similarity to the step-like structures in the larger calcite crystallites found on the

Estaillades and Indiana samples in Chapter 3: *Carbonates*. No examples or indeed traces of calcite were found in the EDX data, as no Ca peak was detected for any of the areas investigated. Calcite is however reported by Yesufu-Rufai *et al.* to make up 7 % of Bandera Brown, so is not an unlikely mineral to identify on its surface.[89]

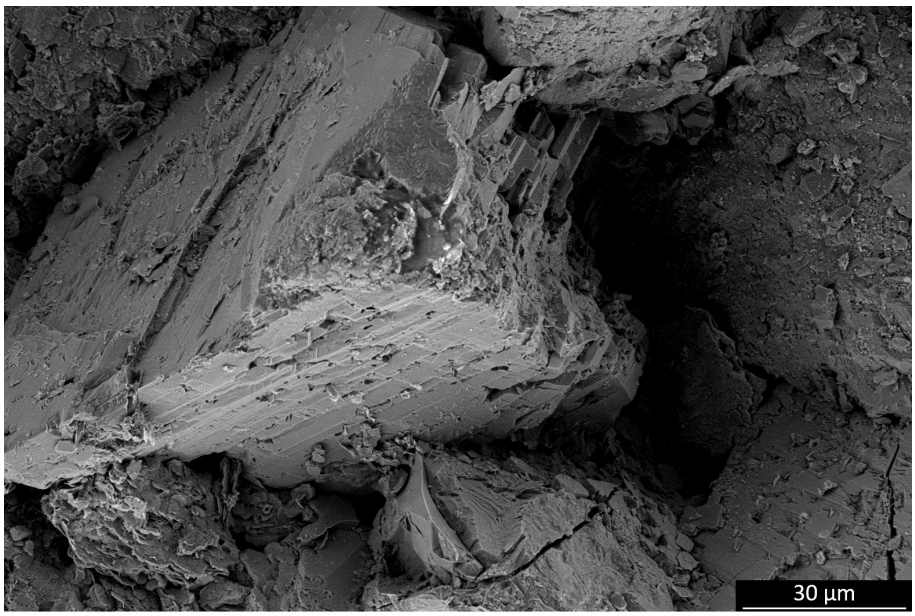



Figure 7.9: Bandera Brown: Calcite
A low-vacuum SEM micrograph of a large feature which is proposed to be calcite, originally shown in Figure 6.6 in Chapter 6: *Bandera Brown*.

#### 7.3.1.6 Hematite

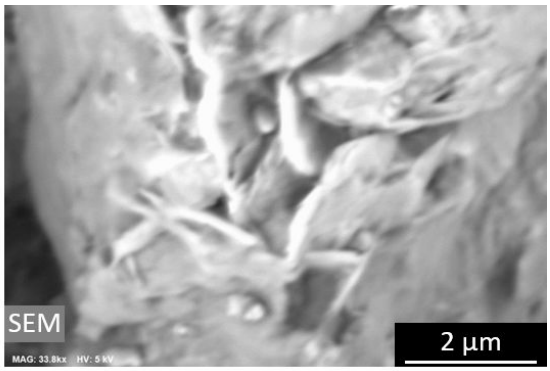
Hematite ($Fe_2O_3$) was first identified from low-vacuum SEM micrographs where small, spikey, star-shaped crystallites can be seen littered across the surface. Examples of hematite were also found in the EDX investigations, one of which is shown in Figure 7.10b. Figure 7.10 compares two low-vacuum SEM micrographs; one of a region where hematite appears to be present (Figure 7.10b), and one of a region which appears to not have any hematite (Figure 7.10a). The associated EDX spectra for Figures 7.10a and 7.10b are shown in Figures 7.10c and 7.10d respectively.

These EDX spectra reveal that the region where hematite appears to be present, Figure 7.10b, shows a more intense Fe signal, having a Fe:Al peak ratio of approximately 0.93:1, compared to the one which appears to not have any hematite present, Figure 7.10a, which has a Fe:Al peak ratio of approximately 0.29:1. This greater Fe content in the region shown in Figure 7.10b aligns with the assessment that hematite crystallites are present across the surface.

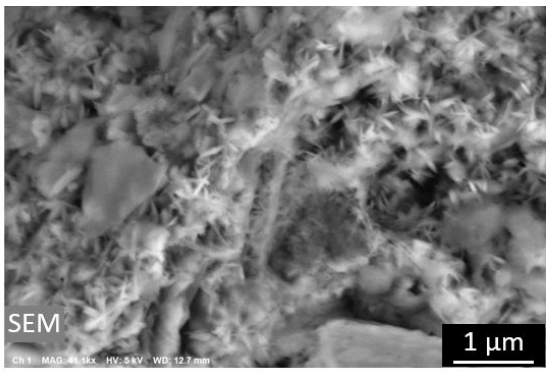
#### 7.3.1.7 Albite and Apatite

Albite ($NaAlSi_3O_8$) and apatite ($Ca_5(PO_4)_3F$) were proposed as explanations for the presence of Na and P respectively in the EDX results for some of the regions under investigation. The relevant data from one of these areas is presented in Figures 7.11 and 7.12. Figure 7.11 shows a low-vacuum SEM micrograph, which from topography alone appears to be a mica/vermiculite section with a small amount of hematite. From the elements detected in the EDX results shown in Figure 7.12, the situation appears to in fact be more complex, as Na and P would not be expected on a mica/vermiculite and hematite surface.

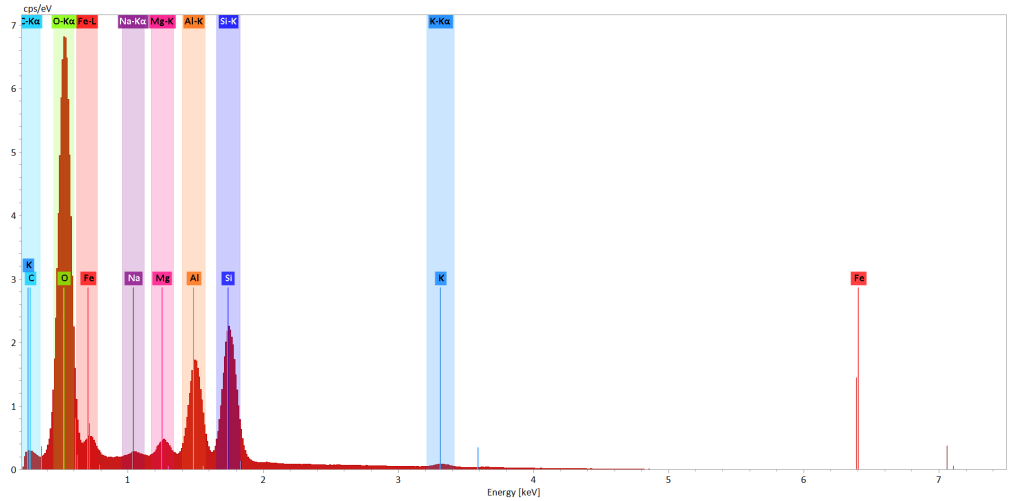
The assignments of albite and apatite were proposed with reference to the list of minerals in Bandera Brown presented by Yesufu-Rufai *et al.*.[89] Apatite is the only listed mineral which contains P, so is an explanation for its presence in the EDX spectrum. Of the minerals listed by Yesufu-Rufai *et al.* which contained Na, most were clays with fairly even Si and Al compositions. The EDX results in Figure 7.12 however show that the Si content (Figure 7.12b) was most concentrated where the Na was most concentrated (Figure 7.12c), but the Al distribution (Figure 7.12a) was not more concentrated. The region where Na is most concentrated is highlighted



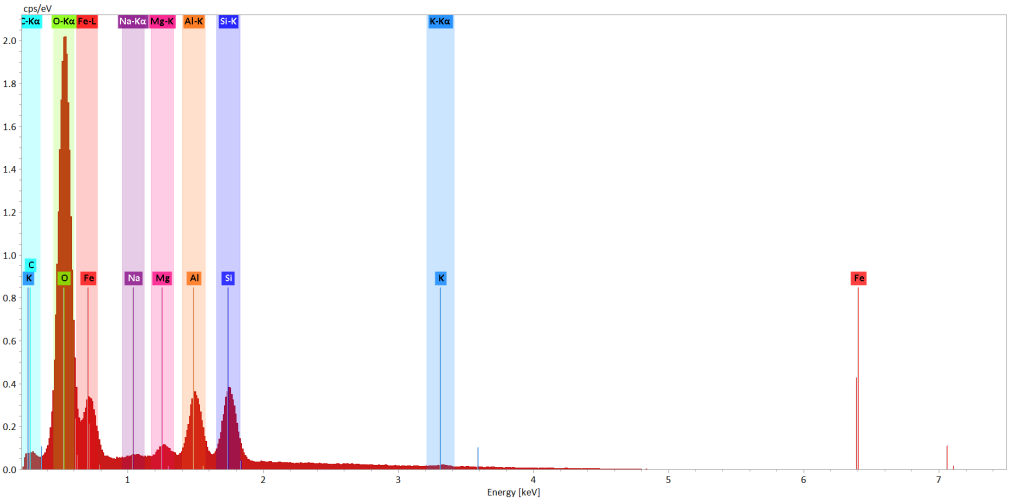

(a) Vermiculite/mica




(b) Hematite-covered




(c) EDX spectrum for the vermiculite/mica surface




(d) EDX spectrum for the hematite-covered surface

Figure 7.10: Hematite evidence in EDX results
Two areas of the Bandera Brown surface studied by EDX in Chapter 6: *Bandera Brown*; (a) and (b) show two high magnification low-vacuum SEM micrographs of what are proposed to be vermiculite/mica and hematite-covered surfaces respectively. The associated EDX spectra for these areas are shown in (c) and (d) respectively. (a) - (d) were originally shown in Figures 6.16a, 6.17e, 6.22a and 6.23e respectively.

by a white circle in all the element distribution maps. Albite was therefore selected as the only Si-rich Na-containing compound in Yesufu-Rufai *et al.*'s list, in order to explain these variations.[89]

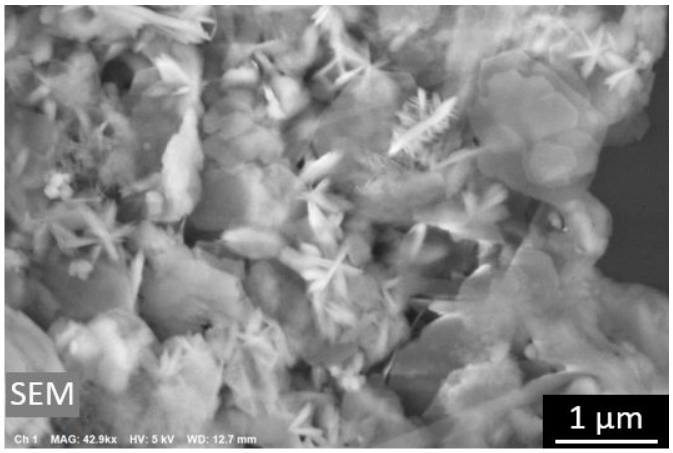
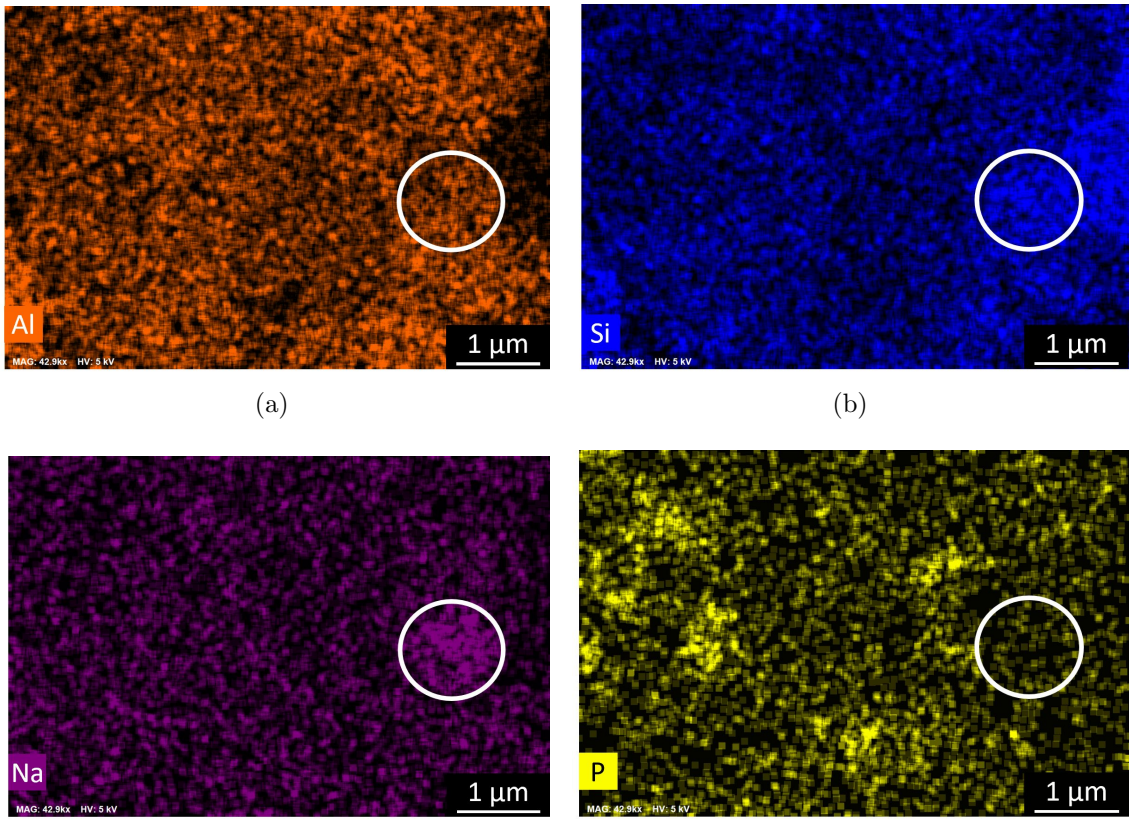



Figure 7.11: Bandera Brown: Albite and apatite locations - SEM micrograph
The low-vacuum SEM micrograph of the Bandera Brown surface previously shown in Figure 6.25 in Chapter 6: *Bandera Brown*. Selected EDX results for this region are shown once more in Figure 7.12.

As can be seen from the EDX spectrum in Figure 7.12e, both the Na and P are present in very small quantities compared to the majority of the other elements which were detected on the surface. There did however appear to be distinct hot-spots in the distribution maps in Figures 7.12c and 7.12d, which could indicate that these signals are not erroneous. These hot spots did not correlate neatly with any of the features visible in the associated low-vacuum SEM micrograph shown in Figure 7.11, which perhaps suggests that these minerals are present just beneath the surface.




(a) (b) (c) (d) (e)

Figure 7.12: Bandera Brown: Albite and apatite locations - EDX results
EDX data for an area of Bandera Brown originally shown in Figures 6.26 and 6.27 in Chapter 6: *Bandera Brown* which shows signals for Na and P. These are proposed to be indicators of the presence of albite and apatite. White guide circles highlight the location where Na is most concentrated on all maps for ease of comparison.

### 7.3.2 The composition of Bandera Brown

As touched upon in Chapter 1: *Introduction*, the literature provides conflicting accounts as to the exact composition of Bandera Brown.[89,98,182] For example, Gamal *et al.* list only six, van den Pol *et al.* list nine, and Yesufu-Rufai *et al.* list 15 different minerals in their reported compositions of Bandera Brown. All three are agreed that quartz is the dominant component, citing 59, 87 and 58.89 % compositions respectively, but the next most dominant listed by Gamal *et al.* is dolomite at 15 %, unlike van den Pol *et al.* and Yesufu-Rufai *et al.* who list plagioclase at 4 and 16.41 % respectively; Gamal *et al.* does not list plagioclase in their nine minerals at all, and dolomite does not feature in van den Pol *et al.*'s six either.[89,98,182] It is possible that all studies are correct to an extent, and that the exact composition of Bandera Brown varies from sample to sample. It is also likely that determining the exact composition of such a complex rock is not trivial, and that mistakes are made in resolving exactly which minerals are present. This is made particularly challenging in the case of Bandera Brown, where a variety of minerals with identical elemental compositions are present. For example, most clays which appear to be present in Bandera Brown are primarily composed of Si, Al and O in varying ratios.[89,98,124,182]

Despite the conflict and the doubt around this information, a broad understanding of Bandera Brown can be drawn. Quartz is clearly likely to be the most dominant component. A variety of clays are also present in all three reports; the three reports are not agreed on all of these minerals, but kaolinite ($Al_2Si_2O_5(OH)_4$), illite ($(K,H_3O)(Al,Mg,Fe)_2(Si,Al)_4O_{10}[(OH)_2,(H_2O)]$), and chlorite ($(Fe, Mg, Al)_6(Si, Al)_4O_{10}(OH)_8$) are all present in these three reports, at a

variety of compositions.[89,98,182]

Based on low-vacuum SEM micrographs and EDX results, and guidance from Dr. Fons Marcelis,[a] nine minerals were tentatively identified as present on the Bandera Brown sample in Chapter 6: *Bandera Brown*, and were summarised in Table 7.3 (page 382). Table 7.4 lists these nine minerals once more, and indicates which of the three reports from Gamal *et al.* van den Pol *et al.* and Yesufu-Rufai *et al.* also found these minerals via XRD (Gamal *et al.* and van den Pol *et al.*) and BSE SEM (Yesufu-Rufai *et al.*) analysis.[89,98,182] From this table, it can be seen that eight out of the nine minerals were also identified by one of these reports.[89,98,182] As previously stated, quartz and kaolinite were identified in all three reports. Albite is named specifically in one report, and the generic classes to which it belongs is listed in the other two reports. Smectite and calcite were identified in two out of the three papers, and apatite, vermiculite and mica were only listed in one of the three papers.

The ninth mineral, hematite ($Fe_2O_3$) was not listed in any of these three papers, but was identified by Dr. Fons Marcelis as being present in some of the low-vacuum SEM micrographs. Iron is a common element in Bandera Brown, and as such it is not improbable that an iron oxide would be present on the surface. Although information relating to hematite on Bandera Brown specifically could not be found, hematite has been found in the literature to be a common iron oxide precipitate on iron-bearing sandstones,[183,184] as well as being found to be naturally present in small inclusions in K-feldspars, which were reported by both Gamal *et al.* and Yesufu-Rufai *et al.* as being present in Bandera Brown.[89,98,185] Additionally, the EDX spectra of areas proposed to be covered with hematite had much higher Fe:Al

[a]Research Geologist at Shell Global Solutions International B.V., Amsterdam, the Netherlands

| Mineral | Gamal *et al.* | van den Pol *et al.* | Yesufu *et al.* |
|---|---|---|---|
| Quartz | ✓ | ✓ | ✓ |
| Mica | | ✓ | |
| Vermiculite | | ✓ | |
| Calcite | | (✓) | ✓ |
| Smectite | | ✓ | ✓ |
| Kaolinite | ✓ | ✓ | ✓ |
| Hematite | | | |
| Albite | ✓ | ✓ | ✓ |
| Apatite | | | ✓ |

Table 7.4: Bandera Brown minerals identified in SEM data compared to literature analyses
The nine minerals which were identified from low-vacuum SEM micrographs and EDX data in Chapter 6: *Bandera Brown*, and which of the three reports from Gamal *et al.* van den Pol *et al.* and Yesufu-Rufai *et al.* also found these minerals in their analyses.[89,98,182] "✓" indicates that the mineral was identified, no symbol indicates that the mineral was not identified, and "(✓)" indicates that the mineral was identified in trace amounts by the associated authors.

peak ratios than areas which appear to not have any hematite present. The data from Chapter 6: *Bandera Brown* which shows this most clearly was re-shown in Figure 7.10 (page 388), where the EDX spectrum for the surface proposed to contain hematite shows an approximately 0.93:1 Fe:Al peak ratio, compared to the EDX spectrum for the region proposed to contain vermiculite or mica showing an approximately 0.29:1 Fe:Al peak ratio. Considering all of the information available, hematite is still proposed to be a valid mineral assignment for the Bandera Brown surface presented in Chapter 6: *Bandera Brown*.

### 7.3.3 Mineral Relevance for PNM

Certain minerals on the Bandera Brown surface are anticipated to have greater relevance than others when serving as inputs for PNM, depending on their abundance and on their charge behaviour towards crude oil under different conditions. Below, the minerals which were identified in the low-vacuum SEM micrographs and associated EDX analyses are discussed; the more relevant surfaces here are of particular interest for topographical and surface charge mapping on the SICM for inputs in PNM.

#### 7.3.3.1 Clays

The clay minerals which were identified on the surface of Bandera Brown: mica, vermiculite, kaolinite and smectite, are all expected to be of significance to PNM of Bandera Brown systems, along with similar sandstone outcrop rocks. From the literature, clays are estimated to make up 7 - 14.88 % of the Bandera Brown surface, so represent a significant proportion of the sample.[89,98,182] Additionally, as previously mentioned in Chapter 4: *Surface Charge Mapping*, Section 4.2.2, clays are thought to play a key role LSF due to their negatively charged surfaces and their interaction with the crude oil.[120,127] In high-salinity brines, the negative charges of the clay and crude oil surfaces are shielded from each other by the abundance of positively charged ions in solution, allowing the crude oil to remain in place within the rock. At lower salinities however, the concentration of positive ions is insufficient to shield the negatively charged surfaces from each other, and the crude oil is thus removed from the rock surface.[120] Kaolinite particles were also discussed (Chapter 4: *Surface*

*Charge Mapping*, Section 4.2.1), due to their pH-dependent surface charge behaviour, becoming predominantly positively charged at pHs below 6 - 6.5; a behaviour which could be exploited in EOR.[118,125] The relative abundance of clays on the Bandera Brown surface, in addition to these environment-dependent behaviours exhibited by them, ultimately mean that inputs such as topography and surface charge mapping for clay surfaces are of key interest for PNM, not just for Bandera Brown, but for all clay-rich outcrop rocks.

#### 7.3.3.2 Quartz

Quartz is also expected to be of importance for accurate PNM of Bandera Brown systems. Quartz has been found in the literature to be the most abundant mineral on Bandera Brown, with proportions ranging between 58.89 - 87 %.[89,98,182] Quartz, like some clays, also exhibits pH-dependent surface charge behaviour, but with a much greater skew towards negative charge; the point of zero charge being around pH 2 - 3, below which a positive charge is observed.[186,187] Although pH $< 2$ is not expected to be encountered frequently in a reservoir environment, so this pH-dependent positive/negative behaviour is not necessarily of interest, it should be noted that the surface charge density of quartz builds slowly from pH 2 - 3 to pH 5 - 6, above which a higher magnitude of negative charge is observed, which may play a role in the strength of surface/crude oil interactions across these pHs, which could have implications for EOR techniques such as LSF.[186,188] These considerations, coupled with quartz being agreed in the literature as the most abundant mineral in Bandera Brown, clearly demonstrate the importance of the study of quartz's topography and surface charge for PNM.[89,98,182]

#### 7.3.3.3 Calcite

Calcite, as shown in Table 7.4, is not consistently reported in the literature as being present in Bandera Brown, however Yesufu-Rufai *et al.* reported 7 % calcite in their sample.[89,98,182] Additionally, a large structure was observed in the low-vacuum SEM micrographs shown in this thesis (Figure 7.9, page 386), which appears to be a calcite crystal. Understanding calcite's environment-dependent surface charge behaviour is of interest to a number of applications, however the dependencies which have been identified are yet to be fully understood.[189] Although changes in pH have been shown to change the surface charge magnitude of calcite via zeta potential measurements, the surface remains strongly positively charged, so this is not anticipated to be of interest to EOR applications.[189,190] Concentrations of certain additives however, for example sodium polyacrylate (NaPA), have been shown in the literature to have a notable effect on the surface charge of calcite, with additions of NaPA as low as 0.2 % to calcite suspensions being reported as demonstrating a switch from the "default" positive to a negative surface charge.[190] Although the surface charge dependencies of calcite would be of interest for understanding and modelling the carbonate outcrop rocks studied in this thesis, it is likely that this is not an important mineral to consider in PNM of Bandera Brown, given its low abundance.[89,98,182]

#### 7.3.3.4 Albite

Albite, a plagioclase and alkali feldspar with the chemical formula $NaAlSi_3O_8$, was assigned in the low-vacuum SEM work presented in this thesis due to EDX maps showing a clear Na hot-spot alongside a Si hot-spot and the presence of Al.[170] Gamal

*et al.* report their Bandera Brown surface as containing 12 % albite; although not specifically named by Yesufu-Rufai *et al.*, they list plagioclases and alkali feldspars as being present at 16.41 and 1.85 % respectively, and van den Pol *et al.* list plagioclases as being present at 4 %, so the literature appears to be in agreement that this could be a significant mineral for PNM studies of Bandera Brown.[89,98] Albite has shown pH-dependent surface charge behaviour in the literature, with a point of zero charge around pH 4; below this the mineral exhibits a positive surface charge, and above this a negative surface charge.[191] The magnitude of this negative surface charge at higher pH has also been shown to be reduced with increasing salt concentration, which could also have useful applications in EOR.[192] From these factors it is clear that albite would be of interest for PNM of Bandera Brown systems, however locating a region of albite on the surface of Bandera Brown with SICM mapping would pose a challenge, as it does not have a distinctive shape, and was only observed in the regions studied with low-vacuum SEM from the EDX analysis.

#### 7.3.3.5 Hematite

Hematite was observed on the low-vacuum SEM micrographs of Bandera Brown presented in this thesis, alongside EDX analysis showing a higher concentration of Fe than would have otherwise not been expected. As mentioned in Section 7.3.2, although hematite is not specifically listed as being present in Bandera Brown in the literature, hematite has been reported in the literature as a common precipitate from iron-bearing sandstones, as well as being naturally present in K-feldspars, which have been reported as being present in Bandera Brown.[89,98,183–185] Hematite, $Fe_2O_3$, has also been shown in the literature to be reducible to magnetite, $Fe_3O_4$, under high

pH and reducing conditions, which could explain the redox-dependent back-pressure behaviour observed by Southwick *et al.* in Bandera Brown core flooding experiments with HPAM.[88,184,193] If an area of hematite crystals was therefore located on the Bandera Brown surface with the SICM, it is likely that any information gathered would be of importance to predicting fluid flow behaviour in Bandera Brown systems using PNM.

#### 7.3.3.6 Apatite

Apatite, like albite, was only identified in the regions imaged by low-vacuum SEM via EDX analysis. The assignment of apatite, $Ca_5(PO_4)_3F$, was given due to the presence of a small P peak in the EDX spectrum, which could only be assigned to apatite, as it was the only mineral reported as present in Bandera Brown in the literature which contained P.[88,89,98] As it was assigned from the EDX alone, not from feature shape, it was not identified in the SICM topographical images. This is however not deemed to be of importance, as it was only found in one report, by Yesufu-Rufai *et al.*, and at only 0.08 %;[89] due to this lack of abundance, it is unlikely that apatite has any significant effect on the behaviour of Bandera Brown systems for the purposes of PNM.

#### 7.3.3.7 Summary

Overall, it is clear that there is no single set of conditions which yield an entirely positive or negative surface charge on sandstone surfaces. For example, clays and quartz exhibit positive surface charge behaviour at low pHs, whereas hematite requires high pHs to be reduced to magnetite and exhibit more favourable conditions for crude oil removal.[88,118,125,186,187] Calcite, by contrast, remains positively charged across the pH range.[189,190] Depending on the relative abundances of the minerals on a given sandstone surface, different EOR techniques would need to be employed to exploit the surface charge-altering behaviours; there is unlikely to be a "one size fits all" approach applicable to all sandstones. It is therefore key that mineral identification is performed on the surface of sandstone samples, not just an assessment of the morphology, prior to any PNM being carried out, to ensure accurate and relevant data is collected.

### 7.3.4 Topographical mapping with SICM

As summarised previously in Table 7.3 (page 382), only mica/vermiculite and smectite clays were identified in the SICM topographical images taken of the Bandera Brown surface. These minerals have relatively similar characteristics, all with feature sizes of 1 - 2 $\mu$m across, which fit well within the fields of view used during SICM imaging. Of the minerals which were not identified during SICM imaging, two of these, albite and apatite, were only identified from EDX data, so were not expected to be possible to identify from the SICM topographical images. The other minerals which were not identified by SICM were quartz, calcite, kaolinite and hematite.

The quartz, calcite and kaolinite structures which were identified in the low-vacuum SEM micrographs were comparatively larger than those of the mica, vermiculite and smectite clays, being $>$ 10, 50 - 90 and 3.5 - 4 $\mu$m across respectively, which may have played a role in why they were not identified in any of the SICM images, as these approach or exceed the fields of view used during SICM imaging. If larger fields of view had been used during the SICM studies, calcite or quartz could have been identifiable, but would not necessarily have been differentiable, as they are both crystallites with smooth surfaces and edges. Kaolinite structures have a distinctive "booklet" structure which would also have been identifiable if one were successfully mapped with the SICM, and their being on the order of 3.5 - 4 $\mu$m across would have allowed them to be entirely captured within the larger 5 $\times$ 5 $\mu$m or 10 $\times$ 10 $\mu$m SICM fields of view. They were however not abundant in the low-vacuum SEM micrographs for Bandera Brown presented in Chapter 6: *Bandera Brown*, so it is possible that their absence from the SICM images is in part

due to their rarity; the XRD data obtained by van den Pol *et al.*, Gamal *et al.* and Yesufu-Rufai *et al.* aligns with this assessment, each stating 3, 3 and 1.24 % kaolinite compositions respectively in their Bandera Brown samples.

The spikey hematite crystallites visible in the low-vacuum SEM micrographs in Figures 7.10b and 7.11 (pages 388 and 389) are estimated to be on the order of 400 - 600 nm across; these structures would therefore not necessarily be resolved in the larger 5 $\times$ 5 $\mu$m or 10 $\times$ 10 $\mu$m SICM images, with pixel sizes typically 50 $\times$ 50 or 100 $\times$ 100 nm, but might have been identifiable in the smaller 2 $\times$ 2 $\mu$m SICM images, with pixel sizes typically 25 $\times$ 25 nm, had they been imaged.

Overall, it is to be expected that the abundant minerals with feature sizes best suited to the sizes of field of view and resolution limits used in the SICM, and those least likely to cause the tip to crash, were the features which were captured successfully in the SICM images of Bandera Brown.

## 7.4 Ageing Studies

Chapters 5: *Carbonate Ageing Studies*, and 6: *Bandera Brown*, presented low-vacuum SEM, AFM and SICM images of three artificially aged samples; calcite, Estaillades and Bandera Brown. Calcite and Estaillades were selected of the four carbonates investigated in Chapter 3: *Carbonates*, as calcite is a predominantly flat sample and thus the most topographically "simple", and Estaillades was the least diverse of the three carbonates, having fewer different surface types than Ketton or Estaillades. Bandera Brown was also aged and studied, as it presented both a more mineralogically and a more topographically complex surface. As was established in Chapters 5: *Carbonate Ageing Studies*, and 6: *Bandera Brown*, samples discussed in this section which have been subjected to the ageing protocol are referred to as "aged", and samples which have not been exposed to crude oil and elevated temperatures are referred to as "unaltered".

Summaries of the surfaces types observed on these three aged materials using low-vacuum SEM before and after mapping on the SICM are given in Tables 7.5 and 7.6 on pages 404 and 405. Aged calcite had the greatest diversity in surface types, presenting four distinct regions across two different samples. Aged calcite sample 1 was predominantly covered by spherical droplet structures 1 - 2 $\mu$m across, which were either by themselves or in small clusters on an otherwise flat surface, surface type 1, or formed larger agglomerates on the order of 10s of $\mu$m across which obscured the flat surface beneath, surface type 2. Surface type 3 represented regions of the aged calcite surface which did not have any droplets present, appearing to reveal the topography of the calcite surface beneath. Aged calcite sample 2 presented

one further surface type, surface type 4. Surface type 4 is similar to surface type 1, in that there are raised features present across an otherwise flat surface. These features are however less rounded, with varied shapes and sizes around 1 - 4 $\mu$m across.

Aged Estaillades and Bandera Brown in contrast did not appear to present any diversity in their crude oil films. The rock surfaces themselves are rougher than calcite, with greater height variations, a suggestion of which is visible beneath the film. Despite the variation beneath, the crude oil films coating these complex topographies are the themselves quite homogeneous, made up of evenly spaced droplet structures which cover the surfaces fully. Tables 7.5 and 7.6 therefore describe only one surface type each for the aged Estaillades and Bandera Brown surfaces.

| Aged Material | Surface Type | Description | EDX Signals | EDX signals on unaltered surface |
|---|---|---|---|---|
| Calcite | 1 | Spherical droplets of 1-2 $\mu$m across on an otherwise smooth crude oil film | N/A | Ca, C and O |
| | 2 | Agglomerates 10s of $\mu$m across of the smaller droplets | | |
| | 3 | Regions which do not have any droplet structures present | | |
| | 4 | Irregular deposits on an otherwise smooth crude oil film | C, O and S | |
| Calcite post-SICM | 1 | Irregular deposits on an otherwise smooth crude oil film | N, little O | |
| | 2 | Smooth surface without any droplets or deposits | N, lots O | |
| Estaillades | 1 | Smooth droplets approximately 1 $\mu$m across agglomerated to form a continuous film | C, S, O and N | Ca, O and Si |
| Estaillades post-SICM | 1 | Smooth droplets approximately 1 $\mu$m across, agglomerated to form a continuous film | N and S | |
| | 2 | Smooth-sided raised structured above the crude oil film | Si, N, Na, O and S | |

Table 7.5: Summary of Aged Carbonate Surface Types
A summary of the different surface types identified on the aged calcite and Estaillades samples: qualitative descriptions based on low-vacuum SEM micrographs and summaries of relevant EDX data from Chapter 5: *Carbonate Ageing Studies.*

| Aged Material | Surface Type | Regions Observed | EDX Signals | EDX signals on unaltered surface |
|---|---|---|---|---|
| Bandera Brown | 1 | Smooth droplets approximately 1-2 $\mu$m across, agglomerated to form a continuous film | N and O | Al, Fe, Si, Mg, O, C, K, Na, occasionally P |
| Bandera Brown post-SICM | 1 | Smooth droplets approximately 1-2 $\mu$m across, agglomerated to form a continuous film | N, O, S and Si | |
| | 2 | Flat, elevated regions, without droplet structures present | | |

Table 7.6: Summary of Aged Bandera Brown Surface Types
A summary of the different surface types identified on the aged Bandera Brown sample: qualitative descriptions based on low-vacuum SEM micrographs and summaries of relevant EDX data from Chapter 6: *Bandera Brown*.

### 7.4.1 SICM and AFM imaging

A summary of the surface types which were identified in the SICM and AFM images of aged calcite, Estaillades and Bandera Brown is presented in Table 7.7. In the case of aged calcite, surface types 1 and 2 were identified in both the SICM and AFM images; as these were the most common surface types observed on aged calcite 1, it is not unexpected that they would be found by both scanning probe microscopies.

| Aged Material | Surface Type | SICM | AFM |
|---|---|---|---|
| Calcite | 1 | ✓ | ✓ |
| | 2 | ✓ | ✓ |
| | 3 | | |
| | 4 | | |
| Estaillades | 1 | ✓ | ✓ |
| Bandera Brown | 1 | ✓ | N/A |

Table 7.7: Aged material surface types identified by SICM or AFM
A summary of the aged material surface types which were identified in the SICM and AFM topographical images in Chapters 5: *Carbonate Ageing Studies*, and 6: *Bandera Brown*. "✓" signifies that the surface type was identified in at least one image and no symbol signifies that no examples of that surface type were identified.

Aged calcite surface types 3 and 4 on the other hand were not found during either SICM or AFM imaging. Aged calcite surface type 3 was the least common surface type observed on aged calcite 1, appearing very infrequently on the regions investigated with low-vacuum SEM, so it is possibly a reflection of its relative rarity that it was not found by the probe microscopies. Aged surface type 4 was the only surface type identified on aged calcite 2. Aged calcite 2 was created to serve as a reference for the post-SICM aged calcite 1 surface, to investigate whether the same surface-altering effects would be achieved if the sample was merely left in air for a few months. To this end, it was therefore not imaged with AFM or SICM. Although

it is therefore perhaps not surprising that no examples of surface type 4 were found in the AFM or SICM images, the row is included in this table to highlight that no examples of surface type 4 were found on the aged calcite 1 in the low-vacuum SEM micrographs or SICM and AFM images.

Aged Estaillades and Bandera Brown only had one identified surface type each in the low-vacuum SEM micrographs. Both SICM and AFM were carried out on aged Estaillades, and both successfully imaged the surface, showing feature sizes and shapes similar to those seen in the low-vacuum SEM micrographs. As AFM had already been utilised to validate the SICM images on the aged carbonate surfaces, only SICM was carried out on the aged Bandera Brown sample; these experiments also successfully yielded images of the surface, which aligned with what was observed in the low-vacuum SEM micrographs.

### 7.4.2 Aged sample variability

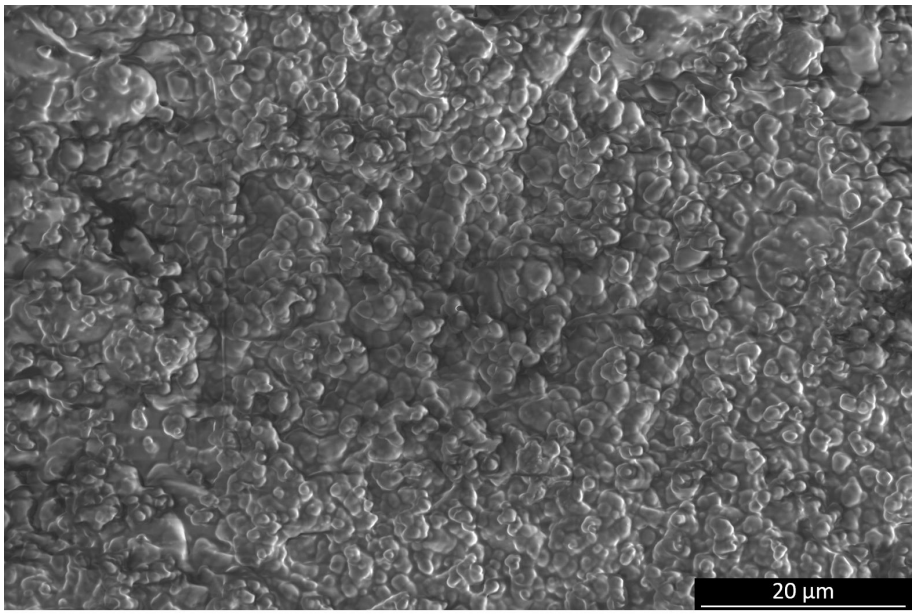
The two aged Estaillades surfaces which were studied with low-vacuum SEM appeared to be quite similar (Figure 7.13), despite being aged at different times. They were however not identical; on the second sample surface the droplet structures were further apart, unlike the first sample which appeared to be covered in a continuous film of droplet structures. This difference might be the result of variations in film thickness, or perhaps a difference in the exact number of days after ageing at which the low-vacuum SEM micrographs were collected. Additionally, although the same type of crude oil was used in both experiments, the crude oil used to age these two

samples were from two different bottles provided by two different laboratories,[a] so there may be some variation in the exact composition of the crude oil used in each ageing process.

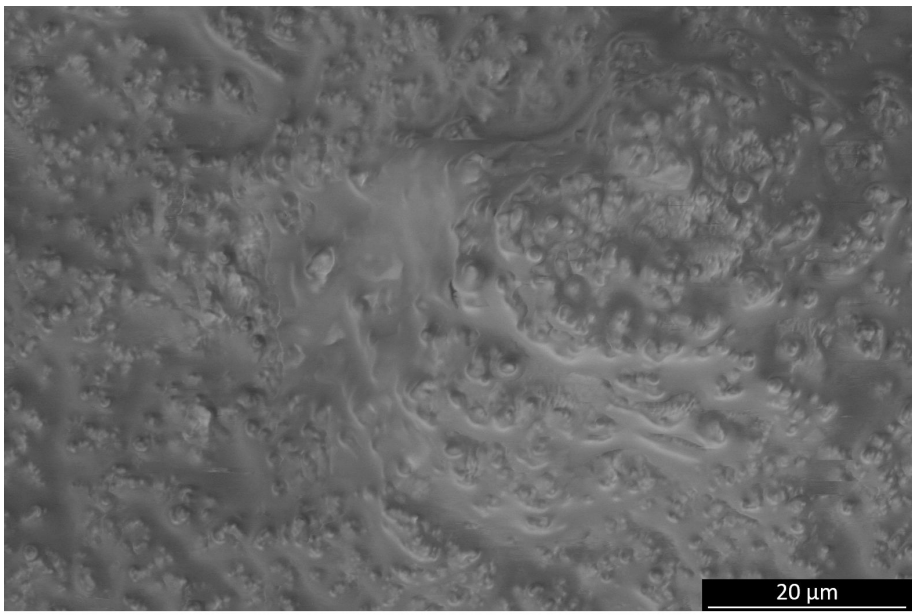
A greater difference is observed between the surfaces of aged calcite samples 1 and 2, highlighted by the low-vacuum SEM micrographs shown in Figure 7.14. On the surface of aged calcite 1 (Figure 7.14a), the raised features present are all around 1 - 2 $\mu$m across and quite rounded in shape. The aged calcite 2's surface on the other hand (Figure 7.14b) has raised features with a greater variation in size, between 1 - 4 $\mu$m, and are a variety of shapes, some with sharp edges. It is possible that these inconsistencies can be explained by two different crude oil sources being used, as was suggested for Estaillades, and thus subtly different deposits are forming. When the aged calcite 2 sample surface is compared to the aged calcite 1 sample after imaging with the SICM, surface type 1 (Figure 7.14c), it can be seen that structures of similar sizes and shapes are present on both surfaces. It is therefore proposed that the inconsistencies between aged calcite 1 and 2 are the result, in part at least, of different times elapsing between sample fabrication and characterisation.

The differences observed between these samples do cast doubt on the reproducibility of the ageing procedure used in these studies; the procedure followed was similar to the accepted procedures in the literature and those conducted by researchers on the SDRP, although across the literature there are variations in duration, temperature and the starting conditions of the outcrop rock core, which are all likely to have an impact the resulting conditions for film topology, redox

[a]one provided by the Luckham group in the Department of Chemical Engineering, and the other from the Blunt group in the Department of Earth Science and Engineering

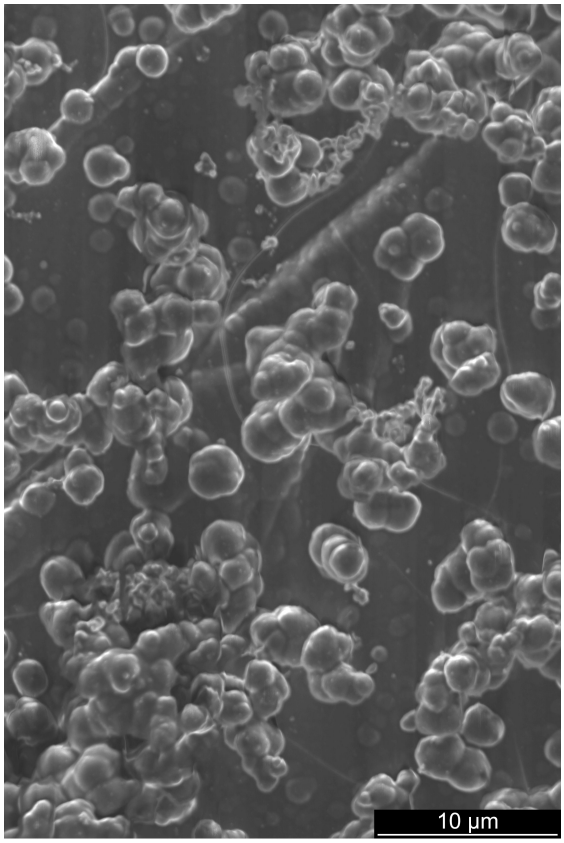



(a) Aged Estaillades 1

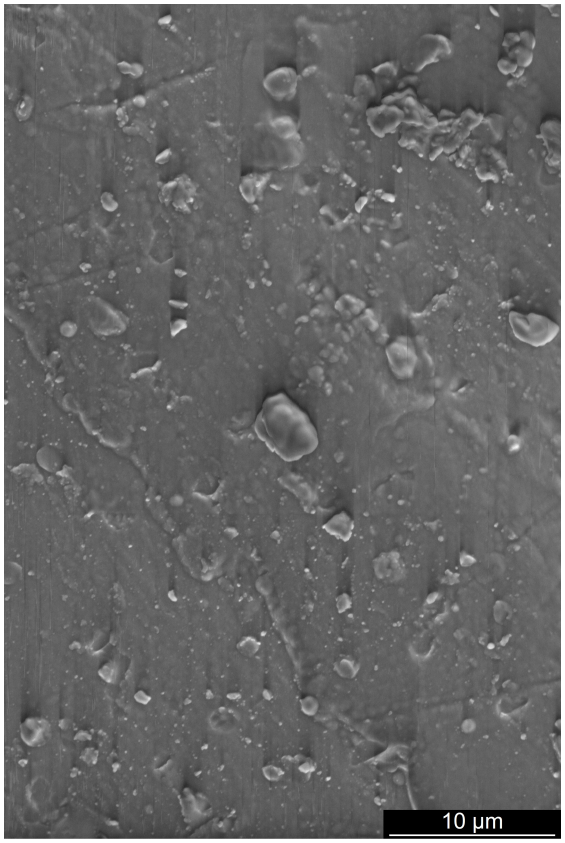



(b) Aged Estaillades 2

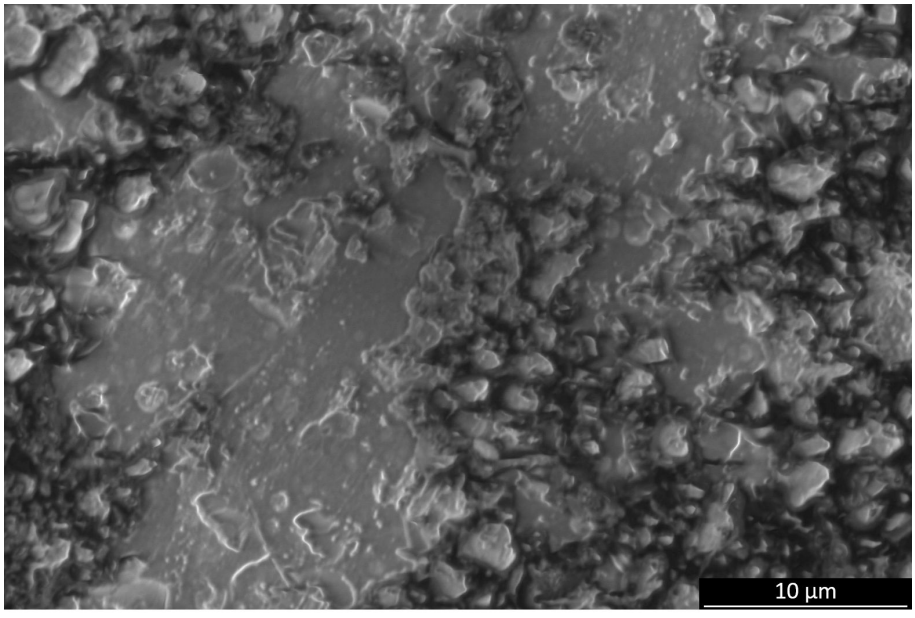
Figure 7.13: Reproducibility of ageing on Estaillades
Two low-vacuum SEM micrographs of aged Estaillades samples 1 and 2. (a) shows a low-vacuum SEM micrograph of aged Estaillades 1 which fully encompasses the region shown in Figure 5.23d in Chapter 3: *Carbonates*. (b) shows the low-vacuum SEM micrograph of aged Estaillades 2 which was originally shown in Figure 5.24b in Chapter 3: *Carbonates*.




(a) Aged Calcite 1




(b) Aged Calcite 2




(c) Aged Calcite 1 post-SICM

Figure 7.14: Reproducibility of ageing on calcite
Two low-vacuum SEM micrographs of calcite samples 1 and 2, and a low-vacuum SEM micrograph of surface type 1 on the aged calcite 1 sample post-SICM. (a), (b) and (c) show the low-vacuum SEM micrographs shown in Figures 5.5b, 5.9a and 5.13b respectively from Chapter 5: *Carbonate Ageing Studies*

state and surface charge distributions.[142–144] From these experiments alone it is not possible to make any conclusive remarks about the reproducibility of this method; further, more extensive studies would be required to understand the dependencies and sensitivities of this procedure.

Two samples of Bandera Brown were also aged, however the surfaces which were observed across both samples were very similar, with no differences of note (Chapter 6: *Bandera Brown*, Section 6.3.1.1). With inconsistencies across the aged Estaillades and calcite samples however, a more in-depth study is required to determine whether these differences are due to air exposure time differences, subtle differences in crude oil composition or perhaps a contamination issue. From the limited data here however, it is not possible to draw any firm conclusions.

### 7.4.3 The impact of SICM imaging

On the aged calcite and Bandera Brown samples, alteration to the crude oil film appeared to occur during imaging with the SICM, which is attributed to the 0.1 M $KCl_{(aq)}$ electrolyte partially removing or altering the film at certain locations. This observation is not unexpected, as brines of varying compositions and concentrations are commonly used in oil recovery techniques such as the EOR technique of LSF.[119,120,126,127]

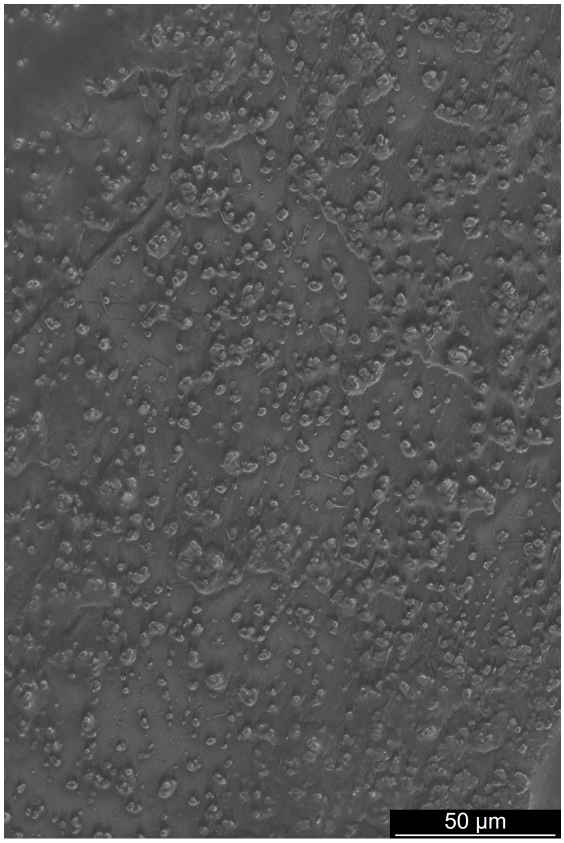
The low-vacuum SEM micrographs which were taken after SICM imaging revealed that the crude oil film had changed morphologically in places, most notably on the aged calcite surface, which presented two new, distinct regions when compared to the surface prior to SICM imaging (Figure 7.15). EDX revealed that one

of these surface types was rich in oxygen, whereas the other was not, unlike the freshly aged sample which had an even distribution of oxygen on the surface. From this information, it was hypothesised that the crude oil film had segregated into its more and less oxygen-rich components. There was no Ca peak present, and therefore there was no evidence of local thinning of the film to $< 2$ $\mu$m.[83]

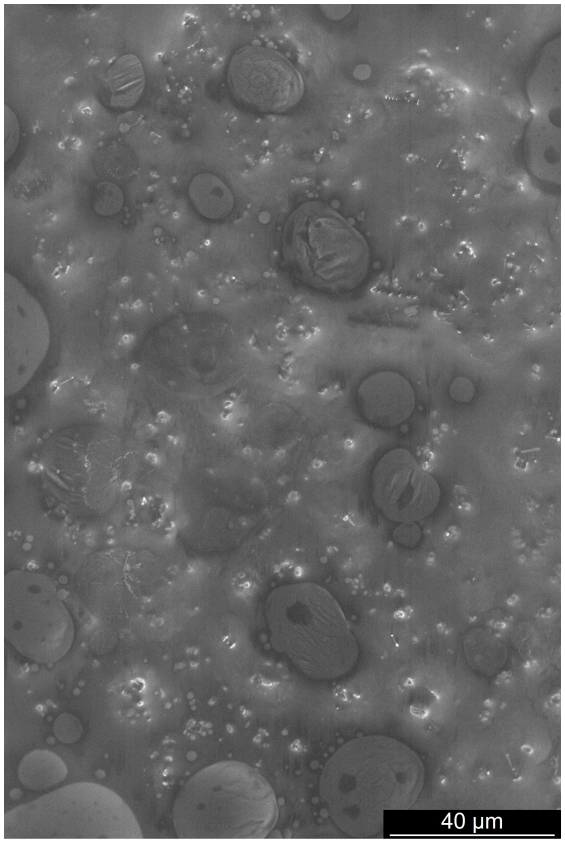
Although the post-SICM crude oil film alteration was not as immediately obvious on the aged Bandera Brown surface from the low-vacuum SEM micrographs alone, as it was for the aged calcite, investigation with EDX showed that crude oil film alteration had occurred (Figures 7.16 and 7.17). EDX mapping of the aged Bandera Brown surface immediately post-ageing revealed only N and O signals from on the surface. Subsequent EDX mapping of the aged Bandera Brown sample after SICM characterisation revealed that additional elements were present, most notably Si was detectable on the surface. Si is present in some minerals in Bandera Brown such as quartz or clays, but is not expected from a crude oil film. As such, the Si signal on the aged Bandera Brown surface after SICM characterisation is proposed to be coming from the Bandera Brown rock itself, and is an indication of the local thinning of the crude oil film such that the signal could be detected. The exposure of Si-bearing minerals, which on Bandera Brown would imply the quartz or clay minerals, by the 0.1 M $KCl_{(aq)}$ electrolyte aligns with the literature surrounding LSF. LSF has been reported as effective and studied extensively on clay- and quartz-rich surfaces, and so it makes sense that the presence of these minerals correlated with where evidence of film-thinning was observed after exposure to a low-concentration salt solution on the aged Bandera Brown surface.[119,120,126,127,188] A detailed explanation

of the mechanism of LSF on negatively-charged surfaces such as quartz and clays can be found in Chapter 4: *Surface Charge Mapping*, Section 4.2.2.

The film alteration on the aged calcite sample can not be explained by chemical heterogeneity, as it is chemically homogeneous, and indeed the very chemically similar aged Estaillades sample did not exhibit any clear evidence of crude oil film alteration after SICM characterisation, so it is not likely that the alteration was influenced by the surface chemistry. It is therefore proposed that the apparent film segregation observed on the aged calcite surface was enabled by the relatively flat, smooth calcite surface itself, allowing different components of the film to move across the surface and agglomerate. The Estaillades sample by contrast is much rougher, and so movement of crude oil components within the film would have been more restricted; it is possible that a similar effect could be replicated on an Estaillades sample, had it been immersed in the $KCl_{(aq)}$ for a longer period of time, but it is not possible to draw any firm conclusions about the mechanism of this apparent film segregation without further work.




(a) Aged Calcite

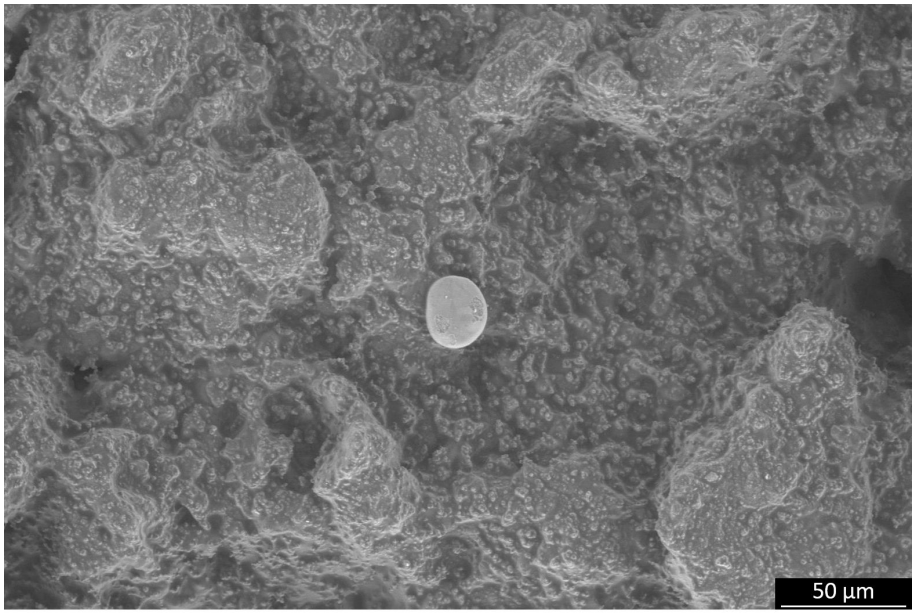



(b) Old Aged Calcite

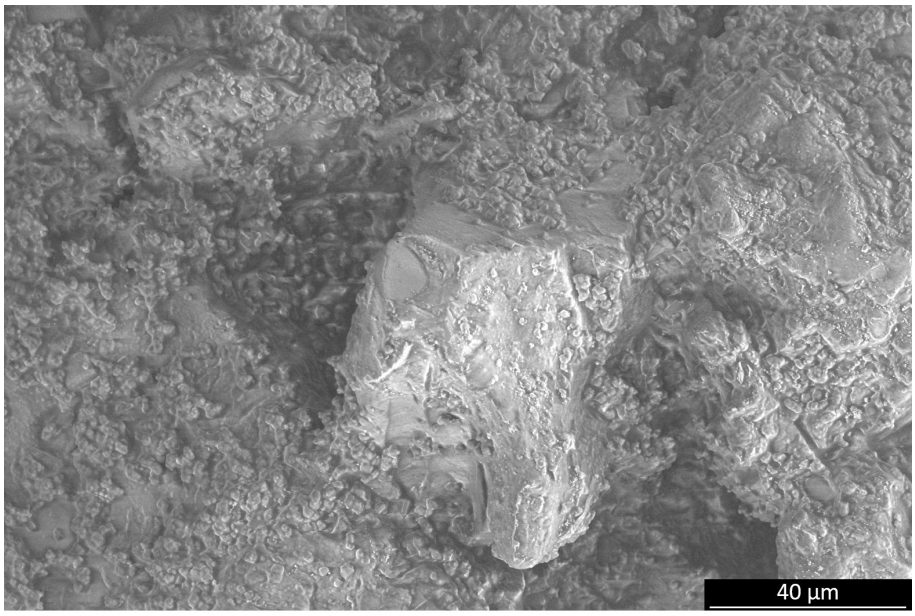



(c) Aged Calcite post-SICM

Figure 7.15: Surface alteration of aged calcite
The three aged calcite surfaces examined with low-vacuum SEM; (a) the freshly aged calcite surface, (b) the aged calcite surface left in air for a few months and (c) the aged calcite surface which had undergone characterisation with SICM. These micrographs were initially shown in Figures 5.9c, 5.18 and 5.14, pages 228, 240 and 235 respectively, in Chapter 5: *Carbonate Ageing Studies*.

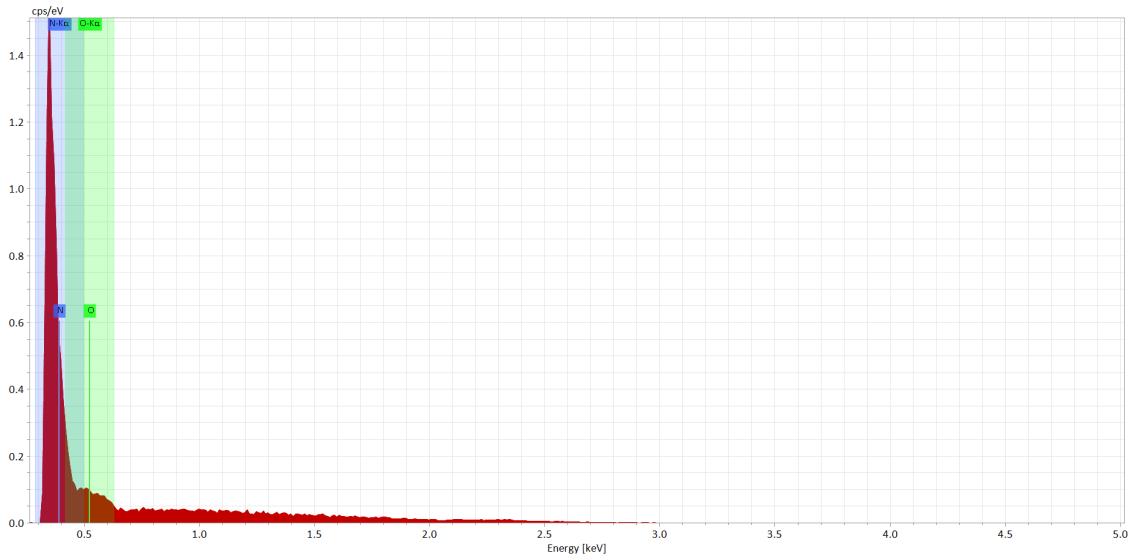



(a) Aged Bandera Brown

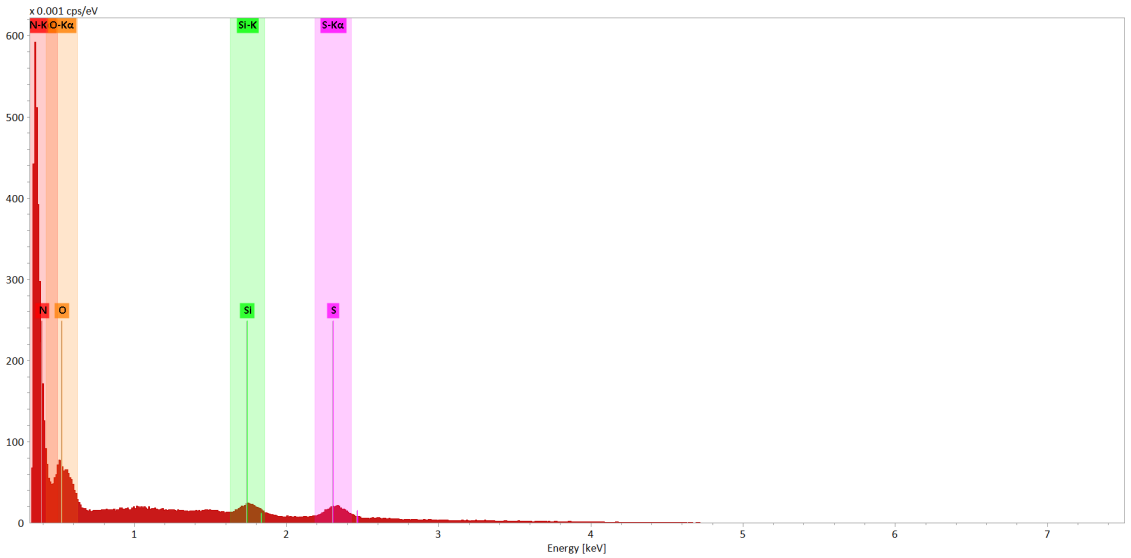



(b) Aged Bandera Brown post-SICM

Figure 7.16: Surface alteration of aged Bandera Brown: SEM
Low-vacuum SEM micrographs of the aged Bandera Brown surface (a) before and (b) after SICM characterisation. (a) was originally shown as part of the overlay in Figure 6.45 and (b) was originally shown in 6.59, both in Chapter 6: *Bandera Brown*.




(a) Aged Bandera Brown



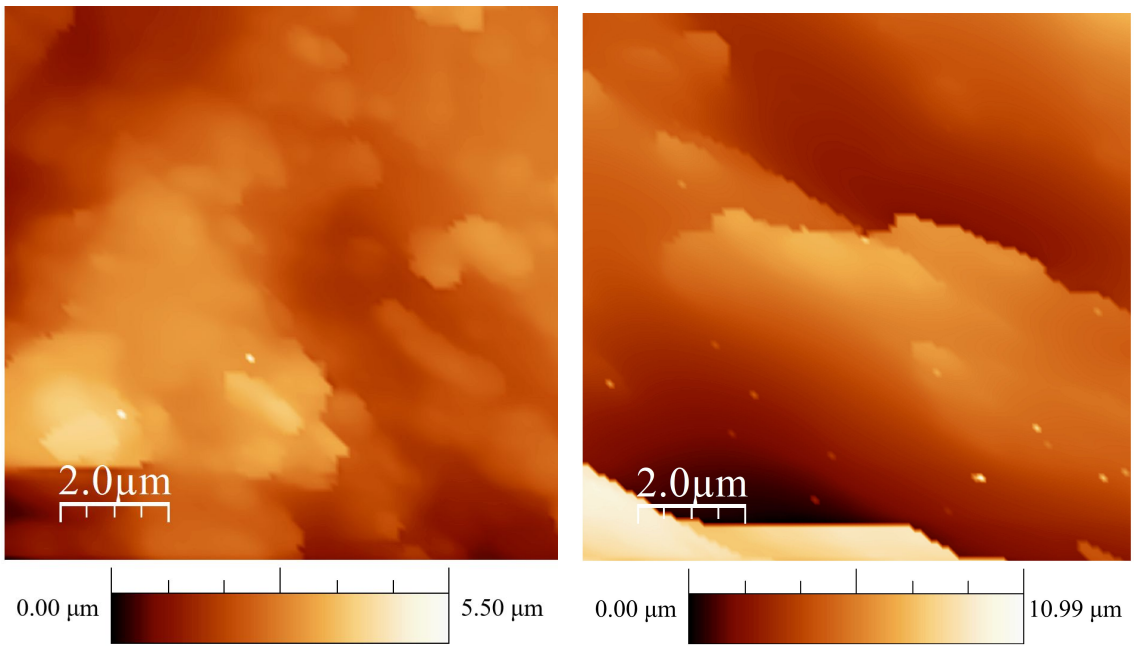

(b) Aged Bandera Brown post-SICM

Figure 7.17: Surface alteration of aged Bandera Brown: EDX
EDX spectra for the low-vacuum SEM micrographs shown in Figure 7.16, which demonstrate the surface alteration before and after SICM imaging. (a) shows the EDX spectrum for the freshly aged Bandera Brown surface, where only N and O signals are present, whereas (b) shows the EDX spectrum for the aged Bandera Brown surface after SICM characterisation, where N, O Si and S signals are all present. These spectra were originally shown in Figures 6.53d and 6.61 in Chapter 6: *Bandera Brown*.

In addition to the information from low-vacuum SEM and EDX experiments, observations were made during characterisation with SICM which are proposed as being the result of crude oil/electrolyte interactions. During the SICM experiments on all of the aged samples, including Estaillades, it was found that the nanopipette became blocked more frequently than during the experiments on the unaltered samples. The nanopipette was deemed to be blocked if the recorded current dropped to 0 nA and remained at 0 nA. This blockage occurring more frequently for aged samples is attributed to crude oil particles from the film coming off into solution and physically blocking the nanopipette opening.

The SICM images which were successfully recorded of the aged surfaces had a blurred quality to them, such that none of the features could be clearly resolved. This can again be explained by the crude oil film partly coming off into the electrolyte directly above the surface. This would have created local artificially lower $K^+$ and $Cl^-$ concentrations, which in turn would cause a current drop when the nanopipette probed these regions. As a consequence of these local low concentrations of charge carriers, the SICM probe would interpret that it had approached the sample surface and be retracted too early. If this crude oil concentration was not perfectly uniform above the surface, then this effect would only occur for some but not all pixels, or to greater or lesser extents, thus the exact location of feature edges would be obscured, causing a "blurring" to occur. An example SICM image of each of the aged materials is shown below in Figure 7.18, which showcases this blurring effect across all three samples.

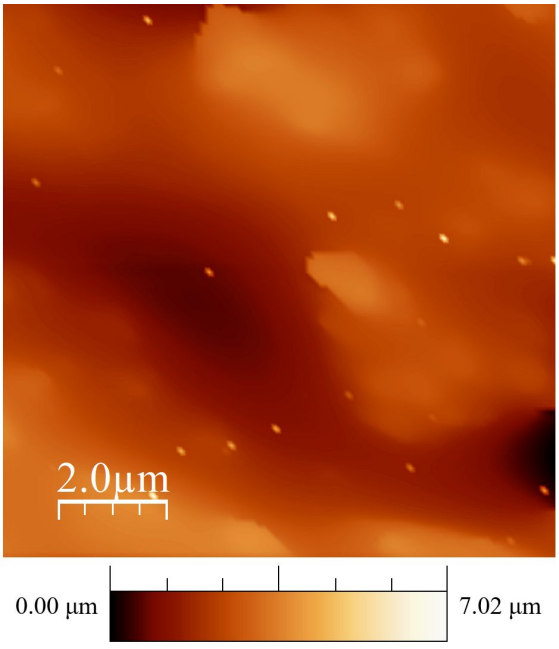
Despite this crude oil film alteration and blurring effect, the SICM images of the aged materials shown across Chapters 5: *Carbonate Ageing Studies* and 6: *Bandera Brown* did still depict surfaces with raised features approximately 1 $\mu$m across, which align with the sizes of the droplet structures observed in the low-vacuum SEM micrographs of these surfaces. In the aged calcite SICM images, some of the droplet structures were observed as separated on a flat crude oil film, whereas others formed agglomerates, consistent with patterns observed in aged calcite surface types 1, 2 and 4. The aged Estaillades and Bandera Brown surfaces did not show any clear heterogeneity in the low-vacuum SEM micrographs, the entirety of both surfaces being coated in a continuous film of droplets, without any flatter areas present in between. The size and distribution of the droplet structures, along with the greater height variation on these rocks are all observed in the SICM images. For example in the SICM images in Figure 7.18, the SICM images for aged Estaillades and Bandera Brown have height ranges of 0 - 10.99 and 7.02 $\mu$m respectively, compared to the aged calcite image's range of 0 - 5.50 $\mu$m. In light of these characteristics being consistent with what was observed in the low-vacuum SEM micrographs, SICM is still proposed to have successfully imaged these surfaces.




(a) Aged Calcite




(b) Aged Estaillades




(c) Aged Bandera Brown

Figure 7.18: SICM images of aged materials
SICM topographical images of (a) aged calcite, (b) aged Estaillades and (c) aged Bandera Brown. These images were originally shown in Figures 5.44b and 5.48 from Chapter 5: *Carbonate Ageing Studies* and Figure 6.55a from Chapter 6: *Bandera Brown* respectively.

## 7.5 Progress towards surface charge mapping

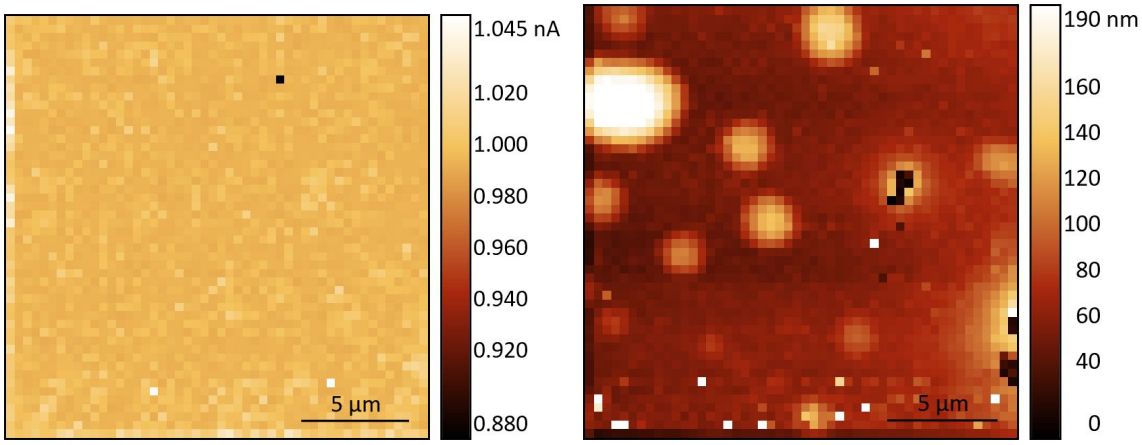
Over the past decade, a number of methods for surface charge determination using SICM have been developed; an overview of which can be found in Chapter 1, Section 1.2.4.[29,41,59,60] The surface charge mapping mode installed on the SICM in the laboratory was based on the pulsed-potential SICM method reported by Page *et al.*, which adds a pulse in the applied bias to a different bias at the top and bottom of each hop, while the current response is recorded.[29] The parameters are selected such that the pulse occurs inside and outside of the DDL, and so the difference between the current responses is dependent on the local surface charge beneath the nanopipette.[29] A more detailed explanation of this method was presented in Chapter 1, Section 1.2.4.2.

As the method installed on the SICM for determining surface charge was based on Page *et al.*'s experiments, their reference sample of a polystyrene film on a glass slide was selected to test that the setup was working as expected, and from low-vacuum SEM and AFM imaging the sample appeared to have been replicated successfully, with the expected features.[29]

Unfortunately, surface charge mapping on the SICM was not successfully performed in the laboratory prior to the project concluding. This was in part due to time constraints; the update to the software allowing for the different pulses at the top and bottom of each hop was delayed numerous times, and ultimately was only installed as the project was reaching its conclusion, giving limited time for experiments to take place. Additionally, although efforts were made to find a location on the polystyrene film where the glass beneath was exposed, no appropriate area was

located on the SICM during the imaging sessions devoted to this sample.

One area of the polystyrene film, successfully topographically imaged on the SICM, appeared to show a dent in the surface which was approximately 100 nm deep; this aligned with the thickness of the polystyrene film observed on Page *et al.*'s sample, and was therefore expected to reveal the glass surface underneath.[29] This area, re-shown in Figure 7.19, was then imaged using the pulsed-potential method to generate a current response map of the area. The current response map for this region, Figure 7.19a, however showed no notable variation in current response, even around the area which was expected to reveal the glass beneath.



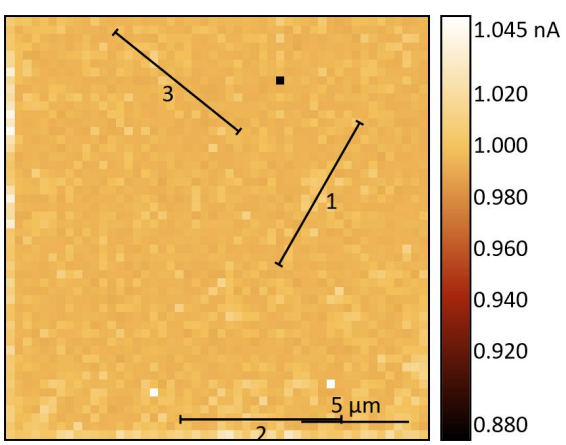

(a) (b)

Figure 7.19: Polystyrene on glass: SICM pulsed-potential attempt
The area imaged by pulsed-potential SICM, originally shown in Chapter 4: *Surface Charge Mapping*, Sections 4.3.2.3, page 212. (a) shows a plot of the differences between the current responses at the top and bottom of each hop, and (b) is the topographical map for the same area collected simultaneously.

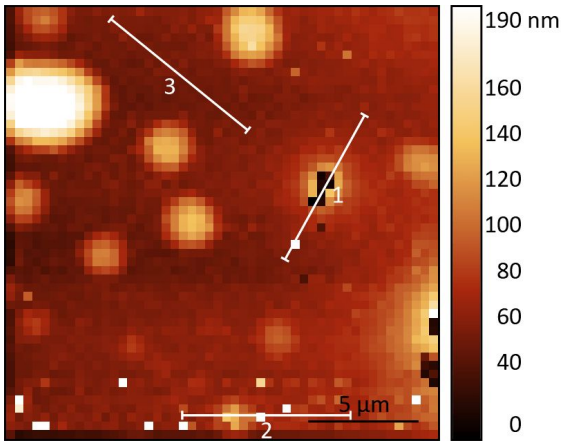
Page *et al.* observed a current difference of around 0.07 - 0.09 nA between the polymer film and the glass surface. The region on the current response map which aligns with the dent in the topographical map in Figure 7.19 showed a difference of only 0.01 nA between what was thought to be the polystyrene film and the glass

surface. This is not deemed to be significant, as it is not as large an increase as was observed by Page *et al.*, and also this difference can be observed on other regions of the current response map, in areas which are not associated with a dent in the surface. Three height and current response profiles showcasing this are shown across Figures 7.20 and 7.21. The lines 1 - 3 are labelled on the current response and topographical map shown in Figures 7.20a and 7.20b, with the associated current and height profiles overlain for each line in Figures 7.20c, 7.21a and 7.21b respectively.

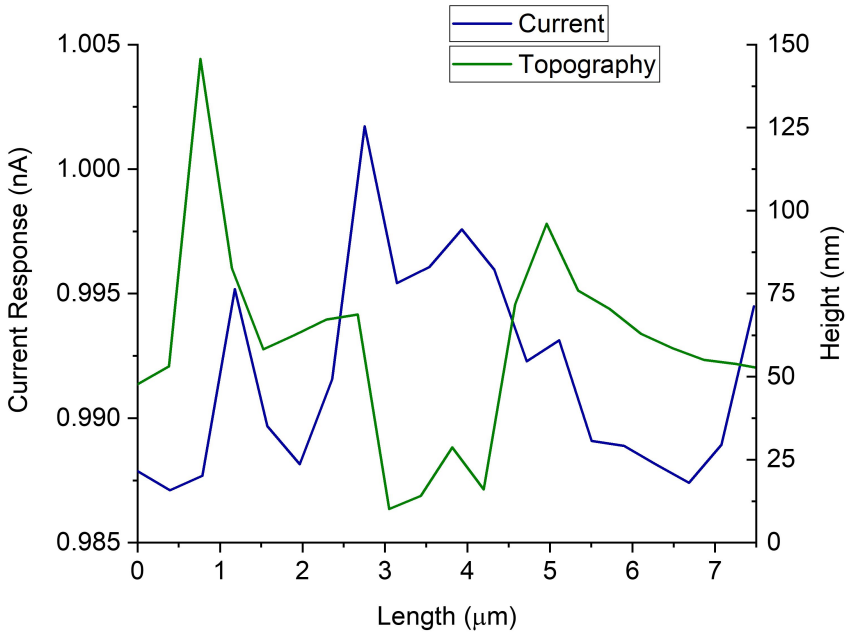
Line 1 crosses the region with a 75 - 100 nm deep dent, and as shown in the current profile in Figure 7.20c, a small increase in the net current response of 0.01 nA is observed in the same place. Line 2 crosses a raised feature on the polystyrene film around 75 nm high, and also shows an associated increase in net current response of 0.01 - 0.015 nA. Line 3 crosses a relatively flat region of the film, with a height variation of $< 10$ nm; a spike in the net current response of 0.015 nA is also observed at this location. It therefore seems likely that the small increase in net current response which aligns with the dent is a coincidence, and not evidence of the glass surface; the polystyrene film at this location is therefore likely to be $> 100$ nm thick, such that the observed dent is just a dent in the polystyrene film, and not a hole revealing the glass surface. No other region of the surface was found with topographical mapping on the SICM which met the critereon for being a good contender for surface charge mapping prior to the conclusion of the project.




(a) Current Response Difference

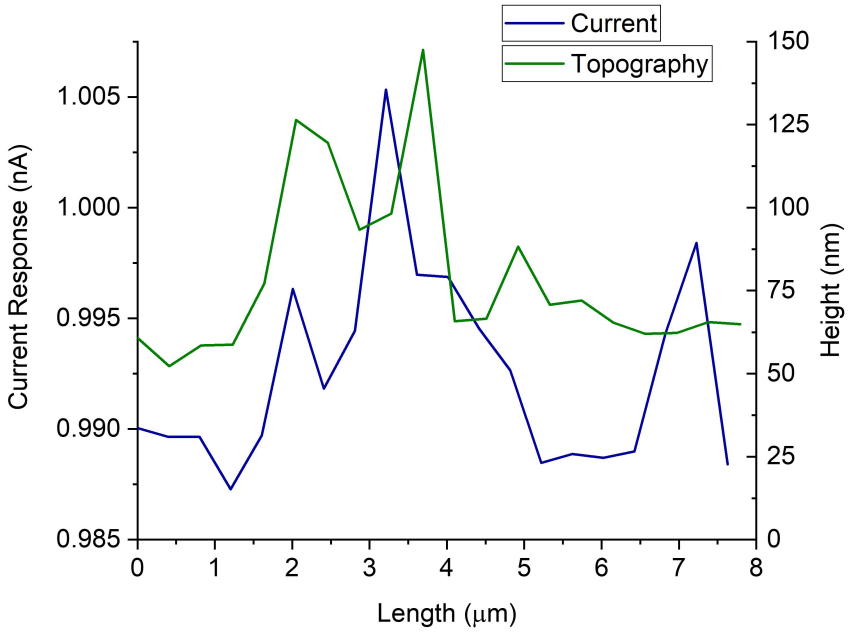



(b) Topography

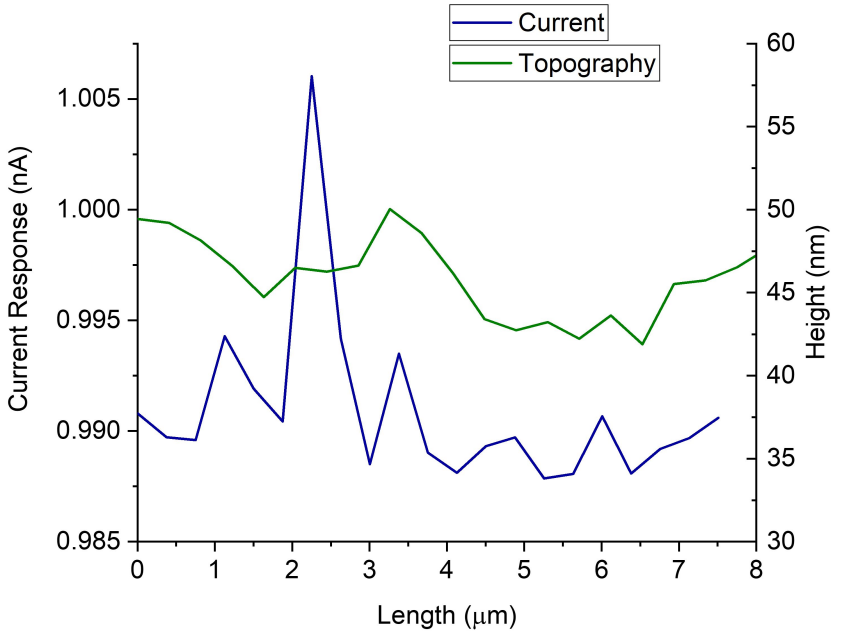



(c) Line 1

Figure 7.20: Polystyrene on glass: current response variations - Part 1
(a) and (b) show the same current response difference map and topographical map shown in Figure 7.19, with three lines labelled 1 - 3 indicated three net current response and height profiles of interest. (c) shows the two profiles for line 1 across two separate y-axes. Associated profiles for lines 2 and 3 can be found in Figure 7.21.




(a) Line 2




(b) Line 3

Figure 7.21: Polystyrene on glass: current response variations - Part 2
(a) and (b) show the profiles for lines 2 and 3 labelled in Figure 7.20 respectively, the net current response and topography for the same pixels shown overlain using two different y-axes.

Although disappointing, the lack of varied current response across the section of the surface imaged using the pulsed-potential method did at least align with the hypothesis that the raised structures seen in the AFM and SICM images across Chapter 4: *Surface Charge Mapping*, Sections 4.3.2.2 and 4.3.2.3, and again in Figure 7.19b, were polystyrene nanostructures on top of a flat polystyrene film, and that the dents visible in these images are therefore dents in the film, and not dents in the glass. If what had been observed was instead polystyrene nanostructures sitting on the bare glass slide for instance, which was a possibility, then there would have been a charge difference between the raised structures and the flat surface in the area selected for pulsed-potential SICM mapping, which was not observed. Everything within the field of view in Figure 7.19b had the same surface charge, and as such it is likely to consist of one material, which we assume to be polystyrene.

# Chapter 8

# Future Work

Chapter 4: *Surface Charge Mapping* described the progress which has been made thus far in establishing the SICM surface charge mapping mode in the laboratory at Imperial. Although AFM has also been shown in the literature to be able to provide surface charge maps,[70,71] SICM was chosen for this work due to it being shown in Chapter 3: *Carbonates* to be better suited to the topographical mapping of the rough outcrop rock surfaces.

A variety of wettability-related phenomena, observed in the literature in studies of reservoir and outcrop rocks, which have been proposed to be the result of surface charge heterogeneities, and their apparent ability to be altered under certain conditions, have yet to be mapped directly with a surface charge mapping technique.[88,89,118–120,125] There is therefore great potential for surface charge mapping on the SICM to contribute to the field of oil and gas recovery. As discussed in Chapter 4: *Surface Charge Mapping*, these applications were: 1) the enhancement of molecular modelling of fluid droplets on surfaces, 2) the mapping of the pH-dependency of

the surface charge polarity on certain clay surfaces, 3) the visualisation of charge magnitude changes in the iron-bearing minerals on a Bandera Brown surface before and after a reducing agent is added, 4) the investigation of a variety of low-salinity brines and their effects on local surface charge magnitudes, and 5) the mapping of the same surface under organic and aqueous electrolytes to investigate any impact on the magnitude or polarity of local surface charges. Practical considerations, in addition to any anticipated limitations of these proposed experiments are discussed below.

## 8.1 Integration with modelling

Zheng *et al.*, as part of the SDRP, carried out work where they performed approximated molecular modelling of the behaviour of an n-decane droplet on a Ketton surface which was re-constructed from an AFM image.[23] The AFM image in question showed a small field of view, only 483 × 483 nm, so an accurate identification of the surface type is challenging, however given the apparent sub-micron diameters of the particles and their irregular shape, see Figure 1 in reference 23, it appears that one of the ooid grain shell surfaces, Ketton surface type 3, 4 or 6, was mapped.[23] This aligns with the work in this thesis, as ooid grain shell surfaces were the only surfaces successfully mapped in the AFM studies of Ketton. It is proposed that modelling work such as the experiments carried out by Zheng *et al.* could be enhanced by using an SICM image of a Ketton surface where a simultaneous surface charge map had also been performed.[23] This would unfortunately come at the expense of resolution; the pixels in the AFM image in Zheng *et al.*'s study being 0.236 × 0.236 nm in

size, whilst the smallest pixel size in the SICM images of Ketton reported in this thesis was 25 × 25 nm.[23] The extra information from SICM surface charge mapping could however allow for even more accurate modelling of fluid behaviour, as real, experimentally determined values of surface charge could serve as inputs for each pixel on the reconstructed surface.

## 8.2 Additives

In order to map the pH-dependency of the surface charge heterogeneities of certain clay particles, or the change in oxidation state of the iron-bearing minerals in Bandera Brown under oxidising and reducing conditions, an additive would be required to be introduced between two surface charge maps of the same region. The use of additives would be relatively straight forward to integrate with the SICM setup, as the sample, electrodes and electrolyte could be predominantly left in place whilst the additive was introduced. Once the additive had diffused through the electrolyte, perhaps with the aid of a syringe, collection of the next surface charge map could proceed with relative ease.

### 8.2.1 Kaolinite

Kaolinite clay booklets, which were observed on the Bandera Brown surface (Figure 8.1), have been hypothesised in the literature to have pH-dependent surface charges, but this has yet to be directly mapped and proven.[118,123] If a kaolinite booklet were located using SICM on a Bandera Brown surface, or indeed another surface where kaolinite is known to be present, then surface charge mapping could

be performed at the same position, above the booklet, in both a low and high pH environment. Additives such as $NaOH_{(aq)}$ or $HCl_{(aq)}$ could be used to tune the pH, as these were previously used in the literature by Hu *et al.* for their pH-dependent behaviour investigations on kaolinite suspensions.[123] Tombàcz and Szekeres later found that the pH at which the charge polarity on certain kaolinite faces appears to change is around 6 - 6.5.[118] Above pH 6 - 6.5 the entirety of the booklet surface is hypothesised to be negatively charged due to the unbound O atoms on the surfaces, but below pH 6 - 6.5 the excess protons in solution were proposed to be drawn to the $SiO^-$ faces, causing a positive charge to build up on one of the booklet faces. The diagram illustrating this from Chapter 4: *Surface Charge Mapping* is shown once more in Figure 8.2 for reference, where the orange faces in the pH $<$ 6 - 6.5 diagram indicate the $SiO^-$ surfaces which bind to the excess protons, and the green face which remains negative represents the alumina surface of the kaolinite booklet.

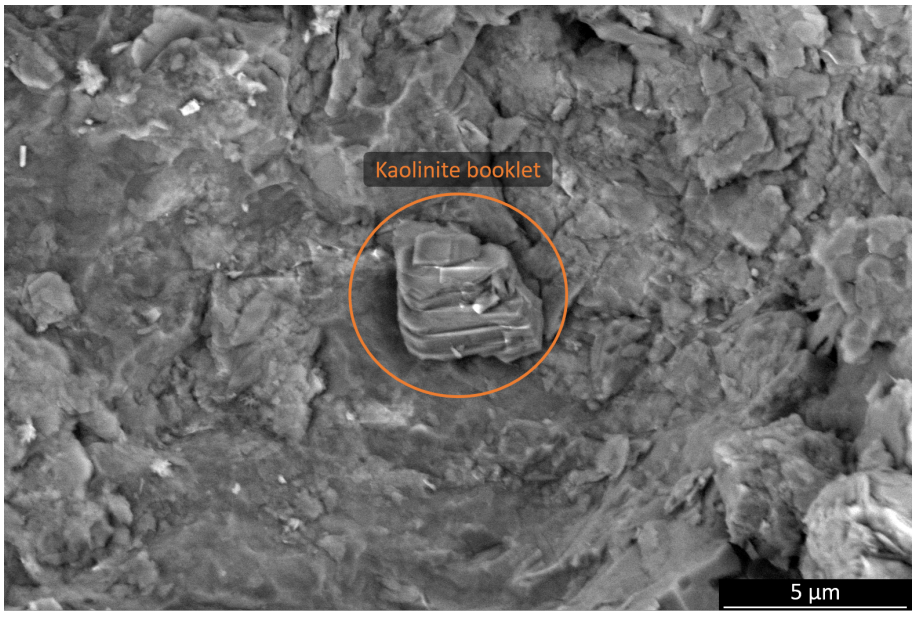



Figure 8.1: Bandera Brown: Kaolinite
A high magnification low-vacuum SEM micrograph of a kaolinite booklet on the Bandera Brown surface, originally shown in Chapter 6: *Bandera Brown*, Figure 6.9, page 290. A section of this image is also shown in reference 99.

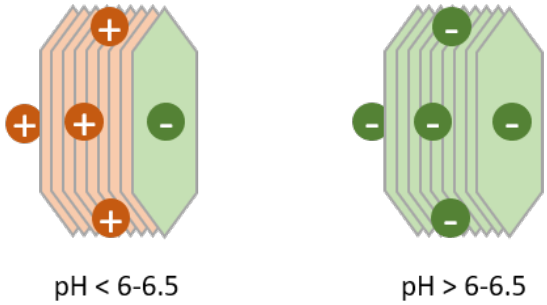



Figure 8.2: Kaolinite surface charge pH-dependency
A diagram of the proposed kaolinite booklet surface charge distributions and how they change with pH, previously shown in Chapter 4: *Surface Charge Mapping*, Figure 4.1b, redrawn from reference 118.

The required additives for these pH-dependency experiments, $HCl_{(aq)}$ and $NaOH_{(aq)}$, are not anticipated to introduce increased obstruction of the nanopipette opening; the only new ion to the $KCl_{(aq)}$ system would be the $Na^{+}_{(aq)}$ cation, which has a hydration radius of 2.3 Å; this is smaller than the $Cl^{-}_{(aq)}$ anion already present, which has a hydration radius of 3.2 Å.[75] The relative rarity of kaolinite clay booklets on the Bandera Brown surface, however, will likely pose a challenge to these experiments; the proportion of kaolinite in Bandera Brown reported in the literature is between 1.24 - 3 %.[89,98,182] Locating a kaolinite booklet on the surface of Bandera Brown on the SICM would therefore most likely be a result of extensive trial and error, so it is proposed that a sample more rich in kaolinite should be investigated initially, to first attempt to prove the hypothesis around kaolinite's pH-dependent surface charges,[118,123] before attempting to locate one on Bandera Brown. Berea, another sandstone outcrop rock which was investigated by the SDRP, has been reported as having twice the amount of kaolinite as Bandera Brown, being composed of 6 - 7 % kaolinite, so this could be a better outcrop rock to use initially.[98,182] Regardless of the success on a sandstone outcrop rock surface, proving this hypothesised

pH-dependent behaviour on a model surface would still generate interest not only in the field of oil and gas extraction research, but also more widely in geology.[118,123]

### 8.2.2 Redox-active iron-bearing species

The oxidising and reducing conditions required to investigate the redox behaviour of the iron-bearing minerals in Bandera Brown could also be generated through the use of an additive. Southwick *et al.* used erythorbic acid in their experiments to perform what they propose is a reduction of the Fe 3+ regions to the Fe 2+ oxidation state.[88] Following on from this work, erythorbic acid could be used an additive in SICM surface charge mapping experiments; once a surface charge map had been collected of an area thought to possibly contain Fe-bearing minerals in a 0.05 M $KCl_{(aq)}$ electrolyte, the erythorbic acid could be added and allowed to diffuse. A second surface charge map could then be collected of the same region, hopefully allowing for the visualisation of what would be expected to be a lower magnitude positive charge on the iron-bearing areas.

Any introduced additive may interfere with the measurement, as was observed during SICM mapping of the artificially aged surfaces where the crude oil film caused a blurring effect in the images. Erythorbic acid (Figure 8.3) is not as large a molecule as the long chain hydrocarbons present in crude oil, and is unlikely to completely block the nanopipette, but it is larger than the ions typically present during an SICM scan. It is therefore possible that erythorbic acid may temporarily partially obstruct the opening, impeding the flow of ions into the nanopipette, affecting the ability of the SICM to image the surface faithfully.

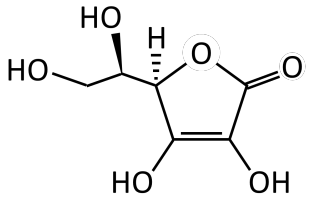



Figure 8.3: Chemical structure of erythorbic acid

Unlike the kaolinite booklets previously discussed, which have a distinctive shape which is expected to be readily identifiable in SICM topographical images, it is not known which minerals will give rise to the Fe redox behaviour which is hypothesised by Southwick *et al.*, and so selecting a location on the Bandera Brown surface upon which to perform these redox-probing experiments will prove a challenge.[88] One approach to these investigations could be to search for hematite-rich locations; as hematite ($Fe_2O_3$) has been shown in the literature to be reducible to magnetite ($Fe_3O_4$) under high pH and reducing conditions.[184,193] The reducing agent could therefore be used with and without a base such as NaOH to provide a high pH to see if this hematite reduction could be replicated on the Bandera Brown surface.[88,184,193] The $< 1$ $\mu$m hematite crystals observed in the low-vacuum SEM micrographs presented in Chapter 6: *Bandera Brown*, an example of which is re-shown in Figure 8.4, would not be expected to be readily discernible on a lower resolution scan, so a narrow field of view such as $2 \times 2$ $\mu$m and around $25 \times 25$ nm pixel size would need to be selected to search the sample surface for these structures.

Should the erythorbic acid successfully reduce the iron-bearing minerals on the Bandera Brown surface, interference with the imaging may arise from the presence of Fe 2+, which is more soluble than Fe 3+ in water. If the surface of interest is itself partially dissolving, this will likely render the surface difficult to map, and

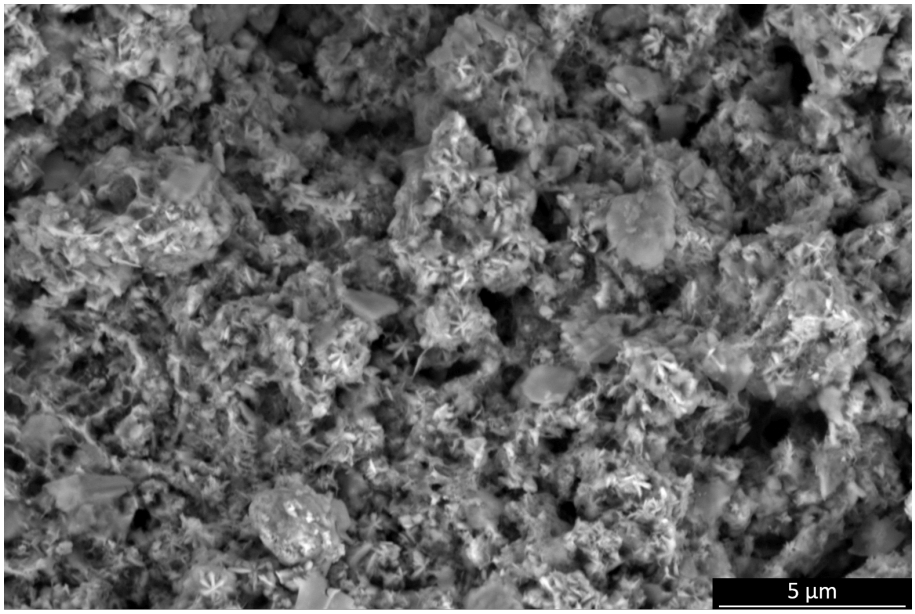



Figure 8.4: Bandera Brown: Hematite
A high magnification low-vacuum SEM micrograph of a region of the Bandera Brown surface covered with star-shaped hematite crystals, originally shown in Chapter 6, Figure 6.12, page 293.

the Fe $2+_{(aq)}$ could also disrupt the DDL and thus the surface charge mapping process.[184] As demonstrated in Chapter 4: *Surface Charge Mapping*, Section 4.3.1, the use of organic electrolytes in air in the SICM is possible, so if the Fe 2+ dissolving in the aqueous electrolyte did cause issues for surface charge mapping, an organic electrolyte could perhaps be utilised instead of an aqueous electrolyte to perform these experiments. This would best be approached by first mapping the surface in the aqueous environment before changing the electrolyte entirely, the method for which is described below in Section 8.3, where the chamber would be flushed and allowed to dry in between mapping the surface in both aqueous and organic electrolytes.

Despite the anticipated challenges to these experiments, the results could be of great importance in the field of oil and gas recovery research. Typically, fluid flow experiments on reservoir rocks conducted in most laboratories, such as micro-CT

experiments, are conducted in air, and thus oxidising conditions. If it were shown directly through surface charge mapping on the SICM that certain components on some rock surfaces were redox active, alongside additional work demonstrating different wettabilities depending whether the rock is exposed to reducing or oxidising conditions, these experimental methods would need to be re-thought. It is generally thought that oil reservoirs are reducing environments, due to the presence of oil and the lack of oxygen brought about by the depth at which these systems sit below the earth's surface. As such, if reducing/oxidising conditions were shown to be of importance, experiments modelling the flow of oil through reservoir rock in laboratories would require a reduction step to ensure that the minerals on the surface were in the correct state for accurate measurements to be obtained.

## 8.3 Changing electrolytes

The proposed avenues of research to investigate the LSF effect by carrying out surface charge maps in different composition brines, and to investigate any potential surface charge alterations which occur when swapping between organic and aqueous electrolytes, would not be as trivial as the work which requires the use of an additive. The requirement to fully swap the electrolyte whilst maintaining the position of the probe and sample adds layers of difficulty which are discussed below.

To increase the likelihood of being able to map the same area of the sample before and after swapping electrolytes, the sample and probe need to be moved as little as possible during electrolyte exchange. To maintain the position of the sample, a sample holder similar to that used by Dr. Sherifat Yesufu-Rufai in her

AFM experiments as part of the SDRP would need to be employed.[89,99] Her setup consisted of a stainless steel petri dish, with the sample fixed in the centre. This petri dish had fluid inlet and outlet ports on opposite sides, such that the sample chamber could be flushed and the fluid replaced between experiments whilst keeping the sample in place. Figure 8.5 shows a diagram illustrating this process. Each time the fluid was replaced, the sample holder was flushed with 10x the volume of the chamber with the new fluid before closing the port taps.[89,99] This extensive flushing resulted in a full removal of the previous fluid prior to the next experiment.

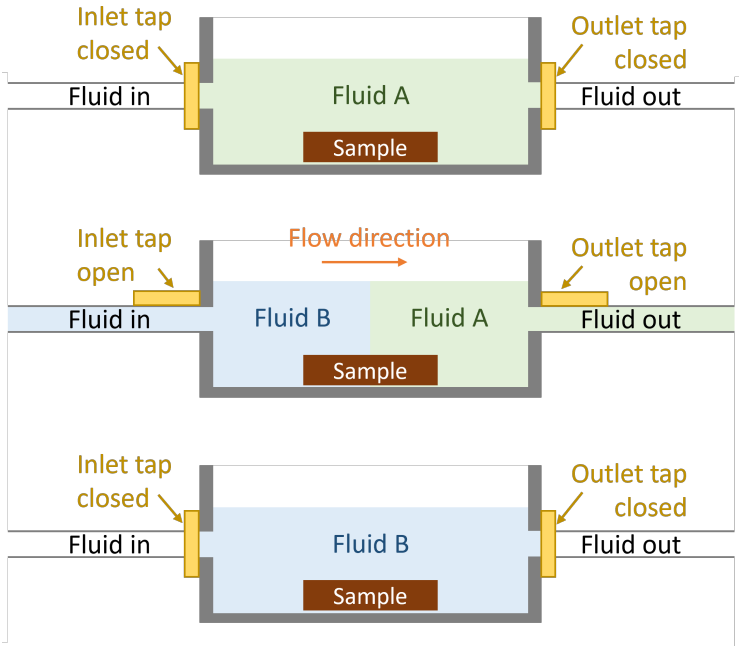



Figure 8.5: Petri dish design for swapping electrolytes between scans
Diagram illustrating the petri dish design and method of fluid replacement used by Dr. Sherifat Yesufu-Rufai on the SDRP to swap solutions between AFM experiments without moving the sample. Drawn with inspiration from references 89 and 99.

### 8.3.1 Low salinity flooding

In the case of the LSF investigations, a similar sample holder to the one shown in Figure 8.5 would probably work well for surface charge mapping on the SICM in different composition/concentration brines.[89,99] In these experiments, particularly for when only the concentration is changed, it may be possible to leave the nanopipette probe in place, and not change the electrolyte inside the nanopipette. Instead, prior to imaging, the nanopipette could be left immersed in solution above the sample surface and allowed to equilibrate with the bulk solution, as this would be expected to have a negligible effect on the overall concentration of the electrolyte. It is not possible to remove the electrolyte from the nanopipette and replace with a new one, so to change the electrolyte in the nanopipette, the nanopipette itself must be replaced; the potential pitfalls of this method are discussed below.

### 8.3.2 Aqueous vs organic electrolytes

Switching between aqueous and organic electrolytes is expected to be less straightforward than changing brines. If the sample was placed in a sample holder similar to that shown in Figure 8.5, and were imaged in an aqueous electrolyte, subsequent flushing through with an organic electrolyte would not necessarily remove the entirety of the aqueous electrolyte, particularly if there were any hydrophilic regions on the sample surface. It is therefore possible that a drying period would perhaps be required between imaging sessions with the two different electrolytes. For example, after imaging the surface under an aqueous electrolyte, the sample could be flushed with distilled water to remove any salt, and then emptied of fluid entirely to allow

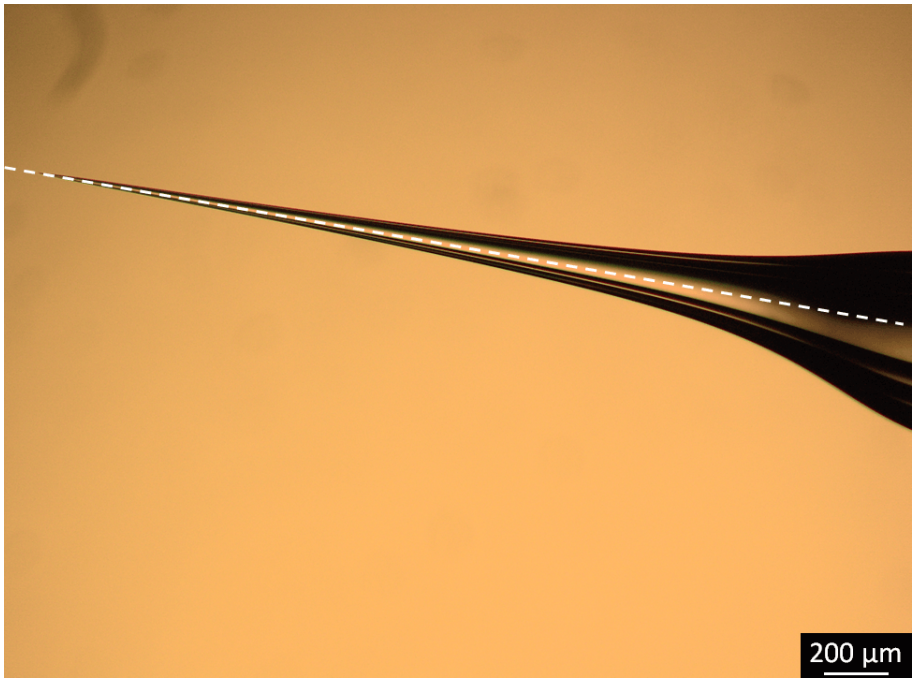
the sample to dry. Once dried, the sample could then be immersed in an organic electrolyte for subsequent surface charge mapping. This drying step would add considerable time to the experiment, but it is probably unavoidable when ensuring that the sample is free of the previous electrolyte.

In order to change the electrolyte from aqueous to organic or *vice versa*, the nanopipette probe would require replacing with a new nanopipette, filled with the new electrolyte. Even if it is assumed that the nanopipette holder would be fitted back into the exact same positionon the nanoscale as it was for the previous scan in the SICM set up, which in itself is unlikely, not all nanopipettes made by the same method are identical. Some do not pull fully symmetrically, and the exact size of the opening does vary somewhat. This is demonstrated in Figure 8.6, where optical microscopy images of two nanopipettes, with openings estimated at 45 nm, pulled from the same capillary pack under identical conditions are presented. White dotted lines on the figures indicate the position and orientation of the centre of the tips, demonstrating how the centre of the tip does not always align with the centre of the capillary. Although this asymmetry is not of importance during routine topographical and surface charge mapping experiments, when attempting to make direct comparisons on the same region of a sample with two different nanopipettes, they prove a notable stumbling block. It is therefore likely that when the new probe approaches the sample in a new electrolyte, that the exact location will have changed.

With these limitations in mind, two approaches could be adopted. One approach would be to carry out significantly larger topographical maps on the SICM, on the




(a)




(b)

Figure 8.6: Asymmetrical pulls on nanopipettes
Two optical microscope images taken of nanopipettes with tip openings estimated at 45 nm. White dotted lines show the centre of the nanopipette tip, and how it does not fully align with the centre of the capillary.

order of 50 × 50 $\mu$m to 100 × 100 $\mu$m, prior to surface charge mapping on a smaller area within that region. When setting up a scan in the second electrolyte, a large topographical scan could be performed once more, with the hope that even if the nanopipette position has moved slightly relative to the sample surface, these large topographical maps in both electrolytes would overlap, allowing for the relocation of the area previously investigated with surface charge mapping. The other approach would be to accept that it is improbable that the same location will be able to be imaged under two different electrolytes, and as such conduct numerous surface charge maps across the surface in each electrolyte. This approach would seek to gather surface charge information on a range of surface types in both electrolytes, which could then be placed into categories using the simultaneous topographical maps and low-vacuum SEM images, akin to the correlative approach for SICM image validation presented in this thesis. The maps which would be identified from the same surface type in different electrolytes could then be compared.

In spite of these anticipated difficulties, the results from these experiments have the potential to be of great use to the field of oil and gas recovery, hence they should be attempted. Being able to directly visualise surface charge alterations as a consequence of changes in environment could provide new inputs and improvements for molecular and pore-scale modelling of reservoir rock networks, feeding upwards into reservoir modelling, and thus delivering improved oil recovery yields through an increased understanding of EOR.

## 8.4 Bandera Brown surface heterogeneity insights

Regardless of the specific application, there would be a clear benefit of simultaneous surface charge mapping with topographical mapping on the SICM for studies on Bandera Brown. In the low-vacuum SEM EDX experiments described in Chapter 6: *Bandera Brown*, initial inspection of the low-vacuum SEM micrographs did not always give the full picture of the mineral distributions on the surface, one such example being re-shown in Figure 8.7. From the SEM micrograph in Figure 8.7a, the surface appears to be a clay surface, predominantly mica/vermiculite, with perhaps a few hematite crystallites across the surface. The element distribution maps in Figures 8.7b - 8.7d shed light on the heterogeneity that exists which is not evident from the topography alone, showing the distributions for Al, Fe and Si respectively. As can be seen from the EDX spectrum in Figure 8.7e, Mg, O, C, K and Na were also identified in this region, but maps for these are not re-shown, as Al, Fe and Si were deemed best suited to showcasing the heterogeneity on the surface. Maps for Mg, O, C, K and Na can be found in the original Figures 6.19 and 6.20 on pages 300 and 301 in Chapter 6: *Bandera Brown*.

Looking at the Si map in Figure 8.7d, there are clear hot-spots across the surface which are Si-rich; this would not be expected from a surface that was entirely one type of clay, so there must be mineralogical heterogeneity present. Three of the larger of these hot spots on the Si map are circled, with circles at the same locations shown on the Fe and Al distribution maps, as well as the SEM micrograph. Looking at these highlighted regions, it can be seen that highest Si concentrations appear at the same locations as low concentrations of Fe and Al. This would not be expected

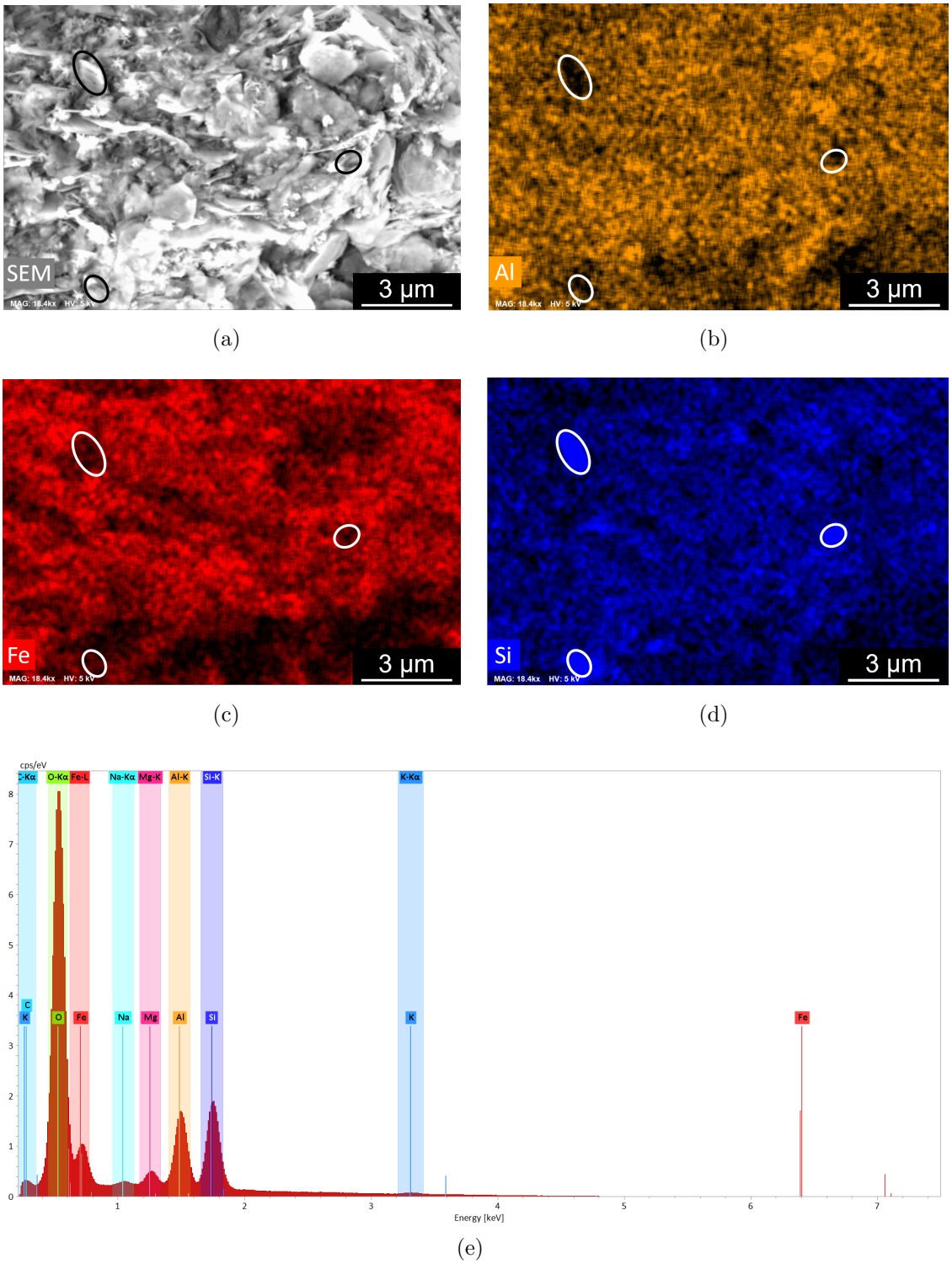



Figure 8.7: Bandera Brown: EDX results showing hidden heterogeneity
A selection of the EDX results originally shown in Figures 6.19 and 6.20 in Chapter 6: *Bandera Brown*. (a) shows the low-vacuum SEM micrograph for the region, (b) - (d) show the associated Al, Fe and Si distribution maps and (e) shows the associated EDX spectrum. Distribution maps for Mg, O, C, K and Na are not re-shown.

from an entirely clay-covered surface, so these hot spots are instead proposed to be quartz ($SiO_2$). From the low-vacuum SEM micrograph alone, this surface was proposed to be predominantly mica/vermiculite, but with the extra information from EDX, it is found that quartz is also present.

A situation analogous to this SEM/EDX example could be found through simultaneous topographical and surface charge mapping on the SICM. The mineralogical distributions on the Bandera Brown surface at these $< 5$ $\mu$m length scales can not always be resolved from the topography alone. Additionally, as the fields of view are not always large enough to capture the full particle, or the resolution may not be fine enough to accurately determine the shape, surface charge mapping may provide insights to allow for mineral identification. Although surface charge mapping would not necessarily allow for such clear identification of minerals, as was the case for quartz in the example in Figure 8.7, a surface charge map alongside a SICM topographical map would still provide a means to gauge the heterogeneity of the surface under investigation. If the entirety of the surface showed the same surface charge, this could be indicative of the presence of only one mineral. If however certain regions showed charges distinct from the rest of the surrounding region, then that would imply that there was a pocket of another mineral present, and allow for more accurate mineral assignment of the regions mapped with SICM.

## 8.5 Integration of other techniques

The workflow put forward in this thesis, incorporating low-vacuum SEM and EDX, AFM and topographical and surface charge mapping on the SICM could be further enhanced by the addition of other nanoscale microscopies and spectroscopies, particularly those which might shed light on the nanoscale chemical heterogeneity of the sample of interest; this would be of particular use for materials like Bandera Brown, which contain a wide range of elements and minerals.

One such technique which could enhance the SEM, AFM, SICM workflow could be transmission X-ray microscopy (TXM). In a TXM experiment, x-rays are transmitted through a sample up to 10 $\mu$m thick, over an area on the sample surface around 10 to 30 $\mu$m across.[194–196] While traversing the sample, these x-rays will interact with the electrons in the bulk material, changing the angle at which the x-rays exit the material, their energy and their intensity; these properties are then recorded by a detector on the other side of the sample from the x-ray source.[194–196] From the gathered x-ray information, 2D and 3D maps of nanoscale structure, crystal grain orientation and charge distributions can be determined with $<$ 100 nm resolutions.[194–196] TXM could be of particular use for the enhanced investigation of Bandera Brown samples, providing crystallographic information as well as charge information which could be used to determine the oxidation state of the iron-bearing minerals after exposure to different conditions.[194]

X-ray photoelectron spectroscopy (XPS) could also provide additional information to the SEM, AFM, SICM workflow, which is unlike TXM in that it investigates just the top few nanometres of a surface of interest, and not the bulk sample.[194,195,197]

In XPS, X-rays are instead used to probe the sample surface, knocking out characteristic photoelectrons, which can be used to determine not only the elemental composition of the surface, but also the oxidation state of the elements present.[197] XPS would again be of particular interest to studies on Bandera Brown, as this could enable the study of surface iron oxidation states before and after a reduction step, to categorically show whether the hypothesised Fe-redox behaviour proposed by Southwick *et al.*, described in more detail in Section 8.2.2, does indeed occur.[88]

Another powerful technique which could contribute to the workflow is AFM-based infrared spectroscopy (AFM-IR), where an infrared (IR) laser probes the sample of interest below the scanning AFM probe tip, which in turn acts as a local IR absorption detector.[198–200] This coupling of techniques allows for IR spectroscopy to be performed at the spatial resolutions achievable by AFM, which depending on the set up can be atomic resolution; this is considerably below the resolution limit of a standard Fourier-transform IR spectrometer, of around 1 $\mu$m.[200,201] In turn, this coupling enhances the AFM topographical mapping, by providing simultaneous chemical analysis.[200] AFM-IR could add value to the workflow put forward in this thesis, particularly in further studies of crude oil films on outcrop rocks. For example, in the aged calcite studies in Chapter 5: *Carbonate Ageing Studies*, it appeared that after SICM imaging, the crude oil film on the calcite surface had segregated into oxygen-rich and oxygen-poor components (Figure 5.15, page 237), however there was insufficient information to draw any firm conclusions. The use of AFM-IR on these surfaces could provide invaluable information to clarify whether there was a difference in the chemical composition of these two film topographies.

# Chapter 9

# Conclusions

SICM was found to be a suitable tool in the mapping of four outcrop rocks: Ketton, Estaillades, Indiana and Bandera Brown. Comparison with low-vacuum SEM and AFM images provided validation of the size and shape of the features which were observed in the SICM images, but also added extra insight.

The low-vacuum SEM micrographs in themselves added to what was already present in the literature. Reports showing SEM micrographs of these reservoir rock materials were commonly either performed at low magnification, or on materials which had been set in resin or coated such that the topography was partly obscured. Even if high enough magnification SEM micrographs were presented which could have visualised the micron-level heterogeneity, reports typically showed only one or two surface types. The work presented in this thesis provides a suite of low-vacuum SEM micrographs on four outcrop rocks, without polishing, coatings or resins, at high magnification, showcasing the range of surface types present at the micron and sub-micron scales. This method of defining surface types from low-vacuum SEM

micrographs also provided an invaluable framework with which to understand the smaller SICM and AFM images on each material, and how these images fitted into the bigger picture.

AFM imaging provided an SPM comparison for the SICM images, allowing for the assessment of feature sizes and heights recorded in the SICM, and subsequently validating the SICM as a suitable SPM for studying these materials. In comparing these images, it was found that the SICM was possibly a more suitable tool than AFM for studying these materials. The SICM being better suited to these outcrop rocks is proposed to hinge on two key factors. The significantly faster scan speeds and smaller hop heights used to obtain the AFM images in this thesis compared to the SICM images, meant that the sharp feature height changes in these materials were not fully resolved, as the tip could not respond fast enough, causing a blurring of feature edges. The other factor is possibly that the AFM probe tip itself was considerably shorter than the SICM probe tip, and so could not reach into the pores on the surface; this left the AFM set up used in these experiments unable to image the same range of surface types present on these materials as the SICM. Some of these issues might have however been resolved if more time had been dedicated to AFM imaging, slower scan speeds used, and if cantilevers with longer tips had been sourced for the project, to access the more recessed features in the surface.

This work also presented the novel mapping of a surface under an organic electrolyte in the SICM in air, which is not only useful for the study of outcrop rocks, but has the potential to be of benefit in other disciplines. The successful use of the SICM for topographical characterisation of these materials in both aqueous and

organic solvents opens up multiple avenues for simultaneous surface charge and topographical mapping of these surfaces. The wealth of information which could be gained ranges from visualising pH-dependent surface charge behaviour on clays, to studying the LSF effect, to understanding the potential redox behaviour proposed for certain iron-bearing sandstones. Although it is unfortunate that this work could not be performed during this project, it is nonetheless promising that the groundwork has been laid for these experiments to take place.

Finally, outcrop rocks which had been exposed to crude oil under artificial ageing conditions were also successfully imaged by SICM. These images were not as well-resolved as those of the un-altered rock surfaces, as crude oil from the dry film appeared to be partially removed by the $KCl_{(aq)}$ electrolyte during imaging, which interfered with the measurements. This hypothesis was strengthened by low-vacuum SEM micrographs taken after SICM imaging, which showed evidence of crude oil film alteration on two of the three samples investigated. Despite the blurring on these SICM images, the approximate feature sizes and shapes observed were in line with what was expected from the low-vacuum SEM micrographs taken beforehand, and so are deemed to be successful.

Overall this thesis has answered the key questions which were asked: the SICM can be used to map outcrop rocks, which was validated with low-vacuum SEM and AFM images. Despite some issues, the SICM has also been shown to be able to map materials which have been artificially aged in crude oil, which also provided insights into possible interactions between the oil and mineral surfaces. As such, future experiments involving crude oil in the SICM can be considered. Now that

topographical mapping on the SICM has been successfully established for these materials, there is scope for surface charge mapping on the SICM to answer a number of pertinent questions about these surfaces.

# Bibliography


[1] BP, *Statistical Review of World Energy 2020*, https://www.bp.com/content/dam/bp/business-sites/en/global/corporate/pdfs/energy-economics/statistical-review/bp-stats-review-2020-full-report.pdf, (accessed 07/10/2020), 2020, 69th Edition.

[2] S. J. Geetha, I. M. Banat and S. J. Joshi, *Biocatalysis and Agricultural Biotechnology*, 2018, **14**, 23–32, DOI: 10.1016/j.bcab.2018.01.010.

[3] A. Muggeridge, A. Cockin, K. Webb, H. Frampton, I. Collins, T. Moulds and P. Salino, *Philos Trans A Math Phys Eng Sci*, 2014, **372(2006)**, 20120320, DOI: 10.1098/rsta.2012.0320.

[4] A. Bera and H. Belhaj, *Journal of Molecular Liquids*, 2016, **224**, 177–188, DOI: 10.1016/j.molliq.2016.09.105.

[5] V. Alvarado and E. Manrique, in *Enhanced Oil Recovery*, ed. V. Alvarado and E. Manrique, Gulf Professional Publishing, Boston, 2010, ch. 2, pp. 7–16, DOI: 10.1016/B978-1-85617-855-6.00008-5.

[6] S. Liang, Y. Liu, N. Zhang and B. Zeng, *J. Petrol. Explor. Prod. Technol.*, 2018, **8**, 861–870, DOI: 10.1007/s13202-017-0379-2.

[7] T. Hao, L. Zhong, J. Liu, X. Han, T. Zhu, X. Zhang, X. Wang and L. Zhang, *J. Petrol. Explor. Prod. Technol.*, 2022, **12**, 743–752, DOI: 10.1007/s13202-021-01323-x.

[8] Y. Ahmadi, M. Mohammadi and M. Sedighi, in *Chemical Methods*, ed. A. Hemmati-Sarapardeh, M. Schaffie, M. Ranjbar, M. Dong and Z. Li, Gulf Professional Publishing, 2022, ch. 1, pp. 1–32, DOI: 10.1016/B978-0-12-821931-7.00002-X.

[9] P. Druetta, P. Raffa and F. Picchioni, *Applied Energy*, 2019, **252**, 113480, DOI: 10.1016/j.apenergy.2019.113480.

[10] T. Bultreys, W. De Boever and V. Cnudde, *Earth-Science Reviews*, 2016, **155**, 93 – 128, DOI: 10.1016/j.earscirev.2016.02.001.

[11] J. H. Stiles and J. M. Hutfilz, *J. Pet. Tech.*, 1992, **44**, 704–713, DOI: 10.2118/18386-PA.

[12] M. Z. Kalam, in *New Technologies in the Oil and Gas Industry*, ed. J. S. Gomes, IntechOpen, London, 2012, ch. 9, pp. 201–226, DOI: 10.5772/52949.

[13] C. A. McPhee, *The Core Analysis Elephant in the Formation Evalutation Room*, SPE Annual Technical Conference and Exhibition, San Antonio, Texas, USA, October 2012, SPE–158087–MS, DOI: 10.2118/158087-MS.

[14] T. Ahmed, in *Reservoir Engineering Handbook*, ed. T. Ahmed, Gulf Professional Publishing, Cambridge, MA, 5th edn., 2019, ch. 4, pp. 167–281, DOI: 10.1016/B978-0-12-813649-2.00004-9.

[15] J. H. Schön, in *Physical Properties of Rocks*, ed. J. H. Schön, Elsevier, Amsterdam, 2nd edn., 2015, ch. 2, pp. 21–84, DOI: 10.1016/B978-0-08-100404-3.00002-0.

[16] M. A. Q. Siddiqui, S. Ali, H. Fei and H. Roshan, *Earth-Science Reviews*, 2018, **181**, 1–11, DOI: 10.1016/j.earscirev.2018.04.002.

[17] J. V. Ferrari, B. M. de Oliveira Silveira, J. J. Arismendi-Florez, T. B. Fagundes, M. A. da Trindade Silva, R. Skinner, C. Ulsen and C. de Carvalho Carneiro, 2021, **199**, 108313, DOI: 10.1016/j.petrol.2020.108313.

[18] G. Mauricio Ceron Lopez, M. B. Myers, Q. Xie, C. D. Wood and A. Saeedi, *Fuel*, 2021, **291**, 120189, DOI: 10.1016/j.fuel.2021.120189.

[19] M. Kanj, S. Sakthivel and E. Giannelis, *Colloids Surf, A Physicochem Eng Asp*, 2020, **598**, 124819, DOI: 10.1016/j.colsurfa.2020.124819.

[20] M. Andrew, B. Bijeljic and M. J. Blunt, *Advances in Water Resources*, 2014, **68**, 24–31, DOI: 10.1016/j.advwatres.2014.02.014.

[21] A. Scanziani, K. Singh, M. J. Blunt and A. Guadagnini, *J. Colloid Interf. Sci.*, 2017, **496**, 51–59, DOI: 10.1016/j.jcis.2017.02.005.

[22] G. C. Savulescu, M. Rücker, A. Scanziani, R. Pini, A. Georgiadis and P. F. Luckham, *J. Colloid Interface Sci.*, 2021, **592**, 397–404, DOI: 10.1016/j.jcis.2021.02.070.

[23] L. Zheng, M. Rücker, T. Bultreys, A. Georgiadis, M. M. Mooijer-van den Heuvel, F. Bresme, J. P. M. Trusler and E. A. Müller, *Energies*, 2020, **13(11)**, 2770, DOI: 10.3390/en13112770.

[24] M. O. Amabeoku, T. M. Al-Ghamdi, Y. Mu and J. Toelke, *Evaluation and Application of Digital Rock Physics (DRP) for Special Core Analysis in Carbonate Formations*, International Petroleum Technology Conference, Beijing, China, March 2013, IPTC–17132–MS, DOI: 10.2523/IPTC-17132-MS.

[25] M. Tembely, A. M. AlSumaiti and W. S. Alameri, *Energy Reports*, 2021, **7**, 1460–1472, DOI: 10.1016/j.egyr.2021.02.065.

[26] T. Bultreys, L. Van Hoorebeke and V. Cnudde, *Advances in Water Resources*, 2015, **78**, 36 – 49, DOI: 10.1016/j.advwatres.2015.02.003.

[27] A. Rabbani, P. Mostaghimi and R. T. Armstrong, *Advances in Water Resources*, 2019, **123**, 70–83, DOI: 10.1016/j.advwatres.2018.11.003.

[28] P. K. Hansma, B. Drake, O. Marti, S. A. C. Gould and C. B. Prater, *Science*, 1989, **243**, 641–643, DOI: 10.1126/science.2464851.

[29] A. Page, D. Perry, P. Young, D. Mitchell, B. G. Frenguelli and P. R. Unwin, *Anal. Chem.*, 2016, **88(22)**, 10854–10859, DOI: 10.1021/acs.analchem.6b03744.

[30] J. Rheinlaender, N. A. Geisse, R. Proksch and T. E. Schäffer, *Langmuir*, 2011, **27(2)**, 697–704, DOI: 10.1021/la103275y.

[31] D. Klenerman, Y. E. Korchev and S. J. Davis, *Current Opinion in Chemical Biology*, 2011, **15**, 696–703, DOI: 10.1016/j.cbpa.2011.04.001.

[32] K. Wang, L. Zhou, J. Li, W. Liu, Y. Wei, Z. Guo, C. Fan, J. Hu, B. Li and L. Wang, *Nano Lett.*, 2020, **20(9)**, 6313–6319, DOI: 10.1021/acs.nanolett.0c01735.

[33] C. Zhu, W. Shi, D. L. Daleke and L. A. Baker, *Analyst*, 2018, **143(5)**, 1087–1093, DOI: 10.1039/C7AN01986F.

[34] Y. Chen, G. B. Sukhorukov and P. Novak, *Nanoscale*, 2018, **10(35)**, 16902–16910, DOI: 10.1039/C8NR03870H.

[35] C. Zhu, K. Huang, N. P. Siepser and L. A. Baker, *Chem. Rev.*, 2021, **121(19)**, 11726–11768, DOI: 10.1021/acs.chemrev.0c00962.

[36] L. Tao, M. Qiao, R. Jin, Y. Li, Z. Xiao, Y. Wang, N. Zhang, C. Xie, Q. He, D. Jiang, G. Yu, Y. Li and S. Wang, *Angewandte Chemie International Edition*, 2018, **58(4)**, 1019–1024, DOI: 10.1002/anie.201810207.

[37] R. Jin, X. Ye, J. Fan, D. Jiang and H.-Y. Chen, *Anal. Chem.*, 2019, **91(4)**, 2605–2609, DOI: 10.1021/acs.analchem.8b05311.

[38] A. L. Lipson, K. Puntambekar, D. J. Comstock, X. Meng, M. L. Geier, J. W. Elam and M. C. Hersam, *Chem. Mater.*, 2014, **26(2)**, 935–940, DOI: 10.1021/cm402451h.

[39] A. L. Lipson, R. S. Ginder and M. C. Hersam, *Adv. Mater.*, 2011, **23**, 5613–5617, DOI: 10.1002/adma.201103094.

[40] C.-C. Chen, Y. Zhou and L. A. Baker, *Annu. Rev. Anal. Chem.*, 2012, **5**, 207–228, DOI: 10.1146/annurev-anchem-062011-143203.

[41] A. Page, D. Perry and P. R. Unwin, *Proc. R. Soc. A*, 2017, **473**, 20160889, DOI: 10.1098/rspa.2016.0889.

[42] C. L. Bentley, D. Perry and P. R. Unwin, *Analytical Chemistry*, 2018, **90(12)**, 7700–7707, DOI: 10.1021/acs.analchem.8b01588.

[43] R. T. Perera and J. K. Rosenstein, *Scientific Reports*, 2018, **8**, 1965, DOI: 10.1038/s41598-018-20412-2.

[44] B. Chen, D. Perry, A. Page, M. Kang and P. R. Unwin, *Anal. Chem.*, 2019, **91(3)**, 2516–2524, DOI: 10.1021/acs.analchem.8b05449.

[45] C.-C. Chen, M. A. Derylo and L. A. Baker, *Anal. Chem.*, 2009, **81**, 4742–4751, DOI: 10.1021/ac900065p.

[46] J. Rheinlaender and T. E. Schäffer, *Anal. Chem.*, 2017, **89(21)**, 11875–11880, DOI: 10.1021/acs.analchem.7b03871.

[47] H. Nitz, J. Kamp and H. Fuchs, *Probe Microscopy*, 1998, **1**, 187–200.

[48] Y. Wang, H. Cai and M. V. Mirkin, *ChemElectroChem*, 2015, **2(3)**, 343–347, DOI: 10.1002/celc.201402328.

[49] P. Novak, C. Li, A. I. Shevchuk, R. Stepanyan, M. Caldwell, S. Hughes, T. G. Smart, J. Gorelik, V. P. Ostanin, M. J. Lab, G. W. J. Moss, G. I. Frolenkov, D. Klenerman and Y. E. Korchev, *Nat. Mater.*, 2009, **6**, 279–281, DOI: 10.1038/nmeth.1306.

[50] A. I. Shevchuk, J. Gorelik, S. E. Harding, M. J. Lab, D. Klenerman and Y. E. Korchev, *Biophys. J.*, 2001, **81(3)**, 1759–1764, DOI: 10.1016/S0006-3495(01)75826-2.

[51] C. Li, N. Johnson, V. Ostanin, A. Shevchuk, L. Ying, Y. Korchev and D. Klenerman, *Prog. Nat. Sci.*, 2008, **18**, 671–677, DOI: 10.1016/j.pnsc.2008.01.011.

[52] Y. Takahashi, Y. Zhou, T. Miyamoto, H. Higashi, N. Nakamichi, Y. Takeda, Y. Kato, Y. Korchev and T. Fukuma, *Anal. Chem.*, 2020, **92(2)**, 2159–2167, DOI: 10.1021/acs.analchem.9b04775.

[53] A. Zhukov, O. Richards, V. Ostanin, Y. Korchev and D. Klenerman, *Ultramicroscopy*, 2012, **121**, 1–7, DOI: 10.1016/j.ultramic.2012.06.015.

[54] S. Wong Su, A. Chieng, J. Parres-Gold, M. Chang and Y. Wang, *Faraday Discuss.*, 2018, **210**, 131–143, DOI: 10.1039/C8FD00059J.

[55] A. Tanaka, R. Tanaka, N. Kasai, S. Tsukada, T. Okajima and K. Sumitomo, *Journal of Structural Biology*, 2015, **191(1)**, 32–38, DOI: 10.1016/j.jsb.2015.06.002.

[56] J. Rheinlaender and T. E. Schäffer, *J Appl. Phys.*, 2009, **105**, 094905, DOI: 10.1063/1.3122007.

[57] S. Del Linz, E. Willman, M. Caldwell, D. Klenerman, A. Fernández and G. Moss, *Analytical Chemistry*, 2014, **86**, 2353–2360, DOI: 10.1021/ac402748j.

[58] A. E. Weber and L. A. Baker, *J. Electrochem. Soc.*, 2014, **161**, H924, DOI: 10.1149/2.0701414jes.

[59] K. McKelvey, S. L. Kinnear, D. Perry, D. Momotenko and P. R. Unwin, *J. Am. Chem. Soc.*, 2014, **136**, 13735–13744, DOI: doi:10.1021/ja506139u.

[60] D. Perry, R. Al Botros, D. Momotenko, S. L. Kinnear and P. R. Unwin, *ACS Nano*, 2015, **9(7)**, 7266–7276, DOI: 10.1021/acsnano.5b02095.

[61] G. Binnig, C. F. Quate and C. Gerber, *Phys. Rev. Lett.*, 1986, **56(9)**, 930 – 933, DOI: 10.1103/PhysRevLett.56.930.

[62] *All Nobel Prizes in Physics*, `https://www.nobelprize.org/prizes/lists/all-nobel-prizes-in-physics/`, (accessed 29/01/2021).

[63] L. Liu, N. Xi, G. Li and H. Chen, in *Nano Optoelectronic Sensors and Devices - Nanophotonics from Design to Manufacturing*, ed. N. Xi and K. W. C. Lai, William Andrew Publishing, Oxford, 1st edn., 2012, ch. 4, pp. 51–79, DOI: 10.1016/B978-1-4377-3471-3.00004-6.

[64] Polymer Solutions Inc., *Atomic Force Microscopy: Imaging and Lithography*, `https://www.polymersolutions.com/blog/atomic-force-microscopy-imaging-and-lithography/`, (accessed 03/03/2020).

[65] P. Eaton and P. West, in *Atomic Force Microscopy*, Oxford University Press, Oxford, Online edn., 2010, ch. 3, pp. 49–81, DOI: 10.1093/acprof:oso/9780199570454.003.0003.

[66] K.-I. Fukui, H. Onishi and Y. Iwasawa, *Chem. Phys. Lett.*, 1997, **280(3)**, 296–301, DOI: 10.1016/S0009-2614(97)01143-3.

[67] S. Orisaka, T. Minobe, T. Uchihashi, Y. Sugawara and S. Morita, *Appl. Surf. Sci.*, 1999, **140(3-4)**, 243–246, DOI: 10.1016/S0169-4332(98)00534-0.

[68] B. W. Hoogenboom, H. J. Hug, Y. Pellmont, S. Martin, P. L. T. M. Frederix, D. Fotiadis and A. Engel, *Appl. Phys. Lett.*, 2006, **88(19)**, 193109, DOI: 10.1063/1.2202638.

[69] T. Fukuma, K. Kobayashi, K. Matsushige and H. Yamada, *Appl. Phys. Lett.*, 2005, **87(3)**, 034101, DOI: 10.1063/1.1999856.

[70] W. F. Heinz and J. H. Hoh, *Biophys. J.*, 1999, **76(1)**, 528–538, DOI: 10.1016/S0006-3495(99)77221-8.

[71] Y. Yang, K. M. Mayer and J. H. Hafner, *Biophys. J.*, 2007, **92(6)**, 1966–1974, DOI: 10.1529/biophysj.106.093328.

[72] K. Umeda, K. Kobayashi, N. Oyabu, K. Matsushige and H. Yamada, *Nanotechnology*, 2015, **26**, 285103, DOI: 10.1088/0957-4484/26/28/285103.

[73] E. Salançon and B. Tinland, *Beilstein J. Nanotechnol.*, 2018, **9**, 2181–2187, DOI: 10.3762/bjnano.9.204.

[74] J. Mähler and I. Persson, *Inorg. Chem.*, 2012, **51(1)**, 425–438, DOI: 10.1021/ic2018693.

[75] K.-L. Yang, S. Yiacoumi and C. Tsouris, *J. Chem. Phys.*, 2002, **117(18)**, 8499–8507, DOI: 10.1063/1.1511726.

[76] A. I. Shevchuk, G. I. Frolenkov, D. Sánchez, P. S. James, N. Freedman, M. J. Lab, R. Jones, D. Klenerman and Y. E. Korchev, *Angew. Chem. Int. Ed.*, 2006, **45**, 2212–2216, DOI: 10.1002/anie.200503915.

[77] E. Tognoni, P. Baschieri, C. Ascoli, M. Pellegrini and M. Pellegrino, *Micron*, 2016, **83**, 11–18, DOI: 10.1016/j.micron.2016.01.002.

[78] M. A. Edwards, C. G. Williams, A. L. Whitworth and P. R. Unwin, *Anal. Chem.*, 2009, **81(11)**, 4482–4492, DOI: 10.1021/ac900376w.

[79] B. Inkson, in *Materials Characterization Using Nondestructive Evaluation (NDE) Methods*, ed. G. Hübschen, I. Altpeter, R. Tschuncky and H.-G. Herrmann, Woodhead Publishing, Duxford, 1st edn., 2016, ch. 2, pp. 17–43, DOI: 10.1016/B978-0-08-100040-3.00002-X.

[80] A. M. Ilyin, in *Microscopy Methods in Nanomaterials Characterization*, ed. S. Thomas, R. Thomas, A. K. Zachariah and R. K. Mishra, Elsevier, Amsterdam, 1st edn., 2017, vol. 1, ch. 11, pp. 363–381, DOI: 10.1016/B978-0-323-46141-2.00011-0.

[81] O. Wells, in *Encyclopedia of Materials: Science and Technology*, ed. K. J. Buschow, R. W. Cahn, M. C. Flemings, B. Ilschner, E. J. Kramer, S. Mahajan and P. Veyssière, Elsevier, Oxford, 2nd edn., 2001, ch. Scanning Electron Microscopy, pp. 8265–8269, DOI: 10.1016/B0-08-043152-6/01479-0.

[82] J. Piños, Š. Mikmeková and L. Frank, *J. Microsc.*, 2017, **266(3)**, 335–342, DOI: 10.1111/jmi.12542.

[83] D. Titus, E. James Jebaseelan Samuel and S. M. Roopan, in *Green Synthesis, Characterization and Applications of Nanoparticles*, ed. A. K. Shukla and S. Iravani, Elsevier, Amsterdam, 2019, ch. 12, pp. 303–319, DOI: 10.1016/B978-0-08-102579-6.00012-5.

[84] R. Kohli and K. Mittal, in *Developments in Surface Contamination and Cleaning, Volume 12*, ed. R. Kohli and K. Mittal, Elsevier, Amsterdam, 2019, ch. 3, pp. 23–105, DOI: 10.1016/B978-0-12-816081-7.00003-6.

[85] nanoScience Instruments, *Scanning Electron Microscopy*, `https://www.nanoscience.com/techniques/scanning-electron-microscopy/`, (accessed 03/03/2020).

[86] H. Miyazaki, H. Uozaki, A. Tojo, S. Hirashima, S. Inaga, K. Sakuma, Y. Morishita and M. Fukayama, *Pathology - Research and Practice*, 2012, **208(9)**, 503–509, DOI: 10.1016/j.prp.2012.05.006.

[87] W. Winoto, N. Loahardjo, X. S. Xie, P. Yin and N. R. Morrow, *Secondary and Tertiary Recovery of Crude Oil from Outcrop and Reservoir Rocks by Low Salinity Waterflooding*, SPE Improved Oil Recovery Symposium, Tulsa, Oklahoma, USA, April 2012, SPE–154209–MS, DOI: 10.2118/154209-MS.

[88] J. G. Southwick, E. van den Pol, C. H. T. van Rijn, D. W. van Batenburg, A. A. B. a Manap, A. A. K. Mastan and N. N. Zulkifli, *Surfactant Flooding in Offshore Environments*, SPE Improved Oil Recovery Conference, Tulsa, Oklahoma, April 2018, SPE–190296–MS, DOI: 10.2118/190296-MS.

[89] S. Yesufu-Rufai, F. Marcelis, A. Georgiadis, S. Berg, M. Rücker, J. van Wunnik and P. Luckham, *Colloids Surf, A Physicochem Eng Asp*, 2020, **597**, 124765, DOI: 10.1016/j.colsurfa.2020.124765.

[90] S. M. Ma and M. Amabeoku, *Interpretation*, 2015, **3(1)**, 1F–T41, DOI: 10.1190/INT-2014-0072.1.

[91] D. Tiab and E. C. Donaldson, in *Petrophysics - Theory and Practice of Measuring Reservoir Rock and Fluid Transport Properties*, ed. D. Tiab and E. C. Donaldson, Gulf Professional Publishing, Boston, 4th edn., 2016, ch. 8, pp. 415–481, DOI: 10.1016/B978-0-12-803188-9.00008-5.

[92] P. Lai, K. Moulton and S. Krevor, *Chem. Geol.*, 2015, **411**, 260–273, DOI: 10.1016/j.chemgeo.2015.07.010.

[93] H. Menke, B. Bijeljic and M. Blunt, *Geochimica et Cosmochimica Acta*, 2017, **204**, 267–285, DOI: 10.1016/j.gca.2017.01.053.

[94] M. Voltolini and J. Ajo-Franklin, *Int. J. Greenh. Gas Control*, 2019, **82**, 38–47, DOI: 10.1016/j.ijggc.2018.12.013.

[95] M. R. Diaz and G. P. Eberli, *Earth-Science Reviews*, 2019, **190**, 536–556, DOI: 10.1016/j.earscirev.2018.12.016.

[96] S. Shah, F. Gray, J. Crawshaw and E. Boek, *Advances in Water Resources*, 2016, **95**, 276–287, DOI: 10.1016/j.advwatres.2015.07.012.

[97] J. Song, S. Rezaee, L. Zhang, Z. Zhang, M. Puerto, O. B. Wani, F. Vargas, S. Alhassan, S. L. Biswal and G. J. Hirasaki, *Energy Fuels*, 2019, **33(2)**, 957–967, DOI: 10.1021/acs.energyfuels.8b03896.

[98] H. Gamal, S. Elkatatny and A. Adebayo, *J. Pet. Sci. Eng.*, 2021, **202**, 108595, DOI: 10.1016/j.petrol.2021.108595.

[99] S. Yesufu-Rufai, M. Rücker, S. Berg, S. F. Lowe, F. Marcelis, A. Georgiadis and P. Luckham, *Fuel*, 2020, **273**, 117807, DOI: 10.1016/j.fuel.2020.117807.

[100] I. Horcas, R. Fernández, J. M. Gómez-Rodríguez, J. Colchero, J. Gómez-Herrero and A. M. Baro, *Rev. Sci. Instrum.*, 2007, **78**, 013705, DOI: 10.1063/1.2432410.

[101] L. A. Espitia, L. Varela, C. Pinedo and A. Tschiptschin, *Wear*, 2013, **301(1-2)**, 449–456, DOI: 10.1016/j.wear.2012.12.029.

[102] D. Semnani, in *Electrospun Nanofibers*, ed. M. Afshari, Woodhead Publishing, 2017, ch. 7 - Geometrical characterization of electrospun nanofibers, pp. 151–180, DOI: 10.1016/B978-0-08-100907-9.00007-6.

[103] L. J. Steinbock, A. Lucas, O. Otto and U. F. Keyser, *Electrophoresis*, 2012, **33**, 3480–3487, DOI: 10.1002/elps.201100663.

[104] K. C. Wu, W. F. Koch and K. W. Pratt, *J. Res. Natl. Inst. Stand. Technol.*, 1991, **96(2)**, 191, DOI: 10.6028/jres.096.008.

[105] M. J. Blunt, B. Bijeljic, H. Dong, O. Gharbi, S. Iglauer, P. Mostaghimi, A. Paluszny and C. Pentland, *Advances in Water Resources*, 2013, **51**, 197–216, DOI: 10.1016/j.advwatres.2012.03.003.

[106] H. Menke, C. Reynolds, M. Andrew, J. Pereira Nunes, B. Bijeljic and M. Blunt, *Chemical Geology*, 2018, **481**, 27–37, DOI: 10.1016/j.chemgeo.2018.01.016.

[107] J. Dautriat, N. Gland, A. Dimanov and J. Raphanel, *Journal of Geophysical Research*, 2011, **116**, B01205, DOI: 10.1029/2009JB000830.

[108] M. Freire-Gormaly, J. S. Ellis, A. Bazylak and H. L. MacLean, *Microporous and Mesoporous Materials*, 2015, **207**, 84–89, DOI: 10.1016/j.micromeso.2015.01.002.

[109] M. Zhang, J. Li, J. Zhao, Y. Cui and X. Luo, *ACS Omega*, 2020, **5(20)**, 11369–11377, DOI: 10.1021/acsomega.0c00345.

[110] K. Kumar, E. K. Dao and K. K. Mohanty, *SPE J.*, 2008, **13(2)**, 137–145, DOI: 10.2118/93009-PA.

[111] O. Seiedi, M. Rahbar, M. Nabipour, M. A. Emadi, M. H. Ghatee and S. Ayatollahi, *Energy Fuels*, 2011, **25(1)**, 183–188, DOI: 10.1021/ef100699t.

[112] T. Hassenkam, L. L. Skovbjerg and S. L. S. Stipp, *PNAS*, 2009, **106(15)**, 6071–6076, DOI: 10.1073/pnas.0901051106.

[113] M. C. Marcano, S. Kim, S. D. Taylor and U. Becker, *Chem. Geol.*, 2019, **525**, 462–478, DOI: 10.1016/j.chemgeo.2019.07.030.

[114] F. M. Etzler and J. Drelich, in *Developments in Surface Contamination and Cleaning*, ed. R. Kohli and K. Mittal, William Andrew Publishing, Oxford, 2012, ch. 6, pp. 307–331, DOI: 10.1016/B978-1-4377-7883-0.00006-7.

[115] H. Hölscher, in *Encyclopedia of Nanotechnology*, ed. B. Bhushan, Springer, Dordrecht, Netherlands, 2012, ch. AFM, Tapping Mode, pp. 99–105, DOI: 10.1007/978-90-481-9751-4_33.

[116] M. J. Wilson, L. Wilson and I. Patey, *Clay Miner.*, 2014, **49(2)**, 147–164, DOI: 10.1180/claymin.2014.049.2.02.

[117] M. S. Nasser and A. E. James, *Sep. Purif. Technol.*, 2006, **52(2)**, 241–252, DOI: 10.1016/j.seppur.2006.04.005.

[118] E. Tombàcz and M. Szekeres, *Appl. Clay Sci.*, 2006, **34(1-4)**, 105–124, DOI: 10.1016/j.clay.2006.05.009.

[119] H. Mahani, A. L. Keya, S. Berg, W.-B. Bartels, R. Nasralla and W. R. Rossen, *Energy Fuels*, 2015, **29(3)**, 1352–1367, DOI: 10.1021/ef5023847.

[120] H. Mahani, S. Berg, D. Ilic, W.-B. Bartels and V. Joekar-Niasar, *SPE J.*, 2015, **20(1)**, 8–20, DOI: 10.2118/165255-PA.

[121] E. V. Lebedeva and A. Fogden, *Environ. Sci. Technol.*, 2010, **44(24)**, 9470–9475, DOI: 10.1021/es102041b.

[122] C. Detellier and S. Letaief, in *Handbook of Clay Science*, ed. F. Bergaya and G. Lagaly, Elsevier, Amsterdam, 2013, vol. 5 of Developments in Clay Science, ch. 13, pp. 707–719, DOI: 10.1016/B978-0-08-098258-8.00022-5.

[123] Y. Hu, X. Liu and Z. Xu, *Minerals Engineering*, 2003, **16(3)**, 219–227, DOI: 10.1016/S0892-6875(02)00368-0.

[124] D. Schulze, in *Encyclopedia of Soils in the Environment*, ed. D. Hillel, Elsevier, Oxford, 2005, ch. CLAY MINERALS, pp. 246–254, DOI: 10.1016/B0-12-348530-4/00189-2.

[125] J. Wan and T. K. Tokunaga, *J. Colloid Interface Sci.*, 2002, **247(1)**, 54–61, DOI: 10.1006/jcis.2001.8132.

[126] A. S. Al-Harrasi, R. S. Al-Maamari and S. Masalmeh, *Laboratory Investigation of Low Salinity Waterflooding for Carbonate Reservoirs*, Abu Dhabi International Petroleum Conference and Exhibition, Abu Dhabi, UAE, November 2012, SPE–161468–MS, DOI: 10.2118/161468-MS.

[127] J. Wang, H. Song and Y. Wang, *Fuel*, 2020, **266**, 117156, DOI: 10.1016/j.fuel.2020.117156.

[128] A. Lager, K. J. Webb, C. J. J. Black, M. Singleton and K. S. Sorbie, *Petrophysics*, 2008, **49(1)**, 28–35.

[129] M. B. Alotaibi, H. A. Nasr-El-Din and J. J. Fletcher, *SPE Reservoir Evaluation Engineering*, 2011, **14(5)**, 594–603, DOI: 10.2118/148701-PA.

[130] D. Baran, R. S. Ashraf, D. A. Hanifi, M. Abdelsamie, N. Gasparini, J. A. Röhr, S. Holliday, A. Wadsworth, S. Lockett, M. Neophytou, C. J. M. Emmott, J. Nelson, C. J. Brabec, A. S. Aram Amassian, T. Kirchartz, J. R. Durrant and I. McCulloch, *Nat. Mat.*, 2016, **16**, 363–369, DOI: 10.1038/nmat4797.

[131] P. Murto, S. Elmas, U. A. Méndez-Romero, Y. Yin, Z. Genene, M. Mone, G. G. Andersson, M. R. Andersson and E. Wang, *Macromolecules*, 2020, **53(24)**, 11106–11119, DOI: 10.1021/acs.macromol.0c02212.

[132] M. Wieland, C. Malacrida, Q. Yu, C. Schlewitz, L. Scapinello, A. Penoni and S. Ludwigs, *Flex. Print. Electron.*, 2020, **5**, 014016, DOI: 10.1088/2058-8585/ab76e0.

[133] R. McGuire Jr., D. K. Dogutan, T. S. Teets, J. Suntivich, Y. Shao-Horn and D. G. Nocera, *Chem. Sci.*, 2010, **1(3)**, 411–414, DOI: 10.1039/C0SC00281J.

[134] C. O. Laoire, S. Mukerjee, K. M. Abraham, E. J. Plichta and M. A. Hendrickson, *J. Phys. Chem. C*, 2010, **114(19)**, 9178–9186, DOI: 10.1021/jp102019y.

[135] N. G. Tsierkezos and A. I. Philippopoulos, *Fluid Phase Equilib.*, 2009, **277(1)**, 20–28, DOI: 10.1016/j.fluid.2008.11.004.

[136] A. Reddy-Marri, E. Marchini, V. Diez Cabanes, R. Argazzi, M. Pastore, S. Caramori and P. C. Gros, *J. Mater. Chem. A*, 2021, **9(6)**, 3540–3554, DOI: 10.1039/D0TA10841C.

[137] F. Frenzel, P. Borchert, A. M. Anton, V. Strehmel and F. Kremer, *Soft Matter*, 2019, **15(7)**, 1605–1618, DOI: 10.1039/C8SM02135J.

[138] D. Guo, J. Li, G. Xie, Y. Wang and J. Luo, *Langmuir*, 2014, **30(24)**, 7206–7212, DOI: 10.1021/la501485e.

[139] A. Rudin and P. Choi, in *The Elements of Polymer Science & Engineering*, ed. A. Rudin and P. Choi, Academic Press, Boston, 3rd edn., 2013, ch. 3, pp. 89–148, DOI: 10.1016/B978-0-12-382178-2.00003-1.

[140] G. D. Bascom and T. Schlick, in *Nuclear Architecture and Dynamics*, ed. C. Lavelle and J.-M. Victor, Academic Press, Boston, 2018, vol. 2, ch. 5, pp. 123–147, DOI: 10.1016/B978-0-12-803480-4.00005-3.

[141] I. Teraoka, in *Polymer Solutions - An Introduction to Physical Properties*, Wiley-Interscience, New York, 1st edn., 2002, ch. 1, pp. 1-68. https://app.knovel.com/hotlink/pdf/id:kt012XT4I1/polymer-solutions-an/experimental-results.

[142] S. Li, M. D. Jackson and N. Agenet, *Fuel*, 2020, **276**, 118097, DOI: 10.1016/j.fuel.2020.118097.

[143] N. Alyafei and M. J. Blunt, *Advances in Water Resources*, 2016, **90**, 36–50, DOI: 10.1016/j.advwatres.2016.02.001.

[144] M. D. Jackson, D. Al-Mahrouqi and J. Vinogradov, *Sci. Rep.*, 2016, **6**, 37363, DOI: 10.1038/srep37363.

[145] World Health Organisation, *INCHEM: Internationally Peer Reviewed Chemical Safety Information*, https://www.inchem.org/#/, (accessed 17/05/2023).

[146] T. Renner, in *Quantities, Units and Symbols in Physical Chemistry*, ed. E. R. Cohen, T. Cvitas, J. G. Frey, B. Holström, K. Kuchitsu, R. Marquardt, I. Mills, F. Pavese, M. Quack, J. Stohner, H. L. Strauss, M. Takami and A. J. Thor, RSC Publishing, Cambridge, UK, 3rd edn., 2007, ch. 2, pp. 11–82, DOI: 10.1039/9781847557889.

[147] K. Kovalev, A. Rashkovskiy, M. Khayrullin, P. Grishin, V. Shklover, N. Artemov and I. Maryasev, *Core Cleaning and Aging Effects of Devonian Carbonate Core at Micro Scale*, SPE Russian Petroleum Technology Conference, Moscow, Russia, October 2018, SPE–191659–18RPTC–MS, DOI: 10.2118/191659-18RPTC-MS.

[148] S. Kumar, P. Panigrahi, R. K. Saw and A. Mandal, *Energy Fuels*, 2016, **30(4)**, 2846–2857, DOI: 10.1021/acs.energyfuels.6b00152.

[149] S.-Y. Chen, K. Kristiansen, D. Seo, N. A. Cadirov, H. A. Dobbs, Y. Kaufman, A. M. Schrader, R. C. Andresen Eguiluz, M. B. Alotaibi, S. C. Ayirala, J. R. Boles, A. A. Yousef and J. N. Israelachvili, *Langmuir*, 2019, **35(1)**, 41–50, DOI: 10.1021/acs.langmuir.8b02711.

[150] A. Gmira, D. K. Cha, S. M. Al-Enezi and A. A. Yousef, *Effect of Salinity on Crude Oil/Brine/Rock Interfaces: A Cryo-BIB-SEM Approach to Carbonates Wettability*, SPE Improved Oil Recovery Conference, Tulsa, Oklahoma, USA, April 2018, SPE–190245–MS, DOI: 10.2118/190245-MS.

[151] S. Moradi, A. A. Isari, Z. Bachari and H. Mahmoodi, *J. Pet. Sci. Eng.*, 2019, **176**, 1–10, DOI: 10.1016/j.petrol.2019.01.043.

[152] J. I. Goldstein, D. E. Newbury, J. R. Michael, N. W. M. Ritchie, J. H. J. Scott and D. C. Joy, in *Scanning Electron Microscopy and X-Ray Microanalysis*, Springer, New York, 4th edn., 2018, ch. 19, pp. 289–307, DOI: 10.1007/978-1-4939-6676-9_19.

[153] E. Stauffer, J. A. Dolan and R. Newman, in *Fire Debris Analysis*, ed. E. Stauffer, J. A. Dolan and R. Newman, Academic Press, Burlington, 2008, ch. 7, pp. 199–233, DOI: 10.1016/B978-012663971-1.50011-7.

[154] J. L. Clabel H., G. Lozano C., I. C. Pinto, R. F. Falci, V. A. G. Rivera, Y. Messaddeq and E. Marega Jr., in *Advances in Glass Research*, ed. S. J. Ikhmayies, Springer, Cham, Switzerland, 1st edn., 2023, ch. 1, pp. 1–52, DOI: 10.1007/978-3-031-20266-7_1.

[155] M. E. J. Haagh, N. Schilderink, M. H. G. Duits, I. Siretanu, P. Krawiec, I. R. Collins and F. Mugele, *Fuel*, 2020, **274**, 117856, DOI: 10.1016/j.fuel.2020.117856.

[156] W. L. Bragg and R. E. Gibbs, *Proc. R. Soc. A*, 1925, **109(751)**, 405–427, DOI: 10.1098/rspa.1925.0135.

[157] L. A. Araujo, C. R. Foschini and C. A. Fortulan, in *Magnetic, Ferroelectric, and Multiferroic Metal Oxides*, ed. B. D. Stojanovic, Elsevier, Amsterdam, 2018, ch. 13, pp. 265–274, DOI: 10.1016/B978-0-12-811180-2.00013-X.

[158] R. Southard, X. Li, E. Eisen and K. Pinkerton, in *Encyclopedia of Toxicology*, ed. P. Wexler, Academic Press, Oxford, 3rd edn., 2014, ch. Silica, Crystalline, pp. 266–269, DOI: 10.1016/B978-0-12-386454-3.00061-0.

[159] A. Matsumoto, Y. Kaimori, T. Kawasaki and K. Soai, in *Advances in Asymmetric Autocatalysis and Related Topics*, ed. G. Pályi, R. Kurdi and C. Zucchi, Academic Press, Oxford, 2017, ch. 18, pp. 337–355, DOI: 10.1016/B978-0-12-812824-4.00018-6.

[160] *a–Quartz (low Quartz) Structure: A2B_hP9_152_c_a*, `http://aflowlib.org/prototype-encyclopedia/A2B_hP9_152_c_a.html`, (accessed April 2021).

[161] M. J. Mehl, D. Hicks, C. Toher, O. Levy, R. M. Hanson, G. Hart and S. Curtarolo, *Computational Materials Science*, 2017, **136**, S1–S828, DOI: 10.1016/j.commatsci.2017.01.017.

[162] D. Hicks, M. J. Mehl, E. Gossett, C. Toher, O. Levy, R. M. Hanson, G. Hart and S. Curtarolo, *Computational Materials Science*, 2019, **161**, S1–S1011, DOI: 10.1016/j.commatsci.2018.10.043.

[163] P.-I. Au, S.-Y. Siow, L. Avadiar, E.-M. Lee and Y.-K. Leong, *Powder Technology*, 2014, **262**, 124–130, DOI: 10.1016/j.powtec.2014.04.078.

[164] A.-N. Nguyen, F. Balima, P. Penhoud, L. Duclaux, L. Mirabel, L. Reinert, F. Muller, S. Le Floch, V. Pischedda, A. San Miguel, A. Beziat, P. Dehaudt and J.-F. Juliaa, *Applied Clay Science*, 2014, **101**, 409–418, DOI: 10.1016/j.clay.2014.09.001.

[165] S. W. Bailey, in *Crystal Structures of Clay Minerals and their X-ray Identification*, ed. G. W. Brindley and G. Brown, Mineralogical Society, London, 1st edn., 1980, vol. 5, ch. 1, pp. 1–124, DOI: 10.1180/mono-5.

[166] O. Fesharaki, E. García-Romero, J. Cuevas-González and N. López-Martínez, *Clay Minerals*, 2007, **42(2)**, 187–201, DOI: 10.1180/claymin.2007.042.2.05.

[167] A. G. Tamirat, J. Rick, A. A. Dubale, W.-N. Su and B.-J. Hwang, *Nanoscale Horiz.*, 2016, **1(4)**, 243–267, DOI: 10.1039/C5NH00098J.

[168] Y. Guo, S. J. Clark and J. Robertson, *J. Phys.: Condens. Matter*, 2012, **24(32)**, 325504, DOI: 10.1088/0953-8984/24/32/325504.

[169] A. C. Thompson, J. Kirz, D. T. Attwood, E. M. Gullikson, M. R. Howells, J. B. Kortright, Y. Liu, A. L. Robinson, J. H. Underwood, K.-J. Kim, I. Lindau, P. Pianetta, H. Winick, G. P. Williams and J. H. Scofield, in *Center for X-Ray Optics and Advanced Light Source: X-Ray Data Booklet*, ed. A. C. Thompson, Lawrence Berkley National Laboratory, University of California, Berkeley, CA, 3rd edn., 2009, ch. 1, pp. 1–1 – 1–53.

[170] B. Li and K. M. Knowles, *Modelling Simul. Mater. Sci. Eng.*, 2013, **21(5)**, 055012, DOI: 10.1088/0965-0393/21/5/055012.

[171] P. Huang and M. Wang, in *Encyclopedia of Soils in the Environment*, ed. D. Hillel, Elsevier, Oxford, 2005, ch. MINERALS, PRIMARY, pp. 500–510, DOI: 10.1016/B0-12-348530-4/00464-1.

[172] I. Parsons and M. R. Lee, *The Canadian Mineralogist*, 2005, **43(6)**, 1959–1992, DOI: 10.2113/gscanmin.43.6.1959.

[173] S. Haldar and J. Tišljar, in *Introduction to Mineralogy and Petrology*, ed. S. Haldar and J. Tišljar, Elsevier, Oxford, 2014, ch. 2, pp. 39–79, DOI: 10.1016/B978-0-12-408133-8.00002-X.

[174] K. Askvik, S. Høiland, P. Fotland, T. Barth, T. Grønn and F. Fadnes, *J. Colloid Interface Sci.*, 2005, **287(2)**, 657–663, DOI: 10.1016/j.jcis.2005.02.031.

[175] M. Rücker, W.-B. Bartels, G. Garfi, M. Shams, T. Bultreys, M. Boone, S. Pieterse, G. C. Maitland, S. Krevor, V. Cnudde, H. Mahani, S. Berg, A. Georgiadis and P. F. Luckham, *J. Colloid Interface Sci.*, 2020, **562**, 159–169, DOI: 10.1016/j.jcis.2019.11.086.

[176] E. M. Ekanem, M. Rücker, S. Yesufu-Rufai, C. Spurin, N. Ooi, A. Georgiadis, S. Berg and P. F. Luckham, *JCIS Open*, 2021, **4**, 100026, DOI: 10.1016/j.jciso.2021.100026.

[177] G. Zhang, S. Foroughi, A. Q. Raeini, M. J. Blunt and B. Bijeljic, *Advances in Water Resources*, 2023, **171**, 104352, DOI: 10.1016/j.advwatres.2022.104352.

[178] L. Feng, S. Li, Y. Li, H. Li, L. Zhang, J. Zhai, Y. Song, B. Liu, L. Jiang and D. Zhu, *Adv. Mat.*, 2002, **14(24)**, 1857–1860, DOI: 10.1002/adma.200290020.

[179] M. Yamamoto, N. Nishikawa, H. Mayama, Y. Nonomura, S. Yokojima, S. Nakamura and K. Uchida, *Langmuir*, 2015, **31(26)**, 7355–7363, DOI: 10.1021/acs.langmuir.5b00670.

[180] Budget Sensors, *Tap300Al-G*, `https://www.budgetsensors.com/tapping-mode-afm-probe-aluminum-tap300al`, (accessed 29/05/2020).

[181] J. Zhao, F. Qin, D. Derome, Q. Kang and J. Carmeliet, *Adv Water Res*, 2020, **145**, 103738, DOI: 10.1016/j.advwatres.2020.103738.

[182] E. van den Pol, C. H. T. van Rijn and J. G. Southwick, *Alkali and Surfactant Consumption in Sandstone Outcrop Rocks*, Conference Proceedings, IOR 2015 - 18th European Symposium on Improved Oil Recovery, European Association of Geoscientists Engineers, 2015, DOI: 10.3997/2214-4609.201412157.

[183] Y. Wang, M. Chan and E. Merino, *Sci. Rep.*, 2015, **5**, 10792, DOI: 10.1038/srep10792.

[184] S. Boggs, Jr., *Principles of Sedimentology and Stratigraphy*, Pearson, New Jersey, 2006.

[185] U. Golla-Schindler, R. Hinrichs, O. Bomati-Miguel and A. Putnis, *Micron*, 2006, **37(5)**, 473–477, DOI: 10.1016/j.micron.2005.11.002.

[186] M. C. Goldberg, E. R. Weiner and P. M. Boymel, *J. Chem. Soc., Faraday Trans. 1*, 1984, **80(6)**, 1491–1498, DOI: 10.1039/F19848001491.

[187] A. Jada, R. Ait Akbour and J. Douch, *Chemosphere*, 2006, **64(8)**, 1287–1295, DOI: 10.1016/j.chemosphere.2005.12.063.

[188] H. N. Al-Saedi, P. V. Brady, R. Flori and P. Heidari, *Novel Insights into Low Salinity Water Flooding Enhanced Oil Recovery in Sandstone: The Clay Role Study*, SPE Improved Oil Recovery Conference, Tulsa, Oklahoma, USA, April 2018, SPE–190215–MS, DOI: 10.2118/190215-MS.

[189] D. Al Mahrouqi, J. Vinogradov and M. D. Jackson, *Adv. Colloid Interface Sci.*, 2017, **240**, 60–76, DOI: https://doi.org/10.1016/j.cis.2016.12.006.

[190] R. Eriksson, J. Merta and J. B. Rosenholm, *J. Colloid Interface Sci.*, 2007, **313(1)**, 184–193, DOI: 10.1016/j.jcis.2007.04.034.

[191] B. Mukhopadhyay and J. V. Walther, *Chem. Geol.*, 2001, **174(4)**, 415–443, DOI: 10.1016/S0009-2541(00)00288-6.

[192] C. Demir, A. A. Abramov and M. S. Çelik, *Miner. Eng.*, 2001, **14(7)**, 733–740, DOI: 10.1016/S0892-6875(01)00069-3.

[193] R. M. Garrels and C. L. Christ, *Solutions, minerals, and equilibria*, Harper & Row, New York, 1965.

[194] S. Spence, W.-K. Lee, F. Lin and X. Xiao, *Nanotechnology*, 2021, **32**, 442003, DOI: 10.1088/1361-6528/ac17ff.

[195] J. C. Andrews, F. Meirer, Y. Liu, Z. Mester and P. Pianetta, *Microsc. Res. Tech.*, 2011, **74(7)**, 671–681, DOI: 10.1002/jemt.20907.

[196] B. Kaulich, P. Thibault, A. Gianoncelli and M. Kiskinova, *J. Phys. Condens. Matter*, 2011, **23(8)**, 083002, DOI: 10.1088/0953-8984/23/8/083002.

[197] D. Nanda Gopala Krishna and J. Philip, *Appl. Surf. Sci. Adv.*, 2022, **12**, 100332, DOI: 10.1016/j.apsadv.2022.100332.

[198] A. Hammiche, H. M. Pollock, M. Reading, M. Clayburn, P. H. Turner and K. Jewkes, *Appl. Spec.*, 1999, **53(7)**, 810–815, DOI: 10.1366/0003702991947379.

[199] M. S. Anderson, *Appl. Spec.*, 2000, **54(3)**, 349–352, DOI: 10.1366/0003702001949618.

[200] A. Dazzi and C. B. Prater, *Chem. Rev.*, 2017, **117(7)**, 5146–5173, DOI: 10.1021/acs.chemrev.6b00448.

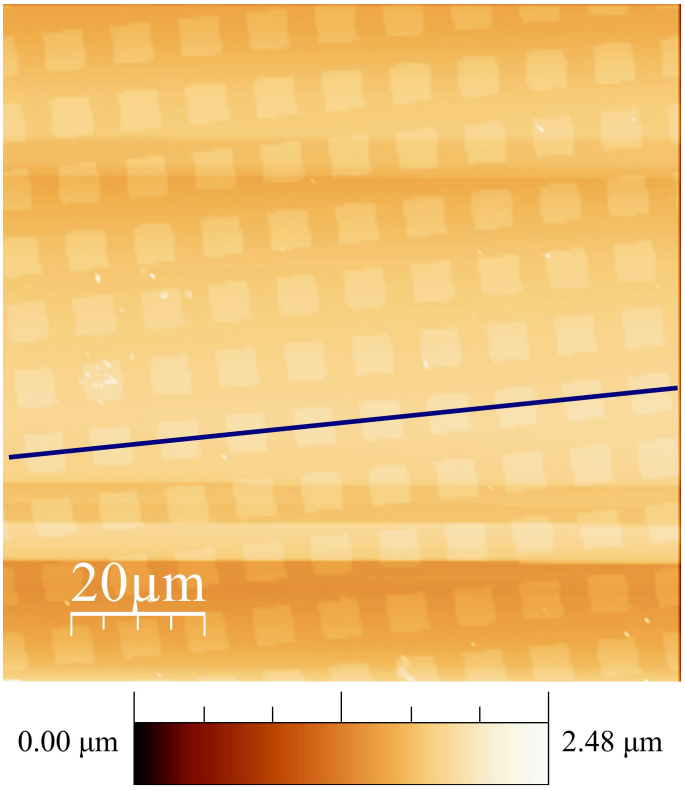
[201] C. R. Findlay, R. Wiens, M. Rak, J. Sedlmair, C. J. Hirschmugl, J. Morrison, C. J. Mundy, M. Kansiz and K. M. Gough, *Analyst*, 2015, **140(7)**, 2493–2503, DOI: 10.1039/C4AN01982B.

# Appendix A

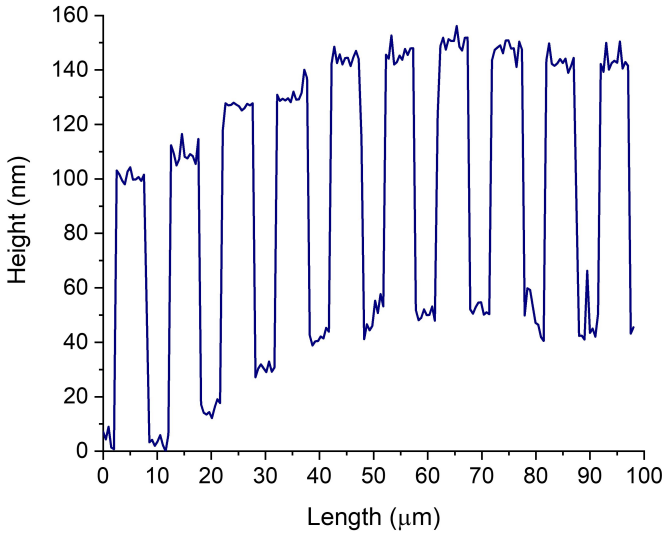
# Methods

## A.1 Calibration Standard

To ensure that the piezos in the SICM scan head were fully calibrated after a period of transit, a HS-100MG calibration standard (BudgetSensors, Bulgaria) with 100 nm step heights was imaged to ensure faithful height recording was taking place. Figures A.1 & A.2 below show a SICM image and a low-vacuum SEM micrograph of this sample respectively. The height profile along the blue line in Figure A.1a is shown in Figure A.1b to demonstrate the accurate recording of the 100 nm step heights.




(a)




(b)

Figure A.1: Calibration Sample: SICM image and height profile
(a) A 100 x 100 $\mu$m SICM image of the HS-100MG calibration standard with 100 nm step heights, with a blue line indicating the position of the height profile shown in (b).

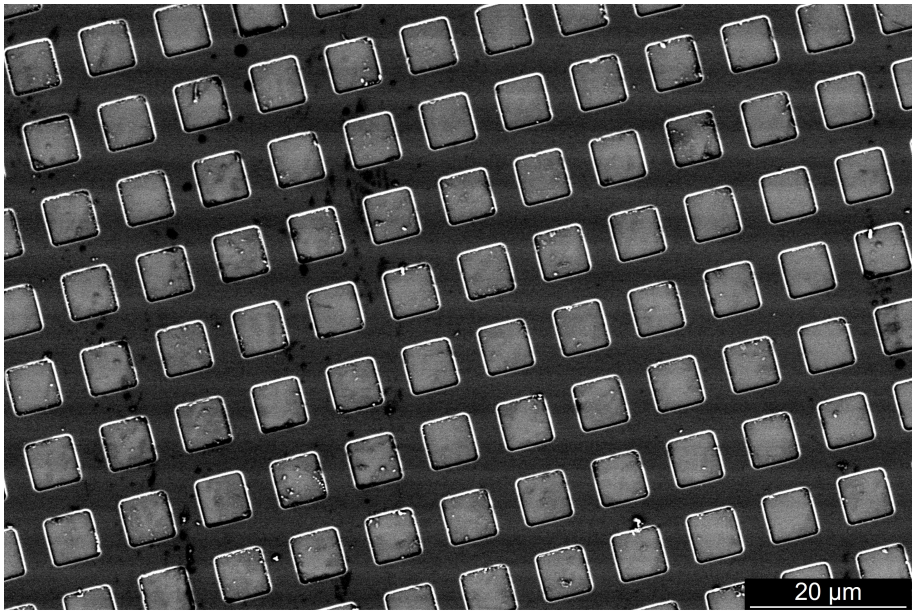



Figure A.2: Calibration Sample: low-vacuum SEM micrograph
A low-vacuum SEM micrograph of the HS-100MG calibration standard on a similar area to that shown in the SICM image in Figure A.1.

## A.2 Nanopipette Characterisation

### A.2.1 Re-arrangement of nanopipette conductance equation

Equation 2.3 in the Methods section was generated by rearranging Equation 2.2 (repeated below in Equation A.1, taken from Steinbock *et al.*) for $d_i$, as follows:[103]

$$G = \frac{d_i D_i \pi g(c)}{4(l + \frac{\pi}{8}(d_i + D_i))} \tag{A.1}$$

Rearranging for the $d_i$ term in the numerator gives:

$$d_i = \frac{4G(l + \frac{\pi}{8}(d_i + D_i))}{D_i \pi g(c)}$$

Which can then be expanded to separate out a second $d_i$ term:

$$d_i = \frac{4G(l + \frac{\pi}{8}d_i + \frac{\pi}{8}D_i)}{D_i\pi g(c)}$$

$$d_i = \frac{4Gl + \frac{\pi}{2}Gd_i + \frac{\pi}{2}GD_i}{D_i\pi g(c)}$$

$$d_i = \frac{4Gl + \frac{\pi}{2}GD_i}{D_i\pi g(c)} + \frac{\frac{\pi}{2}Gd_i}{D_i\pi g(c)}$$

These two $d_i$ terms can thus be combined:

$$d_i \ - \frac{\frac{\pi}{2}Gd_i}{D_i\pi g(c)} = \frac{4Gl + \frac{\pi}{2}GD_i}{D_i\pi g(c)}$$

$$d_i(1 \ - \frac{\frac{\pi}{2}G}{D_i\pi g(c)}) = \frac{4Gl + \frac{\pi}{2}GD_i}{D_i\pi g(c)}$$

To create an equation defining $d_i$:

$$d_i = \frac{4Gl + \frac{\pi}{2}GD_i}{D_i\pi g(c)} \frac{1}{1 \ - \frac{\frac{\pi}{2}G}{D_i\pi g(c)}}$$

Which can thus be simplified to give equation A.2, which is equation 2.3 from the Methods section:

$$d_i = \frac{4Gl + \frac{\pi}{2}GD_i}{D_i\pi g(c)} \frac{D_i\pi g(c)}{D_i\pi g(c) \ - \frac{\pi}{2}G}$$

$$d_i = \frac{D_i\pi g(c)(4Gl + \frac{\pi}{2}GD_i)}{D_i\pi g(c)(D_i\pi g(c) \ - \frac{\pi}{2}G)}$$

$$d_i = \frac{4Gl + \frac{\pi}{2}GD_i}{D_i\pi g(c) \ - \frac{\pi}{2}G} \tag{A.2}$$

### A.2.2 Worked example of nanopipette characterisation

A nanopipette was recorded as having a taper length, $l$, of 2953 $\mu$m and the cyclic voltammogram shown in Figure A.3 when characterised. Figure A.3 also shows a polynomial fit of the curve overlaid over the cyclic voltammogram and the corresponding equation alongside.

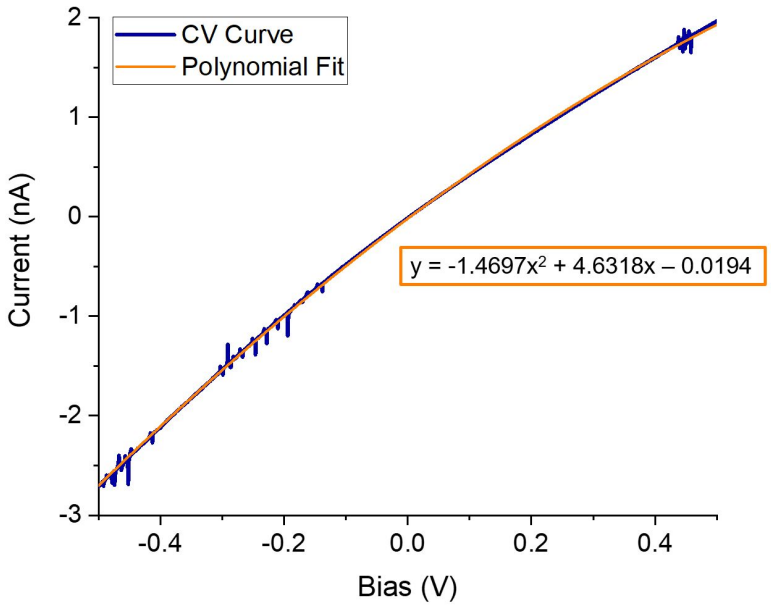



Figure A.3: Nanopipette cyclic voltammogram example
The cyclic voltammogram for the nanopipette in this case study with a $l$ = 2953 $\mu$m. Details of this fit, generated in OriginPro 2018b, are shown in Table A.1.

The gradient of the tangent of the cyclic voltammogram at 0 V, $G$, can be easily calculated from the polynomial fit equation given on Figure A.3 and in re-iterated Equation A.3 below.

$$y = -1.4697x^2 + 4.6318x–0.0194 \tag{A.3}$$

| | |
|---|---|
| Equation | $y = Intercept + Ax^1 + Bx^2$ |
| Intercept | -0.01943 ± 6.58091 × $10^{-4}$ |
| A | 4.63176 ± 0.00152 |
| B | -1.46974 ± 0.00589 |
| $R^2$ | 0.99979 |

Table A.1: Polynomial fit details for the cyclic voltammogram in Figure A.2.2

Differentiating Equation A.3 gives an equation for the gradient, m:

$$\frac{dy}{dx} = -2.9394x + 4.6318 = m$$

$G = m$ when $x = 0$, so when $x = 0$, $m = G = 4.6318$. The conductance, $G$, for this nanopipette is therefore 4.6318 ×$10^{-9}$ A/V ± 1.52×$10^{-12}$ A/V. Plugging our $G$ and $l$ values into equation A.2, using 0.5 mm and 1.28 S/m for $D_i$ & $g(c)$ respectively gives:

$$d_i = \frac{(4 \times (4.6318 \times 10^{-9}) \times (2.953 \times 10^{-3})) + (\frac{\pi}{2} \times (4.6318 \times 10^{-9}) \times (5 \times 10^{-4}))}{(5 \times 10^{-4})1.29\pi \ - (\frac{\pi}{2} \times (4.6318 \times 10^{-9}))}$$

thus the $d_i$ for this nanopipette can be approximated as 29 nm.

# Appendix B

# Carbonates

## B.1 Calcite

### B.1.1 Low-Vacuum Scanning Electron Microscopy

In Chapter 3: *Carbonates*, Section 3.2.1, two overlays of low-vacuum SEM micrographs of two different calcite crystals were presented in Figures 3.2 & 3.3; the individual micrographs without numbers overlain are shown in Figures B.1 - B.4 and B.5 - B.8.

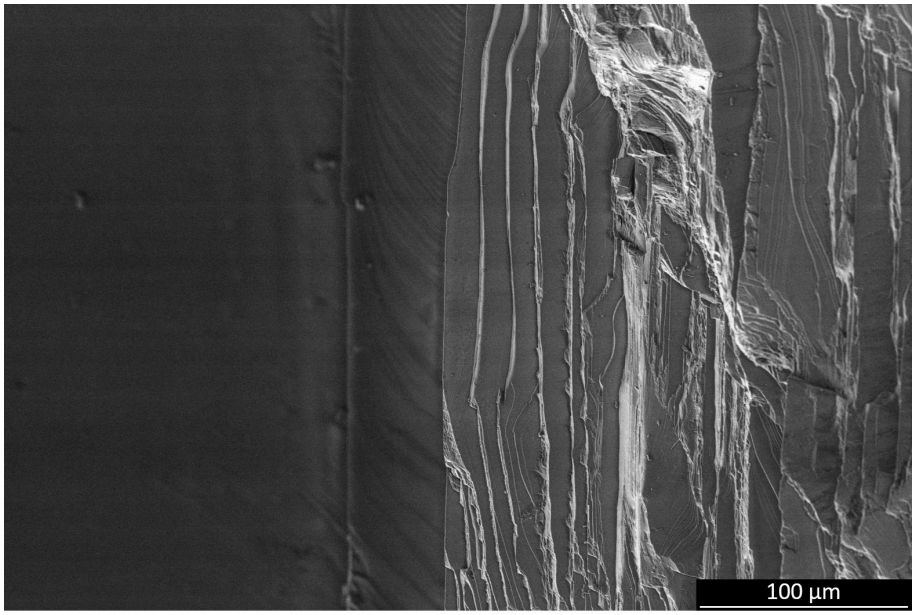



Figure B.1: Low-vacuum SEM: Micrograph 1 of a calcite crystal from Figure 3.2

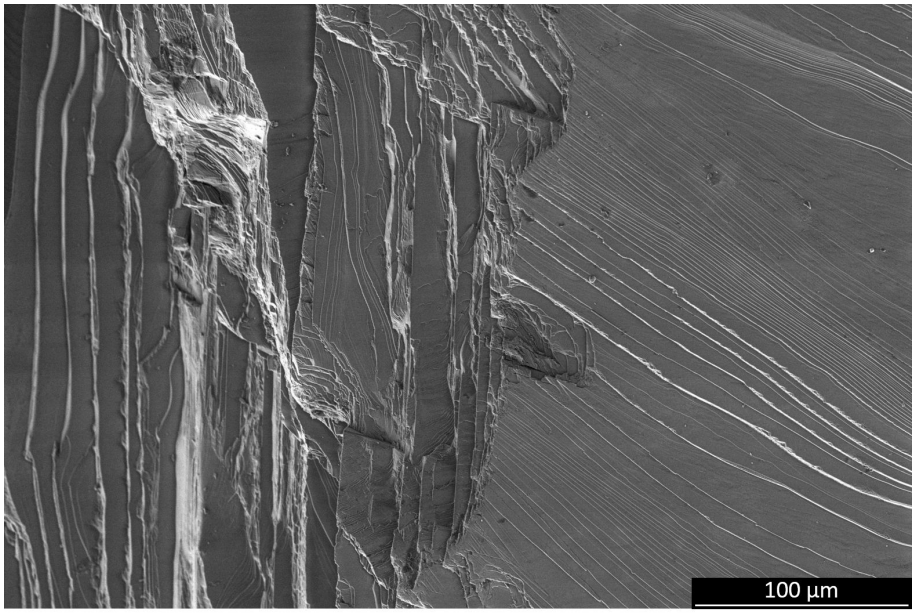



Figure B.2: Low-vacuum SEM: Micrograph 2 of a calcite crystal from Figure 3.2

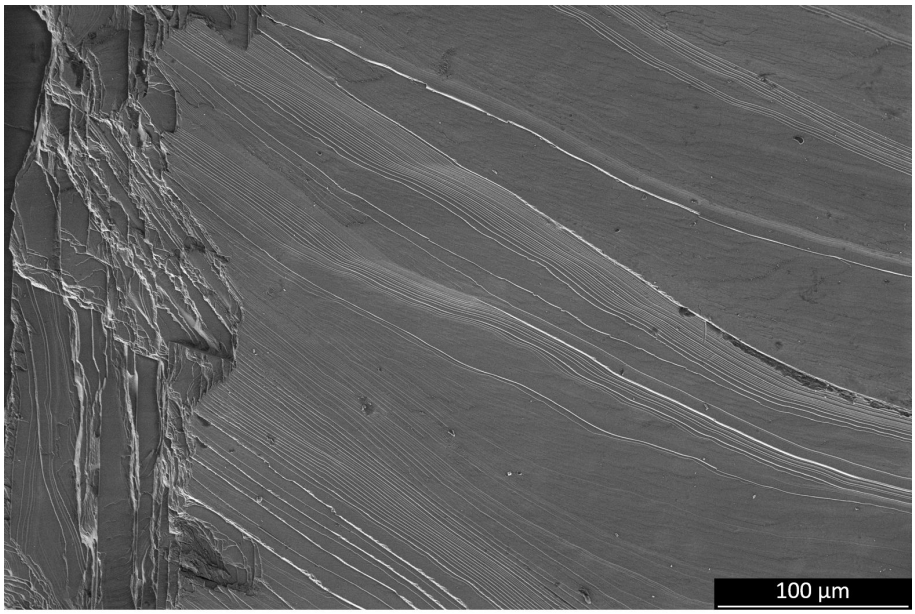



Figure B.3: Low-vacuum SEM: Micrograph 3 of a calcite crystal from Figure 3.2

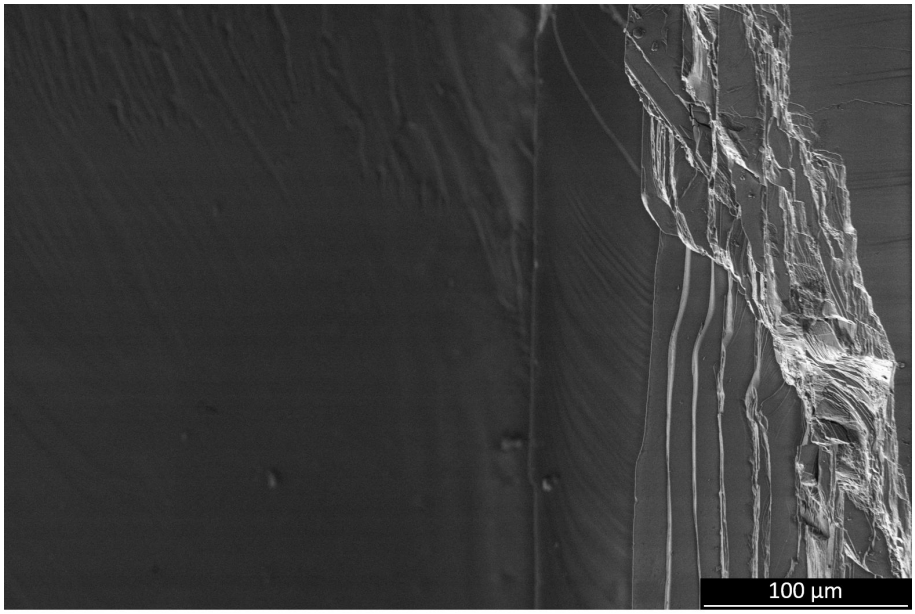



Figure B.4: Low-vacuum SEM: Micrograph 4 of a calcite crystal from Figure 3.2

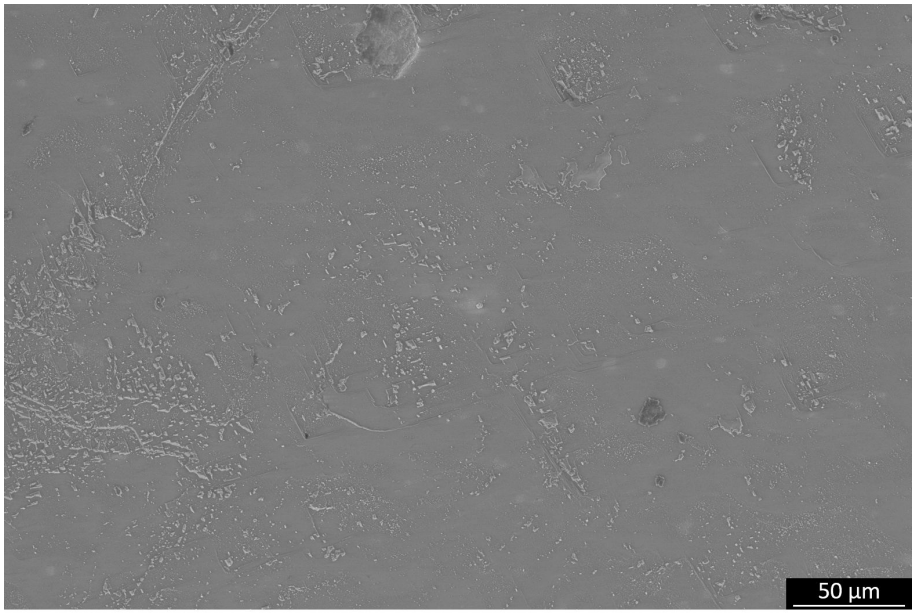



Figure B.5: Low-vacuum SEM: Micrograph 1 of a calcite crystal from Figure 3.3

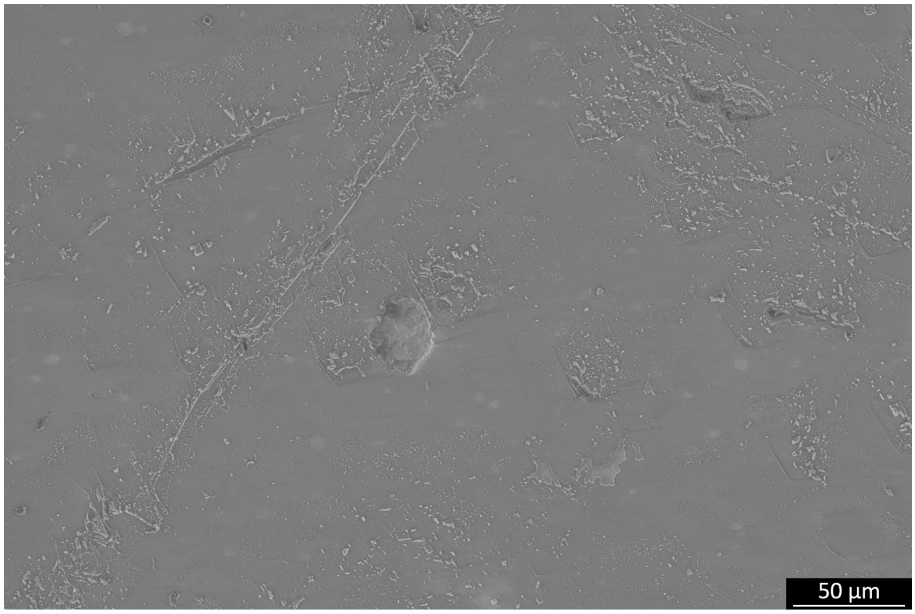



Figure B.6: Low-vacuum SEM: Micrograph 2 of a calcite crystal from Figure 3.3

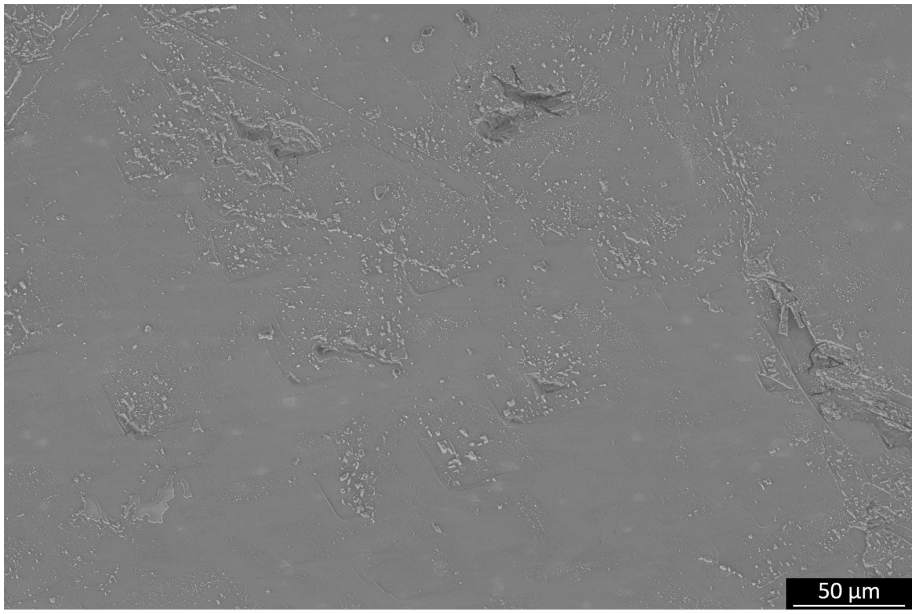



Figure B.7: Low-vacuum SEM: Micrograph 3 of a calcite crystal from Figure 3.3

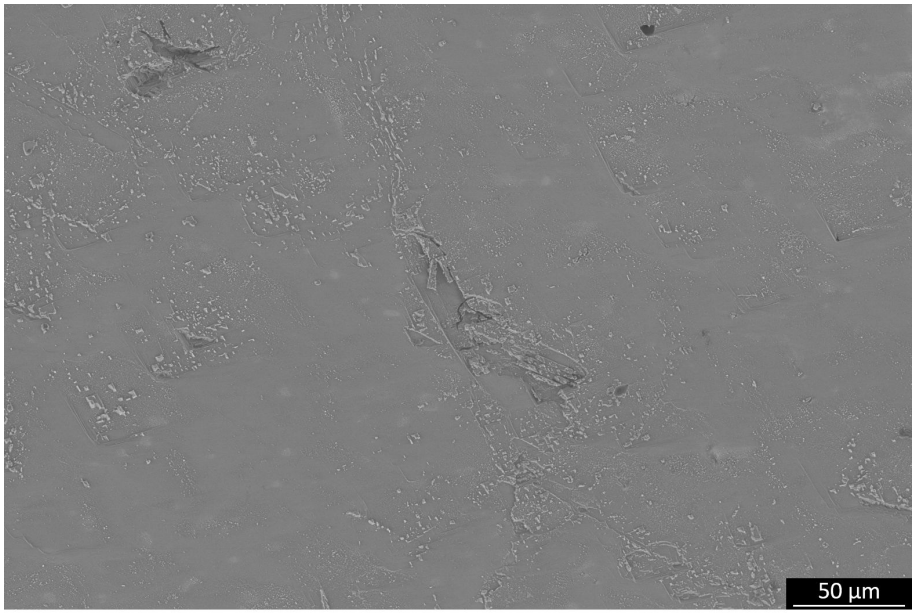



Figure B.8: Low-vacuum SEM: Micrograph 4 of a calcite crystal from Figure 3.3

In Chapter 5: *Carbonate Ageing Studies*, Section 5.3.1.1, two overlays of low-vacuum SEM micrographs of aged calcite surfaces were presented in Figures 5.1 & 5.2; the individual micrographs overlain are shown in Figures B.9 - B.12 & B.13 - B.17 respectively.

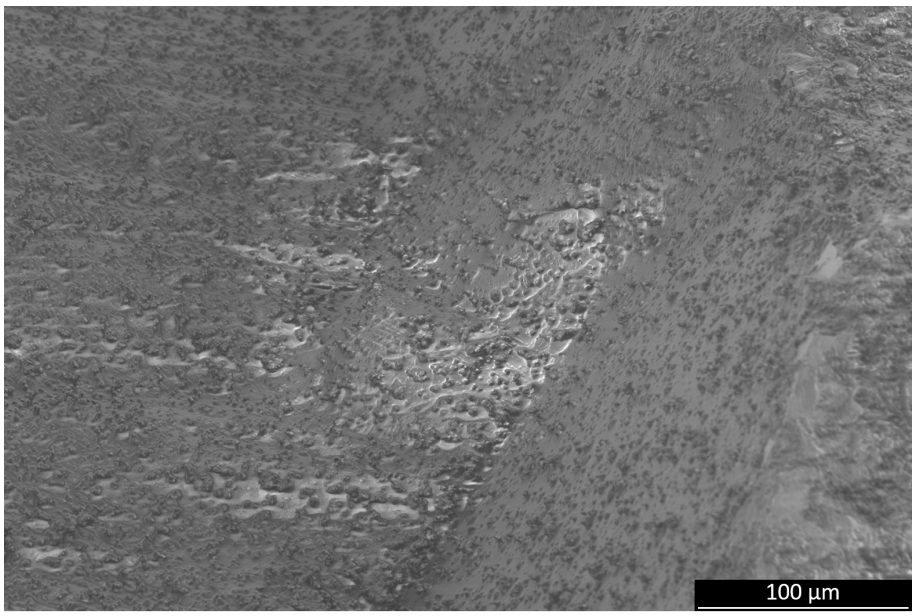



Figure B.9: Low-vacuum SEM: Micrograph 1 of the aged calcite surface shown in Figure 5.1

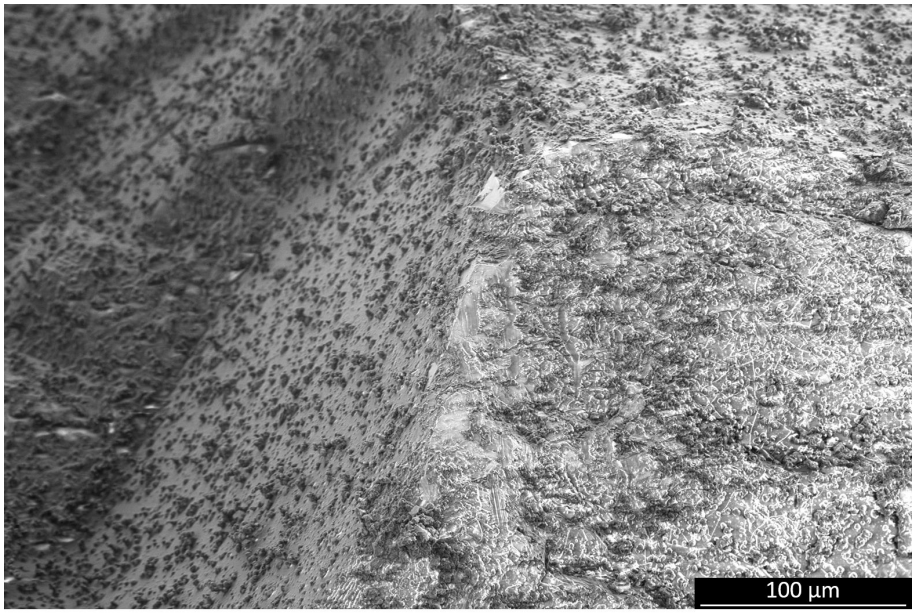



Figure B.10: Low-vacuum SEM: Micrograph 2 of the aged calcite surface shown in Figure 5.1

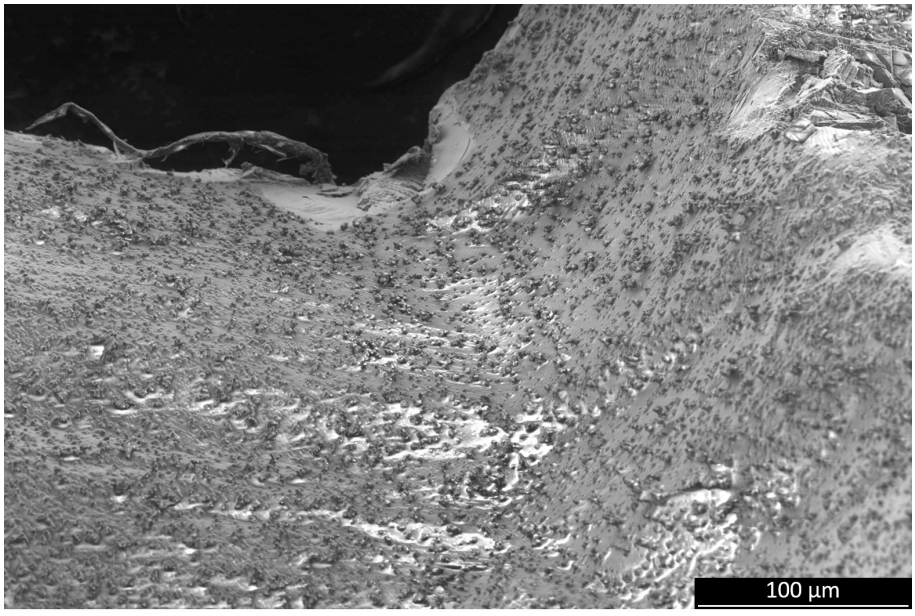



Figure B.11: Low-vacuum SEM: Micrograph 3 of the aged calcite surface shown in Figure 5.1

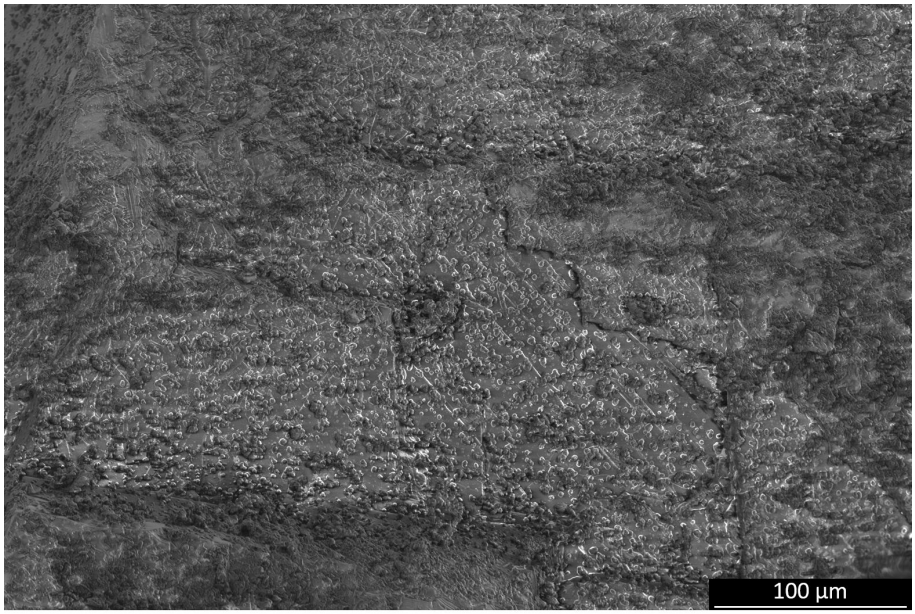



Figure B.12: Low-vacuum SEM: Micrograph 4 of the aged calcite surface shown in Figure 5.1

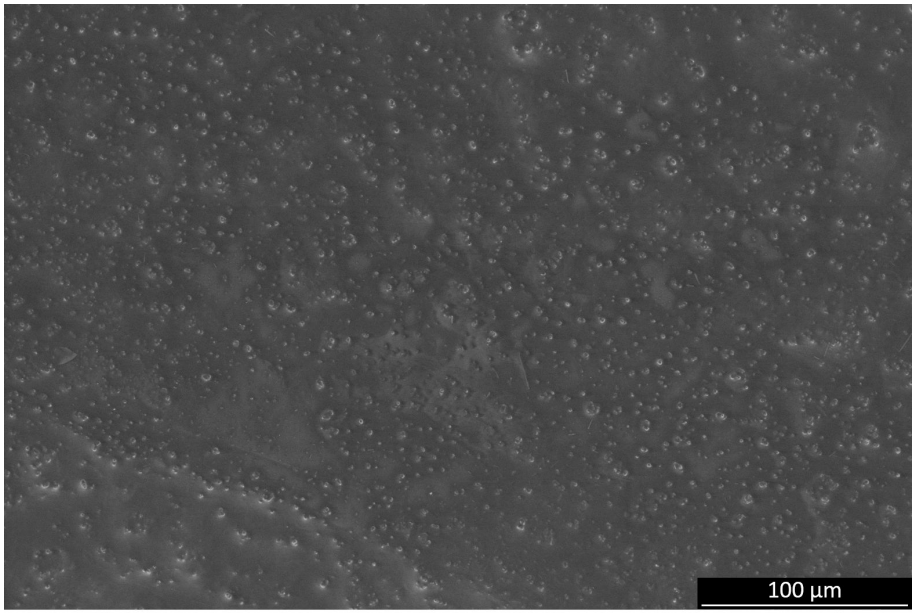



Figure B.13: Low-vacuum SEM: Micrograph 1 of the aged calcite surface shown in Figure 5.2

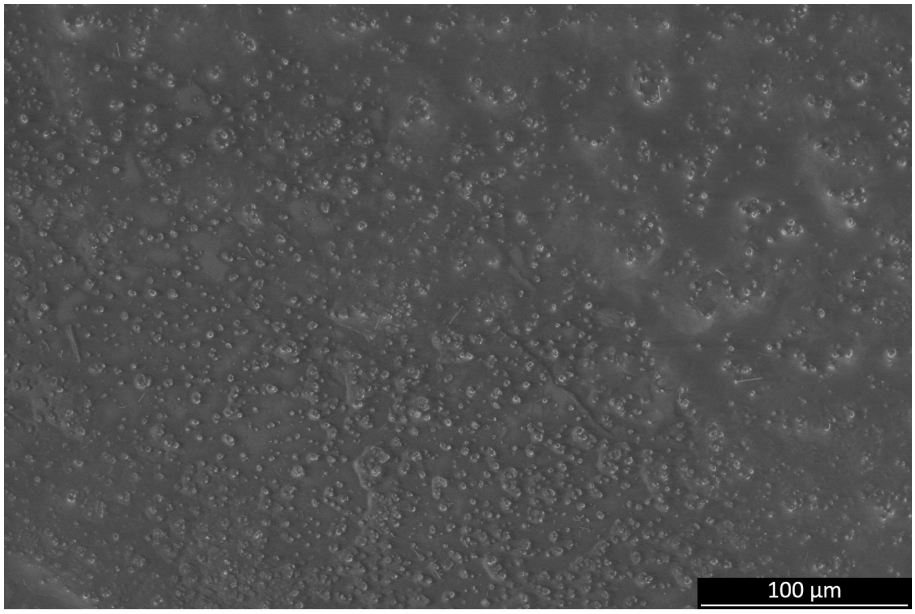



Figure B.14: Low-vacuum SEM: Micrograph 2 of the aged calcite surface shown in Figure 5.2

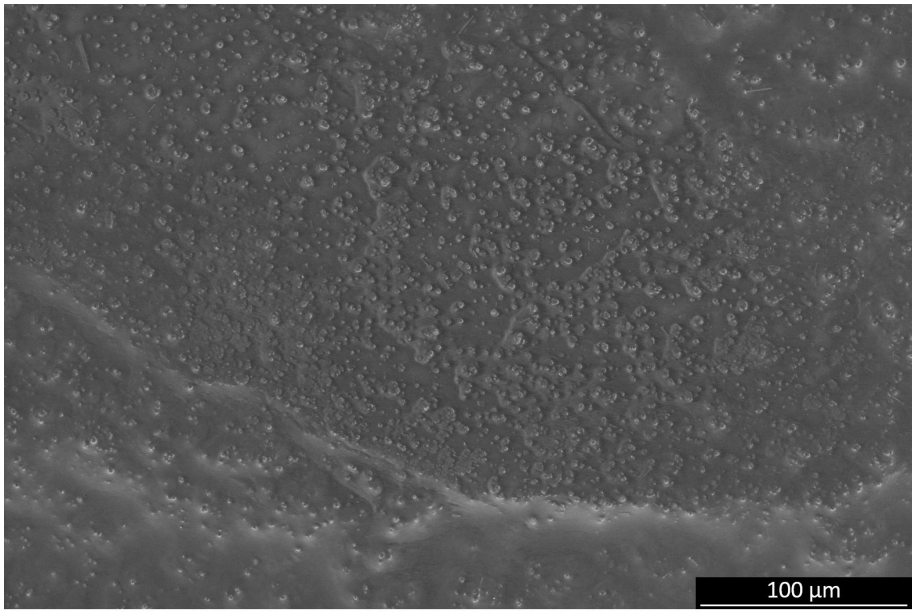



Figure B.15: Low-vacuum SEM: Micrograph 3 of the aged calcite surface shown in Figure 5.2

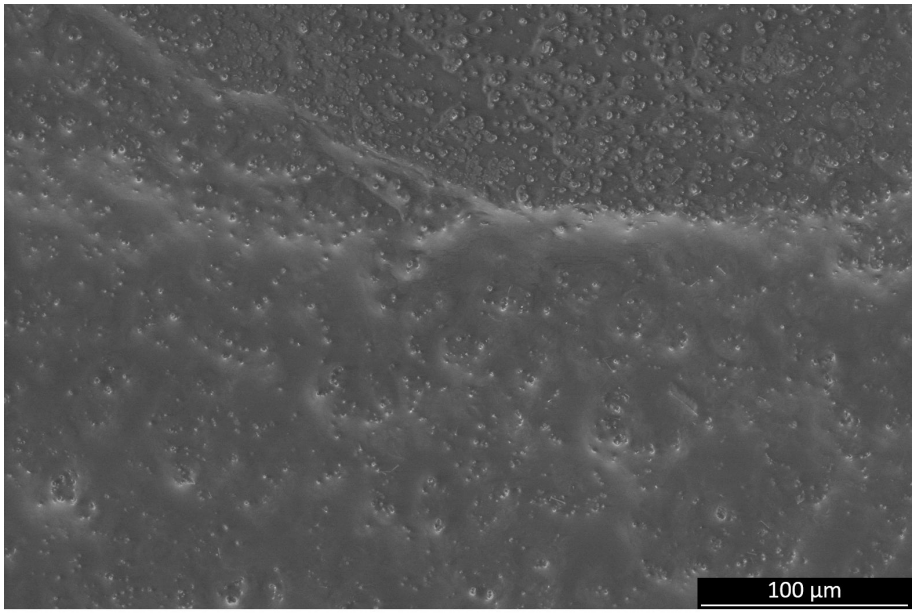



Figure B.16: Low-vacuum SEM: Micrograph 4 of the aged calcite surface shown in Figure 5.2

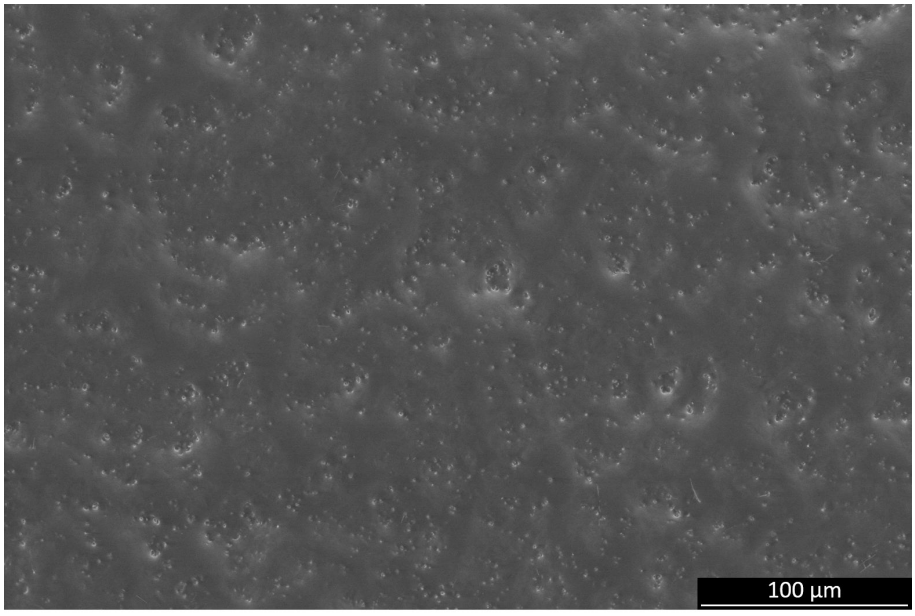



Figure B.17: Low-vacuum SEM: Micrograph 5 of the aged calcite surface shown in Figure 5.2

In Chapter 5: *Carbonate Ageing Studies*, Section 5.3.1.2, an overlay of nine low-vacuum SEM micrographs of an aged calcite surface after SICM measurements had been performed were presented in Figure 5.12; these individual micrographs are shown in Figures B.18 - B.26 below.

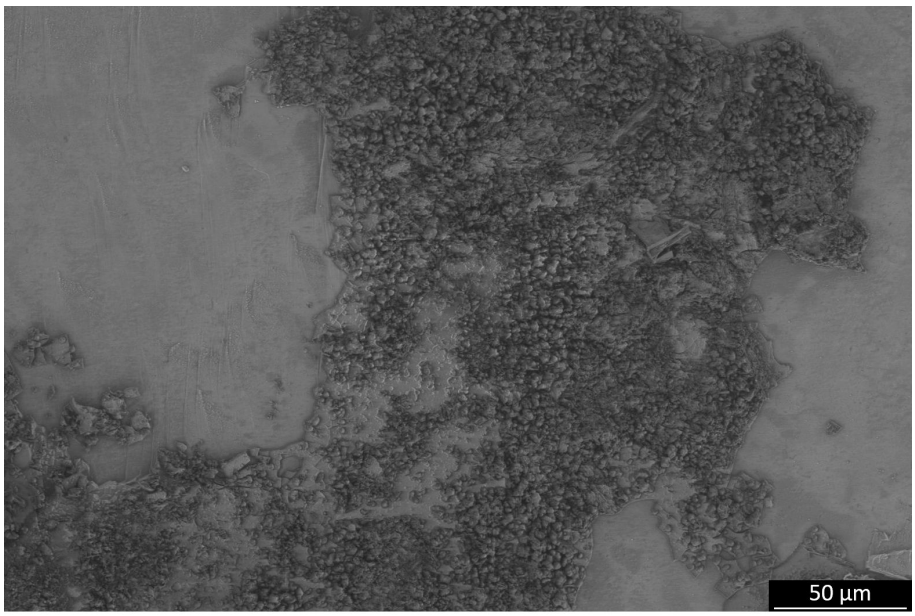



Figure B.18: Low-vacuum SEM: Micrograph 1 of the aged calcite surface after SICM measurements shown in Figure 5.12

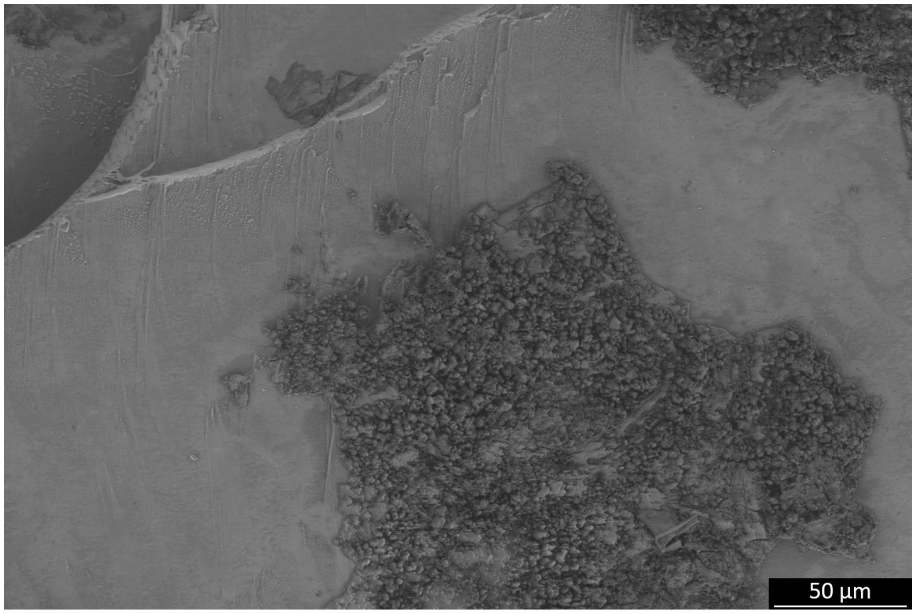



Figure B.19: Low-vacuum SEM: Micrograph 2 of the aged calcite surface after SICM measurements shown in Figure 5.12

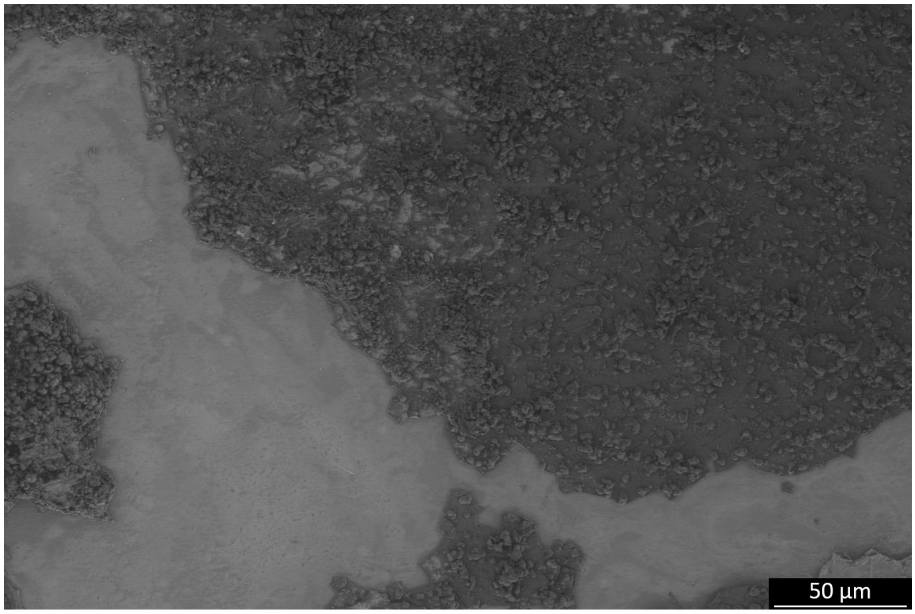



Figure B.20: Low-vacuum SEM: Micrograph 3 of the aged calcite surface after SICM measurements shown in Figure 5.12




Figure B.21: Low-vacuum SEM: Micrograph 4 of the aged calcite surface after SICM measurements shown in Figure 5.12




Figure B.22: Low-vacuum SEM: Micrograph 5 of the aged calcite surface after SICM measurements shown in Figure 5.12

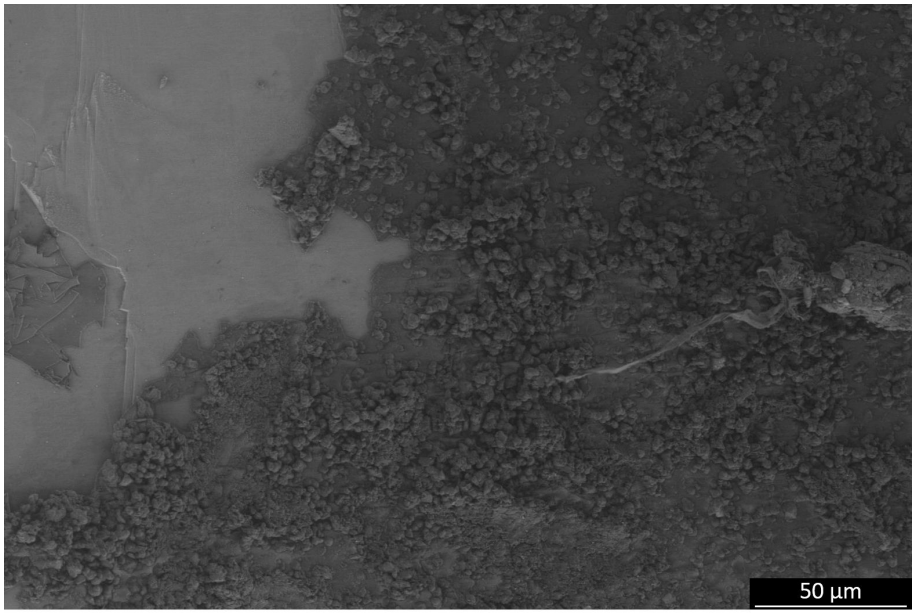



Figure B.23: Low-vacuum SEM: Micrograph 6 of the aged calcite surface after SICM measurements shown in Figure 5.12

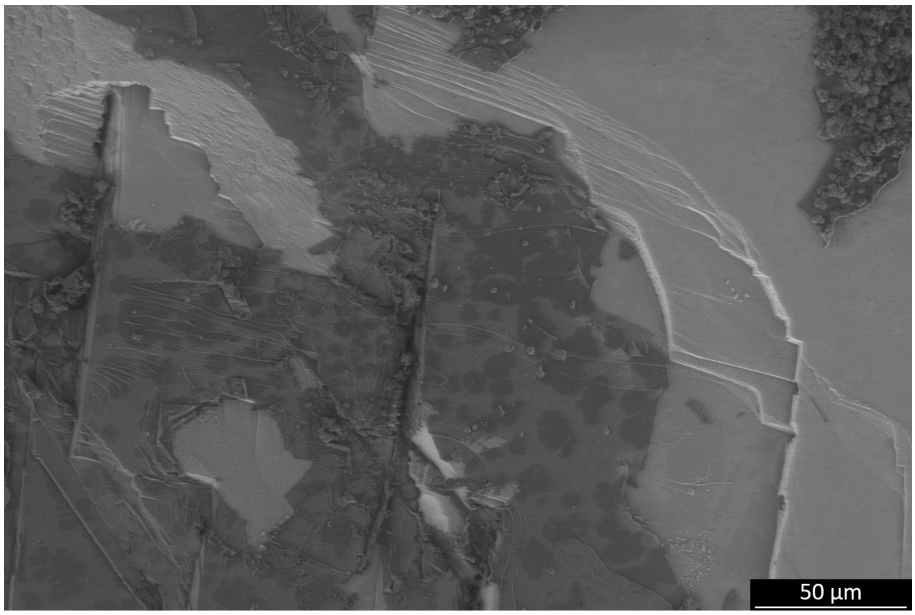



Figure B.24: Low-vacuum SEM: Micrograph 7 of the aged calcite surface after SICM measurements shown in Figure 5.12

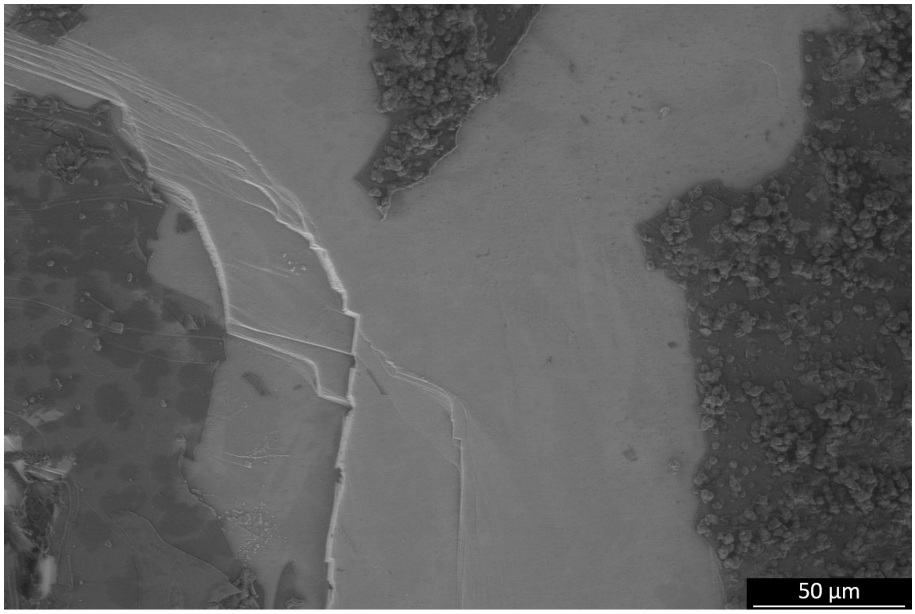



Figure B.25: Low-vacuum SEM: Micrograph 8 of the aged calcite surface after SICM measurements shown in Figure 5.12

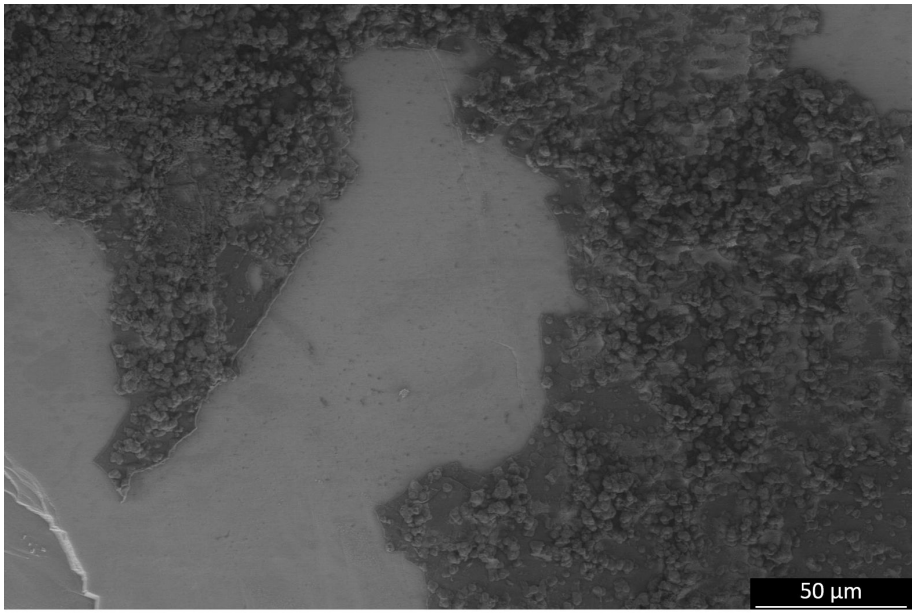



Figure B.26: Low-vacuum SEM: Micrograph 9 of the aged calcite surface after SICM measurements shown in Figure 5.12

In Chapter 5: *Carbonate Ageing Studies*, Section 5.3.1.2, an overlay of five low-vacuum SEM micrographs of an aged calcite surface which had been stored in air for 2 months prior to imaging were presented in Figure 5.16; these individual micrographs are shown in Figures B.27 - B.31 below.

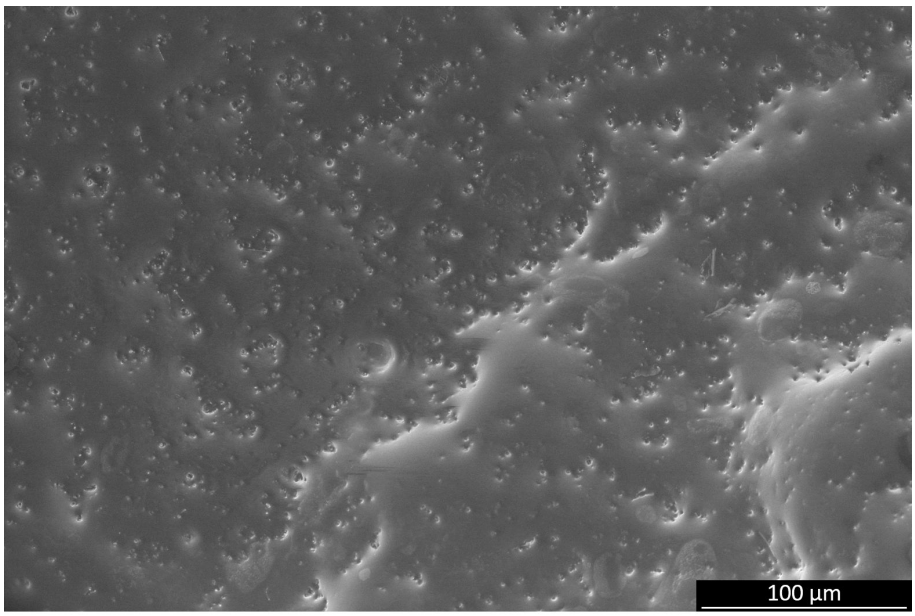



Figure B.27: Low-vacuum SEM: Micrograph 1 of the old aged calcite surface
An image from the overlay of five low-vacuum SEM micrographs of an aged calcite surface which had been stored in air for 2 months prior to imaging which was shown in Figure 5.12.

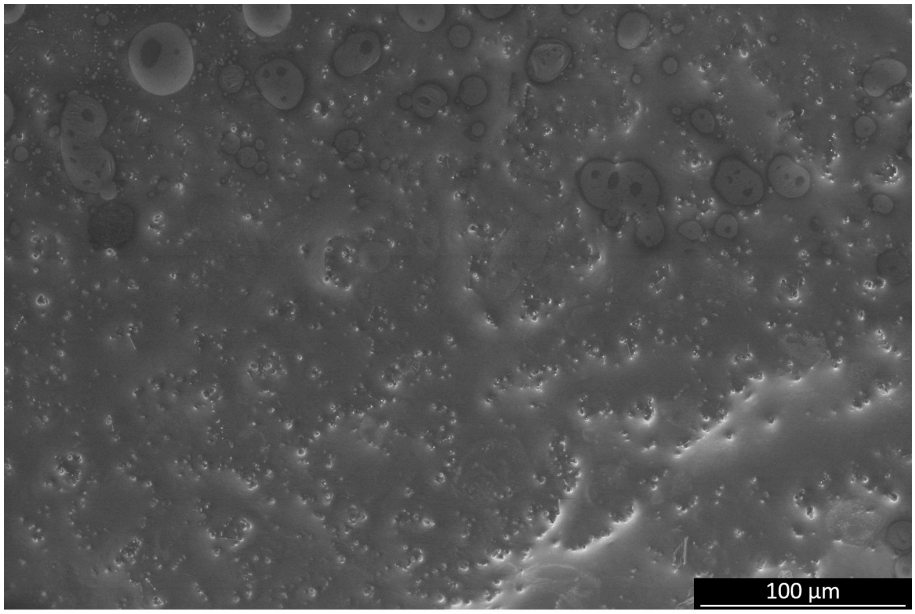



Figure B.28: Low-vacuum SEM: Micrograph 2 of the old aged calcite surface
An image from the overlay of five low-vacuum SEM micrographs of an aged calcite surface which had been stored in air for 2 months prior to imaging which was shown in Figure 5.12.

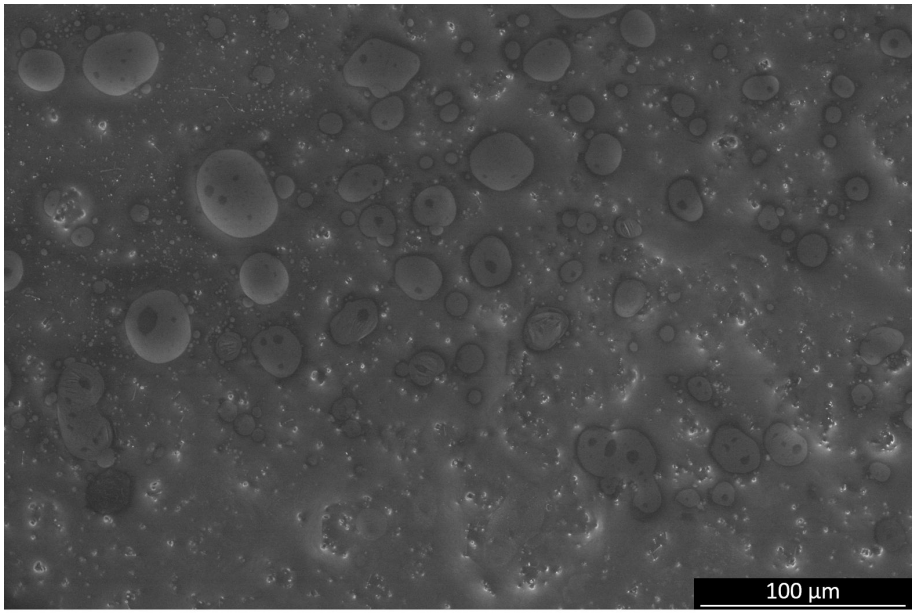



Figure B.29: Low-vacuum SEM: Micrograph 3 of the old aged calcite surface
An image from the overlay of five low-vacuum SEM micrographs of an aged calcite surface which had been stored in air for 2 months prior to imaging which was shown in Figure 5.12.

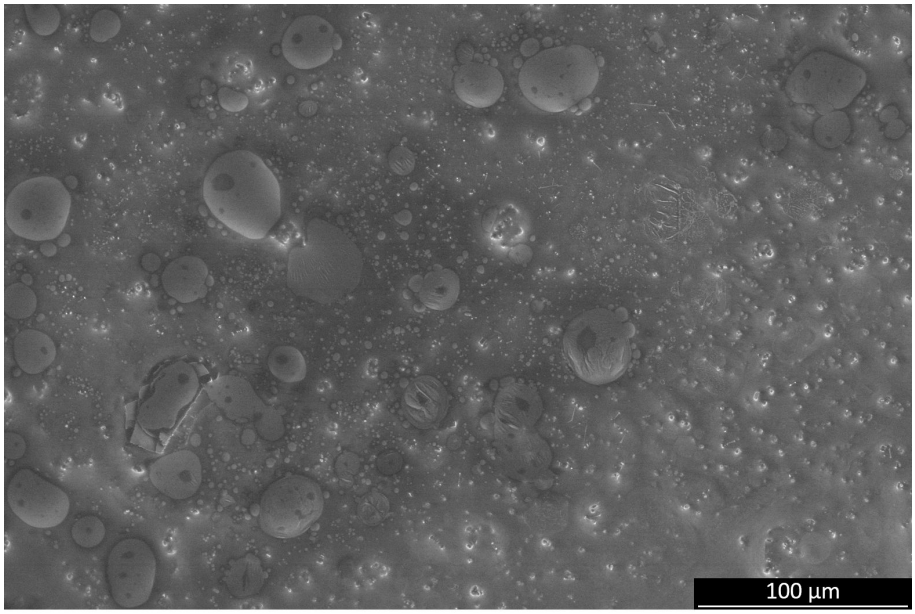



Figure B.30: Low-vacuum SEM: Micrograph 4 of the old aged calcite surface
An image from the overlay of five low-vacuum SEM micrographs of an aged calcite surface which had been stored in air for 2 months prior to imaging which was shown in Figure 5.12.

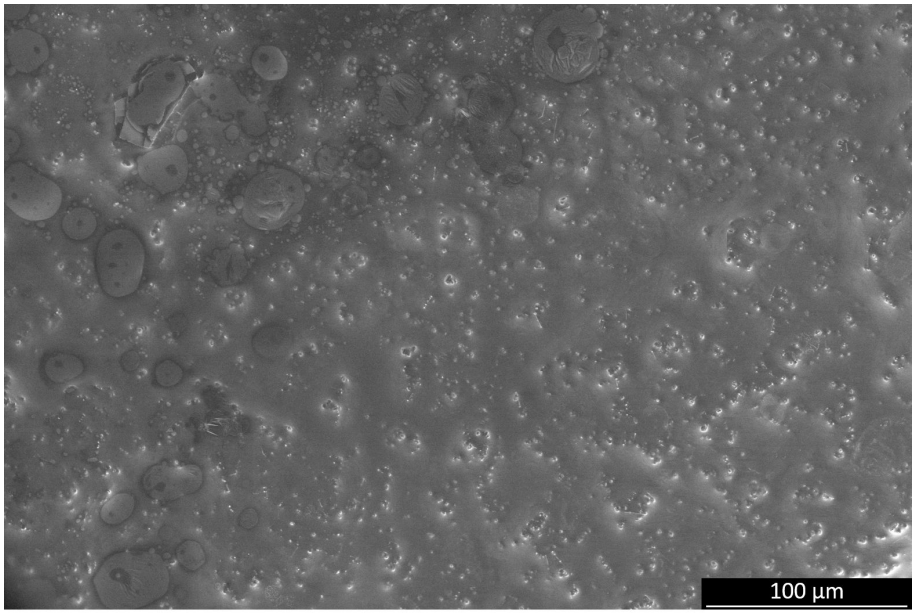


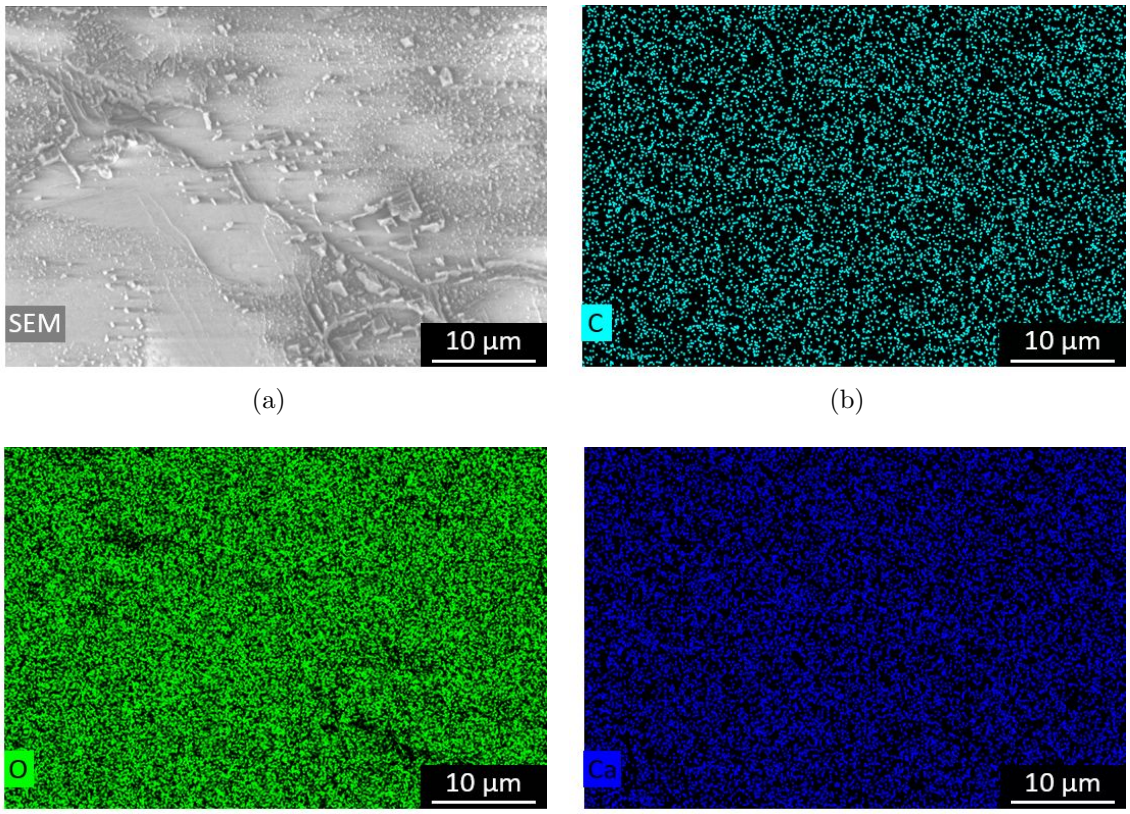

Figure B.31: Low-vacuum SEM: Micrograph 5 of the old aged calcite surface
An image from the overlay of five low-vacuum SEM micrographs of an aged calcite surface which had been stored in air for 2 months prior to imaging which was shown in Figure 5.12.

### B.1.2 Energy-Dispersive X-Ray Spectroscopy

Two areas of an unaltered calcite surface were examined with EDX. The results from calcite surface area 4a (as labelled in Figure 3.3 in Section 3.2.1) were shown in Chapter 5: *Carbonate Ageing Studies*, and results from calcite surface area 4b are shown below in Figure B.32.

Three EDX scans of the Aged Calcite 2 surface were performed on three different areas. One of these areas' results is presented in Section 5.3.1.1 in Figure 5.11. The other two areas' results are presented in B.33 & B.34 below. As was the case with the spectrum in Figure 5.11 in Section 5.3.1.1, the spectra in Figures B.33e & B.34e the position of the Ca peak at 3.69 keV is highlighted to demonstrate how the Ca signal has been masked by the crude oil film.

Three EDX scans of the Aged Calcite 1 surface post-SICM were performed on three different areas. One of these areas' results is presented in Section 5.3.1.2 in Figure 5.15. The other two areas' results are presented in B.35 & B.36 below.




(a) (b) (c) (d) (e)

Figure B.32: EDX: Calcite Surface Type 4b
EDX results for area 4b of the calcite surface defined and labelled in Figure 3.6b in Section 3.2.1. (a) Shows the low-vacuum SEM micrograph of the area, (b), (c) & (d) show the C, O and Ca distribution maps for the area respectively, and (e) shows the X-ray energy spectrum for the image, with element assignments labelled.

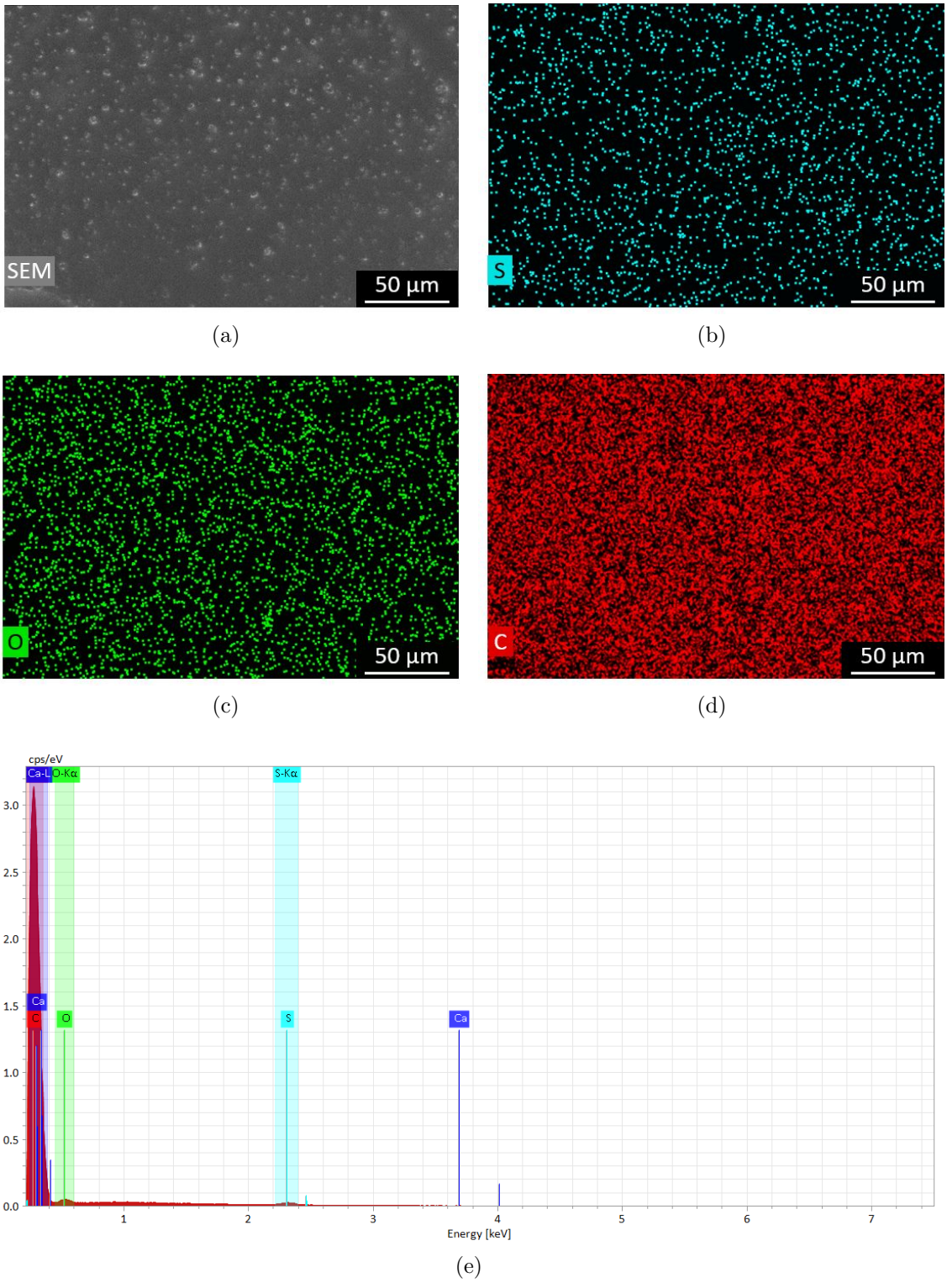



Figure B.33: Aged Calcite 2: EDX Area 2
EDX results for area 2 of the Aged Calcite 2 surface imaged by SEM shown and labelled in Figure 5.2. (a) Shows the low-vacuum SEM micrograph of the area, (b), (c) & (d) show the S, O and C distribution maps for the area respectively, and (e) shows the X-ray energy spectrum for the image, with element assignments labelled.

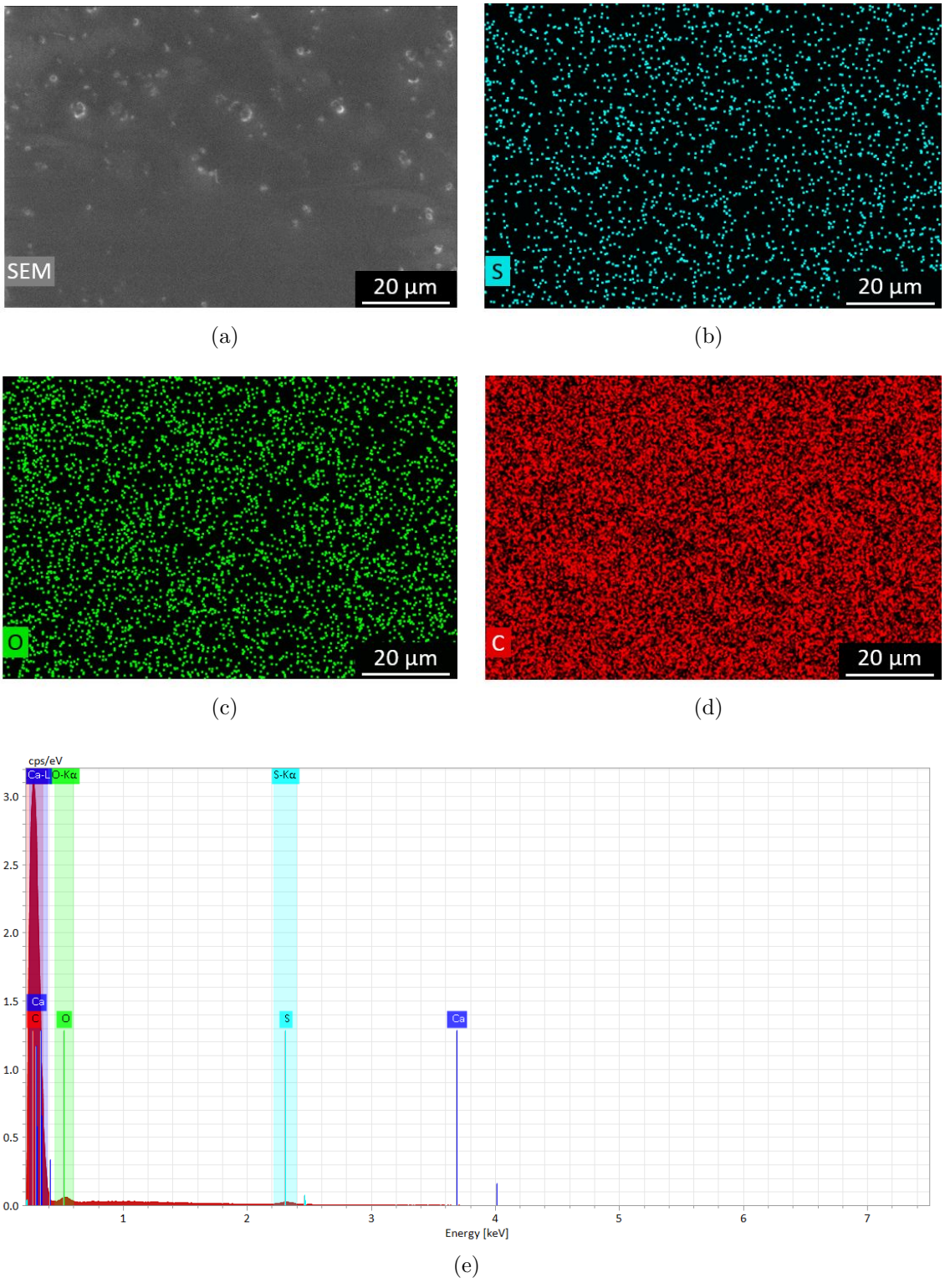
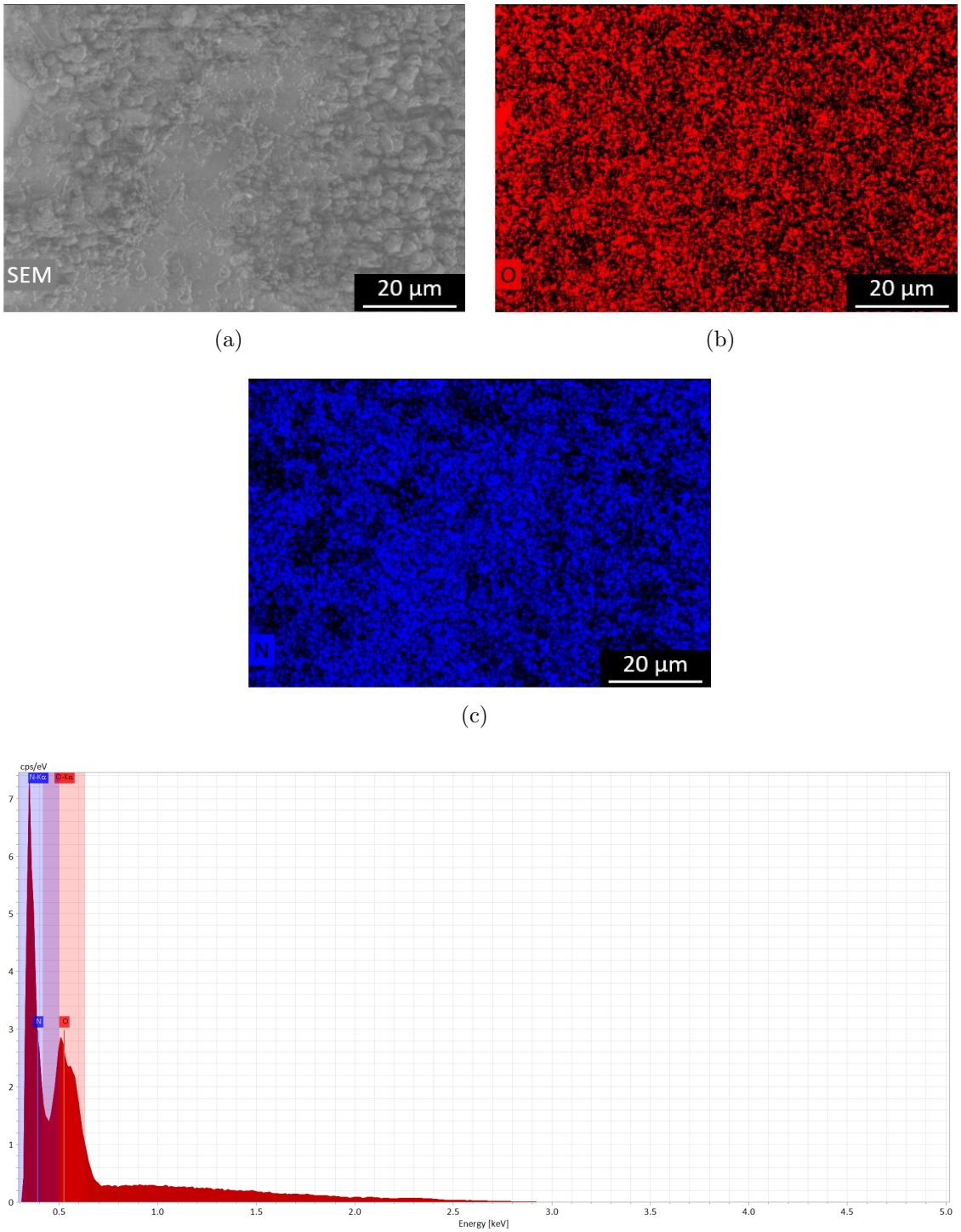
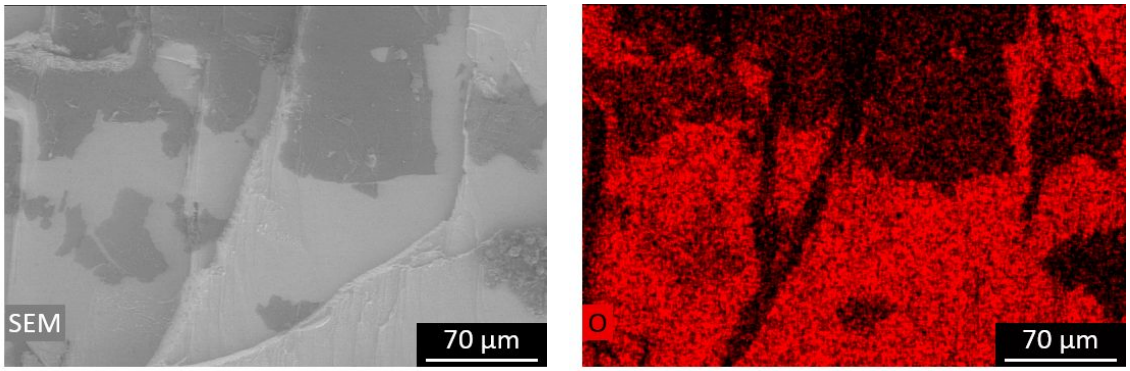



Figure B.34: Aged Calcite 2: EDX Area 3
EDX results for area 3 of the Aged Calcite 2 surface imaged by SEM shown and labelled in Figure 5.2. (a) Shows the low-vacuum SEM micrograph of the area, (b), (c) & (d) show the S, O and C distribution maps for the area respectively, and (e) shows the X-ray energy spectrum for the image, with element assignments labelled.

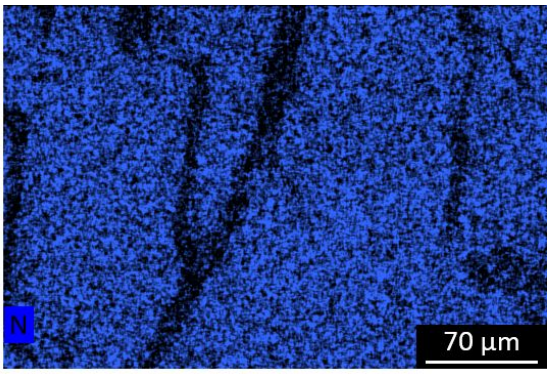



(a) (b) (c) (d)

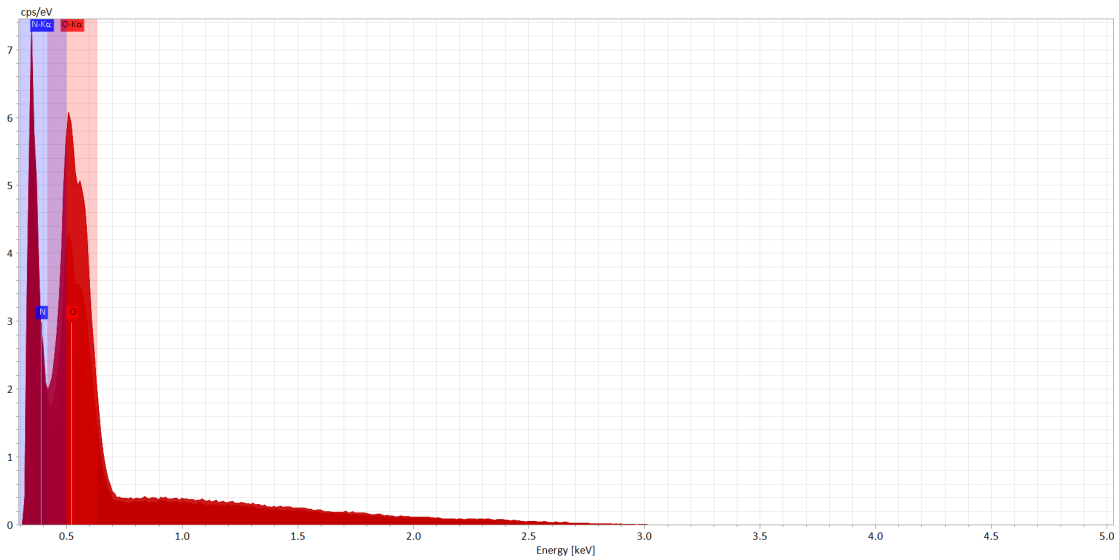
Figure B.35: Aged Calcite post-SICM: EDX Area B
EDX results for area B of the post-SICM measurement Aged Calcite 1 surface imaged by SEM shown and labelled in Section 5.3.1.2, Figure 5.12. (a) Shows the low-vacuum SEM micrograph of the area, (b) & (c) show the O & N distribution maps for the area respectively, and (d) shows the X-ray energy spectrum for the image, with element assignments labelled.




(a) (b)




(c)




(d)

Figure B.36: Aged Calcite post-SICM: EDX Area C
EDX results for area C of the post-SICM measurement Aged Calcite 1 surface imaged by SEM shown and labelled in Section 5.3.1.2, Figure 5.12. (a) Shows the low-vacuum SEM micrograph of the area, (b) & (c) show the O & N distribution maps for the area respectively, and (d) shows the X-ray energy spectrum for the image, with element assignments labelled.

## B.2 Ketton

In Chapter 3: *Carbonates*, Section 3.2.2, two SEM micrograph overlays were presented in Figures 3.7 and 3.8. The micrographs which made up those Figures are presented here, in Figures B.37 - B.42 and Figures B.43 - B.49 respectively.

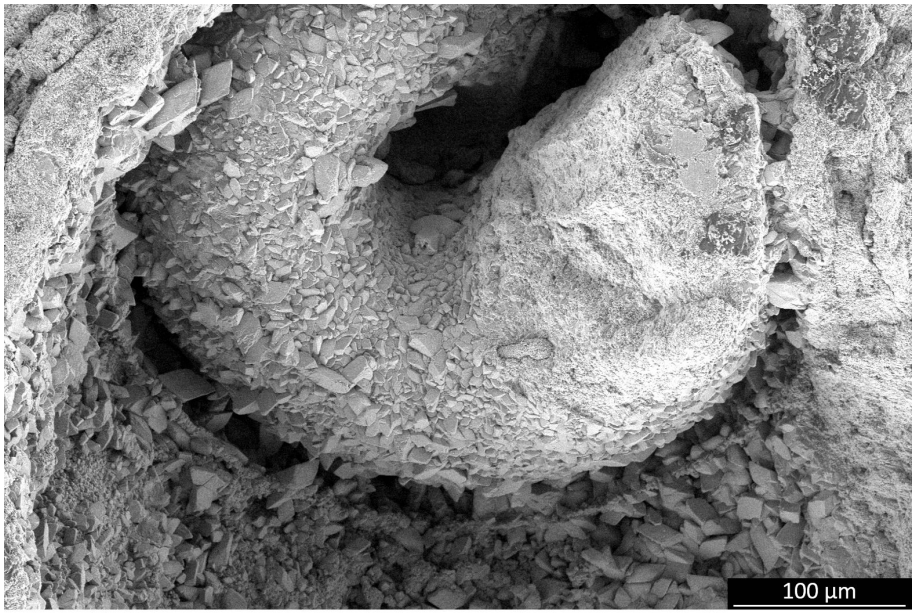



Figure B.37: Low-vacuum SEM: Micrograph 1 of Ketton from Figure 3.7

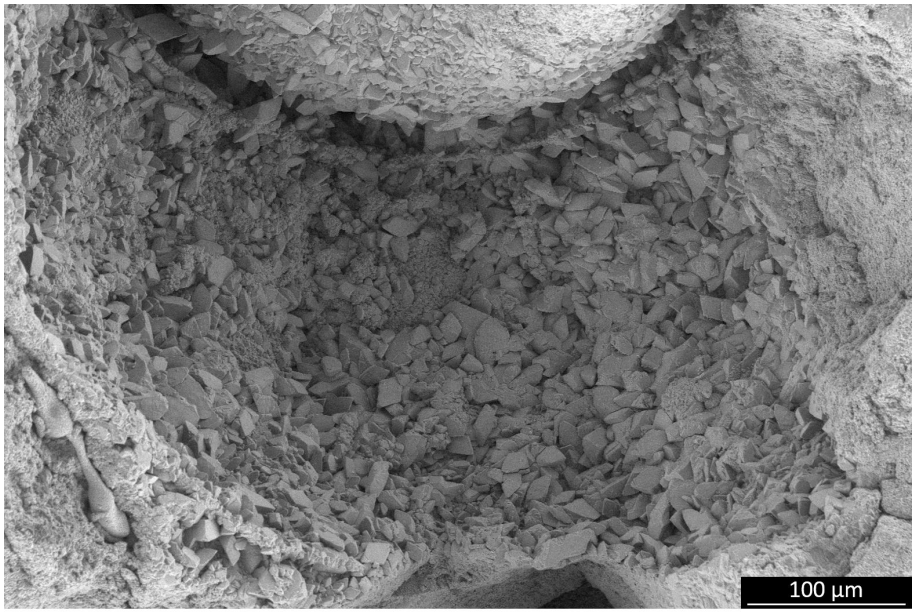



Figure B.38: Low-vacuum SEM: Micrograph 2 of Ketton from Figure 3.7

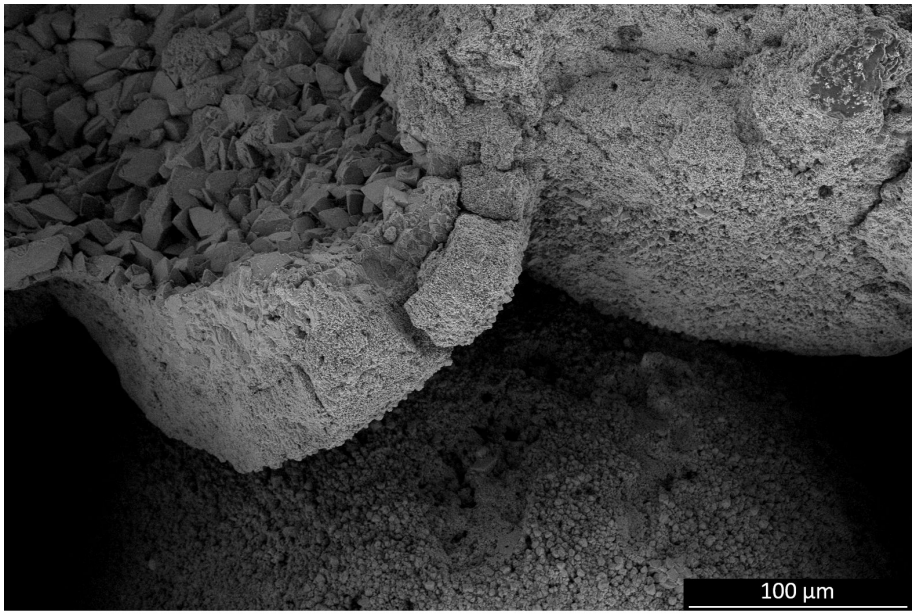



Figure B.39: Low-vacuum SEM: Micrograph 3 of Ketton from Figure 3.7

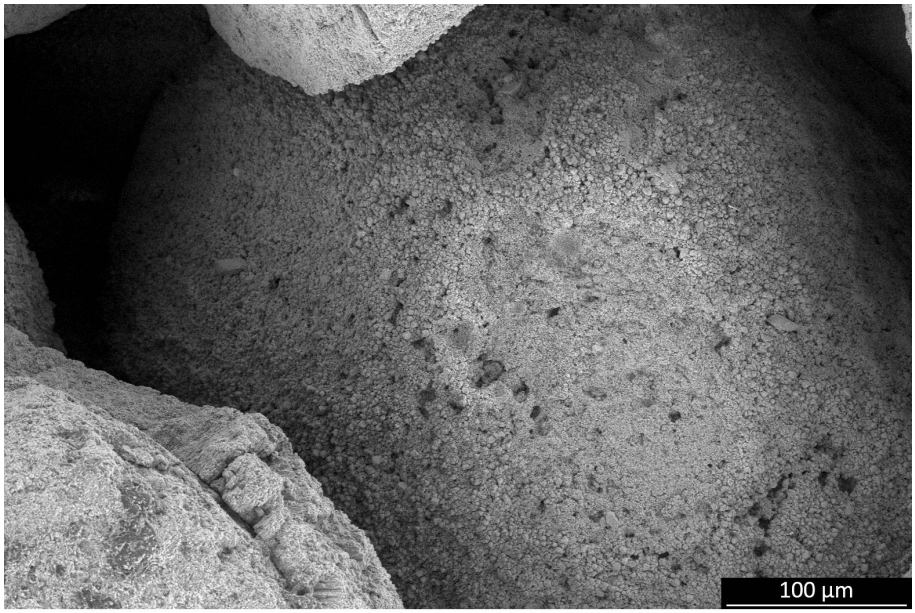



Figure B.40: Low-vacuum SEM: Micrograph 4 of Ketton from Figure 3.7

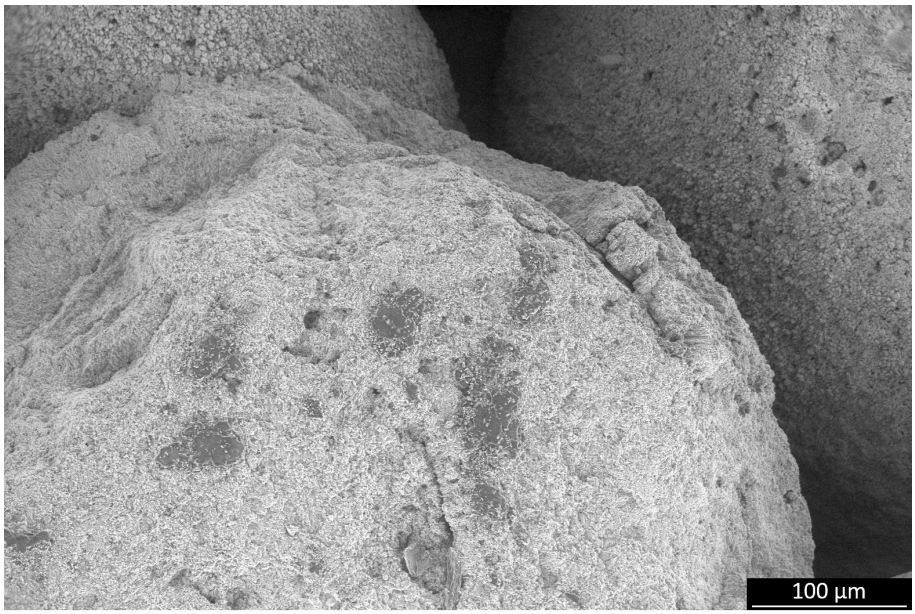



Figure B.41: Low-vacuum SEM: Micrograph 5 of Ketton from Figure 3.7

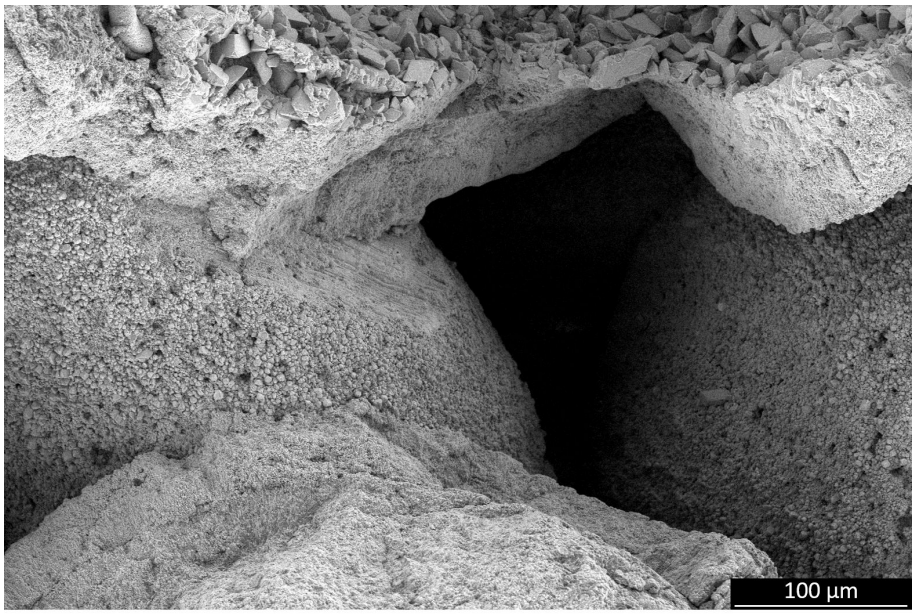



Figure B.42: Low-vacuum SEM: Micrograph 6 of Ketton from Figure 3.7

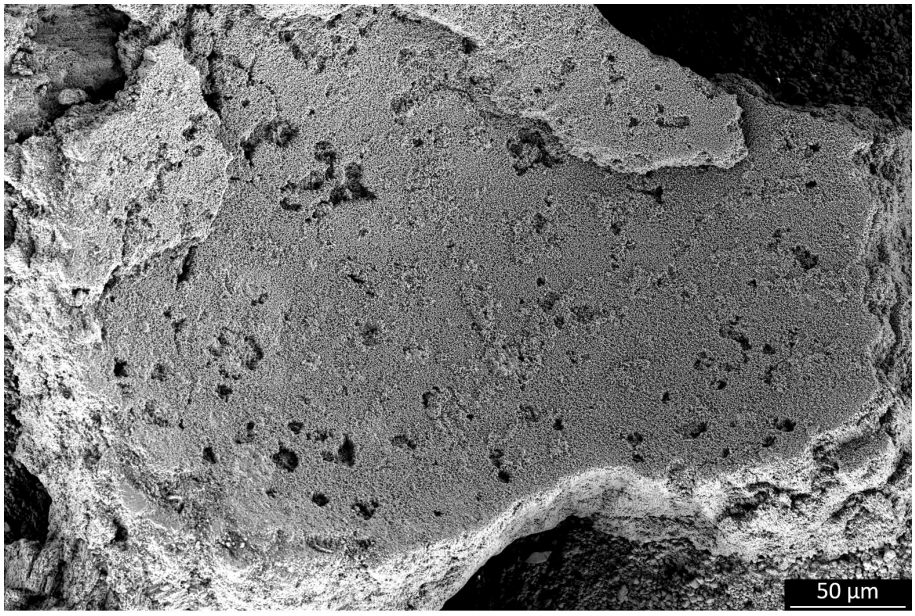



Figure B.43: Low-vacuum SEM: Micrograph 1 of Ketton from Figure 3.8

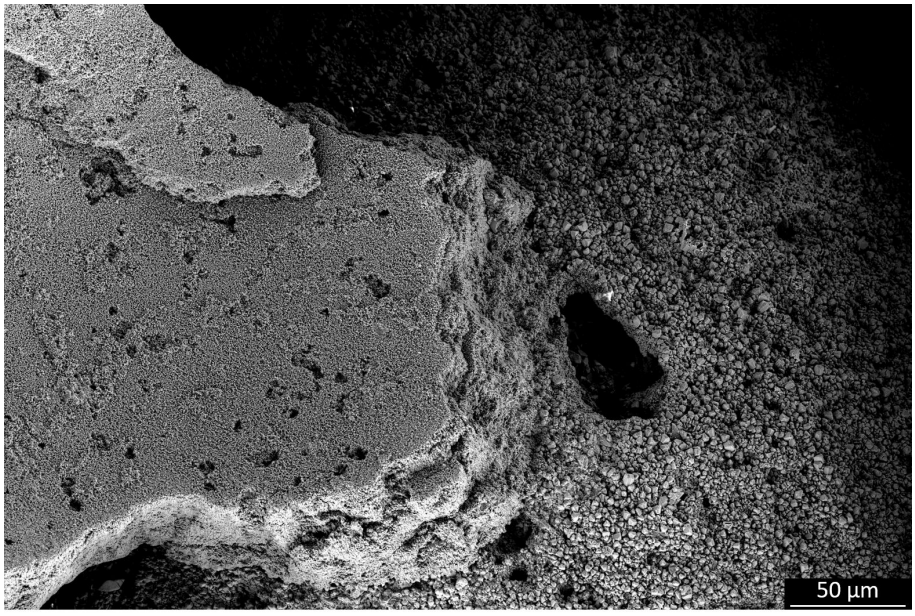



Figure B.44: Low-vacuum SEM: Micrograph 2 of Ketton from Figure 3.8




Figure B.45: Low-vacuum SEM: Micrograph 3 of Ketton from Figure 3.8




Figure B.46: Low-vacuum SEM: Micrograph 4 of Ketton from Figure 3.8

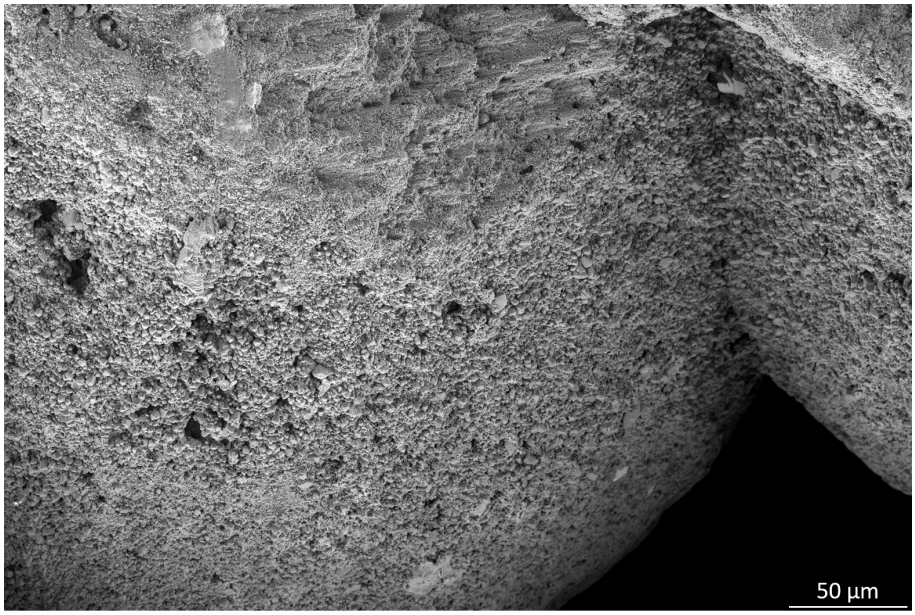



Figure B.47: Low-vacuum SEM: Micrograph 5 of Ketton from Figure 3.8

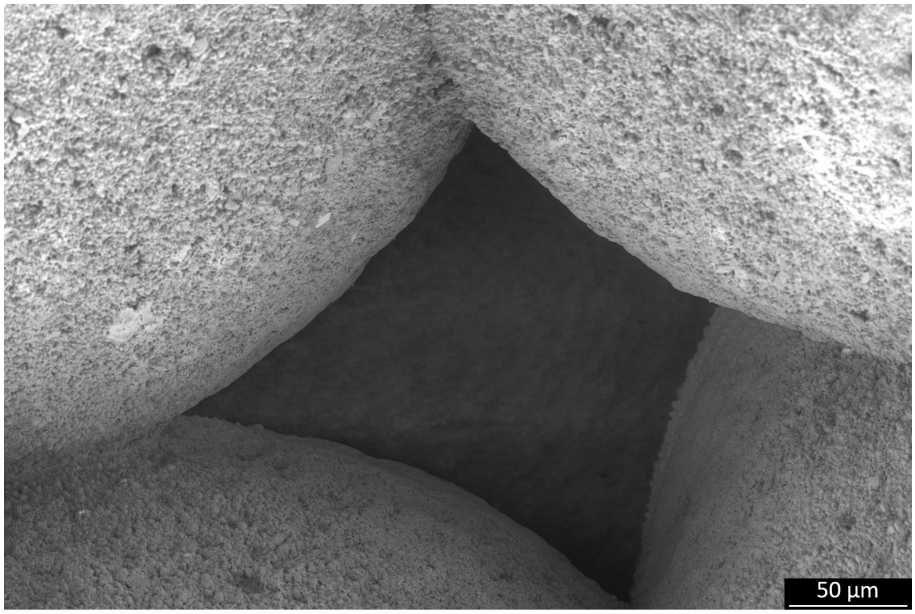



Figure B.48: Low-vacuum SEM: Micrograph 6 of Ketton from Figure 3.8




Figure B.49: Low-vacuum SEM: Micrograph 7 of Ketton from Figure 3.8

## B.3 Estaillades

### B.3.1 Low-Vacuum Scanning Electron Microscopy

In Chapter 3: *Carbonates*, Section 3.2.3, a low-vacuum SEM micrograph overlay was presented in Figure 3.16. The micrographs which made up this Figure are presented in Figures B.50 - B.55. A second overlay was also presented in Figure 3.17, the individual micrographs making up this overlay presented in Figures B.56 & B.57.

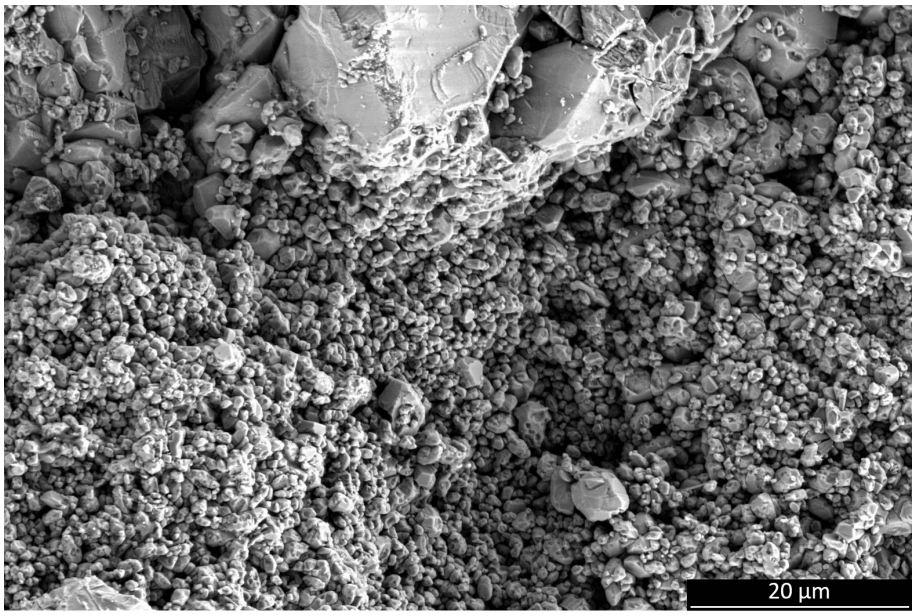



Figure B.50: Low-vacuum SEM: Micrograph 1 of Estaillades from Figure 3.16

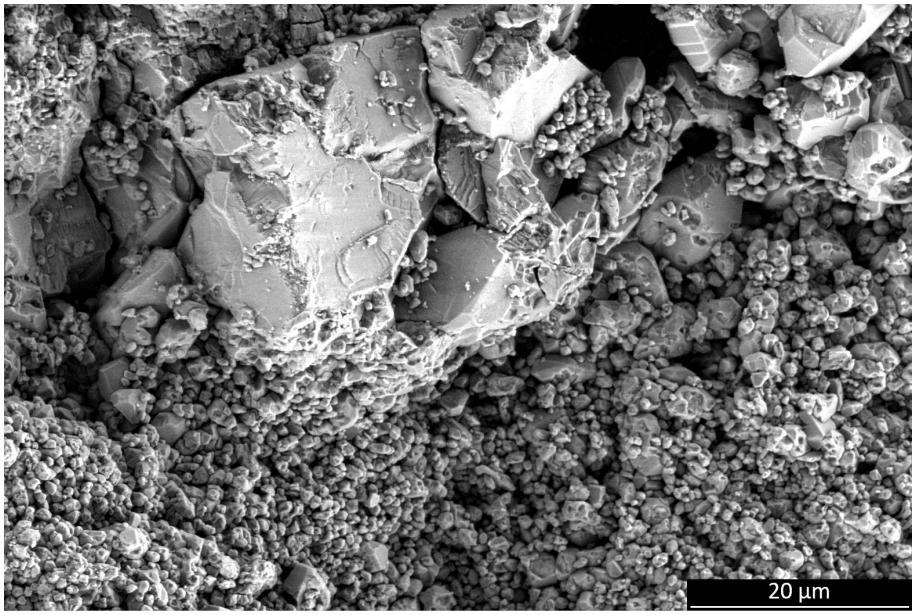



Figure B.51: Low-vacuum SEM: Micrograph 2 of Estaillades from Figure 3.16

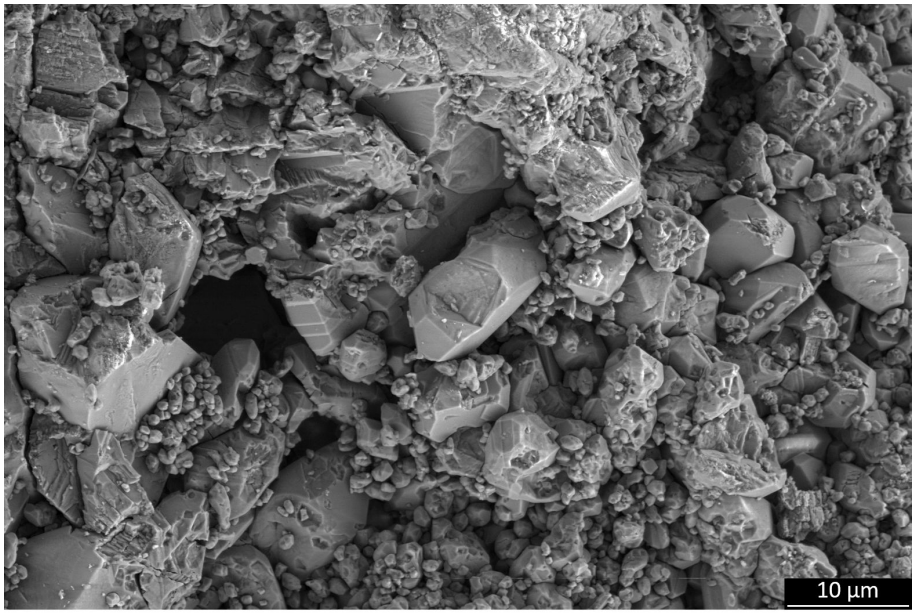



Figure B.52: Low-vacuum SEM: Micrograph 3 of Estaillades from Figure 3.16

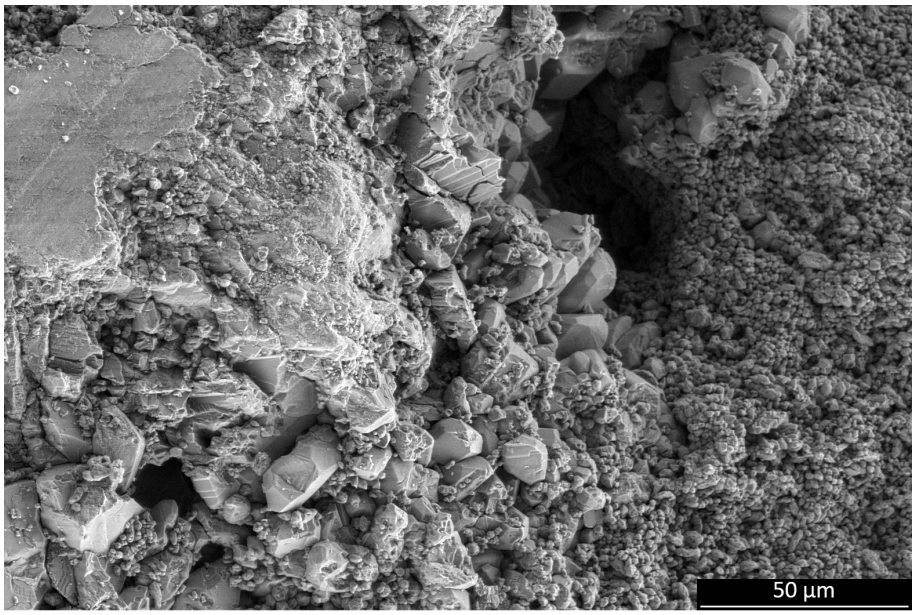



Figure B.53: Low-vacuum SEM: Micrograph 4 of Estaillades from Figure 3.16

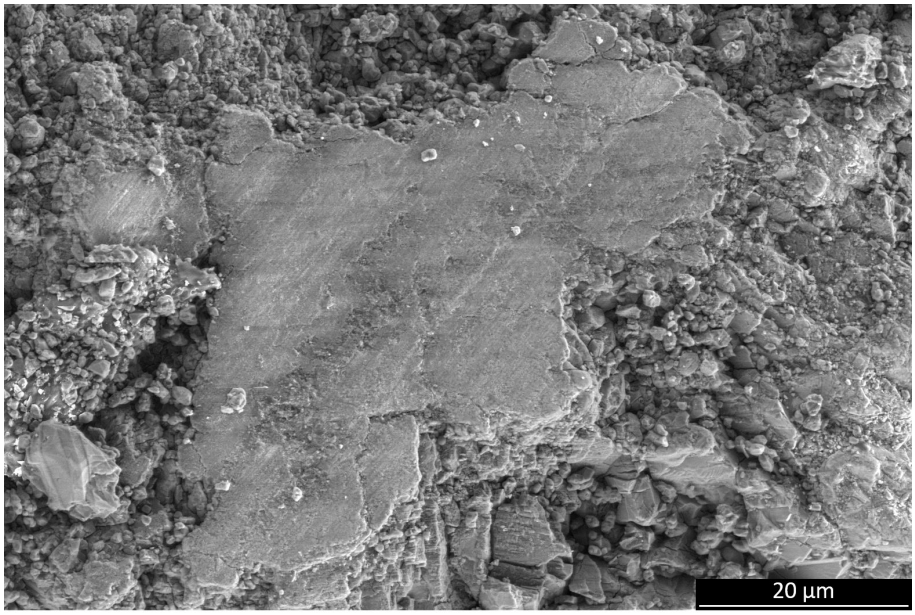



Figure B.54: Low-vacuum SEM: Micrograph 5 of Estaillades from Figure 3.16

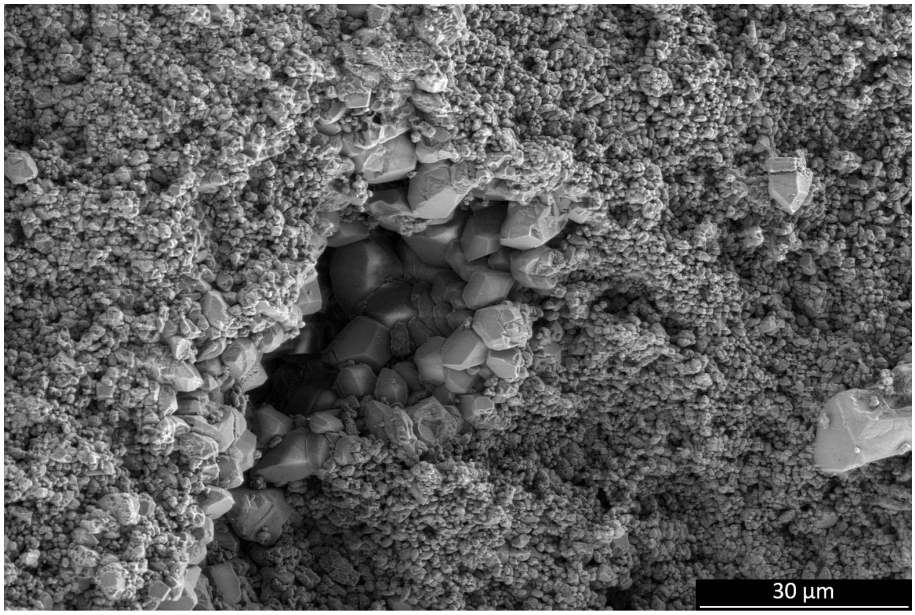



Figure B.55: Low-vacuum SEM: Micrograph 6 of Estaillades from Figure 3.16

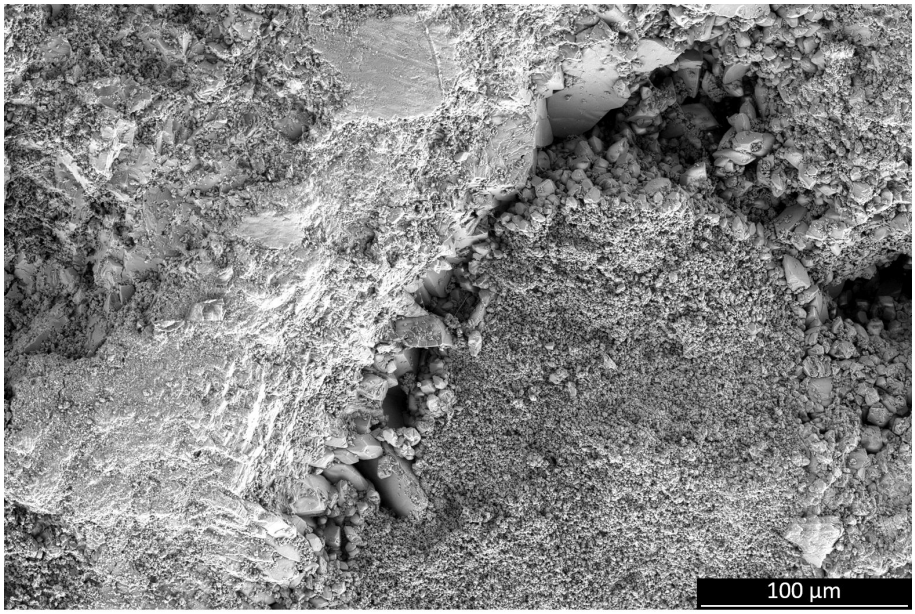



Figure B.56: Low-vacuum SEM: Micrograph 1 of Estaillades from Figure 3.17

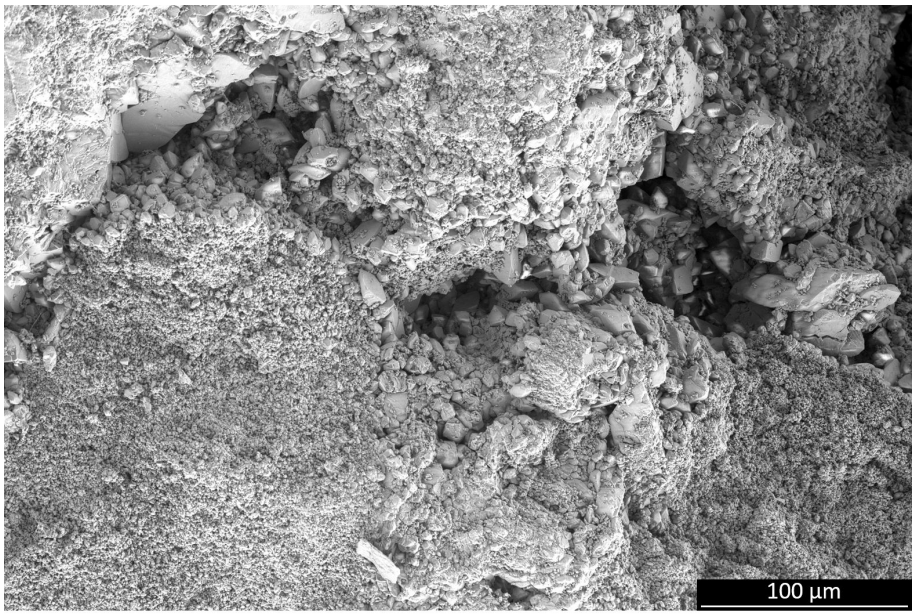



Figure B.57: Low-vacuum SEM: Micrograph 2 of Estaillades from Figure 3.17

In Chapter 5: *Carbonate Ageing Studies*, Section 5.3.2.1, a overlays of low-vacuum SEM micrographs of aged Estaillades surfaces were presented in Figures 5.21 & 5.22; the individual micrographs overlain are shown in Figures B.58 - B.63 & B.64 - B.67 respectively.

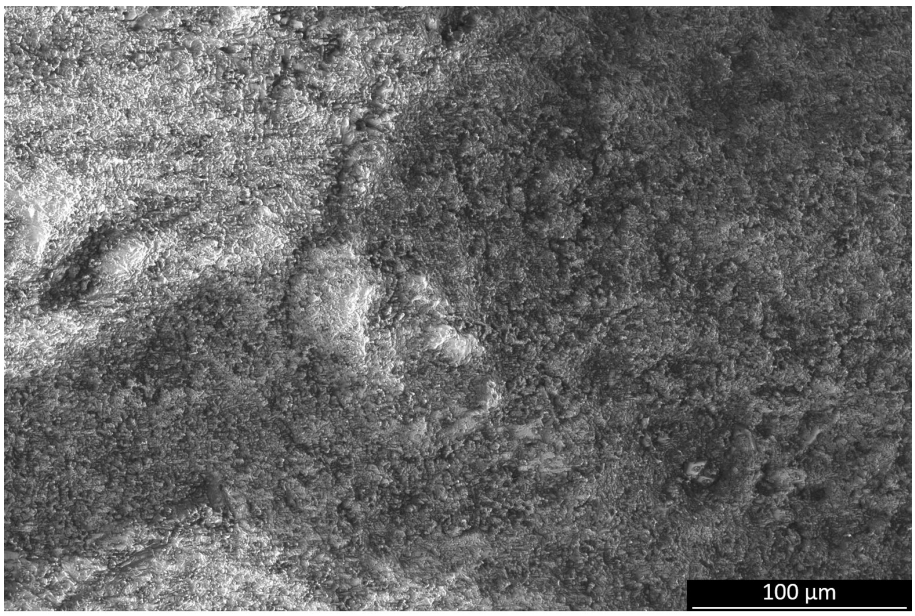



Figure B.58: Low-vacuum SEM: Micrograph 1 of the aged Estaillades surface from Figure 5.21

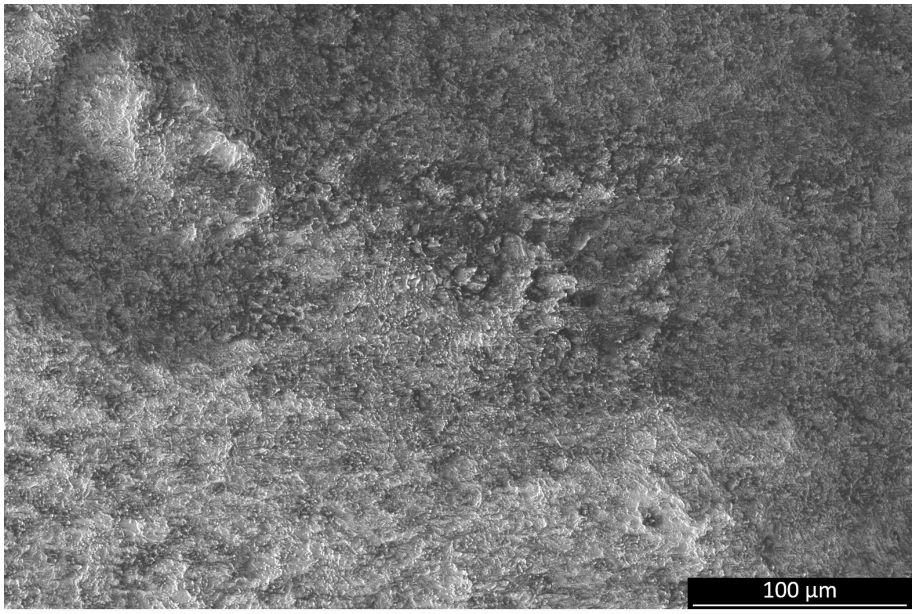



Figure B.59: Low-vacuum SEM: Micrograph 2 of the aged Estaillades surface from Figure 5.21

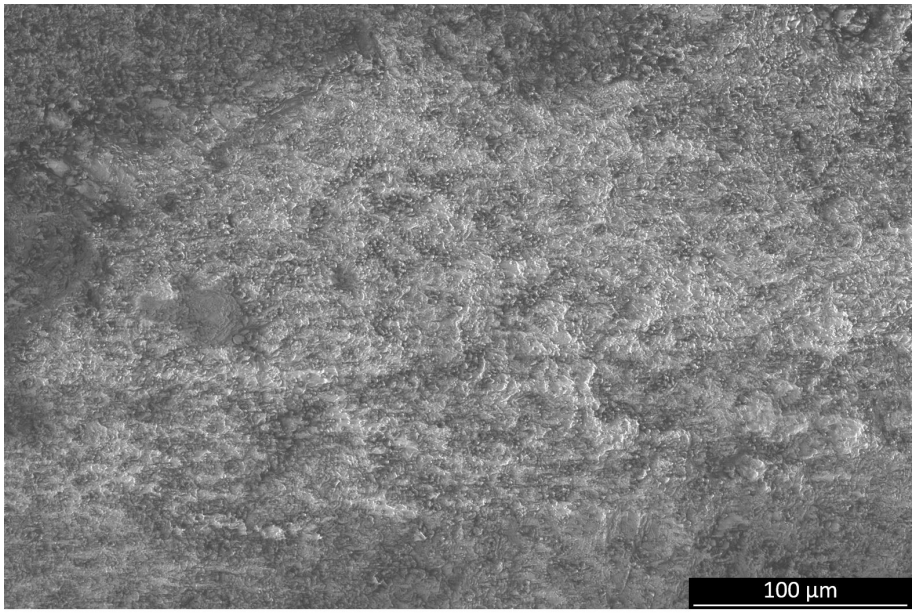



Figure B.60: Low-vacuum SEM: Micrograph 3 of the aged Estaillades surface from Figure 5.21

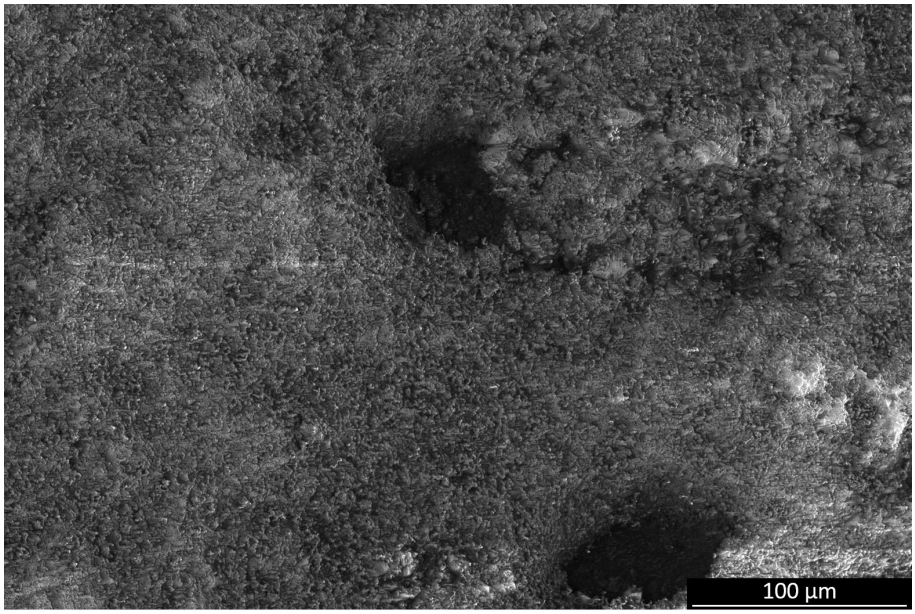



Figure B.61: Low-vacuum SEM: Micrograph 4 of the aged Estaillades surface from Figure 5.21

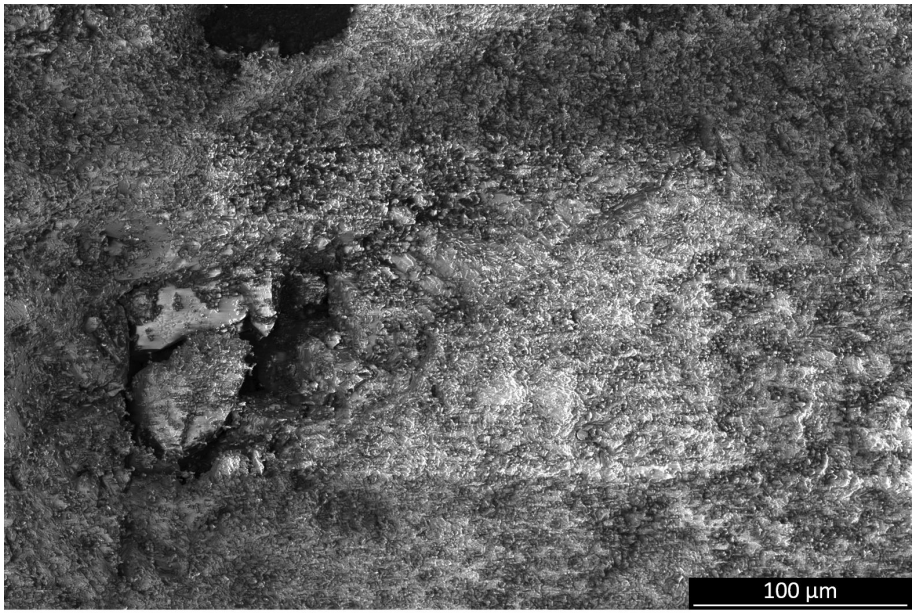



Figure B.62: Low-vacuum SEM: Micrograph 5 of the aged Estaillades surface from Figure 5.21

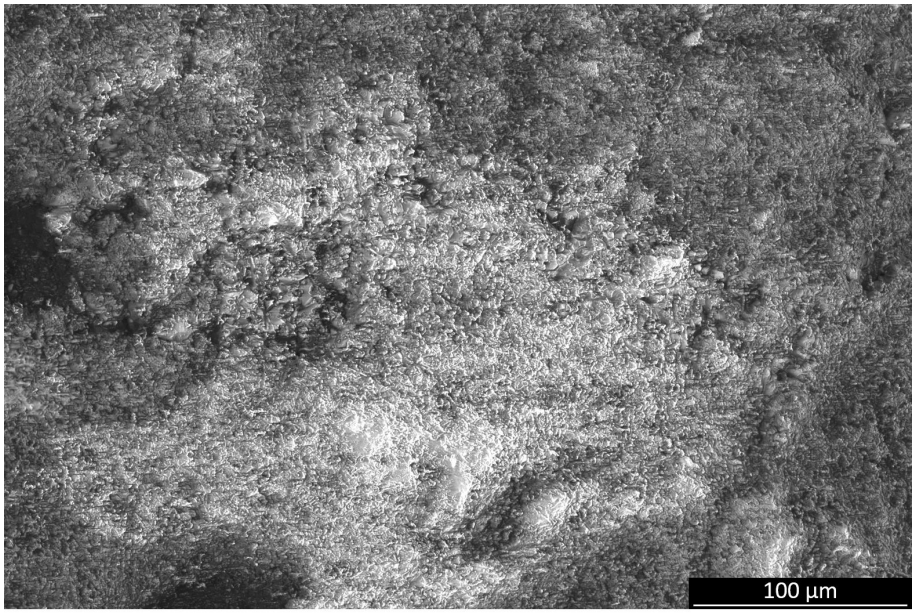



Figure B.63: Low-vacuum SEM: Micrograph 6 of the aged Estaillades surface from Figure 5.21

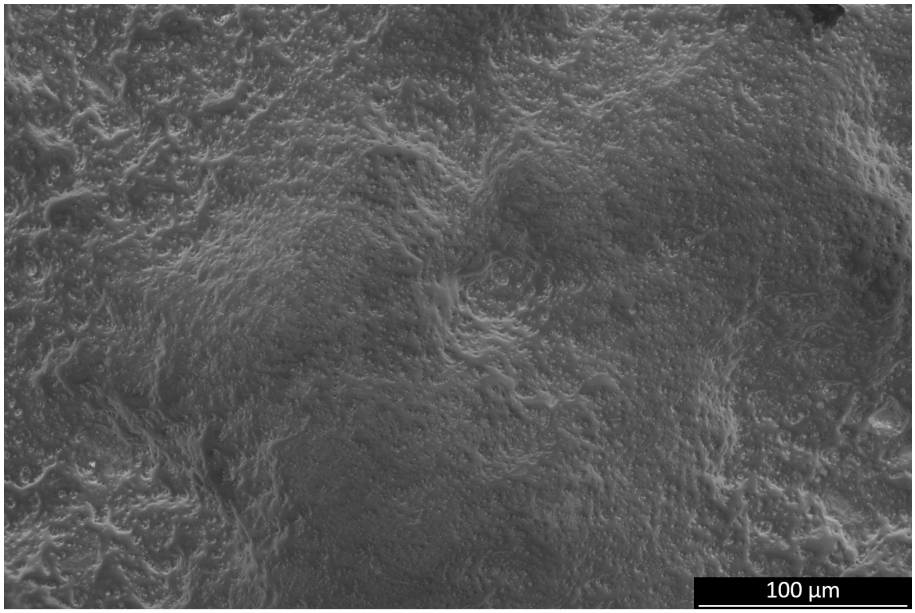



Figure B.64: Low-vacuum SEM: Micrograph 1 of the aged Estaillades surface from Figure 5.22

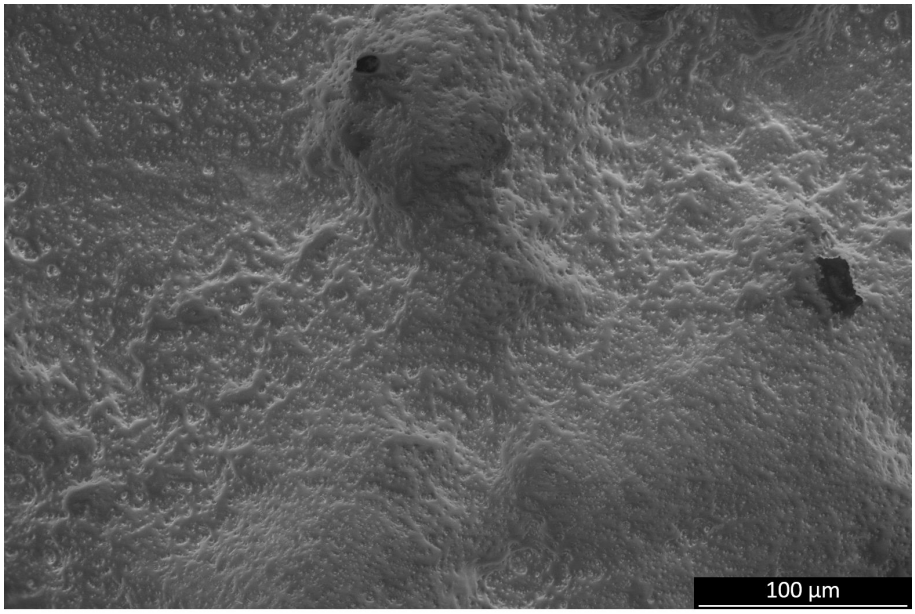



Figure B.65: Low-vacuum SEM: Micrograph 2 of the aged Estaillades surface from Figure 5.22

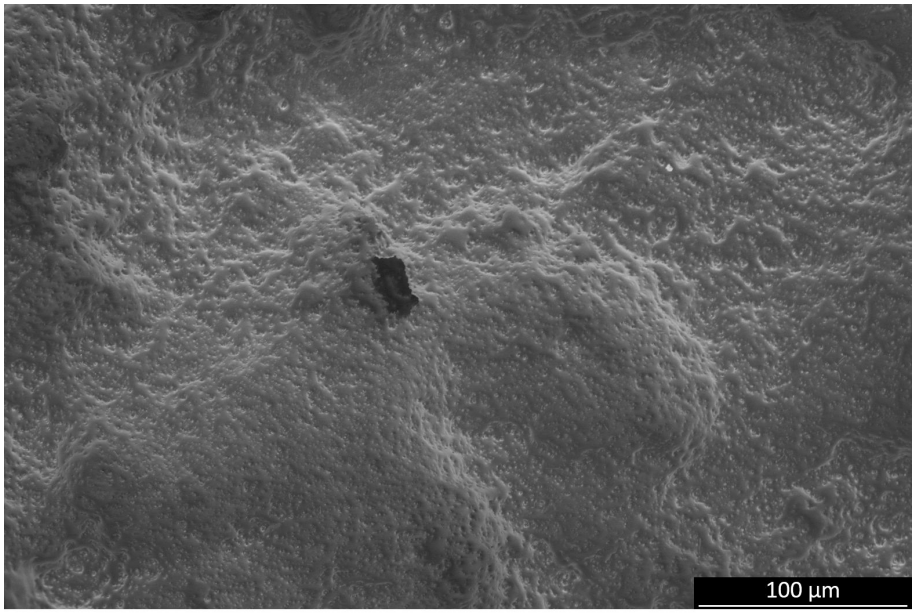



Figure B.66: Low-vacuum SEM: Micrograph 3 of the aged Estaillades surface from Figure 5.22

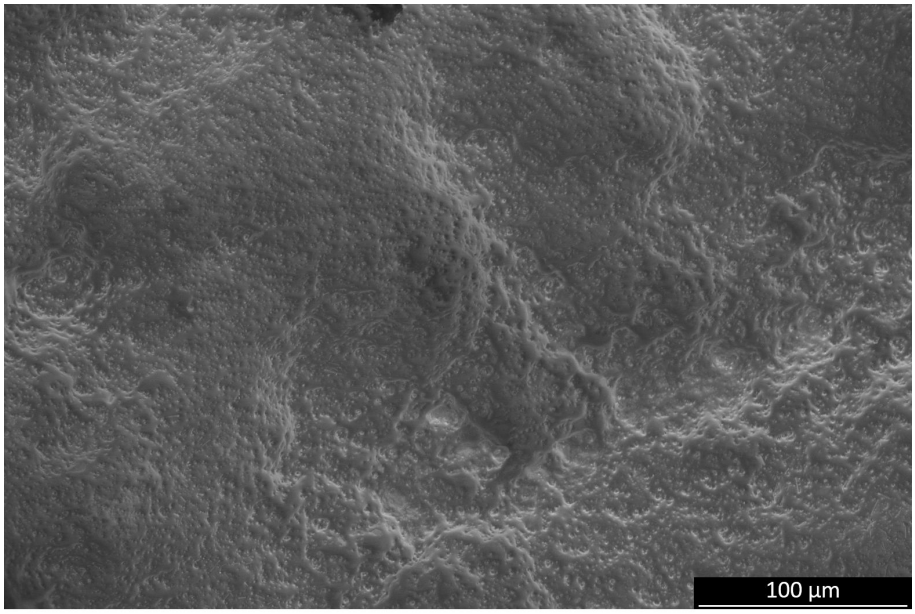



Figure B.67: Low-vacuum SEM: Micrograph 4 of the aged Estaillades surface from Figure 5.22

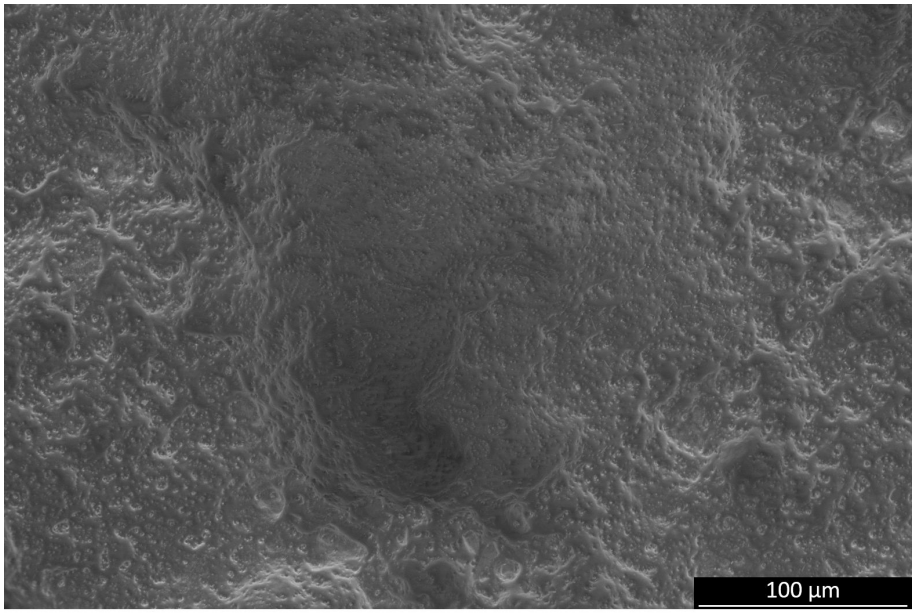



Figure B.68: Low-vacuum SEM: Micrograph 5 of the aged Estaillades surface from Figure 5.22

In Chapter 5: *Carbonate Ageing Studies*, Section 5.3.2.1, an overlay of low-vacuum SEM micrographs of an aged Estaillades surface after SICM measurements was presented in Figure 5.32; the individual micrographs overlain are shown in Figures B.69 - B.74.

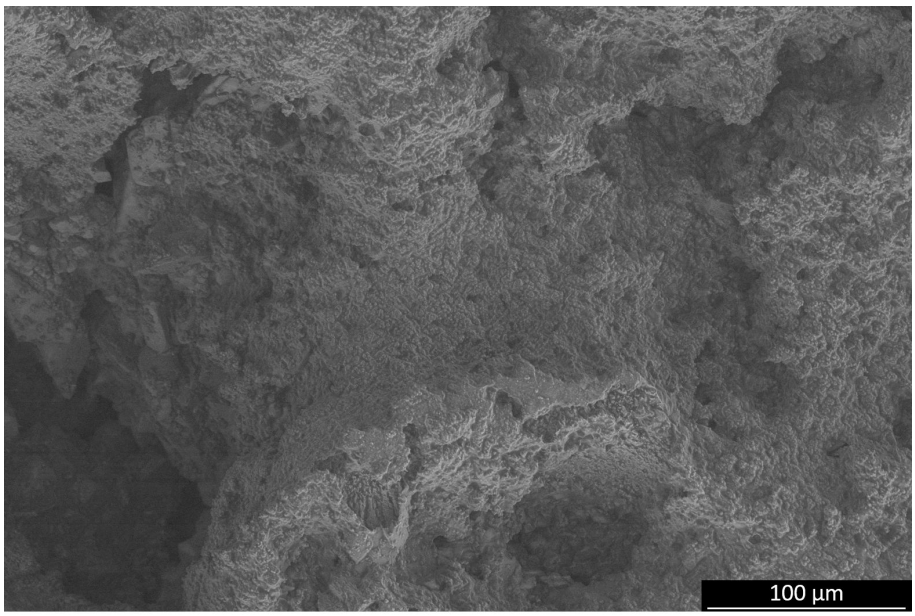



Figure B.69: Low-vacuum SEM: Micrograph 1 of the aged Estaillades surface from Figure 5.32

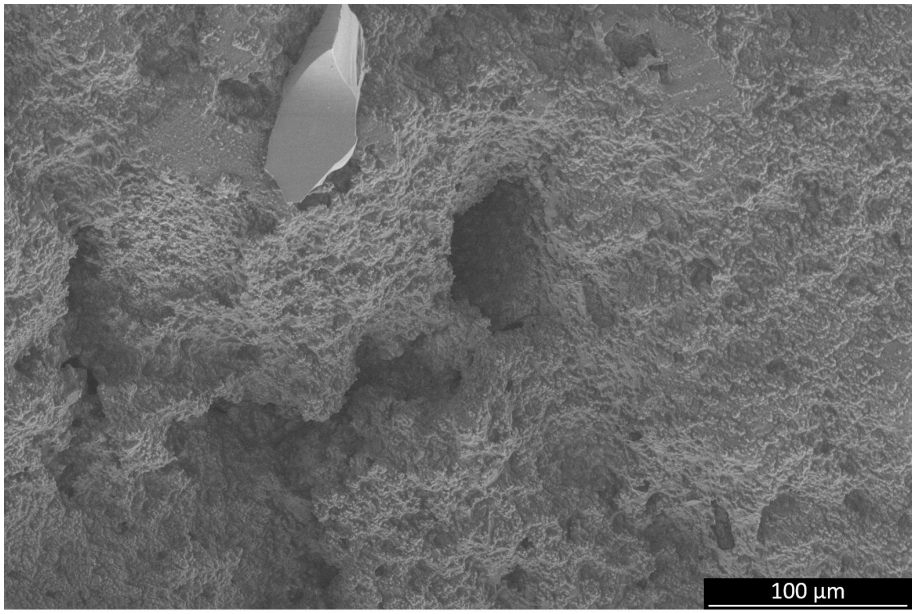



Figure B.70: Low-vacuum SEM: Micrograph 2 of the aged Estaillades surface from Figure 5.32

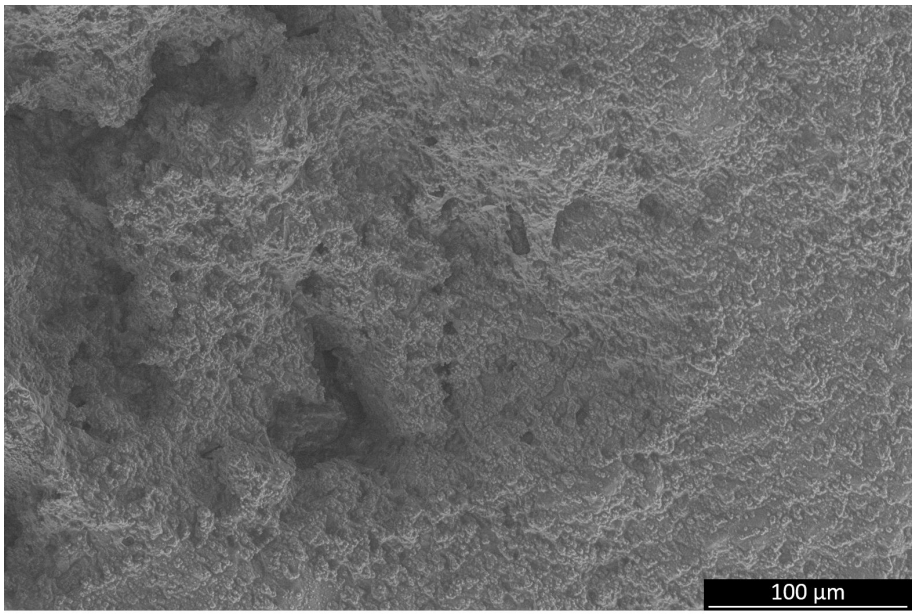



Figure B.71: Low-vacuum SEM: Micrograph 3 of the aged Estaillades surface from Figure 5.32

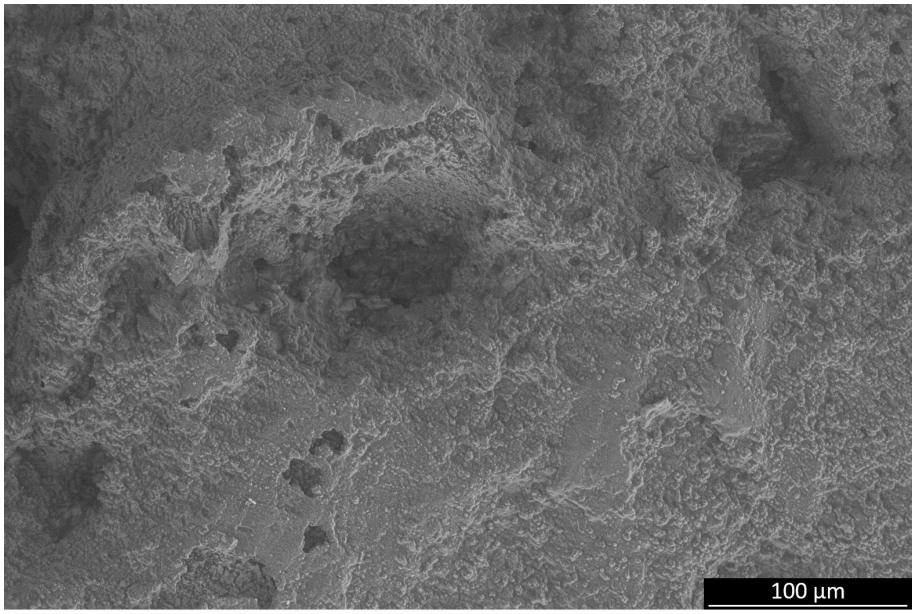



Figure B.72: Low-vacuum SEM: Micrograph 4 of the aged Estaillades surface from Figure 5.32

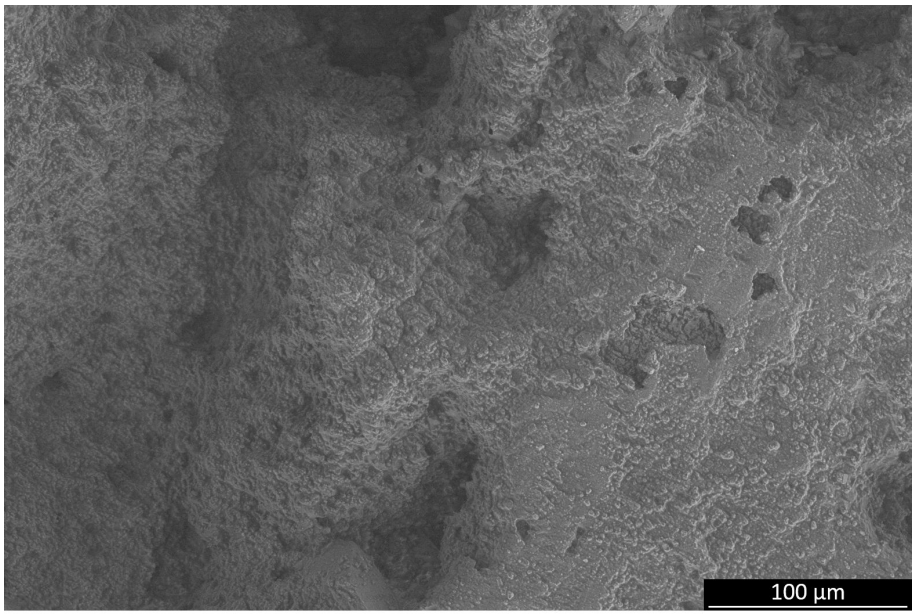



Figure B.73: Low-vacuum SEM: Micrograph 5 of the aged Estaillades surface from Figure 5.32

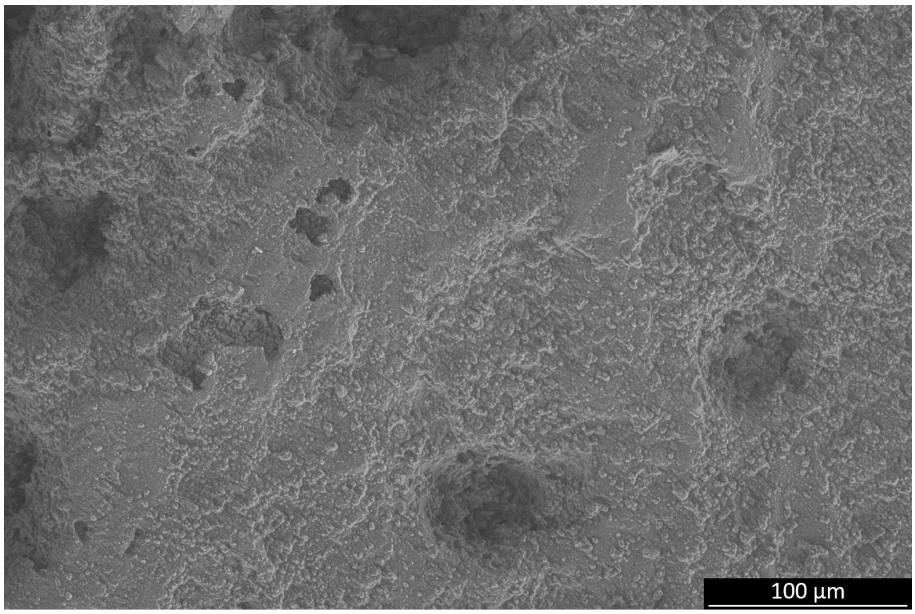



Figure B.74: Low-vacuum SEM: Micrograph 6 of the aged Estaillades surface from Figure 5.32

### B.3.2 Energy-Dispersive X-ray Spectroscopy

EDX scans of Estaillades prior to ageing were performed to provide a comparison for EDX scans post-ageing. Three areas of an unaltered Estaillades surface were examined with EDX, the first two of which were discussed in Chapter 5: *Carbonate Ageing Studies*. The third of which, the area labelled C in Figure B.75, shown at higher magnification in Figure B.76 is an example of Estaillades surface type 1, as were defined in Chapter 3: *Carbonates*, Section 3.2.3.

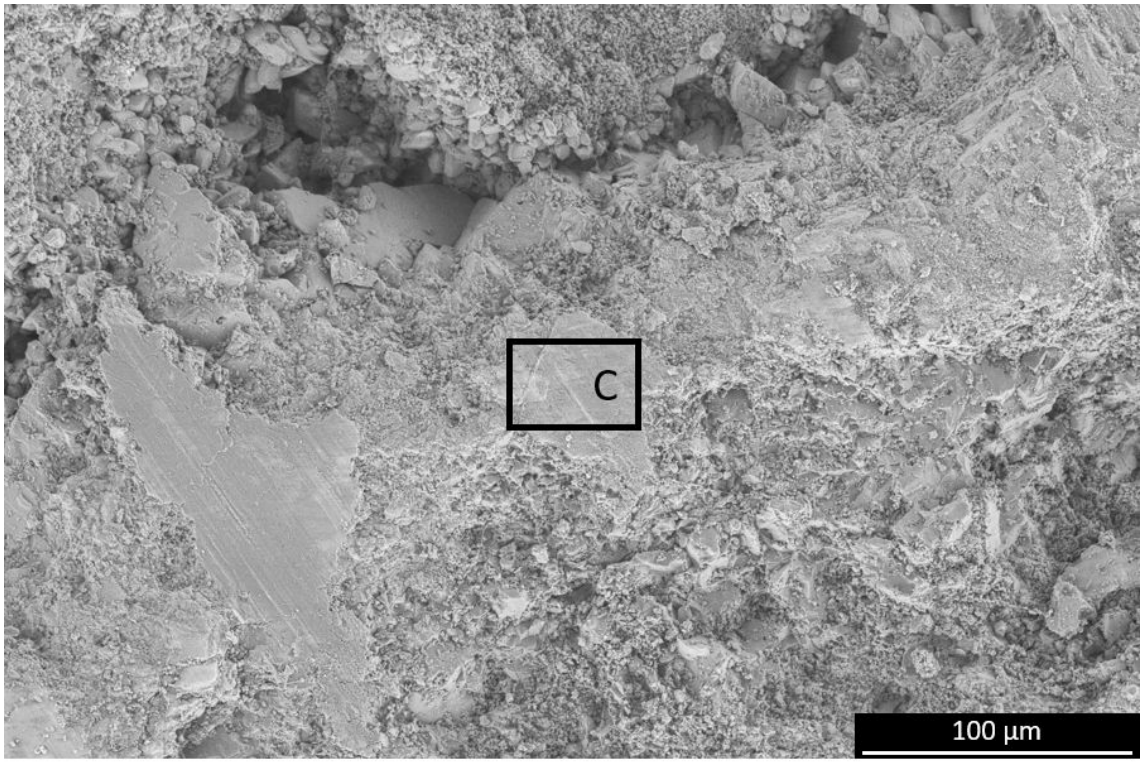
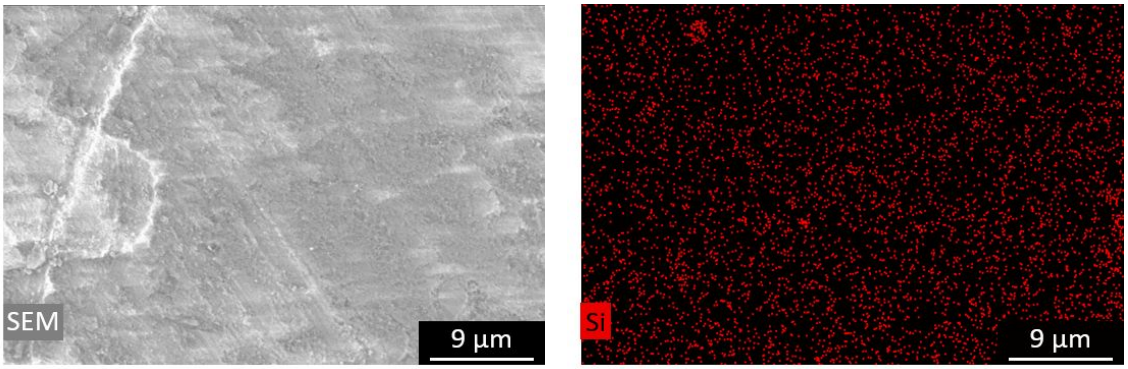


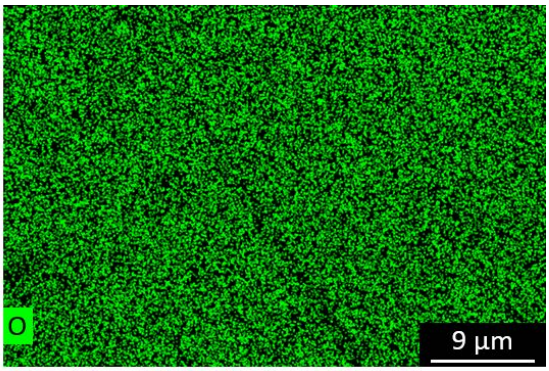

Figure B.75: Estaillades: SEM overview, EDX Area C
A low-vacuum SEM image of Estaillades, with the area (C) studied by EDX below in Figure B.76 labelled.



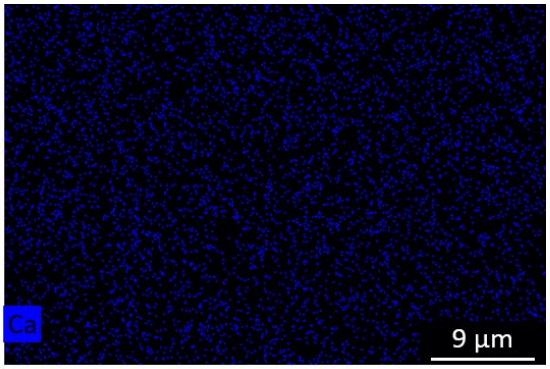

(a)



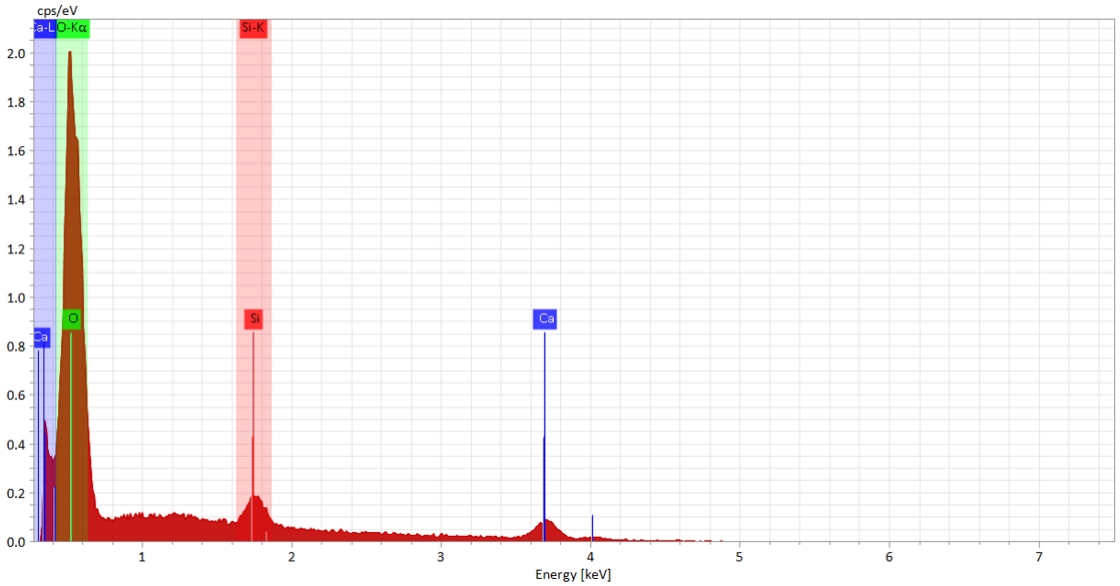

(b)




(c)




(d)




(e)

Figure B.76: Estaillades: EDX Area C
Element distribution maps as determined by EDX for area C of the Estaillades surface imaged by SEM shown and labelled in Figure B.75.

## B.4 Indiana

In Chapter 3: *Carbonates*, Section 3.2.4, an overlay of low-vacuum SEM micrographs of Indiana was presented in Figure 3.22, and a micrograph showing the same surface types was presented in Figure 3.23. The micrographs which made up these Figures without surface type numbers overlain are presented in Figures B.77 - B.83.




Figure B.77: Low-vacuum SEM: Micrograph 1 of Indiana from Figure 3.22

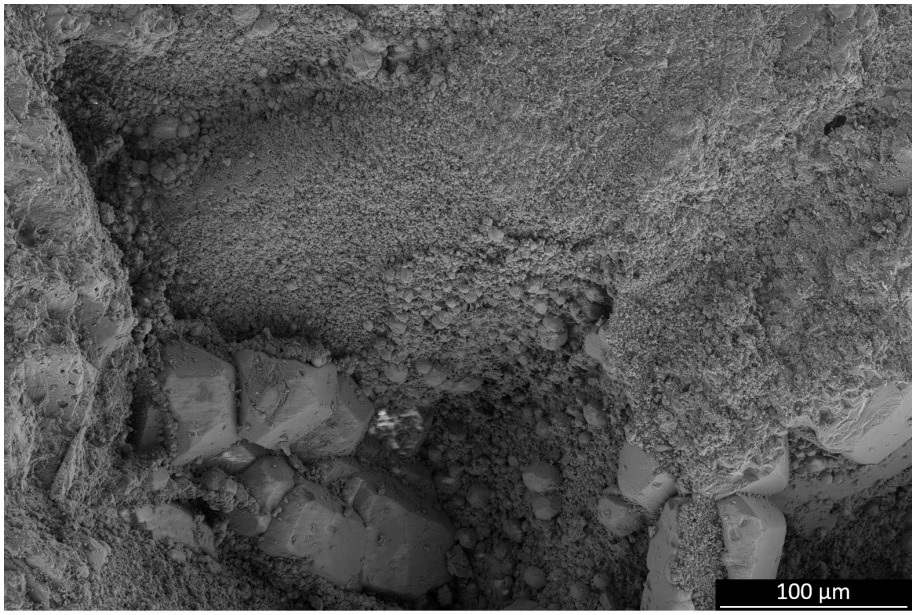



Figure B.78: Low-vacuum SEM: Micrograph 2 of Indiana from Figure 3.22

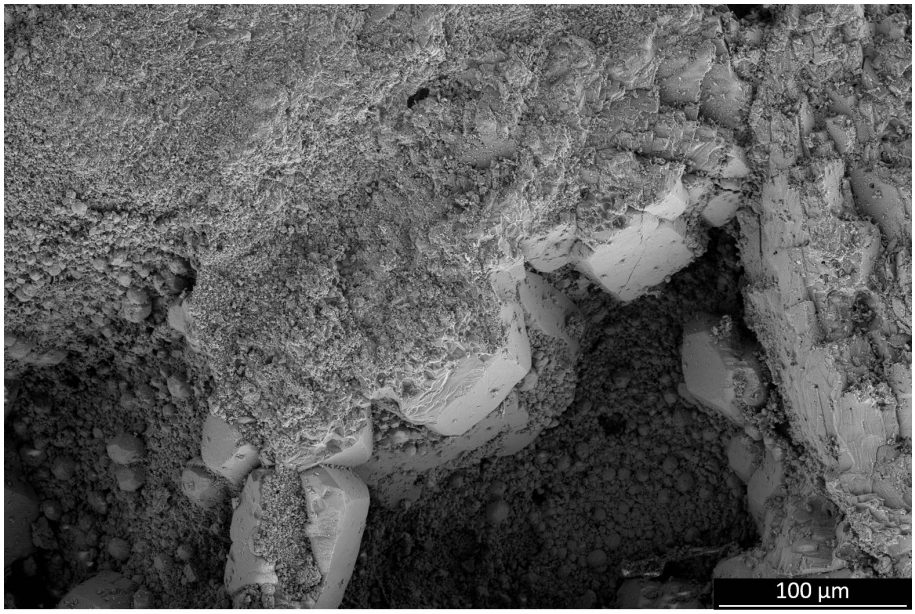



Figure B.79: Low-vacuum SEM: Micrograph 3 of Indiana from Figure 3.22

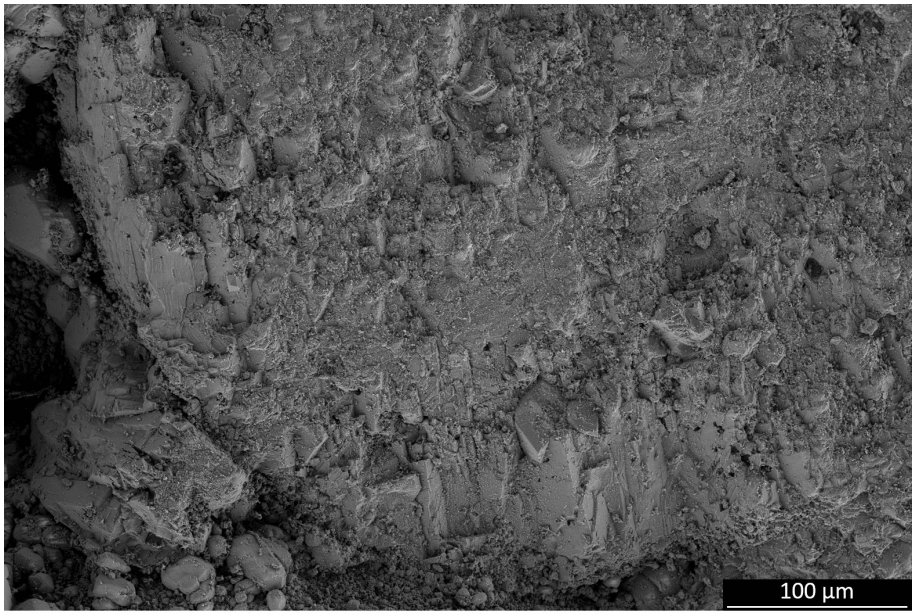



Figure B.80: Low-vacuum SEM: Micrograph 4 of Indiana from Figure 3.22




Figure B.81: Low-vacuum SEM: Micrograph 5 of Indiana from Figure 3.22

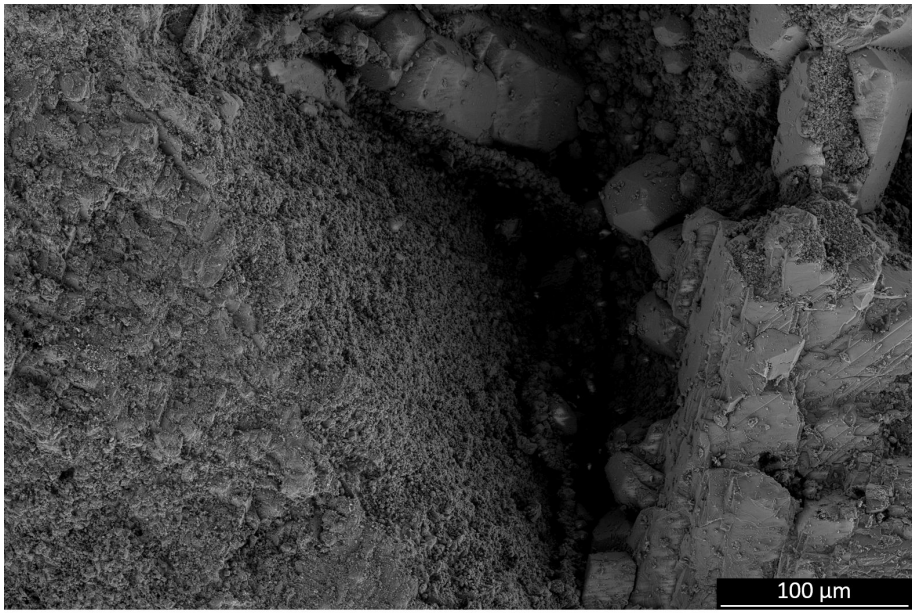



Figure B.82: Low-vacuum SEM: Micrograph 6 of Indiana from Figure 3.22

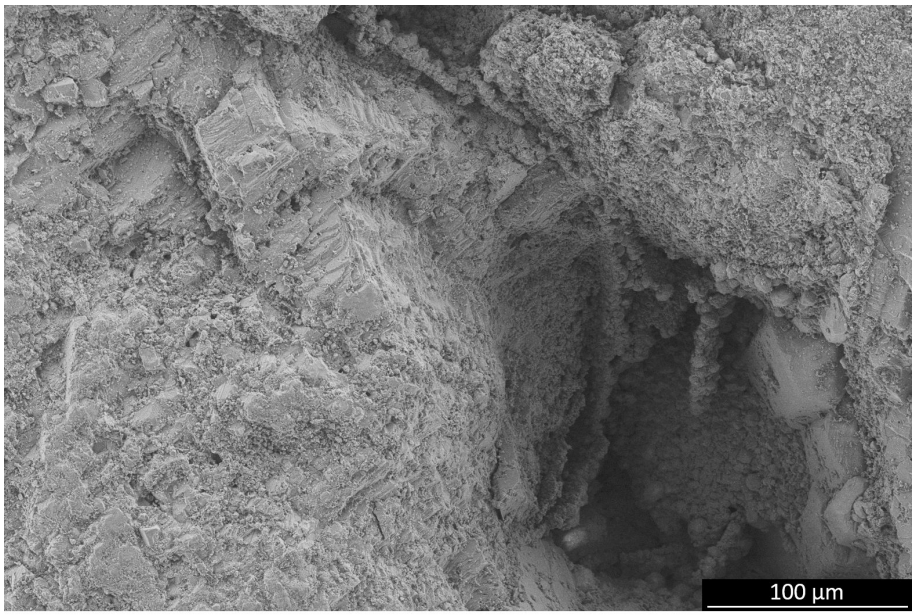



Figure B.83: Low-vacuum SEM: The micrograph of Indiana shown in Figure 3.23, without numbers.

# Appendix C

# Bandera Brown

## C.1 Low-Vacuum Scanning Electron Microscopy

In Chapter 6: *Bandera Brown*, Section 6.2.1.1, two overlays of low-vacuum SEM micrographs of the Bandera Brown surface were presented in Figures 6.1 & 6.14. The low-vacuum micrographs which make up these overlays are presented in Figures C.1 - C.4 and C.5 & C.6 respectively.

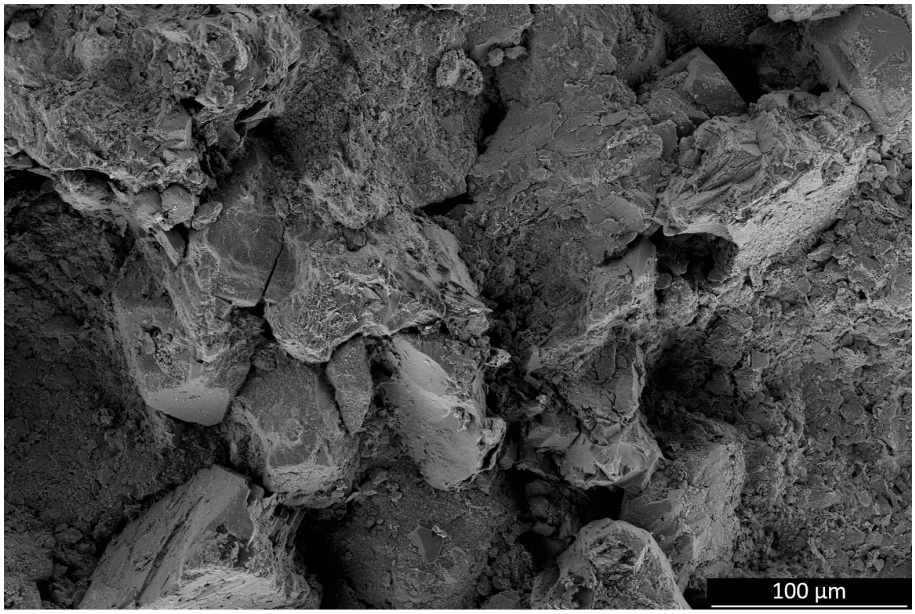



Figure C.1: Low-vacuum SEM: Micrograph 1 of Bandera Brown from Figure 6.1

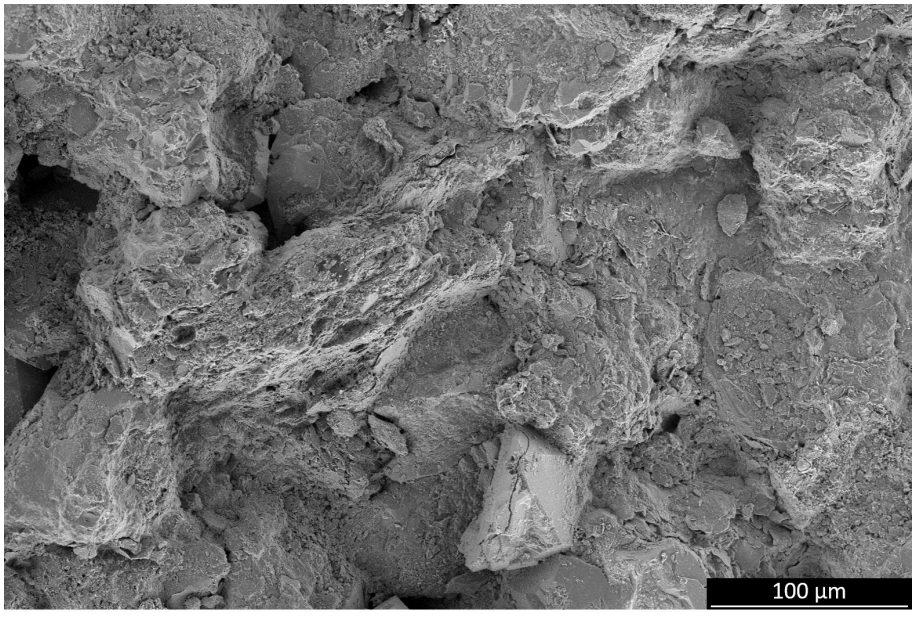



Figure C.2: Low-vacuum SEM: Micrograph 2 of Bandera Brown from Figure 6.1

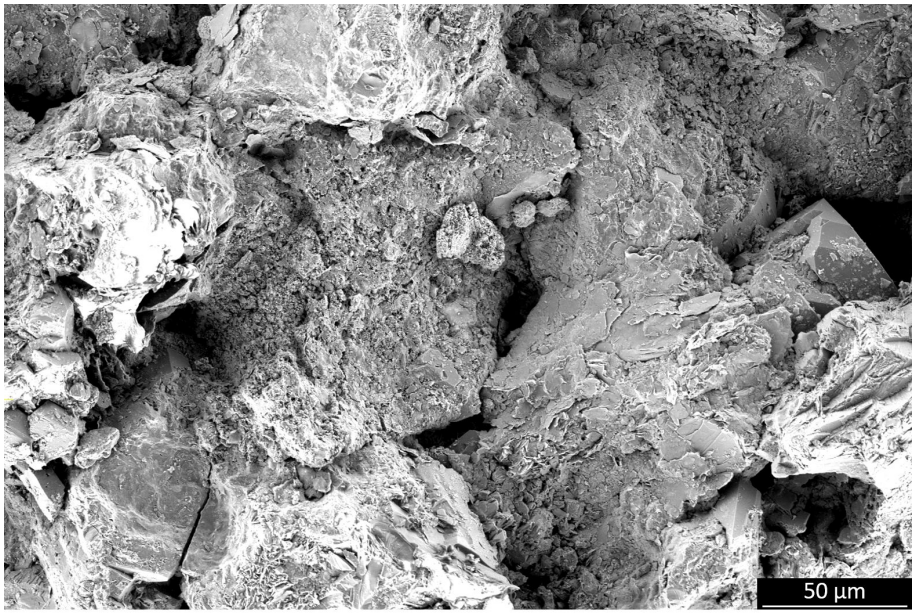



Figure C.3: Low-vacuum SEM: Micrograph 3 of Bandera Brown from Figure 6.1

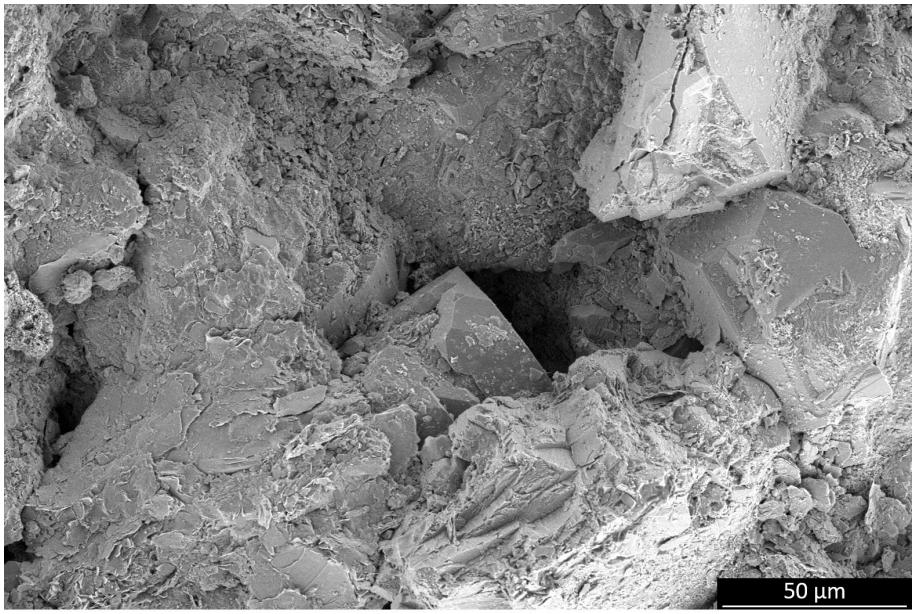



Figure C.4: Low-vacuum SEM: Micrograph 4 of Bandera Brown from Figure 6.1

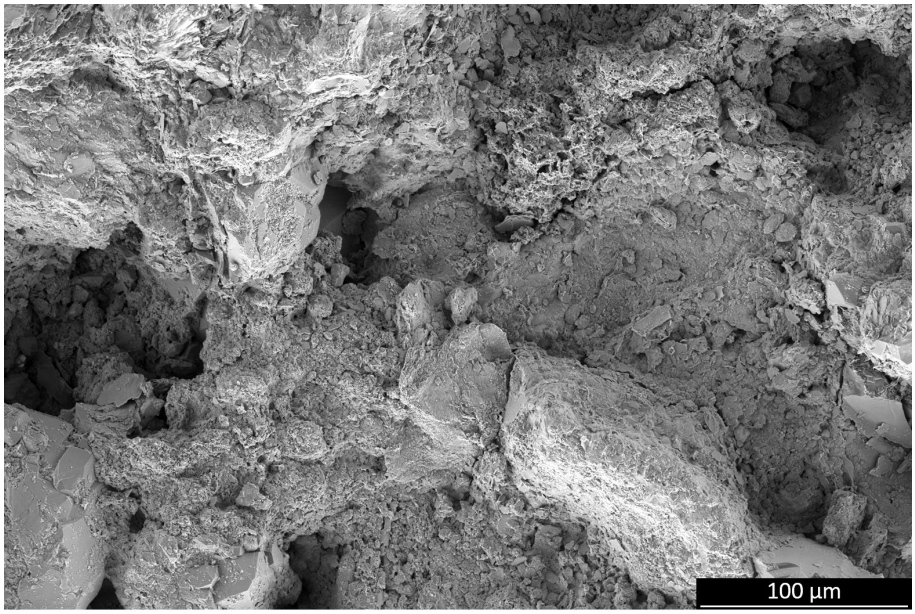



Figure C.5: Low-vacuum SEM: Micrograph 1 of Bandera Brown from Figure 6.14

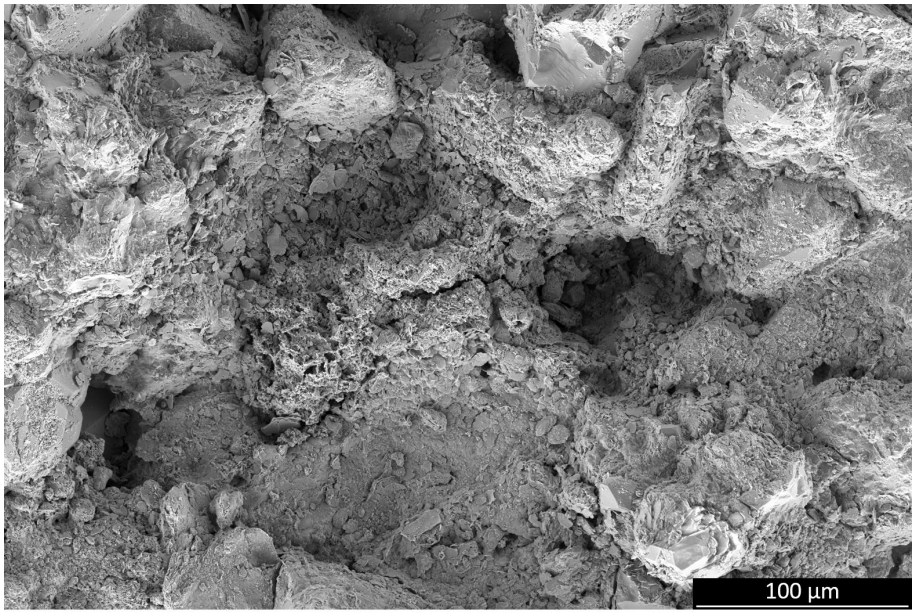



Figure C.6: Low-vacuum SEM: Micrograph 2 of Bandera Brown from Figure 6.14

In Chapter 6: *Bandera Brown*, Section 6.3, two overlays of low-vacuum SEM micrographs of aged Bandera Brown were presented in Figures 6.45 & 6.51. The micrographs which made up these Figures are presented in Figures C.7 - C.13 & C.14 - C.17 respectively.

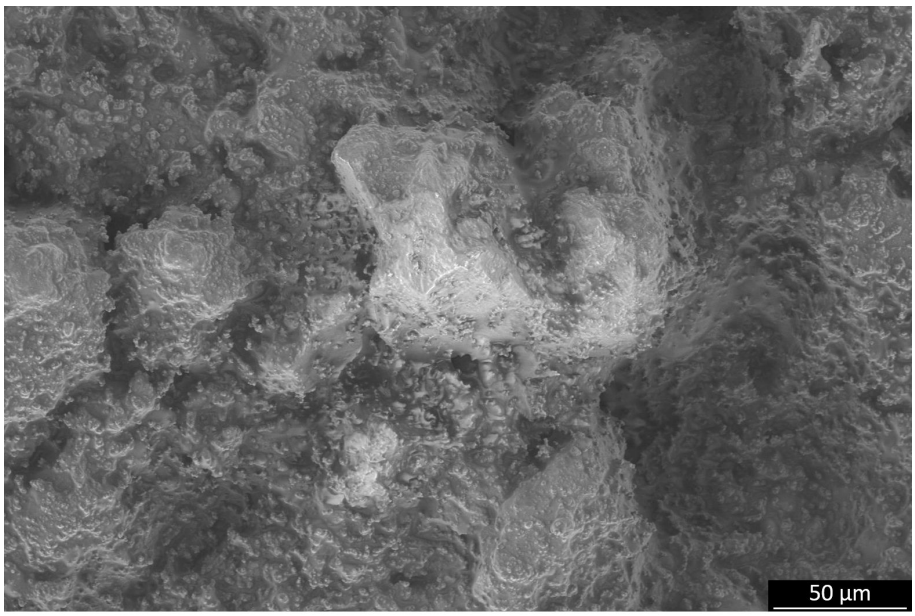



Figure C.7: Low-vacuum SEM: Micrograph 1 of Aged Bandera Brown from Figure 6.45

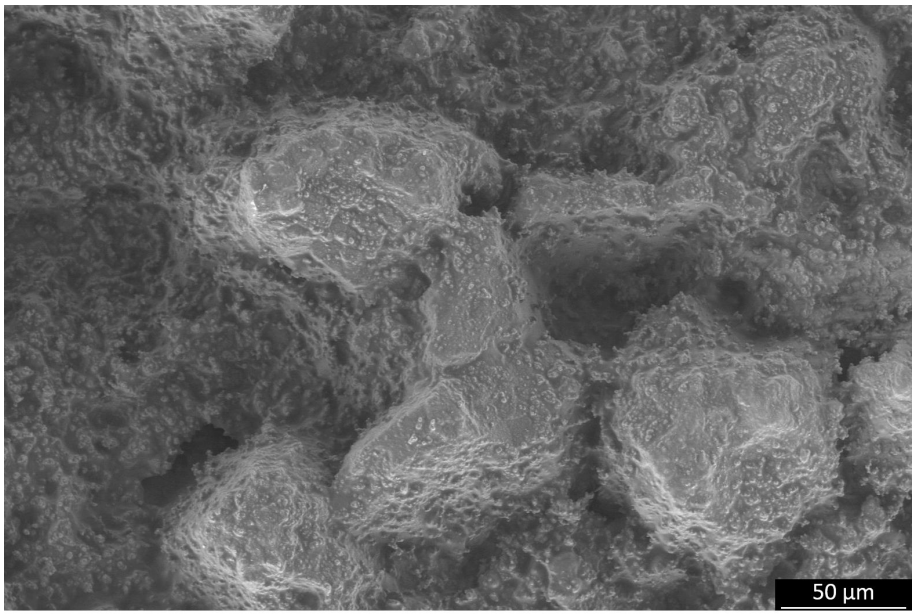



Figure C.8: Low-vacuum SEM: Micrograph 2 of Aged Bandera Brown from Figure 6.45

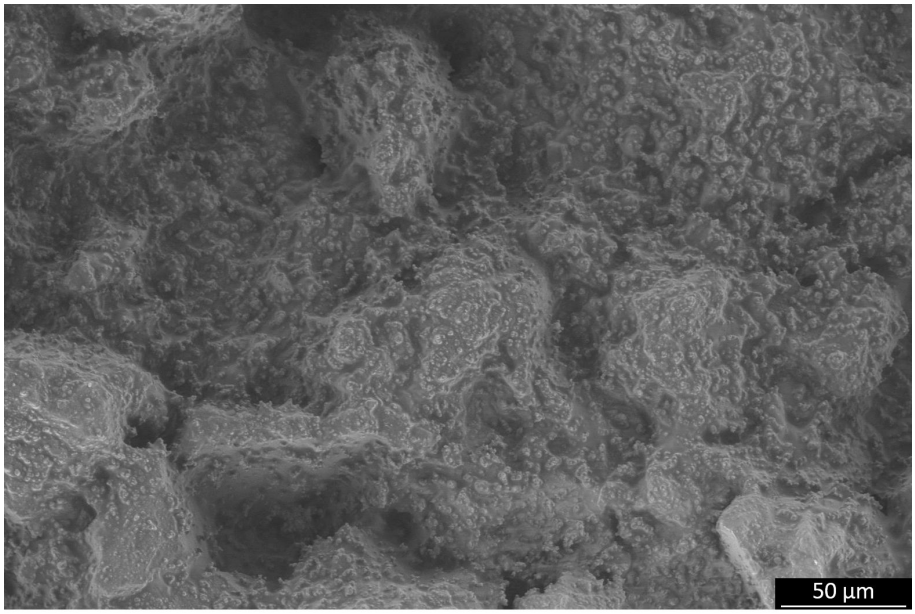



Figure C.9: Low-vacuum SEM: Micrograph 3 of Aged Bandera Brown from Figure 6.45

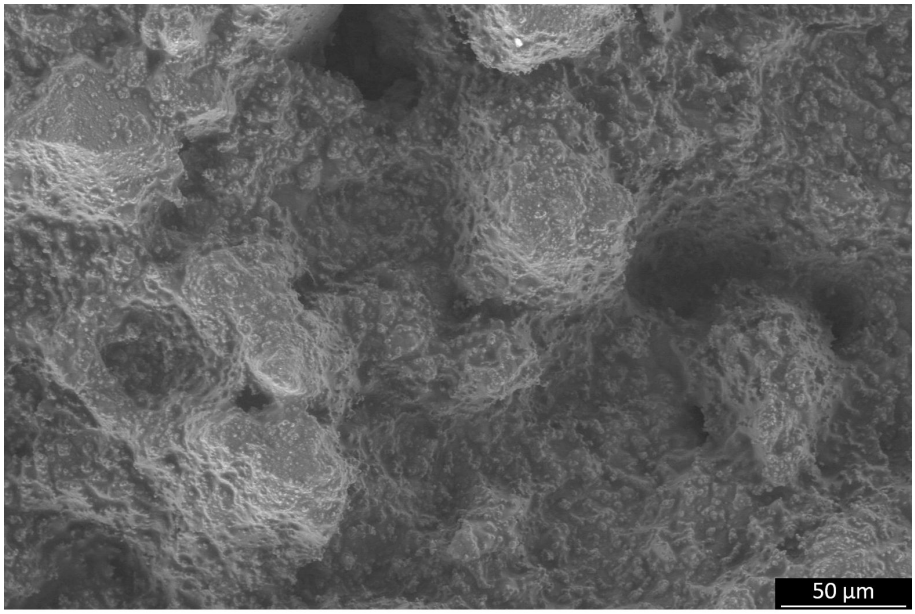



Figure C.10: Low-vacuum SEM: Micrograph 4 of Aged Bandera Brown from Figure 6.45

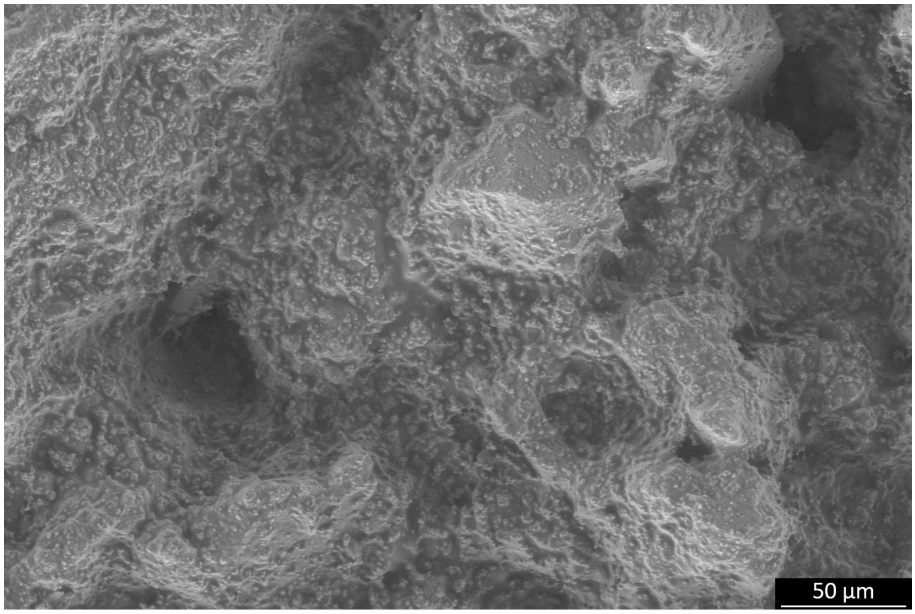



Figure C.11: Low-vacuum SEM: Micrograph 5 of Aged Bandera Brown from Figure 6.45

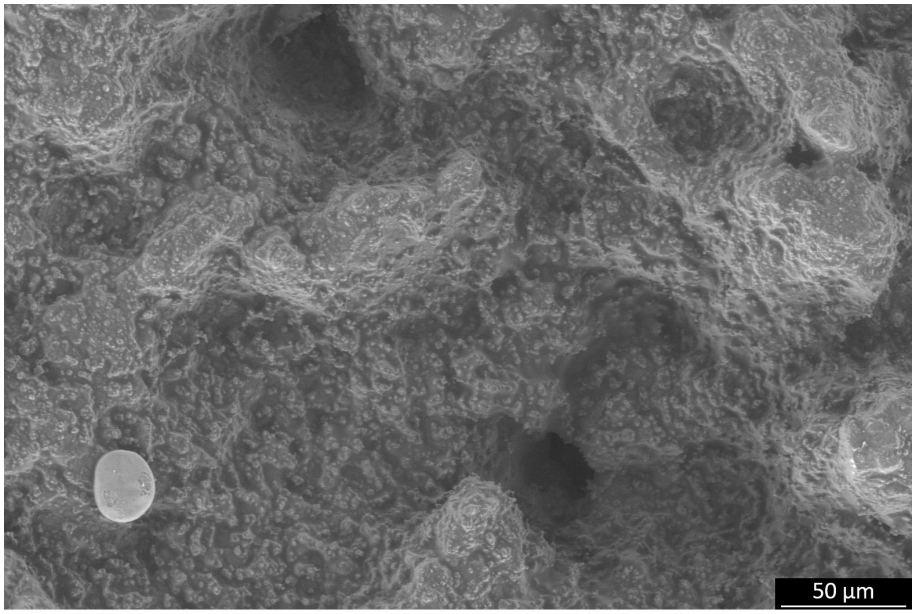



Figure C.12: Low-vacuum SEM: Micrograph 6 of Aged Bandera Brown from Figure 6.45

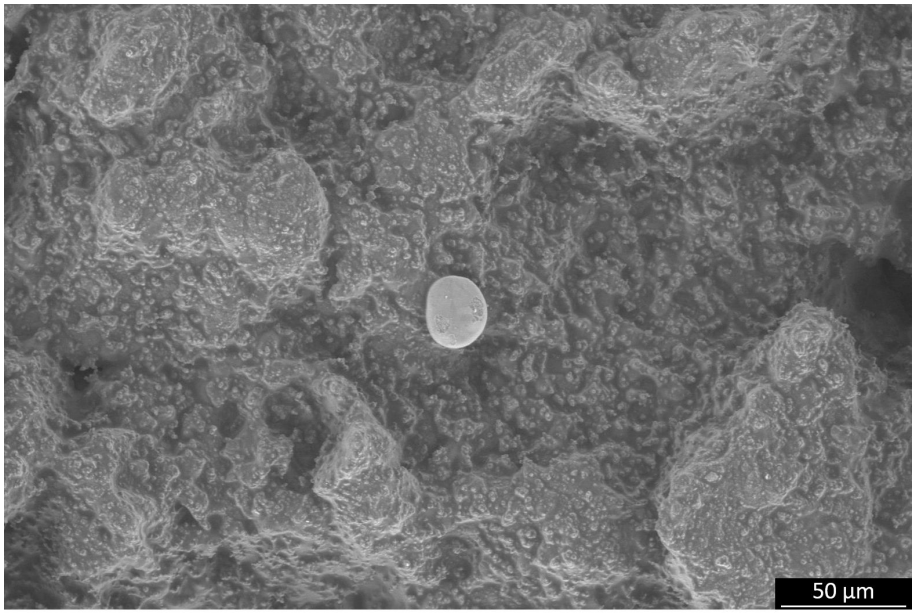



Figure C.13: Low-vacuum SEM: Micrograph 7 of Aged Bandera Brown shown in Figure 6.45

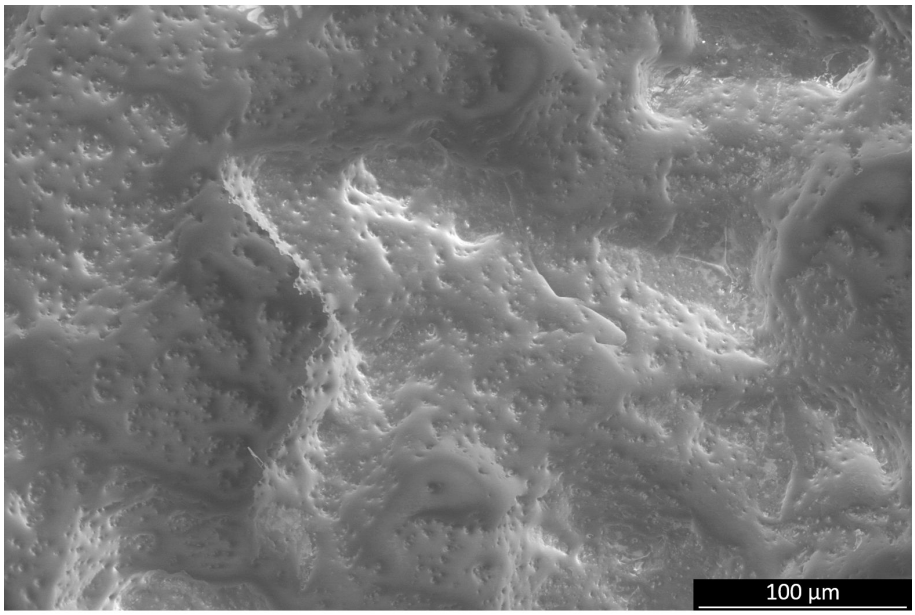



Figure C.14: Low-vacuum SEM: Micrograph 1 of Aged Bandera Brown from Figure 6.51

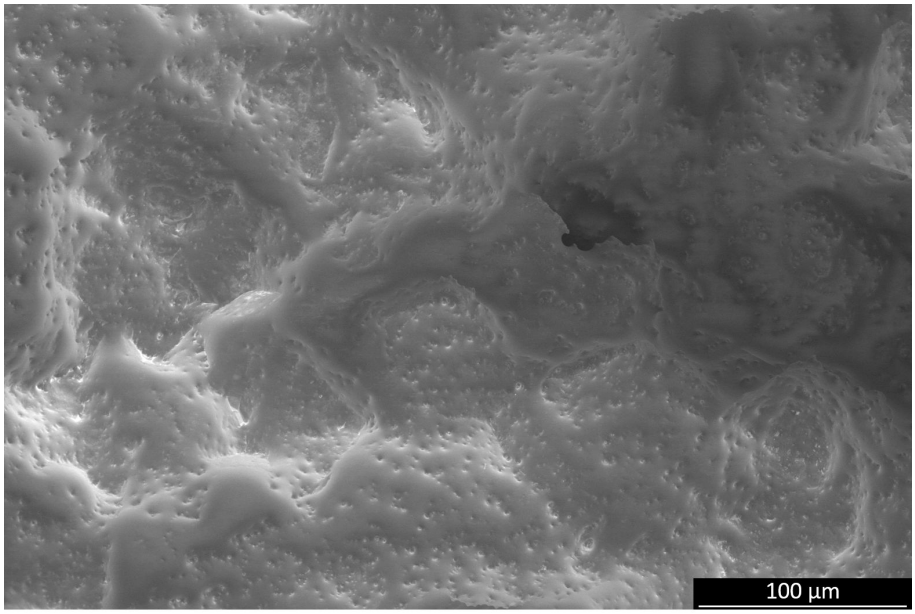



Figure C.15: Low-vacuum SEM: Micrograph 2 of Aged Bandera Brown from Figure 6.51

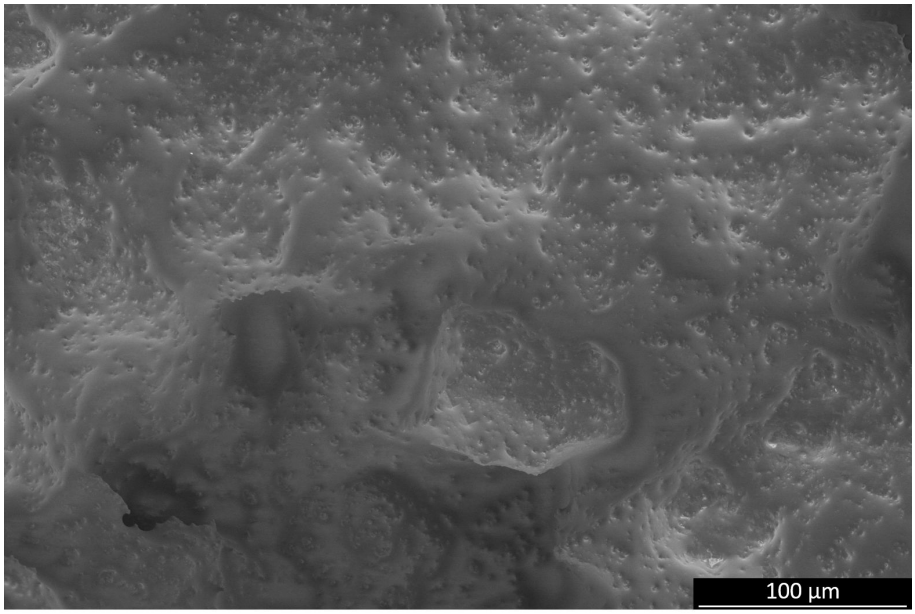



Figure C.16: Low-vacuum SEM: Micrograph 3 of Aged Bandera Brown from Figure 6.51

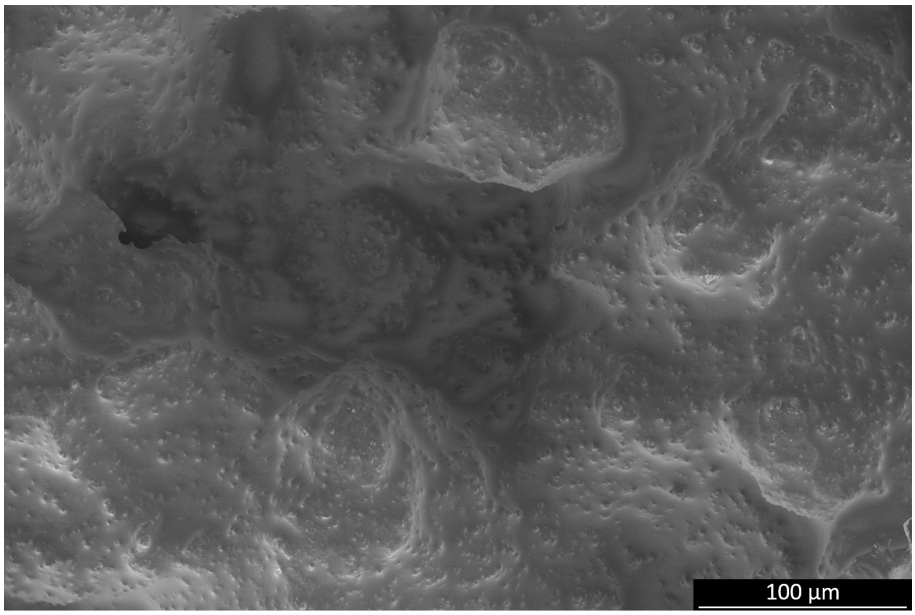



Figure C.17: Low-vacuum SEM: Micrograph 4 of Aged Bandera Brown from Figure 6.51

In Chapter 6: *Bandera Brown*, Section 6.3.3, an overlay of low-vacuum SEM micrographs of aged Bandera Brown after SICM measurements had been performed was presented in Figure 6.58. The micrographs which made up this Figure are presented in Figures C.18 - C.20.

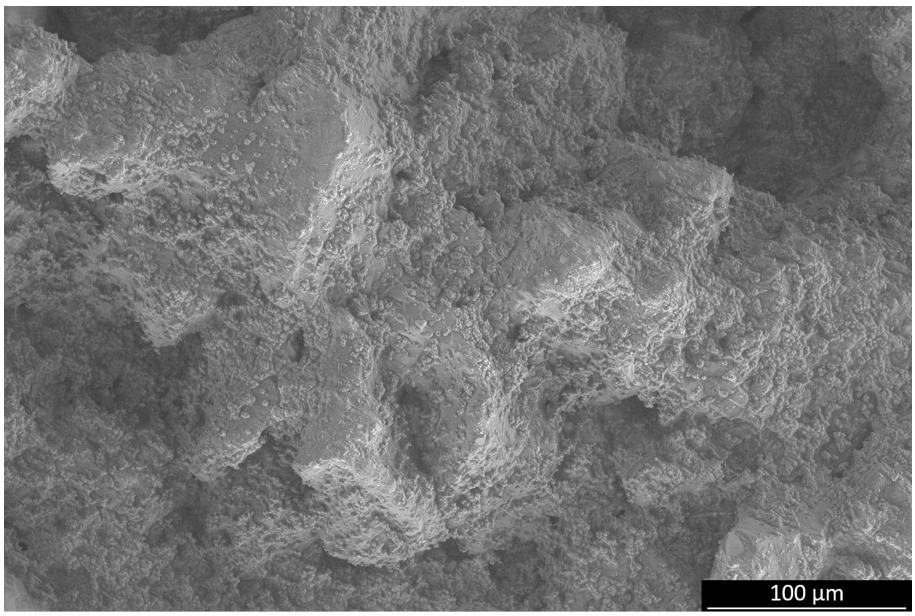



Figure C.18: Low-vacuum SEM: Micrograph 1 of Aged Bandera Brown post SICM from Figure 6.58

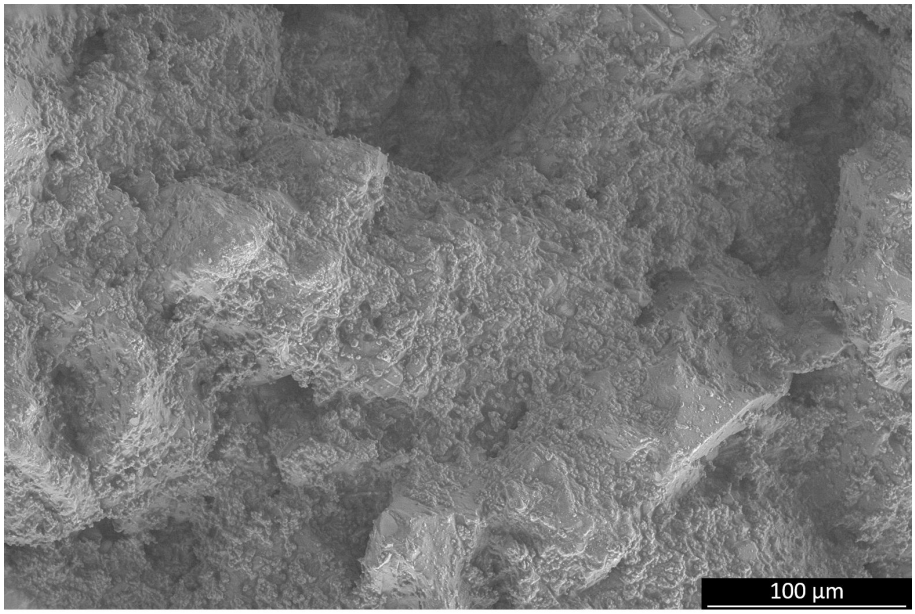



Figure C.19: Low-vacuum SEM: Micrograph 2 of Aged Bandera Brown post SICM from Figure 6.58

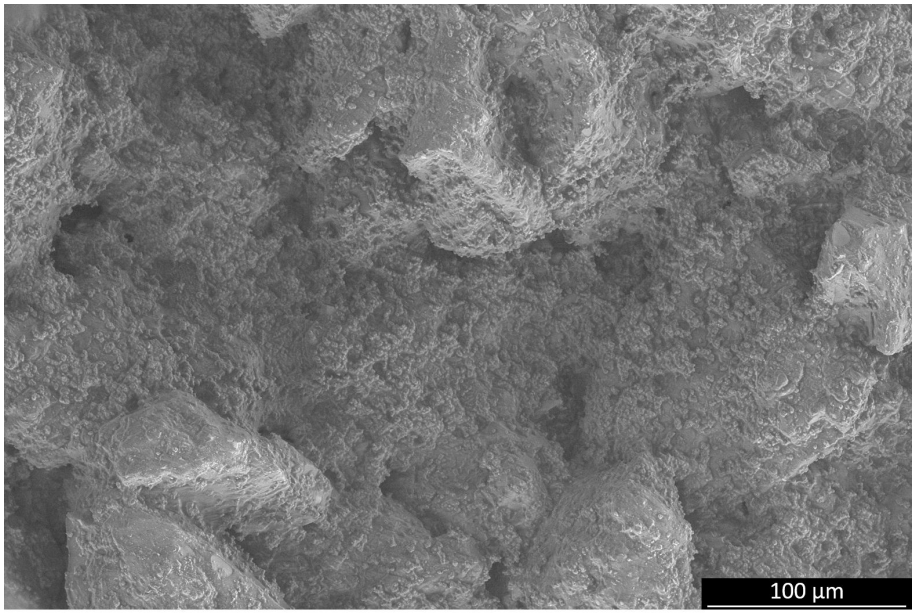



Figure C.20: Low-vacuum SEM: Micrograph 3 of Aged Bandera Brown post SICM from Figure 6.58

# Appendix D

# Polystyrene on Glass

In Chapter 4: *Surface Charge Mapping*, Section 4.3.2.1, an overlay of low-vacuum SEM micrographs of a glass slide dip-coated in polystyrene was presented in Figure 4.5. The micrographs which made up this Figure are presented in Figures D.1 - D.4.

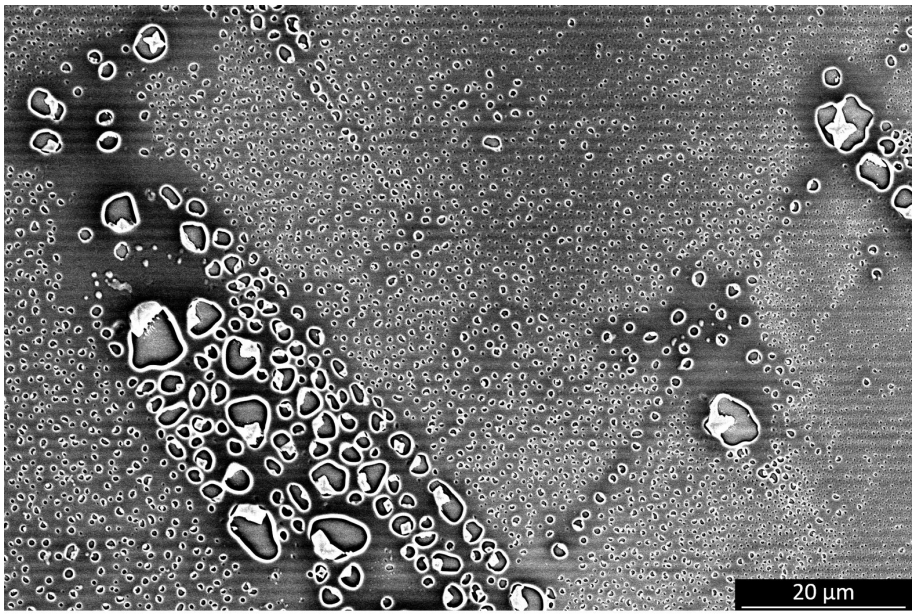



Figure D.1: Low-vacuum SEM: Micrograph 1 of a glass slide dip-coated in polystyrene from Figure 4.5

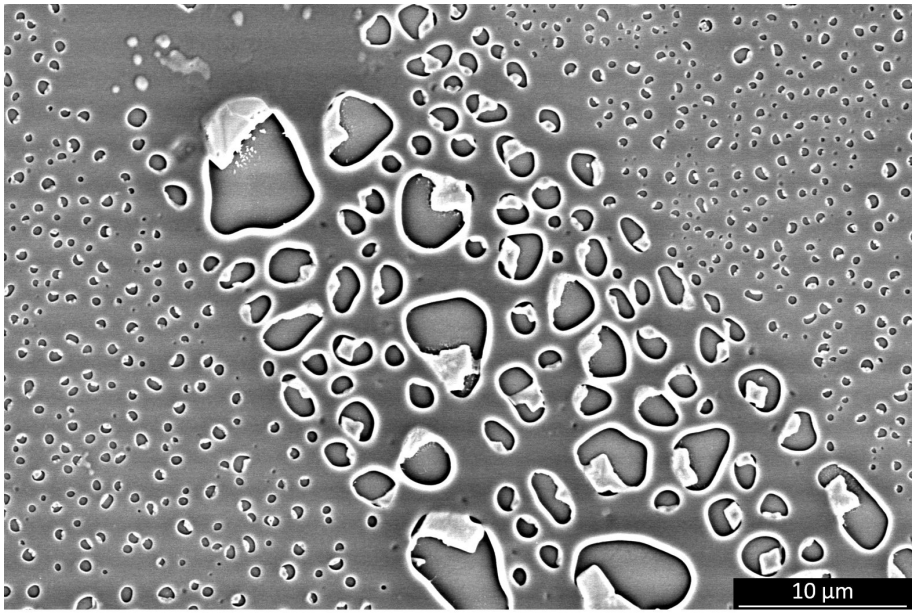



Figure D.2: Low-vacuum SEM: Micrograph 2 of a glass slide dip-coated in polystyrene from Figure 4.5

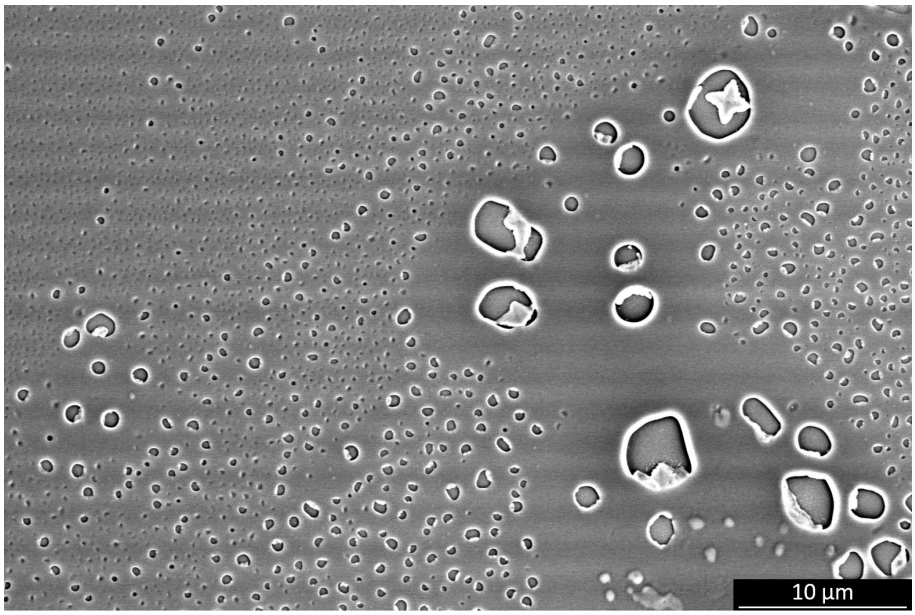



Figure D.3: Low-vacuum SEM: Micrograph 3 of a glass slide dip-coated in polystyrene from Figure 4.5

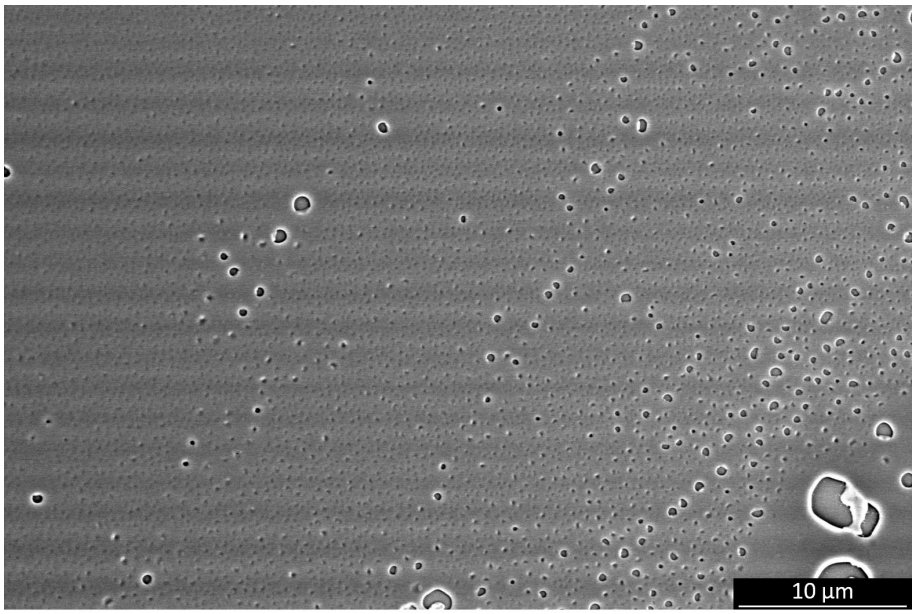



Figure D.4: Low-vacuum SEM: Micrograph 4 of a glass slide dip-coated in polystyrene from Figure 4.5